frontiers | Research Topics

Uncertainty quantification in nuclear physics

Edited by
Maria Piarulli, Evgeny Epelbaum and Christian Forssén

Published in
Frontiers in Physics

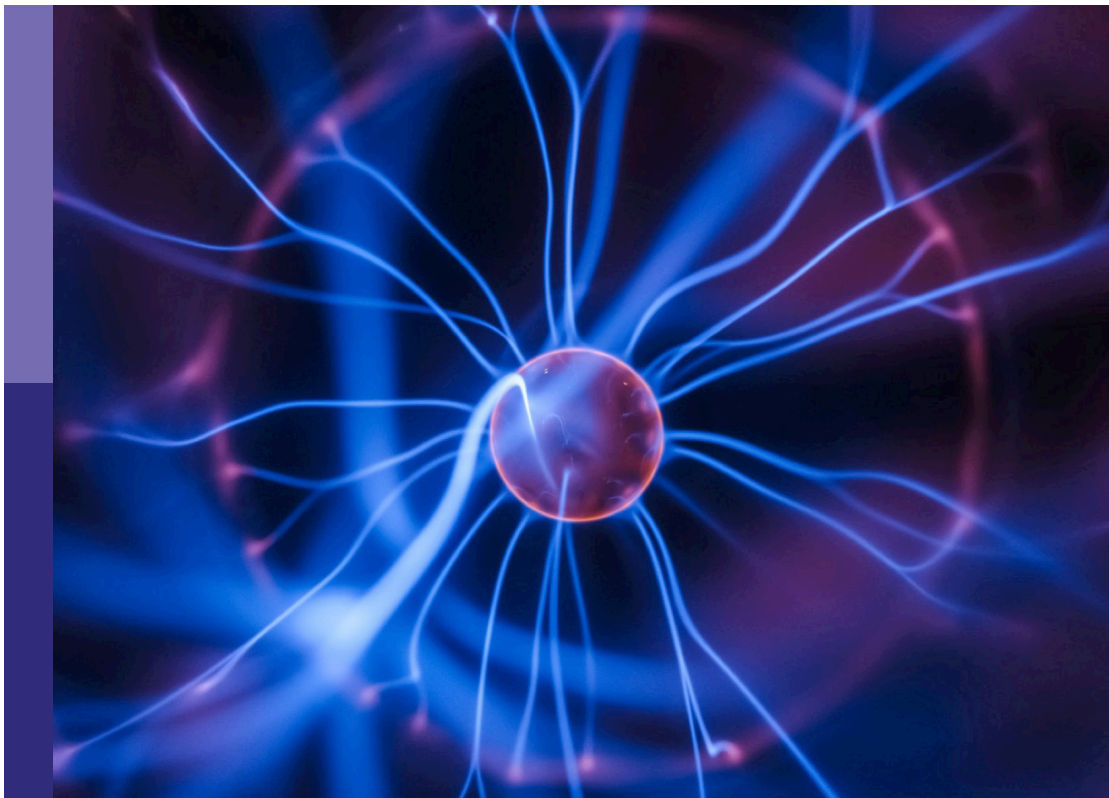

ISSN 1664-8714
ISBN 978-2-8325-3209-6
DOI 10.3389/978-2-8325-3209-6

About Frontiers

Frontiers is more than just an open access publisher of scholarly articles: it is a pioneering approach to the world of academia, radically improving the way scholarly research is managed. The grand vision of Frontiers is a world where all people have an equal opportunity to seek, share and generate knowledge. Frontiers provides immediate and permanent online open access to all its publications, but this alone is not enough to realize our grand goals.

Frontiers journal series

The Frontiers journal series is a multi-tier and interdisciplinary set of open-access, online journals, promising a paradigm shift from the current review, selection and dissemination processes in academic publishing. All Frontiers journals are driven by researchers for researchers; therefore, they constitute a service to the scholarly community. At the same time, the *Frontiers journal series* operates on a revolutionary invention, the tiered publishing system, initially addressing specific communities of scholars, and gradually climbing up to broader public understanding, thus serving the interests of the lay society, too.

Dedication to quality

Each Frontiers article is a landmark of the highest quality, thanks to genuinely collaborative interactions between authors and review editors, who include some of the world's best academicians. Research must be certified by peers before entering a stream of knowledge that may eventually reach the public - and shape society; therefore, Frontiers only applies the most rigorous and unbiased reviews. Frontiers revolutionizes research publishing by freely delivering the most outstanding research, evaluated with no bias from both the academic and social point of view. By applying the most advanced information technologies, Frontiers is catapulting scholarly publishing into a new generation.

What are Frontiers Research Topics?

Frontiers Research Topics are very popular trademarks of the *Frontiers journals series*: they are collections of at least ten articles, all centered on a particular subject. With their unique mix of varied contributions from Original Research to Review Articles, Frontiers Research Topics unify the most influential researchers, the latest key findings and historical advances in a hot research area.

Find out more on how to host your own Frontiers Research Topic or contribute to one as an author by contacting the Frontiers editorial office: frontiersin.org/about/contact

Uncertainty quantification in nuclear physics

Topic editors

Maria Piarulli — Washington University in St. Louis, United States
Evgeny Epelbaum — Ruhr University Bochum, Germany
Christian Forssén — Chalmers University of Technology, Sweden

Citation

Piarulli, M., Epelbaum, E., Forssén, C., eds. (2023). *Uncertainty quantification in nuclear physics*. Lausanne: Frontiers Media SA. doi: 10.3389/978-2-8325-3209-6

Table of contents

frontiers | Frontiers in Physics

TYPE Editorial
PUBLISHED 15 August 2023
DOI 10.3389/fphy.2023.1270577

OPEN ACCESS

EDITED AND REVIEWED BY
Jie Meng,
Peking University, China

*CORRESPONDENCE
Maria Piarulli,
mpiarulli@physics.wustl.edu

RECEIVED 01 August 2023
ACCEPTED 07 August 2023
PUBLISHED 15 August 2023

CITATION
Piarulli M, Epelbaum E and Forssén C (2023), Editorial: Uncertainty quantification in nuclear physics. *Front. Phys.* 11:1270577. doi: 10.3389/fphy.2023.1270577

Editorial: Uncertainty quantification in nuclear physics

Maria Piarulli[1]*, Evgeny Epelbaum[2] and Christian Forssén[3]

[1]Physics Department, Washington University, St. Louis, MO, United States, [2]Institut für Theoretische Physik II, Ruhr-Universität Bochum, Bochum, Germany, [3]Department of Physics, Chalmers University of Technology, Göteborg, Sweden

KEYWORDS

nuclear physics, uncertainty quantification, Bayesian methods, emulators, effective field theory, *ab initio*, many-body physics

Editorial on the Research Topic
Uncertainty quantification in nuclear physics

Uncertainty quantification (UQ) has emerged as a crucial aspect of the interface between theory and experiment in nuclear physics. Over the past decade the field has undergone a transformative shift into the "precision era" due to advancements in *ab initio* many-body methods, computing power, sophisticated theoretical techniques, and the advent of a new generation of experiments.

With experimental procedures now capable of probing observables with greater precision, and in some cases even where data is lacking, the need for theoretical predictions with well-quantified error bars has become more pronounced. This requirement extends not only to ongoing experiments but also to future endeavors seeking accurate measurements of more exotic processes including precision tests of the Standard Model as well as Beyond the Standard Model searches.

The employment of Bayesian approaches, efficient emulators to overcome computational limitations, and machine learning methods has sparked a surge of interest in UQ, revolutionizing the field. These techniques have enabled researchers to assess uncertainties in different theoretical domains, ranging from lattice quantum chromodynamics to nuclear many-body forces to properties of atomic nuclei. Moreover, they have enabled quantitative insights into the role played by future astrophysics and gravitational observations for constraining the equation of state for neutron matter, the determination of nucleon resonances in experimental data, and the development of reliable nuclear-energy-density functionals for extrapolations into unexplored nuclear territories.

To consolidate the expertise and achievements in nuclear physics UQ, this Research Topic aimed to bring together leading contributors in the field. We have received an outstanding Research Topic that highlight recent accomplishments along this line of research and that provide insights into the methodologies being developed and employed.

The Research Topic features 15 articles. Several contributions focus on the uncertainty quantification in nuclear structure calculations. For instance, Alnamlah et al. discuss an effective field theory (EFT) for rotational bands in odd-mass nuclei and employ a Bayesian analysis to estimate uncertainties in rotational energy levels. They consider both experimental and EFT truncation uncertainties, utilizing Markov Chain Monte Carlo (MCMC) sampling to infer low-energy constants and the breakdown scale of the EFT. Becker et al. investigate alpha clustering and collective properties in nuclei using emulators within the *ab initio* symmetry-adapted no-core shell model framework. Their work

highlights the importance of such emulators in quantifying uncertainties and improving the precision of nuclear structure calculations. They utilize the eigenvector continuation technique to study various nuclear properties in ^{6}Li and ^{12}C including excitation energies, point-proton root-mean-square radii, electric quadrupole moments, and transitions.

Furthermore, Maris et al. examine uncertainties in theoretical ground state energies of *p*-shell nuclei using interactions from chiral EFT. They investigate the dependence of these energies on the chiral order and analyze two- and three-body data for fitting, addressing uncertainties stemming from basis truncations, omitted induced many-body forces, and EFT truncation. Acharya et al. focus on quantifying theoretical uncertainties in *ab initio* calculations of electromagnetic observables in light and medium-mass nuclei. They discuss different sources of uncertainties including approximations introduced by few- and many-body solvers and the truncation of the chiral EFT expansion.

Regarding reactions in nuclei, some contributions are particularly noteworthy. Skibiński et al. investigate the nucleon-induced deuteron breakup reaction using the Faddeev approach at specific laboratory energies. They focus on quantifying theoretical uncertainties associated with the predicted cross-section, particularly in relation to the regulator cutoff parameter. Ceccarelli et al. concentrate on UQ for the muon capture reaction $\mu^{-} + d \rightarrow n + n + \nu_{\mu}$ in the doublet hyperfine state. They address four sources of theoretical uncertainty including model dependence, chiral-order convergence, uncertainty in the single-nucleon axial form factor, and numerical techniques used for solving the $A = 2$ systems.

Furthermore, Odell et al. focus on the estimation of uncertainties in resolved resonance cross section data in nuclear physics using the *R*-matrix framework. They introduce the Bayesian *R*-matrix Inference Code Kit (BRICK) by implementing a MCMC sampler, specifically the emcee algorithm, into the *R*-matrix code AZURE2. They apply Bayesian uncertainty estimation to simultaneously fit the ^{3}He(α, γ)^{7}Be and ^{3}He(α, α)^{3}He reactions, aiming to gain insights into the fitting of capture and scattering data. The data from both reactions are relevant to constrain the values of the bound state α-particle asymptotic normalization coefficients in ^{7}Be. Baker et al. investigate the effective interaction between a nucleon and a nucleus based on optical potentials, with a UQ perspective. They extracted elastic scattering observables for ^{4}He, ^{12}C, and ^{16}O at projectile energies between 65 and 200 MeV. Lastly, Vassh et al. employ a MCMC procedure to predict ground state masses for nucleosynthesis calculations and investigate conditions capable of producing the observed solar *r*-process rare-earth abundance peak. They examine how mass predictions change when using a few different sets of *r*-process solar abundance residuals that have been reported in the literature, with focus on uncertainty propagation.

The Research Topic also includes a review article by Ekström et al. that provides a historical overview of the notion of *ab initio* in nuclear physics and discusses its current relationship with theoretical UQ.

Furthermore some of the article discuss various advancements in UQ methodology. One of the topics covered is the use of projection-based, reduced-order emulators as fast surrogate models for complex high-fidelity models. Drischler et al. present a pedagogical introduction to these emulators, which effectively approximate complex models and offer an efficient approach to calculations while addressing the challenges of UQ. Additionally, Rothkopf discusses state-of-the-art methods for extracting spectral functions using Bayesian inference, highlighting the importance of prior domain knowledge for regularization. The use of machine learning for spectral function reconstruction is also mentioned, noting its contribution to the Bayesian community's understanding of the topic.

Verriere et al. focus on the challenges in studying atomic nuclei and the potential of nuclear density functional theory to accurately describe their properties with uncertainties. They explore the application of machine learning and artificial intelligence techniques to enhance DFT calculations and accelerate the understanding of nuclear phenomena. In the paper by Giuliani et al., the authors showcase the application of a principled Bayesian statistical framework for UQ in nuclear physics. By employing the reduced-based emulator and calibrating the energy density functional, they provide accurate model calculations with estimated uncertainties, supporting the nuclear theory community in delivering reliable predictions in the face of increasing data availability.

Lastly, Jiang et al. address the usefulness of the sampling/importance resampling method in UQ for nuclear theory applications. By employing sampling/importance resampling to realistic scenarios, the authors demonstrate its effectiveness in inferring posterior distributions and estimating the predictive probability distribution of observables. Researchers in nuclear theory can benefit from employing this Bayesian sampling method to gain insights into uncertainties and make informed decisions based on the obtained posterior distributions.

In conclusion, this Research Topic presents a comprehensive collection of articles that contributes to the advancement of UQ in nuclear physics. The diverse range of topics and methodologies highlights the progress made in addressing uncertainties and provides a solid foundation for future developments in the field. We are grateful to all the scientists participating in this project and hope that the reader will enjoy this Research Topic.

Author contributions

MP: Writing–original draft, Writing–review and editing. EE: Writing–original draft, Writing–review and editing. CF: Writing–original draft, Writing–review and editing.

Conflict of interest

The authors declare that the research was conducted in the absence of any commercial or financial relationships that could be construed as a potential conflict of interest.

Publisher's note

frontiers | Frontiers in Physics

ORIGINAL RESEARCH
published: 13 June 2022
doi: 10.3389/fphy.2022.888476

Performing Bayesian Analyses With AZURE2 Using BRICK: An Application to the ^{7}Be System

Daniel Odell[1], Carl R. Brune[1], Daniel R. Phillips[1], Richard James deBoer[2] and Som Nath Paneru[1,3]*

[1]Department of Physics and Astronomy, Institute of Nuclear and Particle Physics, Ohio University, Athens, OH, United States, [2]Department of Physics, The Joint Institute for Nuclear Astrophysics, University of Notre Dame, Notre Dame, IN, United States, [3]Facility for Rare Isotope Beams, Michigan State University, East Lansing, MI, United States

Phenomenological *R*-matrix has been a standard framework for the evaluation of resolved resonance cross section data in nuclear physics for many years. It is a powerful method for comparing different types of experimental nuclear data and combining the results of many different experimental measurements in order to gain a better estimation of the true underlying cross sections. Yet a practical challenge has always been the estimation of the uncertainty on both the cross sections at the energies of interest and the fit parameters, which can take the form of standard level parameters. Frequentist (χ^2-based) estimation has been the norm. In this work, a Markov Chain Monte Carlo sampler, `emcee`, has been implemented for the *R*-matrix code AZURE2, creating the Bayesian *R*-matrix Inference Code Kit (BRICK). Bayesian uncertainty estimation has then been carried out for a simultaneous *R*-matrix fit of the ^{3}He $(\alpha,\gamma)^{7}$Be and ^{3}He $(\alpha,\alpha)^{3}$He reactions in order to gain further insight into the fitting of capture and scattering data. Both data sets constrain the values of the bound state α-particle asymptotic normalization coefficients in ^{7}Be. The analysis highlights the need for low-energy scattering data with well-documented uncertainty information and shows how misleading results can be obtained in its absence.

Keywords: R-matrix, Bayesian uncertainty analysis, nuclear astrophysics, Big Bang nucleosynthesis, asymptotic normalization coefficient

OPEN ACCESS

Edited by:
Maria Piarulli, Washington University in St. Louis, United States

Reviewed by:
Petr Navratil, TRIUMF, Canada
Giovanni Luca Guardo, Laboratori Nazionali del Sud (INFN), Italy

****Correspondence:***
Daniel Odell
dodell@ohio.edu

Specialty section:
This article was submitted to Nuclear Physics, a section of the journal Frontiers in Physics

Received: *02 March 2022*
Accepted: *22 April 2022*
Published: *13 June 2022*

Citation:
Odell D, Brune CR, Phillips DR, deBoer RJ and Paneru SN (2022) Performing Bayesian Analyses With AZURE2 Using BRICK: An Application to the ^{7}Be System. Front. Phys. 10:888476. doi: 10.3389/fphy.2022.888476

1 INTRODUCTION

Phenomenological *R*-matrix has been the standard analysis tool for cross section data that exhibit overlapping yet resolved resonances for many years [1]. It is used extensively to evaluate data for applications (e.g., the ENDF/B-VIII.0 evaluation [2]), to perform extrapolations to low, unobserved energies in nuclear astrophysics (e.g., Azuma et al. [3]; Descouvemont et al. [4]), and to extract level parameters for nuclear structure [5]. In all cases, it provides a reaction framework in which experimental information of various different types can be combined to improve estimates of the true cross sections. One challenging aspect of this type of analysis has been reliable uncertainty propagation.

Traditionally, data have been fitted using χ^2 minimization, with uncertainties being estimated using one of two methods. The first is using partial derivatives and the assumption that the quantity of interest is related linearly with the parameters of the model. The second is the assignment of confidence intervals based on some $\Delta\chi^2$ value. The assumption of linearity is often a poor one and the second method can become tedious or impossible to implement for a complicated model. Additional

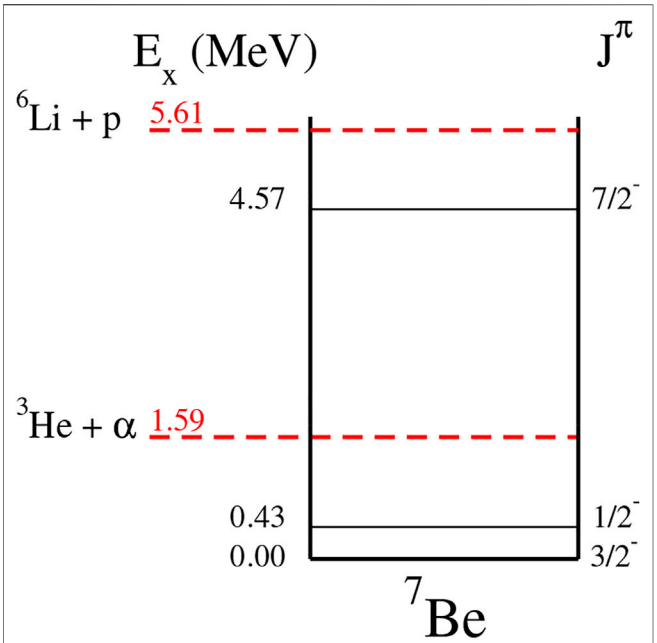

FIGURE 1 | Level diagram of ^{7}Be up to the proton separation energy.

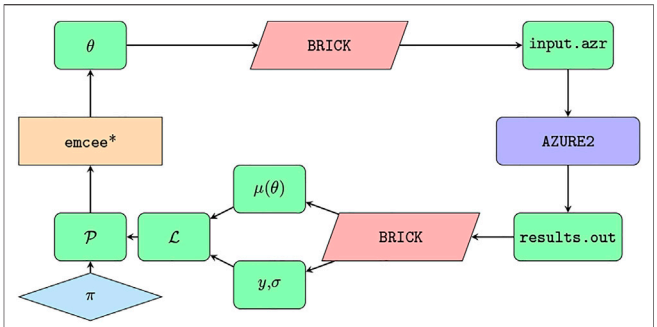

FIGURE 2 | Representation of the different roles of `emcee`, `BRICK`, and `AZURE2` in the Bayesian analysis presented below. The asterisk in the `emcee` rectangle indicates the starting point of the process.

limitations are that one must assume Gaussian uncertainties on the input data and there is almost no ability to include prior information about the parameters. It is known that χ^2 methods may lead to biased results and/or underestimated uncertainties in data evaluations [6]. The reason for these issues is understood to be incomplete documentation or modeling of systematic uncertainties. While systematic uncertainties are a difficult subject in any approach, they are much easier to model and implement using the Bayesian methods described below. Finally, we would like to point out that a mixed approach is possible, where χ^2 minimization is combined with a Monte Carlo simulation of some uncertainties. This method was used by deBoer et al. [7] in a previous analysis of ^{3}He $(\alpha,\gamma)^{7}$Be and ^{3}He $(\alpha,\alpha)^{3}$He.

Bayesian methods are increasingly becoming the standard for performing Uncertainty Quantification in physical sciences and engineering in general, and theoretical nuclear physics in particular [8–34]. In contrast to a traditional χ^2-minimization they offer the opportunity to examine the entire probability distribution for parameters of interest, rather than focusing on the values that maximize the likelihood. Perhaps equally important, in a Bayesian approach it is straightforward—mandatory even—to declare and include prior information on the parameters of interest. Bayesian methods, combined with the possibility to use Markov Chain Monte Carlo sampling to explore a high-dimensional parameter space, allow one to introduce additional parameters without fear of computational instabilities caused by shallow χ^2 minima. The use of MCMC sampling also makes uncertainty propagation straightforward, as we will demonstrate here. And a Bayesian framework is—to our knowledge—the only option if one wishes to incorporate a rigorous formulation of theory uncertainties into the statistical analysis. In this work, Bayesian uncertainty quantification is implemented by pairing the *R*-matrix code `AZURE2` [3,35] with the MCMC Python package `emcee` [36]. The pairing is facilitated by a Python interface `BRICK` (Bayesian R-matrix Inference Code Kit), enabling Bayesian inference in the context of *R*-matrix analyses.

To benchmark this code, it has been applied to the analysis of the ^{3}He $(\alpha,\gamma)^{7}$Be and ^{3}He $(\alpha,\alpha)^{3}$He reactions. The ^{3}He $(\alpha,\gamma)^{7}$Be reaction is a key reaction in modeling the neutrino flux coming from our Sun [37]. It also plays a role in Big Bang Nucleosynthesis (BBN) [38]. The reaction cross section is dominated by the direct capture process, but also has significant contributions from broad resonances (see **Figure 1**). In recent years, high-precision measurements of this reaction have been performed, using direct γ-ray detection [39–41], the activation method [40–44], and a recoil separator [45]. Additional higher energy measurements have also been made recently by Szücs et al. [46], but are outside the energy range of the present analysis. Using these high precision measurements, several analyses have been made to combine these data sets and extrapolate the cross section to low energies using pure external capture [47], *R*-matrix [7], effective field theory [21,22], a modified potential model [48], and *ab initio* calculations [49–52]. These several recent analyses make this reaction an ideal case for benchmarking since they use both more traditional and Bayesian uncertainty estimation methods.

As the energies pertinent to solar fusion and BBN the ^{3}He (α,γ) ^{7}Be cross section has a large contribution from external capture, ^{3}He $(\alpha,\alpha)^{3}$He data, through its constraints on the scattering phase shifts, should also provide an additional source of constraint on the low-energy extrapolation. This type of combined analysis has been reported in deBoer et al. [7], but there it was found that the available scattering data of Barnard et al. [53] was inconsistent with the capture data, perhaps because of incomplete uncertainty documentation in the former. With this in mind, new measurements of the ^{3}He $(\alpha,\alpha)^{3}$He cross section were recently reported by Paneru et al. [54].

In this work, a Bayesian uncertainty analysis is performed on an *R*-matrix fit to the low energy ^{3}He $(\alpha,\gamma)^{7}$Be [39–42,44,45] and ^{3}He $(\alpha,\alpha)^{3}$He [53,54] data. The [54] data is a new measurement performed with the Scattering of Nuclei in Inverse Kinematics

TABLE 1 | Sampled parameters in the *R*-matrix model.

J^{π}	E_{λ} (MeV)	Widths and ANCs	Prior Distributions
$1/2^{-}$	0.4291	C_1	*U* (1, 5 MeV)
$1/2^{-}$	21.6	Γ_{α}	*U* (–200, 200 MeV)
$1/2^{+}$	14	Γ_{α}	*U* (0, 100 MeV)
		$\Gamma_{\gamma,0}$	*U* (0, 10 MeV)
		$\Gamma_{\gamma,1}$	*U* (–10, 10 keV)
$3/2^{-}$	0	C_0	*U* (1, 5 MeV)
$3/2^{-}$	21.6	Γ_{α}	*U* (–100, 100 MeV)
$3/2^{+}$	12	Γ_{α}	*U* (0, 100 MeV)
		$\Gamma_{\gamma,0}$	*U* (–10, 10 keV)
		$\Gamma_{\gamma,1}$	*U* (–3, 3 keV)
$5/2^{-}$	7	Γ_{α}	*U* (0, 100 MeV)
$5/2^{+}$	12	Γ_{α}	*U* (0, 100 MeV)
		$\Gamma_{\gamma,0}$	*U* (–100, 100 MeV)
$7/2^{-}$	*U* (1, 10 MeV)	Γ_{α}	*U* (0, 10 MeV)
		$\Gamma_{\gamma,0}$	*U* (0, 1 keV)

Numbers indicate that the level energies were fixed. A distribution indicates that the corresponding parameter was sampled. The subscripts α and γ indicate the exit particle pair—scattering and capture, respectively. Capture particle pairs are distinguished by ground (0) and excited (1) ^{7}Be states. The signs of the partial widths and ANCs indicate the signs of the corresponding reduced width amplitudes. The second column, E_{λ}, is given in excitation energy relative to the ground state.

TABLE 2 | Common-mode errors associated with the SONIK measurements.

Energy (keV/u)	No of Data points	Common-mode errors
239	17	6.4
291	29	7.6
432	45	9.8
586	46	5.7
711	52	4.5
$873^{(1)}$	52	6.2
$873^{(2)}$	52	4.1
1196	52	7.7
1441	53	6.3
1820	53	8.9

(SONIK) detector. The sensitivity of the fit to the scattering data is the main focus, examining the differences resulting from the two different scattering data sets considered. The mapping of the posterior distributions of the fit parameters, cross sections, phase shifts, and scattering lengths gives new insights into the dependence of these quantities to the input scattering data.

2 WHAT IS BRICK?

BRICK is a python package that acts as an interface between the AZURE2 [3,35] *R*-matrix code and an MCMC sampler. It is not a replacement for AZURE2 nor is it intended to be. The primary functionality that it provides is a user-friendly way to sample parameters that have already been set up with the AZURE2 graphical user interface (GUI) to be varied.

2.1 AZURE2

AZURE2 is a multilevel, multichannel, *R*-matrix code (open source) that was developed under the Joint Institute for Nuclear Astrophysics (JINA) [3,35]. While the code was created primarily to handle the added complexity of charged-particle induced capture reactions [55], also has capability for a wide range of other types of reaction calculations. The code is primarily designed to be used by way of a GUI, but can also be executed in a command line mode for batch processes [35]. The code stores all of its setup information in a simple text input file. While this file is usually edited by way of the GUI, it can also be modified directly. This may be desirable for batch type calculations, as are being used here.

AZURE2 primarily uses the alternative *R*-matrix parameterization of Brune [56]. It has two main advantages. The first is that it eliminates the need for the boundary conditions present in the classical formalism of Lane and Thomas [1]. The second is that the remaining fit parameters become the observed level parameters. The remaining model parameters are the channel radii which are fixed at 4.2 fm in this analysis.

A key advantage in using the parameterization of Brune [56] for the fitting of low energy capture reactions is that level parameters for bound or near threshold resonances can be more directly included in the *R*-matrix analysis [57,58]. The use of the Bayesian uncertainty estimation further facilitates the inclusion of uncertainty information for these parameters. This provides an improved method for communicating the level structure information gained from transfer reaction studies into an *R*-matrix analysis in a statistically rigorous way.

2.2 Implementation

2.2.1 Overview

The role of BRICK in our *R*-matrix calculations is to act as a mediator. It maps proposed parameters—both *R*-matrix parameters and normalization factors—from an MCMC sampler to AZURE2 and *R*-matrix predictions from AZURE2 back to the sampler. First, it accepts proposed points in parameter space, θ, from the sampler—in this analysis we use emcee [36]—and packages them into a format that AZURE2 can read. Then it reads the output from AZURE2 and presents it as a list. Each item of the list contains the predictions, $\mu(\theta)$, and data, y and σ, corresponding to a specific output channel configuration. The likelihood, represented in **Figure 2** by $\mathcal{L}$, can then be calculated according to the user's choice; the Gaussian likelihood chosen for this work is given below in **Eq. 2**. Accompanied by prior distributions, π, one can readily construct a Bayesian posterior, $\mathcal{P}$. Prior distributions chosen in this analysis are given in **Section 3.2**. The posterior value, or rather its logarithm $\ln \mathcal{P}$, is passed back to emcee. Finally, based on the $\ln \mathcal{P}$ value, the MCMC algorithm decides to accept or reject the proposed point, proposes a new θ, and the process repeats. A diagram is provided in **Figure 2** to illustrate the qualitative functionality of the different software packages. The process described above starts at the orange rectangle labeled "emcee."

2.2.2 Details

BRICK is built such that different samplers can be used. The analysis presented in this paper uses emcee, so the details provided in this section will be somewhat specific to it.

TABLE 3 | Details of the capture data considered in this work: number of data points, energy ranges, and common-mode errors (δ_{common}). Energies are given the laboratory frame.

Data set	Total capture	Branching ratio	δ_{common} (%)
Seattle [2]	8 pts (0.57, 2.17 MeV)	8 pts (0.57, 2.17 MeV)	3
Weizmann [42]	4 pts (0.74, 1.67 MeV)	-	3.7
LUNA [41]	7 pts (0.16, 0.30 MeV)	3 pts (0.17, 0.30 MeV)	3.2
ERNA [45]	47 pts (1.23, 5.49 MeV)	6 pts (1.93, 4.55 MeV)	5
Notre Dame [39]	17 pts (0.53, 2.55 MeV)	17 pts (0.53, 2.55 MeV)	8
ATOMKI [44]	5 pts (2.58, 4.43 MeV)	-	6

When initializing an instance of an `EnsembleSampler`, the most relevant argument is `log_prob_fn`, the function that returns the logarithm of the probability. One of the advantages of `emcee` is that it allows the practitioner to perform arbitrary calculations inside that probability function. That function must meet only two requirements: (1) take an array of floating point numbers that represents the vector in parameter space and (2) return a floating point number that represents the logarithm of the probability associated with that array. In between those two steps, one is free to perform whatever calculations one needs. This can be seen on the left-hand side of **Figure 2**. The parameter-space vector, θ, is output from `emcee`. The logarithm of the probability at that point, $\ln \mathcal{P}$, is subsequently input to `emcee`. In this sense, `emcee` is well-suited to the implementation of "black-box" physics models where one has limited access to the source code.

The primary tasks that `BRICK` accomplishes are (1) translating θ into a format that `AZURE2` can read and (2) reading the output from `AZURE2` such that a $\ln \mathcal{P}$ value can be easily calculated. The means of accomplishing these tasks relies on the command-line interface (CLI) to `AZURE2`, which is accessible when installed on Linux machines. The CLI options available to `AZURE2` are well documented in the manual [35]. The most critical argument is the input file, typically accompanied by the file extension `.azr`. This input file contains all of the necessary information to perform an *R*-matrix calculation with a given set of parameters. It is generated when the *R*-matrix and data models are built with the commonly used GUI, which `AZURE2` provides. `BRICK` is not built to replace that GUI. It *accompanies* `AZURE2` by allowing the user to bring their `AZURE2`-prepared *R*-matrix model over and sample what was previously optimized. Accordingly, the default behavior of `BRICK` is to respect the choices made by the user in the `AZURE2` GUI. If a parameter is fixed in `AZURE2`, it is fixed in `BRICK`. If it is varied in `AZURE2`, it is sampled in `BRICK`.

`BRICK` accesses the `AZURE2` CLI through the Python module `subprocess`. But prior to that, `BRICK` must map the values in θ to the proper locations in the input file. This is accomplished by reading the `<levels>` and `<sectionsData>` sections of the input file. `BRICK` reads the appropriate parameters and flags looking for varied parameters. As they are found, their locations are stored. When a new θ is proposed, `BRICK` creates a new input file and maps the values in θ to the varied parameter locations. Then `AZURE2` is called with the newly generated input file. The output from `AZURE2` is written to a sequence of files in the `output` directory by default. Those files are read and the predictions, μ, and experimental data, y, are extracted. A likelihood is then constructed. Under the assumption that the uncertainties associated with y are uncorrelated and normally distributed, this is a multivariate Gaussian distribution. Accompanied by a list of prior distributions corresponding to the preexisting knowledge of the sampled parameters, a posterior is finally constructed and passed back to `emcee`.

Initially, this process was built in a single-threaded manner. As `emcee` is a ensemble sampler, efficient exploration of the posterior relies heavily on many, simultaneous walkers. In order to scale this beyond the most basic calculations, we modified our implementation to allow each walker to write its own input file and read from its own output directory. Inside the log-probability function, there is no access to any kind of walker identifier, so each walker generates a file-space that is uniquely identified by an eight-character random string. This allows each walker to work independently, so on systems where many cores are available, each walker can have a dedicated core. Or at least the time spent waiting for CPU time is minimized. This also allows for an increased number of walkers, which is a common tactic used to decrease autocorrelation time.

3 APPLICATION TO ^{3}He(α, α)^{3}He AND ^{3}He(α, γ)^{7}Be

3.1 The *R*-Matrix Model

The starting point for the *R*-matrix model used here was that of deBoer et al. [7]. In that work, ten levels were used with three particle pairs (^{3}He+α, ^{7}Be+γ_0, and ^{7}Be+γ_1) for a total of 16 *R*-matrix fit parameters. Initial MCMC calculations showed that a $7/2^-$ background level used in deBoer et al. [7] was not statistically significant, and was thus dropped from the calculation. This already demonstrated one of the powerful feature of this type of MCMC analysis, it provided a clear identification of redundant fit parameters. Likewise, we verified that the exact placement of many of the background levels did not effect the fit results, as long as they were placed at sufficiently high energies. The exception to this was the $5/2^-$ background level, placed at 7 MeV. Because there are two real levels at E_x = 6.73 and 7.21 MeV in ^{7}Be, this background level needed to be placed close to their energies. It was found that this single background level was sufficient to model both the contributions from these levels and additional higher energy $5/2^-$ levels. The *R*-matrix model used here thus consisted of nine levels, three particle pairs, and 16 *R*-matrix fit parameters as summarized in **Table 1**.

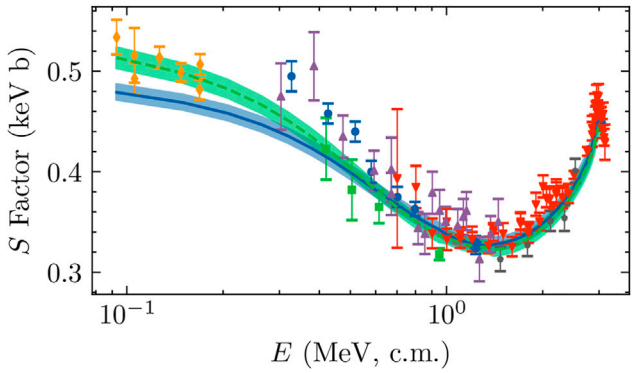

FIGURE 3 | Total capture S factor from Seattle [2] (blue circles) Weizmann [42] (green squares), LUNA [41] (orange diamonds), ERNA [45] (red, downward-pointing triangles), Notre Dame [39] (purple, upward-pointing triangles), and ATOMKI [44] (black stars) data sets are shown with reported error bars. $\mathcal{D}_{CSB}$ and $\mathcal{D}_{CS}$ results are shown with blue and green bands, respectively. The band indicates 68% intervals. The solid, blue line indicates the median prediction from the $\mathcal{D}_{CSB}$ analysis. The dashed, green line indicates the median prediction from the $\mathcal{D}_{CS}$ analysis. Normalization factors have not been applied to either the theory prediction or data, so estimates of the extent to which BRICK's fit agrees with the different data sets are not straightforward to make from the figure.

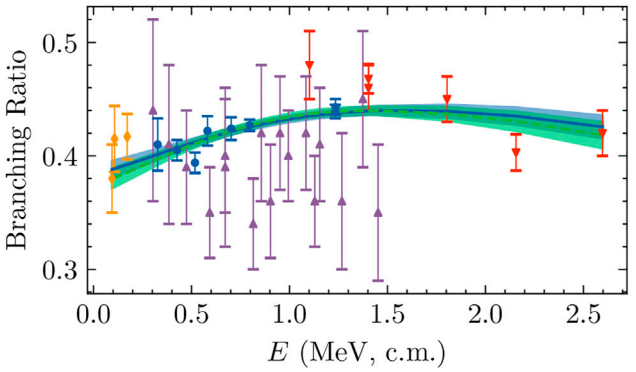

FIGURE 4 | The branching ratio predictions are shown alongside the four analyzed branching ratio data sets: Seattle [2], LUNA [41], ERNA [45], and Notre Dame [39]. Colors, symbols, and line styles are the same as **Panel 3**. Bands indicate 68% intervals.

3.2 Priors on *R*-Matrix Parameters

Because this is a Bayesian analysis, we must choose priors for all R-matrix parameters. We have chosen to use uninformative, uniform priors. However, the signs of the reduced width amplitudes (that is the interference solution), which are implemented in AZURE2 by the signs of the partial widths, were determined by the initial best χ^2 fit using AZURE2. In this case, a unique interference solution was found. This may not always be the case: sometimes other interference solutions may be possible. The emcee sampler may then not be able to easily find these other interference solutions in the parameter space. It seems to be likely that in cases where different interference solutions are possible, each one will require a separate emcee analysis.

One common circumstance where a Bayesian analysis will improve on previous uncertainty estimates is in the ability to give priors for bound state level parameters determined from transfer studies. Unfortunately, in the case of the ^{7}Be system, there is limited information available for the bound state α-particle ANCs. A recent first measurement has been reported by Kiss et al. [59], but the ANCs are rather discrepant from those found from this and past R-matrix analyses of capture data. This inconsistency has not been investigated here, but needs to be addressed in future work. If reliable bound-state ANC determinations become available, that are independent of the capture and scattering data, it provides a path to further decrease the uncertainty in the low energy S-factor extrapolation. One could also adopt priors on the ANCs from *ab initio* calculations, although we have not done so.

It is also tempting to implement more constraining priors into the R-matrix analysis from a compilation like the National Nuclear Data Center or the TUNL Nuclear Data Project [60]. However, great care must be taken to understand the source of the values and uncertainties when weighted averages are used to determine adopted values for level parameters in these compilations. In particular, past analysis of the data being fit in the R-matrix analysis may be a contributor to the evaluation values. Thus blindly using evaluation level parameters and uncertainties can lead to double counting and an erroneous decrease of uncertainties. It is for this reason that uniform priors on parameters are adopted in the present analysis. The posterior shapes then clearly stem solely from the data sets considered in the R-matrix analysis.

The priors for the R-matrix parameters used in this work are listed in **Table 1**. In all but one case, level energies are fixed. The exception is the $7/2^-$ level energy which corresponds to the lowest lying $7/2^-$ resonance. The lowest $1/2^-$ and $3/2^-$ levels and the $7/2^-$ level are the only levels inside or below the energy range covered by the analyzed data. All other levels are background levels. For more details of the choices made in formation of the R-matrix model, see Paneru [61]. The distribution formed by the product of these R-matrix priors and priors on the parameters introduced in the next section is the overall prior π shown in **Figure 2**.

3.3 Modeling Systematic Errors in the Data

3.3.1 Common-Mode Errors

AZURE2 provides a method for the inclusion of a common-mode error for each data set using a modified χ^2 function

$$\chi^2 = \sum_{\alpha=1}^{N_{\text{sets}}} \left(\sum_{j=1}^{N_\alpha} \frac{\left(f\left(x_{\alpha,j}\right) - c_\alpha n_\alpha y_{\alpha,j}\right)^2}{\left(c_\alpha n_\alpha \sigma_{\alpha,j}\right)^2} + \frac{\left((c_\alpha - n_\alpha)/n_\alpha\right)^2}{\delta^2_{c_{exp},\alpha}} \right), \quad (1)$$

where c_α is the normalization fit parameter, n_α is the starting normalization which is set to 1 in the present analysis, $f\left(x_{\alpha,j}\right)$ is the differential scattering cross section form the R-matrix, $y_{\alpha,j}$ is the data point value, $\sigma_{\alpha,j}$ is the combined statistical and point-to-point uncertainty of a data point, and $\delta_{c_{\text{exp}},\alpha}$ is the *fractional* common-mode uncertainty of the data set. The additional term in the χ^2 function is derived by making the approximation that the common-

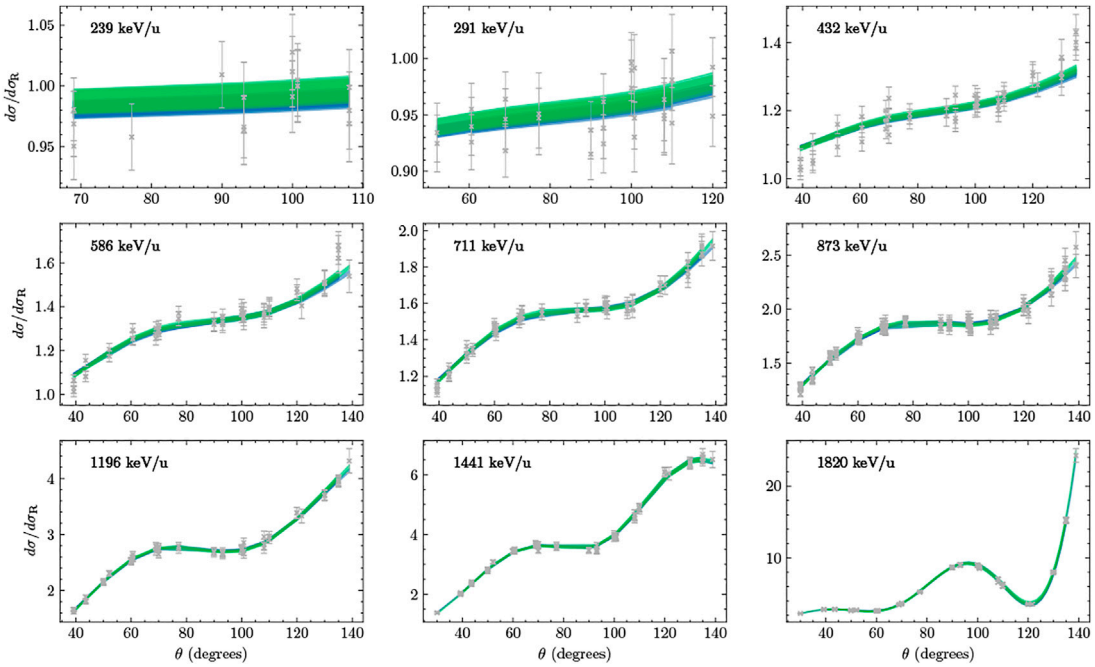

FIGURE 5 | Angular dependence of the differential cross sections of Paneru et al. [54] are shown relative to the Rutherford prediction with grey x's and error bars. Each panel includes the measurements from three interaction regions [61]. Bands indicate 68% intervals. Green bands are generated for the analysis of $\mathcal{D}_{CS}$. Blue bands correspond to $\mathcal{D}_{CSB}$.

mode systematic uncertainty has a Gaussian probability distribution [62]. The accuracy of this approximation is often unclear [6].

Common-mode errors are implemented in the present analysis in BRICK, outside of AZURE2, i.e., the common-mode errors are applied to the AZURE2 output. In BRICK the R-matrix parameter set θ_R is augmented by a set of normalization factors f_α and energy shifts, $\Delta_{E,\alpha}$. (At present energy shifts are only implemented for scattering data.) The overall parameter set θ is then the union of the set θ_R and $\{f_\alpha, \Delta_{E,\alpha}\}$. The likelihood $\mathcal{L}$ is formed as a product of standard Gaussian likelihoods for each data point, but with normalization factors applied to the AZURE2 predictions μ:

$$\mathcal{L} \propto \prod_{\alpha=1}^{N_{\text{sets}}} \prod_{j=1}^{N_\alpha} \exp\left(-\frac{\left(y_{j\alpha} - f_\alpha \mu\left(x_{j\alpha}; \theta_R\right)\right)^2}{2\sigma_{j\alpha}^2} \right), \tag{2}$$

where we have omitted overall factors that do not affect the parameter estimation. Here $x_{j\alpha}$ represents the kinematics of the jth data point in data set α. For scattering data sets, $x_{j\alpha}$ defines the energy and angle at which the measurement was made. In those cases exclusively, $\Delta_{E,\alpha}$ is added to the energy. $\sigma_{j\alpha}$ is the combined statistical and point-to-point uncertainty of the corresponding datum, $y_{j\alpha}$. N_α is the number of points in data set α, and the product over α runs over all the sets that have independent common-mode errors.

The priors on the f_α's are specified by the BRICK user. If a Gaussian prior centered at 1 with a width equal to the common-mode error reported in the original experimental publication is employed for the f_α's, then the product of that prior on the normalization factors and the likelihood **Eq. 2** has the same maximum value as the "extended likelihood" corresponding to **Eq. 1**, that is used to estimate the f_α's in the frequentist framework implemented in AZURE2.

In our analysis of the ^{3}He$(\alpha,\alpha)^{3}$He and ^{3}He$(\alpha,\gamma)^{7}$Be reactions, we adopted such a Gaussian prior, truncated to exclude negative values of the cross section. We used a different f_α for each energy bin in the SONIK data, detailed in **Section 4.2**, with the widths of the prior given by the common-mode errors stated in **Table 2**. The common-mode error associated with the Barnard data, described in **Section 4.1**, is taken to be 5%. The width of the priors for the f_α's to be applied to the capture data, discussed in **Section 4.3**, are specified by the common-mode errors listed in **Table 3**. All normalization-factor priors are of the form

$$T(0,\infty)N\left(1,\sigma_{f\alpha}^2\right), \tag{3}$$

where

$$T(a,b) = \begin{cases} 1 & [a,b] \\ 0 & \text{otherwise} \end{cases}, \tag{4}$$

and $N(\mu,\sigma^2)$ represents a Gaussian distribution centered at μ with a variance of σ^2.

3.3.2 Energy Shifts

BRICK also has the capability of estimating (overall) beam-energy shifts in a particular data set. This is implemented as another parameter to be estimated $\Delta_{E,\alpha}$. This parameter affects all the AZURE2 evaluations for data set α. BRICK implements the energy shift by generating a different input

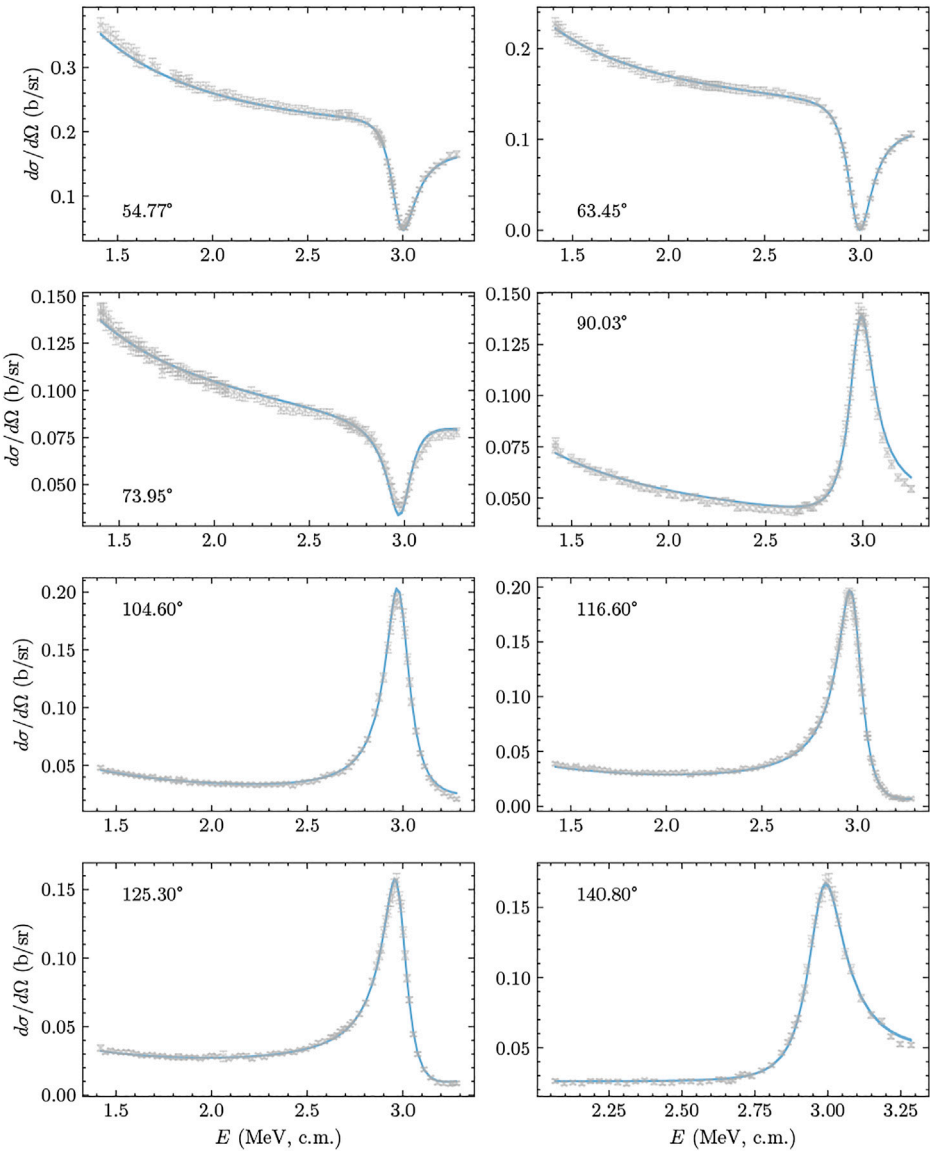

FIGURE 6 | Differential cross section as a function of energy as reported in Barnard et al. [53], shown as grey x's with error bars. Blue bands represent the 68% intervals generated from the $\mathcal{D}_{CSB}$ analysis.

and data files for each value of $\Delta_{E,\alpha}$ under consideration. The flowchart of **Figure 2** is thus not strictly accurate when this feature is included. Gaussian priors were defined, centered at zero, on possible energy shifts for the SONIK data and the Barnard data. The widths of the priors are based on information in the original papers, as summarized in **Sections 4.1, 4.2**. For the SONIK data, the energy-shift parameter's prior has a standard deviation of 3 keV, based on the energy uncertainty quoted in Paneru et al. [54]. Barnard et al. [53] cites a much larger uncertainty of 20–40 keV, depending upon the energy. The standard deviation of the prior on the ΔE parameter is taken to be 40 keV for this data set, a much larger value than for the SONIK data. It should be noted that the energy uncertainty for the Barnard data set is not a constant, but it is not possible to improve our modeling of this uncertainty due to the lack of documentation of its origin.

4 DATA SETS

4.1 ^{3}He-α Elastic Scattering

Measurements of the elastic scattering products resulting from a ^{3}He beam incident on a ^{4}He target were reported in 1964 by Barnard et al. [53], for $2.4 \leq E\,[^{3}\text{He, lab}] \leq 5.7$ MeV ($1.4 \leq E_{\text{c. m.}} \leq 3.3$ MeV). The experiment provides excitation functions of differential cross section at eight center-of-mass (c.m.) angles covering $31.55^{\circ} \leq \theta[^{3}\text{He, lab}] \leq 91.94^{\circ}$ ($54.77^{\circ} \leq \theta_{\text{c.m.}} \leq 140.8^{\circ}$). The

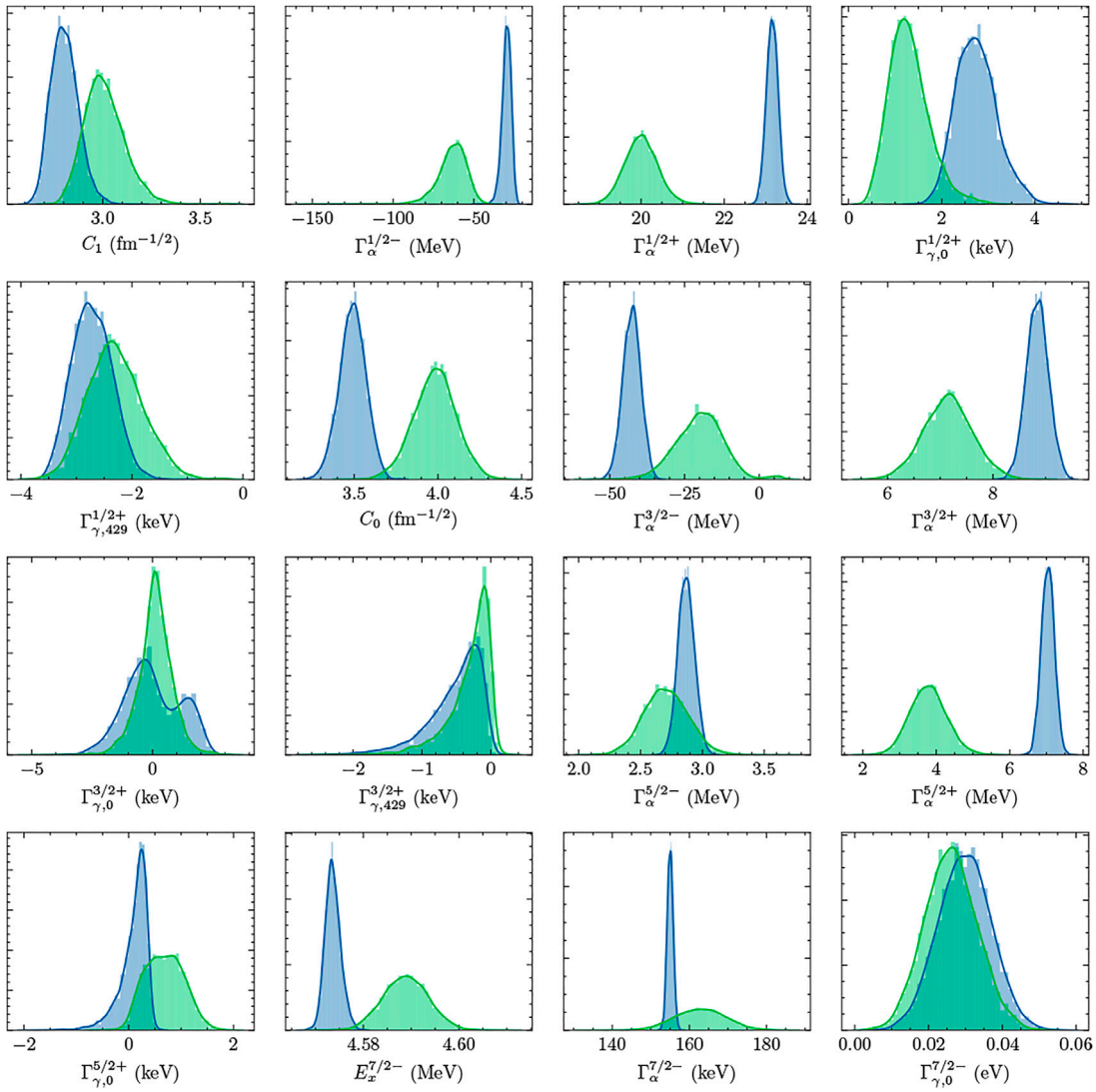

FIGURE 7 | *R*-matrix parameter comparison between $\mathcal{D}_{CS}$ (green) and $\mathcal{D}_{CSB}$ (blue) analyses.

systematic uncertainty in the measurements is estimated to be 5%. Detailed point-to-point uncertainties are not given, but are stated to be about 3%. The measurements are subject to a significant energy uncertainty, estimated to be 20 keV below E [^{3}He, lab] = 4 MeV and 40 keV above that energy. It was also noted by the authors that their beam energy was only reproducible to the level of 20 keV. In total, there are 646 data points collected at 577 unique energies. The data were obtained from EXFOR in the fall of 2021 and converted into the laboratory frame when necessary. All eight angles were included. The previous analysis by deBoer et al. [7] omitted the largest angle.

4.2 Paneru et al. ^{3}He-α Elastic Scattering

A new measurement of ^{3}He+α elastic scattering was performed at TRIUMF using the SONIK [61,63] target and detector system. SONIK was filled with ^{4}He gas maintained at a typical pressure of 5 Torr bombarded with ^{3}He with a beam intensity of about 10^{12} pps. Elastic scattering cross sections were measured at nine different energies from $E_{\mathrm{c.\ m.}}$ = 0.38–3.13 MeV. SONIK covers an angular range of $30^{\circ} < \theta_{\mathrm{c.m.}} < 139^{\circ}$—a markedly larger range than previous measurements. The detectors in SONIK were arranged such that they observed three different points, termed interaction regions, in the gas target along the beam direction. When the beam traversed the gas target it lost energy, so the bombarding energy, and therefore the scattering energy, was slightly different in each of the three interaction regions.

As we will explore further below, the results for the differential scattering cross section from this measurement are consistent with previous determinations but have better precision. The data also extend to markedly lower energies. The uncertainties with this measurement are well quantified and are presented in Paneru et al. [54]. A separate normalization uncertainty is determined for each beam energy. These normalization uncertainties range from 4.1 to 9.8%.

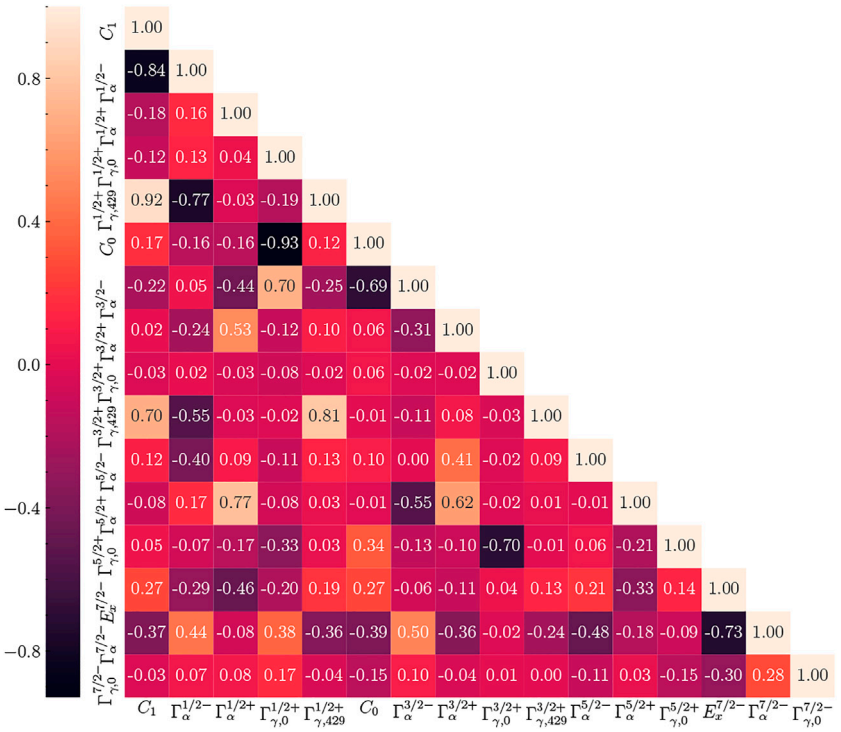

FIGURE 8 | Correlation matrix of *R*-matrix parameters for the $\mathcal{D}_{CS}$ analysis. Parameter chains are centered at zero and scaled to one prior to the computation. The strongest correlations (anti-correlations) are highlighted with lighter (darker) colors.

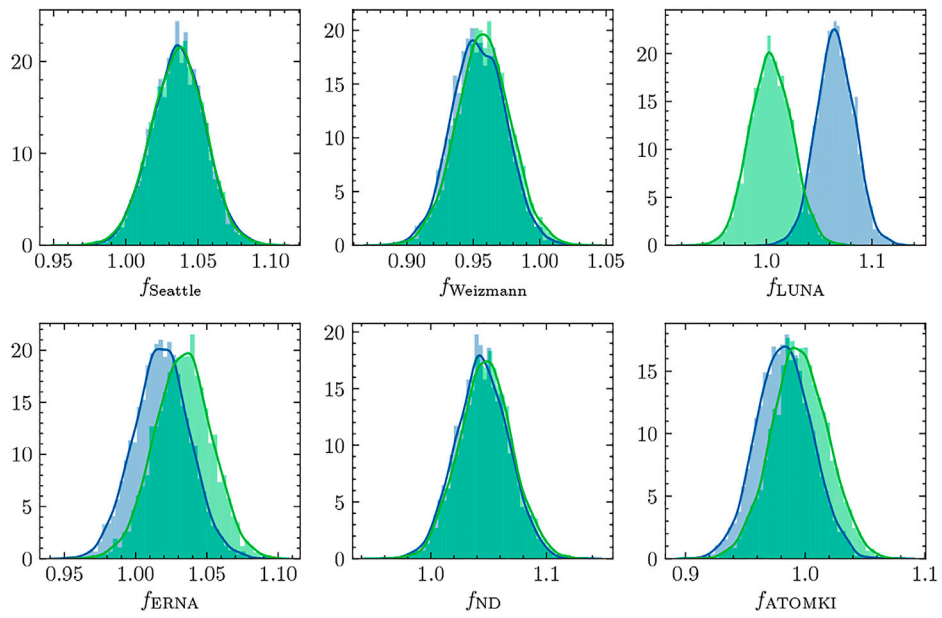

FIGURE 9 | The normalization factors applied to the total cross section predicted by our *R*-matrix model are compared for each of the total capture data sets (Seattle [2] Weizmann [42], LUNA [41], ERNA [45], Notre Dame [39], and ATOMKI [44]). $\mathcal{D}_{CSB}$ (blue) and $\mathcal{D}_{CS}$ (green) results are shown together for each data set.

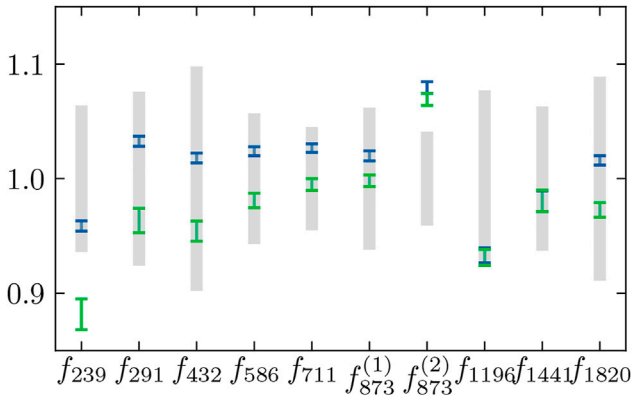

FIGURE 10 | Summaries of the normalization factor posteriors for each SONIK [54] data set are shown for $\mathcal{D}_{\mathrm{CSB}}$ (blue) and $\mathcal{D}_{\mathrm{CS}}$ (green). Error bars represent 68% quantiles. Grey-shaded rectangles indicate the uncertainties reported in [61].

4.3 ^{3}He(α, γ) Data

The data selection [39–42,44,45] for the ^{3}He $(\alpha,\gamma)^7$Be reaction for this work follows that of previous recent works [7,22,47,64]. Note that the LUNA measurements of Gyürky et al. [65] and Confortola et al. [66] are collected in Costantini et al. [41]. The combined data sets cover a wide energy range from $E_{\mathrm{c.\,m.}}$ = 94–3130 keV, but still remain below the proton decay threshold. Older data are not included due to a long history of discrepancies, which manifested as differences between experiments that used either direct detection of γ-rays or the activation technique. More recent measurements have achieved consistency resulting from improved experimental techniques by performing consistency check measurements using both direct detection of γ-rays and the activation technique [47]. Details about the capture data sets, including common-mode errors for cross sections, are listed in **Table 3**.

4.4 Data Models

Two distinct data models are analyzed here, $\mathcal{D}_{\mathrm{CS}}$ and $\mathcal{D}_{\mathrm{CSB}}$, where C indicates the inclusion of the capture data described in **Section 4.3**, S indicates the inclusion of the SONIK data described in **Section 4.2**, and B indicates the inclusion of the Barnard data described in **Section 4.1**. $\mathcal{D}_{\mathrm{CSB}}$ is a more complete data model in the sense that it includes more data and would naively be considered the "best" data model. But, there are notable effects when the data of Barnard et al. [53] are included that are highlighted and discussed in **Section 5**.

5 RESULTS

The results of our analysis are presented here in two subsections. The first discusses results in the energy regime of the data that was analyzed. The second computes extrapolated quantities—observables that lie in energy regimes outside those covered by the analyzed data.

5.1 Fits to Data

First we examine the extent to which our results match experimental data. We do this by comparing predicted and measured observables.

5.1.1 Capture Data

Figure 3 shows the total capture S-factor data alongside bands representing 68% intervals from the analyses of both data models, $\mathcal{D}_{\mathrm{CSB}}$ and $\mathcal{D}_{\mathrm{CS}}$. For energies above 400 keV both analyses give very similar results. However, below that energy, the $\mathcal{D}_{\mathrm{CS}}$ analysis provides a more "natural" agreement with data—see the normalization factor posteriors and the associated discussion below. The LUNA data in particular discriminate between the two data models. The fit to the CSB data includes a normalization factor for the LUNA data that differs from 1 by about three times the stated common-mode error, cf. below. The normalization factors are not applied to the data in **Figure 3**, which is why the CSB band sits well below the LUNA data.

The branching ratio, defined as the ratio of the excited-state cross section to the ground-state cross section, results for both data models—$\mathcal{D}_{\mathrm{CS}}$ and $\mathcal{D}_{\mathrm{CSB}}$—are shown in **Figure 4**. The most prominent differences between the $\mathcal{D}_{CSB}$ and $\mathcal{D}_{CS}$ results occur near the upper and lower ends of the energy range. However, in the context of the experimental uncertainties, these differences

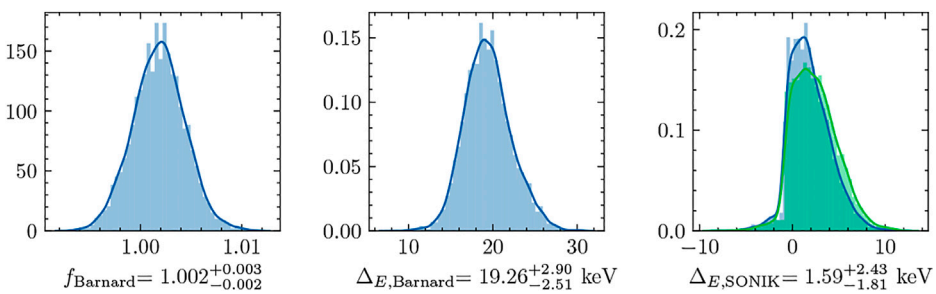

FIGURE 11 | Posteriors of the normalization factor applied to the Barnard data and the energy shifts introduced to the Barnard et al. [53] and SONIK [54] data sets. The Barnard normalization factor is applied to the theory prediction. Energy shifts are presented in keV. These results were obtained exclusively with the $\mathcal{D}_{\mathrm{CSB}}$ data model.

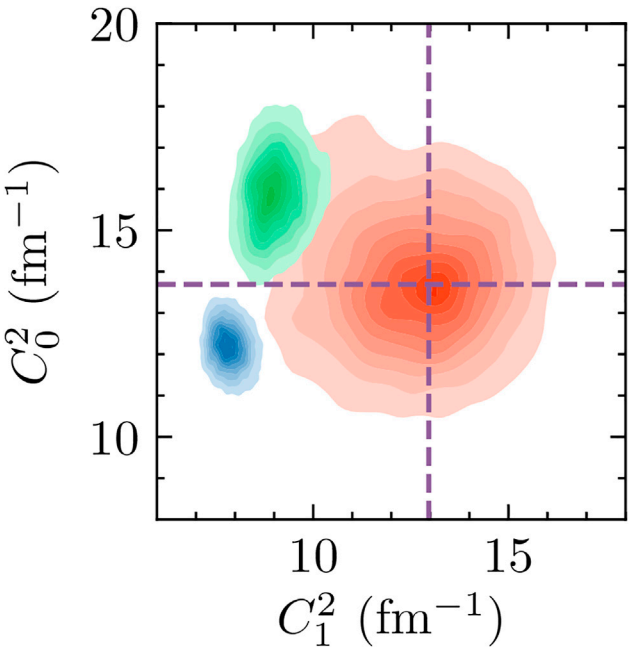

FIGURE 12 | The two-dimensional posterior of the squares of the ANCs, C_0 and C_1. Results for $\mathcal{D}_{CS}$ are shown in green and for $\mathcal{D}_{CSB}$ in blue. The EFT analysis of capture data of Zhang et al. [22] extracted the ANC values shown in red, and in the analysis of Barnard et al. [53] and capture data of deBoer et al. [7] the ANCs were fixed at the location indicated by the purple, dashed lines.

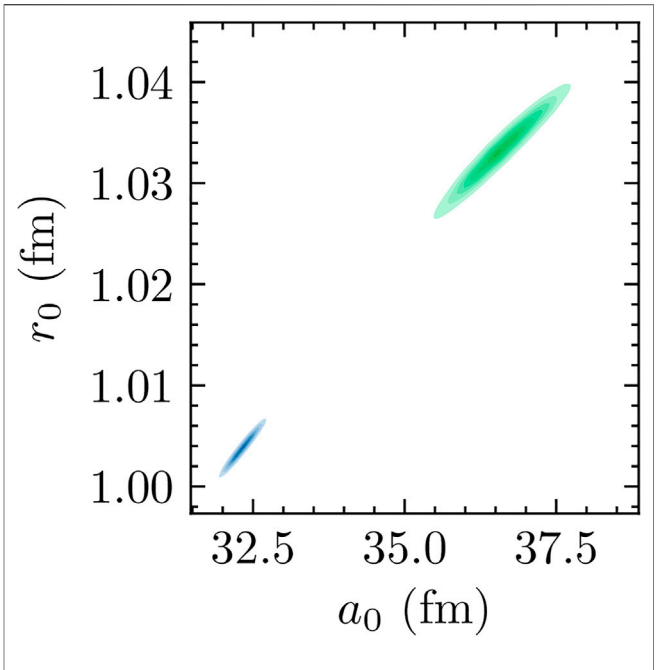

FIGURE 13 | a_0-r_0 correlation for both $\mathcal{D}_{CSB}$ (blue) and $\mathcal{D}_{CS}$ (green) data models.

are not significant. Over the entire energy range, the predictions from $\mathcal{D}_{CS}$ and $\mathcal{D}_{CSB}$ overlap at the 1-σ level.

5.1.2 Scattering Data

The differential cross sections from the SONIK [54] and Barnard et al. [53] measurements are shown in **Figures 5** and **6**, respectively, with the predictions from our analyses. In all cases, both analyses reproduce the data to high accuracy. However, the $\mathcal{D}_{CS}$ analysis results in a much lower χ^2/datum at max ln P: 0.72 for the SONIK [54] data vs. 0.95 for the $\mathcal{D}_{CSB}$ analysis of the SONIK + Barnard [53] data sets.

5.2 Parameter Distributions

Separate corner plots for each data model are provided in the Supplemental Material. There are notable differences in several R-matrix parameters. In particular, the $\mathcal{D}_{CS}$ ANCs are significantly larger and their posterior distributions are noticeably wider. The $\mathcal{D}_{CS}$ analysis also produces a significantly smaller ratio of ANCs, C_1/C_0. This is consistent with the smaller branching ratios at low energies shown in **Figure 4**.

The $\mathcal{D}_{CS}$ partial α widths in the $1/2^+$, $3/2^+$, and $5/2^+$ channels are smaller and separated by more than two standard deviations from the $\mathcal{D}_{CSB}$ widths. The distributions for $\Gamma_{\gamma,0}^{(5/2^+)}$ seem to indicate opposite signs. The $\mathcal{D}_{CSB}E_x^{(7/2^-)}$ posterior is markedly smaller and narrower, and the constraints on $\Gamma_\alpha^{(7/2^-)}$ from $\mathcal{D}_{CSB}$ are dramatically tighter. This is presumably due to the much larger amount of data in the vicinity of the $7/2^-$ resonance that is present in the Barnard et al. [53] data set. It is also worth noting the "non-Gaussian" behavior of several of these distributions—a characteristic that would be difficult to identify in a typical analysis that assumed linear propagation of uncertainties around a minimum of the posterior pdf. Using Gaussian approximations and linearizing would likely underestimate uncertainties in the case of $\Gamma_{\gamma,0}^{(3/2^+)}$, for example.

All parameters shown in **Figure 7** are well-constrained. By comparing to the prior distributions listed in **Table 1**, one can see the dominance of the data's influence over the information in the prior: all posterior distributions are markedly narrower than the priors chosen. As discussed in **Section 3.2**, several R-matrix-model iterations were taken to remove redundant parameters.

The correlation matrix of the R-matrix parameters is shown in **Figure 8**. The figure represents an approximation of the full information contained in the corner plot given in the Supplemental Material. There, significant, often-nonlinear, correlations are observable between several pairs of R-matrix parameters. In particular, the influence of the ANCs over the entire R-matrix parameter space, either directly or indirectly, means that it is very important for scattering data to have well-defined uncertainties over its full energy range.

The normalization factors applied to the theory predictions for each of the total capture data sets are shown for both data models in **Figure 9**. The comparison reveals good agreement between $\mathcal{D}_{CS}$ and $\mathcal{D}_{CSB}$ for all but the LUNA data set [41]—the lowest-energy capture data set in our analysis. The $\mathcal{D}_{CS}$ analysis yields a normalization factor for these data that is very close to 1. In contrast, the $\mathcal{D}_{CSB}$

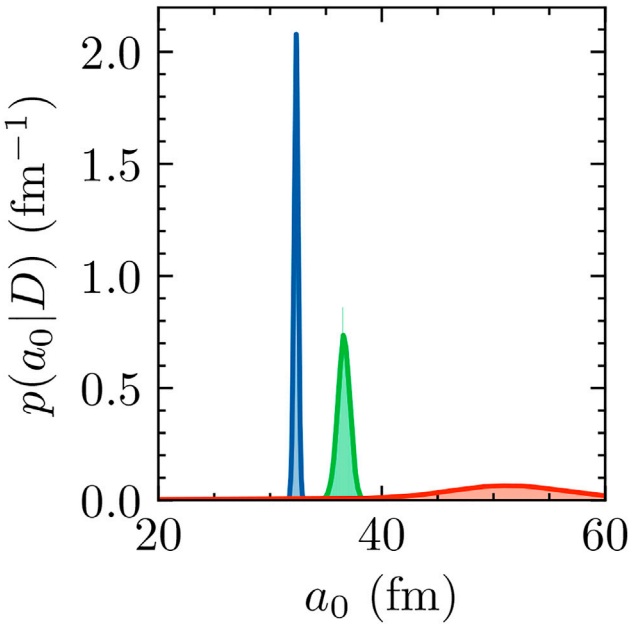

FIGURE 14 | a_0 posteriors obtained from $\mathcal{D}_{CS}$ (green) and $\mathcal{D}_{CSB}$ (blue) analyses. The result from Zhang et al. [22] is shown in red.

analysis requires that the LUNA data be shifted by nearly 10%. (Recall from **Eq. 2**, that f is applied to the theory prediction, and so an $f > 1$ corresponds to a systematic error that reduces the experimental cross section and uncertainties.). To put this in perspective, the LUNA collaboration estimates their common-mode error at 3.2%. Because the LUNA data set is the lowest capture data set, this disagreement between the $\mathcal{D}_{CS}$ and $\mathcal{D}_{CSB}$ analyses corresponds to a significant difference in the extrapolated $S(0)$ of these two analyses.

The normalization factors applied to the theory predictions for each of the SONIK energies are shown in **Figure 10**. When the data of Barnard et al. [53] are included in the analysis, the SONIK normalization factors are significantly larger. This effect is systematically apparent at lower energies. In more than half the cases, the $\mathcal{D}_{CSB}$ and $\mathcal{D}_{CS}$ results are inconsistent with each other. For eight out of ten SONIK energies, the normalization factor obtained from the fit is within the common-mode error estimated by the SONIK collaboration. Note that the common-mode error in this experiment was estimated to be different at different beam energies [61] [1]. This is represented in **Figure 10** by the varying heights of the grey bands, which are priors in accord with these experimentally assigned common-mode errors, see **Table 2**.

The posteriors for f_{Barnard} and the energy shifts for both the Barnard et al. [53] and SONIK [54] data sets (see **Section 3.3**) are shown in **Figure 11**. The result for f_{Barnard} is $1.002^{+0.003}_{-0.002}$: well within the estimated systematic uncertainty of 5% given in Barnard et al. [53]. A shift of $19.26^{+2.90}_{-2.51}$ keV in the energies reported in Barnard et al. [53] is found, but this result is consistent with the energy uncertainty estimates ranging from 20 to 40 keV given in that paper. However, even such a clearly nonzero shift does not seem to significantly impact extrapolated quantities. Finally, the SONIK energy shift indicated by our analyses is $1.59^{+2.43}_{-1.81}$ keV. This result matches very well with the reported energy uncertainty estimate of 3 keV. The prior for this parameter was a normal distribution centered at 0 keV with a 1-σ width of 3 keV. The primary difference between the posterior and the prior for this parameter is the loss of probability in the negative energy region. If any energy shift in the SONIK data [54] is necessary, it is positive, but since 0 keV is well within one standard deviation, there is strong evidence for no shift.

[1]We use slightly different common-mode uncertainty estimates in our prior definitions than those listed in [61]. This update will be reflected in a forthcoming publication by the SONIK collaboration [54].

TABLE 4 | A summary of the posteriors of the extrapolated quantities. Where possible, results from other anlayses are included.

Analysis	$S(0)$ (keV b)	a_0 (fm)	r_0 (fm)
$\mathcal{D}_{CS}$	$0.539^{+0.011}_{-0.012}$	$36.59^{+0.55}_{-0.53}$	$1.033^{+0.003}_{-0.003}$
$\mathcal{D}_{CSB}$	$0.495^{+0.008}_{-0.008}$	$32.32^{+0.18}_{-0.18}$	$1.004^{+0.001}_{-0.001}$
deBoer et al. [7]	$0.542^{+0.023}_{-0.017}$	—	—
Zhang et al. [22]	$0.578^{+0.015}_{-0.016}$	$50.36^{+6.02}_{-7.50}$	$0.974^{+0.025}_{-0.027}$

The ANCs corresponding to the two bound ^{7}Be states are of particular interest for extrapolating threshold quantities. First, we point out that the inclusion of scattering data significantly reduces the uncertainty of the ANCs. Our posterior is much narrower than that obtained using capture-only data in Zhang et al. [22]. This highlights the importance of scattering data in constraining bound-state properties and the amplitudes associated with transitions to them.

Second, the choice of scattering data set matters. The C_1 results from analyzing $\mathcal{D}_{CS}$ and $\mathcal{D}_{CSB}$ are discrepant at the 1-σ level. The C_0 results disagree by approximately 2-σ. The contrast is highlighted in **Figure 12** where the squares C_1^2 and C_0^2 are compared. The differing values directly impact the S-factor extrapolations discussed below.

5.3 Extrapolated Quantities

The Coulomb-modified effective range function is given in Hamilton et al. [67] and van Haeringen [68] as

$$K(E) = k^{2\ell+1}\frac{\eta^{2\ell}}{\Gamma^2(\ell+1)}u_\ell(\eta)\left[C_0^2(\eta)\cot\delta_\ell + 2\eta h(\eta)\right], \quad (5)$$

where k is the relative momentum, ℓ is the angular momentum, η is the Sommerfeld parameter, Γ is the gamma function, $u_\ell(\eta)$ is given by

$$u_\ell(\eta) = \frac{\Gamma^2(2\ell+2)C_\ell^2}{(2\eta)^{2\ell}C_0^2}, \quad (6)$$

with

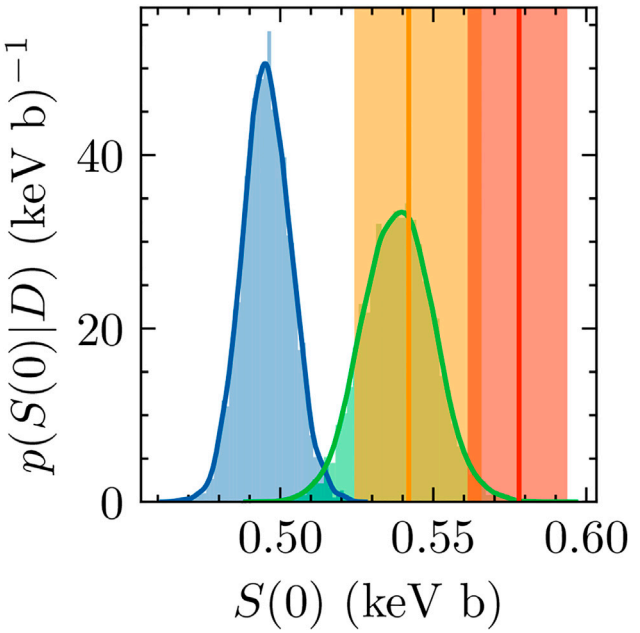

FIGURE 15 | Extrapolated $S(0)$ posteriors from the analyses of both $\mathcal{D}_{\mathrm{CSB}}$ (blue) and $\mathcal{D}_{\mathrm{CS}}$ (green) data models. Previous results from Zhang et al. [22] (red) are deBoer et al. [7] (orange) are also summarized here for comparison.

$$C_\ell = \frac{\left(\ell^2+\eta^2\right)^{1/2}}{\ell\left(2\ell+1\right)} C_{\ell-1}\ , \tag{7}$$

$$C_0 = \left[\frac{2\pi\eta}{e^{2\pi\eta}-1}\right]^{1/2}\ , \tag{8}$$

$$h(\eta) = \frac{1}{2}\left[\Psi(1+i\eta)+\Psi(1-i\eta)\right] - \ln\eta\ , \tag{9}$$

and Ψ representing the digamma function [69]. This effective range function is an analytic function of E (or k^2) near $E = 0$. From the phase shifts, obtained with BRICK, calculated over a range of low momenta, one can fit the scattering length, a_0, and effective range, r_0, according to the low-energy expansion

$$K(E) = -\frac{1}{a_0} + \frac{r_0}{2}k^2 + \ldots \tag{10}$$

Our calculation involves 70 equally spaced phase shifts over a range of low energies from 0.57 keV to 3.93 MeV. The results are used to evaluate the effective range function defined by **Eq. 5**. The energy dependence is then fit to **Eq. 10** using a non-linear least squares fit. In addition to a_0 and r_0 defined in **Eq. 5**, the shape parameter at $\mathcal{O}(k^4)$ was fit to ensure a better determination of a_0 and r_0.

The results from $\mathcal{D}_{\mathrm{CSB}}$ and $\mathcal{D}_{\mathrm{CS}}$ are shown in **Figure 13**. As in the ANC comparison, they are strikingly discrepant. The naive expectation would be that $\mathcal{D}_{CSB}$ distributions would be smaller subsets of the $\mathcal{D}_{CS}$ distributions. For many relevant quantities, this is not the case.

Figure 14 shows a comparison of the scattering lengths obtained from the $\mathcal{D}_{CS}$ and $\mathcal{D}_{CSB}$ analyses. A comparison to Zhang et al. [22], also included in **Figure 14**, reveals the impact of including scattering data: the inclusion of scattering data drives the median downward and constrains the uncertainties significantly. A summary of these posteriors is given in **Table 4**.

The $\mathcal{D}_{CSB}$ scattering length and effective range are both smaller and more tightly constrained. One might have expected that with more data—and more data at lower energies—this extrapolated quantity would become more tightly constrained. The two-dimensional posteriors shown in **Figure 13** seem to lie on the same line or band that defines the correlation between a_0 and r_0, though two extended posteriors is not sufficient to define such a line.

The total capture S factor at zero energy was extrapolated by evaluating the S factor at 100 evenly spaced points between 1 and 100 keV, constructing a cubic-polynomial interpolation function to represent the calculations, and evaluating that function at zero energy. Errors from the interpolation/extrapolation process are negligible when compared to contributions from parameter uncertainties. The results are shown alongside previous results in **Figure 15**. As expected from the different low-energy behaviors shown in **Figure 3**, the $\mathcal{D}_{\mathrm{CS}}$ and $\mathcal{D}_{\mathrm{CSB}}$ results are discrepant, only overlapping at the 2-σ level. The inclusion of the Barnard et al. [53] data reduces the uncertainty in $S(0)$ and pulls the entire distribution downward, outside the uncertainties of the $\mathcal{D}_{CS}$ analysis. This effect is not seen in [7] because the ANCs in that analysis were not varied freely. The $\mathcal{D}_{CSB}$ result is discrepant with the $\mathcal{D}_{CS}$ results *and* those reported in [7,22]. A summary of these posteriors is given in **Table 4**.

Insights into the relevance of parameters can be obtained by examining the correlations between them. In **Figure 16**, the correlations between $S(0)$ and a_0, C_1^2 and C_0^2 are shown. While the $\mathcal{D}_{CS}$ and $\mathcal{D}_{CSB}$ results are discrepant in several astrophysically relevant cases, the discrepancy is consistent, and this figure exposes, to a large extent, why: the ANCs, particularly the ground-state ANC, strongly correlates with $S(0)$. The Barnard et al. [53] data more tightly constrain these parameters at smaller values, and this directly lowers the predicted $S(0)$ extrapolation.

6 CONCLUSION

We have described and applied the Bayesian R-matrix Inference Code Kit (BRICK), which facilitates communication between the phenomenological R-matrix code AZURE2 [3] and a Markov Chain Monte Carlo (MCMC) sampler such as emcee [36]. It thereby enables MCMC sampling of the joint posterior probability density function (pdf) for the R-matrix parameters and normalization factors. With samples that represent such a posterior in hand, the computation of the pdf for any quantity that can be calculated in the R-matrix formalism is straightforward.

While BRICK is a general tool, we have also provided an example of its application to an R-matrix fit of ^{3}He-α scattering and the ^{3}He $(\alpha,\gamma)^{7}$Be capture reaction data, in order to make inferences about the ^{7}Be system. This application was partly

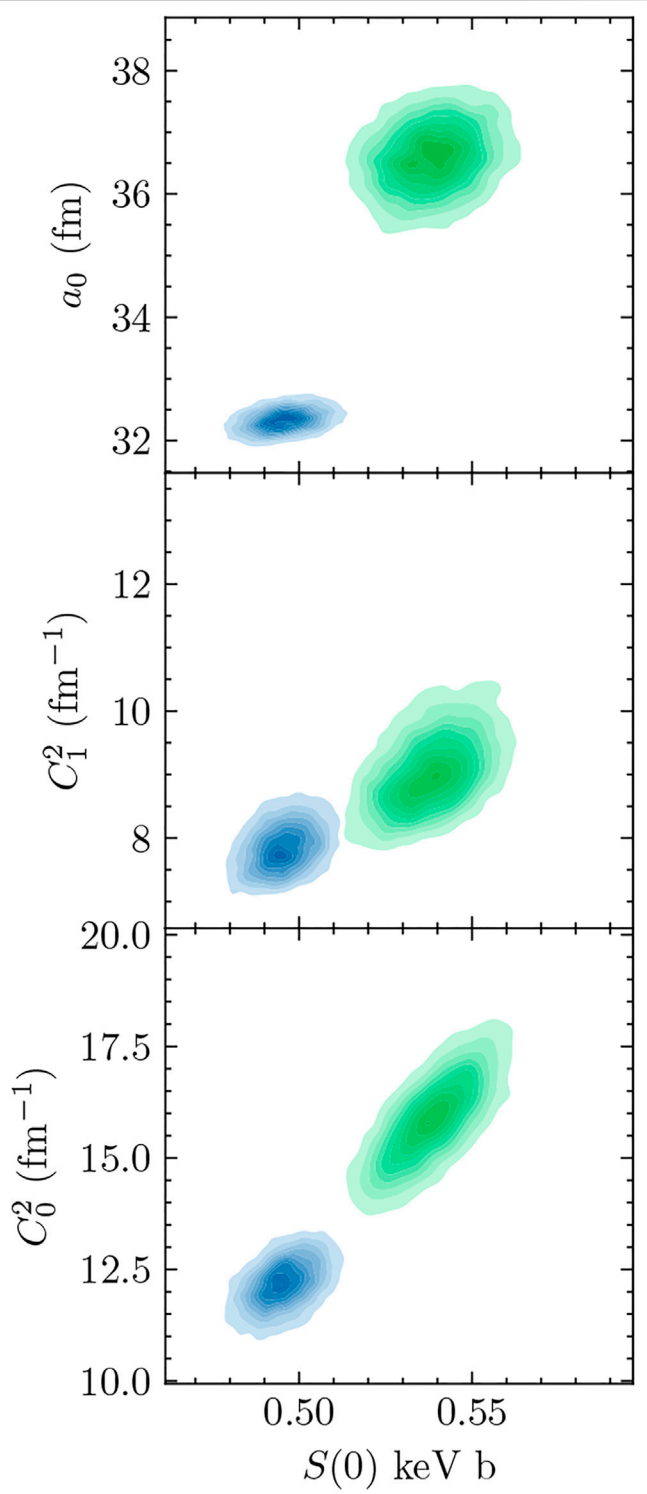

FIGURE 16 | Two-dimensional posteriors are presented for the analyses of both $\mathcal{D}_{CSB}$ (blue) and $\mathcal{D}_{CS}$ (green) data models. The "anchor" parameter is $S(0)$. The top panel gives its correlation with a_0. The middle (bottom) panel corresponds to the square of the excited- (ground-) state ANC.

motivated by the availability of a new ^{3}He-α scattering data set obtained using the SONIK detector at TRIUMF [61] following the suggestion of deBoer et al. [7]. These data have more carefully quantified uncertainties than a previous measurement by Barnard et al. [53]. Our study shows this motivation was well justified, finding discrepant values for extrapolated quantifies when the data of Barnard et al. [53] were included. Our analysis of the SONIK data shows consistency between them and capture data, producing an S factor in accord with analyses of capture data alone: our final $\mathcal{D}_{CS}$ (capture + SONIK data) result for the S-factor at zero energy is $S(0) = 0.539^{+0.011}_{-0.012}$ keV b. When the Barnard et al. [53] data were included in the analysis, the $\mathcal{D}_{CSB}$ results produced significantly lower ANCs and $S(0)$ extrapolation. Indeed, the $\mathcal{D}_{CSB}$ analysis produces values for $S(E)$ at c. m. energies of 10–20 keV that can only be reconciled with the LUNA data [41] if the normalization of these data is adjusted by 2–3 times the quoted common-mode error.

This emphasizes the importance of detailed uncertainty quantification when data sets are to be used for accurate inference of extrapolated quantities, where Barnard et al. [53] does not include these kinds of details regarding the experiment. This makes the tension between the Barnard et al. [53] and SONIK data regarding $S(0)$ difficult to resolve, thus the Barnard et al. [53] data may need to be omitted from future evaluations. We emphasize, though, that these previous data were invaluable in advancing our understanding of the ^{7}Be system to its current state, but data with more well defined uncertainties are needed for current applications.

Zhang, Nollett, and Phillips pointed out that the s-wave ^{3}He-α scattering length is correlated with this result [22]. The $\mathcal{D}_{CS}$ analysis produces $a_0 = 36.59^{+0.55}_{-0.53}$ fm. Premarathna and Rupak simultaneously analysed capture data and ^{3}He-α phase shifts in EFT and found $a_0 = 40^{+5}_{-6}$ fm (Model A II of Premarathna and Rupak [21])—in good agreement with this number. However, it disagrees by 2σ with the a_0 extracted using EFT methods from capture data alone by Zhang et al. [22]: $a_0 = 50^{+6}_{-7}$. Recently Poudel and Phillips [70] performed an EFT analysis of the SONIK data, using priors on the ^{7}Be ANCs from the capture analysis of Zhang et al. [22], and extracted $a_0 = 60 \pm 6$ fm—even further away from the results of this R-matrix analysis.

Improvements in the analyses presented here could occur if there were:

- Better documentation of the energy dependence of systematic uncertainties in published data sets. The Bayesian formalism that underlies `BRICK` allows systematic uncertainties with any correlation structure to be incorporated into the analysis.
- Improved understanding of the way theory uncertainties in the phenomenological R-matrix formalism affect the extrapolation of data.
- Detailed modern data with full uncertainty quantification in the vicinity of the $7/2^{-}$ resonance. This may help resolve some of the ambiguities in results between the $\mathcal{D}_{CS}$ and $\mathcal{D}_{CSB}$ analyses.

- Ab initio constraints, e.g., on ANCs could be incorporated in the analysis.
- Data from transfer reactions that provided complementary information on the ^{7}Be ANCs.

Future applications of BRICK could include posteriors for astrophysical reaction rates. This would enhance BRICK's utility as a tool for performing detailed uncertainty quantification on nuclear reactions, especially those of astrophysical interest. AZURE2 already includes the necessary functionality. Implementing this feature ought to be a straightforward process.

DATA AVAILABILITY STATEMENT

Publicly available datasets were analyzed in this study. This data can be found here: Data are available on the EXFOR data repository https://www-nds.iaea.org/exfor/. The data measured at TRIUMF using the SONIK gas target will be available in an upcoming publication.

AUTHOR CONTRIBUTIONS

CB and DP formulated the conceptual design of the project. DO was the author of the BRICK code and was the author of the first draft of the manuscript. RD consulted DO to facilitate the interface of the BRICK with AZURE2 codes, perform benchmark calculations, and the calculations for the ^{7}Be system. SP supplied their experimental data for the calculations and consulted on its analysis. CB and RD collected and interpreted past experimental data from the literature. All authors contributed to the critical discussions of the research, writing, revising, reading, and approving the submitted manuscript.

FUNDING

This work was supported by the U.S. Department of Energy, National Nuclear Security Agency under Award DE-NA0003883, and Office of Science, Office of Nuclear Physics, under Award DE-FG02-93 ER-40756, as well as by the National Science Foundation under grants OAC-2004601 (CSSI program, BAND collaboration), PHY-2011890 (University of Notre Dame Nuclear Science Laboratory), and PHY-1430152 (the Joint Institute for Nuclear Astrophysics - Center for the Evolution of the Elements). This research utilized resources from the Notre Dame Center for Research Computing.

ACKNOWLEDGMENTS

We thank Maheshwor Poudel and Xilin Zhang for helpful discussions.

SUPPLEMENTARY MATERIAL

The Supplementary Material for this article can be found online at: https://www.frontiersin.org/articles/10.3389/fphy.2022.888476/full#supplementary-material

REFERENCES

1. Lane AM, Thomas RG. *R*-matrix Theory of Nuclear Reactions. *Rev Mod Phys* (1958) 30:257–353. doi:10.1103/RevModPhys.30.257
2. Brown DA, Chadwick MB, Capote R, Kahler AC, Trkov A, Herman MW, et al. ENDF/B-VIII.0: The 8 Th Major Release of the Nuclear Reaction Data Library with CIELO-Project Cross Sections, New Standards and Thermal Scattering Data. *Nucl Data Sheets* (2018) 148:1–142. doi:10.1016/j.nds.2018.02.001
3. Azuma RE, Uberseder E, Simpson EC, Brune CR, Costantini H, de Boer RJ, et al. AZURE: AnR-Matrix Code for Nuclear Astrophysics. *Phys Rev C* (2010) 81:045805. doi:10.1103/PhysRevC.81.045805
4. Descouvemont P, Adahchour A, Angulo C, Coc A, Vangioni-Flam E. Big-Bang Reaction Rates within the *R*-Matrix Model. *Nucl Phys ANuclei Cosmos VIII* (2005) 758:783–6. doi:10.1016/j.nuclphysa.2005.05.140
5. ENSDF. *From ENSDF Database as of April 12, 2022* (2022). Version available from: http://www.nndc.bnl.gov/ensarchivals/ (Accessed January 10, 2021).
6. Smith DL, Badikov SA, Gai EV, Oh S-Y, T. Kawano NML, Pronyaev VG. Perspectives on Peelle's Pertinent Puzzle. In: *International Evaluation of Neutron Cross-Section Standards*. Wagramer Strasse 5, P.O. Box 100, 1400 Vienna, Austria: International Atomic Energy Agency (2007). p. 46–83.
7. deBoer RJ, Görres J, Smith K, Uberseder E, Wiescher M, Kontos A, et al. Monte Carlo Uncertainty of theHe3(α,γ)Be7reaction Rate. *Phys Rev C* (2014) 90:035804. doi:10.1103/PhysRevC.90.035804
8. Schindler MR, Phillips DR. Bayesian Methods for Parameter Estimation in Effective Field Theories. *Ann Phys* (2009) 324:682–708. doi:10.1016/j.aop.2008.09.003
9. Furnstahl RJ, Phillips DR, Wesolowski S. A Recipe for EFT Uncertainty Quantification in Nuclear Physics. *J Phys G: Nucl Part Phys* (2015) 42:034028. doi:10.1088/0954-3899/42/3/034028
10. Furnstahl RJ, Klco N, Phillips DR, Wesolowski S. Quantifying Truncation Errors in Effective Field Theory. *Phys Rev C* (2015) 92:024005. doi:10.1103/PhysRevC.92.024005
11. Zhang X, Nollett KM, Phillips DR. Halo Effective Field Theory Constrains the Solar ^{7}Be + P → ^{8}B + γ Rate. *Phys Lett B* (2015) 751:535–40. doi:10.1016/j.physletb.2015.11.005
12. Melendez JA, Wesolowski S, Furnstahl RJ. Bayesian Truncation Errors in Chiral Effective Field Theory: Nucleon-Nucleon Observables. *Phys Rev C* (2017) 96:024003. doi:10.1103/PhysRevC.96.024003
13. Wesolowski S, Furnstahl RJ, Melendez JA, Phillips DR. Exploring Bayesian Parameter Estimation for Chiral Effective Field Theory Using Nucleon-Nucleon Phase Shifts. *J Phys G: Nucl Part Phys* (2019) 46:045102. doi:10.1088/1361-6471/aaf5fc
14. Neufcourt L, Cao Y, Giuliani S, Nazarewicz W, Olsen E, Tarasov OB. Beyond the Proton Drip Line: Bayesian Analysis of Proton-Emitting Nuclei. *Phys Rev C* (2020) 101:014319. doi:10.1103/PhysRevC.101.014319
15. Neufcourt L, Cao Y, Nazarewicz W, Olsen E, Viens F. Neutron Drip Line in the Ca Region from Bayesian Model Averaging. *Phys Rev Lett* (2019) 122:062502. doi:10.1103/PhysRevLett.122.062502
16. King GB, Lovell AE, Neufcourt L, Nunes FM. Direct Comparison between Bayesian and Frequentist Uncertainty Quantification for Nuclear Reactions. *Phys Rev Lett* (2019) 122:232502. doi:10.1103/PhysRevLett.122.232502
17. Melendez JA, Furnstahl RJ, Phillips DR, Pratola MT, Wesolowski S. Quantifying Correlated Truncation Errors in Effective Field Theory. *Phys Rev C* (2019) 100:044001. doi:10.1103/PhysRevC.100.044001

18. Filin AA, Baru V, Epelbaum E, Krebs H, Möller D, Reinert P. Extraction of the Neutron Charge Radius from a Precision Calculation of the Deuteron Structure Radius. *Phys Rev Lett* (2020) 124:082501. doi:10.1103/PhysRevLett.124.082501
19. Drischler C, Furnstahl RJ, Melendez JA, Phillips DR. How Well Do We Know the Neutron-Matter Equation of State at the Densities inside Neutron Stars? A Bayesian Approach with Correlated Uncertainties. *Phys Rev Lett* (2020) 125: 202702. doi:10.1103/PhysRevLett.125.202702
20. Drischler C, Melendez JA, Furnstahl RJ, Phillips DR. Quantifying Uncertainties and Correlations in the Nuclear-Matter Equation of State. *Phys Rev C* (2020) 102:054315. doi:10.1103/PhysRevC.102.054315
21. Premarathna P, Rupak G. Bayesian Analysis of Capture Reactions $$\varvec{3}\hbox {He}\varvec{(\alpha ,\gamma)7}\hbox {Be}$$ and $$\varvec{3}\hbox {H}\varvec{(\alpha ,\gamma)7}\hbox {Li}$$. *Eur Phys J A* (2020) 56:166. doi:10.1140/epja/s10050-020-00113-z
22. Zhang X, Nollett KM, Phillips DR. S-factor and Scattering-Parameter Extractions from ${}^{3}\mathrm{He}+{}^{4}\mathrm{He}{ \rightarrow }^{7}\mathrm{Be}+\gamma $. *J Phys G: Nucl Part Phys* (2020) 47:054002. doi:10.1088/1361-6471/ab6a71
23. Filin AA, Möller D, Baru V, Epelbaum E, Krebs H, Reinert P. High-accuracy Calculation of the Deuteron Charge and Quadrupole Form Factors in Chiral Effective Field Theory. *Phys Rev C* (2021) 103:024313. doi:10.1103/PhysRevC.103.024313
24. Schunck N, Quinlan KR, Bernstein J. A Bayesian Analysis of Nuclear Deformation Properties with Skyrme Energy Functionals. *J Phys G: Nucl Part Phys* (2020) 47:104002. doi:10.1088/1361-6471/aba4fa
25. Neufcourt L, Cao Y, Giuliani SA, Nazarewicz W, Olsen E, Tarasov OB. Quantified Limits of the Nuclear Landscape. *Phys Rev C* (2020) 101: 044307. doi:10.1103/PhysRevC.101.044307
26. Everett D, Ke W, Paquet J-F, Vujanovic G, Bass SA, Du L, et al. Multisystem Bayesian Constraints on the Transport Coefficients of QCD Matter. *Phys Rev C* (2021) 103:054904. doi:10.1103/PhysRevC.103.054904
27. Catacora-Rios M, King GB, Lovell AE, Nunes FM. Statistical Tools for a Better Optical Model. *Phys Rev C* (2021) 104:064611. doi:10.1103/PhysRevC.104.064611
28. Reinert P, Krebs H, Epelbaum E. Precision Determination of Pion-Nucleon Coupling Constants Using Effective Field Theory. *Phys Rev Lett* (2021) 126: 092501. doi:10.1103/PhysRevLett.126.092501
29. Phillips DR, Furnstahl RJ, Heinz U, Maiti T, Nazarewicz W, Nunes FM, et al. Get on the BAND Wagon: A Bayesian Framework for Quantifying Model Uncertainties in Nuclear Dynamics. *J Phys G: Nucl Part Phys* (2021) 48:072001. doi:10.1088/1361-6471/abf1df
30. Wesolowski S, Svensson I, Ekström A, Forssén C, Furnstahl RJ, Melendez JA, et al. Rigorous Constraints on Three-Nucleon Forces in Chiral Effective Field Theory from Fast and Accurate Calculations of Few-Body Observables. *Phys Rev C* (2021) 104:064001. doi:10.1103/PhysRevC.104.064001
31. Schnabel G, Capote R, Koning A, Brown D. *Nuclear Data Evaluation with Bayesian Networks* (2021).
32. Xu J, Zhang Z, Li B-A. Bayesian Uncertainty Quantification for Nuclear Matter Incompressibility. *Phys Rev C* (2021) 104:054324. doi:10.1103/PhysRevC.104.054324
33. Cao S, Chen Y, Coleman J, Mulligan J, Jacobs PM, Soltz RA, et al. Determining the Jet Transport Coefficient $\hat{q}$ from Inclusive Hadron Suppression Measurements Using Bayesian Parameter Estimation from Inclusive Hadron Suppression Measurements Using Bayesian Parameter Estimation. *Phys Rev C* (2021) 104:024905. doi:10.1103/PhysRevC.104.024905
34. Hamaker A, Leistenschneider E, Jain R, Bollen G, Giuliani SA, Lund K, et al. Precision Mass Measurement of Lightweight Self-Conjugate Nucleus 80Zr. *Nat Phys* (2021) 17:1408–12. doi:10.1038/s41567-021-01395-w
35. Uberseder E, deBoer RJ. *AZURE2 User Manual* (2015).
36. Foreman-Mackey D, Hogg DW, Lang D, Goodman J. Emcee: The MCMC Hammer. *Publications Astronomical Soc Pac* (2013) 125:306–12. doi:10.1086/670067
37. Bahcall JN, Ulrich RK. Solar Models, Neutrino Experiments, and Helioseismology. *Rev Mod Phys* (1988) 60:297–372. doi:10.1103/RevModPhys.60.297
38. Cyburt RH, Fields BD, Olive KA, Yeh T-H. Big Bang Nucleosynthesis: Present Status. *Rev Mod Phys* (2016) 88:015004. doi:10.1103/RevModPhys.88.015004
39. Kontos A, Uberseder E, deBoer R, Görres J, Akers C, Best A, et al. AstrophysicalSfactor of ^{3}He(α,γ)^{7}Be. *Phys Rev C* (2013) 87:065804. doi:10.1103/PhysRevC.87.065804
40. Brown TAD, Bordeanu C, Snover KA, Storm DW, Melconian D, Sallaska AL, et al. ^{3}He+^{4}He→^{7}Be astrophysical *S* factor. *Phys Rev C* (2007) 76:055801. doi:10.1103/PhysRevC.76.055801
41. Costantini H, Bemmerer D, Confortola F, Formicola A, Gyürky G, Bezzon P, et al. The S-Factor at Solar Energies: The Prompt γ experiment at LUNA. *Nucl Phys A* (2008) 814:144–58. doi:10.1016/j.nuclphysa.2008.09.014
42. Singh BS, Hass M, Nir-El Y, Haquin G. New Precision Measurement of the ^{3}He(^{4}He, γ) ^{7}Be Cross Section Cross Section. *Phys Rev Lett* (2004) 93:262503. doi:10.1103/PhysRevLett.93.262503
43. Carmona-Gallardo M, Nara Singh BS, Borge MJG, Briz JA, Cubero M, Fulton BR, et al. New Measurement of the ^{3}He(α,γ)^{7}Be Cross Section at Medium Energies. *Phys Rev C* (2012) 86:032801. doi:10.1103/PhysRevC.86.032801
44. Bordeanu C, Gyürky G, Halász Z, Szücs T, Kiss GG, Elekes Z, et al. Activation Measurement of the Reaction Cross Section at High Energies. *Nucl Phys A* (2013) 908:1–11. doi:10.1016/j.nuclphysa.2013.03.012
45. Di Leva A, Gialanella L, Kunz R, Rogalla D, Schürmann D, Strieder F, et al. Stellar and Primordial Nucleosynthesis of ^{7}Be: Measurement of ^{3}He(α,γ)^{7}Be. *Phys Rev Lett* (2009) 102:232502. doi:10.1103/PhysRevLett.102.232502
46. Szücs T, Kiss GG, Gyürky G, Halász Z, Szegedi TN, Fülöp Z. Cross Section of ^{3}He(α,γ)^{7}Be Around the ^{7}Be Proton Separation Threshold. *Phys Rev C* (2019) 99:055804. doi:10.1103/PhysRevC.99.055804
47. Adelberger EG, García A, Robertson RGH, Snover KA, Balantekin AB, Heeger K, et al. Solar Fusion Cross Sections. II. Theppchain and CNO Cycles. *Rev Mod Phys* (2011) 83:195–245. doi:10.1103/RevModPhys.83.195
48. Tursunov EM, Turakulov SA, Kadyrov AS. Analysis of the ^{3}He(α,γ)^{7}Be and ^{3}H(α,γ)^{7}Li Astrophysical Direct Capture Reactions in a Modified Potential-Model Approach. *Nucl Phys A* (2021) 1006:122108. doi:10.1016/j.nuclphysa.2020.122108
49. Nollett KM. Radiativeα-capture Cross Sections from Realistic Nucleon-Nucleon Interactions and Variational Monte Carlo Wave Functions. *Phys Rev C* (2001) 63:054002. doi:10.1103/PhysRevC.63.054002
50. Neff T. Microscopic Calculation of the ^{3}He(α,γ)^{7}Be and ^{3}H(α,γ)^{7}Li Capture Cross Sections Using Realistic Interactions. *Phys Rev Lett* (2011) 106:042502. doi:10.1103/PhysRevLett.106.042502
51. Dohet-Eraly J, Navrátil P, Quaglioni S, Horiuchi W, Hupin G, Raimondi F. ^{3}He(α,γ)^{7}Be and ^{3}H(α,γ)^{7}Li Astrophysical S Factors from the No-Core Shell Model with Continuum. *Phys Lett B* (2016) 757:430–6. doi:10.1016/j.physletb.2016.04.021
52. Vorabbi M, Navrátil P, Quaglioni S, Hupin G. ^{7}Be and ^{7}Li Nuclei within the No-Core Shell Model with Continuum. *Phys Rev C* (2019) 100:024304. doi:10.1103/PhysRevC.100.024304
53. Barnard ACL, Jones CM, Weil JL. Elastic Scattering of 2-11 MeV Protons by He^{4}. *Nucl Phys* (1964) 50:604–20. doi:10.1016/0029-5582(64)90233-0
54. Paneru SN, Brune CR, Connolly D, Karpesky J, Davids B, Ruiz C, et al. *Elastic Scattering of ^{3}He + ^{4}He with SONIK* (2022). Unpublished.
55. deBoer RJ, Görres J, Wiescher M, Azuma RE, Best A, Brune CR, et al. The ^{12}C(α,γ)^{16}O Reaction and its Implications for Stellar Helium Burning. *Rev Mod Phys* (2017) 89:035007. doi:10.1103/RevModPhys.89.035007
56. Brune CR. Alternative Parametrization ofR-Matrix Theory. *Phys Rev C* (2002) 66:044611. doi:10.1103/PhysRevC.66.044611
57. Mukhamedzhanov AM, Tribble RE. Connection between Asymptotic Normalization Coefficients, Subthreshold Bound States, and Resonances. *Phys Rev C* (1999) 59:3418–24. doi:10.1103/PhysRevC.59.3418
58. Mukhamedzhanov AM, Gagliardi CA, Tribble RE. Asymptotic Normalization Coefficients, Spectroscopic Factors, and Direct Radiative Capture Rates. *Phys Rev C* (2001) 63:024612. doi:10.1103/PhysRevC.63.024612
59. Kiss GG, La Cognata M, Spitaleri C, Yarmukhamedov R, Wiedenhöver I, Baby LT, et al. Astrophysical S-Factor for the ^{3}He(α,γ)^{7}Be Reaction via the Asymptotic Normalization Coefficient (ANC) Method. *Phys Lett B* (2020) 807:135606. doi:10.1016/j.physletb.2020.135606
60. Tilley DR, Cheves CM, Godwin JL, Hale GM, Hofmann HM, Kelley JH, et al. Energy Levels of Light Nuclei A=5, 6, 7. *Nucl Phys A* (2002) 708:3–163. doi:10.1016/S0375-9474(02)00597-3
61. Paneru SN. *Elastic Scattering of ^{3}He+^{4}He with SONIK*. Ph.D. thesis. Athens, OH, USA: Ohio University (2020).

62. D'Agostini G. On the Use of the Covariance Matrix to Fit Correlated Data. *Nucl Instr Methods Phys Res Section A: Acc Spectrometers, Detectors Associated Equipment* (1994) 346:306–11. doi:10.1016/0168-9002(94)90719-6
63. Connolly D. *Radiative Alpha Capture on S_{34} at Astrophysically Relevant Energies and Design of a Scattering Chamber for High Precision Elastic Scattering Measurements for the DRAGON experiment*. Ph.D. thesis. Golden, CO, USA: Colorado School of Mines (2015).
64. Cyburt RH, Davids B. Evaluation of modern ^{3}He(α,γ)^{7}Be data. *Phys Rev C* (2008) 78:064614. doi:10.1103/PhysRevC.78.064614
65. Gyürky G, Confortola F, Costantini H, Formicola A, Bemmerer D, Bonetti R, et al. ^{3}He(α,γ)^{7}Be cross Section at Low Energies. *Phys Rev C* (2007) 75:035805. doi:10.1103/PhysRevC.75.035805
66. Confortola F, Bemmerer D, Costantini H, Formicola A, Gyürky G, Bezzon P, et al. AstrophysicalSfactor of the ^{3}He(α,γ)^{7}Be reaction Measured at Low Energy via Detection of Prompt and Delayed γ Rays. *Phys Rev C* (2007) 75:065803. doi:10.1103/PhysRevC.75.065803
67. Hamilton J, Øverbö I, Tromborg B. Coulomb Corrections in Non-relativistic Scattering. *Nucl Phys B* (1973) 60:443–77. doi:10.1016/0550-3213(73)90193-4
68. van Haeringen H. T Matrix and Effective Range Function for Coulomb Plus Rational Separable Potentials Especially for I=1. *J Math Phys* (1977) 18:927–40. doi:10.1063/1.523373
69. Humblet J. Bessel Function Expansions of Coulomb Wave Functions. *J Math Phys* (1985) 26:656–9. doi:10.1063/1.526602
70. Poudel M, Phillips DR. *Effective Field Theory Analysis of ^{3}He-α Scattering Data* (2021).

Conflict of Interest: The authors declare that the research was conducted in the absence of any commercial or financial relationships that could be construed as a potential conflict of interest.

frontiers | Frontiers in Physics

TYPE Original Research
PUBLISHED 22 August 2022
DOI 10.3389/fphy.2022.901954

OPEN ACCESS

EDITED BY
Christian Forssén,
Chalmers University of Technology, Sweden

REVIEWED BY
Norbert Kaiser,
Technical University of Munich, Germany
Christopher Koerber,
Ruhr University Bochum, Germany

*CORRESPONDENCE
I. K. Alnamlah,
ialnamlah@ksu.edu.sa

SPECIALTY SECTION
This article was submitted to Nuclear Physics, a section of the journal Frontiers in Physics

RECEIVED 22 March 2022
ACCEPTED 05 July 2022
PUBLISHED 22 August 2022

CITATION
Alnamlah IK, Coello Pérez EA and Phillips DR (2022), Analyzing rotational bands in odd-mass nuclei using effective field theory and Bayesian methods.
Front. Phys. 10:901954.
doi: 10.3389/fphy.2022.901954

Analyzing rotational bands in odd-mass nuclei using effective field theory and Bayesian methods

I. K. Alnamlah[1,2]*, E. A. Coello Pérez[3] and D. R. Phillips[1]

[1]Institute of Nuclear and Particle Physics and Department of Physics and Astronomy, Ohio University, Athens, OH, United States, [2]Department of Physics and Astronomy, King Saud University, Riyadh, Saudi Arabia, [3]Lawrence Livermore National Laboratory, Livermore, CA, United States

We recently developed an Effective Field Theory (EFT) for rotational bands in odd-mass nuclei. Here we use EFT expressions to perform a Bayesian analysis of data on the rotational energy levels of ^{99}Tc, ^{155,157}Gd, ^{159}Dy, ^{167,169}Er, ^{167,169}Tm, ^{183}W, ^{235}U and ^{239}Pu. The error model in our Bayesian analysis includes both experimental and EFT truncation uncertainties. It also accounts for the fact that low-energy constants (LECs) at even and odd orders are expected to have different sizes. We use Markov Chain Monte Carlo (MCMC) sampling to explore the joint posterior of the EFT and error-model parameters and show both the LECs and the breakdown scale can be reliably determined. We extract the LECs up to fourth order in the EFT and find that, provided we correctly account for EFT truncation errors in our likelihood, results for lower-order LECs are stable as we go to higher orders. LEC results are also stable with respect to the addition of higher-energy data. We extract the expansion parameter for all the nuclei listed above and find a clear correlation between the extracted and the expected value of the inverse breakdown scale, W, based on the single-particle and vibrational energy scales. However, the W that actually determines the convergence of the EFT expansion is markedly smaller than would be naively expected based on those scales.

KEYWORDS

EFT, bayesian analysis, rotational bands, collective models, nuclear structure

1 Introduction

Rotational bands are ubiquitous in the spectra of medium-mass and heavy nuclei. As has been known for 70 years [1], they emerge in a description of the nucleus as a nearly rigid axially-symmetric rotor [2]. For even-even nuclei the simplest rotational bands consist of 0^+, 2^+, ... states and their energies are described by an expansion in powers of $I(I+1)$, where I is the spin of the rotational state [3, 4]. This behavior has recently been obtained in *ab initio* calculations of the Be isotope chain [5–9] and ^{34}Mg [10].

Odd-mass neighbors of a rotor nucleus can then be understood as a fermion coupled to the rotor. The fermion dynamics is simpler in the intrinsic frame in which the nucleus is not rotating, but this frame is non-inertial, so solving the problem there induces a Coriolis

force proportional to $\vec{j}\cdot\vec{I}$, the dot product of the single-fermion angular momentum and the total angular momentum of the fermion-rotor system. When combined with other mechanisms, such as excitation of the fermion to higher-single particle states and the fermion disturbing the rotor, this induces a string of terms in the energy-level formula [11]. Odd powers of I appear, and produce staggering between adjacent levels. Which powers of I are present depends on the value of the quantum number, K, the projection of the fermion angular momentum on the rotor axis. For $K = 1/2$ bands the energy-level formula is:

$$E(I) = A_K I(I+1) + E_K + A_1(-1)^{I+1/2}(I+1/2) + B_1 I(I+1)(-1)^{I+1/2}\left(I+\frac{1}{2}\right) + B_K[I(I+1)]^2 \quad (1)$$

where A_K, E_K, A_1, B_1, and B_K are parameters, related to rotor properties and single-particle matrix elements, that need to be either derived from a microscopic model or estimated from data.

Over the years a number of models have had success describing this pattern from underlying density functional theory [12–15] or shell-model [15–18] dynamics. The models also predict specific values for the coefficients that appear in Eq. 1. In Ref. [19] we took a different approach, organizing formula (1) as an effective field theory (EFT) expansion in powers of the small parameter, Q. For values of I appreciably larger than one the expansion parameter should be modified to $Q = I/I_{\{br\}}$, with $I_{\{br\}}$ the spin of the nuclear state at which dynamical effects associated with single-particle and/or vibrational degrees of freedom cause the polynomial expansion in powers of I to break down. To simplify our later presentation we notate the inverse of the breakdown scale as $W \equiv 1/I_{\{br\}}$. We then have Q=IW. This description of rotational bands in odd-mass nuclei builds on the successful EFT developed for even-even nuclei in Refs. [3, 4]. Other efforts to develop an EFT for these rotational bands can be found in Refs. [20, 21].

In the odd-mass rotor EFT, Eq. 1 is the next-to-next-to-next-to-next-to leading order (N^{4}LO) result for the energies, and the first corrections to it are $\mathcal{O}(EQ^4)$. The EFT analysis of Eq. 1 organizes it in terms of increasingly accurate predictions: the N^{k}LO energy-level formula has accuracy $\mathcal{O}(EQ^k)$. All short-distance/high-energy physical mechanisms that affect the energies up to that accuracy are subsumed into the parameters or low-energy constants (LECs) that multiply the I-dependent terms in Eq. 1. In Ref. [19] we determined these LECs by fitting the lowest levels in the different rotational bands we analyzed. However, this runs the risk of fine-tuning the values of the LECs to those levels, and it does not provide uncertainty estimates for them. Better parameter estimation would use all the data available on a particular band, and account for the $\mathcal{O}(EQ^k)$ truncation uncertainty present at order N^{k}LO [31, 32].

Bayesian methods for EFT parameter estimation do just that [32–35]. Reference [34] showed that the effect of neglected terms in the EFT expansion could be included in the error model by modifying the likelihood so that the covariance matrix that appears there includes both experimental uncertainties and EFT truncation errors. More recently, Ref. [35] showed that MCMC sampling of that likelihood enabled the simultaneous determination of the LECs and the parameters of the error model, i.e., the value of W and the typical size of the "order one" dimensionless coefficients that appear in the EFT expansion.

In this work we apply the EFT parameter estimation technology developed in Refs. [32–35] to the problem of rotational bands in odd-mass nuclei. We consider $K = 1/2$ bands in ^{99}Tc, ^{167,169}Er, ^{167,169}Tm, ^{183}W, ^{235}U and ^{239}Pu as well as $K = 3/2$ bands in ^{155,157}Gd and ^{159}Dy. Section 2 summarizes the elements of the EFT that are relevant for this paper. Section 3 then develops the Bayesian statistical model we use to analyze data on rotational bands. We first write down the likelihood that includes both experimental and theory uncertainties, and then explain how we use known information on the expected size of the LECs and the expansion parameter to set priors. A novel feature of this work, compared to earlier Bayesian EFT parameter-estimation studies, is that our statistical model incorporates the possibility that the LECs at even and odd orders have different typical sizes. This reflects the physics of odd-order LECs that are associated with matrix elements of the fermion spin, while even-order LECs contain a combination of effects from the rotor and the fermion. Section 4 contains details of our Markov Chain Monte Carlo sampler, and then Section 5 presents the results for LECs and the inverse breakdown scale, W, that we obtain from sampling the Bayesian posterior. We conclude in Section 6. All the results and figures generated from this work can be reproduced using publicly available Jupyter notebooks [36].

2 Rotational EFT background

Here we summarize the results of the EFT for rotational bands in odd-mass nuclei that was developed up to fourth order in the angular velocity of the system in Ref. [19]. This theory constructs the Lagrangian of the particle-rotor system using its angular velocity and the angular momentum of the unpaired fermion, $\vec{j}$, as building blocks. The resulting Lagrangian corrects that of a rigid rotor with contributions arranged as a series in powers of a small expansion parameter, $Q = W*I$, according to a power-counting scheme that counts powers of the system's angular velocity. Naively, we expect W to be of order $E_{\rm rot}/E_{\rm high}$, where $E_{\rm rot}$ is the energy scale at which rotational excitation take place and $E_{\rm high}$ is the scale of high-energy physics not explicitly taken into account by the EFT. At leading order (LO), the energy of a rotational band on top of a bandhead with spin K is

$$E_{\rm LO}(I,K) = A_{\rm rot} I(I+1) + E_K, \quad (2)$$

where I is the spin of the rotational state (or, equivalently, the total angular momentum of the fermion-rotor system), and $A_{\rm rot}$ and E_K are LECs that must be fitted to experimental data. $A_{\rm rot}$ is determined by the moment of inertia of the even-even nucleus (the rotor) to which the unpaired fermion is coupled.

At next-to-leading order (NLO) rotational bands with $K = 1/2$ are affected by a term that takes the same $\vec{j}\cdot\vec{I}$ form as the Coriolis force. This produces:

$$E_{\rm NLO}(I,K) = A_{\rm rot} I(I+1) + E_K + A_1(-1)^{I+1/2}\left(I+\frac{1}{2}\right)\delta^K_{1/2}, \tag{3}$$

where $\delta^K_{K'}$ is the Kronecker delta. The LEC A_1 is expected to be of order $A_{\rm rot}$ times a sum of matrix elements involving the fermion's total angular momentum operator (for details see Ref. [19]). From previous studies we see that $A_1/A_{\rm rot} < 1$. This correction, sometimes called the signature term, causes staggering between adjacent states in $K = 1/2$ bands.

The energy of a rotational band at next-to-next-to-leading order (N^{2}LO) is

$$E_{\rm N^2LO}(I,K) = A_K I(I+1) + E_K + A_1(-1)^{I+1/2}\left(I+\frac{1}{2}\right)\delta^K_{1/2}. \tag{4}$$

The term proportional to A_K combines the LO term proportional to $A_{\rm rot}$ and corrections entering at this order with the same spin dependence. From our power counting we expect the shift $\Delta A = A_{\rm rot} - A_K$ to be of order $A_{\rm rot}W$. In contrast to $A_{\rm rot}$, A_K is band dependent and so should be fitted to data on the rotational band of interest.

The N^{3}LO corrections to the energy of a rotational band are both $\sim I^3$ for $I \gg 1$, but take a different form in the $K = 1/2$ and $K = 3/2$ bands:

$$\Delta E_{\rm N^3LO}(I,K) = B_1(-1)^{I+1/2}\left(I+\frac{1}{2}\right)I(I+1)\delta^K_{1/2} + A_3(-1)^{I+3/2}\left(I+\frac{1}{2}\right)\left(I-\frac{1}{2}\right)\left(I+\frac{3}{2}\right)\delta^K_{3/2}. \tag{5}$$

with B_1 and A_3 expected to be of order A_1W^2. Last, at N^{4}LO we have the additional term:

$$\Delta E_{\rm N^4LO}(I,K) = B_K[I(I+1)]^2. \tag{6}$$

with B_K expected to be of order $A_{\rm rot}W^3$.

This pattern continues: at odd orders we add terms that correct the staggering term and have LECs of order A_1W^{n-1}, while the even-order terms provide the overall trend with I and have LECs of order $A_{\rm rot}W^{n-1}$. (In both cases n is the order of our expansion.) This difference in the expected sizes of odd and even LECs comes from the physics. Odd-order LECs are associated with operators in the effective Lagrangian that couple rotor and fermionic degrees of freedom, while even-order LECs encode both rotor-fermion interactions and effects coming from the non-rigidity of the rotor itself.

In what follows we denote the LECs A_1, ΔA, B_1, and B_K generically as $\{a_n: n = 1, \ldots, k\}\equiv\mathbf{a}_k$, where k is the order of the EFT calculation. (In the case of $K = 3/2$ bands the set is ΔA, A_3, and B_K, and $a_1 = 0$.) We then divide the nth-order LEC, a_n, by the reference scale and the power of the inverse breakdown scale assigned to it by the EFT power counting, i.e., construct:

$$c_n = \frac{a_n}{A_{\rm rot}W^{n-1}}. \tag{7}$$

We expect these coefficients c_n to be of order one, i.e., they should be natural coefficients. However, because sets of odd and even natural coefficients seem to have different sizes we will assume the even and odd c_n's are drawn from two different distributions with different characteristic sizes that we denote by $\bar{c}_{even}$ and $\bar{c}_{odd}$.

3 Building the Bayesian model

3.1 Building the posterior

Our goal in this analysis is to use the information on the expected size of LECs to stablize the extraction of their values as we add more levels to the analysis, or as we use energy-level formulae computed at different EFT orders. At the same time, we want to estimate the inverse breakdown scale, W, of the theory, as well as the characteristic sizes for even and odd coefficients, $\bar{c}_{even}$ and $\bar{c}_{odd}$.

We want to obtain the posterior distribution for all the LECs that appear at order k, a set we collectively denote by $\mathbf{a}_k$. Here we will obtain the joint posterior pdf of $\mathbf{a}_k$, the inverse breakdown scale, W, and the characteristic sizes. To do this we follow the successful endeavor by the BUQEYE collaboration in Refs. [33–35], and write the posterior, given experimental data, $\vec{y}_{exp}$, and prior information on the model, $P*$, as

$$\begin{aligned}\mathrm{pr}\left(\mathbf{a}_k, W, \bar{c}_{even}, \bar{c}_{odd}|\vec{y}_{exp}, P*\right) = {}& \mathrm{pr}\left(\mathbf{a}_k|W, \bar{c}_{even}, \bar{c}_{odd}, \vec{y}_{exp}, P*\right)\\ &\times \mathrm{pr}\left(W|\bar{c}_{even}, \bar{c}_{odd}, \vec{y}_{exp}, P*\right)\\ &\times \mathrm{pr}\left(\bar{c}_{even}|\bar{c}_{odd}, \vec{y}_{exp}, P*\right)\\ &\times \mathrm{pr}\left(\bar{c}_{odd}|\vec{y}_{exp}, P*\right).\end{aligned} \tag{8}$$

Marginalization of this posterior distribution over W, $\bar{c}_{even}$ and $\bar{c}_{odd}$ yields the posterior distribution for $\mathbf{a}_k$. Other marginalizations can be carried out to obtain posteriors for W, $\bar{c}_{even}$ and $\bar{c}_{odd}$.

This joint posterior distribution tells us the probability of the LECs and the error model parameters given experimental data. We could use this posterior distribution to get other quantities or observables, such as the energy of a particular rotational level, which depend on the LECs or the error model parameters. These are now represented by distributions and not single numbers. Their distributions are called posterior predictive distributions (PPD). We write the PPD of an observable $\mathcal{O}$ as

$$\mathrm{pr}\left(\mathcal{O}|\vec{y}_{exp}, P*\right) = \int d\vec{\theta}\delta\left(\mathcal{O} - \mathcal{O}\left(\vec{\theta}\right)\right)\mathrm{pr}\left(\vec{\theta}|\vec{y}_{exp}, P*\right) \quad (9)$$

where $\vec{\theta}$ represents the LECs and the error model parameters. Calculating the observable at each point in the parameter space $\vec{\theta}$ and then integrating over the parameters $\vec{\theta}$ allows one to carefully account for correlations between the parameters.

Using Bayes' theorem, we can express the posterior of Eq. 8 as

$$\begin{aligned}\mathrm{pr}\left(\mathbf{a}_k, W, \bar{c}_{even}, \bar{c}_{odd}|\vec{y}_{exp}, P*\right) = \mathrm{pr}\left(\vec{y}_{exp}|\mathbf{a}_k, W, \bar{c}_{even}, \bar{c}_{odd}, P*\right)\\ \times \mathrm{pr}\left(\mathbf{a}_k|W, \bar{c}_{even}, \bar{c}_{odd}, P*\right)\\ \times \mathrm{pr}\left(W|\bar{c}_{even}, \bar{c}_{odd}, P*\right)\\ \times \mathrm{pr}\left(\bar{c}_{even}|P*\right)\mathrm{pr}\left(\bar{c}_{odd}|P*\right)\\ \times \frac{1}{\mathrm{pr}\left(\vec{y}_{exp}|P*\right)}.\end{aligned} \quad (10)$$

The terms on the right-hand side of Eq. 10 have the following interpretations:

1. $\mathrm{pr}\left(\vec{y}_{exp}|\mathbf{a}_k, W, \bar{c}_{even}, \bar{c}_{odd}, P*\right)$ is the likelihood of the experimental data given specific values of both the LECs that appear in the energy formula at order k and the parameters in our error model.
2. $\mathrm{pr}\left(\mathbf{a}_k|W, \bar{c}_{even}, \bar{c}_{odd}, P*\right)$ is the prior distribution of the LECs given the parameters encoding the systematic expansion of the EFT.
3. $\mathrm{pr}\left(W|\bar{c}_{even}, \bar{c}_{odd}, P*\right)$ is the prior distribution of the inverse breakdown scale given the characteristic sizes of even and odd natural coefficients.
4. $\mathrm{pr}\left(\bar{c}_{even}|P*\right)$ and $\mathrm{pr}\left(\bar{c}_{odd}|P*\right)$ are the prior distributions of the even and odd characteristic sizes (In Eq. 10 we assume an uncorrelated prior on $\bar{c}_{even}$ and $\bar{c}_{odd}$.).
5. $\mathrm{pr}\left(\vec{y}_{exp}|P*\right)$ is the evidence, which we drop in what follows as it does not depend on the parameters we are interested in extracting and functions only as a normalization constant.

3.2 Building the likelihood

We now build the likelihood function accounting for the expected error between the experimental and theoretical values, for data on $K = 1/2$ rotational bands. The corresponding likelihood for $K = 3/2$ bands is built analogously. Following [34] we start by writing our observable (the energy of a particular rotational level) at order k as

$$\begin{aligned}E(I) = A_{\mathrm{rot}}I(I+1)\\ \left\{1 + \sum_{n=odd}^{k} c_n W^{n-1}(-1)^{I+1/2}\left(I+\frac{1}{2}\right)[I(I+1)]^{(n-3)/2}\right.\\ \left. + \sum_{n=even}^{k} c_n W^{n-1}[I(I+1)]^{(n-2)/2}\right\}.\end{aligned} \quad (11)$$

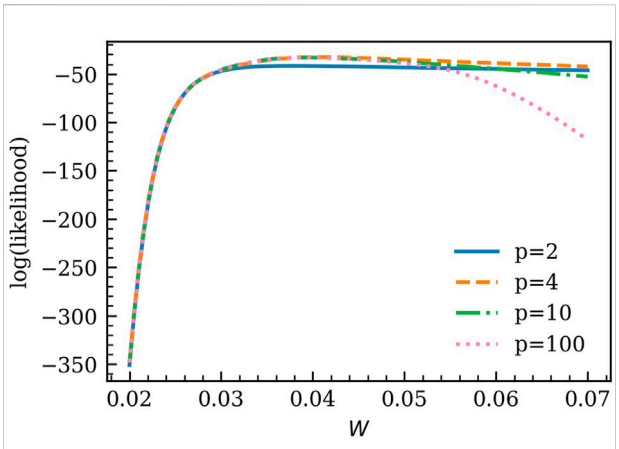

FIGURE 1
Comparing the log of the likelihood when accounting for different number of omitted terms, p, in the theory error. Apart from W, the parameters that enter the likelihood were chosen to be the median parameters after we had sampled the posterior distribution for ^{169}Er.

We choose the leading-order energy for each level, $A_{\mathrm{rot}}I(I+1)$, to be the reference scale E_{ref} for the observable. The dimensionless coefficients c_n (see Eq. 7) are assumed to be $\mathcal{O}(1)$. The theory error $\vec{\sigma}_{th}$ at any order is due to terms omitted from the summations in Eq. 11. Its most significant contribution comes from the first omitted term in the EFT expansion. Accounting only for this term yields an estimate for the theory error that is fully correlated across levels if $k+1$ is even, and anticorrelated for adjacent levels if $k+1$ is odd. To account for this correlation or anticorrelation we write the theory covariance matrix as the outer product of a vector representing the theory error, $\Sigma_{th} \equiv \vec{\sigma}_{th} \otimes \vec{\sigma}_{th}$. The vector $\vec{\sigma}_{th}$ contains the value of the first omitted term for each of the m energy levels that enter the likelihood. We also account for experimental errors by writing the covariance matrix as

$$\Sigma = \Sigma_{th} + \Sigma_{exp} \quad (12)$$

where we take $(\Sigma_{exp})_{ij} \equiv (\vec{\sigma}_{exp})_i^2\delta_{ij}$. The likelihood function is then

$$\mathrm{pr}\left(\vec{y}_{exp}|\mathbf{a}_k, W, \bar{c}_{even}, \bar{c}_{odd}, P*\right) = \sqrt{\frac{1}{(2\pi)^m|\Sigma|}}\exp\left(-\frac{1}{2}\vec{r}^{\,T}\Sigma^{-1}\vec{r}\right), \quad (13)$$

where $\vec{r} \equiv \vec{y}_{exp} - \vec{y}_{th}$ is the residual between the central experimental energy for a level and the theory result from Eq. 11 and m is the number of levels included in the likelihood estimation.

We note that since the theory error is the outer product of the theory error with itself, the theory covariance Σ_{th} is singular. Including the experimental error solves this singularity problem

for the covariance Σ. However, Σ can still become ill-conditioned for higher values of W if the experimental errors are too small; numerical issues then arise when we try to invert the covariance matrix.

Including more terms in the estimate for the theoretical error produces a steeper peak in the likelihood function, see Figure 1, which, in turn, restricts the values sampled for W to a narrower region. Because it precludes the sampler exploring large values of W, this inclusion of more omitted terms in the model of the theoretical error solves the numerical problem of ill-conditioned matrices and gives a more accurate extraction of the LECs and the error-model parameters.

In what follows we estimate the theory error including omitted terms up to a certain cutoff order $k_{\max}$. Our theory error estimate for the level with spin I is then

$$\sigma_{th}(I) = A_{\rm rot} \sum_{l=k+1}^{k_{max}} \bar{c}_{even,odd} W^{l-1} P_l(I), \tag{14}$$

where the $\bar{c}$ that is used here is $\bar{c}_{even}$ for even values of l and $\bar{c}_{odd}$ otherwise. The I-dependence of the lth term is chosen to match that in Eq. 11, and is denoted here by $P_l(I)$, a polynomial of power l. We arrange the contributions to the theory error, Eq. 14 as the p columns of a $m \times p$ matrix σ_{th}, where $p = k_{\max} - k$ is the number of omitted terms. Each column in this matrix then corresponds to the theory-error structure, while each row corresponds to a different energy level. To obtain Σ_{th} we then again take the outer product of σ_{th} with itself, i.e., we construct an outer product in our m-dimensional data space, while also taking an inner product in order space. This results in the theory error associated with different orders being added in quadrature, while maintaining the correlation structure of the theory error across the data space.

3.3 Building the priors

The prior distributions for an order-n LEC is taken to be a Gaussian with mean zero and standard deviation

$$\sigma_n = \begin{cases} A_{\rm rot} \bar{c}_{even} W^{n-1} & \text{if } n \text{ is even;} \\ A_{\rm rot} \bar{c}_{odd} W^{n-1} & \text{if } n \text{ is odd,} \end{cases} \tag{15}$$

encoding the EFT expectations for the sizes of the LECs arising from the power counting described in Section 2. The standard deviation in Eq. 15 allows the possibility for even and odd LECs to have different typical sizes. Combining the Gaussian priors for the LECs yields

$$\mathrm{pr}(\mathbf{a}_k | W, \bar{c}_{even}, \bar{c}_{odd}, P*) = \frac{1}{\bar{E}\sqrt{2\pi}} exp\left(-\frac{E_k^2}{2\bar{E}^2}\right)$$

$$\prod_{n=1}^{k} \frac{1}{\sigma_n \sqrt{2\pi}} \exp\left(-\frac{a_n^2}{2\sigma_n^2}\right). \tag{16}$$

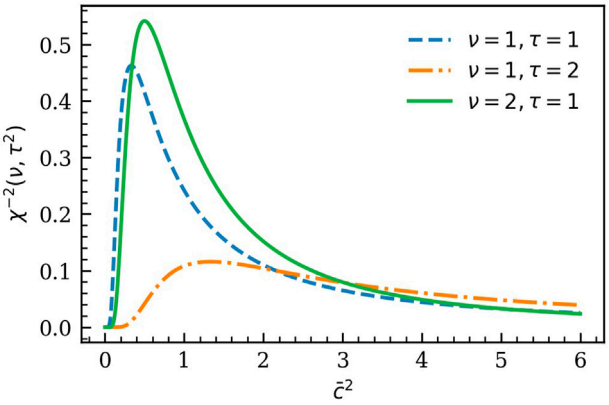

FIGURE 2
Prior distribution of the size of the dimensionless natural coefficients, $\bar{c}$.

The LEC E_K is just an energy shift and its size is not determined by the EFT power counting. We set the prior on it to be Gaussian with mean zero and a standard deviation, $\bar{E}$, that is wide enough to capture its value. The value for $\bar{E}$ is determined from the energy of the bandhead and $A_{\rm rot}$ by means of Eq. 3.

We choose not to impose any expectations regarding the size of the expansion parameter in the prior for W and so take it to be flat between two limits:

$$\mathrm{pr}(W | \bar{c}_{even}, \bar{c}_{odd}, P*) \propto \begin{cases} 1 & W \in (0, W_{cut}) \\ 0 & \text{otherwise.} \end{cases} \tag{17}$$

Limiting W from above restricts the sampler from going to high values of W, as they make the covariance matrix ill-conditioned and harder to invert. For all cases we check that the posterior for W is confined to values well below W_{cut}.

The priors on the characteristic sizes $\bar{c}_{even}$ and $\bar{c}_{odd}$, are taken to be identical scaled-inverse-χ^2 distributions

$$\mathrm{pr}(\bar{c}_l^2 | P*) \propto \begin{cases} \chi^{-2}(\nu = 1, \tau^2 = 1) & \bar{c}_l^2 \in (0, \bar{c}_{cut}^2) \\ 0 & \text{otherwise,} \end{cases} \tag{18}$$

where the cutoff $\bar{c}_{cut}$ prevents numerical issues inverting the covariance matrix. The scaled-inverse-χ^2 distribution, given by

$$\chi^{-2}(x; \nu, \tau^2) = \frac{(\tau^2 \nu/2)^{\nu/2}}{\Gamma(\nu/2)} \frac{\exp\left[-\frac{\nu\tau^2}{2x}\right]}{x^{1+\nu/2}}, \tag{19}$$

is shown for different values of ν and τ in Figure 2. We stress that we chose identical priors for $\bar{c}_{even}$ and $\bar{c}_{odd}$ even though we expect the former to be larger than the latter based on previous analyses of data on rotational bands [19]. We did not want to bias our analysis by imposing this hierarchy on the prior, instead

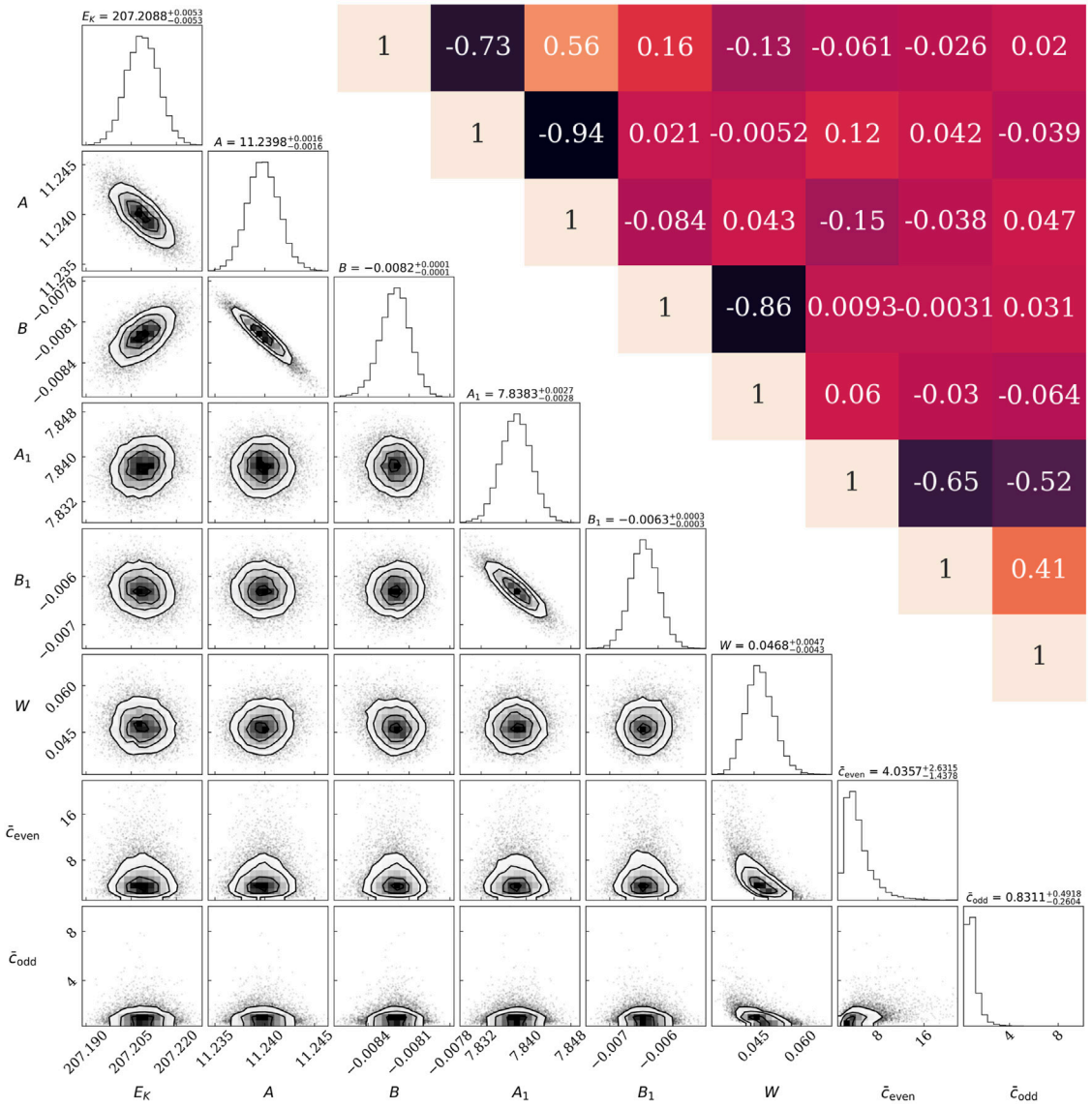

FIGURE 3
Corner plot for the marginalized distributions of the LECs and the error-model parameters at N^{4}LO for ^{167}Er including all adopted rotational levels (I_{max} =16.5) and accounting for six omitted terms in the theory error. The inset in the top right corner shows the correlations between posterior parameters. The order of the parameters on the corner plot is the same on the correlations plot. (Here E_K and all the EFT LECs are expressed in keV. The error-model parameters are dimensionless.)

anticipating that it will emerge naturally in the posteriors for those parameters.

The scaled-inverse-χ^2 favors small values of $\bar{c}^2$ and has long tails. This allows the sampler to explore higher values of $\bar{c}^2$. The sharp decrease in this distribution for very small values of $\bar{c}^2$ could be a problem for cases where $\bar{c}_{odd}$ is much smaller than one. This is a concern in some $K = 3/2$ bands where we expect smaller odd-order corrections to the leading-order energy than in $K = 1/2$ bands.

4 Running the sampler

To sample the posterior distribution in Eq. 10 we use the Python ensemble sampling toolkit for affine-invariant MCMC (emcee) [37]. We run the sampler for each nucleus at a certain EFT order using the m rotational levels from the bandhead up to some I_{max} and accounting for p omitted terms in the theory error. We use 64 walkers to sample the posterior distribution for an initial 10,000 steps. We then continue running the sampler with

3,000 step increments. After every 3,000 steps we calculate the autocorrelation time, τ_α, where α indexes an LEC or an error-model parameter. We declare the sampler to be converged if the sampler meets two criteria. First, the number of steps has to be more than 50 times the highest τ_α. Second, the change in any of the τ_α's has to be less than 2% from its value after the last 3,000 step increment.

To get the posterior distributions we discard 2 ×max (τ_α) steps from the beginning of the chain (*burn-in*) and 0.5 ×min (τ_α) steps in between steps we accept (*thinning*).

A sample corner plot of the marginalized distributions of the LECs and the error-model parameters W, $\bar{c}_{even}$ and $\bar{c}_{odd}$, for the case of ^{167}Er is shown in Figure 3. This figure clearly shows that the posterior distributions for all parameters are fully converged. For this particular case we set $W_{cut} = 0.16$ and $\bar{c}_{cut} = 22$ for both $\bar{c}_{even}$ and $\bar{c}_{odd}$. As explained in Section 3.3, the cutoffs on W and the characteristic sizes prevent the covariance matrix from being ill-conditioned. We also ran the sampler for ^{167}Er at different values of W_{cut} and $\bar{c}_{cut}$ and found that different choices of these hyperparameters do not result in a significant change in the posterior distributions.

For some cases, namely ^{99}Tc and ^{183}W, the posterior distribution of W was initially at the upper limit of the prior. We then ran into numerical problems when increasing W_{cut} trying to encompass the entire posterior. This problem was solved by decreasing the number of levels included in the analysis, i.e., decreasing $I_{\max}$. It was then possible to increase W_{cut} without encountering problems with degenerate matrices. This means that for ^{99}Tc we were only able to extract the LECs and W at $I_{\max} = 11.5$. We note that this is beyond the breakdown scale for this particular nucleus and therefore we believe that the extraction of the LECs and the error model parameters is not as reliable as for the other nuclei considered in this work. For ^{183}W we needed to remove two levels from the upper end of the data set for the sampler to be numerically stable.

In Figure 3 we see clear correlations between E_K, A, and B and also between A_1 and B_1. (Here we have dropped the subscript K on A and B; it is to be understood that all LECs are band dependent.) The correlation coefficients given in the inset in the top-right corner of the figure make the block-diagonal structure of the covariance matrix clear. To a good approximation the correlation matrix can be decomposed into a correlation matrix for even-order LECs, one for odd-order LECs, and one for the error-model parameters.

We note that, as expected, $\bar{c}_{odd}$ is smaller than $\bar{c}_{even}$. Corrections to the energy levels carrying odd powers of I are smaller than those carrying even powers of I. This size difference is connected to different physics correcting the effective Lagrangian at even and odd orders.

To see which of the parameters has the narrowest distribution and therefore places the strongest constraint on the posterior distribution, we did a Singular Value Decomposition (SVD) of the Hessian matrix. We found that the eigenvector with the highest eigenvalue, i.e., the parameter combination with smallest absolute error, is made up mostly of the highest-order LEC. This is unsurprising, since that LEC, B, is markedly smaller than the others (we note that its relative error is actually larger than that on, e.g., A_1).

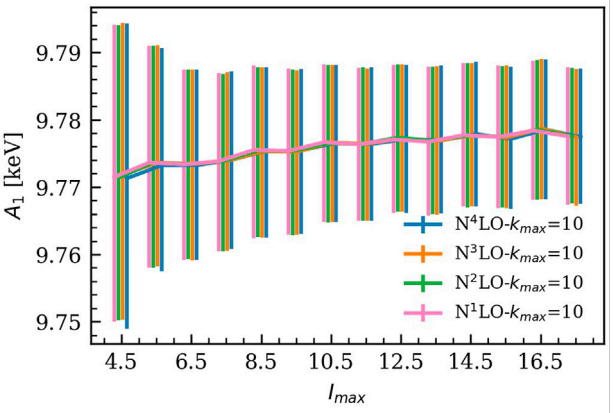

FIGURE 4
Posteriors for A_1 describing ^{169}Er as a function of $I_{\max}$ at different EFT orders. The solid line connects the median values and the error bands encompass the 16th and 84th percentiles of the marginalized distribution.

We initially found a peculiar correlation between LECs in some cases where the rotational band was built on the ground state of the nucleus we were looking at. There we found the eigenvector with the highest eigenvalue was a very particular linear combination that involved all the LECs. We ultimately traced this correlation to the fact that the ground state experimental error had been set to zero, and so the combination of LECs that entered the formula for the ground-state energy was very well constrained (theory error is also very small there). This problem was solved by adding a small experimental error to the ground state. We chose it to be equal to the error that the NNDC quotes on the energy of the first excited state.

5 Results

In this section we show results for our Bayesian analysis of the rotational energy levels in ^{99}Tc, ^{155,157}Gd, ^{159}Dy, ^{167,169}Er, ^{167,169}Tm, ^{183}W, ^{235}U and ^{239}Pu. The experimental data are taken from the National Nuclear Data Center (NNDC) [22–30]. Except for the cases of ^{99}Tc and ^{183}W noted above, we included all levels in a certain rotational band according to the adopted level determination in the NNDC.

5.1 Stable LEC extraction across EFT orders and additional data

In this subsection we show that lower-order LECs extracted for the selected rotational bands are stable across EFT orders and with the addition of high-energy data, provided that we account for enough omitted terms when treating the theory error. For ^{169}Er, ^{167}Er, ^{169}Tm, and ^{239}Pu including omitted terms up to $k_{\max} = 10$,

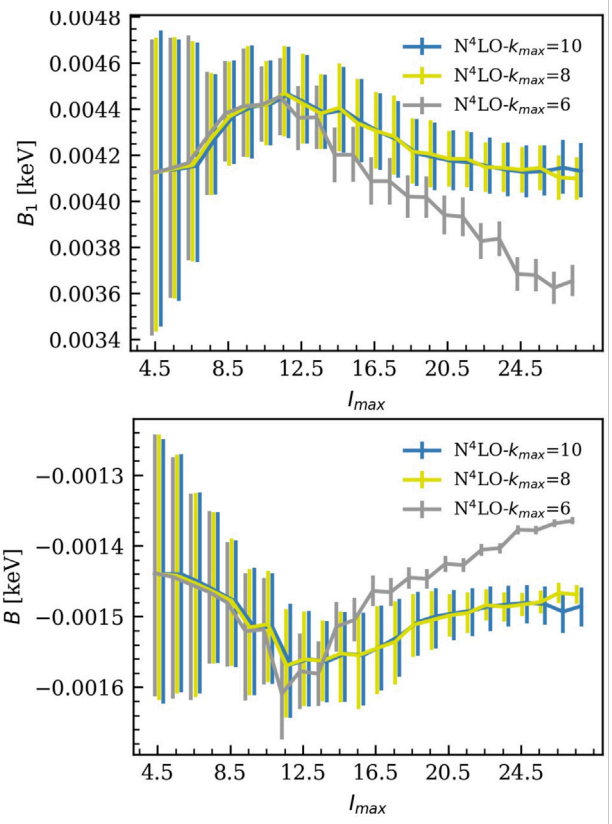

FIGURE 5
Posteriors for B_1 and B describing ^{239}Pu a function of I_{max} for different values of k_{max}. The solid line connects the median values and the error bands encompass the 16th and 84th percentiles in the marginalized distribution.

i.e., accounting for six omitted terms at N^{4}LO, was enough to stabilize the extraction of the LECs.

As an example, we show the stability of the extracted LEC, A_1, across number of levels included at different EFT orders in Figure 4. In this figure, I_{max} is the spin of the highest-energy level included in a particular analysis. The central values of the resulting posteriors are consistent with each other within 68% credible intervals, shown as error bars in the figure. Adding more levels to the analysis narrows the posteriors for the LECs up to a certain I_{max}, after which the widths of these distributions saturate. Figure 4 also demonstrates striking agreement between the distributions obtained at low and high EFT orders: they are almost identical as long as omitted terms up to the same k_{max} are accounted for in both analyses.

The importance of including more than one omitted term in the theory error estimate is evident in Figure 5. The top and bottom panels of the figure show the way that posteriors for B_1 and B evolve as I_{max} increases. This is done using three error models that include different numbers of omitted terms. These results show that including more omitted terms in the model of the theory error removes the drifting and staggering of the central values.

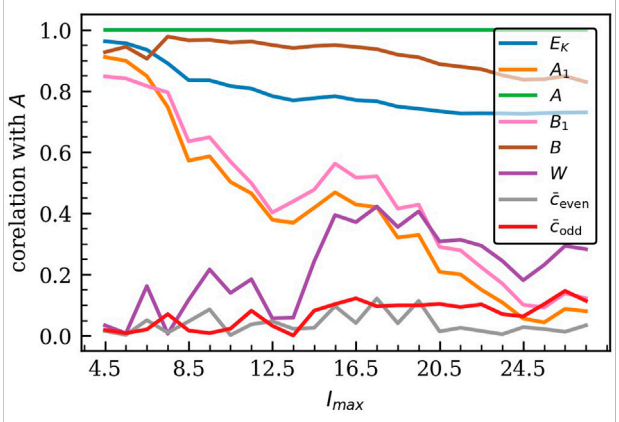

FIGURE 6
Correlations between LECs and error-model parameters as a function of I_{max}, resulting from the analysis on the lowest K =1/2 rotational band in ^{239}Pu at N^{4}LO with k_{max} =10.

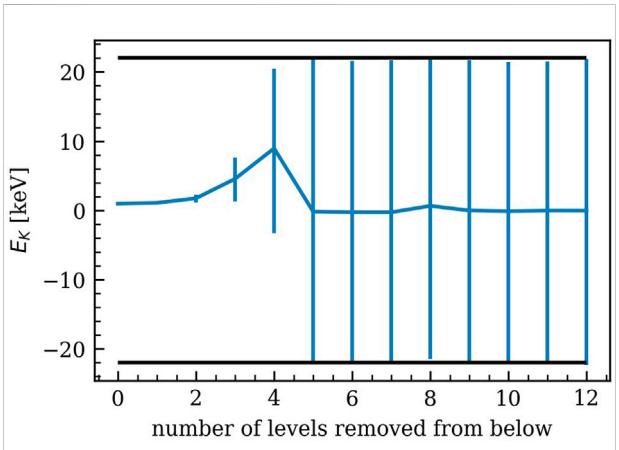

FIGURE 7
The distribution of E_K for ^{169}Er at N^{4}LO and k_{max} =10 as we successively remove the lowest energy levels from the data set D. The solid blue line connects the median values and the error bands encompass uncertainties between on the 16th and 84th percentiles of the samples in the marginalized distribution. The solid black lines show to size of the standard deviation set with the Gaussian prior on E_K.

For both cases the distributions at k_{max} = 10 agree within errors as we go higher in I_{max}. The narrowing of the distribution as we go higher in I_{max} is clearly seen in those two figures. In addition to having less data, the broadening of the error bands at low I_{max} comes from the fact that including less levels in the analysis leads to highly correlated LECs. This allows the numerically larger errors on the lower-order LECs to contribute to the errors on the higher-order LECs, thereby enhancing them.

In Figure 6 we show the decrease in the correlations between the LECs as I_{max} increases. The high correlation between the LECs at

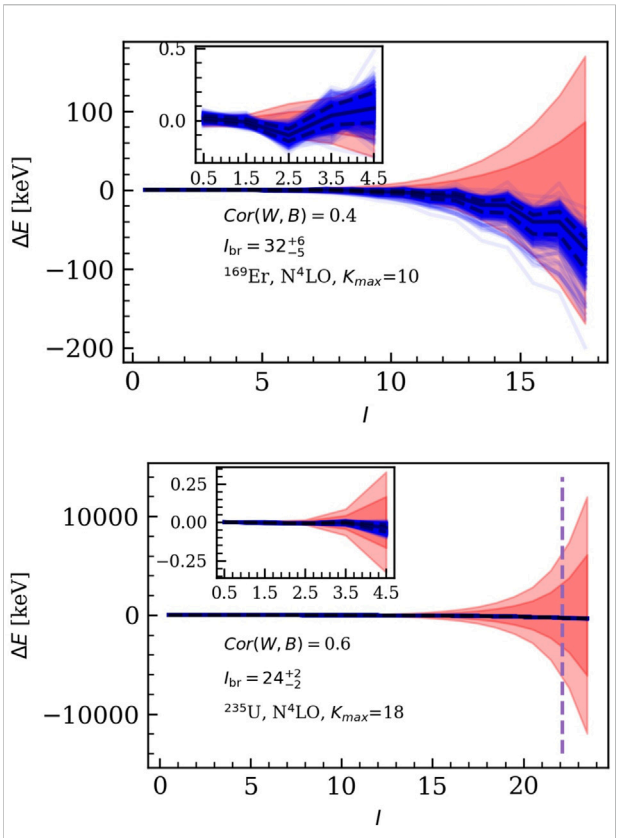

FIGURE 8
The posterior predictive distribution for energy-level residuals at N^{4}LO and k_{max} =10 for ^{169}Er and I_{max} =17.5 (top panel) and at k_{max} =18 for ^{235}U and I_{max} =23.5 (bottom panel). The dark and light red bands show the truncation error plus the experimental error at 68% and 95% credible levels respectively. The lighter blue lines connect the energy residuals calculated from the distribution of the LECs. The solid black line represents the median of the distribution and the dashed lines indicate the 16th and 84th percentiles. The correlation shown on the plot is the highest correlation between any LEC and any error-model parameter. I_{br} was determined from the distribution of W. The dashed purple line shows the lower limit of I_{br}. The inset on the plot shows the residuals on the first five levels with an altered y-axis scale.

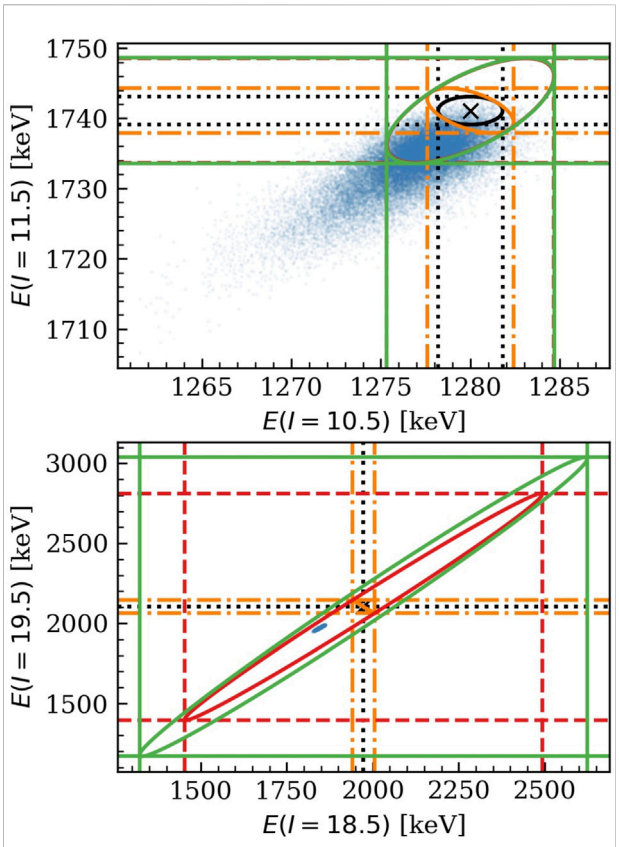

FIGURE 9
A 2D cut of the posterior predictive distribution at N^{4}LO and k_{max} =10 for ^{169}Er and I_{max} =17.5 (top panel) and at k_{max} =18 for ^{235}U and I_{max} =23.5 (bottom panel). The blue dots show the energies calculated from the distribution of the LECs. The black cross shows the experimental value and the black lines and black ellipse shows the corresponding experimental uncertainty. The remaining ellipses and lines show the truncation error and the experimental error added in quadrature. (All the ellipses are centered at the experimental value.) The orange, red and green account for 1, two and six omitted terms in the theory error respectively (In the top panel the red ellipse is completely covered by the green ellipse.)

low I_{max} occurs because these analyses do not include enough data to constrain all LECs independently. Furthermore, the high correlation between the LECs at low I_{max} also results in an unreliable extraction of the inverse breakdown scale W. This comes from the fact that at low energies the theory truncation error is very small compared to the experimental error. Indeed, adding more terms to our EFT error model (i.e., increasing k_{max}) leads to higher correlation between the LECs at low I_{max}. Thus, the number of levels required to reliably extract W increases with increasing k_{max}.

Starting instead at the low-I end of the data: when we progressively remove the lowest-energy levels from the data set D used to construct the likelihood we rapidly lose the ability to reliably extract the LECs. Figure 7 shows that the distribution for E_K starts narrow and broadens as we remove levels from below. When we remove the six lowest energy levels the distribution of E_K is exactly the same as the prior distribution: the likelihood is making no contribution to the E_K posterior.

The previous results were nearly the same for all cases considered in this work. However, even for k_{max} = 10, staggering and shifting of the LECs remains sizable for the K = 1/2 bands in ^{183}W, ^{167}Tm and ^{235}U. In ^{183}W and ^{167}Tm, these effects could be attributed to large expansion parameters, as they translate to large omitted contributions to the energies of the rotational levels. In ^{235}U, the fermionic matrix elements could be larger than naively expected, causing the systematic expansion of the EFT to be questionable as discussed in Ref. [19]. For ^{167}Tm we needed to go to k_{max} = 12 to get stable results, and for ^{235}U and ^{183}W we needed to go to k_{max} = 18.

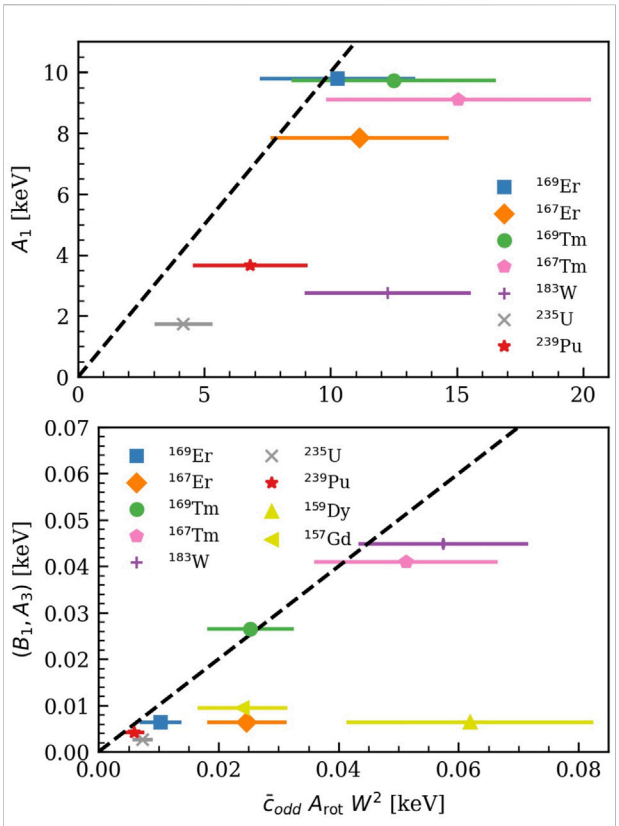

FIGURE 10
The size of the NLO LEC, A_1 (top panel) and the N^{3}LO LEC, B_1 for K =1/2 bands and A_3 for K =3/2 bands (bottom panel), on the y-axis, compared to its expected size from the EFT power counting, on the x-axis. Error bands on the LEC distribution are small and can not been seen on the plot. The error bands on the x-axis encompass the 16th and 84th percentiles. Different nuclei are labeled in the legend of the plot. The black dashed line has slope =1 and is plotted to facilitate comparison of prior expectation and results from the posterior. The yellow colored symbols are results for rotational bands with bandheads K =3/2, all the others are K =1/2 bands. K =3/2 rotational bands do not have a parameter A_1 and we do not have them in the top panel. ^{99}Tc and ^{155}Gd are outliers and we exclude them from the plots (LECs values for these nuclei can be found in Table 1).

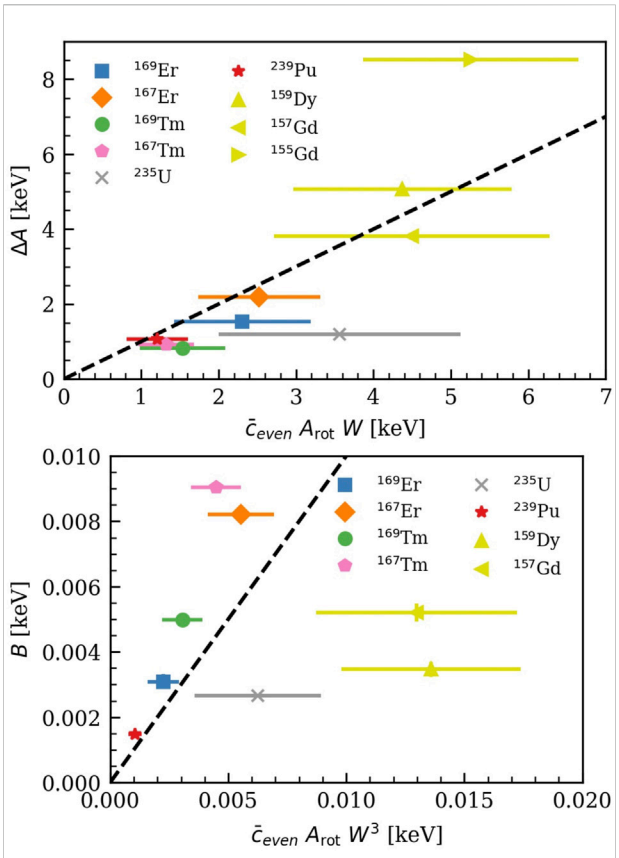

FIGURE 11
The size of the N^{2}LO LEC, ΔA (top panel) and the N^{4}LO LEC, B (bottom panel), on the y-axis, compared to its expected size from the EFT power counting, on the x-axis. Error bands on the LEC distribution are small and can not been seen on the plot. The error bands on the x-axis encompass uncertainties between the 16th and 84th percentiles. Different nuclei are labeled in the legend of the plot. The black dashed line has slope =1 and is plotted to facilitate comparison of prior expectation with results from the posterior. The yellow colored symbols are results for rotational bands with bandheads K =3/2, all the others are K =1/2 bands. ^{99}Tc and ^{183}W are outliers and we exclude them from the both plots. We also exclude ^{155}Gd from the bottom plot only (LEC values for these nuclei can be found in Table 1).

For K = 3/2 bands, we were able to extract stable LECs from the ^{159}Dy analysis by setting I_{max} = 15.5. This extraction required us to consider omitted terms up to k_{max} = 16. This is because the spin at which the EFT breaks in this nucleus is $I_{br} \approx 15.5$. (This, then, is the third case in which we do not use all the NNDC energy-level data available on a particular band.) ^{157}Gd is stable across orders and I_{max} and we get stable results at k_{max} = 12, while ^{155}Gd exhibits shifting and staggering due to a larger inverse breakdown scale, $W \approx 0.07$, and we needed to go to k_{max} = 18 to get stable results.

The values of the LECs and the error-model parameters at N^{4}LO for the nuclei considered in this work are given in Tables 1, 2 respectively.

5.2 Prior sensitivity

In addition to using the scaled-inverse-χ^2 distribution as a prior for $\bar{c}_{even}$ and $\bar{c}_{odd}$ we tried truncated Gaussians with mean zero and standard deviations σ = 7 and σ = 3 respectively for all cases. These truncated Gaussian priors allow for smaller values of the characteristic sizes. But the standard deviations were chosen to still allow values for $\bar{c}_{odd}$ and $\bar{c}_{even}$ larger than those resulting from scaled-inverse-χ^2 priors with ν = 1 and τ^2 = 1.

The change in prior for $\bar{c}_{odd}$ and $\bar{c}_{even}$ does not significantly change the posteriors for the LECs: the corresponding central values differ by less than 1%, and are consistent with each other

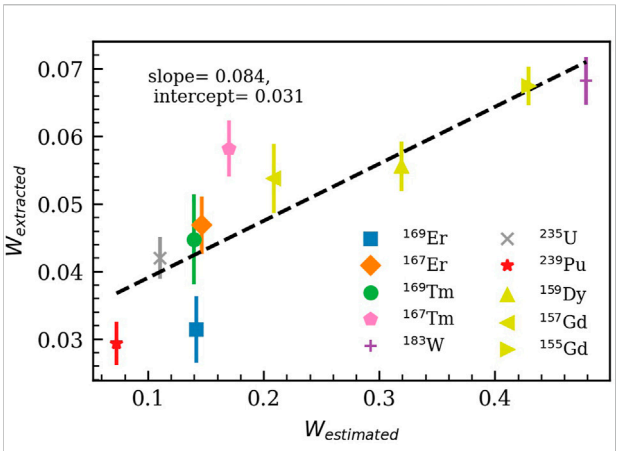

FIGURE 12
The extracted inverse breakdown scale W from the marginalized posterior distribution obtained by sampling compared to its naively expected size. The expected size is taken to be the maximum of E_{rot}/E_{sp} and E_{rot}/E_{vib}. The dashed black line shows the best linear fit and its parameters are printed on the plot. The yellow colored symbols are results for rotational bands with bandheads K =3/2, all the others are K =1/2 bands. ^{99}Tc is an outlier and we exclude it from the plot (its values can be seen in Table 2).

within the 68% credible intervals. Central values of the posteriors for W differ by less than 15%, and were similarly consistent.

The strongest dependence on the prior is that exhibited by the posteriors for $\bar{c}_{odd}$ and $\bar{c}_{even}$: the central values differ in some cases by more than 50%. However, even these values are consistent with each other within 68% credible intervals, since the posteriors for the characteristic sizes are broad.

The changes in the posteriors of W on one hand and $\bar{c}_{odd}$ & $\bar{c}_{even}$ on the other are anticorrelated. We only care about combinations of them to set the size of the theory error and the expected size of the LECs. Thus, the dependence of the theory error and the expected size of the LECs on the prior for the characteristic sizes is less profound. The difference in sizes of the theory error resulting from the chosen priors is less than 20% for all cases except ^{157}Gd, where the difference is about 40%.

For all results that follow we used the scaled-inverse-χ^2 distribution with ν = 1 and τ^2 = 1 as the prior for both $\bar{c}_{odd}$ and $\bar{c}_{even}$, in keeping with the naturalness assumption.

5.3 Posterior predictive distributions

Figure 8 shows the PPDs (in blue) of the energy residuals as a function of the spin I for two cases considered in this work. These distributions are calculated using Eq. 9. In each figure, translucent blue lines connect energy residuals resulting from different LECs sets sampled from the posterior distribution in Eq. 8. The solid black line represents the median of the PPD, and the dashed lines encompass the region between the 16th and 84th percentiles. Meanwhile, the dark and light red bands show the truncation error and the experimental error added in quadrature at 68% and 95% credible levels respectively. To calculate the truncation error, we consider a theory error that accounts for p omitted terms. The omitted terms are combined in quadrature, just as they are in the likelihood defined in Section 3. This calculation was done using Eq. 9 i.e., by calculating the theory error at each point in the sample space and then marginalizing over the error parameters. The dependence of the size of the theory error on the prior on $\bar{c}_{even}$ and $\bar{c}_{odd}$ is small in these cases: the theory error changes by about 10% when the prior is changed.

The correlation coefficient written in the legend in Figure 8 is the largest between any LEC and any error-model parameter for the shown analysis. When this value is small, the truncation error and the propagated LEC error could in principle be added together in quadrature.

In viewing Figure 8 it is important to remember that the truncation error on the energy residuals is highly correlated across levels. This comes from the high correlation between levels when building the correlation matrix that goes into the likelihood. This correlation also flows into a correlation between levels in the PPD of the energies. A correlation plot between two energy levels, like the ones in Figure 9, gives a 2D cut of this multi-dimensional correlation.

In both panels we see the importance of accounting for more than one omitted term in the theory error. This is clearly shown in the reverse in the direction of the correlation from a negative to a positive correlation when going from the orange ellipse to the red ellipse. The orange ellipse is obtained when we account for only one omitted term, while the red ellipse includes the effect of two omitted terms. After accounting for six omitted terms the green ellipse is obtained and the 68% ellipse in principle expands. This is more clearly seen when we go to high-energy levels plotted in the lower panel in Figure 9. Note also that for lower-energy levels the correlation is smaller since the experimental error dominates over the truncation error, and we assumed that the experimental errors are not correlated across energy levels.

5.4 Model checking

In Figures 10, 11 we compare the marginalized posterior distributions of the LECs, on the y-axis, with their expected sizes from the EFT power counting, on the x-axis. Since we also extract the theory error parameters from the sampler and they are highly correlated among themselves, we calculate the expected size from the distributions of the error model parameters using Eq. 9. We notice that the error on the distribution of the LECs is very small compared to the error on the expected sizes that comes from the distribution of the theory error parameters.

As these graphs are model-checking graphs, and since the estimates of LEC sizes plotted on the x-axis are meant as order-

TABLE 1 The median value of the LECs at N^{4}LO compared with the standard deviation of their Gaussian priors with zero mean [see Eq. 15]. We see that, for nearly all cases, the LECs fall within this standard deviation. The uncertainties encompass the 16th and 84th percentiles of the samples in the marginalized distributions. K =3/2 rotational bands do not have a parameter A_1 and the parameters (B_1, A_3) refer to K =1/2 and K =3/2 bands respectively. All the numbers are in units of keV.

Nucleus	E_K	$\bar{E}$	A_1	σ_1	ΔA	σ_2	(B_1, A_3)	σ_3	B	σ_4
^{99}Tc	$147.3113^{0.0141}_{-0.0142}$	160	$70.1913^{0.0102}_{-0.0103}$	121^{48}_{-35}	$-7.6608^{0.0085}_{-0.0086}$	$33.8^{6.4}_{-7.9}$	$-7.5851^{0.0022}_{-0.0022}$	$5.058^{1.614}_{-1.177}$	$-2.9916^{0.0008}_{-0.0008}$	$1.3614^{0.3417}_{-0.2508}$
^{155}Gd	$-45.1106^{0.0178}_{-0.0180}$	77	-	-	$-8.5265^{0.0060}_{-0.0059}$	$5.3^{2.2}_{-1.4}$	$-0.0043^{0.0006}_{-0.0006}$	$0.499^{0.201}_{-0.168}$	$0.0076^{0.0005}_{-0.0005}$	$0.0240^{0.0086}_{-0.0055}$
^{157}Gd	$-41.3384^{0.0155}_{-0.0160}$	56	-	-	$-3.8064^{0.0040}_{-0.0039}$	$4.5^{3.6}_{-1.8}$	$-0.0094^{0.0002}_{-0.0002}$	$0.024^{0.013}_{-0.007}$	$-0.0052^{0.0003}_{-0.0003}$	$0.0130^{0.0074}_{-0.0043}$
^{159}Dy	$-42.7894^{0.0159}_{-0.0152}$	62	-	-	$-5.0705^{0.0036}_{-0.0040}$	$4.4^{2.7}_{-1.4}$	$-0.0063^{0.0003}_{-0.0002}$	$0.062^{0.038}_{-0.021}$	$-0.0035^{0.0003}_{-0.0002}$	$0.0136^{0.0066}_{-0.0038}$
^{167}Er	$207.2088^{0.0054}_{-0.0054}$	230	$7.8383^{0.0028}_{-0.0028}$	11^{7}_{-4}	$-2.1898^{0.0016}_{-0.0016}$	$2.5^{1.4}_{-0.8}$	$-0.0063^{0.0003}_{-0.0003}$	$0.025^{0.012}_{-0.007}$	$-0.0082^{0.0001}_{-0.0001}$	$0.0055^{0.0023}_{-0.0014}$
^{169}Er	$0.9672^{0.0196}_{-0.0198}$	22	$9.7776^{0.0101}_{-0.0100}$	10^{6}_{-3}	$-1.5382^{0.0058}_{-0.0054}$	$2.3^{1.6}_{-0.9}$	$-0.0064^{0.0008}_{-0.0009}$	$0.010^{0.006}_{-0.003}$	$-0.0031^{0.0002}_{-0.0002}$	$0.0022^{0.0012}_{-0.0007}$
^{167}Tm	$-18.4633^{0.0160}_{-0.0164}$	22	$-9.1088^{0.0075}_{-0.0074}$	15^{10}_{-5}	$-0.9198^{0.0028}_{-0.0027}$	$1.3^{0.6}_{-0.4}$	$0.0410^{0.0007}_{-0.0007}$	$0.051^{0.028}_{-0.015}$	$-0.0090^{0.0001}_{-0.0001}$	$0.0045^{0.0017}_{-0.0011}$
^{169}Tm	$-19.0532^{0.0011}_{-0.0011}$	22	$-9.7205^{0.0008}_{-0.0008}$	12^{8}_{-4}	$-0.8269^{0.0006}_{-0.0006}$	$1.5^{1.0}_{-0.5}$	$0.0264^{0.0002}_{-0.0002}$	$0.025^{0.013}_{-0.007}$	$-0.0050^{0.0001}_{-0.0001}$	$0.0031^{0.0015}_{-0.0009}$
^{183}W	$-6.8489^{0.0065}_{-0.0043}$	22	$2.7630^{0.0041}_{-0.0028}$	12^{5}_{-3}	$-3.9299^{0.0029}_{-0.0044}$	$16.3^{4.9}_{-5.5}$	$-0.0448^{0.0006}_{-0.0009}$	$0.057^{0.023}_{-0.014}$	$0.0229^{0.0006}_{-0.0004}$	$0.0746^{0.0188}_{-0.0201}$
^{235}U	$-6.1892^{0.0009}_{-0.0009}$	22	$-1.7294^{0.0007}_{-0.0008}$	4^{2}_{-1}	$-1.1971^{0.0006}_{-0.0005}$	$3.6^{2.9}_{-1.6}$	$0.0025^{0.0001}_{-0.0001}$	$0.007^{0.003}_{-0.002}$	$-0.0027^{0.0000}_{-0.0001}$	$0.0062^{0.0047}_{-0.0027}$
^{239}Pu	$-8.3577^{0.0019}_{-0.0019}$	22	$-3.6560^{0.0011}_{-0.0011}$	7^{4}_{-2}	$-1.0715^{0.0004}_{-0.0004}$	$1.2^{0.7}_{-0.4}$	$0.0041^{0.0001}_{-0.0001}$	$0.006^{0.003}_{-0.002}$	$-0.0015^{0.0000}_{-0.0000}$	$0.0010^{0.0005}_{-0.0003}$

TABLE 2 The median value of the error model parameters at N^{4}LO and the estimated expansion parameters based on rotational and single particle energy scales. The uncertainties encompass the 16th and 84th percentiles of the samples in the marginalized distributions.

Nucleus	W	$E_{\rm rot}/E_{\rm vib}$	$E_{\rm rot}/E_{\rm sp}$	$\bar{c}_{even}$	$\bar{c}_{odd}$
^{99}Tc	$0.204^{0.021}_{-0.015}$	0.396	1.020	$1.9^{0.4}_{-0.5}$	$1.3^{0.5}_{-0.4}$
^{155}Gd	$0.067^{0.003}_{-0.003}$	0.181	0.429	$3.8^{1.7}_{-1.1}$	$5.4^{2.7}_{-2.1}$
^{157}Gd	$0.054^{0.005}_{-0.005}$	0.085	0.209	$5.7^{5.4}_{-2.5}$	$0.6^{0.3}_{-0.2}$
^{159}Dy	$0.056^{0.004}_{-0.004}$	0.104	0.319	$4.8^{3.3}_{-1.7}$	$1.2^{0.9}_{-0.5}$
^{167}Er	$0.047^{0.005}_{-0.004}$	0.102	0.147	$4.0^{2.6}_{-1.4}$	$0.8^{0.5}_{-0.3}$
^{169}Er	$0.031^{0.006}_{-0.005}$	0.097	0.142	$5.6^{5.1}_{-2.5}$	$0.8^{0.4}_{-0.2}$
^{167}Tm	$0.058^{0.004}_{-0.004}$	0.102	0.170	$1.7^{0.9}_{-0.5}$	$1.1^{0.8}_{-0.4}$
^{169}Tm	$0.045^{0.008}_{-0.007}$	0.097	0.140	$2.6^{2.3}_{-1.1}$	$0.9^{0.6}_{-0.3}$
^{183}W	$0.068^{0.005}_{-0.004}$	0.082	0.479	$14.4^{5.0}_{-5.3}$	$0.7^{0.3}_{-0.2}$
^{235}U	$0.042^{0.003}_{-0.003}$	0.047	0.111	$11.7^{10.0}_{-5.3}$	$0.6^{0.3}_{-0.2}$
^{239}Pu	$0.029^{0.004}_{-0.003}$	0.073	0.059	$5.6^{4.0}_{-2.2}$	$0.9^{0.6}_{-0.3}$

of-magnitude estimates, we do not expect perfect linear correlations. Nevertheless, the top panel in Figure 11 shows that, for all K = 1/2 bands considered, the LEC ΔA agrees with its expected size within error bands. This result is surprisingly better than expected. In contrast, the size of ΔA for K = 3/2 bands is larger than expected, especially for ^{155}Gd (see yellow symbols in Figure 11). There are two factors that could contribute to this. First, the K = 3/2 bands have larger fermionic matrix elements. This could hinder the systematic expansion of the EFT. Second, the K = 3/2 bands have relatively larger expansion parameters, see Figure 12.

The same discussion applies to the results in the remaining panels in Figures 10, 11, where we see good agreement between the LECs and their expected sizes for K = 1/2 bands. The disagreement with power-counting estimates for K = 3/2 bands at N^{3,4}LO is less of a concern than the one at N^{2}LO seen in the top panel of Figure 11, since these higher-order LECs are smaller than their expected sizes. This doesn't undermine the convergence of the EFT expansion.

We also note here that the scale of the x-axis is prior dependent and could change by more than 50% in some nuclei, depending on the choice of prior on $\bar{c}_{even}$ and $\bar{c}_{odd}$. For ^{157}Gd changing the prior on $\bar{c}_{even}$ and $\bar{c}_{odd}$ to a truncated normal allowed for smaller values of $\bar{c}_{odd}$ and A_3 was then equal to the expected size (i.e., the point for ^{157}Gd then falls exactly on the line in the bottom panel of Figure 10). This did not happen when the truncated normal is chosen as a prior for the analysis in ^{155}Gd and ^{159}Dy; this may occur because there is strong N^{5}LO energy-level staggering present in the data for these nuclei.

The size of $\bar{c}_{even}$ and $\bar{c}_{odd}$ is constrained by both the sizes of the LECs and the size of the theory error. In a good systematic expansion the tension between those factors on setting the size of the $\bar{c}$'s would be small and one number apiece would suffice to represent the even and odd order corrections. However when the systematic expansion is hindered, as in the case for K = 3/2 bands due to large fermionic matrix elements, this tension becomes clear. One example of this is seen in Figure 11 for K = 3/2 bands. There ΔA is large and favors large values of $\bar{c}_{even}$, however, B is small and favors smaller values of $\bar{c}_{even}$. The eventual result is a compromise. This tension may be exacerbated by the truncation error also providing information on the size of the $\bar{c}$'s.

5.5 Higher than expected break-down scale

In Figure 12 we see a clear correlation between the extracted values of W and those that are expected based on each nucleus' single-particle and vibrational energy scales, E_{sp} and E_{vib}. The expected W is the larger of E_{rot}/E_{sp} and E_{rot}/E_{vib}, while the extracted W comes from sampling the posterior in Eq. 10. This extracted W is what actually determines the convergence of the EFT expansion. It is markedly smaller than would be naively expected. The break-down scale of the theory is thus higher than naively expected: our rotational EFT works to much higher I than energy-scale arguments would suggest. This could occur because coupling between the higher rotational states explicitly included in the EFT and the high-energy states that are not explicitly included in our EFT is hindered by the large difference in angular momentum between them.

6 Conclusion

We performed a Bayesian analysis to extract the LECs and inverse breakdown scale W describing the rotational energy levels of diverse odd-mass nuclei within a recently developed EFT. This analysis corroborates the EFT organization for energy-level formulae which results from the assumed power-counting scheme: the extracted LECs of order k scale as W^{k-1}, i.e., according to EFT expectations. While our analysis reached this conclusion for both $K = 1/2$ and $K = 3/2$ rotational bands, the sizes of the LECs describing the latter exhibit larger deviations from their expected values than those describing the former. We attribute this behavior to the size of fermionic matrix elements, assumed to be of order one while organizing energy-level formulae. Since these matrix elements involve the angular momentum of the fermion, $\vec{j}$, we cannot exclude the possibility that the systematic behavior of the EFT is hindered in bands build on top of single-particle orbitals with larger values of K. For the $K = 3/2$ bands studied in this work, however, this discrepancy does not destroy the systematic improvement of calculated energies up to N^{4}LO, as the sizes of extracted LECs are smaller that expected.

In order to ensure that the extracted values are independent of the EFT order and number of energy levels entering the analysis, we employed a theory error beyond the first-omitted-term approximation, considering omitted terms in the expansion for the energy of rotational levels up to order k_{max}. As we increased the number of omitted terms considered in the theory error, the corresponding log likelihood exhibited steeper and steeper peaks. Therefore, the 'widths' of the sampled posteriors decrease as k_{max} increases. Considering up to fourteen omitted terms at N^{4}LO enabled a stable extraction of the LECs and breakdown scale describing the levels of interest. The shapes of posteriors for low-order LECs extracted at this order and those extracted using lower-order energy formulae are, for all practical purposes, identical. On the other hand, the shapes of the posteriors depend strongly on the number of levels informing the model, narrowing as more levels are included. Nevertheless, the 68% credible intervals of these posteriors possess significant overlap, facilitating reliable LEC extraction.

In addition to the posteriors for the LECs and the inverse breakdown scales, our analysis yielded distributions for the characteristic sizes of even and odd c_n's, $\bar{c}_{even}$ and $\bar{c}_{odd}$. The values of $\bar{c}_{odd}$ are typically smaller than those for $\bar{c}_{even}$, in agreement with results from previous studies where the LECs were fitted to the smallest possible data sets. The difference of the characteristic sizes of even and odd LECs has its origin in the physics behind the corresponding contributions to the effective Lagrangian: while odd-order contributions correct the particle-rotor interaction, even-order contributions include terms that depend exclusively on the rotor degrees of freedom, thus correcting the physics of the core to which the particle is coupled. Here this conclusion was reached solely on the basis of experimental data; we assumed equal priors for both characteristic sizes.

Although the distributions of $\bar{c}_{odd}$ and $\bar{c}_{even}$ change depending on the choice of the their priors, that does not significantly change the distributions of the LECs. Altering the priors also does not have a large effect on the size of the theory error, which changes by less than 20% for nearly all cases.

These considerations mean that our extractions of the LECs and the theory error parameters in the EFT of rotational bands in odd-mass nuclei are robust under the choice of prior. The formalism presented here also gives robust results for LECs across orders and as more data is added to the analysis. We conclude that a Bayesian framework that incorporates theory errors in the likelihood offers significant advantages for LEC extraction in EFTs. This methodology has already been used for the extraction of LECs in the NN potential from phase shifts [34] and to constrain parameters of the three-nucleon force [35]. But it is a very general approach which should improve the parameter estimation for LECs in any EFT.

Data availability statement

The datasets presented in this study can be found in the online repository: https://github.com/inamlah/brb.

Author contributions

This work has been conceptualized by DP and IA. Both IA and EACP have contributed to writing the code. IA, EACP and DP have all contributed to analyzing the results and writing the manuscript.

Funding

This work was supported by the US Department of Energy, contract DE-FG02-93ER40756 (IKA, DRP) by the National Science Foundation CSSI program Award OAC-2004601 (DRP), and under the auspices of the US Department of Energy by Lawrence Livermore National Laboratory under Contract DE-AC52-07NA27344 (EACP). IKA acknowledges the support of King Saud University and the Ministry of Education in Saudi Arabia.

Acknowledgments

We thank Dick Furnstahl and Jordan Melendez for useful discussions. We are also grateful for Daniel Odell's significant conceptual and computational assistance.

Conflict of interest

The authors declare that the research was conducted in the absence of any commercial or financial relationships that could be construed as a potential conflict of interest.

The handling editor CF declared a past co-authorship with the author DRP.

Publisher's note

Supplementary material

The Supplementary Material for this article can be found online at: https://www.frontiersin.org/articles/10.3389/fphy.2022.901954/full#supplementary-material

References

1. Bohr A. On the quantization of angular momenta in heavy nuclei. *Phys Rev* (1951) 81:134–8. doi:10.1103/PhysRev.81.134

2. Rowe DJ. *Nuclear collective motion: Models and theory*. Singapore: World Scientific (2010). Chapter 6.

3. Papenbrock T. Effective theory for deformed nuclei. *Nucl Phys A* (2011) 852: 36–60. [arXiv:1011.5026 [nucl-th]]. doi:10.1016/j.nuclphysa.2010.12.013

4. Coello Pérez EA, Papenbrock T. Effective theory for the nonrigid rotor in an electromagnetic field: Toward accurate and precise calculations ofE2transitions in deformed nuclei. *Phys Rev C* (2015) 92(no. 1):014323. [arXiv:1502.04405 [nucl-th]]. doi:10.1103/PhysRevC.92.014323

5. Caprio MA, Maris P, Vary JP. Emergence of rotational bands in *ab initio* no-core configuration interaction calculations of light nuclei. *Phys Lett B* (2013) 719:179–84. [arXiv:1301.0956 [nucl-th]]. doi:10.1016/j.physletb.2012.12.064

6. Maris P, Caprio MA, Vary JP. Erratum: Emergence of rotational bands in *ab initio* no-core configuration interaction calculations of the Be isotopes. *Phys Rev Cphys Rev C* (2015) 91(no.2):014310. 029902. [erratum:[arXiv:1409.0881 [nucl-th]]. 10.1103/physrevc.99.029902. doi:10.1103/PhysRevC.91.014310

7. Jansen GR, Signoracci A, Hagen G, Navrátil P. Open s d-shell nuclei from first principles. *Phys Rev C* (2016) 94(no.1):011301. [arXiv:1511.00757 [nucl-th]]. doi:10.1103/PhysRevC.94.011301

8. Caprio MA, Fasano PJ, Maris P, McCoy AE, Vary JP. Probing *ab initio* emergence of nuclear rotation. *Eur Phys J A* (2020) 56(no.4):120. [nucl-th]]. doi:10.1140/epja/s10050-020-00112-0

9. McCoy AE, Caprio MA, Dytrych T, Fasano PJ. Emergent sp(3, R) dynamical symmetry in the nuclear many-body system from an *ab initio* description. *Phys Rev Lett* (2020) 125(no.10):102505. [nucl-th]]. doi:10.1103/physrevlett.125.102505

10. Hagen G, Novario SJ, Sun ZH, Papenbrock T, Jansen GR, Lietz JG, et al. Angular-momentum projection in coupled-cluster theory: Structure of Mg34. *Phys Rev C* 105(6). [arXiv:2201.07298 [nucl-th]]. doi:10.1103/physrevc.105.064311

11. Bohr A, Mottelson B. *Nuclear structure, volume II: Deformations*. Singapore: World Scientific (1998).

12. Dudek J, Nazarewicz W, Szymański J. Independent quasiparticle analysis of rotational bands in^{156}Er. *Phys Scr* (1981) 24:309–11. doi:10.1088/0031-8949/24/1b/029

13. Cwiok S, Nazarewicz W, Dudek J, Szymanski Z. Analysis of the backbending effect inYb166, Yb168, andYb170within the Hartree-Fock-Bogolyubov cranking method. *Phys Rev C* (1980) 21:448–52. doi:10.1103/PhysRevC.21.448

14. Afanasjev AV, Abdurazakov O. Pairing and rotational properties of actinides and superheavy nuclei in covariant density functional theory. *Phys Rev C* (2013) 88(no.1):014320. [arXiv:1307.4131 [nucl-th]]. doi:10.1103/PhysRevC.88.014320

15. Zhang ZH, Huang M, Afanasjev AV. Rotational excitations in rare-earth nuclei: A comparative study within three cranking models with different mean fields and treatments of pairing correlations. *Phys Rev C* (2020) 101(no.5):054303. arXiv:2003.07902 [nucl-th]]. doi:10.1103/PhysRevC.101.054303

16. Inglis DR. Particle derivation of nuclear rotation properties associated with a surface wave. *Phys Rev* (1954) 96:1059–65. doi:10.1103/PhysRev.96.1059

17. Velazquez V, Hirsch JG, Sun Y, Guidry MW. Backbending in Dy isotopes within the projected shell model. *Nucl Phys A* (1999) 653:355–71. [arXiv:nucl-th/9901044 [nucl-th]]. doi:10.1016/S0375-9474(99)00238-9

18. Liu SX, Zeng JY, Yu L. Particle-number-conserving treatment for the backbending in Yb isotopes. *Nucl Phys A* (2004) 735:77–85. doi:10.1016/j.nuclphysa.2004.02.007

19. Alnamlah IK, Pérez EAC, Phillips DR. Effective field theory approach to rotational bands in odd-mass nuclei. *Phys Rev C* (2021) 104(no.6):064311. [arXiv:2011.01083 [nucl-th]]. doi:10.1103/PhysRevC.104.064311

20. Papenbrock T, Weidenmüller HA. Effective field theory for deformed odd-mass nuclei. *Phys Rev C* (2020) 102(no.4):044324. [nucl-th]. doi:10.1103/physrevc.102.044324

21. Chen QB, Kaiser N, Meißner UG, Meng J. Effective field theory for triaxially deformed odd-mass nuclei. [arXiv:2003.04065 [nucl-th]].

22. Baglin CM. Nuclear data sheets for A = 169. *Nucl Data Sheets* (2008) 109(no.9):2033–256. doi:10.1016/j.nds.2008.08.001

23. Baglin CM. Nuclear data sheets for A = 167. *Nucl Data Sheets* (2000) 90(3): 431–644. doi:10.1006/ndsh.2000.0012

24. Browne E, Tuli JK. Nuclear data sheets for A = 239. *Nucl Data Sheets* (2014) 122:293–376. doi:10.1016/j.nds.2014.11.003

25. Browne E, Tuli JK. Nuclear data sheets for A = 235. *Nucl Data Sheets* (2014) 122:205–92. doi:10.1016/j.nds.2014.11.002

26. Reich CW. Nuclear data sheets for A = 159. *Nucl Data Sheets* (2012) 113(no.1):157–363. doi:10.1016/j.nds.2012.01.002

27. Nica N. Nuclear data sheets for A=155. *Nucl Data Sheets* (2019) 160:1–404. doi:10.1016/j.nds.2019.100523

28. Nica N. Nuclear data sheets for A = 157. *Nucl Data Sheets* (2016) 132:1–256. doi:10.1016/j.nds.2016.01.001

29. Browne E, Tuli JK. Nuclear data sheets for A = 99. *Nucl Data Sheets* (2017) 145:25–340. doi:10.1016/j.nds.2017.09.002

30. Baglin CM. Nuclear data sheets for A = 183. *Nucl Data Sheets* (2016) 134: 149–430. doi:10.1016/j.nds.2016.04.002

31. Furnstahl RJ, Phillips DR, Wesolowski S. A recipe for EFT uncertainty quantification in nuclear physics. *J Phys G: Nucl Part Phys* (2015) 42(no.3): 034028. [nucl-th]]. doi:10.1088/0954-3899/42/3/034028

32. Schindler MR, Phillips DR. Bayesian methods for parameter estimation in effective field theories. *Ann Phys (N Y)* (2009) 324:682–708. [arXiv:0808.3643 [hep-ph]]. doi:10.1016/j.aop.2008.09.003

33. Wesolowski S, Klco N, Furnstahl RJ, Phillips DR, Thapaliya A. Bayesian parameter estimation for effective field theories. *J Phys G: Nucl Part Phys* (2016) 43(7):074001. [nucl-th]]. doi:10.1088/0954-3899/43/7/074001

34. Wesolowski S, Furnstahl RJ, Melendez JA, Phillips DR. Exploring Bayesian parameter estimation for chiral effective field theory using nucleon–nucleon phase shifts. *J Phys G: Nucl Part Phys* (2019) 46(no.4):045102. [arXiv:1808.08211 [nucl-th]]. doi:10.1088/1361-6471/aaf5fc

35. Wesolowski S, Svensson I, Ekström A, Forssén C, Furnstahl RJ, Melendez JA, et al. Rigorous constraints on three-nucleon forces in chiral effective field theory from fast and accurate calculations of few-body observables. *Phys Rev C* (2021) 104(no.6):064001. arXiv:2104.04441 [nucl-th]]. doi:10.1103/PhysRevC.104.064001

36. Alnamlah IK, Coello Pérez EA, Phillips DR. Bayesian rotational bands. *GitHub repository* (2022). Available at: http://github.com/inamlah/brb.

37. Foreman-Mackey D, Hogg DW, Lang D, Goodman J. EMCEE: the MCMC hammer. *Publ Astron Soc Pac* (2013) 125:306–12. arXiv:1202.3665 [astro-ph.IM]]. doi:10.1086/670067

frontiers | Frontiers in Physics

TYPE Original Research
PUBLISHED 03 November 2022
DOI 10.3389/fphy.2022.1058809

OPEN ACCESS

EDITED BY
Michele Viviani,
National Institute of Nuclear Physics of Pisa, Italy

REVIEWED BY
Saori Pastore,
Washington University in St. Louis, United States
Bijaya Acharya,
Oak Ridge National Laboratory (DOE), United States

*CORRESPONDENCE
Weiguang Jiang,
wjiang@uni-mainz.de

SPECIALTY SECTION
This article was submitted to Nuclear Physics, a section of the journal Frontiers in Physics

RECEIVED 30 September 2022
ACCEPTED 20 October 2022
PUBLISHED 03 November 2022

CITATION
Jiang W and Forssén C (2022), Bayesian probability updates using sampling/importance resampling: Applications in nuclear theory.
Front. Phys. 10:1058809.
doi: 10.3389/fphy.2022.1058809

Bayesian probability updates using sampling/importance resampling: Applications in nuclear theory

Weiguang Jiang* and Christian Forssén

Department of Physics, Chalmers University of Technology, Göteborg, Sweden

We review an established Bayesian sampling method called sampling/importance resampling and highlight situations in nuclear theory when it can be particularly useful. To this end we both analyse a toy problem and demonstrate realistic applications of importance resampling to infer the posterior distribution for parameters of ΔNNLO interaction model based on chiral effective field theory and to estimate the posterior probability distribution of target observables. The limitation of the method is also showcased in extreme situations where importance resampling breaks.

KEYWORDS

bayesian inference, probability updates, importance resampling, uncertainty quantification, ab initio nuclear theory, low-energy constants

1 Introduction

Bayesian inference is an appealing approach for dealing with theoretical uncertainties and has been applied in different nuclear physics studies [1–16]. In the practice of Bayesian analyses, a sampling procedure is usually inevitable for approximating the posterior probability distribution of model parameters and for performing predictive computations. Various Markov chain Monte Carlo (MCMC) methods [17–21] are often used for this purpose, even for complicated models with high-dimensional parameter spaces. However, MCMC sampling typically requires many likelihood evaluations, which is often a costly operation in nuclear theory, and there is a need to explore other sampling techniques. In this paper, we review an established method called sampling/importance resampling (S/IR) [22–24] and demonstrate its use in realistic nuclear physics applications where we also perform comparisons with MCMC sampling.

In recent years, there has been an increasing demand for precision nuclear theory. This implies a challenge to not just achieve accurate theoretical predictions but also to quantify accompanying uncertainties. The use of *ab initio* many-body methods and nuclear interaction models based on chiral effective field theory (χEFT) has shown a potential to describe finite nuclei and nuclear matter based on extant experimental data (e.g. nucleon-nucleon scattering, few-body sector) with controlled approximations [25–29]. The interaction model is parametrized in terms of low-energy constants (LECs), the number of which is growing order-by-order according to the rules of a

corresponding power counting [30–32]. Very importantly, the systematic expansion allows to quantify the truncation error and to incorporate this knowledge in the analysis [4–6, 10–14]. Indeed, Bayesian inference is an excellent framework to incorporate different sources of uncertainty and to propagate error bars to the model predictions. Starting from Bayes' theorem

$$\mathrm{pr}(\boldsymbol{\theta}|\mathcal{D}) \propto \mathcal{L}(\boldsymbol{\theta})\mathrm{pr}(\boldsymbol{\theta}), \tag{1}$$

where $\mathrm{pr}(\boldsymbol{\theta}|\mathcal{D})$ is the posterior probability density function (PDF) for the vector $\boldsymbol{\theta}$ of LECs (conditional on the data $\mathcal{D}$), $\mathcal{L}(\boldsymbol{\theta}) \equiv \mathrm{pr}(\mathcal{D}\,|\boldsymbol{\theta})$ is the likelihood and $\mathrm{pr}(\boldsymbol{\theta})$ is the prior. Then for any model prediction one needs to evaluate the expectation value of a function of interest $\mathbf{y}(\boldsymbol{\theta})$ (target observables) according to the posterior. This involves integrals such as

$$\int d\boldsymbol{\theta}\boldsymbol{y}(\boldsymbol{\theta})\mathrm{pr}(\boldsymbol{\theta}|\mathcal{D}), \tag{2}$$

which can not be analytically solved for realistic cases. Fortunately, integrals such as Eq. 2 can be approximately evaluated using a finite set of samples $\{\boldsymbol{\theta}_i\}_{i=1}^N$ from $\mathrm{pr}(\boldsymbol{\theta}|\mathcal{D})$. MCMC sampling methods are the main computational tool for providing such samples, even for high-dimensional parameter volumes [16]. However the use of MCMC in nuclear theory typically requires massive computations to record sufficiently many samples from the Markov chain. There are certainly situations where MCMC sampling is not ideal, or even becomes infeasible:

1) When the posterior is conditioned on some calibration data for which our model evaluations are very costly. Then we might only afford a limited number of full likelihood evaluations and our MCMC sampling becomes less likely to converge.
2) Bayesian posterior updates in which calibration data is added in several different stages. This typically requires that the MCMC sampling must be carried out repeatedly from scratch.
3) Model checking where we want to explore the sensitivity to prior assignments. This is a second example of posterior updating.
4) The prediction of target observables for which our model evaluations become very costly and the handling of a large number of MCMC samples becomes infeasible.

These are situations where one might want to use the S/IR method [23, 24], which can exploit the previous results of model evaluations to allow posterior probability updates at a much smaller computational cost compared to the full MCMC method. In the following sections we first review the S/IR method and then present both toy and realistic applications in which its performance is compared with full MCMC sampling. Finally, we illustrate limitations of the method by considering cases where S/IR fails and we highlight the importance of the so-called effective number of samples. More difficult scenarios, in which the method fails without a clear warning, are left for the concluding remarks.

2 Sampling/importance resampling

The basic idea of S/IR is to utilize the inherent duality between samples and the density (probability distribution) from which they were generated [23]. This duality offers an opportunity to indirectly recreate a density (that might be hard to compute) from samples that are easy to obtain. Here we give a brief review of the method and illustrate with a toy problem.

Let us consider a target density $h(\boldsymbol{\theta})$. In our applications this target will be the posterior PDF $\mathrm{pr}(\boldsymbol{\theta}|\mathcal{D})$ from Eq. 1. Instead of attempting to directly collect samples from $h(\boldsymbol{\theta})$, as would be the goal in MCMC approaches, the S/IR method uses a detour. We first obtain samples from a simple (even analytic) density $g(\boldsymbol{\theta})$. We then resample from this finite set using a resampling algorithm to approximately recreate samples from the target density $h(\boldsymbol{\theta})$. There are (at least) two different resampling methods. In this paper we only focus on one of them called weighted bootstrap (more details of resampling methods can be found in Refs. [22, 23]).

Assuming we are interested in the target density $h(\boldsymbol{\theta}) = f(\boldsymbol{\theta})/\int f(\boldsymbol{\theta})\,\mathrm{d}\boldsymbol{\theta}$, the procedure of resampling *via* weighted bootstrap can be summarized as follows:

1) Generate the set $\{\boldsymbol{\theta}_i\}_{i=1}^n$ of samples from a sampling density $g(\boldsymbol{\theta})$.
2) Calculate $\omega_i = f(\boldsymbol{\theta}_i)/\, g(\boldsymbol{\theta}_i)$ for the n samples and define importance weights as: $q_i = \omega_i\, /\sum_{j=1}^n \omega_j$.
3) Draw N new samples $\{\boldsymbol{\theta}_i^*\}_{i=1}^N$ from the discrete distribution $\{\boldsymbol{\theta}_i\}_{i=1}^n$ with probability mass q_i on $\boldsymbol{\theta}_i$.
4) The set of samples $\{\boldsymbol{\theta}_i^*\}_{i=1}^N$ will then be approximately distributed according to the target density $h(\boldsymbol{\theta})$.

Intuitively, the distribution of $\boldsymbol{\theta}^*$ should be good approximation of $h(\boldsymbol{\theta})$ when n is large enough. Here we justify this claim *via* the cumulative distribution function of θ^* (for the one-dimensional case)

$$\mathrm{pr}(\theta^* \le \mathrm{a}) = \sum_{i=1}^{n} q_i \cdot H(a-\theta_i) = \frac{\frac{1}{n}\sum_{i=1}^{n}\omega_i \cdot H(a-\theta_i)}{\frac{1}{n}\sum_{i=1}^{n}\omega_i}$$
$$\underset{n\to\infty}{\longrightarrow} \frac{\mathbb{E}_g\left[\frac{f(\theta)}{g(\theta)}\cdot H(a-\theta)\right]}{\mathbb{E}_g\left[\frac{f(\theta)}{g(\theta)}\right]} = \frac{\int_{-\infty}^{a} f(\theta)\,d\theta}{\int_{-\infty}^{\infty} f(\theta)\,d\theta} = \int_{-\infty}^{a} h(\theta)\,d\theta, \tag{3}$$

with $\mathbb{E}_g[X(\theta)] = \int_{-\infty}^{\infty} X(\theta)g(\theta)\,d\theta$ the expectation value of $X(\theta)$ with respect to $g(\theta)$, and H Heaviside step function such that

$$H(a-\theta) = \begin{cases} 1 & \text{if } \theta \le a, \\ 0 & \text{if } \theta > a. \end{cases} \tag{4}$$

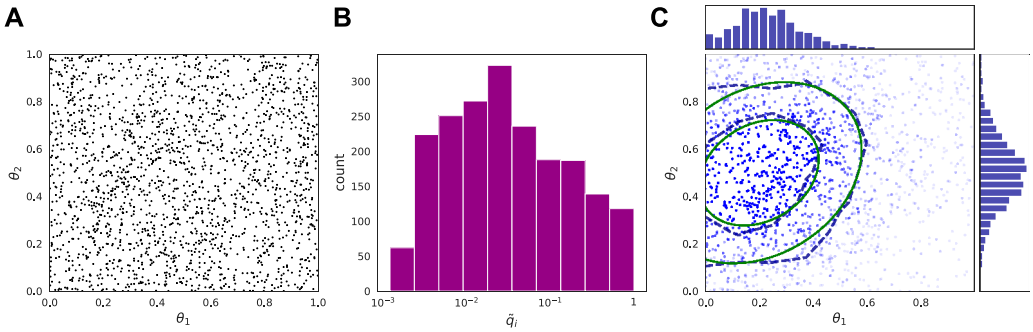

FIGURE 1
Illustration of S/IR procedures. **(A)** Samples $\{\boldsymbol{\theta}\}_{i=1}^{n}$ from the uniform prior in a unit square (n = 2000 samples are shown). **(B)** Histogram of rescaled importance weights $\tilde{q}_i = q_i/\max(\{q\})$ where $q_i = \mathcal{L}(\boldsymbol{\theta}_i)/\sum_{j=1}^{n}\mathcal{L}(\boldsymbol{\theta}_j)$ with $\mathcal{L}(\boldsymbol{\theta})$ as in Eq. 6. The number of effective samples is $n_{\text{eff}} = 214.6$. Note that the samples are drawn from a unit square and that the tail of the target distribution is not covered. **(C)** Samples $\{\boldsymbol{\theta}^{\star}\}_{i=1}^{N}$ of the posterior (blue dots with 10% opacity) resampled from the prior samples with probability mass q_i. The contour lines for the 68% and 90% credible regions of the posterior samples (blue dashed) are shown and compared with those of the exact bivariate target distribution (green solid). Summary histograms of the marginal distributions for θ_1 and θ_2 are shown in the top and right subplots.

The above resampling method can be applied to generate samples from the posterior PDF $h(\boldsymbol{\theta}) = \text{pr}(\boldsymbol{\theta}|\mathcal{D})$ in a Bayesian analysis. It remains to choose a sampling distribution, $g(\boldsymbol{\theta})$, which in principle could be any continuous density distribution. However, recall that $h(\boldsymbol{\theta})$ can be expressed in terms of an unnormalized distribution $f(\boldsymbol{\theta})$, and using Bayes' theorem 1) we can set $f(\boldsymbol{\theta}) = \mathcal{L}(\boldsymbol{\theta})\text{pr}(\boldsymbol{\theta})$. Thus, choosing the prior $\text{pr}(\boldsymbol{\theta})$ as the sampling distribution $g(\boldsymbol{\theta})$ we find that the importance weights are expressed in terms of the likelihood, $q_i = \mathcal{L}(\boldsymbol{\theta}_i)/\sum_{j=1}^{n}\mathcal{L}(\boldsymbol{\theta}_j)$. Assuming that it is simple to collect samples from the prior, the costly operation will be the evaluation of $\mathcal{L}(\boldsymbol{\theta}_i)$. Here we make the side remark that an effective and computationally cost-saving approximation can be made if we manage to perform a pre-screening to identify (and ignore) samples that will give a very small importance weight. We also note that the above choice of $g(\boldsymbol{\theta}) = \text{pr}(\boldsymbol{\theta})$ is purely for simplicity and one can perform importance resampling with any $g(\boldsymbol{\theta})$.

In Figure 1 we follow the above procedure and give a simple example of S/IR to illustrate how to get samples from a posterior distribution. We consider a two-dimensional parametric model with $\boldsymbol{\theta} = (\theta_1, \theta_2)$. Given data $\mathcal{D}$ obtained under the model we have:

$$\text{pr}(\theta_1, \theta_2|\mathcal{D}) = \frac{\mathcal{L}(\theta_1, \theta_2)\text{pr}(\theta_1, \theta_2)}{\iint \mathcal{L}(\theta_1, \theta_2)\text{pr}(\theta_1, \theta_2)\, d\theta_1 d\theta_2}. \tag{5}$$

For simplicity and illustration, the joint prior distribution for θ_1, θ_2 is set to be uniform over the unit square as shown in Figure 1A. In this example we also assume that the data $\mathcal{D}$ follows a multivariate Student-t distribution such that the likelihood function is

$$\mathcal{L}(\theta_1, \theta_2) = \frac{\Gamma[(\nu + p)/2]}{\Gamma(\nu/2)\nu^{p/2}\pi^{p/2}|\boldsymbol{\Sigma}|^{1/2}}\left[1 + \frac{1}{\nu}(\boldsymbol{\theta} - \boldsymbol{\mu})^T\boldsymbol{\Sigma}^{-1}(\boldsymbol{\theta} - \boldsymbol{\mu})\right]^{-(\mu+p)/2}, \tag{6}$$

where the dimension $p = 2$, the degrees of freedom $\nu = 2$, the mean vector $\boldsymbol{\mu} = (0.2, 0.5)$ and the scale matrix $\boldsymbol{\Sigma} = [[0.02, 0.005], [0.005, 0.02]]$.

The importance weights q_i are then computed for $n = 2000$ samples drawn from the prior (these prior samples are shown in Figure 1A). The resulting histogram of importance weights is shown in Figure 1B. Here the weights have been rescaled as $\tilde{q}_i = q_i/\max(\{q\})$ such that the sample with the largest probability mass corresponds to 1 in the histogram. We also define the effective number of samples, n_{eff}, as the sum of rescaled importance weights, $n_{\text{eff}} = \sum_{i=1}^{n}\tilde{q}_i$. Finally, in Figure 1C we show $N = 20,000$ new samples $\{\boldsymbol{\theta}_i^{\star}\}_{i=1}^{N}$ that are drawn from the prior samples $\{\boldsymbol{\theta}_i\}_{i=1}^{n}$ according to the probability mass q_i for each $\boldsymbol{\theta}_i$. The blue and green contour lines represent (68% and 90%) credible regions for the resampled distribution and for the

TABLE 1 Target values, z, and error assignments, ε, for observables used in the model calibration and for predictions. Energies in [MeV], point-proton radii in [fm], and the deuteron quadrupole moment in [e^2fm^2].

Calibration observables

Observable	z	ε_{exp}	$\varepsilon_{\text{model}}$	$\varepsilon_{\text{method}}$	ε_{em} (%)
$E(^2\text{H})$	−2.2298	0	0.05	0.0005	0.001
$R_p(^2\text{H})$	1.976	0	0.005	0.0002	0.0005
$Q(^2\text{H})$	0.27	0.01	0.003	0.0005	0.001
Predicted observables					
$E(^3\text{H})$	−8.4818	0	0.17	0.0005	0.01
$E(^4\text{He})$	−28.2956	0	0.55	0.0005	0.01
$R_p(^4\text{He})$	1.455	0	0.016	0.0002	0.003

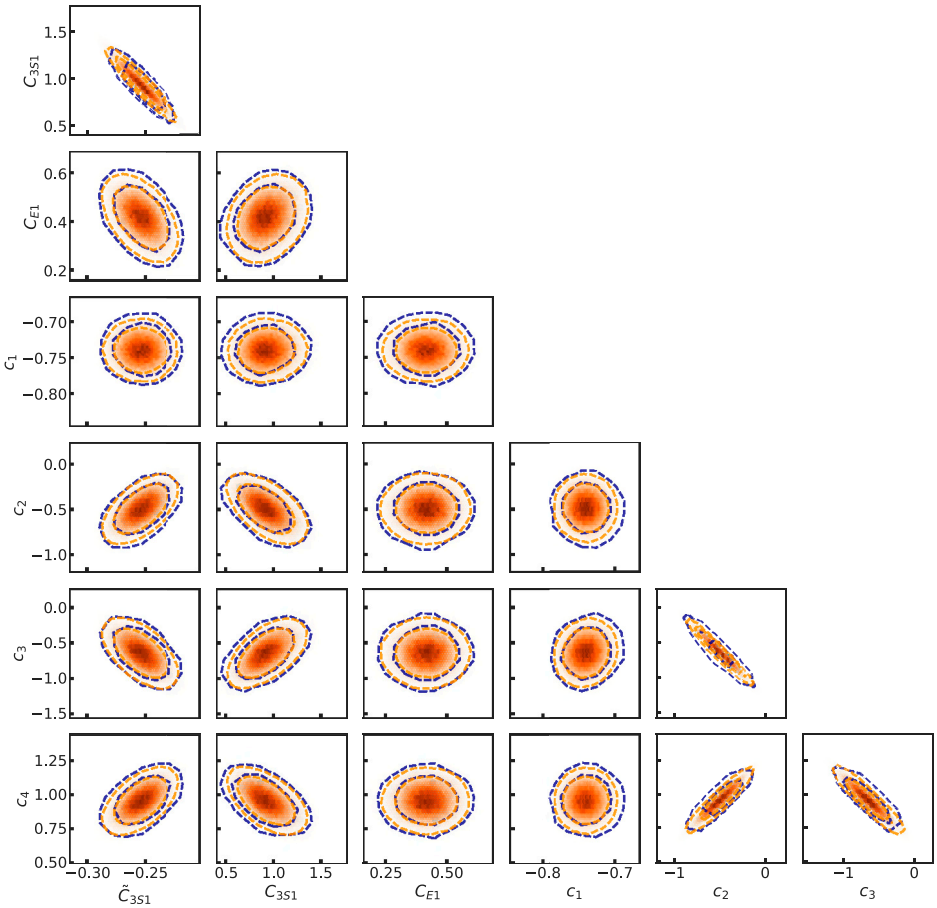

FIGURE 2
The joint posterior of LECs sampled with S/IR (blue) compared with MCMC sampling (orange). The LECs are shown in units of 10^4 GeV^{-1}, 10^4 GeV^{-2} and 10^4 GeV^{-4} for c_i, $\tilde{C}_i$ and C_i, respectively. The likelihood observables and assigned errors are given in Table 1. The contour lines indicate 68% and 90% credible regions.

Student-t distribution, respectively. This result demonstrates that the samples generated by the S/IR method give a very good approximation of the target posterior distribution.

3 Nuclear physics applications

Now that we have reviewed the basic idea of the S/IR method, we move on to present realistic applications of the resampling technique in nuclear structure calculations. Here we study Bayesian inference involving the ΔNNLO chiral interaction [33] with explicit inclusion of delta isobar degree of freedom at next-to-next-to-leading order. In Weinberg's power counting the ΔNNLO interaction model is parametrized by 17 LECs, with four pion-nucleon LECs ($c_{1,2,3,4}$) that are inferred from pion-nucleon scattering data and 13 additional LECs that should be inferred from extant experimental data of low-energy nucleon-nucleon scattering and bound-state nuclear observables.

For this application we treat only a subset of the parameters as active and keep the other LECs fixed at values taken from the $\Delta\text{NNLO}_{\text{GO}}(450)$ interaction [34]. Specifically, we consider deuteron observables and use seven active model parameters: $c_{1,2,3,4}$, $\tilde{C}_{3S1}$, C_{3S1}, C_{E1}. Our Gaussian likelihood contains three data wih independent errors: the deuteron ground state energy E, its point-proton radius R_{p} and one-body quadrupole moment Q with experimental and theoretical targets from Refs. [35–37]. Note that the target point-proton radii were transformed from experimental charge radii using the same relation as in Ref. [38]. For the target Q we use the theoretical result obtained by the CD-Bonn [37] model. With these simplified conditions, we perform S/IR as well as MCMC sampling to study 1) the posterior PDF for the LECs and 2) posterior predictive distributions (PPDs) for selected few-body observables. This application therefore allows a straightforward comparison of the two different sampling methods in a realistic setting. We note that the inclusion of all 17 LECs as active parameters would have required more

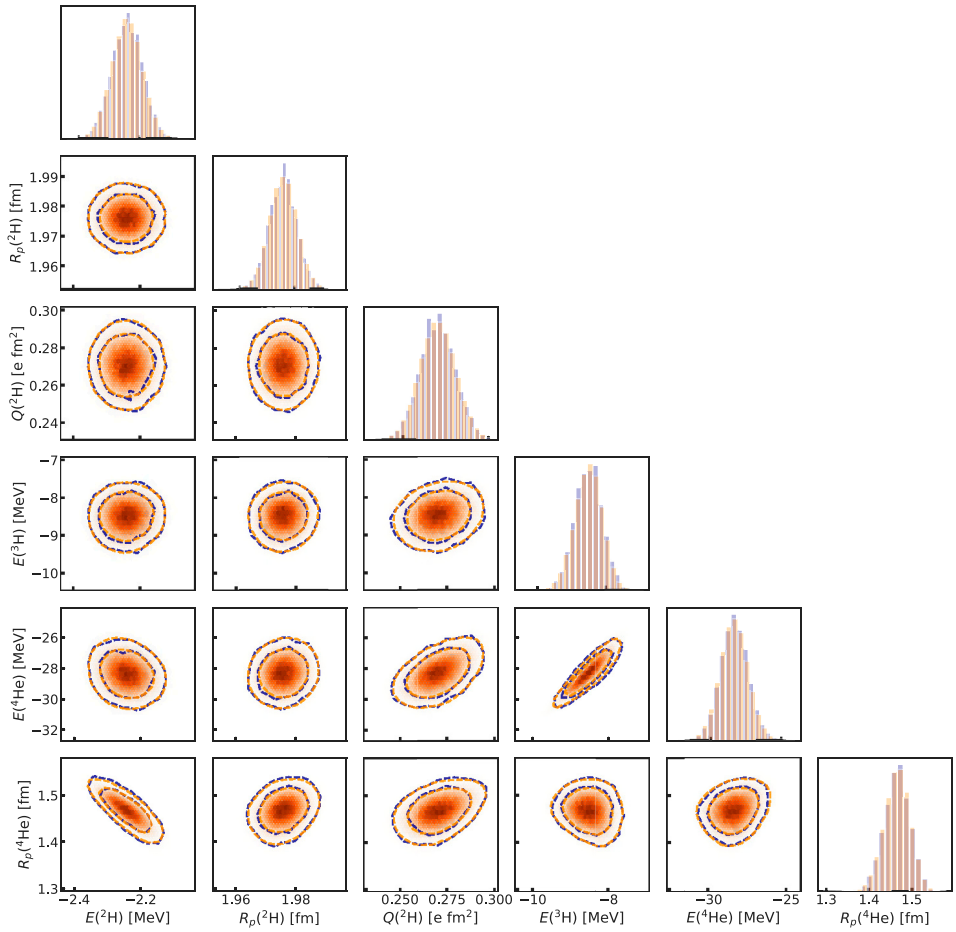

FIGURE 3
The PPD obtained from samples of the LECs posterior distribution as shown in Figure 2. The bivariate histograms and the corresponding contour lines denote the joint distribution of observables generate by S/IR (blue) and MCMC sampling (orange). The marginal distributions of the observables are shown in the diagonal panels.

careful tuning of the MCMC sampling algorithm and corresponding convergence studies.

It is the computation of observables, e.g., for likelihood evaluations, which is usually the major, time-consuming bottleneck in Bayesian analyses using MCMC methods. In this application, the statistical analysis is enabled by the use of emulators which mimic the outputs of many-body solvers but are faster by orders of magnitude. The emulators employed here for the ground-state observables of the deuteron, and later for few-body observables, are based on eigenvector continuation [39–41]. These emulators allow to reduce the computation time from seconds to milliseconds while keeping the relative error (compared with full no-core shell model calculation) within 0.001%. Unfortunately, emulators are not yet available for all nuclear observables. The MCMC sampling of posterior PDFs, or the evaluation of expectation integrals such as Eq. 2, will typically not work for models with observables that require heavy calculations.

The experimental target values and error assignments for the calibration observables used to condition the posterior PDF are listed in the upper half of Table 1. In this study we assume a normally-distributed likelihood, and consider different sources of error when calibrating the model predictions with experimental data. The errors are assumed to be independent. They include experimental, $\varepsilon_{\mathrm{exp}}$, model ($\chi$EFT truncation) discrepancy, $\varepsilon_{\mathrm{model}}$, many-body method, $\varepsilon_{\mathrm{method}}$, and emulator, $\varepsilon_{\mathrm{em}}$, errors. The χEFT truncation errors are estimated based on order-by-order calculations as in Ref. [33]. More details on the determination of the error scales can be found in Ref. [42].

Furthermore, we take advantage of previous studies and incorporate information about $c_{1,2,3,4}$ from a Roy-Steiner analysis of pion-nucleon scattering data [43] and identify a non-implausible domain for $\tilde{C}_{3S1}$, C_{3S1}, C_{E1} from a history matching approach in Ref. [42]. With this prior knowledge we

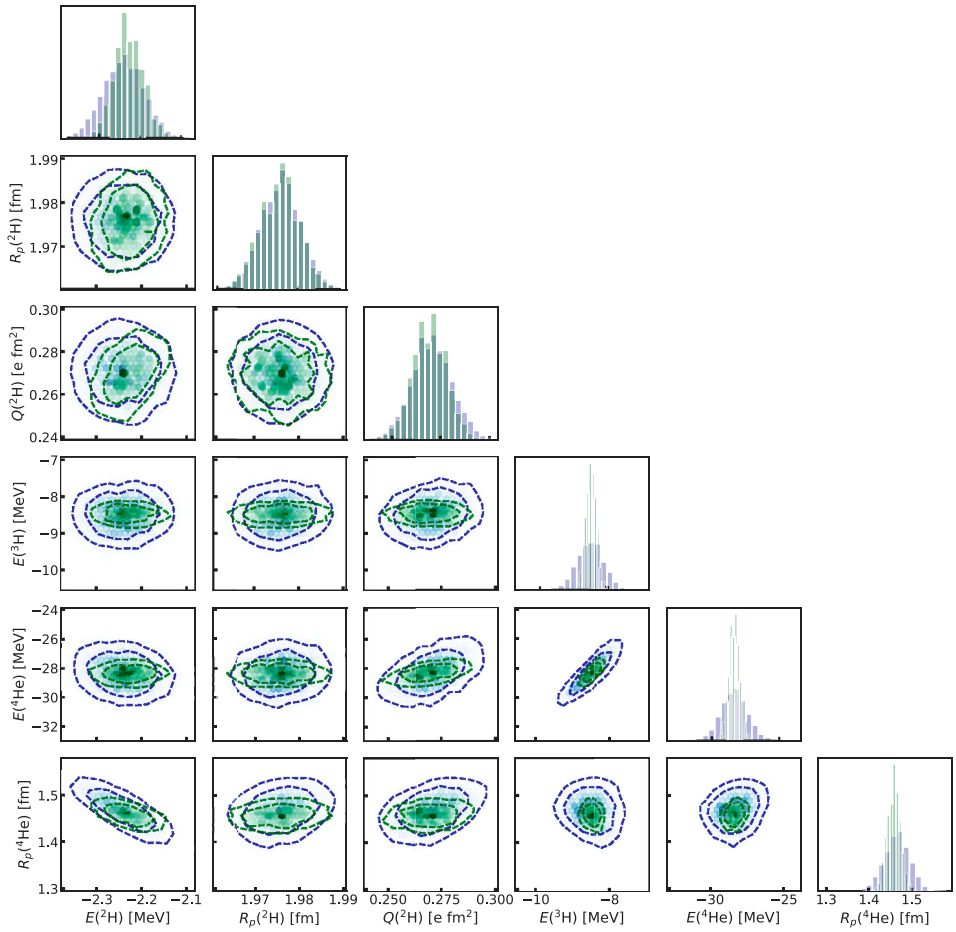

FIGURE 4
The posterior predictive distribution from sampling over two different posterior distributions. $PPD_{A=2}$ (blue) is calibrated by the deuteron observables while $PPD_{A=2,3,4}$ (green) is calibrated by the deuteron, ^{3}H and ^{4}He observables. The marginal distributions of the observables are shown in the diagonal panels.

set up the prior distribution of the seven LECs as the product of a multivariate Gaussian for $c_{1,2,3,4}$ and a uniform distribution for $\tilde{C}_{3S1}$, C_{3S1}, C_{E1}[1]. We note that the use of history matching is very beneficial for both S/IR and MCMC sampling. For S/IR it allows to select a sampling distribution that promises a large overlap with the target distribution and it identifies prior samples that are likely to have large weights in the resampling step. For MCMC, the non-implausible samples from history matching serve as good starting points for the walkers and thereby give faster convergence.

1 Specifically we use the non-implausible domain that was identified in wave 2 of the history matching performed in Ref. [42]. This wave only included deuteron observables.

3.1 Posterior sampling

Once we have the prior and the likelihood function we are able to draw samples from the posterior PDF and to analyze the *ab initio* description of few-nucleon systems with the present interaction model. The joint posterior of the LECs is shown in Figure 2, where we compare bivariate, marginal distributions from S/IR and MCMC sampling. For the MCMC sampling we employed an open-source Python toolkit called emcee [44] that performs affine-invariant ensemble sampling. We use 150 walkers that are warmed up with 5,000 initial steps and then move for 5×10^5 steps. This amounts to 7.6×10^7 likelihood evaluations. The positions of the walkers are recorded every 500 steps which gives 1.5×10^5 samples from the posterior distribution of the LECs. On the other hand, for S/IR we first acquire 2×10^4 samples from the prior distribution and perform the same number of likelihood evaluations to get the importance weights. From this limited set we then draw $1.5 \times$

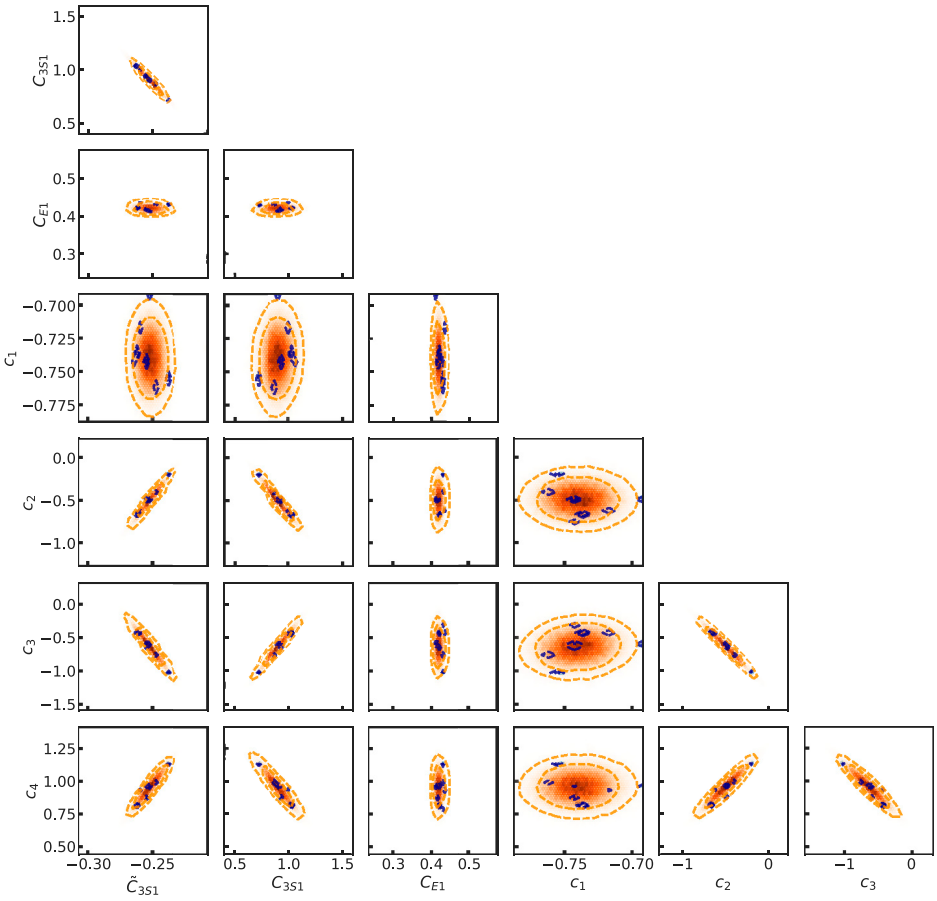

FIGURE 5
The posterior of LECs sampled with S/IR (blue) compared with MCMC sampling (orange) for a situation when the deuteron calibration observables are associated with errors that have been reduced by an order of magnitude (see text for details). The LECs are shown in units of 10^4 GeV^{-1}, 10^4 GeV^{-2} and 10^4 GeV^{-4} for c_i, $\tilde{C}_i$ and C_i, respectively.

10^5 samples using resampling (the same final number as in MCMC). Note that several prior samples occur more than once in the final sample set. Here the number of effective samples for S/IR is $n_{\text{eff}} = 1589.9$. As we can see from Figure 2, the contour lines of both sampling methods are in good agreement and, e.g., the correlation structure of the LEC pairs are equally well described. The histograms of S/IR and MCMC samples are both plotted in the figure but are almost impossible to distinguish.

As a second stage we use the inferred model to perform model checking of the calibration observables and to predict the ^{3}H ground-state energy and the ^{4}He ground-state energy and point-proton radius (see Table 1). For this purpose the PPD is defined as the set

$$\{\mathbf{y}_{\text{th}}(\boldsymbol{\theta}):\ \boldsymbol{\theta} \sim \text{pr}(\boldsymbol{\theta}\,|\,\mathcal{D})\}, \tag{7}$$

where $\mathbf{y}_{\text{th}}(\boldsymbol{\theta})$ is the theoretical predictions of selected observables using the model parameter vector $\boldsymbol{\theta}$. Figure 3 illustrate the PPD of the three deuteron observables using S/IR (blue) and MCMC sampling (orange). The marginal histograms of the observable predictions are shown in the diagonal panels of the corner plot. In this study both sampling methods give very similar distributions for all observables. Note that the predictive distributions for the three deuteron observables can be considered as model checking since they appeared in the likelihood function and therefore conditioned the LEC posterior. The ^{3}H and ^{4}He observables, on the other hand, are predictions in this study. Their distributions are characterized by larger variances compared to the deuteron predictions.

3.2 Posterior probability updates

As mentioned in the introduction, the S/IR method requires a minimum amount of computation to produce new samples when the posterior PDF is updated for various reasons. Here we present

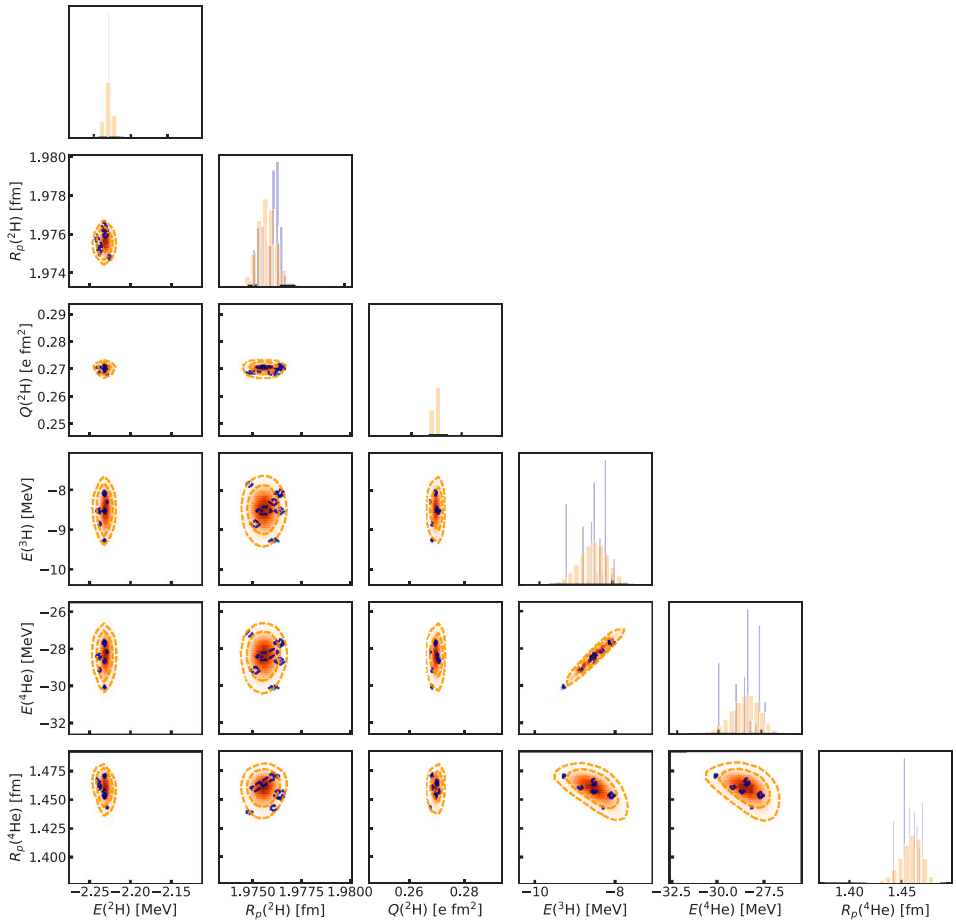

FIGURE 6
The PPD generated using S/IR (blue) and MCMC sampling (orange) for the posterior distributions shown in Figure 5. Marginal histograms of the observables are shown in the diagonal panels.

one likely scenario where the posterior is changed due to different choices of calibration data (for instance the inclusion of newly-accessible observables). Let us start from the previously described calibration of our interaction model with three selected deuteron observables. If we add ^{3}H and ^{4}He observables into the calibration (experimental target values and error assignments as in Table 1) to further condition the model, the likelihood function needs to be updated accordingly. The sampling of the posterior PDF should be repeated from the beginning and the new samples should be used to construct PPDs. However, using S/IR we resample from the same set of prior samples—only with different importance weights. The same set of samples also appear in the sampling of PPDs. To distinguish the original and the updated posteriors we use the notation $PPD_{A=2}$ to denote predictions with only deuteron observable as calibration data and $PPD_{A=2,3,4}$ with ^{3}H and ^{4}He added to the likelihood. These two different PPDs, generated by S/IR, are shown in Figure 4. Note that the $PPD_{A=2}$ (blue) is the same as in Figure 3, and is shown here as a benchmark. As expected we observe that the description of ^{3}H and ^{4}He observables is more accurate and more precise (smaller variations) with $PPD_{A=2,3,4}$ (green) as compared with $PPD_{A=2}$ (blue). We also find that the deuteron ground state energy is slightly improved with the updated posterior. This can be explained by the anti-correlation between $R_p(^4\mathrm{He})$ and $E(^2\mathrm{H})$. The additional constraints imposed by $R_p(^4\mathrm{He})$ through the likelihood function propagates to $E(^2\mathrm{H})$ *via* the correlation structure.

3.3 S/IR limitations

So far we have focused on the feasibility and advantage of the S/IR approach. However, there are some important limitations and we recommend users to be mindful of the number of effective samples. In Figure 4, we found that our S/IR sampling of $PPD_{A=2}$ has $n_{\mathrm{eff}} = 1589.9$, while for $PPD_{A=2,3,4}$ it drops to $n_{\mathrm{eff}} = 314.9$. This can be understood by the resampling from a fixed set of prior samples. The more

complex the likelihood function, the less effective the samples. As seen in Figure 4, the contour lines of $PPD_{A=2,3,4}$ is less smooth then those obtained from $PPD_{A=2}$ due to the smaller number of effective samples. The S/IR method will eventually break when n_{eff} becomes too small. An intermediate remedy could be the use of kernel density estimators, although that approach typically introduces an undesired sensitivity to the choice of kernel widths.

A similar situation occurs when the target observables are characterized by very small error assignments. This leads to a sharply peaked likelihood function and a decreased overlap with the prior samples. The resulting large variance of importance weights implies that the final set representing the posterior distribution will be dominated by a very small number of samples. Here we show such an example where resampling no longer works. We attempted to reconstruct a PPD with only deuteron observables in the calibration, but where all error assignments in Table 1 had been reduced by an order of magnitude. The results of this analysis are shown in Figures 5, 6 which display the PDFs and PPDs, respectively, generated by S/IR (blue) and compared with MCMC (orange). The S/IR method does not perform well in this case. With $n_{\text{eff}} = 4.4$ the PDF and PPD generated by S/IR are represented by a few samples. The MCMC sampling, on the other hand, does manage to identify the updated distribution.

Unfortunately one can also envision more difficult scenarios in which S/IR could fail without any clear signatures. For example, if the prior has a very small overlap with the posterior there is a risk that many prior samples get a similar importance weight (such that the number of effective samples is large) but that one has missed the most interesting region. Again, history matching is a very useful tool in the analysis as it can be used to ensure that we are focusing on the LECs domain that covers the mode(s) of the posterior.

4 Summary

In this paper we reviewed an established sampling method known as S/IR. Specifically, we applied importance resampling using the weighted bootstrap algorithm and sampled the posterior PDF for selected LECs of the ΔNNLO interaction model conditioned on deuteron observables. The resulting PDF and PPD were compared with those obtained from MCMC sampling and a very good agreement was found. We also demonstrated Bayesian updating using S/IR by the addition of ^{3}H and ^{4}He observables to the calibration data set. As expected, the predictions of ^{3}H and ^{4}He observables were improved, but also the description of the deuteron ground-state energy which could be explained by the correlation structure between $E(^2\text{H})$ and $R_p(^4\text{He})$. Finally, we illustrated some limitations of the S/IR method that were signaled by small numbers of effective samples. We found that such situations occured when the likelihood became too complex for the limited model, or when prior samples failed to resolve a very peaked posterior that resulted from small tolerances. We also argued that prior knowledge of the posterior landscape is very useful to avoid possible failure scenarios that might not be signaled by the number of effective samples.

Data availability statement

The original contributions presented in the study are included in the article/Supplementary Material, further inquiries can be directed to the corresponding author.

Author contributions

WJ and CF contributed equally in this paper.

Funding

This work was supported by the European Research Council under the European Unions Horizon 2020 research and innovation program (Grant No. 758027) and the Swedish Research Council (Grant Nos 2017-04234 and 2021-04507). The computations and data handling were enabled by resources provided by the Swedish National Infrastructure for Computing (SNIC) at Chalmers Centre for Computational Science and Engineering (C3SE), and the National Supercomputer Centre (NSC) partially funded by the Swedish Research Council through Grant No. 2018-05973.

Conflict of interest

The authors declare that the research was conducted in the absence of any commercial or financial relationships that could be construed as a potential conflict of interest.

Publisher's note

References

1. Schindler MR, Phillips DR. Bayesian methods for parameter estimation in effective field theories. *Ann Phys (N Y)* (2009) 324:682–708. doi:10.1016/j.aop.2008.09.003

2. Caesar C, Simonis J, Adachi T, Aksyutina Y, Alcantara J, Altstadt S, et al. Beyond the neutron drip line: The unbound oxygen isotopes ^{25}o and ^{26}o. *Phys Rev C* (2013) 88:034313. doi:10.1103/PhysRevC.88.034313

3. Furnstahl RJ, Klco N, Phillips DR, Wesolowski S. Quantifying truncation errors in effective field theory. *arXiv e-prints* (2015).

4. Wesolowski S, Furnstahl RJ, Melendez JA, Phillips DR. Exploring bayesian parameter estimation for chiral effective field theory using nucleon–nucleon phase shifts. *J Phys G: Nucl Part Phys* (2019) 46:045102. doi:10.1088/1361-6471/aaf5fc

5. Melendez JA, Furnstahl RJ, Phillips DR, Pratola MT, Wesolowski S. Quantifying correlated truncation errors in effective field theory. *Phys Rev C* (2019) 100:044001. doi:10.1103/PhysRevC.100.044001

6. Epelbaum E, Golak J, Hebeler K, Kamada H, Krebs H, MeiBner UG, et al. Towards high-order calculations of three-nucleon scattering in chiral effective field theory. *Eur Phys J A* (2020) 56:92. doi:10.1140/epja/s10050-020-00102-2

7. Yang L, Lin C, Zhang Y, Wen P, Jia H, Wang D, et al. Bayesian analysis on interactions of exotic nuclear systems. *Phys Lett B* (2020) 807:135540. doi:10.1016/j.physletb.2020.135540

8. Phillips DR, Furnstahl RJ, Heinz U, Maiti T, Nazarewicz W, Nunes FM, et al. Get on the band wagon: A bayesian framework for quantifying model uncertainties in nuclear dynamics. *J Phys G: Nucl Part Phys* (2021) 48:072001. doi:10.1088/1361-6471/abf1df

9. Drischler C, Furnstahl RJ, Melendez JA, Phillips DR. How well do we know the neutron-matter equation of state at the densities inside neutron stars? A bayesian approach with correlated uncertainties. *Phys Rev Lett* (2020) 125:202702. doi:10.1103/PhysRevLett.125.202702

10. Drischler C, Melendez JA, Furnstahl RJ, Phillips DR. Quantifying uncertainties and correlations in the nuclear-matter equation of state. *Phys Rev C* (2020) 102:054315. doi:10.1103/PhysRevC.102.054315

11. Maris P, Epelbaum E, Furnstahl RJ, Golak J, Hebeler K, Huther T, et al. Light nuclei with semilocal momentum-space regularized chiral interactions up to third order. *Phys Rev C* (2021) 103:054001. doi:10.1103/PhysRevC.103.054001

12. Wesolowski S, Svensson I, Ekström A, Forssén C, Furnstahl RJ, Melendez JA, et al. Rigorous constraints on three-nucleon forces in chiral effective field theory from fast and accurate calculations of few-body observables. *Phys Rev C* (2021) 104:064001. doi:10.1103/PhysRevC.104.064001

13. Djärv T, Ekström A, Forssén C, Johansson HT. Bayesian predictions for A=6 nuclei using eigenvector continuation emulators. *Phys Rev C* (2022) 105:014005. doi:10.1103/PhysRevC.105.014005

14. Svensson I, Ekström A, Forssén C. Bayesian parameter estimation in chiral effective field theory using the Hamiltonian Monte Carlo method. *Phys Rev C* (2022) 105:014004. doi:10.1103/PhysRevC.105.014004

15. Acharya B, Bacca S. Gaussian process error modeling for chiral effective-field-theory calculations of np ↔dγ at low energies. *Phys Lett B* (2022) 827:137011. doi:10.1016/j.physletb.2022.137011

16. Svensson I, Ekström A, Forssén C. Bayesian estimation of the low-energy constants up to fourth order in the nucleon-nucleon sector of chiral effective field theory. arXiv 2206.08250 (2022). doi:10.48550/arXiv.2206.08250

17. Metropolis N, Rosenbluth AW, Rosenbluth MN, Teller AH, Teller E. Equation of state calculations by fast computing machines. *J Chem Phys* (1953) 21:1087–92. doi:10.1063/1.1699114

18. Hastings WK. Monte Carlo sampling methods using Markov chains and their applications. *Biometrika* (1970) 57:97–109. doi:10.1093/biomet/57.1.97

19. Hitchcock DB. A history of the metropolis–hastings algorithm. *The Am Statistician* (2003) 57:254–7. doi:10.1198/0003130032413

20. von Toussaint U. Bayesian inference in physics. *Rev Mod Phys* (2011) 83:943–99. doi:10.1103/RevModPhys.83.943

21. Brooks S, Gelman A, Jones G, Meng X. *Handbook of Markov chain Monte Carlo*. Florida, United States: Chapman & Hall/CRC Handbooks of Modern Statistical Methods CRC Press (2011).

22. Rubin DB. Using the sir algorithm to simulate posterior distributions. *Bayesian Stat* (1988) 3:395–402.

23. Smith AFM, Gelfand AE. Bayesian statistics without tears: A sampling-resampling perspective. *Am Stat* (1992) 46:84–8. doi:10.2307/2684170

24. Bernardo J, Smith A. Bayesian theory. In: *Wiley series in probability and statistics*. New Jersey, United States: John Wiley & Sons Canada, Limited (2006).

25. Kolck UV. Effective field theory of nuclear forces. *Prog Part Nucl Phys* (1999) 43:337–418. doi:10.1016/S0146-6410(99)00097-6

26. Bogner SK, Kuo TTS, Schwenk A. Model-independent low momentum nucleon interaction from phase shift equivalence. *Phys Rep* (2003) 386:1–27. doi:10.1016/j.physrep.2003.07.001

27. Epelbaum E, Hammer HW, Meißner UG. Modern theory of nuclear forces. *Rev Mod Phys* (2009) 81:1773–825. doi:10.1103/RevModPhys.81.1773

28. Bogner S, Furnstahl R, Schwenk A. From low-momentum interactions to nuclear structure. *Prog Part Nucl Phys* (2010) 65:94–147. doi:10.1016/j.ppnp.2010.03.001

29. Machleidt R, Entem D. Chiral effective field theory and nuclear forces. *Phys Rep* (2011) 503:1–75. doi:10.1016/j.physrep.2011.02.001

30. Weinberg S. Nuclear forces from chiral Lagrangians. *Phys Lett B* (1990) 251:288–92. doi:10.1016/0370-2693(90)90938-3

31. Weinberg S. Effective chiral Lagrangians for nucleon-pion interactions and nuclear forces. *Nucl Phys B* (1991) 363:3–18. doi:10.1016/0550-3213(91)90231-L

32. Kaplan DB, Savage MJ, Wise MB. A new expansion for nucleon-nucleon interactions. *Phys Lett B* (1998) 424:390–6. doi:10.1016/S0370-2693(98)00210-X

33. Ekström A, Hagen G, Morris TD, Papenbrock T, Schwartz PD. Δ isobars and nuclear saturation. *Phys Rev C* (2018) 97:024332. doi:10.1103/PhysRevC.97.024332

34. Jiang WG, Ekström A, Forssén C, Hagen G, Jansen GR, Papenbrock T. Accurate bulk properties of nuclei from $A = 2$ to ∞ from potentials with Δ isobars. *Phys Rev C* (2020) 102:054301. doi:10.1103/PhysRevC.102.054301

35. Wang M, Huang WJ, Kondev FG, Audi G, Naimi S. The AME 2020 atomic mass evaluation (II). Tables, graphs and references. *Chin Phys C* (2021) 45:030003. doi:10.1088/1674-1137/abddaf

36. Angeli I, Marinova K. Table of experimental nuclear ground state charge radii: An update. *Data Nucl Data Tables* (2013) 99:69–95. doi:10.1016/j.adt.2011.12.006

37. Machleidt R. High-precision, charge-dependent Bonn nucleon-nucleon potential. *Phys Rev C* (2001) 63:024001. doi:10.1103/PhysRevC.63.024001

38. Ekström A, Jansen GR, Wendt KA, Hagen G, Papenbrock T, Carlsson BD, et al. Accurate nuclear radii and binding energies from a chiral interaction. *Phys Rev C* (2015) 91:051301. doi:10.1103/PhysRevC.91.051301

39. Frame D, He R, Ipsen I, Lee D, Lee D, Rrapaj E. Eigenvector continuation with subspace learning. *Phys Rev Lett* (2018) 121:032501. doi:10.1103/PhysRevLett.121.032501

40. König S, Ekström A, Hebeler K, Lee D, Schwenk A. Eigenvector continuation as an efficient and accurate emulator for uncertainty quantification. *Phys Lett B* (2020) 810:135814. doi:10.1016/j.physletb.2020.135814

41. Ekström A, Hagen G. Global sensitivity analysis of bulk properties of an atomic nucleus. *Phys Rev Lett* (2019) 123:252501. doi:10.1103/PhysRevLett.123.252501

42. Hu B, Jiang W, Miyagi T, Sun Z, Ekstrom A, Forssen C, et al. *Ab initio* predictions link the neutron skin of ^{208}Pb to nuclear forces. *Nat Phys* (2022) 18:1196–200. doi:10.1038/s41567-022-01715-8

43. Siemens D, Ruiz de Elvira J, Epelbaum E, Hoferichter M, Krebs H, Kubis B, et al. Reconciling threshold and subthreshold expansions for pion–nucleon scattering. *Phys Lett B* (2017) 770:27–34. doi:10.1016/j.physletb.2017.04.039

44. Foreman-Mackey D, Hogg DW, Lang D, Goodman J. emcee: The MCMC hammer. *Publications Astronomical Soc Pac* (2013) 125:306–12. doi:10.1086/670067

frontiers | Frontiers in Physics

TYPE Original Research
PUBLISHED 08 November 2022
DOI 10.3389/fphy.2022.1028370

OPEN ACCESS

EDITED BY
Christian Forssén,
Chalmers University of Technology, Sweden

REVIEWED BY
Daniel Phillips,
Ohio University, United States
Markus Kortelainen,
University of Jyväskylä, Finland

*CORRESPONDENCE
Nicolas Schunck,
schunck1@llnl.gov

SPECIALTY SECTION
This article was submitted to Nuclear Physics, a section of the journal Frontiers in Physics

RECEIVED 25 August 2022
ACCEPTED 19 October 2022
PUBLISHED 08 November 2022

CITATION
Verriere M, Schunck N, Kim I, Marević P, Quinlan K, Ngo MN, Regnier D and Lasseri RD (2022), Building surrogate models of nuclear density functional theory with Gaussian processes and autoencoders.
Front. Phys. 10:1028370.
doi: 10.3389/fphy.2022.1028370

Building surrogate models of nuclear density functional theory with Gaussian processes and autoencoders

Marc Verriere[1], Nicolas Schunck[1]*, Irene Kim[2,3], Petar Marević[1,4,5], Kevin Quinlan[6], Michelle N. Ngo[6,7], David Regnier[8,9] and Raphael David Lasseri[4]

[1]Nuclear and Data Theory Group, Nuclear and Chemical Science Division, Lawrence Livermore National Laboratory, Livermore, CA, United States, [2]Machine Intelligence Group, Center for Applied Scientific Computing, Lawrence Livermore National Laboratory, Livermore, CA, United States, [3]Sensing and Intelligent Systems Group, Global Security Computing Applications Division, Lawrence Livermore National Laboratory, Livermore, CA, United States, [4]Centre Borelli, ENS Paris-Saclay, Université Paris-Saclay, Cachan, France, [5]Physics Department, Faculty of Science, University of Zagreb, Zagreb, Croatia, [6]Applied Statistics Group, Lawrence Livermore National Laboratory, Livermore, CA, United States, [7]Center for Complex Biological Systems, University of California Irvine, Irvine, CA, United States, [8]Université Paris-Saclay, CEA, Laboratoire Matière en Conditions Extrêmes, Bruyères-le-Châtel, France, [9]CEA, DAM, DIF, Bruyères-le-Châtel, France

From the lightest Hydrogen isotopes up to the recently synthesized Oganesson (Z = 118), it is estimated that as many as about 8,000 atomic nuclei could exist in nature. Most of these nuclei are too short-lived to be occurring on Earth, but they play an essential role in astrophysical events such as supernova explosions or neutron star mergers that are presumed to be at the origin of most heavy elements in the Universe. Understanding the structure, reactions, and decays of nuclei across the entire chart of nuclides is an enormous challenge because of the experimental difficulties in measuring properties of interest in such fleeting objects and the theoretical and computational issues of simulating strongly-interacting quantum many-body systems. Nuclear density functional theory (DFT) is a fully microscopic theoretical framework which has the potential of providing such a quantitatively accurate description of nuclear properties for every nucleus in the chart of nuclides. Thanks to high-performance computing facilities, it has already been successfully applied to predict nuclear masses, global patterns of radioactive decay like β or γ decay, and several aspects of the nuclear fission process such as, e.g., spontaneous fission half-lives. Yet, predictive simulations of nuclear spectroscopy—the low-lying excited states and transitions between them—or of nuclear fission, or the quantification of theoretical uncertainties and their propagation to basic or applied nuclear science applications, would require several orders of magnitude more calculations than currently possible. However, most of this computational effort would be spent into generating a suitable basis of DFT wavefunctions. Such a task could potentially be considerably accelerated by borrowing tools from the field of machine learning and artificial intelligence. In this paper, we review

different approaches to applying supervised and unsupervised learning techniques to nuclear DFT.

KEYWORDS

nuclear density functional theory, Gaussian process, deep learning, autoencoders, resnet

1 Introduction

Predicting all the properties of every atomic nucleus in the nuclear chart, from Hydrogen all the way to superheavy elements, remains a formidable challenge. Density functional theory (DFT) offers a compelling framework to do so, since the computational cost is, in principle, nearly independent of the mass of the system Eschrig [1]. Because of our incomplete knowledge of nuclear forces and of the fact that the nucleus is a self-bound system, the implementation of DFT in nuclei is slightly different from other systems such as atoms or molecules and is often referred to as the energy density functional (EDF) formalism Schunck [2].

Simple single-reference energy density functional (SR-EDF) calculations of atomic nuclei can often be done on a laptop. However, large-scale SR-EDF computations of nuclear properties or higher-fidelity simulations based on the multi-reference (MR-EDF) framework can quickly become very expensive computationally. Examples where such computational load is needed range from microscopic fission theory Schunck and Regnier [3]; Schunck and Robledo [4] to parameter calibration and uncertainty propagation Kejzlar et al. [5]; Schunck et al. [6] to calculations at the scale of the entire chart of nuclides Erler et al. [7]; Ney et al. [8] relevant, e.g., for astrophysical simulations Mumpower et al. [9]. Many of these applications would benefit from a reliable emulator of EDF models.

It may be useful to distinguish two classes of quantities that such emulators should reproduce. What we may call "integral" quantities are quantum-mechanical observables such as, e.g., the energy, radius, or spin of the nucleus, or more complex data such as decay or capture rates. By contrast, we call "differential" quantities the basic degrees of freedom of the theoretical model. In this article, we focus on the Hartree-Fock-Bogoliubov (HFB) theory, which is both the cornerstone of the SR-EDF approach and provides the most common basis of generator states employed in MR-EDF calculations. In the HFB theory, all the degrees of freedom are encapsulated into three equivalent quantities: the quasiparticle spinors, as defined either on some spatial grid or configuration space; the full non-local density matrix $\rho(\boldsymbol{r}\sigma\tau, \boldsymbol{r}'\sigma'\tau')$ and pairing tensor $\kappa(\boldsymbol{r}\sigma\tau, \boldsymbol{r}'\sigma'\tau')$, where $\boldsymbol{r}$ refers to spatial coordinates, $\sigma = \pm 1/2$ to the spin projection and $\tau = \pm 1/2$ to the isopin projection Perlińska et al. [10]; the full non-local HFB mean-field and pairing potentials, often denoted by h $(\boldsymbol{r}\sigma\tau, \boldsymbol{r}'\sigma'\tau')$ and $\Delta(\boldsymbol{r}\sigma\tau, \boldsymbol{r}'\sigma'\tau')$.

Obviously, integral quantities have the clearest physical meaning and can be compared to data immediately. For this reason, they have been the focus of most of the recent efforts in applying techniques of machine learning and artificial intelligence (ML/AI) to low-energy nuclear theory, with applications ranging from mass tables Utama et al. [11]; Utama and Piekarewicz [12,13]; Niu and Liang [14]; Neufcourt et al. [15]; Lovell et al. [16]; Scamps et al. [17]; Mumpower et al. [18], β-decay rates Niu et al. [19], or fission product yields Wang et al. [20]; Lovell et al. [21]. The main limitation of this approach is that it must be repeated for every observable of interest. In addition, incorporating correlations between such observables, for example the fact that β-decay rates are strongly dependent on Q_β-values which are themselves related to nuclear masses, is not easy. This is partly because the behavior of observables such as the total energy or the total spin is often driven by underlying shell effects that can lead to very rapid variations, e.g. at a single-particle crossing. Such effects could be very hard to incorporate accurately in a statistical model of integral quantities.

This problem can in principle be solved by emulating what we called earlier differential quantities. For example, single-particle crossings might be predicted reliably with a good statistical model for the single-particle spinors themselves. In addition, since differential quantities represent, by definition, all the degrees of freedom of the SR-EDF theory, any observable of interest can be computed from them, and the correlations between these observables would be automatically reproduced. In this sense, an emulator of differential quantities is truly an emulator for the entire SR-EDF approach and can be thought of as a variant of intrusive, model-driven, model order reduction techniques discussed in Melendez et al. [22]; Giuliani et al. [23]; Bonilla et al. [24]. In the much simpler case of the Bohr collective Hamiltonian, such a strategy gave promising results Lasseri et al. [25].

The goal of this paper is precisely to explore the feasibility of training statistical models to learn the degrees of freedom of the HFB theory. We have explored two approaches: a simple one based on independent, stationary Gaussian processes and a more advanced one relying on deep neural networks with autoencoders and convolutional layers.

In Section 2, we briefly summarize the nuclear EDF formalism with Skyrme functionals with a focus on the HFB theory preserving axial symmetry. Section 3 presents the results obtained with Gaussian processes. After recalling some general notions about Gaussian processes, we analyze the results of fitting HFB potential across a two-dimensional potential energy surface in ^{240}Pu. Section 4 is devoted to autoencoders. We discuss choices

made both for the network architecture and for the training data set. We quantify the performance of autoencoders in reproducing canonical wavefunctions across a potential energy surface in ^{98}Zr and analyze the structure of the latent space.

2 Nuclear density functional theory

In very broad terms, the main assumption of density functional theory (DFT) for quantum many-body systems is that the energy of the system of interest can be expressed as a functional of the density of particles Parr and Yang [26]; Dreizler and Gross [27]; Eschrig [1]. Atomic nuclei are a somewhat special case of DFT, since the nuclear Hamiltonian is not known exactly and the nucleus is a self-bound system Engel [28]; Barnea [29]. As a result, the form of the energy density functional (EDF) is often driven by underlying models of nuclear forces, and the EDF is expressed as a function of non-local, symmetry-breaking, intrinsic densities Schunck [2]. In the single-reference EDF (SR-EDF) approach, the many-body nuclear state is approximated by a simple product state of independent particles or quasiparticles, possibly with some constraints reflecting the physics of the problem. We notate $|\Phi(\boldsymbol{q})\rangle$ such as state, with $\boldsymbol{q}$ representing a set of constraints. The multi-reference EDF (MR-EDF) approach builds a better approximation of the exact many-body state by mixing together SR-EDF states.

2.1 Energy functional

The two most basic densities needed to build accurate nuclear EDFs are the one-body density matrix ρ and the pairing tensor κ (and its complex conjugate κ^*). The total energy of the nucleus is often written as

$$E[\rho,\kappa,\kappa^\star] = E_{\text{nuc}}[\rho] + E_{\text{Cou}}[\rho] + E_{\text{pair}}[\rho,\kappa,\kappa^\star], \tag{1}$$

where $E_{\text{nuc}}[\rho]$ represents the particle-hole, or mean-field, contribution to the total energy from nuclear forces, $E_{\text{Cou}}[\rho]$ the same contribution from the Coulomb force, and $E_{\text{pair}}[\rho, \kappa, \kappa^*]$ the particle-particle contribution to the energy[1]. In this work, we model the nuclear part of the EDF with a Skyrme-like term

$$E_{\text{nuc}}[\rho] = \sum_{t=0,1}\int \mathrm{d}^3\boldsymbol{r}\,\chi_t(\boldsymbol{r}), \tag{2}$$

which includes the kinetic energy term and reads generically

$$\chi_t(\boldsymbol{r}) = C_t^{\rho\rho}\rho_t^2 + C_t^{\rho\tau}\rho_t\tau_t + C_t^{JJ}\mathbf{J}_t^2 + C_t^{\rho\Delta\rho}\rho_t\Delta\rho_t + C_t^{\rho\nabla J}\rho_t\boldsymbol{\nabla}\cdot\boldsymbol{J}_t. \tag{3}$$

In this expression, the index t refers to the isoscalar ($t = 0$) or isovector ($t = 1$) channel and the terms $C_t^{uu'}$ are the coupling constants associated with the energy functional. The particle density $\rho_t(\boldsymbol{r})$, kinetic energy density $\tau_t(\boldsymbol{r})$, spin-current tensor $\mathbf{J}_t(\boldsymbol{r})$, and vector density $\boldsymbol{J}_t(\boldsymbol{r})$ are all derived from the full one-body, non-local density $\rho(\boldsymbol{r}\sigma\tau, \boldsymbol{r}'\sigma'\tau')$ where $\boldsymbol{r}$ are spatial coordinates, σ is the intrinsic spin projection, $\sigma = \pm 1/2$, and $\tau = \pm 1/2$ is the isospin projection; see Engel et al. [30]; Dobaczewski and Dudek [31]; Bender et al. [32]; Perlińska et al. [10]; Lesinski et al. [33] for their actual definition. Since we do not consider any proton-neutron mixing, all densities are diagonal in isospin space. The two remaining terms in Eq. 1 are treated in exactly the same way as in Schunck et al. [34]. In particular, the pairing energy is derived from a surface-volume density-dependent pairing force

$$V^{(\tau)}(\boldsymbol{r},\boldsymbol{r}') = V_0^{(\tau)}\left[1 - \frac{1}{2}\frac{\rho(\boldsymbol{r})}{\rho_c}\right]\delta(\boldsymbol{r}-\boldsymbol{r}'), \tag{4}$$

where $\rho_c = 0.16$ fm^{-3} is the saturation density of nuclear matter.

2.2 Hartree-Fock-Bogoliubov theory

The actual densities in (3) are obtained by solving the Hartree-Fock-Bogoliubov (HFB) equation, which derives from applying a variational principle and imposing that the energy be minimal under variations of the densities Schunck [2]. The HFB equation is most commonly solved in the form of a non-linear eigenvalue problem. The eigenfunctions define the quasiparticle (q.p.) spinors. Without proton-neutron mixing, we can treat neutrons and protons separately. Therefore, for any one type of particles, the HFB equation giving the μ^{th} eigenstate reads in coordinate space Dobaczewski et al. [35].

$$\begin{gathered}\int \mathrm{d}^3\boldsymbol{r}'\sum_{\sigma'}\begin{pmatrix} h(\boldsymbol{r}\sigma,\boldsymbol{r}'\sigma') - \lambda\delta_{\sigma\sigma'} & \tilde{h}(\boldsymbol{r}\sigma,\boldsymbol{r}'\sigma') \\ \tilde{h}^*(\boldsymbol{r}\sigma,\boldsymbol{r}'\sigma') & -h(\boldsymbol{r}\sigma,\boldsymbol{r}'\sigma') + \lambda\delta_{\sigma\sigma'}\end{pmatrix} \\ \begin{pmatrix} U(E_\mu,\boldsymbol{r}'\sigma') \\ V(E_\mu,\boldsymbol{r}'\sigma')\end{pmatrix} = E_\mu\begin{pmatrix} U(E_\mu,\boldsymbol{r}\sigma) \\ V(E_\mu,\boldsymbol{r}\sigma)\end{pmatrix},\end{gathered} \tag{5}$$

where $h(\boldsymbol{r}\sigma, \boldsymbol{r}'\sigma')$ is the mean field, $\tilde{h}(\boldsymbol{r}\sigma,\boldsymbol{r}'\sigma')$ the pairing field[2] and λ the Fermi energy. Such an eigenvalue problem must be solved for protons and for neutrons.

For the case of Skyrme energy functionals and zero-range pairing functionals, both the mean field h and pairing field $\tilde{h}$ become semi-local functions of $\boldsymbol{r}$ (semi-local refers to the fact that these potentials involve differential operators). We refer to

1 The pairing contribution lumps together terms coming from nuclear forces, Coulomb forces and possibly rearrangement terms.

2 Following Dobaczewski et al. [35,117], we employ the 'russian' convention where the pairing field is defined from the pairing density $\tilde{\rho}(\boldsymbol{r}\sigma,\boldsymbol{r}'\sigma')$ rather than the pairing tensor. The quantity $\tilde{h}$ is related to the more traditional form of the pairing field Δ through: $\tilde{h}(\boldsymbol{r}\sigma,\boldsymbol{r}'\sigma') = -2\sigma'\Delta(\boldsymbol{r}\sigma,\boldsymbol{r}'-\sigma')$.

Vautherin and Brink [36]; Engel et al. [30] for an outline of the derivations leading to the expressions of the mean field in the case of Skyrme functionals and to, e.g., Dobaczewski and Dudek [37]; Bender et al. [38]; Hellemans et al. [39]; Ryssens et al. [40] for the expression of the mean field in terms of coupling constants rather than the parameters of the Skyrme potential. In the following, we simply recall the essential formulas needed in the rest of the manuscript.

Expression 5 is written in coordinate space. In configuration space, i.e., when the q.p. spinors are expanded on a suitable basis of the single-particle (s.p.) Hilbert space, the same equation becomes a non-linear eigenvalue problem that can be written as

$$\begin{pmatrix} h-\lambda & \tilde{h} \\ \tilde{h}^{\star} & -h^{\star}+\lambda \end{pmatrix}\begin{pmatrix} U & V^{\star} \\ V & U^{\star} \end{pmatrix} = \begin{pmatrix} U & V^{\star} \\ V & U^{\star} \end{pmatrix}\begin{pmatrix} -E & 0 \\ 0 & E \end{pmatrix}, \quad (6)$$

where h, $\tilde{h}$, U and V are now $N_{\text{basis}} \times N_{\text{basis}}$ matrices, with N_{basis} the number of basis states. Eigenvalues are collected in the diagonal $N_{\text{basis}} \times N_{\text{basis}}$ matrix E. The set of all eigenvectors define the Bogoliubov matrix,

$$\mathcal{W} = \begin{pmatrix} U & V^{\star} \\ V & U^{\star} \end{pmatrix}, \quad (7)$$

which is unitary: $\mathcal{W}\mathcal{W}^{\dagger} = \mathcal{W}^{\dagger}\mathcal{W} = 1$. Details about the HFB theory can be found in the standard references Valatin [41]; Mang [42]; Blaizot and Ripka [43]; Ring and Schuck [44].

2.3 Mean-field and pairing potentials

The mean fields are obtained by functional differentiation of the scalar-isoscalar energy functional (1) with respect to all relevant isoscalar or isovector densities, ρ_0, ρ_1, τ_0, etc. For the case of a standard Skyrme EDF when time-reversal symmetry is conserved, the corresponding mean-field potentials in the isoscalar-isovector representation become semi-local Dobaczewski and Dudek [37,45]; Stoitsov et al. [46]; Hellemans et al. [39].

$$h_t(\boldsymbol{r}) = -\boldsymbol{\nabla} M_t^{*}(\boldsymbol{r})\boldsymbol{\nabla} + U_t(\boldsymbol{r}) + \frac{1}{2i}\sum_{\mu\nu}\left(\nabla_\mu \sigma_\nu B_{t,\mu\nu}(\boldsymbol{r}) + B_{t,\mu\nu}(\boldsymbol{r})\nabla_\mu \sigma_\nu\right), \quad (8)$$

where, as before, $t = 0$, 1 refers to the isoscalar or isovector channel and the various contributions are.

$$M_t(\boldsymbol{r}) = \frac{\hbar^2}{2m} + C_t^{\rho\tau}\rho_t, \quad (9a)$$

$$U_t(\boldsymbol{r}) = 2C_t^{\rho\rho}\rho_t + C_t^{\rho\tau}\tau_t + 2C_t^{\rho\Delta\rho}\Delta\rho_t + C_t^{\rho\nabla J}\boldsymbol{\nabla}\cdot\boldsymbol{J}_t + U_t^{(\text{rear})}, \quad (9b)$$

$$B_{t,\mu\nu}(\boldsymbol{r}) = 2C_t^{\rho J}J_{t,\mu\nu} - C_t^{\rho\Delta J}\nabla_\mu \rho_{t,\nu}. \quad (9c)$$

In these expressions, μ, ν label spatial coordinates and $\boldsymbol{\sigma}$ is the vector of Pauli matrices in the chosen coordinate system. For example, in Cartesian coordinates, $\mu, \nu \equiv x, y, z$ and $\boldsymbol{\sigma} = (\sigma_x, \sigma_y, \sigma_z)$.

The term $U_t^{(\text{rear})}$ is the rearrangement potential originating from the density-dependent part of the energy. The resulting isoscalar and isovector mean-field and pairing potentials can then recombined to give the neutron and proton potentials,

$$h^{(n)} = h_0 + h_1, \qquad h^{(p)} = h_0 - h_1. \quad (10)$$

Note that the full proton potential should also contain the contribution from the Coulomb potential.

The pairing field is obtained by functional differentiation of the same energy functional (1), this time with respect to the pairing density. As a result, one can show that it is simply given by

$$\tilde{h}^{(\tau)}(\boldsymbol{r}) = V_0^{(\tau)}\left[1 - \frac{1}{2}\frac{\rho_0(\boldsymbol{r})}{\rho_c}\right]\tilde{\rho}^{(\tau)}(\boldsymbol{r}). \quad (11)$$

2.4 Collective space

Nuclear fission or nuclear shape coexistence are two prominent examples of large-amplitude collective motion of nuclei Schunck and Regnier [3]; Heyde and Wood [47]. Such phenomena can be accurately described within nuclear DFT by introducing a small-dimensional collective manifold, e.g., associated with the nuclear shape, where we assume the nuclear dynamics is confined Nakatsukasa et al. [48]; Schunck [2]. The generator coordinate method (GCM) and its time-dependent extension (TDGCM) provide quantum-mechanical equations of motion for such collective dynamics Griffin and Wheeler [49]; Wa Wong [50]; Reinhard and Goeke [51]; Bender et al. [32]; Verriere and Regnier [52]. In the GCM, the HFB solutions are generator states, i.e., they serve as a basis in which the nuclear many-body state is expanded. The choice of the collective manifold, that is, of the collective variables, depends on the problem at hand. For shape coexistence or fission, these variables typically correspond to the expectation value of multipole moment operators on the HFB state. A pre-calculated set of HFB states with different values for the collective variables defines a potential energy surface (PES).

In practice, PES are obtained by adding constraints to the solutions of the HFB equation. This is achieved by introducing a set of constraining operators $\hat{Q}_a$ capturing the physics of the problem at hand. The set of all such constraints $\boldsymbol{q} \equiv (q_1, \ldots, q_N)$ defines a point in the PES. In this work, our goal is to design emulators capable of reproducing the HFB solutions at any given point $\boldsymbol{q}$ of a PES. Throughout this article, we consider exclusively two-dimensional collective spaces spanned by the expectation values of the axial quadrupole $\hat{Q}_{20}$ and axial octupole $\hat{Q}_{30}$ moment operators. In the presence of constraints, the mean-field potential in the HFB equation is modified as follows

$$h(\boldsymbol{r}\sigma,\boldsymbol{r}'\sigma') - \lambda\delta_{\sigma\sigma'} \quad \rightarrow \quad h(\boldsymbol{r}\sigma,\boldsymbol{r}'\sigma') - \left(\lambda + \sum_a \lambda_a Q_a(\boldsymbol{r})\right)\delta_{\sigma\sigma'}. \tag{12}$$

As is well known, the Fermi energies play in fact the role of the Lagrange parameters λ_a for the constraints on particle number. When performing calculations with constraints on the octupole moment, it is also important to fix the position of the center of mass. This is typically done by adding a constraint on the dipole moment $\hat{Q}_{10}$. In the following, we note $q_{\lambda\mu}$ the expectation value of the operator $\hat{Q}_{\lambda\mu}$ on the quasiparticle vacuum, $q_{\lambda\mu} = \langle\Phi(\boldsymbol{q})|\hat{Q}_{\lambda\mu}|\Phi(\boldsymbol{q})\rangle$.

Potential energy surfaces are a very important ingredient in a very popular approximation to the GCM called the Gaussian overlap approximation (GOA) Brink and Weiguny [53]; Onishi and Une [54]; Une et al. [55]. By assuming, among other things, that the overlap between two HFB states with different collective variables $\boldsymbol{q}$ and $\boldsymbol{q}'$ is approximately Gaussian, the GOA allows turning the integro-differential Hill-Wheeler-Griffin equation of the GCM into a much more tractable Schrödinger-like equation. The time-dependent version of this equation reads as Verriere and Regnier [52].

$$i\hbar\frac{\partial}{\partial t}g(\boldsymbol{q},t) = \left[-\frac{\hbar^2}{2}\sum_{\alpha\beta}\frac{\partial}{\partial q_\alpha}B_{\alpha\beta}(\boldsymbol{q})\frac{\partial}{\partial q_\beta} + V(\boldsymbol{q})\right]g(\boldsymbol{q},t), \tag{13}$$

where the probability to be at point $\boldsymbol{q}$ of the collective space at time t is given by $|g(\boldsymbol{q},t)|^2$, $V(\boldsymbol{q})$ is the actual PES, typically the HFB energy as a function of the collective variables $\boldsymbol{q}$ (sometimes supplemented by some zero-point energy correction) and $B_{\alpha\beta}(\boldsymbol{q})$ the collective inertia tensor. In (13), indices α and β run from 1 to the number N_{col} of collective variables. While the HFB energy often varies smoothly with respect to the collective variables, the collective inertia tensor can exhibit very rapid variations near level crossings.

2.5 Canonical basis

The Bloch-Messiah-Zumino theorem states that the Bogoliubov matrix $\mathcal{W}$ of (7) can be decomposed into a product of three matrices Ring and Schuck [44]; Bloch and Messiah [56]; Zumino [57].

$$\mathcal{W} = \mathcal{D}\bar{\mathcal{W}}\mathcal{C} = \begin{pmatrix} D & 0 \\ 0 & D^* \end{pmatrix}\begin{pmatrix} \bar{U} & \bar{V} \\ \bar{V} & \bar{U} \end{pmatrix}\begin{pmatrix} C & 0 \\ 0 & C^* \end{pmatrix}, \tag{14}$$

where D and C are unitary matrices. The matrices $\bar{U}$ and $\bar{V}$ take the very simple canonical form

$$\bar{U} = \begin{pmatrix} 0 & & & & \\ & \ddots & & & \\ & & u_k & 0 & \\ & & 0 & u_{\bar{k}} & \\ & & & \ddots & \\ & & & & 0 \end{pmatrix}, \qquad \bar{V} = \begin{pmatrix} 0 & & & & \\ & \ddots & & & \\ & & 0 & v_k & \\ & & v_{\bar{k}} & 0 & \\ & & & \ddots & \\ & & & & 0 \end{pmatrix}. \tag{15}$$

Starting from an arbitrary s.p. basis $(\hat{c},\hat{c}^\dagger)$ of the Hilbert space, the transformation characterized by the matrix $\mathcal{D}$ leads to a new basis $(\hat{a},\hat{a}^\dagger)$ that diagonalizes the density matrix ρ and puts the pairing tensor κ into the canonical form similar to that of $\bar{V}$. This new basis is called the canonical basis of the HFB theory. Properties of the canonical basis are discussed in details in the literature; see, e.g., Ring and Schuck [44]; Schunck [2]. In the HFB theory, quasiparticles are superpositions of particle operators $\hat{a}^\dagger$ and hole operators $\hat{a}$. Thus, the canonical basis is transformed according to the matrix $\bar{\mathcal{W}}$ to obtain a set of quasiparticle operators $(\hat{\alpha},\hat{\alpha}^\dagger)$. There is another transformation of these operators associated with the matrix $\mathcal{C}$. However, the most important property for the purpose of this paper is that physical observables associated with HFB solutions do not depend on that last transformation.

In addition to simplifying the calculation of many-body observables, the canonical basis is also computationally less expensive than the full Bogoliubov basis[3]. As an illustration, let us take the example of the local density $\rho(\boldsymbol{r})$. Assuming the s.p. basis $(\hat{c},\hat{c}^\dagger)$ is represented by the basis functions $\{\psi_n(\boldsymbol{r},\sigma)\}_{n\in\mathbb{N}}$, the local density (for isospin τ) is obtained from the matrix of the Bogoliubov transformation by

$$\rho(\boldsymbol{r}) = \sum_\sigma\sum_\mu\sum_{mn} V^*_{m\mu}V_{n\mu}\,\psi_m(\boldsymbol{r},\sigma)\psi^*_n(\boldsymbol{r},\sigma). \tag{16}$$

Notwithstanding the constraints imposed by the orthonormality of the q.p. spinors, the number of independent parameters in this expression approximately scales like $2\times N^2_{\text{basis}}\times N_{\text{qp}}\times N_{\boldsymbol{r}}$, where N_{basis} is the size of the s.p. basis, N_{qp} the number of q.p. states μ and $N_{\boldsymbol{r}}$ the total number of points in the spatial grid $\boldsymbol{r}$ (which depends on the symmetries imposed). In the canonical basis, and assuming that the state $\hat{a}_\mu|0\rangle$ is associated with the wavefunction $\varphi_\mu(\boldsymbol{r},\sigma)$, the same object is represented by

$$\rho(\boldsymbol{r}) = \sum_\sigma\sum_\mu v^2_\mu|\varphi_\mu(\boldsymbol{r},\sigma)|^2. \tag{17}$$

The number of data points now scales like $2\times N_{\text{qp}}\times N_{\boldsymbol{r}} + N_{\text{qp}}$, or about N^2_{basis} smaller than before. For calculations with $N_{\text{basis}}\approx$ 1,000 the compression enabled by the canonical basis is of the order of 10^6.

2.6 Harmonic oscillator basis

All calculations in this article were performed with the HFBTHO code Marević et al. [58]. Recall that HFBTHO works by expanding the solutions on the axially-deformed

3 This statement is obviously not true when solving the HFB equation directly in coordinate space. In the case of the local density discussed here, the expression $\rho(\boldsymbol{r}) = \sum_\sigma\sum_\mu V_\mu(\boldsymbol{r},\sigma)V^*_\mu(\boldsymbol{r},\sigma)$ is just as computationally expensive as the canonical basis expression $\rho(\boldsymbol{r}) = \sum_\sigma\sum_\mu v^2_\mu|\varphi_\mu(\boldsymbol{r},\sigma)|^2$.

harmonic oscillator basis Stoitsov et al. [46]. Specifically, the HO basis functions are written

$$\psi_{\boldsymbol{n}}(\boldsymbol{r},\sigma) = \psi^{\Lambda}_{n_r}(r)\psi_{n_z}(z)\frac{e^{i\Lambda\theta}}{\sqrt{2\pi}}\chi_{\Sigma}(\sigma), \tag{18}$$

where $\boldsymbol{n} \equiv (n_r, n_z, \Lambda, \Omega = \Lambda \pm \Sigma)$ are the quantum numbers labeling basis states and.

$$\psi^{\Lambda}_{n_r}(r) = N_{n_r}\beta_{\perp}\sqrt{2}\eta^{|\Lambda|/2}e^{-\eta/2}L^{|\Lambda|}_{n_r}(\eta), \tag{19a}$$

$$\psi_{n_z}(z) = N_{n_z}\sqrt{\beta_z}e^{-\xi^2/2}H_{n_z}(\xi), \tag{19b}$$

With $\eta = \beta_{\perp}^2 r^2$ and $\xi = \beta_z z$ dimensionless variables, $L^{|\Lambda|}_{n_r}$ the associated Laguerre polynomials of order n_r and H_{n_z} the Hermite polynomial of order n_z. The oscillator scaling factors $\beta_{\perp}$ and β_z are the inverse of the oscillator lengths, i.e., $\beta_z = 1/b_z$.

All integrations are performed by Gauss quadrature, namely Gauss-Hermite for integrations along the ξ-axis of the intrinsic reference frame and Gauss-Laguerre for integrations along the perpendicular direction characterized by the variable η. In the following, we note N_z the number of Gauss-Hermite nodes and $N_{\perp}$ the number of Gauss-Laguerre nodes.

3 Supervised learning with Gaussian processes

Gaussian processes (GPs) are a simple yet versatile tool for regression that has found many applications in low-energy nuclear theory over the past few years, from determining the nuclear equation of state Drischler et al. [59], quantifying the error of nuclear cross sections calculations Kravvaris et al. [60]; Acharya and Bacca [61] to modeling of neutron stars Pastore et al. [62]. In the context of nuclear DFT, they were applied to build emulators of χ_2 objective functions in the UNEDF project Kortelainen et al. [63–65]; Higdon et al. [66]; McDonnell et al. [67]; Schunck et al. [6], of nuclear mass models Neufcourt et al. [15,68–70], or of potential energy surfaces in actinides Schunck et al. [34]. In this section, we test the ability of GPs to learn directly the HFB potentials across a large, two-dimensional collective space.

3.1 Gaussian processes

Gaussian processes are commonly thought of as the generalization of normally-distributed random variables (Gaussian distribution) to functions. There exists a considerable field of applications for GPs and we refer to the reference textbook by Rasmussen and Williams for a comprehensive review of the formalism and applications of GPs Rasmussen and Williams [71]. For the purpose of this work, we are only interested in the ability of GPs to be used as a regression analysis tool and we very briefly outline below some of the basic assumptions and formulas.

We assume that we have a dataset of observations $\{\mathbf{y} = y_i\}_{i=1,\ldots,n}$ and that these data represent n realizations of

$$y = f(\mathbf{x}) + \epsilon, \tag{20}$$

where f: $\mathbf{x}\mapsto f(\mathbf{x})$ is the unknown function we are seeking to learn from the data. Saying that a function f is a Gaussian process means that every finite collection of function values $\mathbf{f} = (f(\mathbf{x}_1), \ldots, f(\mathbf{x}_p))$ follows a p-dimensional multivariate normal distribution. In other words, we assume that the unknown function f follows a normal distribution in 'function space'. This is denoted by

$$f(\mathbf{x}) \sim \mathcal{GP}(m(\mathbf{x}), k(\mathbf{x},\mathbf{x}')), \tag{21}$$

where m: $\mathbf{x}\mapsto m(\mathbf{x})$ is the mean function and k: $(\mathbf{x}, \mathbf{x}')\mapsto k(\mathbf{x}, \mathbf{x}')$ the covariance function, which is nothing but the generalization to functions of the standard deviation,

$$k(\mathbf{x},\mathbf{x}') = \mathbb{E}[(f(\mathbf{x}) - m(\mathbf{x}))(f(\mathbf{x}') - m(\mathbf{x}'))]. \tag{22}$$

Thanks to the properties of Gaussian functions, the mean and covariance functions have analytical expressions as a function of the test data $\mathbf{y}$ and covariance k; see Eqs (2.25)-(2.26) in Rasmussen and Williams [71].

The covariance function is the central object in GP regression. It is typically parametrized both with a functional form and with a set of free parameters called hyperparameters. The hyperparameters are determined from the observed data by maximizing the likelihood function. In our tests, the covariance matrix is described by a standard Matérn 5/2 kernel,

$$k(\mathbf{x},\mathbf{x}') = \left(1 + \frac{\sqrt{5}}{\ell}\|\mathbf{x}-\mathbf{x}'\| + \frac{5}{3\ell^2}\|\mathbf{x}-\mathbf{x}'\|^2\right)\exp\left(-\frac{\sqrt{5}}{\ell}\|\mathbf{x}-\mathbf{x}'\|\right), \tag{23}$$

where ℓ is the length-scale that characterizes correlations between values of the data at different locations. The length-scale is a hyper-parameter that is optimized in the training phase of the Gaussian process. In this work, we only considered stationary GPs: the correlation between data points $\mathbf{x}$ and $\mathbf{x}'$ only depends on the distance $\|\mathbf{x}-\mathbf{x}'\|$ between these points, not on their actual value.

3.2 Study case

3.2.1 HFB potentials

Section 2.2 showed that the HFB mean-field potential involves several differential operators. When the HFB matrix is constructed by computing expectation values of the HFB potential on basis functions, differentiation is carried over to the basis functions and computed analytically—one of the many advantages of working with the HO basis. In practice, this means that the elements of the HFB matrix are computed by multiplying

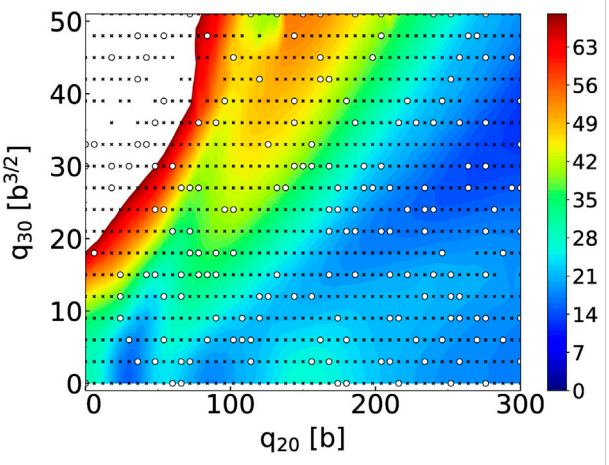

FIGURE 1
Potential energy surface of ^{240}Pu with the SkM* EDF for the grid (q_{20}, q_{30}) ∈ [0 b, 300 b] × [0 b$^{3/2}$, 51 b$^{3/2}$] with steps δq_{20} = 6 b and δq_{30} = 3 b$^{3/2}$. The black crosses are the training points, the white circles the validation points. Energies indicated by the color bar are in MeV relatively to −1820 MeV.

spatial kernels with different objects representing either the original HO functions or their derivatives. This means that we cannot consider a single emulator for the entire HFB potential. Instead, we have to build several different ones for each of its components: the central potential U (derivative of the EDF with respect to ρ), the r- and z-derivatives of the effective mass M^* (derivative with respect to the kinetic density τ), the r- and z-derivatives of the spin-orbit potential W, and the pairing field $\tilde{h}$. There are six such functions for neutrons and another six for protons. We denote this set of twelve functions as $\{f_i\}_{i=1,\ldots,12}$.

At any given point $\boldsymbol{q}$ of the *collective* space, these functions are all local, scalar functions of η and ξ, $f_i(\boldsymbol{q}) \equiv f_i$: $(\eta, \xi) \mapsto f_i(\eta, \xi; \boldsymbol{q})$ where (η, ξ) are the nodes of the Gauss-Laguerre and Gauss-Hermite quadrature grid. We note generically $f_{ik}(\boldsymbol{q})$ the value at point k of the quadrature grid (linearized) of the sample at point $\boldsymbol{q}$ of the function f_i. When fitting Gaussian process to reproduce mean-field and pairing potentials, we consider a quadrature grid of $N_z \times N_\perp$ = 3,200 points. Our goal is thus to build 3,200 different emulators, one for each point k of that grid, for each of the 12 local functions characterizing the mean-field and pairing potentials. This gives a grand total of 38,400 emulators to build. While this number is large, it is still easily manageable on standard computers. It is also several orders of magnitude smaller than emulating the full set of quasiparticle spinors, as we will see in the next section.

In addition, the value of all the Lagrange parameters used to set the constraints must also be included in the list of data points. In our case, we have 5 of them: the two Fermi energies λ_n and λ_p and the three constraints on the value of the dipole, quadrupole and octupole moments, λ_1, λ_2 and λ_3, respectively. Finally, we also fit the expectation value of the three constraints on $\hat{Q}_{10}$, $\hat{Q}_{20}$ and $\hat{Q}_{30}$. We thus have a grand total of 38,408 functions of $\boldsymbol{q}$ to emulate.

3.2.2 Training data and fitting procedure

We show in Figure 1 the potential energy surface that we are trying to reconstruct. This PES is for the ^{240}Pu nucleus and was generated with the SkM* parameterization of the Skyrme energy functional Bartel et al. [72]. The pairing channel is described with the zero-range, density-dependent pairing force of Eq. 4 that has exactly the same characteristics as in Schunck et al. [73].

We imposed constraints on the axial quadrupole and octupole moments such that: 0 b ≤ q_{20} ≤ 300 b and 0 b$^{3/2}$ ≤ q_{30} ≤ 51 b$^{3/2}$ with steps of δq_{20} = 6 b and δq_{30} = 3 b$^{3/2}$, respectively. The full PES should thus contain 918 collective points. In practice, we obtained N_p = 887 fully converged solutions. Calculations were performed with the HFBTHO solver by expanding the solutions on the harmonic oscillator basis with N_{max} = 28 deformed shells and a truncation in the number of states of N_{basis} = 1,000. At each point of the PES, the frequency ω_0 and deformation β_2 of the HO basis are set according to the empirical formulas given in Schunck et al. [73]. Following standard practice, we divided the full N_p = 887 dataset of points into a training (80% of the points) and validation (20% of the points) set. The selection was done randomly and resulted in N_{train} = 709 training points and $N_{valid.}$ = 178 validation points. The training points are marked as small black crosses in Figure 1 while the validation points are marked as larger white circles.

Based on the discussion in Section 3.2.1, we fit a Gaussian process to each of the 38,408 variables needed to characterize completely the HFB matrix. Since we work in a two-dimensional collective space, we have two features and the training data is represented by a two-dimensional array X of dimension ($n_{samples}$, $n_{features}$) with $n_{samples} = N_p$ and $n_{features}$ = 2. The target values Y (= the value at point k on the quadrature grid of any of the functions f_i) are contained in a one-dimensional array of size N_p. Prior to the fit, the data is normalized between 0 and 1. The GP is based on a standard Matérn kernel with ν = 2.5 and length-scale ℓ. In practice, we use different length-scales for the q_{20} and q_{30} directions so that $\ell = \boldsymbol{\ell}$ is a vector. We initialized these values at the spacing of the grid $\boldsymbol{\ell} = (\delta q_{20}, \delta q_{30})$. We added a small amount of white noise to the Matérn kernel to account for the global noise level of the data.

3.2.3 Performance

Once the GP has been fitted on the training data, we can estimate its performance on the validation data. For each of the $N_{valid.}$ = 178 validation points, we used the GP-fitted HFB potentials to perform a single iteration of the HFB self-consistent loop and extract various observables from this single iteration. Figure 2 focuses on the total HFB energy and the zero-point energy correction ε_0. Together, these two quantities define the collective potential energy in the

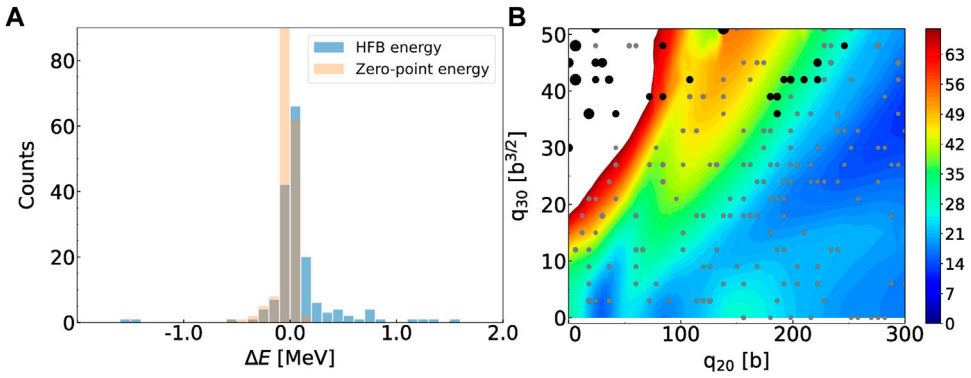

FIGURE 2
(A): Histogram of the error on the GP-predicted total HFB energy and zero-point energy correction across the validation points. Bin size is 100 keV. **(B)**: Size of the error on the GP-predicted total HFB energy across the validation set. Gray circles have an error lower than 500 keV and the size of the markers correspond to energy bins of 100 keV. Black circles have an error greater than 500 keV and are binned by 400 keV units. Energies indicated by the color bar are in MeV relatively to −1820 MeV.

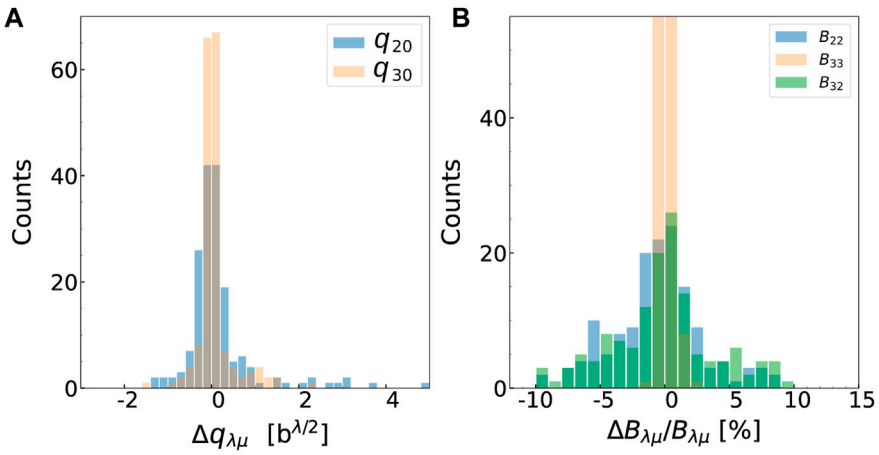

FIGURE 3
(A): Histogram of the error on the GP-predicted values of the multipole moments. The bin size is 0.2 $b^{\lambda/2}$ with $\lambda = 2$ (quadrupole moment) or $\lambda = 3$ (octupole moment). **(B)**: Histogram of the relative error, in percents, on the GP-predicted values of the components of the collective inertia tensor. The bin size is 1, corresponding to 1% relative errors.

collective Hamiltonian (13) of the GCM. The left panel of the figure shows the histogram of the error $\Delta E = E_{\mathrm{HFB}}^{(\mathrm{true})} - E_{\mathrm{HFB}}^{(\mathrm{GP})}$, where $E_{\mathrm{HFB}}^{(\mathrm{true})}$ is the result from the fully converged HFB solution and $E_{\mathrm{HFB}}^{(\mathrm{GP})}$ is the value predicted by the Gaussian process. The bin size is 100 keV. Overall, we find that the large majority of the error is within ±200 keV. This is a rather good result considering the span of the PES and the fact that basis truncation errors can easily amount to a few MeV Schunck [74].

To gain additional insight, we draw in the right panel of Figure 2 each of the validation points with a marker, the size of which is proportional to the error of the prediction. To further distinguish between most points and the few outliers, we show in gray the points for which the absolute value of the error is less than 500 keV and in black the points for which it is greater than 500 keV. For the gray points, we use 5 different marker sizes corresponding to energy bins of 100 keV: the smaller grey symbol corresponds to an error smaller than 100 keV, the larger one between 400 and 500 keV. Similarly, the larger black circles have all an error greater than 500 keV and are ordered by bins of 400 keV (there are only two points for which the error is larger than 4 MeV). Interestingly, most of the larger errors are concentrated in the region of small elongation $q_{20} < 80$ b and high asymmetry $q_{30} > 30\,\mathrm{b}^{3/2}$. This region of the collective space is very high in energy (more than 100 MeV above the ground state) and plays no role in the collective dynamics.

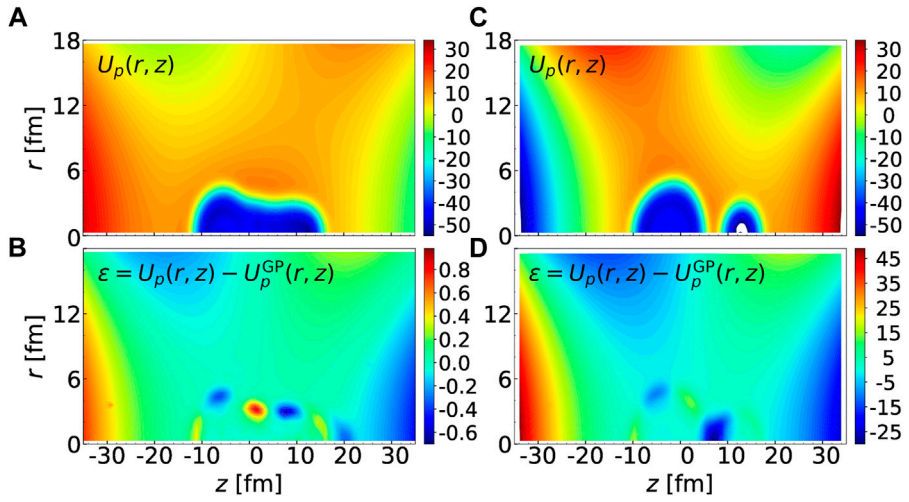

FIGURE 4
(A): Central part of the mean-field potential for protons, $U_p(r, z)$ for the configuration (q_{20}, q_{30}) = (198 b, 30 $b^{3/2}$); **(B)**: Error in the GP fit for that same configuration. **(C)**: Central part of the mean-field potential for protons, $U_p(r, z)$ for the configuration (q_{20}, q_{30}) = (138 b, 51 $b^{3/2}$); **(D)**: Error in the GP fit for that same configuration. In all figures, the energy given by the error bar is in MeV. Note the much smaller energy scale for the bottom left panel.

Note that the expectation values of the multipole moments themselves are not reproduced exactly by the GP: strictly speaking, the contour plot in the right panel of Figure 2 is drawn based on the requested values of the constraints, not their actual values as obtained by solving the HFB equation once with the reconstructed potentials. The histogram in the left panel of Figure 3 quantifies this discrepancy. It shows the absolute error $\Delta q_{\lambda\mu} = q_{\lambda\mu}^{(\mathrm{true})} - q_{\lambda\mu}^{(\mathrm{GP})}$, where $q_{\lambda\mu}^{(\mathrm{true})}$ is the result from the fully converged HFB solution and $q_{\lambda\mu}^{(\mathrm{true})}$ is the value predicted by the Gaussian process. On average, the error remains within ±0.5 b for q_{20} and ±0.5 $b^{3/2}$ for q_{30}, which is significantly smaller than the mesh size.

The collective potential energy is only one of the two ingredients used to simulate fission dynamics. As mentioned in Section 2.4, see Eq. 13, the collective inertia tensor is another essential quantity Schunck and Robledo [4]; Schunck and Regnier [3]. In this work, we computed the collective inertia at the perturbative cranking approximation Schunck and Robledo [4]. Since we work in two-dimensional collective spaces, the collective inertia tensor B has three independent components, hereafter labeled B_{22}, B_{33} and $B_{32} = B_{23}$. Figure 3 shows the relative error on these quantities, defined as $\epsilon = (B_{\lambda\lambda'}^{(\mathrm{true})} - B_{\lambda\lambda'}^{(\mathrm{GP})})/B_{\lambda\lambda'}^{(\mathrm{true})}$. Overall, the error is more spread than for the energy but rarely exceeds five percents[4].

Both the total energy and the collective mass tensor are computed from the HFB solutions. However, since the GP fit is performed directly on the mean-field and pairing potentials, one can analyze the error on these quantities directly. In Figure 4, we consider two different configurations. The configuration $\mathcal{C}_1 = (q_{20}, q_{30}) = (198\,\mathrm{b}, 30\,\mathrm{b}^{3/2})$ is very well reproduced by the GP with an error in the HFB energy of 4.4 keV and a relative error on B_{22} of -0.43% and B_{22} of -0.84% only. In contrast, the configuration $\mathcal{C}_2 = (q_{20}, q_{30}) = (138\,\mathrm{b}, 51\,\mathrm{b}^{3/2})$ is one of the worst possible cases, with a total error on the HFB energy of 9.0 MeV and relative errors on B_{22} of -71.0% and B_{22} of -13.7%. For each of these two configurations, we look at the central part of the mean-field potential for protons, the term $U_p = U_0 - U_1$ of (9b). The left side of Figure 4 shows, respectively, the actual value of $U_p(r, z)$ across the quadrature grid (top panel) and the difference between the true value and the GP fit (bottom panel) for the configuration $\mathcal{C}_1$. The right side of the figure shows the same quantity for the configuration $\mathcal{C}_2$. In all four plots, the energy scale is in MeV; it is identical for the two panels at the top, but it is different for the two at the bottom.

We see that for the "good" configuration $\mathcal{C}_1$, the error is between −0.6 MeV and 1.0 MeV but is mostly occurring at the surface of the nucleus and at the edges of the domain. Conversely, the "bad" configuration $\mathcal{C}_2$ actually corresponds to a scissioned configuration: the mean-field potential (upper right panel) shows two different regions corresponding to fully separated fragments[5]. Such a geometric configuration is very different

4 Note that B_{32} vanishes for axially-symmetric shapes. As a result, the relative error can be artificially large for values of $q_{30} \approx 0$ $b^{3/2}$.

5 This particular scission configuration corresponds to what is called cluster radioactivity Warda and Robledo [118]; Warda et al. [119]; Matheson et al. [120]. The heavy fragment is much larger than the light one. Here, $\langle A_{\mathrm{H}} \rangle$ = 205.6, $\langle A_{\mathrm{L}} \rangle$ = 34.4.

from the rest of the potential energy surface shown in Figure 1, which contains mostly non-scissioned configurations. As a result, the error in the GP fit is very large in the region between the two fragments since it predicts this configuration to be non-scissioned. Note that in HFBTHO, the representation of the potentials on the quadrature points does not contain the exponential factor $\exp(-\beta_z\xi^2)\exp(-\beta_\perp^2\xi^2)$ which is factored in the quadrature weights. Therefore, the large errors at the edges of the domain, for $z \approx -30$ fm, $z \approx +30$ fm or $r \approx 18$ fm are not significant since they are entirely absorbed by this exponential factor.

Overall, Gaussian processes seem to provide an efficient way to predict HFB solutions across potential energy surfaces. Their primary advantage is that they are very simple to implement, with several popular programming environments offering ready-to-use, full GP packages, and very fast to train (a few minutes at most for a few hundreds of samples). As our examples suggest, GPs are very good at interpolating across a domain where solutions behave smoothly. In the case of PES, this implies that the training data must not contain, e.g., scissioned and non-scissioned configurations. More generally, it should not feature too many discontinuities Dubray and Regnier [75]. When these conditions are met, GPs can be used to quickly and precisely densify a PES, e.g., to obtain more precise fission paths in spontaneous fission half-live calculations Sadhukhan [76].

However, Gaussian processes are intrinsically limited. In our example, we treated the value of each potential at each point of the quadrature mesh as an independent GP. Yet, such data are in reality heavily correlated. To incorporate such correlations requires generalizing from scalar GPs to vector, or multi-output GPs Bruinsma et al. [77]. In our example of nuclear potentials, the output space would be $\mathbb{R}^D$ with $D \approx 32{,}008$. An additional difficulty is related to choosing the kernel that is appropriate to describe the correlated data and identifying what the prior distribution should be Álvarez et al. [78]. Yet another deficiency of standard Gaussian processes, especially in contrast to the deep-learning techniques discussed below, is that they are not capable to learn a latent representation of the data. For these reasons, we consider such techniques helpful mostly to densify existing potential energy surfaces.

4 Deep learning with autoencoders

Even though self-consistent potential energy surfaces are key ingredients in the microscopic theory of nuclear fission Bender et al. [79], we must overcome two significant obstacles to generate reliable and complete PES. First, the computational cost of nuclear DFT limits the actual number of single-particle d.o.f. When solving the HFB equation with basis-expansion methods, for example, the basis must be truncated (up to a maximum of about a few thousand states, typically), making the results strongly basis-dependent Schunck [80]; even in mesh-based methods, the size of the box and lattice spacing also induce truncation effects Ryssens et al. [81]; Jin et al. [82]. Most importantly, the number of collective variables that can be included in the PES is also limited: in spontaneous fission calculations, which do not require a description of the PES up to scission, up to $N_{\text{col}} = 5$ collective variables have been incorporated Sadhukhan [76]; when simulating the PES up to scission, only 2 collective variables are included with only rare attempts to go beyondRegnier et al. [83]; Zhao et al. [84]. As a consequence, the combination of heavily-truncated collective spaces and the adiabatic hypothesis inherent to such approaches leads to missing regions in the PES and spurious connections between distinct channels with unknown effects on physics predictions Dubray and Regnier [75]; Lau et al. [85]. The field of deep learning may offer an appealing solution to this problem by allowing the construction of low-dimensional and continuous surrogate representations of potential energy surfaces. In the following, we test the ability of autoencoders—a particular class of deep neural networks—to generate accurate low-dimensional representations of HFB solutions.

4.1 Network architecture

The term 'deep learning' encompasses many different types of mathematical and computational techniques that are almost always tailored to specific applications. In this section, we discuss some of the specific features of the data we seek to encode in a low-dimensional representation, which in turn help constrain the network architecture. The definition of a proper loss function adapted to quantum-mechanical datasets is especially important.

4.1.1 Canonical states

We aim at building a surrogate model for determining canonical wavefunctions as a function of a set of continuous constraints. Canonical states are denoted generically $\varphi_\mu^{(\tau)}(\boldsymbol{r},\sigma)$ with $\boldsymbol{r} \equiv (r, z, \theta)$ the cylindrical coordinates and $\sigma = \pm 1/2$ the spin. Fully characterizing an HFB state requires the set of canonical wavefunctions for both neutrons and protons, which are distinguished by their isospin quantum number $\tau = +1/2$ (neutrons) and $\tau = -1/2$ (protons). As mentioned in Section 2, an HFB solution $|\Phi(\boldsymbol{q})\rangle$ is entirely determined up to a global phase by the set of all canonical states $\{\varphi_\mu^{(\tau)}(\boldsymbol{r},\sigma)\}_\mu$ and their associated occupation amplitudes $\{v_\mu^{(\tau)}\}_\mu$.

In this work, we restrict ourselves to axially-symmetric configurations. In that case, the canonical wavefunctions are eigenstates of the projection of the total angular momentum on the symmetry axis $\hat{J}_z$ with eigenvalue Ω and acquire the same separable structure (18) as the HO basis functions,

$$\varphi_{\mu}^{(\tau)}(\boldsymbol{r},\sigma) = \varphi_{\mu}^{(\tau)}(r,z,\sigma)\frac{e^{i\Lambda\theta}}{\sqrt{2\pi}}, \tag{24}$$

where $\varphi_{\mu}^{(\tau)}(r,z,\sigma)$ is the canonical wavefunction at $\theta = 0$. In this initial work, we only consider even-even nuclear systems and time-reversal symmetric nuclear Hamiltonians. Therefore, Kramer's degeneracy ensures that paired particles in the canonical basis are time-reversal partners of each other: $\varphi_{\bar{\mu}}^{(\tau)}(\boldsymbol{r},\sigma) = 2\sigma\varphi_{\mu}^{(\tau)*}(\boldsymbol{r},-\sigma)$. This guarantees that the canonical wavefunction at $\theta = 0$ can be chosen purely real. Incidentally, it also means that we only need to describe one wavefunction per pair of particles. Using these properties, we can completely describe a canonical wavefunction in our model by only predicting a single pair of real-valued functions (one for each spin projection σ).

As shown by Eqs 8, Eqs 9a–9c, all mean-field and pairing potentials are functions of the Skyrme densities. The kinetic energy density $\tau(r, z)$, spin-current tensor $\mathsf{J}(r,z)$, and vector density $\boldsymbol{J}(r, z)$ involve derivatives of the quasiparticle spinors or, in the canonical basis, of the canonical wavefunctions on the quadrature grid Stoitsov et al. [46]. We compute these derivatives by first extracting the coefficients $\alpha_{n\mu}^{(\tau)}$ of the expansion of the canonical wavefunctions $\varphi_{\mu}^{(\tau)}(\boldsymbol{r},\sigma)$ in the HO basis

$$\varphi_{\mu}^{(\tau)}(\boldsymbol{r},\sigma) = \sum_{\boldsymbol{n}} \alpha_{\boldsymbol{n}\mu}^{(\tau)}\psi_{\boldsymbol{n}}(\boldsymbol{r},\sigma) \Rightarrow \alpha_{\boldsymbol{n}\mu}^{(\tau)} = \int \mathrm{d}^3\boldsymbol{r}\,\psi_{\boldsymbol{n}}^{\star}(\boldsymbol{r},\sigma)\varphi_{\mu}^{(\tau)}(\boldsymbol{r},\sigma), \tag{25}$$

using Gauss-Laguerre and Gauss-Hermite quadrature. Since all the derivatives of the HO functions can be computed analytically, the expansion (25) makes it very easy to compute partial derivatives with respect to r or z, for example,

$$\frac{\partial\varphi_{\mu}^{(\tau)}}{\partial z}(\boldsymbol{r},\sigma) = \sum_{\boldsymbol{n}} \alpha_{\boldsymbol{n}\mu}^{(\tau)}\frac{\partial\psi_{\boldsymbol{n}}}{\partial z}(\boldsymbol{r},\sigma). \tag{26}$$

4.1.2 Structure of the predicted quantity

In the ideal case, the canonical wavefunctions evolve smoothly with the collective variables. The resulting continuity of the many-body state with respect to collective variables is a prerequisite for a rigorous description of the time evolution of fissioning systems, yet it is rarely satisfied in practical calculations. We discuss below the three possible sources of discontinuity of the canonical wavefunctions in potential energy surfaces.

First, the canonical wavefunctions are invariant through a global phase. Since the quantity we want to predict is real, the orbitals can be independently multiplied by an arbitrary sign. Even though this type of discontinuity does not impact the evolution of global observables as a function of deformation, it affects the learning of the model: since we want to obtain continuous functions, a flipping of the sign would be seen by the neural network as a discontinuity in the input data. We address this point through the choice of the loss, as discussed in Section 4.1.3, and through the determination of the training set, as detailed in Section 4.2.

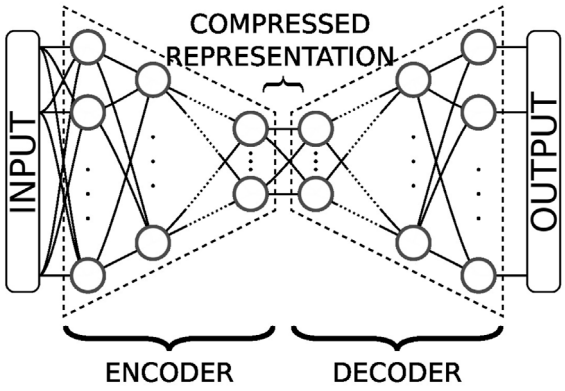

FIGURE 5
An autoencoder is the association of two blocks. The first one, on the left, compresses the input data into a lower-dimensional representation, or code, in the latent space. The second one, on the right, decompresses the code back into the original input.

Second, we work within the adiabatic approximation, which consists in building PES by selecting the q.p. vacuum that minimizes the energy at each point. When the number N_{col} of collective variables of the PES is small, this approximation may lead to discontinuities Dubray and Regnier [75]. These discontinuities correspond to missing regions of the collective space and are related to the inadequate choice of collective variables. Since we want to obtain a continuous description of the fission path, we must give our neural network the ability to choose the relevant degrees of freedom. This could be achieved with autoencoders. Autoencoders are a type of neural networks analogous to the zip/unzip programs. They are widely used and greatly successful for representation learning—the field of Machine Learning that attempts to find a more meaningful representation of complex data Baldi [86]; Burda et al. [87]; Chen et al. [88]; Gong et al. [89]; Bengio et al. [90]; Zhang et al. [91]; Yu et al. [92] and can be viewed as a non-linear generalization of principal component analysis (PCA). As illustrated in Figure 5, an autoencoder Ξ typically consists of two components. The encoder E ($T^{(\varphi)}$) encodes complex and/or high-dimensional data $T^{(\varphi)}$ to a typically lower-dimensional representation $\boldsymbol{v}^{(\varphi)}$. The *latent space* is the set of all possible such representations. The decoder D ($\boldsymbol{v}^{(\varphi)}$) takes the low-dimensional representation of the encoder and uncompresses it into a tensor $T^{(\phi)}$ as close as possible to $T^{(\varphi)}$. Such architectures are trained using a *loss function* that quantifies the discrepancy between the initial input and the reconstructed output,

$$\mathcal{L}_{\mathrm{rec.}}\left(T^{(\phi)}\right) = d\left(T^{(\varphi)}, T^{(\phi)}\right), \tag{27}$$

where $d(.,.)$ defines the metric in the space of input data. We discuss the choice of a proper loss in more details in Section 4.1.3.

Third, the evolution of the q.p. wavefunctions as a function of the collective variables $\boldsymbol{q}$ may lead to specific values $\boldsymbol{q}_i$ where the q.p. solutions are degenerate. These degeneracies form a sub-manifold of dimension at most $D-2$, where D is the number of collective d.o.f.s. As a consequence, they cannot appear in one-dimensional PES: q.p. solutions with the same symmetry "cannot cross" (the famous no-crossing rule von Neuman and Wigner [93]). In multi-dimensional spaces, this rule does not hold anymore: when following a closed-loop trajectory around such a degeneracy, the sign of the q.p. wavefunctions is flipped, in a similar manner that we flip side when winding around a Moebius strip Teller [94]; Longuet-Higgins et al. [95]; Longuet-Higgins [96]. In the field of quantum chemistry, such degeneracies are referred to as diabolical points or conical intersections Domcke et al. [97]; Larson et al. [98]. The practical consequence of conical intersections for deep learning is that the manifold of all the q.p. wavefunctions cannot be embedded in a D-dimensional latent space. Such singularities can be treated in two ways: (i) by using a latent space of higher dimension than needed or (ii) by implementing specific neural network layers capable of handling such cases. For now, we do not consider these situations.

4.1.3 Loss functions and metrics

As already discussed in Section 4.1.2, autoencoders are trained through the minimization of a loss function that contains a reconstruction term of the form (27). As suggested by its name, this term ensures that the autoencoder can correctly reconstruct the input tensor $T^{(\varphi)}$ from its compressed representation. It depends on a definition for the metric d (., .) used to compare the different elements of the input space. Since our canonical wavefunctions φ_μ are expanded on the axial harmonic oscillator basis of Section 2.6, they are discretized on the Gauss quadrature mesh without any loss of information. Therefore, both the input and output tensors of our surrogate model are a rank-3 tensor $T^{(\phi)} \equiv T^{(\varphi)} \equiv T_{ijk}$ of dimensions $N_\perp \times N_z \times 2$, where i is the index of the Gauss-Laguerre node along the r-axis, j the index of the Gauss-Hermite node along the z-axis, and k the index of the spin component.

A standard loss used with autoencoders is the mean-square-error (MSE). Because of the structure of our input data, see Section 4.1.1, the MSE loss reads in our case

$$d_{\mathrm{MSE}}\left(T^{(\varphi)}, T^{(\phi)}\right) = \frac{1}{N_\perp \times N_z \times 2} \sum_{i=0}^{N_\perp - 1} \sum_{j=0}^{N_z - 1} \sum_{i=0}^{1} \left(T^{(\phi)}_{ijk} - T^{(\varphi)}_{ijk}\right)^2. \tag{28}$$

The MSE is very general and can be thought of, quite simply, as the mean squared "distance" between the initial and reconstructed data. However, this generality implies that it does not contain any information about the properties of the data one tries to reconstruct.

Indeed, we can define a metric that is better suited to the physics we aim to describe. Let us recall that our goal is to compute potential energy surfaces that can be used, e.g., for fission simulations. These PES are nothing but generator states for the (TD)GCM mentioned in Section 2.4. The GCM relies on the norm kernel $\mathcal{N}(\boldsymbol{q}, \boldsymbol{q}')$ and the Hamiltonian kernel $\mathcal{H}(\boldsymbol{q}, \boldsymbol{q}')$, which are defined as.

$$\mathcal{N}(\boldsymbol{q}, \boldsymbol{q}') = \langle \Phi(\boldsymbol{q}) | \Phi(\boldsymbol{q}') \rangle, \tag{29}$$

$$\mathcal{H}(\boldsymbol{q}, \boldsymbol{q}') = \langle \Phi(\boldsymbol{q}) | \hat{H} | \Phi(\boldsymbol{q}') \rangle. \tag{30}$$

Since the norm kernel involves the standard inner product in the many-body space, it represents the topology of that space. Therefore, it should be advantageous to use for the loss a metric induced by the same inner product that defines the norm kernel.

In our case, we want to build an AE where the encoder $\boldsymbol{v}^{(\varphi)} = E\left(T^{(\varphi)}\right)$ compresses the *single-particle*, canonical orbitals $\{\varphi_\mu\}_\mu$ associated with $|\Phi\rangle$ into a low-dimensional vector $\boldsymbol{v}^{(\varphi)}$ and where the decoder $T^{(\phi)} = D\left(\boldsymbol{v}^{(\varphi)}\right)$ is used to compute the set of reconstructed canonical orbitals $\{\phi_\mu\}_\mu$. Most importantly, this reconstruction should be such that the reconstructed *many-body* state $|\Psi\rangle$ is as close as possible to the original state $|\Phi\rangle$. In other words, we need to use a loss that depends on the norm overlap (between many-body states) but since we work with single-particle wavefunctions, we must have a way to relate the norm overlap to these s.p. wavefunctions. This can be achieved with Equations 5.4 and (5.6) of Haider and Gogny [99], which relate the inner product $\langle \Phi | \Psi \rangle$ in the many-body space with the inner product (overlap) $\langle \varphi_\mu | \phi_\nu \rangle$ between the related canonical orbitals φ_μ and ϕ_ν,

$$\langle \varphi_\mu | \phi_\nu \rangle \equiv \tau^{(\varphi\phi)}_{\mu\nu} = \left\{ \hat{a}^{(\varphi)\dagger}_\mu, \hat{a}^{\phi}_\nu \right\} = \sum_\sigma \int \mathrm{d}^3\boldsymbol{r}\, \varphi^\star_\mu(\boldsymbol{r}, \sigma) \phi_\nu(\boldsymbol{r}, \sigma) \tag{31}$$

and with the occupation amplitudes. However, it assumes that the canonical wavefunctions of each many-body state are orthogonal. This property is not guaranteed for our *reconstructed* canonical wavefunctions. In fact, because of this lack of orthogonality, the reconstructed wavefunctions cannot be interpreted as representing the canonical basis of the Bloch-Messiah-Zumino decomposition of the quasiparticle vacuum and the Haider and Gogny formula cannot be applied 'as is'. However, we show in Supplementary Appendix S1 that it is possible to find a set of transformations of the reconstructed wavefunctions that allows us to define such as genuine canonical basis.

We want the loss function to depend only on the error associated with the reconstructed orbital ϕ_μ. Therefore, we should in principle consider the many-body state $|\tilde{\Phi}_\mu\rangle$ where only the orbital φ_μ is substituted by its reconstruction ϕ_μ. We can then compute the inner product between $|\Phi\rangle$ and $|\tilde{\Phi}_\mu\rangle$ using Supplementary Appendix S1 and deduce any induced metric f

$$d^f_{\mathrm{exact}}\left(T^{(\varphi)}, T^{(\phi)}\right) = f\left(\frac{\langle \Phi | \tilde{\Phi}_\mu \rangle}{\sqrt{\langle \tilde{\Phi}_\mu | \tilde{\Phi}_\mu \rangle}}\right). \tag{32}$$

However, computing this metric is too computationally involved to be carried out explicitly for each training data at each epoch. Instead, we keep this metric for comparing *a posteriori* the performance of our model.

Instead of explicitly determining $d^{f}_{\text{exact}}(T^{(\varphi)}, T^{(\phi)})$, we focus on reproducing canonical orbitals using the metrics of the one-body Hilbert space. In practice we considered the distance noted $d^{(0)}_{\circ}$ that is induced by the inner product between normalized functions in the one-body Hilbert space, that is,

$$d^{(0)}_{\circ}(\varphi,\phi) \equiv \left(\frac{\langle\varphi|}{\sqrt{\langle\varphi|\varphi\rangle}} - \frac{\langle\phi|}{\sqrt{\langle\phi|\phi\rangle}}\right)\left(\frac{|\varphi\rangle}{\sqrt{\langle\varphi|\varphi\rangle}} - \frac{|\phi\rangle}{\sqrt{\langle\phi|\phi\rangle}}\right), \tag{33}$$

which is nothing but

$$d^{(0)}_{\circ}(\varphi,\phi) = \sum_{\sigma}\int \mathrm{d}^3\boldsymbol{r}\left|\varphi(\boldsymbol{r},\sigma) - \phi(\boldsymbol{r},\sigma)\right|^2, \tag{34}$$

where the $\varphi(\boldsymbol{r}, \sigma)$ and $\phi(\boldsymbol{r}, \sigma)$ have been normalized. Since all wavefunctions are discretized on the Gauss quadrature mesh, this distance reads

$$d^{(0)}_{\circ}(\varphi,\phi) = \sum_{n_\perp n_z n_\sigma} W_{n_\perp n_z}\left|T^{(\varphi)}_{n_\perp n_z n_\sigma} - T^{(\phi)}_{n_\perp n_z n_\sigma}\right|^2, \tag{35}$$

where the weights W are given by

$$W_{n_\perp n_z} = \frac{w^{\mathrm{GL}}_{n_\perp}}{2b_\perp^2} \times 2\pi \times \frac{w^{\mathrm{GH}}_{n_z}}{b_z}. \tag{36}$$

These weights, which depend on the indices $n_\perp$ and n_z in the summation, are the only difference between the squared distance loss (Eq. 35) and the MSE loss (Eq. 28). Although the distance (Eq. 35) is norm-invariant[6], it still depends on the global phase of each orbital. We have explored other possible options for the loss based on norm- and phase-invariant distances; see Supplementary Appendix S2 for a list. However, we found in our tests that the distance $d^{(0)}_{\circ}$ systematically outperformed the other ones and, for this reason, only show results obtained with this one.

4.1.4 Physics-informed autoencoder

From a mathematical point of view, deep neural networks can be thought of as a series of compositions of functions. Each composition operation defines a new layer in the network. Networks are most often built with alternating linear and nonlinear layers. The linear part is a simple matrix multiplication. Typical examples of nonlinear layers include sigmoid, tanh, Rectified Linear Unit (ReLU) functions. In addition to these linear and nonlinear layers, there could be miscellaneous manipulations of the model for more specific purposes, such as adding batch normalization layers Ioffe and Szegedy [100], applying dropout Srivastava et al. [101] to some linear layers, or skip connection He et al. [102] between layers.

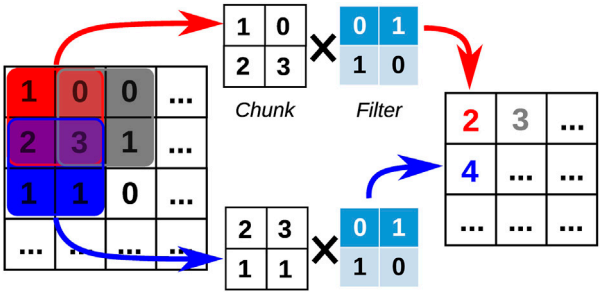

FIGURE 6
Schematic example of a convolutional layer. For any 2 × 2 chunk C of the input image on the left, this convolutional layer performs the point-wise multiplication of C with the filter F followed by the addition of all elements. This compresses the initial chunk of the image into a single integer.

Our data is a smooth function defined over a $N_\perp \times N_z = 60 \times 40$ grid and is analogous to a small picture. For this reason, we chose a 2D convolutional network architecture. Convolutional layers are popular for image analysis, because they incorporate the two-dimensional pixel arrangement in the construction of the weights of the network. These two-dimensional weights, or filters, capture local shapes and can model the dependent structure in nearby pixels of image data. Given a 2D $m \times m$ input array, a 2D filter F is a $n \times n$ matrix, usually with $n \ll m$. If we note I^n the space of $n \times n$ integer-valued matrices, then the convolutional layer $\mathcal{C}$ is an operation of the $\mathcal{C}$: $(I^n, I^n) \to \mathbb{N}$ that is applied to all pairs (F, C) where C is any $n \times n$ chunk of the input image; see Figure 6 for an example. This way, the resulting output summarizes the strength and location of that particular filter shape within the image. As the model gets trained, the filter parameters are fitted to a shape that is learned to be important in the training data. Convolutional neural network are very effective for image analysis and are currently widely used Krizhevsky et al. [103]; Zeiler and Fergus [104]; Sermanet et al. [105]; Szegedy et al. [106].

In this work, we used the Resnet 18 model as our encoder and constructed the decoder from a transposed convolution architecture of the Resnet 18. The Resnet 18 model was first introduced by He *et al.* as a convolutional neural network for image analysis He et al. [102]. It was proposed as a solution to the degradation of performance as the network depth increases. Resnet branches an identity-function addition layer to sub-blocks (some sequential layers of composition) of a given network. While a typical neural network sub-block input and output could be represented by x and $f(x)$, respectively, a Resnet sub-block would output $f(x) + x$ for the same input x, as in Figure 2 of He et al. [102]. This architecture is called 'skip

6 A distance $d(u, v)$ is norm-invariant if for any positive real number α and β, we have $d(\alpha u, \beta v) = d(u, v)$.

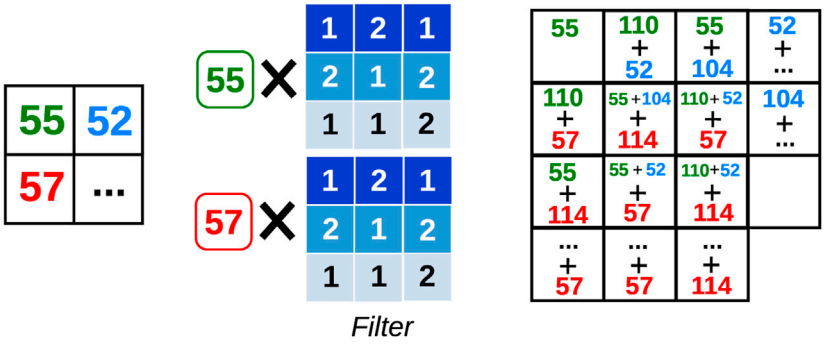

FIGURE 7
Schematic illustration of the 2D-transposed convolution. Each input value, e.g., 55, 57, etc., is multiplied by the entire kernel resulting in a 3 × 3 matrix. These matrices are then added to one another in a sliding and overlapping way.

connection' and was shown to be helpful for tackling multiple challenges in training deep neural network such as vanishing gradient problem and complex loss function Li et al. [107]; He et al. [102]. Since then, the Resnet architecture has been widely successful, often being used as a baseline for exploring new architectures Zhang et al. [108]; Radosavovic et al. [109] or as the central model for many analyses Cubuk et al. [110]; Yun et al. [111]; Zhang et al. [112]. In a few cases, it was also combined with autoencoders for feature learning from high-dimensional data Wickramasinghe et al. [113].

For the decoder part, we designed a near-mirror image of the encoder using transposed convolution. Transposed convolution is essentially the opposite operation to convolution in terms of input and output dimensions. Here the meaning of transpose refers to the form of the filter matrix when the convolution layer is represented by a 1D vector input obtained from linearizing the 2D input. Note that the mirror-located filters in the decoder are independent parameters and not the actual transposed filter matrix of the encoder. Such a construction ensures symmetrical encoder and decoder models, making the decoder model close to the inverse shape of the encoder model. Figure 7 illustrates the operation: one input value is multiplied by the entire kernel (filter) and is added to the output matrix at its corresponding location. The corresponding output location for each colored input number are color-coded and show how the addition is done.

The first and the last layer of the Resnet architecture are mostly for resizing and were minimally modified from the original Resnet 18 model since the size of our input data is significantly smaller than typical image sizes used for Resnet image classification analyses. We also modified the number of input channels of the first layer of the encoder to be 2 (for each of the spin components of the nuclear wavefunction) instead of the usual number 3 (for the RGB colors of colored images) or 1 (for black-and-white images). The spin components are closely related to each other with covariance structure, similar to how colors interact within an image. Therefore, we treat a pair of spin components as a single sample and treat each component as an input channel. The same applies to the output channel of the decoder.

The full network is represented schematically in Figure 8. Parametric Rectified Linear Unit, or PRELU, layers were added to impose nonlinearity in the model He et al. [114]. PRELU layers are controlled by a single hyperparameter that is trained with the data. Batch normalization is a standardizing layer that is applied to each batch by computing its mean and standard deviation. It is known to accelerate training by helping with optimization steps Ioffe and Szegedy [100]. The average pooling layer (bottom left) averages each local batch of the input and produces a downsized output. The upsampling layer (top right) upsamples the input using a bilinear interpolation.

4.2 Training

As mentioned in Section 4.1.4, the loss is the discrepancy between the input of the encoder and the output of the decoder. The minimization of the loss with respect to all the model parameters w, such as the filter parameters, is the training process. We used the standard back-propagation algorithm to efficiently compute the gradient of the loss function with respect to the model parameters. The gradient computation is done with the chain rule, iterating from the last layer in the backward direction. We combined this with the mini-batch gradient descent algorithm: ideally, one would need the entire dataset to estimate the gradient at the current model parameter value. However, with large datasets, this becomes computationally inefficient. Instead we use a random subset of the entire data, called mini-batch, to approximate the gradient, and expedite the convergence of the optimization. For each mini-batch, we update each parameter w by taking small steps of gradient descent, $w_{t+1} = w_t - \alpha \frac{\partial \mathcal{L}}{\partial w_t}$. At step t, or at tth mini-batch, the average loss

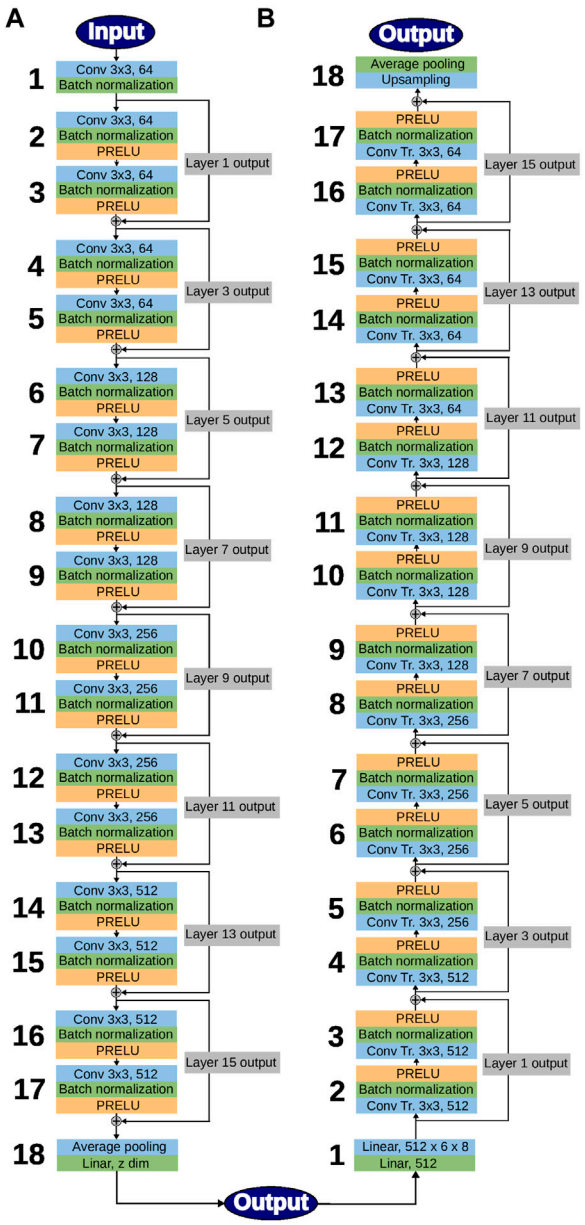

FIGURE 8
Representation of our modified Resnet 18 architecture for the encoder **(A)** and the decoder **(B)**. Large numbers on the left of each side label the different layers. Numbers such as 64, 128, etc. refer to the size of the filer; see text for a discussion of some of the main layers.

$\mathcal{L}$ and the gradient with respect to current model parameter w_t are computed. Then α-sized gradient descent step is taken to update the model parameters. Instead of using the current gradient for the update, one can use a weighted average of past gradients. We employed the well-known Adam algorithm, which uses the exponential moving average of current and past gradients Kingma and Ba [115].

Iterating over the entire dataset once, using multiple mini-batches, is called an epoch. Typically a deep neural network needs hundreds to thousands of epochs for the algorithm to converge. Parameters such as the batch size or learning rate, the parameters of the optimizer itself (Adam's or other), and the number of epochs are hyper-parameters that must be tuned for model fitting. For our training, we used the default initialization method in PyTorch for the model parameters. The linear layers were initialized with a random uniform distribution over $[-1/k, 1/k]$, where k is the size of the weight. For example, if there are 2 input channels and 3×3 convolution filters are used, $k = 2 \times 3 \times 3$. PRELU layers were initialized with their default PyTorch value of 0.25. We proceeded with mini-batches of size 32 with the default $\beta_1 = 0.9$, $\beta_2 = 0.999$ and $\epsilon = 10^{-8}$: all these numbers refer to the PyTorch implementation of the Adam's optimizer. For α, we used 0.001 as starting value and used a learning rate scheduler, which reduces the α value by a factor of 0.5 when there is no improvement in the loss for 15 epochs. After careful observation of the loss curves, we have estimated that at least 1,000 epochs are needed to achieve convergence.

To mitigate the problem of the global phase invariance of the canonical wavefunctions discussed in Section 4.1.2, we doubled the size of the dataset: at each point $\boldsymbol{q}$ of the collective space (=the sample), we added to each canonical wavefunction $\varphi_\mu(\boldsymbol{r}, \sigma)$ the same function with the opposite sign $-\varphi_\mu(\boldsymbol{r}, \sigma)$. The resulting dataset was then first split into three components, training, validation and test datasets, which represent 70%, 15%, and 15% of the entire data respectively. Training data is used for minimizing the loss with respect to the model parameters as explained above. Then we choose the model at the epoch that performs the best with the validation dataset as our final model. Finally, the model performance is evaluated using the test data.

4.3 Results

In this section, we summarize some of the preliminary results we have obtained after training several variants of the AE. In Section 4.3.1, we give some details about the training data and the quality of the reconstructed wavefunctions. We discuss some possible tools to analyze the structure of the latent space in Section 4.3.2. In these two sections, we only present results obtained for latent spaces of dimension $D = 20$. In Section 4.3.3, we use the reconstructed wavefunctions to recalculate HFB observables with the code HFBTHO. We show the results of this physics validation for both $D = 20$ and $D = 10$.

4.3.1 Performance of the network

Figure 9 shows the initial potential energy surface in ^{98}Zr used in this work. Calculations were performed for the SkM* parametrization of the Skyrme potential with a surface-volume, density-dependent pairing force with $V_0^{(n)} = -199.69$ MeV.fm^{-3}, $V_0^{(p)} = -223.59$ MeV.fm^{-3} and an "infinite" pairing cutoff. The

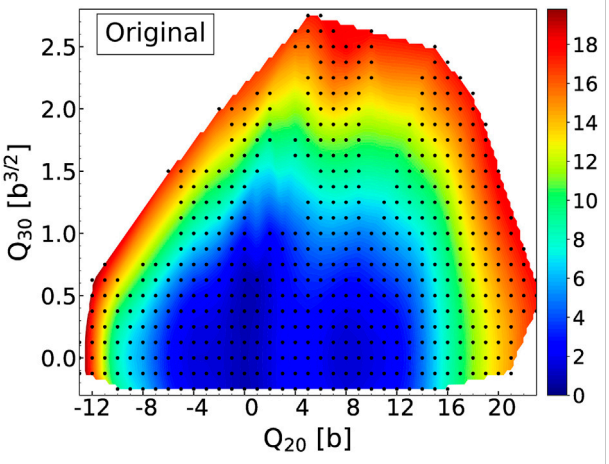

FIGURE 9
Potential energy surface of ^{98}Zr in the (q_{20}, q_{30}) plane. Converged HFBTHO solutions are represented by black dots. Energies given by the color bar are in MeV relatively to the ground state.

basis was identical for all points with oscillator length b_0 = 1.971 fm, deformation β_0 = 0.3 and number of shells N_{basis} = 20. The PES contains 548 HFB calculations with constraints on the axial quadrupole, $q_{20} = \langle\hat{Q}_{20}\rangle$, and axial octupole moment, $q_{30} = \langle\hat{Q}_{30}\rangle$. The mesh was: $-$ 12.5 b $\leq q_{20} \leq$ 25.0 b with steps δq_{20} = 1 b and 0.0 b3/2 $\leq q_{30} \leq$ 3.0 b$^{3/2}$ with step δq_{30} = 0.125 b$^{3/2}$. The black dots in Figure 9 indicate the location of the converged solutions. For each solution, the n_p = 60 highest-occupation proton and n_n = 87 highest-occupation neutron canonical wavefunctions were used as training data for the network[7].

For each of the losses discussed in Supplementary Appendix S2, we trained the AE with the slightly modified Resnet 18 architecture described in Section 4.1.4. It is important to keep in mind that the value of these losses should not be compared with one another. The only rigorous method to compare the performance of both networks would be to compute the many-body norm overlap across all the points in each case—or to perform *a posteriori* physics validation with the reconstructed data, as will be shown in Section 4.3.3.

To give an idea of the quality of the AE, we show in Figure 10 one example of the original and reconstructed canonical wavefunctions. Specifically, we consider the configuration (q_{20}, q_{30}) = ($-$ 7.0 b, $-$ 0.25 b$^{3/2}$) in the collective space and look at the neutron wavefunction with occupation number v_μ^2 = 0.945255, which is located near the Fermi surface. This example was obtained for an AE trained with the $d_o^{(0)}$ loss and compressed to D = 20. The figure shows, in the left panel, the logarithm of the squared norm of the original wavefunction across the quadrature mesh, $\ln|\varphi_\mu|^2 \equiv \ln|T^{(\varphi_\mu)}_{n_\perp n_z n_\sigma}|^2$, in the middle panel, the same quantity for the reconstructed wavefunction, and in the right panel the logarithm of the absolute value of the difference between the two. On this example, the AE can reconstruct the wavefunction with about 3% error.

7 Since time-reversal symmetry is conserved, the Fermi energy is located around states with indices $\mu_p \approx 20$ and $\mu_n \approx 29$. Therefore, our choice implies that in our energy window, about 1/3 of all states are below the Fermi level and about 2/3 of them are above it.

4.3.2 Structure of the latent space

One of the advantages of AEs is the existence of a low-dimensional representation of the data. In principle, any visible structure in this latent space would be the signal that the network has properly learned, or encoded, some dominant features of the dataset. Here, our latent space has dimension D = 20. This means that every canonical wavefunction, which is originally a matrix of size $n = N_\perp \times N_z$, is encoded into a single vector of size D. From a mathematical point of view, the encoder is thus a function

$$\begin{aligned} \hat{E}\colon \mathbb{R}^n &\to \mathbb{R}^D \\ \varphi &\longmapsto \boldsymbol{v} = \hat{E}(\varphi) \end{aligned} \tag{37}$$

Let us consider some (scalar) quantity P associated with the many-body state $|\Phi(\boldsymbol{q})\rangle$ at point $\boldsymbol{q}$. Such a quantity could be an actual observable such as the total energy but it could also be an auxiliary object such as the expectation value of the multipole moment operators. In fact, P could also be a quantity associated with the individual degrees of freedom at point $\boldsymbol{q}$, for example the q.p. energies. In general terms, we can think of P as the output value of the function

$$\begin{aligned} \hat{P}\colon \mathbb{R}^n &\to \mathbb{R} \\ \varphi &\longmapsto P = \hat{P}(\varphi) \end{aligned} \tag{38}$$

For example, if P represents the s.p. canonical energies, then the function $\hat{P}$ is the one that associates with each canonical wavefunction its s.p. energy. Therefore, for every canonical wavefunction, there is a different value of P. Conversely, if $P = \langle\hat{Q}_{20}\rangle$, there is a single value for all the canonical wavefunctions at point $\boldsymbol{q}$. Since there is a vector in the latent space for each canonical wavefunction, and there is also a value for the quantity P for each such function, we can then define the new function $\hat{\mathcal{P}}$ acting on vectors of the *latent space* and defined as

$$\begin{aligned} \hat{\mathcal{P}}\colon \mathbb{R}^D &\to \mathbb{R} \\ \boldsymbol{v} &\longmapsto P = \hat{\mathcal{P}}(\boldsymbol{v}) \end{aligned} \tag{39}$$

and it is straightforward to see that: $\hat{P} = \hat{\mathcal{P}} \circ \hat{E}$. Our goal is now to try to analyze where various quantities P are located in the latent space and whether one can identify some specific features of these locations.

Since we have a total of n_t = 147 wavefunctions for each of the N_p = 552 points in the collective space, the encoder yields a set of $n_t \times N_p$ vectors of dimension D. This means that, in the latent space, every quantity P above is also represented by a cloud of

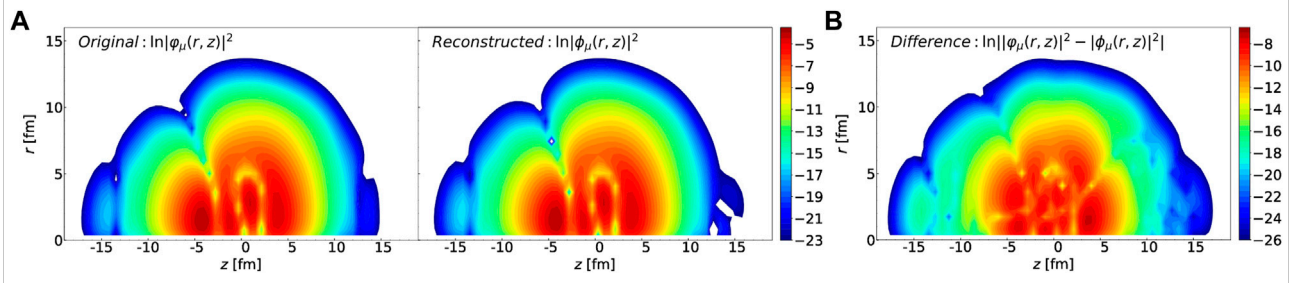

FIGURE 10
(A): Contour plot of the logarithm of the squared norm of the neutron canonical wavefunction with occupation number $v_\mu^2 = 0.945255$ (without the exponential factor). Middle: Same for the reconstructed wavefunction. **(B)**: Logarithm of the difference between the squared norm of the original and reconstructed wavefunctions.

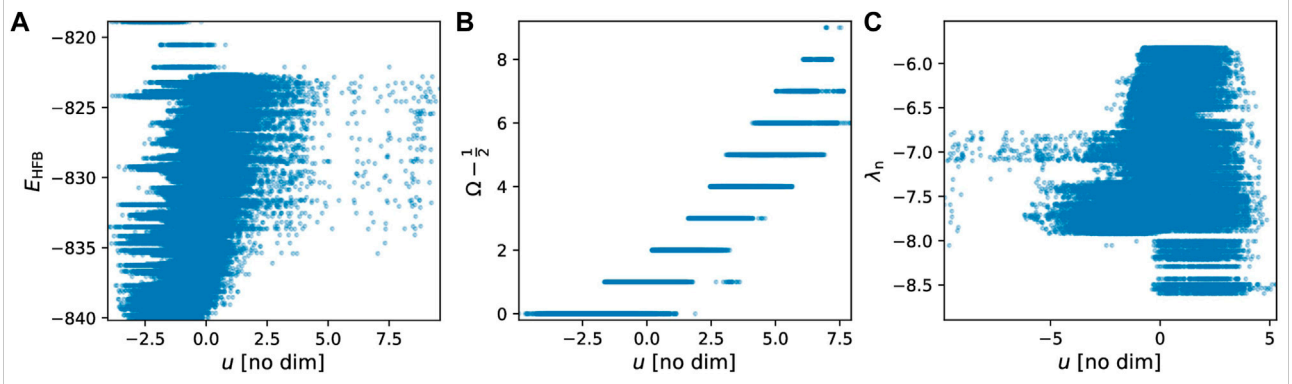

FIGURE 11
One-dimensional projections of the D-dimensional linear fit for the total energy E_{HFB} **(A)**, the projection Ω of the canonical state **(B)** and the neutron Fermi energy λ_n **(C)**. Each point represents one of these quantities for a canonical wavefunction μ and a point $\boldsymbol{q}$ in the collective space.

$n_t \times N_p$ such vectors. This is obviously impossible to visualize. For this reason, we introduce the following analysis. First, we perform a linear regression in the D-dimensional latent space of a few select quantities of interest P, that is, we write

$$P = \boldsymbol{\alpha} \cdot \boldsymbol{\nu} + b, \tag{40}$$

where $\boldsymbol{\alpha}$ is a D-dimensional vector, $\boldsymbol{\nu}$ is the vector associated with the quantity P in the latent space and $b \in \mathbb{R}$. The unit vector $\boldsymbol{u} = \boldsymbol{\alpha}/\|\boldsymbol{\alpha}\|$ can be interpreted as representing the leading direction in the latent space. The quantity $u = \boldsymbol{u} \cdot \boldsymbol{\nu}$ is a scalar which we obtain easily from the result of the linear regression. We can thus plot the function P: $u \mapsto P(u)$. Examples of such functions are shown in Figure 11. Each point in the figures represents the value $P = \hat{\mathcal{P}}(\boldsymbol{\nu})$ of some characteristic quantity at point $u = \boldsymbol{u} \cdot \boldsymbol{\nu}$.

The three cases shown in Figure 11 illustrate that the network has not always identified relevant features. The case of Ω, middle panel, is the cleanest: there is a clear slope as a function of u: if one sets $u = 1$, for example, then only values of $7/2 \leq \Omega \leq 15/2$ are possible. Conversely, the AE has not really discovered any feature in the neutron Fermi energy (right panel): for any given value of u, there is a large range of possible values of Fermi energies. In the case of the total energy (left panel), the situation is somewhat intermediate: there is a faint slope suggesting a linear dependency of the energy as a function of u.

4.3.3 Physics validation

The results presented in the Section 4.3.1 suggest the AE has the ability to reproduce the canonical wavefunctions with good precision. To test this hypothesis, we recalculated the HFB solution at all the training, validation and testing points by substituting in the HFBTHO binary files the original canonical wavefunctions by the ones reconstructed by the AE. Recall that only the lowest n_t wavefunctions with the largest occupation were encoded in the AE ($n_n = 87$ for neutrons and $n_p = 60$ for protons); the remaining ones were unchanged. In practice, their occupation is so small that their contribution to nuclear observables is very small (< 10 keV for the total energy, for example).

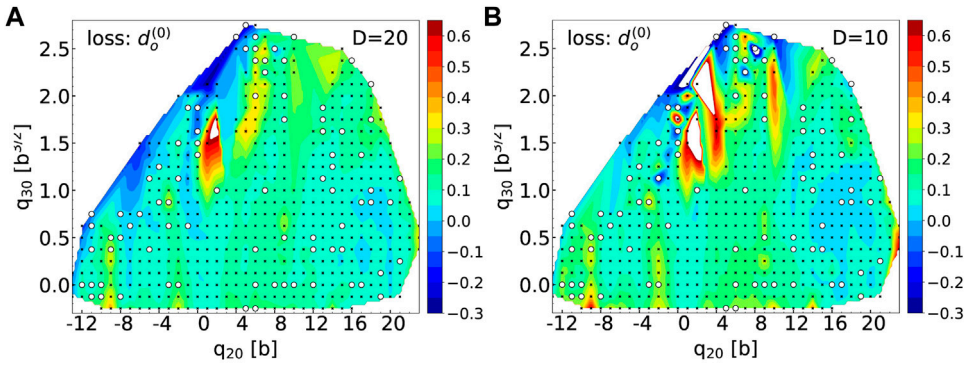

FIGURE 12
(A): Potential energy surface in the (q_{20}, q_{30}) plane for ^{98}Zr obtained after replacing the first n_n = 87 and n_p = 60 highest-occupation canonical wavefunctions by their values reconstructed by the AE for a latent space of dimension D = 20. The black dots show the location of the training points only, the white circles the location of the validation points. **(B)**: same figure for a latent space of dimension D = 10. For both figures, energies are given in MeV.

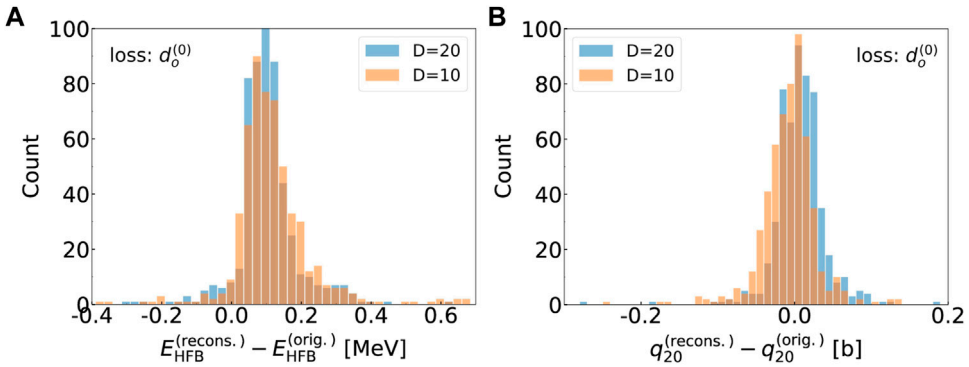

FIGURE 13
(A): Histogram of the difference in total HFB energy between the original HFBTHO calculation and the result obtained by computing the energy in the canonical basis with the reconstructed wavefunctions (see text for details). Calculations were performed both for a D = 20 and D = 10 latent space. **(B)**: Similar histogram for the expectation value of the axial quadrupole moment.

Figure 12 shows the error on the potential energy across the (q_{20}, q_{30}) collective space obtained with the reconstructed canonical wavefunctions for latent spaces of dimension D = 20 (left) and D = 10 (right). In each case, we only show results obtained when using the $d_o^{(0)}$ loss, which gives the best results. The black crosses denote the location of all the original points; the white circles show the location of the validation points. Overall, the results are very encouraging. In both cases, most of the error is concentrated near regions of the PES where there are discontinuities (hence, the lack of converged solutions). Everywhere else, the error is small and mostly randomly distributed across the PES, that is, it is not systematically larger at the validation points. As expected, the quality of the reconstruction is a little worse when D = 10: one can notice about a dozen points for which the error is significantly larger, in absolute value. Examples include (q_{20}, q_{30}) = (− 5.0 b, 1.125 b$^{3/2}$) or (q_{20}, q_{30}) = (+ 8.0 b, 2.5 b$^{3/2}$) in the validation set, and (q_{20}, q_{30}) = (0.0 b, 1.75 b$^{3/2}$) or the region around 1 b ≤ q_{20} ≤ 4 b and 1.5 b$^{3/2}$ ≤ q_{30} ≤ 2.25 b$^{3/2}$ in the training set. These may suggest that for D = 10, the loss may not have fully converged yet. Because of the existence of discontinuities near these points, this could also be the manifestation that our continuous AE cannot build a continuous representation of the data everywhere. However, the fact that an increase of the compression by a factor 2, from D = 20 to D = 10, does not substantially degrade the performance of the AE is very promising.

The two histograms in Figure 13 give another measure of the quality of the AE. The histogram in the left shows the distribution of the error on the HFB energy for two sizes of the latent space, D = 20 and D = 10. For the D = 20 case, the mean error is $\overline{\Delta E}$ =

104 keV and the standard deviation $\sigma_E = 89$ keV. These numbers increase a little bit in the case of $D = 10$: $\overline{\Delta E} = 122$ keV and $\sigma_E = 153$ keV. To better estimate the quality of the AE, we applied the same Gaussian process technique as described in Section 3 to the dataset in ^{98}Zr. Since GPs are interpolators and reproduce the training data, we can only test them across the validation set, which, in the case of ^{98}Zr contains only 110 configurations. After computing the energy with the HFB potentials obtained from the GP across this set, we obtain: $\overline{\Delta E}^{(\mathrm{GP})} = -32$ keV and $\sigma_E^{(\mathrm{GP})} = 225$ keV. This is comparable to what the AE predicts. As mentioned before, it is important to bear in mind that, for the AE, the points with the higher error $\Delta E < -150$ keV or $\Delta E > 250$ keV do not correspond to testing points only.

The histogram on the right shows the distribution of the error for q_{20}, in units of b. Here, the mean and standard deviation of the error are: $\overline{\Delta q_{20}} = 6.8$ mb and $\sigma_q = 33.0$ mb for $D = 20$, and $\overline{\Delta q_{20}} = -7.4$ mb and $\sigma_q = 48.2$ mb for $D = 10$. For comparison, the results obtained (across the validation set only) with the GP are: $\overline{\Delta q_{20}} = -12.7$ mb and $\sigma_q = 68.3$ mb. Once again, the AE performs just as well, if not slightly better, than the GP fit.

5 Conclusion

Nuclear density functional methods are amenable to large-scale calculations of nuclear properties across the entire chart of isotopes relevant for, e.g., nuclear astrophysics simulations or uncertainty quantification. However, such calculations remain computationally expensive and fraught with formal and practical issues associated with self-consistency or reduced collective spaces. In this article, we have analyzed two different techniques to build fast, efficient and accurate surrogate models, or emulators, or DFT objects.

We first showed that Gaussian processes could reproduce reasonably well the values of the mean-field and pairing-field potentials of the HFB theory across a large two-dimensional potential energy surface. The absolute error on the total energy was within ±100 keV and the relative errors on the collective inertia tensor smaller than 5%. However, GPs require the training data to be "smoothly-varying", i.e., they should not include phenomena such as nuclear scission or, more generally, discontinuities in the PES. It is well known that GPs are not reliable for extrapolation: such a technique can thus be very practical to densify (=interpolate) an existing potential energy surface but must not be applied outside its training range.

Our implementation of standard versions of GPs is fast and simple to use, but it misses many of the correlations that exist between the values of the HFB potentials on the quadrature grid: (i) all components of the full Skyrme mean field (central, spin-orbit, etc.) are in principle related to one another through their common origin in the non-local one-body density matrix; (ii) the correlations between the value of any given potential at point (r, z) and at point (r', z') were not taken into account; (iii) the correlations between the variations of the mean fields at different deformations was also neglected. Incorporating all these effects may considerably increase the complexity of the emulator. In such a case, it is more natural to directly use deep-learning techniques. In this work, we reported the first application of autoencoders to emulate the canonical wavefunctions of the HFB theory. Autoencoders are a form of deep neural network that compresses the input data, here the canonical wavefunctions, into a small-dimensional space called the latent representation. The encoder is trained simultaneously with a decoder by enforcing that the training data is left invariant after compression followed by decompression. In practice, the measure of such "invariance" is set by what is called the loss of the network. We discussed possible forms of the loss that are best adapted to learning quantum-mechanical wavefunctions of many-body systems such as nuclei. We showed that such an AE could successfully reduce the data into a space of dimension $D = 10$ while keeping the total error on the energy lower than $\Delta E = 150$ keV (on average). The analysis of the latent space revealed well-identified structures in a few cases, which suggests the network can learn some of the physics underlying the data. This exploratory study suggests that AE could serve as reliable canonical wavefunctions generators. The next step will involve learning a full sequence of such wavefunctions, i.e., an ordered list, in order to emulate the full HFB many-body state.

Data availability statement

The raw data supporting the conclusions of this article will be made available by the authors, without undue reservation.

Author contributions

MV led the study of autoencoders for canonical wavefunctions: design of the overall architecture of the autoencoders, development of the software stack and analysis of the results. NS led the study of Gaussian process for mean-field potentials—training and validation runs, code development and HFBTHO calculations—and supervised the whole project. IK implemented, tested and trained different architectures of autoencoders and helped with the analysis of the results. PM developed an HFBTHO module to use canonical wavefunctions in HFB calculations. KQ provided technical expertise about Gaussian processes and supervised MN, who implemented and fitted Gaussian processes to mean-field potentials. DR and RL provided technical consulting on deep neural network and the architecture of autoencoders. All authors contributed to the writing of the manuscript, and read and approved the submitted version.

Funding

This work was performed under the auspices of the United States Department of Energy by Lawrence Livermore National Laboratory under Contract DE-AC52-07NA27344. Computing support came from the Lawrence Livermore National Laboratory (LLNL) Institutional Computing Grand Challenge program.

Conflict of interest

The authors declare that the research was conducted in the absence of any commercial or financial relationships that could be construed as a potential conflict of interest.

Publisher's note

All claims expressed in this article are solely those of the authors and do not necessarily represent those of their affiliated organizations, or those of the publisher, the editors and the reviewers. Any product that may be evaluated in this article, or claim that may be made by its manufacturer, is not guaranteed or endorsed by the publisher.

Supplementary material

The Supplementary Material for this article can be found online at: https://www.frontiersin.org/articles/10.3389/fphy.2022.1028370/full#supplementary-material

References

1. Eschrig R. *Fundamentals of density functional theory*. Leipzig: Teubner (1996).

2. Schunck N. *IOP expanding physics*. Bristol, UK: IOP Publishing (2019).Energy density functional methods for atomic nuclei.

3. Schunck N, Regnier D. Theory of nuclear fission. *Prog Part Nucl Phys* (2022) 125:103963. doi:10.1016/j.ppnp.2022.103963

4. Schunck N, Robledo LM. Microscopic theory of nuclear fission: A review. *Rep Prog Phys* (2016) 79:116301. doi:10.1088/0034-4885/79/11/116301

5. Kejzlar V, Neufcourt L, Nazarewicz W, Reinhard PG. Statistical aspects of nuclear mass models. *J Phys G: Nucl Part Phys* (2020) 47:094001. doi:10.1088/1361-6471/ab907c

6. Schunck N, O'Neal J, Grosskopf M, Lawrence E, Wild SM. Calibration of energy density functionals with deformed nuclei. *J Phys G: Nucl Part Phys* (2020) 47: 074001. doi:10.1088/1361-6471/ab8745

7. Erler J, Birge N, Kortelainen M, Nazarewicz W, Olsen E, Perhac AM, et al.The limits of the nuclear landscape. *Nature* (2012) 486:509–12. doi:10.1038/nature11188

8. Ney EM, Engel J, Li T, Schunck N. Global description of β^- decay with the axially deformed Skyrme finite-amplitude method: Extension to odd-mass and odd-odd nuclei. *Phys Rev C* (2020) 102:034326. doi:10.1103/PhysRevC.102.034326

9. Mumpower MR, Surman R, McLaughlin GC, Aprahamian A. The impact of individual nuclear properties onr-process nucleosynthesis. *Prog Part Nucl Phys* (2016) 86:86–126. doi:10.1016/j.ppnp.2015.09.001

10. Perlińska E, Rohoziński SG, Dobaczewski J, Nazarewicz W. Local density approximation for proton-neutron pairing correlations: Formalism. *Phys Rev C* (2004) 69:014316. doi:10.1103/PhysRevC.69.014316

11. Utama R, Piekarewicz J, Prosper HB. Nuclear mass predictions for the crustal composition of neutron stars: A bayesian neural network approach. *Phys Rev C* (2016) 93:014311. doi:10.1103/PhysRevC.93.014311

12. Utama R, Piekarewicz J. Refining mass formulas for astrophysical applications: A bayesian neural network approach. *Phys Rev C* (2017) 96: 044308. doi:10.1103/PhysRevC.96.044308

13. Utama R, Piekarewicz J. Validating neural-network refinements of nuclear mass models. *Phys Rev C* (2018) 97:014306. doi:10.1103/PhysRevC.97.014306

14. Niu ZM, Liang HZ. Nuclear mass predictions based on Bayesian neural network approach with pairing and shell effects. *Phys Lett B* (2018) 778:48–53. doi:10.1016/j.physletb.2018.01.002

15. Neufcourt L, Cao Y, Nazarewicz W, Olsen E, Viens F. Neutron drip line in the Ca region from bayesian model averaging. *Phys Rev Lett* (2019) 122:062502. doi:10.1103/PhysRevLett.122.062502

16. Lovell AE, Mohan AT, Sprouse TM, Mumpower MR. Nuclear masses learned from a probabilistic neural network. *Phys Rev C* (2022) 106:014305. doi:10.1103/PhysRevC.106.014305

17. Scamps G, Goriely S, Olsen E, Bender M, Ryssens W. Skyrme-Hartree-Fock-Bogoliubov mass models on a 3D mesh: Effect of triaxial shape. *Eur Phys J A* (2021) 57:333. doi:10.1140/epja/s10050-021-00642-1

18. Mumpower MR, Sprouse TM, Lovell AE, Mohan AT. Physically interpretable machine learning for nuclear masses. *Phys Rev C* (2022) 106:L021301. doi:10.1103/PhysRevC.106.L021301

19. Niu ZM, Liang HZ, Sun BH, Long WH, Niu YF. Predictions of nuclear β-decay half-lives with machine learning and their impact on r-process nucleosynthesis. *Phys Rev C* (2019) 99:064307. doi:10.1103/PhysRevC.99.064307

20. Wang ZA, Pei J, Liu Y, Qiang Y. Bayesian evaluation of incomplete fission yields. *Phys Rev Lett* (2019) 123:122501. doi:10.1103/PhysRevLett.123.122501

21. Lovell AE, Mohan AT, Talou P. Quantifying uncertainties on fission fragment mass yields with mixture density networks. *J Phys G: Nucl Part Phys* (2020) 47: 114001. doi:10.1088/1361-6471/ab9f58

22. Melendez JA, Drischler C, Furnstahl RJ, Garcia AJ, Zhang X. Model reduction methods for nuclear emulators. *J Phys G: Nucl Part Phys* (2022) 49:102001. doi:10.1088/1361-6471/ac83dd

23. Giuliani P, Godbey K, Bonilla E, Viens F, Piekarewicz J. *Bayes goes fast: Uncertainty quantification for a covariant energy density functional emulated by the reduced basis method* (2022). [Dataset]. doi:10.48550/ARXIV.2209.13039

24. Bonilla E, Giuliani P, Godbey K, Lee D. *Training and projecting: A reduced basis method emulator for many-body physics* (2022). [Dataset]. doi:10.48550/ARXIV.2203.05284

25. Lasseri RD, Regnier D, Ebran JP, Penon A. Taming nuclear complexity with a committee of multilayer neural networks. *Phys Rev Lett* (2020) 124:162502. doi:10.1103/PhysRevLett.124.162502

26. Parr R, Yang W. *International series of monographs on chemistry*. New York: Oxford University Press (1989).Density functional theory of atoms and molecules

27. Dreizler R, Gross E. *Density functional theory: An approach to the quantum many-body problem*. Springer-Verlag (1990). doi:10.1007/978-3-642-86105-5

28. Engel J. Intrinsic-density functionals. *Phys Rev C* (2007) 75:014306. doi:10.1103/PhysRevC.75.014306

29. Barnea N. Density functional theory for self-bound systems. *Phys Rev C* (2007) 76:067302. doi:10.1103/PhysRevC.76.067302

30. Engel YM, Brink DM, Goeke K, Krieger SJ, Vautherin D. Time-dependent Hartree-Fock theory with Skyrme's interaction. *Nucl Phys A* (1975) 249:215–38. doi:10.1016/0375-9474(75)90184-0

31. Dobaczewski J, Dudek J. Time-Odd components in the rotating mean field and identical bands. *Acta Phys Pol B* (1996) 27:45.

32. Bender M, Heenen PH, Reinhard PG. Self-consistent mean-field models for nuclear structure. *Rev Mod Phys* (2003) 75:121–80. doi:10.1103/RevModPhys.75.121

33. Lesinski T, Bender M, Bennaceur K, Duguet T, Meyer J. Tensor part of the Skyrme energy density functional: Spherical nuclei. *Phys Rev C* (2007) 76:014312. doi:10.1103/PhysRevC.76.014312

34. Schunck N, Quinlan KR, Bernstein J. A Bayesian analysis of nuclear deformation properties with Skyrme energy functionals. *J Phys G: Nucl Part Phys* (2020) 47:104002. doi:10.1088/1361-6471/aba4fa

35. Dobaczewski J, Flocard H, Treiner J. Hartree-Fock-Bogolyubov description of nuclei near the neutron-drip line. *Nucl Phys A* (1984) 422:103–39. doi:10.1016/0375-9474(84)90433-0

36. Vautherin D, Brink DM. Hartree-Fock calculations with skyrme's interaction. I. Spherical nuclei. *Phys Rev C* (1972) 5:626–47. doi:10.1103/PhysRevC.5.626

37. Dobaczewski J, Dudek J. Solution of the Skyrme-Hartree-Fock equations in the Cartesian deformed harmonic oscillator basis I. The method. *Comput Phys Commun* (1997) 102:166–82. doi:10.1016/S0010-4655(97)00004-0

38. Bender M, Bennaceur K, Duguet T, Heenen PH, Lesinski T, Meyer J. Tensor part of the Skyrme energy density functional. II. Deformation properties of magic and semi-magic nuclei. *Phys Rev C* (2009) 80:064302. doi:10.1103/PhysRevC.80.064302

39. Hellemans V, Heenen PH, Bender M. Tensor part of the Skyrme energy density functional. III. Time-odd terms at high spin. *Phys Rev C* (2012) 85:014326. doi:10.1103/PhysRevC.85.014326

40. Ryssens W, Hellemans V, Bender M, Heenen PH. Solution of the skyrme-hf+BCS equation on a 3D mesh, II: A new version of the Ev8 code. *Comput Phys Commun* (2015) 187:175–94. doi:10.1016/j.cpc.2014.10.001

41. Valatin JG. Generalized Hartree-Fock method. *Phys Rev* (1961) 122:1012–20. doi:10.1103/PhysRev.122.1012

42. Mang HJ. The self-consistent single-particle model in nuclear physics. *Phys Rep* (1975) 18:325–68. doi:10.1016/0370-1573(75)90012-5

43. Blaizot JP, Ripka G. *Quantum theory of finite systems*. Cambridge: The MIT Press (1985).

44. Ring P, Schuck P. The nuclear many-body problem. In: *Texts and monographs in physics*. Springer (2004).

45. Dobaczewski J, Dudek J. Time-odd components in the mean field of rotating superdeformed nuclei. *Phys Rev C* (1995) 52:1827–39. doi:10.1103/PhysRevC.52.1827

46. Stoitsov MV, Dobaczewski J, Nazarewicz W, Ring P. Axially deformed solution of the Skyrme-Hartree-Fock-Bogolyubov equations using the transformed harmonic oscillator basis. The program HFBTHO (v1.66p). *Comput Phys Commun* (2005) 167:43–63. doi:10.1016/j.cpc.2005.01.001

47. Heyde K, Wood JL. Shape coexistence in atomic nuclei. *Rev Mod Phys* (2011) 83:1467–521. doi:10.1103/RevModPhys.83.1467

48. Nakatsukasa T, Matsuyanagi K, Matsuo M, Yabana K. Time-dependent density-functional description of nuclear dynamics. *Rev Mod Phys* (2016) 88:045004. doi:10.1103/RevModPhys.88.045004

49. Griffin JJ, Wheeler JA. Collective motions in nuclei by the method of generator coordinates. *Phys Rev* (1957) 108:311–27. doi:10.1103/PhysRev.108.311

50. Wa Wong C. Generator-coordinate methods in nuclear physics. *Phys Rep* (1975) 15:283–357. doi:10.1016/0370-1573(75)90036-8

51. Reinhard PG, Goeke K. The generator coordinate method and quantised collective motion in nuclear systems. *Rep Prog Phys* (1987) 50:1–64. doi:10.1088/0034-4885/50/1/001

52. Verriere M, Regnier D. The time-dependent generator coordinate method in nuclear physics. *Front Phys* (2020) 8:1. doi:10.3389/fphy.2020.00233

53. Brink DM, Weiguny A. The generator coordinate theory of collective motion. *Nucl Phys A* (1968) 120:59–93. doi:10.1016/0375-9474(68)90059-6

54. Onishi N, Une T. Local Gaussian approximation in the generator coordinate method. *Prog Theor Phys* (1975) 53:504–15. doi:10.1143/PTP.53.504

55. Une T, Ikeda A, Onishi N. Collective Hamiltonian in the generator coordinate method with local Gaussian approximation. *Prog Theor Phys* (1976) 55:498–508. doi:10.1143/PTP.55.498

56. Bloch C, Messiah A. The canonical form of an antisymmetric tensor and its application to the theory of superconductivity. *Nucl Phys* (1962) 39:95–106. doi:10.1016/0029-5582(62)90377-2

57. Zumino B. Normal forms of complex matrices. *J Math Phys* (1962) 3:1055–7. doi:10.1063/1.1724294

58. Marević P, Schunck N, Ney EM, Navarro Pérez R, Verriere M, O'Neal J. Axially-deformed solution of the Skyrme-Hartree-Fock-Bogoliubov equations using the transformed harmonic oscillator basis (iv) HFBTHO (v4.0): A new version of the program. *Comput Phys Commun* (2022) 276:108367. doi:10.1016/j.cpc.2022.108367

59. Drischler C, Furnstahl RJ, Melendez JA, Phillips DR. How well do we know the neutron-matter equation of state at the densities inside neutron stars? A bayesian approach with correlated uncertainties. *Phys Rev Lett* (2020) 125:202702. doi:10.1103/PhysRevLett.125.202702

60. Kravvaris K, Quinlan KR, Quaglioni S, Wendt KA, Navrátil P. Quantifying uncertainties in neutron-α scattering with chiral nucleon-nucleon and three-nucleon forces. *Phys Rev C* (2020) 102:024616. doi:10.1103/PhysRevC.102.024616

61. Acharya B, Bacca S. Gaussian process error modeling for chiral effective-field-theory calculations of $np \leftrightarrow dy$ at low energies. *Phys Lett B* (2022) 827:137011. doi:10.1016/j.physletb.2022.137011

62. Pastore A, Shelley M, Baroni S, Diget CA. A new statistical method for the structure of the inner crust of neutron stars. *J Phys G: Nucl Part Phys* (2017) 44:094003. doi:10.1088/1361-6471/aa8207

63. Kortelainen M, Lesinski T, Moré J, Nazarewicz W, Sarich J, Schunck N, et al.Nuclear energy density optimization. *Phys Rev C* (2010) 82:024313. doi:10.1103/PhysRevC.82.024313

64. Kortelainen M, McDonnell J, Nazarewicz W, Reinhard PG, Sarich J, Schunck N, et al.Nuclear energy density optimization: Large deformations. *Phys Rev C* (2012) 85:024304. doi:10.1103/PhysRevC.85.024304

65. Kortelainen M, McDonnell J, Nazarewicz W, Olsen E, Reinhard PG, Sarich J, et al.Nuclear energy density optimization: Shell structure. *Phys Rev C* (2014) 89:054314. doi:10.1103/PhysRevC.89.054314

66. Higdon D, McDonnell JD, Schunck N, Sarich J, Wild SM. A Bayesian approach for parameter estimation and prediction using a computationally intensive model. *J Phys G: Nucl Part Phys* (2015) 42:034009. doi:10.1088/0954-3899/42/3/034009

67. McDonnell JD, Schunck N, Higdon D, Sarich J, Wild SM, Nazarewicz W. Uncertainty quantification for nuclear density functional theory and information content of new measurements. *Phys Rev Lett* (2015) 114:122501. doi:10.1103/PhysRevLett.114.122501

68. Neufcourt L, Cao Y, Nazarewicz W, Viens F. Bayesian approach to model-based extrapolation of nuclear observables. *Phys Rev C* (2018) 98:034318. doi:10.1103/PhysRevC.98.034318

69. Neufcourt L, Cao Y, Giuliani S, Nazarewicz W, Olsen E, Tarasov OB. Beyond the proton drip line: Bayesian analysis of proton-emitting nuclei. *Phys Rev C* (2020) 101:014319. doi:10.1103/PhysRevC.101.014319

70. Neufcourt L, Cao Y, Giuliani SA, Nazarewicz W, Olsen E, Tarasov OB. Quantified limits of the nuclear landscape. *Phys Rev C* (2020) 101:044307. doi:10.1103/PhysRevC.101.044307

71. Rasmussen CE, Williams CKI. Gaussian Processes for machine learning. *Adaptive computation and machine learning*. Cambridge, Mass: MIT Press (2006).

72. Bartel J, Quentin P, Brack M, Guet C, Håkansson HB. Towards a better parametrisation of skyrme-like effective forces: A critical study of the SkM force. *Nucl Phys A* (1982) 386:79–100. doi:10.1016/0375-9474(82)90403-1

73. Schunck N, Duke D, Carr H, Knoll A. Description of induced nuclear fission with Skyrme energy functionals: Static potential energy surfaces and fission fragment properties. *Phys Rev C* (2014) 90:054305. doi:10.1103/PhysRevC.90.054305

74. Schunck N. Density functional theory approach to nuclear fission. *Acta Phys Pol B* (2013) 44:263. doi:10.5506/APhysPolB.44.263

75. Dubray N, Regnier D. Numerical search of discontinuities in self-consistent potential energy surfaces. *Comput Phys Commun* (2012) 183:2035. doi:10.1016/j.cpc.2012.05.001

76. Sadhukhan J. Microscopic theory for spontaneous fission. *Front Phys* (2020) 8:567171. doi:10.3389/fphy.2020.567171

77. Bruinsma W, Perim E, Tebbutt W, Hosking S, Solin A, Turner R. Scalable exact inference in multi-output Gaussian processes. *Proceedings of the 37th international Conference on machine learning* (PMLR). *Proc Machine Learn Res* (2020) 119:1190.

78. Álvarez MA, Rosasco L, Lawrence ND. Kernels for vector-valued functions: A review. *FNT Machine Learn* (2012) 4:195–266. doi:10.1561/2200000036

79. Bender M, Bernard R, Bertsch G, Chiba S, Dobaczewski J, Dubray N, et al.Future of nuclear fission theory. *J Phys G: Nucl Part Phys* (2020) 47:113002. doi:10.1088/1361-6471/abab4f

80. Schunck N. Microscopic description of induced fission. *J Phys : Conf Ser* (2013) 436:012058. doi:10.1088/1742-6596/436/1/012058

81. Ryssens W, Heenen PH, Bender M. Numerical accuracy of mean-field calculations in coordinate space. *Phys Rev C* (2015) 92:064318. doi:10.1103/PhysRevC.92.064318

82. Jin S, Bulgac A, Roche K, Wlazłowski G. Coordinate-space solver for superfluid many-fermion systems with the shifted conjugate-orthogonal conjugate-gradient method. *Phys Rev C* (2017) 95:044302. doi:10.1103/PhysRevC.95.044302

83. Regnier D, Dubray N, Schunck N, Verrière M. Microscopic description of fission dynamics: Toward a 3D computation of the time dependent GCM equation. *EPJ Web Conf* (2017) 146:04043. doi:10.1051/epjconf/201714604043

84. Zhao J, Nikšić T, Vretenar D. Microscopic self-consistent description of induced fission: Dynamical pairing degree of freedom. *Phys Rev C* (2021) 104: 044612. doi:10.1103/PhysRevC.104.044612

85. Lau NWT, Bernard RN, Simenel C. Smoothing of one- and two-dimensional discontinuities in potential energy surfaces. *Phys Rev C* (2022) 105:034617. doi:10.1103/PhysRevC.105.034617

86. Baldi P. Autoencoders, unsupervised learning, and deep architectures. In Proceedings of ICML workshop on unsupervised and transfer learning (JMLR Workshop and Conference Proceedings) (2012), 37–49.

87. Burda Y, Grosse R, Salakhutdinov R. *Importance weighted autoencoders* (2015). *arXiv preprint arXiv:1509.00519*.

88. Chen M, Xu Z, Weinberger K, Sha F. *Marginalized denoising autoencoders for domain adaptation* (2012). *arXiv preprint arXiv:1206.4683*.

89. Gong D, Liu L, Le V, Saha B, Mansour MR, Venkatesh S, et al.Memorizing normality to detect anomaly: Memory-augmented deep autoencoder for unsupervised anomaly detection. In: Proceedings of the IEEE/CVF International Conference on Computer Vision. October 2019 (2019). p. 1705–14.

90. Bengio Y, Courville A, Vincent P. Representation learning: A review and new perspectives. *IEEE Trans Pattern Anal Mach Intell* (2013) 35:1798–828. doi:10.1109/tpami.2013.50

91. Zhang F, Du B, Zhang L. Saliency-guided unsupervised feature learning for scene classification. *IEEE Trans Geosci Remote Sens* (2014) 53:2175–84. doi:10.1109/tgrs.2014.2357078

92. Yu J, Hong C, Rui Y, Tao D. Multitask autoencoder model for recovering human poses. *IEEE Trans Ind Electron* (2017) 65:5060–8. doi:10.1109/tie.2017.2739691

93. von Neuman J, Wigner E. Uber merkwürdige diskrete Eigenwerte. Uber das Verhalten von Eigenwerten bei adiabatischen Prozessen. *Physikalische Z* (1929) 30: 467–70.

94. Teller E. The crossing of potential surfaces. *J Phys Chem* (1937) 41:109–16. doi:10.1021/j150379a010

95. Longuet-Higgins HC, Öpik U, Pryce MHL, Sack RA. Studies of the jahn-teller effect. II. The dynamical problem. *Proc R Soc Lond A* (1958) 244:1. doi:10.1098/rspa.1958.0022

96. Longuet-Higgins H. The intersection of potential energy surfaces in polyatomic molecules. *Proc R Soc Lond A* (1975) 344:147. doi:10.1098/rspa.1975.0095

97. W Domcke, D Yarkony, H Köppel, editors. *Conical intersections: Theory, computation and experiment*. *Advanced series in physical chemistry*, Vol. 17. World Scientific (2011). doi:10.1142/7803

98. Larson J, Sjöqvist E, Öhberg P. Intersections in physics. An introduction to synthetic gauge theories. In *Lecture notes in physics*. Springer (2020). doi:10.1007/978-3-030-34882-3

99. Haider Q, Gogny D. Microscopic approach to the generator coordinate method with pairing correlations and density-dependent forces. *J Phys G: Nucl Part Phys* (1992) 18:993–1022. doi:10.1088/0954-3899/18/6/003

100. Ioffe S, Szegedy C. Batch normalization: Accelerating deep network training by reducing internal covariate shift. In: *International conference on machine learning (PMLR)* (2015). p. 448–56.

101. Srivastava N, Hinton G, Krizhevsky A, Sutskever I, Salakhutdinov R. Dropout: A simple way to prevent neural networks from overfitting. *J machine Learn Res* (2014) 15:1929–58.

102. He K, Zhang X, Ren S, Sun J. Deep residual learning for image recognition. In: Proceedings of the IEEE conference on computer vision and pattern recognition. June 2016 (2016). p. 770–8.

103. Krizhevsky A, Sutskever I, Hinton GE. Imagenet classification with deep convolutional neural networks. *Adv Neural Inf Process Syst* (2012) 25.

104. Zeiler MD, Fergus R. Visualizing and understanding convolutional networks. In: *European conference on computer vision*. Springer (2014). p. 818–33.

105. Sermanet P, Eigen D, Zhang X, Mathieu M, Fergus R, LeCun Y. *Overfeat: Integrated recognition, localization and detection using convolutional networks* (2013). *arXiv preprint arXiv:1312.6229*.

106. Szegedy C, Ioffe S, Vanhoucke V, Alemi AA. *Inception-v4, inception-resnet and the impact of residual connections on learning*. San Francisco, CA: Thirty-first AAAI conference on artificial intelligence (2017).

107. Li H, Xu Z, Taylor G, Studer C, Goldstein T. Visualizing the loss landscape of neural nets. *Adv Neural Inf Process Syst* (2018) 31.

108. Zhang H, Wu C, Zhang Z, Zhu Y, Lin H, Zhang Z, et al. Resnet: Split-attention networks. Proceedings of the IEEE/CVF Conference on Computer Vision and Pattern Recognition September 2022 (2022), 2736–46.

109. Radosavovic I, Kosaraju RP, Girshick R, He K, Dollár P. Designing network design spaces. In Proceedings of the IEEE/CVF conference on computer vision and pattern recognition. June 2020. Seattle, WA, USA. IEEE (2020). p. 10428–36.

110. Cubuk ED, Zoph B, Shlens J, Le QV. Randaugment: Practical automated data augmentation with a reduced search space. In Proceedings of the IEEE/CVF conference on computer vision and pattern recognition workshops. June 2020. Seattle, WA, USA. IEEE (2020). p. 702–3.

111. Yun S, Han D, Oh SJ, Chun S, Choe J, Yoo Y. Cutmix: Regularization strategy to train strong classifiers with localizable features. In Proceedings of the IEEE/CVF international conference on computer vision. May 2019. IEEE (2019). p. 6023–32.

112. Zhang H, Cisse M, Dauphin YN, Lopez-Paz D. *mixup: Beyond empirical risk minimization*. *arXiv preprint arXiv:1710.09412* (2017).

113. Wickramasinghe CS, Marino DL, Manic M. Resnet autoencoders for unsupervised feature learning from high-dimensional data: Deep models resistant to performance degradation. *IEEE Access* (2021) 9:40511–20. doi:10.1109/ACCESS.2021.3064819

114. He K, Zhang X, Ren S, Sun J. Delving deep into rectifiers: Surpassing human-level performance on imagenet classification. In Proceedings of the IEEE international conference on computer vision February 2015 (2015), 1026–34.

115. Kingma DP, Ba J. *Adam: A method for stochastic optimization* (2014). *arXiv preprint arXiv:1412.6980*.

116. Deza M, Deza E. *Encyclopedia of distances*. Springer (2009). doi:10.1007/978-3-642-00234-2

117. Dobaczewski J, Nazarewicz W, Werner TR, Berger JF, Chinn CR, Dechargé J. Mean-field description of ground-state properties of drip-line nuclei: Pairing and continuum effects. *Phys Rev C* (1996) 53:2809–40. doi:10.1103/PhysRevC.53.2809

118. Warda M, Robledo LM. Microscopic description of cluster radioactivity in actinide nuclei. *Phys Rev C* (2011) 84:044608. doi:10.1103/PhysRevC.84.044608

119. Warda M, Zdeb A, Robledo LM. Cluster radioactivity in superheavy nuclei. *Phys Rev C* (2018) 98:041602(R). doi:10.1103/PhysRevC.98.041602

120. Matheson Z, Giuliani SA, Nazarewicz W, Sadhukhan J, Schunck N. Cluster radioactivity. *Phys Rev C* (2019) 99:041304. doi:10.1103/PhysRevC.99.041304of $^{294}_{118}\mathrm{Og}_{176}$

frontiers | Frontiers in Physics

TYPE Review
PUBLISHED 14 December 2022
DOI 10.3389/fphy.2022.1028995

OPEN ACCESS

EDITED BY
Evgeny Epelbaum,
Ruhr University Bochum, Germany

REVIEWED BY
Attila Pásztor,
Eötvös Loránd University, Hungary
Jon-Ivar Skullerud,
Maynooth University, Ireland

*CORRESPONDENCE
Alexander Rothkopf,
alexander.rothkopf@uis.no

SPECIALTY SECTION
This article was submitted to Nuclear Physics,
a section of the journal
Frontiers in Physics

RECEIVED 26 August 2022
ACCEPTED 25 November 2022
PUBLISHED 14 December 2022

CITATION
Rothkopf A (2022), Bayesian inference of real-time dynamics from lattice QCD. *Front. Phys.* 10:1028995.
doi: 10.3389/fphy.2022.1028995

Bayesian inference of real-time dynamics from lattice QCD

Alexander Rothkopf*

Faculty of Science and Technology, University of Stavanger, Stavanger, Norway

The computation of dynamical properties of nuclear matter, ranging from parton distribution functions of nucleons and nuclei to transport properties in the quark-gluon plasma, constitutes a central goal of modern theoretical physics. This real-time physics often defies a perturbative treatment and the most successful strategy so far is to deploy lattice QCD simulations. These numerical computations are based on Monte-Carlo sampling and formulated in an artificial Euclidean time. Real-time physics is most conveniently formulated in terms of spectral functions, which are hidden in lattice QCD behind an ill-posed inverse problem. I will discuss state-of-the art methods in the extraction of spectral functions from lattice QCD simulations, based on Bayesian inference and emphasize the importance of prior domain knowledge, vital to regularizing the otherwise ill-posed extraction task. With Bayesian inference allowing us to make explicit the uncertainty in both observations and in our prior knowledge, a systematic estimation of the total uncertainties in the extracted spectral functions is nowadays possible. Two implementations of the Bayesian Reconstruction (BR) method for spectral function extraction, one for MAP point estimates and one based on an open access Monte-Carlo sampler are provided. I will briefly touch on the use of machine learning for spectral function reconstruction and discuss some new insight it has brought to the Bayesian community.

KEYWORDS

Bayesian inference, lattice QCD, spectral functions, strong interaction, inverse problem

1 Introduction

1.1 The physics challenge

After a successful decade of studying the static properties of the strong interactions, such as their phase diagram (for reviews see e.g. [1, 2]) and equation of state (for recent studies see e.g., [3–5]) through relativistic heavy-ion collisions (for an overview see e.g., [6]) and more recently through the multi-messenger observations of colliding neutron stars (for a review see e.g. [7]), high energy nuclear physics sets out to make decisive progress in the understanding of real-time dynamics of quarks and gluons in the coming years.

The past heavy-ion collision campaigns at collider facilities such as RHIC at Brookhaven National Laboratory (BNL) and the LHC at the European Center for Nuclear Physics (CERN) provided conclusive evidence for the existence of a distinct high-temperature state of nuclear matter, the quark-gluon-plasma (for a review see e.g., [8]). At the same time, theory, by use of high-performance computing, predicted the thermodynamic properties, such as the equation of state [9–13] of hot nuclear matter from first principles. When data and theory were put to the test in the form of phenomenological models based on relativistic hydrodynamics, excellent agreement was observed (for a review see e.g., [14]).

Similarly past e^{-}+p collider experiments at HERA (DESY) revealed (for a review see [15]) that the properties of nucleons can only be understood when in addition to the three valence quarks of the eponymous quark-model also the virtual excitations of quarks and gluons are taken into account. In particular the emergent phenomenon of asymptotic freedom manifests itself clearly in their data, as the coupling between quarks and gluons becomes weaker with increasing momentum exchange in a collision (for the current state-of-the art see e.g., [16]). Simulations of the strong interactions are by now able to map this intricate behavior of the strong coupling over a wide range of experimentally relevant scales, again leading to excellent agreement between theory and experiment (for a community overview see Chapter 9 of [17]).

Going beyond the static or thermodynamic properties of nuclear matter proves to be challenging for both theory and experiment. In heavy-ion collisions most observed particles in the final state at best carry a memory on the whole time-evolution of the collision. This requires phenomenology to disentangle the physics of the QGP from other effects e.g., those arising in the early partonic stages or the hadronic aftermath of the collision. It turns out that in order to construct accurate multi-stage models of the collision dynamics (see e.g., [18–20]), a variety of first-principles insight is needed. The dynamics of the bulk of the light quarks and gluons which make up the QGP produced in the collision is conveniently characterized by transport coefficients. Of central interest are the viscosities of deconfined quarks and gluons and their electric charge conductivity. The physics of hard probes, such as fast jets (see e.g., [21]) or slow heavy quark bound states (see e.g., [22]), which traverse the bulk nearly as test particles on the other hand requires insight into different types of dynamical quantities. In this context first principles knowledge of the complex in-medium potential between a heavy quark and antiquark, the heavy quark diffusion constant or the so-called jet quenching parameter $\hat{q}$, which summarizes the momentum broadening of a parton jet is called for. As it turns out computing any of these quantities represents a major challenge for numerical simulation methods of the strong interactions.

Going beyond merely establishing asymptotic freedom and instead revealing the full 6-dimensional phase space (i.e., spatial and momentum distribution) of partons inside nucleons and nuclei is the aim of an ambitious collider project just green-lit in the United States. The upcoming electron-ion collider [23] will be able to explore the quark and gluon content of nucleons in kinematic regimes previously inaccessible and opens up the first opportunity to carry out precision tomography of nuclei using well-controlled point-particle projectiles. Simulations have already revealed that the virtual particle content of nucleons is vital for the overall angular momentum budget of the proton (see e.g., [24, 25]). A computation of the full generalized transverse momentum distribution [26] however has not been achieved yet. This quantity describes partons in terms of their longitudinal momentum fraction x, the impact parameter of the collision b_{T} and the transverse momentum of the parton k_{T}. Integrating out different parts of the transverse kinematics leads to simpler object, such as transverse momentum distributions (TMDs, integrated over b_{T}) or generalized parton distributions (GPDs, integrated over k_{T}). Integrating all transverse dependence leads eventually to the conventional parton distribution functions (PDFs), which depend only on the longitudinal Bjorken x variable. A vigorous research community has made significant conceptual and technical progress over the past years, moving towards the first-principles determination of PDFs and more recently GPDs and TMDs from lattice QCD (for a community overview see [27]). Major advances in the past years include the development of the quasi PDF [28] and pseudo PDF [29] formalism, which offer complementary access to PDFs besides their well-known relation to the hadronic tensor [30]. With the arrival of the first exascale supercomputer in 2022, major improvements in the precision and accuracy of parton dynamics from lattice QCD are on the horizon.

1.2 Lattice QCD

In order to support experiment and phenomenology, theory must provide model independent, i.e., first-principles insight into the dynamics of quarks and gluons in nuclei and within the QGP. This requires the use of quantum chromo dynamics (QCD), the renormalizable quantum field theory underlying the strong interactions. Renormalizability refers to the fact that one only needs to provide a limited number of experimental measurements to calibrate each of its input parameters (strong coupling constant and quark masses) before being able to make predictions at any scale. In order to utilize this vast predictive power of QCD however we must be able to evaluate correlation functions of observables from their defining equations in terms of Feynman's path integral

$$\langle O(t_1)\tilde{O}(t_2)\rangle = \frac{1}{Z}\int \mathcal{D}\left[A_a^\mu, \psi_f^a, \bar{\psi}_f^a\right] O(t_1)\tilde{O}(t_2) \exp\left[iS_{\mathrm{QCD}}\left[A_a^\mu, \psi_f^a, \bar{\psi}_f^a\right]\right], \tag{1}$$

where A_a^μ denotes the gluon fields and ψ_f^a the color charged quarks of flavor f. The path integral weight is given by the

exponentiated QCD action denoted by S_{QCD} (for more details see [31]) and the normalization Z refers to the path integral evaluated in the absence of observables in the integrand.

Computing the dynamical properties of quarks and gluons both inside nucleons as well as in the experimentally accessible QGP requires us to evaluate the above path integral in the presence of strong fluctuations, which invalidate commonly used weak-coupling expansions of the path integral weight. Instead a non-perturbative evaluation of observables is called for. While progress has been made in non-perturbative analytic approaches to QCD, such as the functional renormalization group [32, 33] or Dyson-Schwinger equations [34, 35], I focus here on the most prominent numerical approach: lattice QCD (for textbooks see e.g., [36, 37]).

In lattice QCD four-dimensional spacetime is discretized on a hypercube with N^4 grid points $\mathbf{n}$, separated by a lattice spacing a. In order to maintain the central defining property of QCD, the invariance of observables under local $SU(3)$ rotations of quark and gluon degrees of freedom, in such a discrete setting, one introduces gauge link variables $U_\mu(x) = \exp[-igA^a_\mu(x+\frac{1}{2}a\hat{\mu})T^a]$, which connect the nodes of the grid in direction $\hat{\mu}$. Here g denotes the strong coupling constant and T^a refers to the Gell-Mann matrices defining the gauge group $SU(3)$. From the closed products of four or more link variables, as well as the quark fermion fields, discrete but fully gauge invariant actions can be constructed (the simplest one called the Wilson action). This action allows to formulate a discretized version of Feynman's path integral.

It is the next and final step in the formulation of lattice QCD, which is crucial to understand the challenge we face in extracting dynamical properties from its simulations. The path integral of QCD, while already formulated in a discrete fashion, still contains the canonical complex Feynman weight $\exp[-iS_{\mathrm{QCD}}[U,\psi,\bar{\psi}]]$. So far, even though progress is being made, no universal numerical method to evaluate such highly dimensional oscillatory integrals has been developed, a challenge often referred to as the sign problem (see e.g., [38, 39]). Instead one circumvents this difficulty by making use of complex analysis and analytically continues the Minkowski time variable t onto the imaginary axis in the lower half complex plane $\tau = it$. The additional factors of the imaginary unit, which arise from this manipulation can be conveniently combined to cancel the prefactor of i in the Feynman weight leading to

$$\langle O_{\boldsymbol{n}_1}\tilde{O}_{\boldsymbol{n}_2}\rangle = \frac{1}{Z}\int\prod_{\boldsymbol{n}}\prod_{\mu} dU_{\mu,\boldsymbol{n}}d\left[\psi_{f,\boldsymbol{n}},\bar{\psi}_{f,\boldsymbol{n}}\right] O_{\boldsymbol{n}_1}\tilde{O}_{\boldsymbol{n}_2} \exp[S_{\mathrm{E}}[U,\psi,\bar{\psi}]]. \tag{2}$$

The action $S_{\mathrm{E}} \in \mathbb{R}$ one obtains after analytic continuation is referred to as Euclidean action. As a curiosity of quantum field theory one should note that due to a subtle relation between the Boltzmann factor, which describes thermal systems and time evolution in imaginary time, the extent of the imaginary time axis is directly linked to the inverse temperature $\beta = 1/T$ of the system [40]. By varying the length of the imaginary time axis it is therefore possible to change between a scenario at $T \approx 0$ relevant for nucleon structure and $T > 0$ relevant for the study of the QGP.

Besides allowing us to incorporate the concept of temperature in a straight forward manner, this Euclidean path integral is now amenable to standard methods of stochastic integration, since the Euclidean Feynman weight is real and bounded from below. Using established Markov-Chain Monte Carlo techniques one generates ensembles of gauge field configurations distributed according to $\frac{1}{Z}\exp[-S_{\mathrm{E}}[U,\psi,\bar{\psi}]]$. Evaluating (measuring) correlation functions $D(\tau = \tau_2 - \tau_1) = \langle O(\tau_1)O(\tau_2)\rangle$ on N_{conf} statistically independent field realizations $U^{(k)}$ and computing the mean, systematically estimates the quantum statistical expectation value

$$D(\tau) = \langle O(\tau_1)O(\tau_2)\rangle = \frac{1}{N_{\mathrm{conf}}}\sum_{k=1}^{N_{\mathrm{conf}}} O\left(\tau_1;U^{(k)}\right)O\left(\tau_2;U^{(k)}\right) + \mathcal{O}\left(1/\sqrt{N_{\mathrm{conf}}}\right). \tag{3}$$

here the error decreases with the number of generated configurations independent of the dimensionality of the underlying integral.

To avoid misunderstandings, let me emphasize that results obtained from lattice QCD at finite lattice spacing may not be directly compared to physical measurements. A valid comparison requires that the so-called continuum limit is taken $a \to 0$, while remaining close to the thermodynamic limit $V \to \infty$. Different lattice discretizations may yield deviating results, as long as this limit has not been adequately performed. For precision lattice QCD computations a community quality control has been established through the FLAG working group [17] to catalog different simulation results including information on the limits taken.

2 The inverse problem

The technical challenge we face is now laid bare: in order to make progress in the study of the dynamics of the strong interactions we need to evaluate Minkowski time correlation functions in QCD, related to parton distribution functions in nucleons or the dynamical properties of partons in the QGP. The lattice QCD simulations we are able to carry out however are restricted to imaginary time. Reverting back to the real-time domain as it turns out presents an ill-posed inverse problem.

The key to attacking this challenge is provided by the spectral representation of correlation functions [40]. It tells us that different incarnations of relevant correlation functions (e.g. the retarded or Euclidean correlators) share common information content in the form of a so-called spectral

function [41]. The Källén–Lehmann representation reveals that the retarded correlator of fields in momentum space may be written as

$$D^{\mathrm{R}}(p_0, \mathbf{p}) = \frac{i}{\pi} \int d\mu \, \frac{1}{p_0 - \mu + i\epsilon} \rho(\mu, \mathbf{p}), \tag{4}$$

while the same correlator in Euclidean time is given as

$$D^{\mathrm{E}}(\tau, \mathbf{p}) = \int d\mu \, \frac{e^{-\tau\mu}}{1 \mp e^{-\beta\mu}} \rho(\mu, \mathbf{p}), \tag{5}$$

where the sign in the denominator differs between bosonic (−) and fermionic (+) correlators. Both real-time and Euclidean correlator therefore can be expressed by the same spectral function, integrated over different analytically known kernel functions.

As we do have access to the Euclidean correlator, extracting the spectral function from it in principle gives us direct access to its Minkowski counterpart. It is important to note that often phenomenologically relevant physics is encoded directly and intuitively in the structures of the spectral function, making an evaluation of the real-time correlator superfluous. Transport coefficients e.g., can be read off from the low frequency behavior of the zero-momentum spectral function of an appropriate correlation function [42].

For the extraction of parton distribution functions similar challenges ensue. PDFs can be computed from a quantity christened the hadronic tensor $W^{\mathrm{M}}(t)$ [30], a four-point correlation function of quark fields in Minkowski time. The Euclidean hadronic tensor on the lattice is related to its real-time counterpart *via* a Laplace transform

$$W^{\mathrm{E}}(\tau) = \int d\mu \, e^{-\mu\tau} \, W^{\mathrm{M}}(\mu) \tag{6}$$

that needs to be inverted. Recently the pseudo PDF approach [29] has shown how a less numerically costly three-point correlation function $\mathcal{M}^{\mathrm{Ioffe}}$ can be used to extract similar information on e.g., quark distributions $q(x)$. It too is hidden behind an inverse problem of the form

$$\mathcal{M}^{\mathrm{Ioffe}}(\nu) = \int dx \, \cos(\nu x) \, q(x), \tag{7}$$

where the Ioffe-time matrix elements $\mathcal{M}^{\mathrm{Ioffe}}(\nu)$ are accessible on the lattice.

All the above examples of inverse problems share that they are in fact ill-posed. The concept of well- and conversely ill-posedness has been studied in detail and was first formalized by Hadamard [43]. Three conditions characterize a well posed problem: its solution exists, the solution is unique and the solution changes continuously with given initial conditions (which in our case refers to the supplied input data for the reconstruction task).

In the context of spectral function reconstruction, the latter two criteria present central challenges. Not only is the Euclidean correlator from the lattice D_i known only at N_τ discrete points τ_i, but in addition, as it arises from Monte-Carlo simulations, it also carries a finite error $\Delta D/D \neq 0$. This entails that in practice an infinite number of spectral functions exist, which all reproduce the input data within their statistical uncertainties.

Even in the case that one could simulate a continuous correlator, the stability of the inversion remains an issue. The reason is that as one simulates on limited domains, be it limited in Euclidean time due to a finite temperature (transport coefficients) or limited in Ioffe time (PDFs) the inversion exhibits strong sensitivity on uncertainties in the input data. The presence of exponentially small eigenvalues in the kernel K renders the inversion task in general ill-conditioned.

To be more concrete, let us write down the discretized spectral representation in terms of a spectral function ρ_l discretized at frequencies μ_l along N_μ equidistant frequency bins of with $\Delta\mu_l$ and the discretized kernel matrix K_{il}

$$D_i^{\rho} = \frac{1}{2}\Delta\mu_1 K_{i1} \, \rho_1 + \sum_{l=2}^{N_\mu - 1} \Delta\mu_l K_{il} \, \rho_l + \frac{1}{2}\Delta\mu_{N_\mu} K_{iN_\mu} \, \rho_{N_\mu}. \tag{8}$$

The task at hand is to solve the inverse problem of determining the parameters ρ_l from the sparse and noisy D_i's. The ill-posedness of this inverse problem is manifest in Eq. 8 in two aspects:

State-of-the-art lattice QCD simulations provide only around $\mathcal{O}(10 - 100)$ points along imaginary time τ. From it we must reconstruct the function ρ, which often contains intricate patterns at different scales. The fact that $N_\mu \gg N_\tau$ entails that many degenerate sets of ρ_l exist, which all reproduce the input data D_i within their statistical uncertainty. The inverse problem is thus highly degenerate.

In addition many of the kernel functions we have to deal with are of exponential form. This entails a strong loss of information between the spectral function and the Euclidean correlator. In other words, large changes in the spectral function translate into minute changes in the Euclidean correlator. Indeed, each of the tiny eigenvalues of the kernel is associated with a mode along frequencies, which can be added to the spectral function without significantly changing the correlator. Reference [44] has recently investigated this fact in detail analytically for the bosonic finite temperature kernel relevant in transport coefficient computations.

Even the at first sight benign cos kernel matrix arising in the pseudo PDF approach turns out to feature exponentially diminishing eigenvalues [45] as the lattice simulation cannot access the full Brillouin zone in ν. I.e., the matrix K_{il} is in general ill-conditioned, making its inversion unstable even if no noise is present. In the presence of noise the exponentially small eigenvalues lead to a strong enhancement of even minute uncertainties in the correlation functions rendering the inversion meaningless without further regularization.

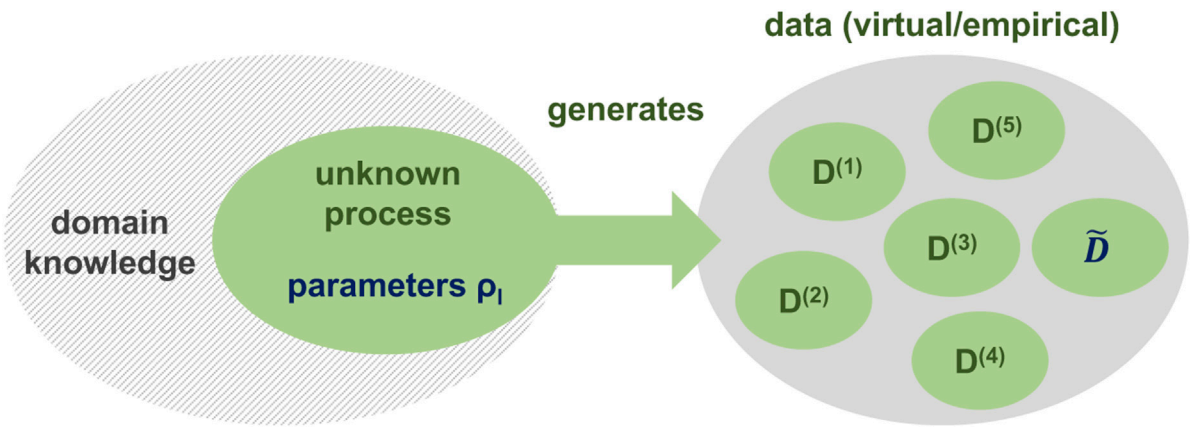

FIGURE 1
Statistical inference attempts to estimate from observed data $D^{(k)}$ the unknown process parameters ρ_I and as of yet unobserved data $\tilde{D}$. Bayesian inference exploits the fact that in many instances our model of the unknown process is embedded in a domain from which prior knowledge can be derived.

We will see in the next section how Bayesian inference and in particular the inclusion of prior knowledge can be used to mitigate the ill-posed (and ill-conditioned) nature of the inversion task and give meaning to the spectral function reconstruction necessary for extracting real-time dynamics from lattice QCD.

3 Bayesian inference of spectral functions

The use of Bayesian inference to extract spectral functions from lattice QCD simulations was pioneered by a team of researchers from Japan in two seminal papers [46, 47]. Inspired by prior work in condensed matter physics [48] and image reconstruction [49], the team successfully transferred the approach to the extraction of QCD real-time information. The work sparked a wealth of subsequent studies, which have applied and further developed Bayesian techniques to the extraction of real-time information from lattice QCD in various contexts, zero temperature hadron spectra and excited states [50–52], parton-distribution functions [45, 53], in-medium hadrons [54–67], sum rules [68, 69], transport coefficients [42, 70–76, 76], the complex in-medium heavy quark potential [77–80] and parton spectral properties [81–83].

The following discussion focuses on the Bayesian extraction of spectral functions that does not rely on a fixed parametrization of the functional form of ρ. If strong prior information exists, e.g. if vacuum hadronic spectral functions consist of well separated delta peaks, direct Bayesian parameter fitting methods are applicable [84] and may be advantageous. Similarly, some studies of in-medium spectra and transport phenomena deploy explicit parametrization of the spectral function derived from model input, whose parameters can be fitted in a Bayesian fashion (see Ref. [85] for a recent example). Our goal here is to extract spectral features for systems in which no such apriori parametrization is known.

3.1 Bayesian inference

Bayesian inference is a sub-field of statistical data analysis (for an excellent introduction see e.g., [86, 87]), which focuses on the estimation of unobserved quantities, based on incomplete and uncertain observed data (see Figure 1). The term unobserved is used to refer to the unknown parameters governing the process, which generates the observed data or to as of yet unobserved future data. In the context of the inverse problem in lattice QCD, the Euclidean correlation functions produced by a Monte-Carlo simulation take on the role of the observed data while the unobserved parameters are the values of the discretized spectral function ρ_I. Future observations can be understood as further realizations of the Euclidean correlator along the Markov-Chain of the simulation.

What makes Bayesian inference particularly well suited to attack the inverse problem is that it offers an explicit and well controlled strategy to incorporate information (I) beyond the measured data (D) into the reconstruction of spectral functions (ρ). It does so by using a more flexible concept of probability, which does not necessarily rely on the outcome of a large number of repeatable trials but instead assigns a general degree of uncertainty.

To be more concrete, Bayesian inference asks us to acknowledge that any model of a physical process is constructed within the context of its specific domain, in our case strong interaction physics. I.e., the structure of the model and its parameters are chosen according to prior information

obtained within its domain. Bayesian inference then requires us to explicitly assign degrees of uncertainty to all these choices and propagate this uncertainty into a generalized probability distribution called the posterior $P[\rho|D, I]$. Intuitively it describes how probable it is that a test function ρ is the correct spectral function, given simulated data D and prior knowledge I.[1]

The starting point of any inference task is the joint probability distribution $P[\rho, D, I]$. As it refers to the parameters ρ, data D and prior information I it combines information about the specific process generating the data as well as the domain it is embedded in. After applying the rules of conditional probability one obtains the work-horse of Bayesian inference, the eponymous Bayes theorem

$$\underbrace{P[\rho|D,I]}_{\text{posterior}} = \underbrace{P[D|I,\rho]}_{\text{likelihood}}\ \underbrace{P[\rho|I]}_{\text{prior}} / \underbrace{P[D|I]}_{\text{evidence}}. \tag{9}$$

It tells us how the posterior $P[\rho|D, I]$ can be efficiently computed. The likelihood denotes the probability for the data D to be generated from QCD given a fixed spectral function ρ. The prior probability quantifies how compatible ρ is compared to our domain knowledge. Historically the ρ independent normalization has been called the evidence. Let us construct the different ingredients to Bayes theorem in the following.

What is the likelihood in the case of spectral function reconstruction? In Monte-Carlo simulations one usually computes sub-averages of correlation functions on each of the N_{conf} generated gauge field configurations. For many commonly studied correlation functions, thanks to the central limit theorem, such data already approximate a normal distribution to a good degree. It is prudent to check the approach to Gaussianity for individual correlation functions, as it has been revealed in Refs. [88, 89] that some actually exhibit a log-normal distribution which converges only very slowly.

In case that the input data is approximately normal distributed, the corresponding likelihood probability $P[D|\rho, I] \propto \exp[-L]$, written in terms of the likelihood function L, too is a multidimensional Gaussian

$$P[D|\rho,I] = \mathcal{N}[D^\rho, C] \propto \exp\left[-\sum_{ij}\frac{1}{2}\left(D_i - D_i^\rho\right)C_{ij}^{-1}\left(D_j - D_j^\rho\right)\right], \tag{10}$$

where D_i denotes the mean of the simulated data at the ith Euclidean time step and D_i^ρ the corresponding Euclidean datapoint, arising from inserting the parameters ρ_l into the spectral representation Eq. 8. C_{ij} refers to the covariance matrix of the mean

$$C_{ij} = \frac{1}{N_{\text{conf}}\left(N_{\text{conf}}-1\right)}\sum_{k=1}^{N_{\text{conf}}}\left(D_i^{(k)} - D_i\right)\left(D_j^{(k)} - D_j\right), \tag{11}$$

where the individual measurements enter as $D^{(k)}$. Note that in order to obtain an accurate estimate of C_{ij}, the number of samples N_{conf} must be significantly larger than the number of data along imaginary time. In particular C_{ij} develops exact zero eigenvalues if the number of configurations is less than that of the datapoints.

In lattice QCD simulations, which are based on Monte-Carlo sampling, correlators computed on subsequent lattices are often not statistically independent. At the same time Eq. 11 assumes that all samples are uncorrelated. Several strategies are deployed in the literature to address this discrepancy. One common approach is to rely on resampling methods, such as the (blocked) Jackknife (for an introduction see Ref. [90]) or similar bootstrap methods in order to estimate the true covariance matrix. Alternatively one may compute the exponential autocorrelation time τ_{D_i} for each correlator data D_i along Monte-Carlo time (see e.g., Chapter 7 of [36]). This quantity encodes how many subsequent lattices remain statistically correlated. To account for finite autocorrelation in Eq. 11, one multiplies C_{ij} with the prefactor $\tau_{D_i}\tau_{D_j}$.

A speedup in the computation of the likelihood can be achieved in practice if, following Ref. [46], one computes the eigenvalues σ_i and eigenvectors of C and changes both the kernel and the input data into the coordinate system where $S^tCS = \text{diag}[\sigma_i]$ becomes diagonal. Then the two sums in Eq. 10 collapse onto a single one $L = \sum_i \frac{1}{2}(\tilde{D}_i - \tilde{D}_i^\rho)^2/\sigma_i^2$ with $\tilde{D}_i^\rho = S_{ij}^t K_{jl}\rho_l$ and $\tilde{D}_i = S_{ij}^t D_j$.

Since the likelihood is a central ingredient in the posterior, all Bayesian reconstruction methods ensure that the reconstructed spectral function, when inserted into the spectral representation will reproduce the input data within their uncertainty. I.e., they will always produce a valid statistical hypothesis for the simulation data. This crucial property distinguishes the Bayesian approach from competing non-Bayesian methods, such as the Backus-Gilbert method and the Padé reconstruction (see examples in e.g., [91, 92]), in which the reconstructed spectral function does not necessarily reproduce the input data.

In case that we do not possess any prior information we have $P[\rho|I] = 1$ and Bayes theorem only contains the likelihood. Since the functional L is highly degenerate in terms of ρ_l's, the question of what is the most probable spectral function, i.e., the maximum likelihood estimate of ρ, does not make sense at this point. Only by supplying meaningful prior information can we regularize and thus give meaning to the inverse problem.

3.2 Bayesian spectral function reconstruction

Different Bayesian strategies to attack the ill-posed spectral function inverse problem differ by the type of domain

1 This prior knowledge may be supplied by a quantum field theory such as QCD and QED but also from experiment.

information they incorporate in the prior probability $P[\rho|I] \propto \exp[S]$, where S is called the regulator functional. Once the prior probability is constructed, the spectral reconstruction consists of evaluating the posterior probability $P[\rho|D, I]$, which informs us of the distribution of the values of ρ_l in each frequency bin μ_l.

The versatility of the Bayesian approach actually allows us to reinterpret several classic regularization prescriptions in the language of Bayes theorem, providing a unifying language to seemingly different strategies.

When surveying approaches to inverse problems in other fields, Tikhonov regularization [93] is by far the most popular regularization prescription. It amounts to choosing an independent Gaussian prior probability for each parameter

$$P[\rho|I] = \prod_{l=1}^{N_\mu} \mathcal{N}[m_l, 1/\sqrt{\alpha_l}] \propto \exp\left[-\sum_{l=1}^{N_\mu} \alpha_l \frac{1}{2} (\rho_l - m_l)^2\right]. \quad (12)$$

Each normal distribution is characterized by its maximum (mean) denoted here by m_l and width (uncertainty) $1/\sqrt{\alpha_l}$. In the literature m_l is usually referred to as the default model and α_l simply as hyperparameter. The significance of the two quantities is that in the absence of simulation data, m_l denotes the most probable apriori value of ρ_l with intrinsic uncertainty $1/\sqrt{\alpha_l}$. Since these parameters, even though they are constrained by QCD, will be known only up to a some uncertainty, the Bayesian strategy requires us to assign distributions $P[m]$ and $P[\alpha]$ to these model parameters. This is a first example of a so-called hierarchical model, where each level of the model encodes the uncertainties and correlations among model (hyper-)parameters in the subsequent layer. It then remains the task of the user to extract from QCD domain knowledge appropriate uncertainty budgets for m and α.

Another regularization deployed in the field of image reconstruction is the so-called total variation approach [94]. Here the difference between neighboring parameters ρ_l and ρ_{l+1}, i.e., $\Delta\rho_l$, is modelled [95] as a Laplace distribution

$$P[\Delta\rho|I] = \prod_{l=1}^{N_\mu-1} \text{Laplace}[m_l, \alpha_l] \propto \exp\left[-\sum_{l=1}^{N_\mu-1} \alpha_l |(\rho_{l+1} - \rho_l) - m_l|\right]. \quad (13)$$

Since $\Delta\rho_l$ is related to the first derivative of the spectral function this regulator incorporates knowledge about rapid changes, such as kinks, in spectral features. Choosing α_l and m_l appropriately one may e.g., prevent the occurrence of kink features in the reconstructed spectral function, if it is known that the underlying true QCD spectral function is smooth.

In Ref. [96] I proposed a regulator related to the derivative of ρ, with a different physical meaning

$$P[\Delta\rho|I] = \prod_{l=1}^{N_\mu-1} \mathcal{N}[m_l, \alpha_l] \propto \exp\left[-\sum_{l=1}^{N_\mu-1} \alpha_l ((\rho_{l+1} - \rho_l) - m_l)^2\right]. \quad (14)$$

Often spectral reconstructions, which are based on a relatively small number of input data, suffer from ringing artifacts, similar to the Gibbs ringing arising in the inverse problem of the Fourier series. These artifacts lead to a reconstructed spectral function with a similar area as the true spectral function but with a much larger arc length due to the presence of unphysical wiggles. Since such ringing is not present in the true QCD spectral function we may apriori suppress it by penalizing arc length $\ell = \int d\mu \sqrt{1 + (d\rho/d\mu)^2}$. And since the square root is monotonic, we may remove it for our purposes, as well as discard the addition of unity, as it is absorbed into the normalization of the corresponding prior distribution. The hyperparameters of such a prior must be chosen appropriately, since the remedy to one artifact, ringing, can lead to the introduction of a different artifact, which is over-damping of reconstructed spectral features. The relevant ranges for α and m, as e.g., in Ref. [67], can be established using mock data tests.

If our prior domain knowledge contains information about the smoothness and the absence of ringing then it is of course possible to combine different regulators by multiplying the prior probabilities. The reconstruction of the first picture of a black hole e.g., combined the Tikhonov and total variation regularization [97]. In the presence of multiple regulators, the hyperparameters α and m of each of these distributions need to be assigned an (independent) uncertainty distribution.

One may ask, whether a proliferation of such parameters spoils the benefit of the Bayesian approach? The answer is that in practice one can estimate the probable ranges of these parameters by use of mock data. One carries out the spectral function reconstruction, i.e., the estimation of the posterior probability $P[\rho|D, I]$, using data, which has been constructed from known spectral functions with realistic features and which has been distorted with noise similar to those occurring in Monte-Carlo simulations (see e.g., [67]). One may then observe from such test data sets, what the most probable values of the hyperparameters are and in what interval they vary, depending on different spectral features present in the input data.

The three priors discussed so far are not commonly used as stand-alone regulators in the reconstruction of hadron spectral functions from lattice QCD in practice. The reason is that neither of them can exploit a central prior information available in the lattice context, which is the positivity [36] of the most relevant hadronic spectral functions. I.e., in most of the relevant reconstruction tasks from lattice QCD, the problem can be formulated in terms of a positive definite spectral function, which significantly limits the function space of potential solutions. Methods that are unable to exploit this prior information, such as the Backus-Gilbert method have therefore been shown to perform poorly relative to the Bayesian approaches, when it comes to the reconstruction of well-defined spectral features (see e.g., [53]).

In the following let us focus on two prominent Bayesian methods, which have been deployed in the reconstruction of positive spectral functions from lattice QCD, the Maximum Entropy Method (MEM) and the Bayesian Reconstruction (BR) method.

The MEM [47–49, 98] has originally been constructed to attack image reconstruction problems in astronomy. It therefore focuses on two-dimensional input data and deploys the Shannon-Jaynes entropy S_{SJ} as regulator:

$$P[\rho|I] \propto \exp\left[\sum_{l=1}^{N_\mu} \alpha_l \, \Delta\mu \left(\rho_l - m_l - \rho_l \log\left[\frac{\rho_l}{m_l}\right]\right)\right]. \tag{15}$$

Its regulator is based on four axioms [49], which specify the prior information the method exploits. They are subset independence, which states that prior information on ρ_l's at different discrete frequency bins l can be combined in a linear fashion within S_{SJ}. The second axiom enforces that S_{SJ} has its maximum at the default model, which establishes the meaning of m_l as the apriori most probable value of ρ_l in the absence of data. These two axioms are not specific to the MEM and find use in different Bayesian methods. It is the third and fourth axiom that distinguish the MEM from other approaches: coordinate invariance requires that ρ itself should transform as a dimensionless probability distribution. To be more concrete, as MEM was constructed with image reconstruction in mind, this axiom requires that the reconstructed image (in our case the spectral function) should be invariant under a common coordinate transformation of the two-dimensional input data and the prior. The last axiom is system independence and requires that in a two-dimensional reconstructed image no additional correlations between the two dimensions of the image are introduced, beyond those that are already contained in the data (for more details see Ref. [99]).

From the appearance of the logarithm in S_{SJ} it is clear that the MEM can exploit the positivity of the spectral function. Due to the fact that the logarithm is multiplied by ρ, S_{SJ} is actually able to accommodate exact zero values of a spectral function. Since the reconstruction task in lattice QCD is one-dimensional, it is not obvious how to directly translate system independence. An intuitive way of interpreting this axiom using e.g. the kangaroos example of Ref. [48] is that the MEM shall not introduce correlations among ρ_l's where the data does not require it. This is a quite restrictive property, as it is exactly prior information, which should help us to limit the potential solutions space by providing as much information about the structure of ρ as possible. Similarly, the assumption that ρ must transform as a probability distribution, while appropriate for a distribution of dimensionless pixel values in an image, does not necessarily apply to spectral functions. These are in general dimensionful quantities and may even contain UV divergences when evaluated naively.

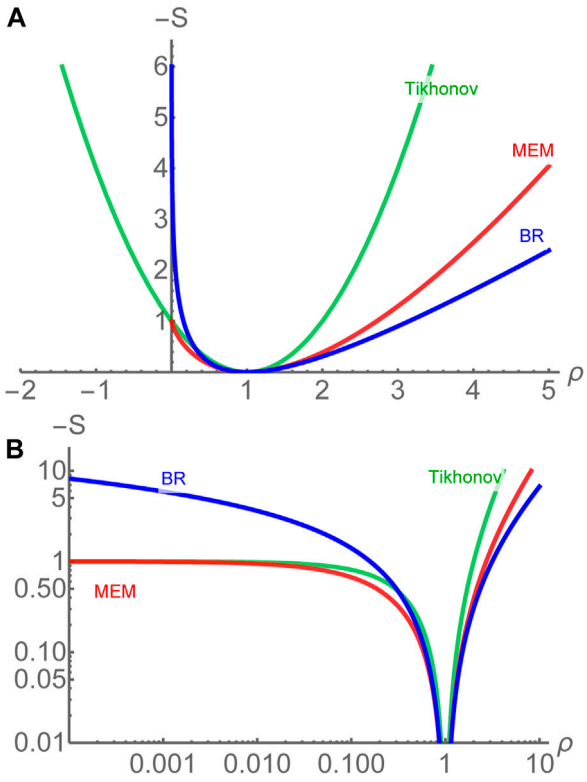

FIGURE 2
Comparison of the regulators of the Tikhonov approach (green), the MEM (red) and the BR method (blue) in linear scale **(A)** and double logarithmic scale **(B)** for the choice of $m = 1$. The Shannon-Jaynes regulator accommodates $\rho = 0$ but appears flat for spectral functions with values close to zero. The BR prior shows the weakest curvature for $\rho > m$ among all regulators.

To overcome these conceptual difficulties the BR method was developed in Ref. [100] with the one-dimensional reconstruction problem of lattice QCD real-time dynamics in mind. The BR method features a regulator S_{BR} related to the Gamma distribution

$$\begin{aligned} P[\rho|I] &= \prod_{l=1}^{N_\mu} \mathrm{Gamma}\left[1 + \Delta\mu\alpha_l, \Delta\mu\alpha_l/m_l\right], \\ &\propto \exp\left[\sum_{l=1}^{N_\mu} \alpha_l \, \Delta\mu \left(1 - \frac{\rho_l}{m_l} + \log\left[\frac{\rho_l}{m_l}\right]\right)\right], \end{aligned} \tag{16}$$

which looks similar to the Shannon-Jaynes entropy but differs in crucial ways. Its construction shares the first two axioms of the MEM but replaces the third and fourth axiom with the following: scale invariance enforces that the posterior may not depend on the units of the spectral function, leading to only ratios between ρ_l and the default model m_l, which by definition must share the same units. The use of ratios also requires that neither ρ nor m vanishes. S_{BR} differs therefore from the Shannon-Jaynes regulator where the integrand of S_{SJ} is dimensionful. The units of $\Delta\mu$ enter as multiplicative scale and can be absorbed

into a redefinition of α (and which will be marginalized over as described in Section 3.3). Furthermore, one introduces a smoothness axiom, which requires the spectral function to be twice differentiable. While it may appear that the latter axiom is at odds with the potential presence of delta-function like structures in spectral functions, it ensures that one smoothly approximates such well defined peaks as the input data improves.

Let us compare the regulators of the Tikhonov approach, the MEM and the BR method in Figure 2, which plots the negative of the integrand for the choice of $m = 1$. The top panel shows a linear plot, the bottom panel a double logarithmic plot. By construction, all feature an extremum at $\rho = m$.

The functional form of the BR regulator turns out to be the one with the weakest curvature among all three for $\rho > m$, while it still manages to regularize the inverse problem. Note that the weaker the regulator, the more efficiently it allows information in the data to manifest itself (it is actually the weakest on the market). At the same time a weaker regulator is less potent in suppressing artifacts, such as ringing, which may affect spectral function reconstruction based on very small number of datapoints.[2]

Note that the BR regulator requires ρ to be positive definite, whereas the MEM accommodates spectral functions and default models that vanish identically over a range of frequencies. In hadronic spectra, e.g., it is known that the spectral function can vanish in regions below threshold. While in the MEM this fact can be incorporated naturally, in the BR method a small but finite value must be supplied in the default model everywhere. In practice this is most often not a problem, since it is below threshold where the non-perturbative bound state structures lie that one wishes to reconstruct. Hence reliable prior information is in general not available and one chooses an uninformative finite, i.e. constant default model there.

Having focused primarily on positive spectral functions so far, let us briefly discuss some of the Bayesian approaches used in the literature to study non-positive spectral functions. This task may arise in the context of hadron spectral functions if correlators with different source and sink operators are investigated (see e.g., Discussion in [101]) or if the underlying lattice simulation deploys a Szymanzik improved action (see e.g., [102]). The quasiparticle spectral functions of quarks and gluons are known to exhibit positivity violation, their study from lattice QCD therefore apriori requires methods that can accommodate spectral functions with both positive and negative values. We already saw that the Tikhonov approach with Gaussian prior does not place restrictions on the values of the spectral function and has therefore been deployed in the study of gluon spectral functions in the past [81, 83]. After the development of the MEM, Hobson and Lasenby [103] extended the method by decomposing general spectral functions into a positive (semi-)definite and negative (semi-)definite part. To each of these a Shannon-Jaynes prior is assigned. The third approach on the market is an extension of the BR method [104], which relaxes the scale invariance axiom and proposes a regulator that is symmetric around $\rho = m$. This method has been deployed in the study of gluon spectral functions [82] and in the extraction of parton distribution functions [45].

An alternative that is independent of the underlying Bayesian approach (see e.g., [105]) is to add to the input data that of a known, large and positive mock-spectral function, which will compensate for any negative values in the original spectral function. After using a Bayesian method for the reconstruction of positive ρs from the modified data, one can subtract from the result the known mock spectral function. In practice this strategy is found to require very high quality input data to succeed.

The challenge one faces in the reconstruction of non-positive spectral functions is that the inversion task becomes significantly more ill-posed in the sense of non-uniqueness. Positivity is a powerful constraint that limits admissible functions that are able to reproduce the input data. In its absence, many of the functions associated with small and even vanishing singular values of the kernel K can contaminate the reconstruction. Often these spurious functions exhibit oscillatory behavior which interferes with the identification of genuine physical peak structures encoded in the data (see also discussion in [91]).

Having surveyed different regulator choices, we are ready to carry out the Bayesian spectral reconstruction. I.e. after choosing according to one's domain knowledge a prior distribution $P[\rho|I(m, \alpha)]$ and assigning appropriate uncertainty intervals to their hyperparameters $P[\alpha]$ and $P[m]$ *via* mock-data studies, we can proceed to evaluate the posterior distribution $P[\rho|D, I]$. If we can access this highly dimensional object through a Monte-Carlo simulation (see e.g., Section 4.3) it provides us not only with the information of what the most probable spectral function is, given our simulation data, but also contains the complete uncertainty budget, including both statistical (data related) and systematic errors (hyperparameter related). The maximum of the prior defines the most probable value for each ρ_l and its spread allows a robust uncertainty quantification beyond a simple Gaussian approximation (i.e., standard deviation) as it may contain tails that lead to a deviation of the mean from the most probable value.

3.3 Uncertainty quantification for point estimates

While access to the posterior allows for a comprehensive uncertainty analysis, a full evaluation of $P[\rho|D, I]$ historically remained computationally prohibitive. Thus the community focused predominantly[3] on determining a point estimate of

2 To avoid this complication, the BR regulator has been successfully combined with the arc-length penalty regulator in Ref. [67].

3 A few works have explored stochastic strategies for the evaluation of the posterior in the context of the SOM [106] or the stochastic analytic continuation (SAI) method [107, 108], of which the MEM is a special limit [109].

the most probable spectral function from the posterior $P[\rho|D, I]$, also called MAP, the maximum aposteriori estimate

$$\frac{\delta}{\delta\rho} P[\rho|D,I]\Big|_{\rho=\rho^{\mathrm{MAP}}} = 0 \qquad \text{OR} \qquad \frac{\delta}{\delta\rho} \mathcal{Q}[\rho|D,I]\Big|_{\rho=\rho^{\mathrm{MAP}}} = 0, \tag{17}$$

where in practice often the logarithm of the posterior is used in the actual optimization $\mathcal{Q} = \log[P[\rho|D, I]]$.

While estimating the MAP, i.e., carrying out a numerical optimization, is much simpler than sampling the full posterior, only a fraction of the information contained in $P[\rho|D, I]$ is made accessible. In particular most information related to uncertainty remains unknown and thus needs to be approximated separately.

The above optimization problem in general can be very demanding as the posterior may contain local extrema in addition to the global one that defines ρ^{MAP} (see sketch in Figure 3). At least in the case of the Tikhonov, MEM and BR method it is possible to prove that if an extremum for Eq. 17 exists it must be unique. The reason is that all three regulators are convex. The proof of this statement does not rely on a specific parametrization of the spectral function and therefore promises that standard (quasi) Newton methods, such as Levenberg-Marquardt or LBFGS (see e.g., Ref. [110]) can be used to locate this unique global extremum in the N_μ dimensional search space.

Also from an information point of view it is fathomable that at this point a unique solution to the former ill-posed inverse problem can be found. We need to estimate the most probable values of N_μ parameters ρ_l and have now provided N_τ simulation data D_i, as well as N_μ pieces of information in the form of the m_l's and α_l's each. I.e., the number of knowns $2N_\mu+N_\tau > N_\mu$ is larger than the number of unknowns, making a unique determination possible. The proof presented in Ref. [47] formalizes this intuitive statement.

In practice it turns out that the finite intercept of the Shannon-Jaynes entropy for $\rho = 0$ can lead to slow convergence if spectral functions with wide ranges of values close to zero are reconstructed. In lattice QCD this occurs regularly when e.g. hadronic spectral functions contain sharp and well separated peak structures. S_{SJ} for very small values (see Figure 2) is effectively flat and thus unable to efficiently guide the optimizer toward the unique minimum and convergence slows down.

It is therefore that one finds in the literature that the extremum Eq. 17 in the MEM is accepted for tolerances around $\Delta \approx 10^{-7}$, which is much larger than zero in machine (double-)precision. Such a large tolerance does not guarantee bitwise identical results when starting the optimization from different initial conditions. Note that the definition of Δ varies in the literature and we here define it *via* the relative step size in the minimization of the optimization functional $\mathcal{Q}$.

The BR prior on the other hand does not exhibit a finite intercept at $\rho = 0$ and therefore avoids this slow convergence problem. It has been found to be capable of locating the unique extremum ρ^{MAP} in real-world settings down to machine precision, which guarantees that the reconstruction result is independent of the starting point of the optimizer.

Bayesian inference, through the dependencies of the posterior $P[\rho|D, I]$, forces us to acknowledge that the result of the reconstruction is affected by two sources of uncertainty: statistical uncertainty in the data and systematic uncertainty associated with the choice and parameters of the prior probability.

Before continuing to the technical details of how to estimate uncertainty, let us focus on the role of prior information first. It enters both through the selection of a prior probability and the choice of the distributions $P[m]$ and $P[\alpha]$. It is important to recognize that already from an information theory viewpoint, one needs to supply prior information if the goal is to give meaning to an ill-posed inverse problem: originally we started out to estimate $N_\mu \gg N_\tau$ parameters ρ_l from N_τ noisy input data D_i.

I.e., in order to select among the infinitely many degenerate parameter sets ρ_l a single one as the most probable, we need information beyond the likelihood. Conversely any method that offers a unique answer to the inverse problem utilizes some form of prior information, whether it acknowledges it or not. Bayesian inference, by making the role of prior knowledge explicit in Bayes theorem, allows us to straight forwardly explore the dependence of the result on our choices related to domain information. It is therefore ideally suited to assess the influence of prior knowledge on reconstructed spectral functions. This distinguishes it from other approaches, such as the Backus Gilbert method, where a similarly clear distinction of likelihood and prior is absent. The Tikhonov method is another example. Originally formulated with a vanishing default model, one can find statements in the literature that it is default model independent. Reformulated in the Bayesian language, we however understand that its original formulation just referred to one specific choice of model, which made the presence of prior knowledge hard to spot.

The presence of the prior as regulator also entails that among the structures in a reconstructed spectral function only some are constrained by the simulation data and others are solely constrained by prior information. It is only in the Bayesian continuum limit, which refers to taking simultaneously the error on the input data to zero while increasing the number of available datapoints toward infinity, that the whole of the spectral function is fixed by input data alone. Our choice of regulator determines how efficiently we converge to this limit and which type of artifacts (e.g., ringing or over-damping) one will encounter on the way. One important element of uncertainty analysis in Bayesian spectral reconstruction therefore amounts to exploring how reconstructed spectra improve as the data improves.[4] This is a well-established practice in the community.

4 In lattice QCD it is often easier to collect more samples than to simulate on grids with more points along Euclidean time. Then at least the improvement of the reconstruction with increasing statistics needs to be considered.

When reconstructing the spectral function according to a given set of Monte–Carlo estimates D_i^k of a lattice QCD correlator D_i, we need to reliably estimate the statistical and systematic uncertainty budget. It is important to recognize that these may be related, e.g., increasing the precision of input data often makes the reconstructed spectrum less susceptible to changes in m or α. An often deployed strategy is to nevertheless estimate the effects separately: In order to assess statistical uncertainty we may use established bootstrap methods or the (blocked) Jackknife (see Ref. [90]), where the reconstruction is performed repeatedly on subensembles of the input data D_i^k and the variance among the reconstructed spectra provides a direct estimate of their statistical uncertainty.

In the case of point estimates, one usually decides apriori on a regulator and fixes to a certain value of the default model m and of the hyperparameter α, before carrying out the reconstruction. The freedom in all these choices enters the systematic uncertainty budget.

Often the user has access to a reliable default model $m(\omega)$ only along a limited range of frequencies μ. In lattice QCD such information is often obtained from perturbative computations describing the large frequency and momentum behavior of the spectral function (see e.g. [111–114]). When considering continuum perturbative results as default model one must account for the finite lattice spacing by introducing a cutoff by hand. In addition the different (re-)normalization schemes in perturbation theory and on the lattice often require an appropriate rescaling. Subsequently, perturbative default models can reproduce input datapoints dominated by the spectrum at large frequencies (e.g., small Euclidean times). One additional practical challenge lies in the functional form of spectral functions obtained from (lattice) perturbation theory, since they may exhibit kink structures. If supplied as default model, as is, such structures may induce ringing artifacts in the reconstructed result. In practice one therefore smooths out kink structures when constructing $m(\omega)$.

In the low frequency part of the spectrum, where non-perturbative physics dominates, we often do not possess relevant information about the functional form of ρ. It is then customary to extend the default model into the non-perturbative regime using simple and smooth functional forms that join up in the perturbative regime.

In practice the user repeats the reconstruction using different choices for the unknown parts of m, e.g., different polynomial dependencies on the frequency and subsequently uses the variation in the end result as indicator of the systematic uncertainty. It is important to note that if there exist different regulators that encode compatible and complementary prior information that one should also consider repeating the reconstruction based on different choices of $P[\rho|I]$ itself.

Since we have access to the likelihood and prior, we may ask whether a combined estimation of the statistical and systematic uncertainty can be carried out even in the case of a point estimate. Since the reconstructed spectrum ρ^{MAP} denotes a minimum of the posterior, one may try to compute the curvature of the (log) posterior $L-S$ around that minimum, which would indicate how steep or shallow that minimum actually is. This is the strategy laid out e.g., in Ref. [47]. In practice it relies on a saddle point approximation of the posterior and therefore can lead to an underestimation of the uncertainty. Many recent studies thus deploy a combination of the Jackknife and a manual variation of the default model.

Since the treatment of hyperparameters differs among the various Bayesian methods, let me discuss it here in more detail. Appropriate ranges for the values of m can often be estimated from mock data studies and since the functional dependence of the default model is varied as part of the uncertainty estimation discussed above, we focus here on the treatment of α. I.e., we will treat the values of m as fixed and consider the effect of $P[\alpha]$. If alpha is taken to be small, a large uncertainty in the value m ensues, which leads to a weak regularization and therefore to large uncertainty in the posterior. If α is large it constrains the posterior to be close to the prior and limits the information that data can provide to the posterior.

Three popular strategies are found in the literature to treat α. Note that in the context of the MEM, a common value is assigned to all hyperparameters α_l, i.e., the same uncertainty is assigned to the default model parameters m_l at all frequencies, an *ad hoc* choice.

The simplest treatment of α, also referred to as the Morozov criterion or historic MEM is motivated by the goal to avoid over fitting of the input data. It argues that if we knew the correct spectral function and were to compute the corresponding likelihood function L, it would on average evaluate to $\langle L\rangle = \frac{1}{2}N_\tau$ i.e. half the number of datapoints. Therefore one should tune the value of α such that the likelihood reproduces this value.

The second and third strategy are based directly on Bayes theorem. The Bayesian way of handling uncertainties in model parameters is to make their dependence explicit in the joint probability distribution $P[\rho,\ D,\ I(m,\ \alpha)]$. Now that the distribution depends on more than three elements, application of conditional probabilities leads to

$$\begin{aligned} P[\rho, D, \alpha, m] &= P[D|\rho, \alpha, m]P[\rho|\alpha, m]P[\alpha, m], \\ &= P[\alpha|\rho, D, m]P[\rho|D, m]P[D, m]. \end{aligned} \tag{18}$$

The modern MEM approach solves Eq. 18 for $P[\alpha|\rho, D, m]$. It then integrates point estimates $\rho_\alpha^{\mathrm{MAP}}$ obtained for fixed values of α over that probability distribution. In order to compute $P[\alpha|\rho, D, m]$ two ingredients are necessary: the full posterior $P[\rho|D, \alpha, m]$ and the distribution $P[\alpha]$. The former is in general not analytically known and therefore is in practice approximated by a saddle point approximation. The latter is in the literature either chosen as constant or as $P[\alpha] \propto 1/\alpha$, a choice referred to as Jeffrey's prior.

Let me briefly clarify the often opaque notion of Jeffrey's prior [115]. Given a probability distribution $P[x|\boldsymbol{\alpha}, \mathbf{m}]$ and a choice of parameter, e.g., $\boldsymbol{\alpha}$, Jeffrey's prior refers to the unique distribution $P_J[\boldsymbol{\alpha}] = \sqrt{\det[I(\boldsymbol{\alpha})]}$ defined from the

Fisher information matrix $I(\boldsymbol{\alpha})$. This definition is considered to be uninformative, as it remains invariant under a change of coordinates of $\boldsymbol{\alpha}$. Using the one-dimensional Gaussian distribution as example, we can obtain an intuitive understanding of its role. Let $P[x|\sigma, m] = \mathcal{N}[x|\sigma, m]$, then

$$P_J[m] = \sqrt{\int dx \mathcal{N}[x|\sigma,m]\left(\frac{d}{dm}\mathcal{N}[x|\sigma,m]\right)^2} = \sqrt{\frac{1}{\sigma^2}} = \text{const.}, \tag{19}$$

$$P_J[\sigma] = \sqrt{\int dx \mathcal{N}[x|\sigma,m]\left(\frac{d}{d\sigma}\mathcal{N}[x|\sigma,m]\right)^2} = \sqrt{\frac{2}{\sigma^2}} = \sqrt{2}\ \frac{1}{\sigma}. \tag{20}$$

Jeffrey's prior for m is independent of m and thus refer to the unique translation invariant distribution on the real values (Haar-measure for addition). It therefore does not impart any information on the location of the peak of the normal distribution. Similarly $P_J[\sigma]$ is a scale invariant distribution on the positive real values (Haar-measure for multiplication). Since the uncertainty parameter σ enters as a multiplicative scale in the normal distribution its Jeffrey's prior also does not introduce any additional information. Both priors investigated here are improper distributions, i.e., they are well-defined only in products with proper probability distributions.

The third strategy to treat the parameters α_l has been put forward in the context of the BR method. It sets out to overcome the two main limitations of the MEM approach: the need for saddle point approximations in the handling of α and the overly restrictive treatment of assigning a common uncertainty to all m_l's. The BR method succeeds in doing so, by using Bayes theorem to marginalize the parameters α_l apriori, making the (highly conservative) assumption that no information about α_l is known, i.e., $P[\alpha_l] = 1$. It benefits from the fact that in contrast to the Shannon-Jaynes prior, the BR-prior is analytically tractable and its normalization can be expressed in closed form.

We start from Eq. 18 and assume that the parameters α and m are independent, so that their distributions factorize. Marginalizing a parameter simply means integrating the posterior over the probability distribution of that parameter. Via application of conditional probabilities it is possible to arrive at the corresponding expression

$$\begin{aligned}\prod_l \int d\alpha_l P[\alpha|\rho,D,m]P[\rho|D,m] &= \frac{P[D|\rho,I]}{P[D|m]P[m]} \\ &\prod_l \int d\alpha_l P[\rho|\alpha,m]P[\alpha]P[m], \\ P[\rho|D,m] &= \frac{P[D|\rho,I]}{P[D|m]} \\ &\prod_l \int d\alpha_l P[\rho|\alpha,m]P[\alpha],\end{aligned} \tag{21}$$

where $P[\rho|D, m]$ does not depend on α anymore and by definition of probabilities $\int d\alpha P[\alpha|\rho, D, m] = 1$. The posterior $P[\rho|D, m]$ now includes all effects arising from the uncertainty of α without referring to that variable anymore. Due to the form of the BR prior $P[\rho|\alpha, m]$, the integral over α_l is well defined, even though we used the improper distribution $P[\alpha] = 1$. One may wonder whether integrating over α_l impacts the convexity of the prior. While not proven rigorously, in practice it turns out that the optimization of the marginalized posterior $P[\rho|D, m]$ in the BR method does not suffer from local extrema.

A user of the BR method therefore only needs to provide a set of values for the default model m_l to compute the most probable spectral function

$$\frac{\delta}{\delta\rho}P[\rho|D,m]\Big|_{\rho=\rho_{\text{BR}}^{\text{MAP}}} = 0. \tag{22}$$

By carrying out several reconstructions and varying the functional form of m within reasonable bounds, established by mock-data tests, the residual dependence on the default model can be quantified.

So far we have discussed the inherent uncertainties from the use of Bayesian inference and how to assess them. Another source of uncertainty in spectral reconstructions arises from specific implementation choices. Let me give an example based on the Maximum Entropy Method. In order to save computational cost, the MEM historically is combined with a singular value decomposition to limit the dimensionality of the solution space. The argument by Bryan [116] suggests that instead of having to locate the unique extremum of $P[\rho|D, I]$ in the full N_μ dimensional search space of parameters ρ_l, it is sufficient to use a certain parametrization of $\rho(\mu)$ in terms of N_τ parameters, the number of input data points. The basis functions are obtained from a singular value decomposition (SVD) of the transpose of the kernel matrix K^t. Bryan's argument only refers to the functional form of the Kernel K and the number of data points N_τ in specifying the parametrization of $\rho(\mu)$. If true in general, this would lead to an enormous reduction in computational complexity. However, I have put forward a counter example to Bryan's argument (originally in [117]) including numerical evidence, which shows that in general the extremum of the prior is not part of Bryan's reduced search space.

One manifestation of the artificial limitation of Bryan's search space is a dependence of the MEM resolution on the position of a spectral feature along the frequency axis. As shown in Figure 3 of Ref. [118], if one reconstructs a single delta peak located at different positions μ_0 with the MEM, one finds that the reconstructed spectral functions show a different width, depending on the value of μ_0. This can be understood by inspecting the SVD basis functions, which are highly oscillatory close to μ_{min} the smallest frequency chosen to discretize the μ range. At larger values of μ these functions however

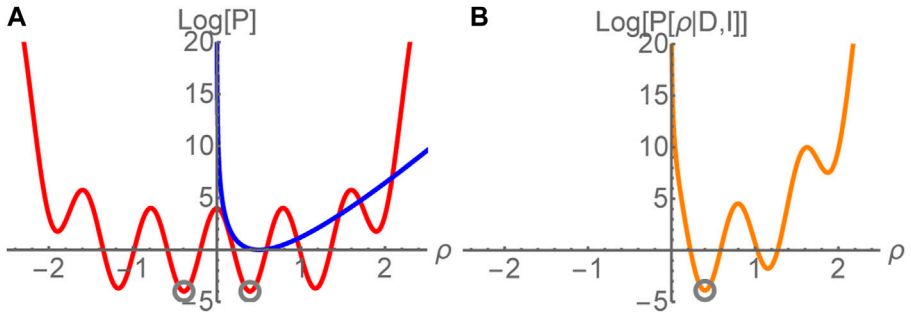

FIGURE 3
Sketch of how the confluence of **(A)** likelihood (red) and (a convex) prior (blue) in the posterior [orange, **(B)**] leads to a regularization of the inverse problem. Instead of multiple degenerate minima in the likelihood (gray circles) only a single unique one remains in the posterior.

damp towards zero. I.e. if the relevant spectral feature is located in the μ range where the basis functions have structure, it is possible to reconstruct a sharp peak reasonable well, while if it is located at larger μ the resolution of the MEM decreases rapidly. The true Bayesian ρ^{MAP}, i.e. the global extremum of the MEM posterior, however does not exhibit such a resolution restriction, as one can see when changing the parametrization of the spectral function to a different basis, e.g., the Fourier basis consisting of cos and sin functions. In addition Ref. [57] in its Figure 28 showed that using a different parametrization of the spectral function, which restricts ρ to a space that is equivalent to the SVD subspace from a linear algebra point of view, one obtains a different result. This, too, emphasizes that the unique global extremum of the posterior is not accessible within these restricted search spaces. Note that one possible explanation for the occurrence of the extremum of $P[\rho|D, I]$ outside of the SVD space lies the fact that in constrained optimization problems (here the constraint is positivity), the extremum can either be given by the stationarity condition of the optimization functional in the interior of the search space or it can lie on the boundary of the search space restricted by the constraint.

I.e., in addition to artifacts introduced into the reconstructed spectrum *via* a particular choice of prior distribution and handling of its hyperparameters (e.g., ringing or over-damping), one also must be aware of additional artifacts arising from choices in the implementation of each method.

The dependence of Bryan's MEM on the limited search space was among the central reasons for the development of the BR method. The advantageous form of the BR prior, which does not suffer from slow convergence in finding ρ^{MAP} in practice, allows one to carry out the needed optimization in the full N_μ dimensional solution space to $P[\rho|D, I]$ with reasonable computational cost. The proof from Ref. [47] which also applies to the convex BR prior, guarantees that in the full search space a single unique Bayesian solution can be located if it exists.

In Section 4 we will take a look at hands-on examples of using the BR method to extract spectral functions and estimating their reliability.

3.4 Two lattice QCD uncertainty challenges

Spectral function reconstruction studies from lattice QCD have encountered two major challenges in the past.

The first one is related to the number of available input data points, which, compared to simulations in e.g. condensed matter physics is relatively small, of the order $O(10-100)$. Especially when analyzing datasets at the lower end of this range, the sparsity of the D_i's along Euclidean time τ often translates into ringing artifacts. Due to the restricted search space of Bryan's MEM, this phenomenon may be hidden, while the global extremum of the MEM posterior $\rho^{\mathrm{MAP}}_{\mathrm{MEM}}$, as well as the BR method MAP estimate $\rho^{\mathrm{MAP}}_{\mathrm{BR}}$ do show ringing. Since ringing leads to spectral functions with a too large arc length compared to the true spectral function one can treat this artifact by combining either the MEM or the BR prior with the arc-length penalty regulator discussed in Section 3.2. The additional hyperparameters associated with this penalty term can be estimated using realistic mock data, as shown e.g., in Ref. [67]. The benefit of this genuine Bayesian approach is that the mechanism by which ringing is suppressed is made explicit and is not hidden in a particular choice of basis function.

The second challenge affects predominantly spectral reconstructions at finite temperature, in particular their comparability at different temperatures. In lattice QCD, temperature is encoded in the length of the imaginary time axis. I.e., simulations at lower temperature have access to a larger τ regime, as those at higher temperature. Since the

available Euclidean time range affects the resolution capabilities of any spectral reconstruction it is important to calibrate one's results to a common baseline. I.e., one needs to establish how the accuracy of the reconstruction method changes as one increases temperature. Otherwise changes in the reconstructed spectral functions are attributed to physics, while they actually represent simply a degradation of the method's resolution. The concept of the reconstructed correlator [55] is an important tool in this regard. Assume we have a correlator encoding a certain spectral function at temperature T_1 with N_τ^{T1} points. We can now ask: how would the correlator look like where the same spectral function is encoded at a higher temperature T_2, i.e., within a smaller Euclidean time window of N_τ^{T2} points. Since the underlying kernel relating spectral function and correlator is often temperature dependent, this question is not easily answered by just discarding imaginary time datapoints from the large τ region of the original correlator.[5] Instead if one wishes to evaluate the corresponding higher temperature correlator Ref. [60] showed that for the bosonic finite temperature kernel $K^{T>0}(\mu,\ \tau) = \cosh[\mu(\tau-\beta/2)]/\sinh[\mu\beta/2]$, relevant for studies of relativistic bosonic spectral functions, one has to form the following quantity

$$D_{\mathrm{rec}}(\tau, T_2|T_1) = \sum_{\tau'/a=\tau/a,\Delta\tau'/a=N_\tau^{T1}}^{N_\tau^{T1}-N_\tau^{T2}+\tau/a} D_{\mathrm{lattice}}(\tau'|T_1). \qquad (23)$$

By carrying out a reconstruction based on two correlators at different Euclidean extent $D_{\mathrm{lattice}}(\tau|T_1)$ and $D_{\mathrm{lattice}}(\tau|T_2)$ one will in general obtain two different spectral functions. Only when one compares the reconstruction based on $D_{\mathrm{rec}}(\tau, T_2|T_1)$ with that of $D_{\mathrm{lattice}}(\tau|T_2)$ is it possible to disentangle the genuine effects of a change in temperature from the one's induced by the reduction in access to Euclidean time. This reconstruction strategy has been first deployed for relativistic correlators in Ref. [66]. A similar analysis in the context of non-relativistic spectral functions in Ref. [67] showed that the temperature effect of a negative mass shift for in-medium hadrons was only observable, if the changes in resolution of the reconstruction had been taken into account.

4 Hands-on spectral reconstruction with the BR method

This publication is accompanied by two open-source codes. The first [119], written in the C/C++ language, implements the BR method (and the MEM) in its traditional form to compute MAP estimates with arbitrary precision arithmetic. The second [120], written in the Python language uses standard double precision arithmetic and utilizes the modern MCStan Monte-Carlo sampler to evaluate the full BR posterior.

4.1 BR MAP implementation in C/C++

The BR MAP code deploys arbitrary precision arithmetics, based on the GMP [121] and MPFR [122] libraries, which offers numerical stability for systems where exponential kernels are evaluated over large frequency ranges. A run-script called BAYES.scr is provided in which all parameters of the code can be specified.

The kernel for a reconstruction task is apriori known and depends on the system in question. The BR MAP code implements three common types encountered in the context of lattice QCD (see parameter KERNELTYPE). Both zero temperature kernel $K^{T=0}(\mu,\ \tau) = \exp[-\mu\tau]$, and the naive finite temperature kernel for bosonic correlators $K^{T>0}(\mu,\ \tau) = \cosh[\mu(\tau-\beta/2)]/\sinh[\mu\beta/2]$ are available. Here β refers to the extend of the imaginary time axis. The third option is the regularized finite temperature kernel $K^{T>0}_{\mathrm{reg}}(\mu,\tau) = \frac{\beta}{2\pi}\mathrm{atan}[\mu]K^{T>0}(\mu,\tau)$ suggested in Ref. [60] (see also [72, 123]). It lifts the divergence of the kernel at $\mu = 0$, which is related to the antisymmetry of bosonic spectral functions at $T > 0$. Note that when redefining the kernel, one also redefines the spectral function to reconstruct and thus an appropriately modified default model must be supplied.

Next, the discretization of the frequency interval μ needs to be decided on (see parameters WMIN and WMAX). When relativistic lattice QCD correlators are investigated, the lattice cutoff $\pm\sqrt{3}\ \frac{\pi}{a}$ provides a reliable estimate up to where spectral structures will be present. It is often a good crosscheck to use a larger range of frequencies beyond where the input data can provide constraining information, in order to see that the reconstructed spectral function in that regime is correctly given by the supplied default model. In case that lattice effective field theory correlators are investigated, the user has to keep in mind that their spectra may be populated beyond the naive lattice cutoff. In some cases the appropriate range can be estimated from an inspection of semi-analytically tractable free theory spectral functions. A rough guess for the UV cutoff can be obtained by fitting an exponential to the first few correlator points at small imaginary time τ. Depending on the resolution required for the encoded spectral features, the number of frequency bins N_μ can be chosen *via* NOMEGA. If a very sharp peak feature is present, one can use the parameters HPSTART, HPEND and HPNUM to define a high resolution window along μ for which HPNUM of the NOMEGA points are used.

The number of points along the Euclidean time axis of the lattice simulation is specified by NT and its extend noted by BETA. Depending on the form of the kernel and the choices for β

5 In cases where the kernel is temperature independent, e.g., for lattice effective field theory correlators, discarding large τ datapoints is equivalent to computing the reconstructed kernel.

and $\mu_{\max}$ the dynamic range of the kernel matrix may be large and one has to choose an appropriate precision NUMPREC for the arithmetic operations used.

For the analysis of lattice QCD correlators FILEFORMAT 4 is most useful. Each of the total NUMCONF measurements of a correlator is expected to be placed in individual files with a common name DATANAME (incl. directory information) and a counter as extension, which counts upward from FOFFSET. The format of each file is expected to contain two columns in ASCII format, the first denoting the Euclidean time step as integer and the second one the real-valued Euclidean correlator. Via TMIN and TMAX the user can specify which are the smallest and largest Euclidean times provided in each input data file, while TUSEMIN and TUSEMAX define which of these datapoints are used for the reconstruction.

In order to robustly estimate the statistical uncertainty of the input data, the code is able to perform an analysis of the autocorrelation among the different measurements. The value of ACTHRESH is used to decide to which threshold the normalized autocorrelation function [36] must have decayed, for us to consider subsequent measurements as uncorrelated. To test the quality of the estimated errors one can manually enlarge or shrink the assigned error values using the parameter ERRADAPTION.

As discussed in the previous section, a robust estimate of the statistical uncertainty of the spectral reconstruction can be obtained from a Jackknife analysis. The code implements this type of error estimate when the number of Jackknife blocks are set to a value larger than two in JACKNUM. The NUMCONF measurements are divided into consecutive blocks and in each iteration of the Jackknife a single block is remove when computing the mean of the correlator. If JACKNUM is set to zero a single reconstruction based on the full available statistics is carried out.

Once the data is specified, we have to select the default model. The default model can either be chosen to take on a simple functional form choosing values 1 or 2 for PRIORMODEL. The latter corresponds to a constant given by MFAC. The former leads to $m(\mu) = m_0/(\mu - \mu_{\min} + 1)^{\text{power}}$, where the power is set *via* the parameter PRIORPOWER and m_0 *via* MFAC. To supply more elaborate default models the user can set PRIORMODEL to 4 and provide a file `prior.0` in the working directory of the code that contains two columns, the first with the frequencies μ and the second with the values of m. Note that we have already marginalized over the uncertainty of the default model using $P[\alpha] = 1$ so that specifying m suffices for the BR method.

In the present implementation of the BR method (ALGORITHM value 1) the integration over α is implemented in a semi-analytic fashion, which is based on a large S expansion. In practice this simply means that one must avoid to start the minimizer from the default model for which $S = 0$.

The original Ref. [100] conservatively stated that it is advantageous with regards to avoiding overfitting to instruct the minimizer to keep the values of the likelihood close to the number of provided datapoints. The code maintains this condition within a tolerance that is specified by a combination of the less than ideal named ALPHAMIN and ANUM parameters. The reconstruction will be performed ANUM times where in each of the iterations counted internally by a variable ACNT the likelihood is constrained to fulfill $|L - N_{\text{data}}| = (1/\text{ALPHAMIN} \times 10^{\text{ACNT}})$.

The search for $\rho_{\text{BR}}^{\text{MAP}}$ is carried out internally using the LBFGS minimization algorithm [124]. It terminates when the relative step size of the minimizer falls below the threshold MINTOL. Note that for high precision arithmetic a correspondingly small threshold should be specified (e.g., for NUMPREC = 128 MINTOL = 10^{-30} or for NUMPREC = 256 MINTOL = 10^{-60}). The results of the minimizer are output into the folder RESULTNAME every 2,000 steps in files called BAYES_rhovalues_A(ANUM-ACNT).dat and the final result is found in the file spec_rec.dat. The spectra are also collected in the file PROB_ESTIMATES_FREQ.dat in column 6, where the frequencies are listed in column 4. If the Jackknife analysis is selected then this file contains multiple spectra for each Jackknife subaverage counted by the value in column 8.

To speed up the convergence in case that very high precision data is supplied (i.e. when very sharp valleys exist in the likelihood) it is advantageous to carry out the reconstruction first with artificially enlarged errorbars *via* ERRADAPTION > 1. The corresponding result in file BAYES_rhovalues_A(ANUM).dat if copied into the working directory of the code with the name `start.0` can be used as starting point for the next minimization with the actual errorbars, by selecting the value 2 for the parameter RESTARTPREV.

The code, when compiled with the preprocessor macro VERBOSITY set to value one, will give ample output about each step of the reconstruction. It will output the frequency discretization, the values for the Euclidean times used, as well as show which data from each datafile has been read-in. In addition it presents the estimated autocorrelation and the eigenvalues of the covariance matrix, before outputting each step of the minimizer to the terminal. This comprehensive output allows the user to spot potential errors during data read-in and allows easy monitoring whether the minimizer is proceeding normally. The incorrect estimation of the covariance matrix due to autocorrelations is a common issue, which can prevent the minimizer to reach the target of minimizing the likelihood down to values close to the number of input data. Enlarging the errorbars until the likelihood reaches small enough values provides a first indication of how badly the covariance matrix is affected by autocorrelations. Another diagnosis step is to only consider the diagonal entries of the covariance matrix, which can be selected using the preprocessor macro DIAGCORR set to 1.

4.2 MEM MAP implementation in C/C++

The provided C/C++ code also allows to perform the MAP estimation based on the MEM prior using arbitrary precision arithmetic. By setting the parameter ALGORITHM to value 2 one can choose Bryan's implementation, where the spectral function is parametrized *via* the SVD of the kernel matrix. The standard implementation uses as many SVD basis functions as input datapoints are provided. By varying the SVDEXT parameter the user may choose to include more or reduce the number of SVD basis function deployed. Alternatively by using the value 3 the user can deploy the Fourier basis functions introduced in Ref. [118] and for value 4 $\rho^{\mathrm{MAP}}_{\mathrm{MEM}}$ is searched for in the full N_μ dimensional search space. Due to the proof of uniqueness of the extremum, even searching in the full space is supposed to locate a single Bayesian answer $\rho^{\mathrm{MAP}}_{\mathrm{MEM}}$ to the inverse problem.

In the MEM, the common uncertainty parameter α for the default model m_l is still part of the posterior and needs to be treated explicitly. To this end the MEM reconstruction is repeated ANUM times, scanning a range of α values between ALPHAMIN and ALPHAMAX. Since apriori the appropriate range of values is not known, the user is recommended to carry out reconstructions with artificially enlarged errorbars *via* ERRADAPTION that converge quickly and which allow to scan a large range between usually $\alpha \in [0; 100]$.

The LBFGS minimizer will be used to find the point estimates $\rho^{\mathrm{MAP}}_{\alpha}$ for each fixed value of the hyperparameter and then according to Ref. [47] estimate the probability distribution $P[\alpha|D, I]$ over which a weighted average is computed. The values of α and the probabilities are output to the 4th and 6th column of the file Probabilities.dat respectively. The final result is then outputted in the file spec_rec.dat in column 4 with the frequencies located in column 3. Intermediate steps of the minimizer are output to files MEM_rhovalues_A(ACNT).dat, where ACNT refers to the step along the alpha interval. In case of a Jackknife analysis all reconstructed spectra can be found in PROB_ESTIMATES_FREQ.dat in column 6, where the frequencies are listed in column 4.

Note that due to the functional form of the Shannon-Jaynes prior the convergence for spectral functions with large regions of vanishing values is often slow, which is why in practice the tolerance for convergence is chosen by MINTOL around 10^{-7}.

Note that the estimation of the α probabilities involves the computation of eigenvalues of a product of the kernel with itself. In turn this step may require additional numerical precision *via* NUMPREC if an exponential kernel is used. If the precision is insufficient, the determination of the eigenvalues might fail and the final integrated spectral function will show NAN values, while intermediate results in MEM_rhovalues_A(ACNT).dat are well behaved. In that case rerunning the reconstruction with higher precision will remedy the issue.

4.3 Full Monte-Carlo based BR method in python

In many circumstances the MAP point estimate of spectral functions already provides relevant information to answer questions about real-time physics from lattice QCD. However, as discussed in the previous section Section 3.3, its full uncertainty budget may be challenging to estimate. It is therefore that I here discuss a modern implementation of the BR method, allowing for access to the posterior distribution *via* Monte-Carlo sampling.

The second code provided with this publication is a Python script based on the MCStan Monte-Carlo sampler library [125, 126]. It uses the same parameters for the description of frequency and imaginary time as the C/C++ code but works solely with double precision arithmetic. Since different kernels are easily re-implemented, the script contains as single example the zero temperature kernel $K^{\mathrm{T}=0}(\tau, \mu)$.

In order to sample from the posterior, we must define all the ingredients of our Bayesian model in the MCStan language. A simple model consists of three sections, data, parameters and the actual model. In data the different variables and vectors used in the evaluation of the model are specified. It contains e.g. the number of datapoints sNt and the number of frequency bins sNw. The decorrelated kernel is provided in a two-dimensional matrix datatype Kernel, while the decorrelated simulation data come in the form of a vector D. The eigenvalues of the covariance matrix enter *via* the vector Uncertainty. The values of the default model are stored in the vector DefMod. In the original BR method we would assume full ignorance of the uncertainty parameters α_l with $P[\alpha] = 1$. Such improper priors may lead to inefficient sampling in MCStan, which is why in this example script a lognormal distribution is used. It draws α values from a range considered relevant in mock data tests. The user can always check self consistently whether the sampling range of α's was chosen appropriately by interrogating the marginalized posterior for α itself, making sure that its maximum lies well within the sampling range.

After selecting how many Markov-chains to initialize *via* NChain and how many steps in Monte Carlo time to proceed *via* NSamples the Monte-Carlo sampler of MCStan is executed using the sample command. MCStan automatically adds additional steps for thermalization of the Markov chain. Depending on how well localized the histrograms for each ρ_l are, the number of samples must be adjusted. Since the BR prior is convex, initializing different chains in different regions of parameter space does not affect the outcome as long as enough samples are drawn.

We may then subsequently estimate the spectral function reconstruction from the posterior by inspecting the histograms for each parameter. Since in this case we have access to the full posterior distribution we can now answer not only what the most probable value for ρ_l is but also compute its mean and median,

giving us relevant insight about the skewness of the distribution of values.

4.4 Mock data

Both code packages contain two realistic mock-data test sets, which have been used in the past to benchmark the performance of Bayesian methods. They are based on the Euclidean Wilson loop computed in first order hard-thermal-loop perturbation theory, for which the temperature independent kernel $K(\tau, \mu) = \exp[-\tau\mu]$ is appropriate. The correlator included here corresponds to the one computed at $T = 631$ MeV in Ref. [127] and which is evaluated at $r = 0.066$ fm, as well as $r = 0.264$ fm spatial extend. The continuum correlator is discretized with 32 steps in Euclidean time. The underlying spectral functions are provided in the folder `MockSpectra` in separate files for comparison.

To stay as close to the scenario of a lattice simulation, based on the ideal correlator data, a set of 1,000 individual datafiles is generated in the folder `MockData` in which the imaginary time data is distorted with Gaussian noise. The noise strength is set to give a constant $\Delta D/D = 10^{-4}$ relative error on the mean when all samples are combined. The user is advised to skip both the first $D(0)$ and last datapoint $D(\tau_{\max})$ in the dataset, which are contaminated by unphysical artifacts related to the regularization of the Wilson loop computation.

The reader will find that this mock data provides a challenging setting for any reconstruction method, as it requires the reconstruction both of a well defined peak, as well as of a broad background structure. It therefore is well suited to test the resolution capabilities of reconstruction methods, as well as their propensity for ringing and over-damping artifacts.

For the `C/C++` implementation of the BR MAP estimation a set of example scripts are provided. The user can first execute e.g. `BAYESMOCK066_precon.scr` to carry out a preconditioning run with enlarged errorbars. In a second step one provides the outcome of the preconditioning run as file `start.0` and executes `BAYESMOCK066.scr` to locate the global extremum of the BR posterior. The outcome of these sample scripts is given for reference in Figure 4 compared to the semi-analytically computed HTL spectral functions in `SpectrumWilsonLoopHTLR066.dat`.

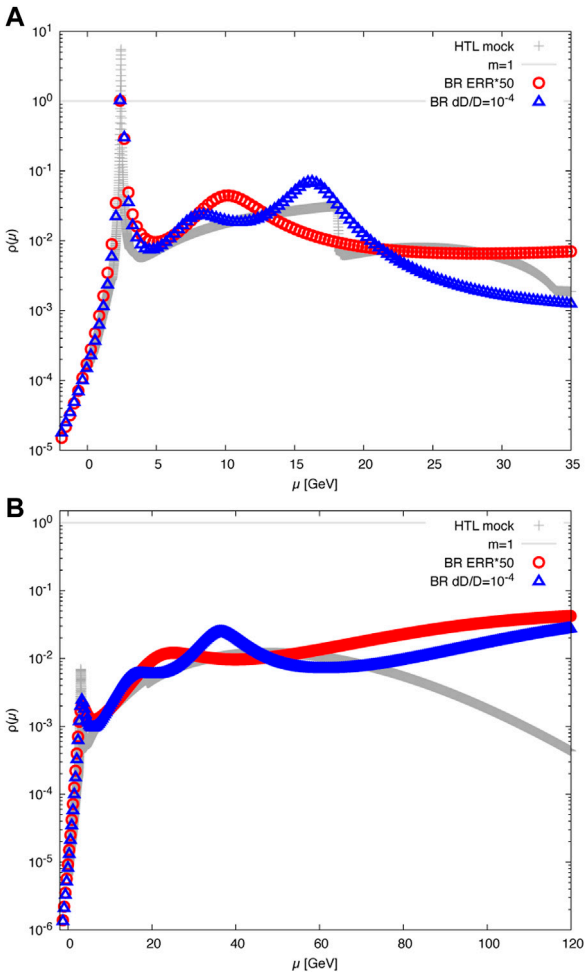

FIGURE 4
BR MAP reconstructions of the HTL Wilson loop spectral function (gray points) evaluated at $T = 631$ MeV and spatial separation distance $r = 0.066$ fm **(A)** and $r = 0.264$ fm **(B)**. The reconstruction based on $N_\tau = 32$ Euclidean data and a frequency range between $\mu a \in [-5, 25]$ with $N_\omega = 1{,}000$ are shown as colored open symbols. The red data denotes the reconstruction based on the preconditioning `ERRADAPTION` = 50 while the final result exploting the full $\Delta D/D = 10^{-4}$ is given in blue.

5 New insight from machine learning

Over the past years interest in machine learning approaches to spectral function reconstruction has increased markedly (see also [128]). Several groups have put forward pioneering studies that explore how established machine learning strategies, such as supervised kernel ridge regression [129, 130], artificial neural networks [44, 45, 131–135] or Gaussian processes [136, 137] can be used to tackle the inverse problem in the context of extracting spectral functions from Euclidean lattice correlators. The machine learning mindset has already lead to new developments in the spectral reconstruction community, by providing new impulses to regularization of the ill-posed problem.

As a first step let us take a look at how machine learning strategies incorporate the necessary prior knowledge to obtain a unique answer to the reconstruction task. While in the Bayesian approach this information enters explicitly through the prior probability and its hyperparameters, it does so in the machine-learning context in three separate ways: To train supervised reconstruction algorithms a training dataset needs to be provided, often consisting of pairs of correlators and information on the encoded spectral functions. Usually a limited

selection of relevant structures is included in this training data set, which amounts to prior knowledge on the spectrum. Both supervised and unsupervised machine learning is build around the concept of a cost- or optimization functional, which contains information on the provided data. It most often also features regulator terms, which can be of similar form as those discussed in Section 3.2. This in particular means that these regulators define the most probable values for the ρ_l's in the absence of data and therefor take on a similar role as a Bayesian default model. The third entry point for prior knowledge lies in the choice of structures used to compose the machine learning model. In case that e.g. Gaussian processes are used, the choice of kernel of the common normal distribution for observed and unobserved data is based on prior knowledge, as is the selection of its hyperparameters. In case that neural networks are used, the number and structure of the deployed layers and activation functions similarly imprint additional prior information on the reconstructed spectral function, such as e.g., their positivity.

Direct applications of machine learning approaches developed in the context of image reconstruction to positive spectral function reconstruction have shown good performance on-par with Bayesian algorithms, such as the BR method or the MEM.

Can we understand why machine learning so far has not outpaced Bayesian approaches? One potential answer lies in the information scarcity of the input correlators themselves. If there is no unused information present in the correlator also sophisticated machine learning cannot go beyond what Bayesian approaches utilize. As shown in recent mock-data tests in the context of finite temperature hadron spectral functions in Ref. [67], increasing the number of available datapoints in imaginary time (i.e., going closer to the continuum limit) does not necessarily improve the reconstruction outcome significantly. One can see what is happening, when investigating the Matsubara frequency correlator, obtained from Euclidean input data *via* Fourier transform. As one decreases the temporal lattice spacing, the range of accessible high lying Matsubara frequencies increases but their coarseness, given by the inverse temperature of the system, remains the same. Of course formally all thermal real-time information can be reconstructed from access to the exact values of the (discrete) Matsubara frequency correlator. In practice, in the presence of finite errors, one finds that the in-medium correlator only at the lowest Matsubara frequencies shows significant changes compared to the $T = 0$ correlator and agrees with it within uncertainties at higher lying Matsubara frequencies. I.e. the contribution of thermal physics diminishes rapidly at higher Matsubara frequencies, which may in practice require increasingly smaller uncertainties on the input data for successful reconstruction at higher temperatures.

This information scarcity dilemma asks us to provide our reconstruction algorithms with more QCD specific prior information. So far the Bayesian priors have focused on very generic properties, such as positivity and smoothness. It is here that machine learning can and already has provided new impulses to the community.

One promising approach is to use neural networks as parametrization of spectral functions or parton distribution functions. First introduced in the context of PDFs in Ref. [45] and recently applied to the study of finite temperature spectra in Ref. [44] this approach allows to infuse the reconstruction with additional information about the analytic properties of ρ. Traditionally one would choose a specific parametrization apriori such as rational functions (Padé) or SVD basis functions (Bryan) and vary their parameters. The more versatile NN approach, thanks to the universal approximation theorem, allows us instead to explore different types of basis functions and assign an uncertainty to each choice.

The concept of learning can also be brought to the prior probability or regulator itself. Instead of constructing a regulator based on generic axioms, one may consider it as a neural network mapping the parameters ρ_l to a single penalty value $P[\rho|I]$. Training an optimal regulator within a Bayesian setting, based e.g., on realistic mock data, promises to capture more QCD specific properties than what is currently encoded in the BR or MEM. Exploring this path is work in progress.

6 Summary and conclusion

Progress in modern high-energy nuclear physics depends on first-principle knowledge of QCD dynamics, be it in the form of transport properties of quarks and gluons at high temperatures or the phase-space distributions of partons inside nucleons at low temperatures. Lattice QCD offers non-perturbative access to these quantities but due to its formulation in imaginary time, hides them behind an ill-posed inverse problem. The inverse problem is most succinctly stated in terms of a spectral decomposition, where the Euclidean correlator accessible on the lattice is expressed as integral over a spectral function multiplied by an analytic kernel. The real-time information of interest can often be read-off directly from the structures occurring in the spectral function. The determination of PDFs from the hadronic tensor and *via* pseudo PDFs can be formulated in terms of a similar inversion problem.

Bayesian inference provides a versatile tool set for the reconstruction of spectral functions. It gives meaning to the ill-posed inverse problem by incorporating relevant domain knowledge with an associated uncertainty budget through the prior probability distribution. Evaluating the posterior distribution, defined through Bayes theorem, gives access to the most probable values of the spectral function based on simulation data and prior knowledge. In addition it also encodes the full uncertainty budget through its spread. Traditionally predominantly MAP point estimates were computed due to lower computational cost of the corresponding optimization problem, compared to full Monte-Carlo sampling of the posterior. In that case information about the uncertainty budget is hidden from the user and it must be estimated manually. Several relevant challenges for uncertainty estimation in the lattice QCD context were discussed, including the problem of ringing and those related to comparing reconstructions based on different Euclidean time extents.

A brief user guide described how to run two open access codes accompanying this publication. One focuses on the determination of MAP point estimates based on the BR and MEM prior. The other utilizes a modern Monte-Carlo library to sample from the full BR posterior.

Last but not least a brief look is taken at machine learning approaches to spectral function reconstruction. The need for providing prior information is discussed and a common challenge among all reconstruction approaches, information scarcity in the input data, is pointed out. Two venues for combining the machine-learning viewpoint with the Bayesian strategy are touched upon.

With the concrete conceptual and technical discussions contained in this publication, the reader is equipped with a solid basis to carry out Bayesian spectral reconstructions. The provided open-access source codes offer a quick entry into the research field and can be modified according to different needs in regards to kernels arising in different lattice QCD studies.

Author contributions

AR: Conception, literature study, code development, writing, and editing.

Funding

Some of the spectral function reconstruction code has been developed in the context of the project NN9578K-QCDrtX "Real-time dynamics of nuclear matter under extreme conditions" funded by UNINETT Sigma2—the National Infrastructure for High Performance Computing and Data Storage in Norway. The author gladly acknowledges support by the Research Council of Norway under the FRIPRO Young Research Talent grant 286883.

Acknowledgments

The author thanks the referees for their valuable suggestions.

Conflict of interest

The author declares that the research was conducted in the absence of any commercial or financial relationships that could be construed as a potential conflict of interest.

Publisher's note

References

1. Guenther JN. Overview of the QCD phase diagram: Recent progress from the lattice. *Eur Phys J A* (2021) 57(4):136. doi:10.1140/epja/s10050-021-00354-6

2. Fukushima K, Hatsuda T. The phase diagram of dense QCD. *Rep Prog Phys* (2011) 74:014001. doi:10.1088/0034-4885/74/1/014001

3. Borsanyi S, Fodor Z, Giordano M, Guenther JN, Katz SD, Pasztor A, Wong CH. *Equation of state of a hot-and-dense quark gluon plasma: Lattice simulations at real μ_B vs. extrapolations* (2022). arXiv:2208.05398.

4. Bazavov A, Ding HT, Hegde P, Kaczmarek O, Karsch F, Laermann E, et al. QCD equation of state to O(μB6) from lattice QCD. *Phys Rev D* (2017) 95(5): 054504. doi:10.1103/PhysRevD.95.054504

5. Borsanyi S, Fodor Z, Guenther JN, Kara R, Parotto P, Pasztor A, et al. Resummed lattice QCD equation of state at finite baryon density: Strangeness neutrality and beyond. *Phys Rev D* (2022) 105(11):114504. doi:10.1103/PhysRevD.105.114504

6. Busza W, Rajagopal K, van der Schee W. Heavy ion collisions: The big picture, and the big questions. *Annu Rev Nucl Part Sci* (2018) 68:339–76. doi:10.1146/annurev-nucl-101917-020852

7. Kojo T. QCD equations of state and speed of sound in neutron stars. *AAPPS Bull* (2021) 31(1):11. doi:10.1007/s43673-021-00011-6

8. Pasechnik R, Šumbera M. Phenomenological review on quark–gluon plasma: Concepts vs. Observations. *Universe* (2017) 3(1):7. doi:10.3390/universe3010007

9. Bazavov A, Petreczky P, Weber JH. Equation of state in 2+1 flavor QCD at high temperatures. *Phys Rev D* (2018) 97(1):014510. doi:10.1103/PhysRevD.97.014510

10. Borsanyi S, Fodor Z, Guenther J, Kampert KH, Katz SD, Kawanai T, et al. Calculation of the axion mass based on high-temperature lattice quantum chromodynamics. *Nature* (2016) 539(7627):69–71. doi:10.1038/nature20115

11. Bazavov A, Bhattacharya T, DeTar C, Ding HT, Gottlieb S, Gupta R, et al. Equation of state in (2+1)-flavor QCD. *Phys Rev D* (2014) 90:094503. doi:10.1103/PhysRevD.90.094503

12. Burger F, Ilgenfritz EM, Lombardo MP, Müller-Preussker M. Equation of state of quark-gluon matter from lattice QCD with two flavors of twisted mass Wilson fermions. *Phys Rev D* (2015) 91(7):074504. doi:10.1103/PhysRevD.91.074504

13. Borsanyi S, Fodor Z, Hoelbling C, Katz SD, Krieg S, Szabo KK. Full result for the QCD equation of state with 2+1 flavors. *Phys Lett B* (2014) 730:99–104. doi:10.1016/j.physletb.2014.01.007

14. Jaiswal A, Roy V. Relativistic hydrodynamics in heavy-ion collisions: General aspects and recent developments. *Adv High Energ Phys* (2016) 2016:1–39. doi:10.1155/2016/9623034

15. Klein M, Yoshida R. Collider physics at HERA. *Prog Part Nucl Phys* (2008) 61: 343–93. doi:10.1016/j.ppnp.2008.05.002

16. d'Enterria D, Kluth S, Zanderighi G, Ayala C, Benitez-Rathgeb MA, Bluemlein J, Boito D. *The strong coupling constant: State of the art and the decade ahead* (2022). arXiv:2203.08271.

17. Aoki Y, Blum T, Colangelo G, Collins S, Della Morte M, Dimopoulos P, et al. *FLAG review 2021* (2021). arXiv:2111.09849.

18. Lin ZW, Ko CM, Li BA, Zhang B, Pal S. Multiphase transport model for relativistic heavy ion collisions. *Phys Rev C* (2005) 72:064901. doi:10.1103/PhysRevC.72.064901

19. Petersen H, Steinheimer J, Burau G, Bleicher M, Stöcker H. Fully integrated transport approach to heavy ion reactions with an intermediate hydrodynamic stage. *Phys Rev C* (2008) 78:044901. doi:10.1103/PhysRevC.78.044901

20. Bratkovskaya EL, Cassing W, Konchakovski VP, Linnyk O. Parton-hadron-string dynamics at relativistic collider energies. *Nucl Phys A* (2011) 856:162–82. doi:10.1016/j.nuclphysa.2011.03.003

21. Cao S, Wang XN. Jet quenching and medium response in high-energy heavy-ion collisions: A review. *Rep Prog Phys* (2021) 84(2):024301. doi:10.1088/1361-6633/abc22b

22. Rothkopf A. Heavy quarkonium in extreme conditions. *Phys Rep* (2020) 858: 1–117. doi:10.1016/j.physrep.2020.02.006

23. Abdul Khalek R, D'Alesio U, Arratia M, Bacchetta A, Battaglieri M, Begel M, et al. Snowmass 2021 white paper: Electron ion collider for high energy physics. In: *2022 snowmass summer study* (2022). 2203.13199.

24. Alexandrou C, Bacchio S, Constantinou M, Finkenrath J, Hadjiyiannakou K, Jansen K, et al. Complete flavor decomposition of the spin and momentum fraction of the proton using lattice QCD simulations at physical pion mass. *Phys Rev D* (2020) 101(9):094513. doi:10.1103/PhysRevD.101.094513

25. Wang G, Yang YB, Liang J, Draper T, Liu KF. Proton momentum and angular momentum decompositions with overlap fermions. *Phys Rev D* (2022) 106(1): 014512. doi:10.1103/PhysRevD.106.014512

26. Meissner S, Metz A, Schlegel M. Generalized parton correlation functions for a spin-1/2 hadron. *J High Energ Phys* (2009) 08:056. doi:10.1088/1126-6708/2009/08/056

27. Constantinou M, Debbio LD, Ji X, Lin HW, Liu KF, Monahan C, et al. *Lattice QCD calculations of parton physics* (2022). arXiv:2202.07193.

28. Ji X. Parton physics on a euclidean lattice. *Phys Rev Lett* (2013) 110:262002. doi:10.1103/PhysRevLett.110.262002

29. Radyushkin AV. Quasi-parton distribution functions, momentum distributions, and pseudo-parton distribution functions. *Phys Rev D* (2017) 96(3):034025. doi:10.1103/PhysRevD.96.034025

30. Liu KF, Dong SJ. Origin of difference between$\bar{u}$and$\bar{d}$partons in the nucleon. *Phys Rev Lett* (1994) 72:1790–3. doi:10.1103/PhysRevLett.72.1790

31. Schwartz MD. *Quantum field theory and the standard model*. Cambridge: Cambridge University Press (2014).

32. Dupuis N, Canet L, Eichhorn A, Metzner W, Pawlowski JM, Tissier M, et al. The nonperturbative functional renormalization group and its applications. *Phys Rep* (2021) 910:1–114. doi:10.1016/j.physrep.2021.01.001

33. Blaizot JP, Pawlowski JM, Reinosa U. Functional renormalization group and 2PI effective action formalism. *Ann Phys (N Y)* (2021) 431:168549. doi:10.1016/j.aop.2021.168549

34. Fischer CS. Infrared properties of qcd from dyson–schwinger equations. *J Phys G: Nucl Part Phys* (2006) 32(8):253–91. doi:10.1088/0954-3899/32/8/r02

35. Roberts CD. Strong QCD and dyson-schwinger equations. *IRMA Lect Math Theor Phys* (2015) 21:355–458. 1203.5341.

36. Montvay I, Münster G. *Quantum fields on a lattice*. Cambridge: Cambridge Monographs on Mathematical Physics. Cambridge University Press (1994).

37. Gattringer C, Lang CB. *Quantum chromodynamics on the lattice vol. 788*. Berlin: Springer (2010). doi:10.1007/978-3-642-01850-3

38. Gattringer C, Langfeld K. Approaches to the sign problem in lattice field theory. *Int J Mod Phys A* (2016) 31(22):1643007. doi:10.1142/S0217751X16430077

39. Berger CE, Rammelmüller L, Loheac AC, Ehmann F, Braun J, Drut JE. Complex Langevin and other approaches to the sign problem in quantum many-body physics. *Phys Rep* (2021) 892:1–54. doi:10.1016/j.physrep.2020.09.002

40. Bellac ML. *Thermal field theory*. Cambridge: Cambridge Monographs on Mathematical Physics. Cambridge University Press (2011). doi:10.1017/CBO9780511721700

41. Ghiglieri J, Kurkela A, Strickland M, Vuorinen A. Perturbative thermal QCD: Formalism and applications. *Phys Rep* (2020) 880:1–73. doi:10.1016/j.physrep.2020.07.004

42. Meyer HB. Transport properties of the quark-gluon plasma: A lattice QCD perspective. *Eur Phys J A* (2011) 47:86. doi:10.1140/epja/i2011-11086-3

43. Hadamard J. *Sur les problèmes aux dérivées partielles et leur signification physique*. Princeton, NJ, USA: Princeton university bulletin (1902). p. 49–52.

44. Shi S, Wang L, Zhou K. *Rethinking the ill-posedness of the spectral function reconstruction - why is it fundamentally hard and how Artificial Neural Networks can help* (2022). arXiv:2201.02564.

45. Karpie J, Orginos K, Rothkopf A, Zafeiropoulos S. Reconstructing parton distribution functions from Ioffe time data: From bayesian methods to neural networks. *J High Energ Phys* (2019) 04:057. doi:10.1007/JHEP04(2019)057

46. Nakahara Y, Asakawa M, Hatsuda T. Hadronic spectral functions in lattice QCD. *Phys Rev D* (1999) 60:091503. doi:10.1103/PhysRevD.60.091503

47. Asakawa M, Hatsuda T, Nakahara Y. Maximum entropy analysis of the spectral functions in lattice QCD. *Prog Part Nucl Phys* (2001) 46:459–508. doi:10.1016/S0146-6410(01)00150-8

48. Jarrell M, Gubernatis JE. Bayesian inference and the analytic continuation of imaginary-time quantum Monte Carlo data. *Phys Rep* (1996) 269(3):133–95. doi:10.1016/0370-1573(95)00074-7

49. Skilling J, Gull SF. Bayesian maximum entropy image reconstruction. *Lecture Notes-Monograph Ser* (1991) 1991:341–67.

50. Yamazaki T, Aoki S, Burkhalter R, Fukugita M, Hashimoto S, Ishizuka N, et al. Spectral function and excited states in lattice qcd with the maximum entropy method. *Phys Rev D* (2001) 65:014501. doi:10.1103/PhysRevD.65.014501

51. Sasaki K, Sasaki S, Hatsuda T. Spectral analysis of excited nucleons in lattice qcd with maximum entropy method. *Phys Lett B* (2005) 623(3):208–17. doi:10.1016/j.physletb.2005.07.026

52. Fiebig HR. Spectral density analysis of time correlation functions in lattice qcd using the maximum entropy method. *Phys Rev D* (2002) 65:094512. doi:10.1103/PhysRevD.65.094512

53. Liang J, Draper T, Liu KF, Rothkopf A, Yang YB. Towards the nucleon hadronic tensor from lattice QCD. *Phys Rev D* (2020) 101(11):114503. doi:10.1103/PhysRevD.101.114503

54. Asakawa M, Hatsuda T. J/ψandηcin the deconfined plasma from lattice QCD. *Phys Rev Lett* (2004) 92:012001. doi:10.1103/PhysRevLett.92.012001

55. Datta S, Karsch F, Petreczky P, Wetzorke I. Behavior of charmonium systems after deconfinement. *Phys Rev D* (2004) 69:094507. doi:10.1103/PhysRevD.69.094507

56. Umeda T, Nomura K, Matsufuru H. Charmonium at finite temperature in quenched lattice QCD. *Eur Phys J C* (2005) 39S1:9–26. doi:10.1140/epjcd/s2004-01-002-1

57. Jakovac A, Petreczky P, Petrov K, Velytsky A. Quarkonium correlators and spectral functions at zero and finite temperature. *Phys Rev D* (2007) 75:014506. doi:10.1103/PhysRevD.75.014506

58. Aarts G, Allton C, Kim S, Lombardo MP, Oktay MB, Ryan SM, et al. What happens to the Υ and η_b in the quark-gluon plasma? Bottomonium spectral functions from lattice QCD. *J High Energ Phys* (2011) 11:103. doi:10.1007/JHEP11(2011)103

59. Aarts G, Allton C, Kim S, Lombardo MP, Oktay MB, Ryan SM, et al. S wave bottomonium states moving in a quark-gluon plasma from lattice NRQCD. *J High Energ Phys* (2013) 03:084. doi:10.1007/JHEP03(2013)084

60. Ding HT, Francis A, Kaczmarek O, Karsch F, Satz H, Soeldner W. Charmonium properties in hot quenched lattice QCD. *Phys Rev D* (2012) 86: 014509. doi:10.1103/PhysRevD.86.014509

61. Aarts G, Allton C, Kim S, Lombardo MP, Ryan SM, Skullerud JI. Melting of P wave bottomonium states in the quark-gluon plasma from lattice NRQCD. *J High Energ Phys* (2013) 12:064. doi:10.1007/JHEP12(2013)064

62. Aarts G, Allton C, Harris T, Kim S, Lombardo MP, Ryan SM, et al. The bottomonium spectrum at finite temperature from $N_f = 2 + 1$ lattice QCD. *J High Energ Phys* (2014) 07:097. doi:10.1007/JHEP07(2014)097

63. Borsanyi S, Durr S, Fodor Z, Hoelbling C, Katz SD, Krieg S, et al. Charmonium spectral functions from 2+1 flavour lattice QCD. *J High Energ Phys* (2014) 04:132. doi:10.1007/jhep04(2014)132

64. Kim S, Petreczky P, Rothkopf A. Lattice NRQCD study of S- and P-wave bottomonium states in a thermal medium with $N_f = 2 + 1$ light flavors. *Phys Rev D* (2015) 91:054511. doi:10.1103/PhysRevD.91.054511

65. Ikeda A, Asakawa M, Kitazawa M. In-medium dispersion relations of charmonia studied by the maximum entropy method. *Phys Rev D* (2017) 95(1): 014504. doi:10.1103/PhysRevD.95.014504

66. Kelly A, Rothkopf A, Skullerud JI. Bayesian study of relativistic open and hidden charm in anisotropic lattice QCD. *Phys Rev D* (2018) 97(11):114509. doi:10.1103/PhysRevD.97.114509

67. Kim S, Petreczky P, Rothkopf A. Quarkonium in-medium properties from realistic lattice NRQCD. *J High Energ Phys* (2018) 11:088. doi:10.1007/JHEP11(2018)088

68. Gubler P, Morita K, Oka M. Charmonium spectra at finite temperature from QCD sum rules with the maximum entropy method. *Phys Rev Lett* (2011) 107: 092003. doi:10.1103/PhysRevLett.107.092003

69. Araki KJ, Ohtani K, Gubler P, Oka M. QCD sum rules on the complex Borel plane. *Prog Theor Exp Phys* (2014) 2014:73B03–0. doi:10.1093/ptep/ptu092

70. Meyer HB. Calculation of the shear viscosity in SU(3) gluodynamics. *Phys Rev D* (2007) 76:101701. doi:10.1103/PhysRevD.76.101701

71. Meyer HB. Calculation of the bulk viscosity in SU(3) gluodynamics. *Phys Rev Lett* (2008) 100:162001. doi:10.1103/PhysRevLett.100.162001

72. Aarts G, Allton C, Foley J, Hands S, Kim S. Spectral functions at small energies and the electrical conductivity in hot, quenched lattice QCD. *Phys Rev Lett* (2007) 99:022002. doi:10.1103/PhysRevLett.99.022002

73. Ding HT, Francis A, Kaczmarek O, Karsch F, Laermann E, Soeldner W. Thermal dilepton rate and electrical conductivity: An analysis of vector current correlation functions in quenched lattice QCD. *Phys Rev D* (2011) 83:034504. doi:10.1103/PhysRevD.83.034504

74. Aarts G, Allton C, Amato A, Giudice P, Hands S, Skullerud JI. Electrical conductivity and charge diffusion in thermal QCD from the lattice. *J High Energ Phys* (2015) 02:186. doi:10.1007/JHEP02(2015)186

75. Amato A, Aarts G, Allton C, Giudice P, Hands S, Skullerud JI. Electrical conductivity of the quark-gluon plasma across the deconfinement transition. *Phys Rev Lett* (2013) 111(17):172001. doi:10.1103/PhysRevLett.111.172001

76. Astrakhantsev N, Braguta V, Kotov A. Temperature dependence of shear viscosity of *SU*(3)–gluodynamics within lattice simulation. *J High Energ Phys* (2017) 04:101. doi:10.1007/JHEP04(2017)101

77. Rothkopf A, Hatsuda T, Sasaki S. Complex heavy-quark potential at finite temperature from lattice QCD. *Phys Rev Lett* (2012) 108:162001. doi:10.1103/PhysRevLett.108.162001

78. Burnier Y, Kaczmarek O, Rothkopf A. Static quark-antiquark potential in the quark-gluon plasma from lattice QCD. *Phys Rev Lett* (2015) 114(8):082001. doi:10.1103/PhysRevLett.114.082001

79. Burnier Y, Kaczmarek O, Rothkopf A. Quarkonium at finite temperature: Towards realistic phenomenology from first principles. *J High Energ Phys* (2015) 12:101–34. doi:10.1007/JHEP12(2015)101

80. Burnier Y, Rothkopf A. Complex heavy-quark potential and Debye mass in a gluonic medium from lattice QCD. *Phys Rev D* (2017) 95(5):054511. doi:10.1103/PhysRevD.95.054511

81. Dudal D, Oliveira O, Silva PJ. Källén-Lehmann spectroscopy for (un)physical degrees of freedom. *Phys Rev D* (2014) 89(1):014010. doi:10.1103/PhysRevD.89.014010

82. Ilgenfritz EM, Pawlowski JM, Rothkopf A, Trunin A. Finite temperature gluon spectral functions from $N_f = 2 + 1 + 1$ lattice QCD. *Eur Phys J C* (2018) 78(2):127. doi:10.1140/epjc/s10052-018-5593-7

83. Dudal D, Oliveira O, Roelfs M, Silva P. Spectral representation of lattice gluon and ghost propagators at zero temperature. *Nucl Phys B* (2020) 952:114912. doi:10.1016/j.nuclphysb.2019.114912

84. Lepage GP, Clark B, Davies CTH, Hornbostel K, Mackenzie PB, Morningstar C, et al. Constrained curve fitting. *Nucl Phys B - Proc Supplements* (2002) 106:12–20. doi:10.1016/S0920-5632(01)01638-3

85. Burnier Y, Ding HT, Kaczmarek O, Kruse AL, Laine M, Ohno H, et al. Thermal quarkonium physics in the pseudoscalar channel. *J High Energ Phys* (2017) 11:206. doi:10.1007/JHEP11(2017)206

86. McElreath R. *Statistical rethinking: A bayesian course with examples in R and stan*. 2nd ed. Boca Raton, FL, USA: CRC Press (2020).

87. Bishop CM. *Pattern recognition and machine learning (information science and statistics)*. Berlin, Heidelberg: Springer (2006).

88. Endres MG, Kaplan DB, Lee JW, Nicholson AN. Listening to noise. *PoS LATTICE* (2011) 2011:017. doi:10.22323/1.139.0017

89. DeGrand T. Log-normal distribution for correlators in lattice QCD? *Phys Rev D* (2012) 86:014512. doi:10.1103/PhysRevD.86.014512

90. Efron B, Tibshirani RJ. *An introduction to the bootstrap. Monographs on statistics and applied probability, vol. 57*. Boca Raton, Florida, USA: Chapman & Hall/CRC (1993).

91. Cyrol AK, Pawlowski JM, Rothkopf A, Wink N. Reconstructing the gluon. *Scipost Phys* (2018) 5(6):065. doi:10.21468/SciPostPhys.5.6.065

92. Binosi D, Tripolt RA. Spectral functions of confined particles. *Phys Lett B* (2020) 801:135171. doi:10.1016/j.physletb.2019.135171

93. Tikhonov AN. On the stability of inverse problems. *Dokl Akad Nauk SSSR* (1943) 39:195–8.

94. Rudin LI, Osher S, Fatemi E. Nonlinear total variation based noise removal algorithms. *Physica D: Nonlinear Phenomena* (1992) 60(1-4):259–68. doi:10.1016/0167-2789(92)90242-F

95. Bardsley JM. Laplace-distributed increments, the laplace prior, and edge-preserving regularization. *J Inverse Ill-Posed Probl* (2012) 20(3):271–85. doi:10.1515/jip-2012-0017

96. Fischer CS, Pawlowski JM, Rothkopf A, Welzbacher CA. Bayesian analysis of quark spectral properties from the Dyson-Schwinger equation. *Phys Rev D* (2018) 98(1):014009. doi:10.1103/PhysRevD.98.014009

97. Event Horizon Telescope Collaboration, Akiyama K, Alberdi A, Alef W, Asada K, Azulay R, et al. First M87 event horizon telescope results. I. The shadow of the supermassive black hole. *Astrophys J* (2019) 875(1):1. doi:10.3847/2041-8213/ab0ec7

98. Narayan R, Nityananda R. Maximum entropy image restoration in astronomy. *Annu Rev Astron Astrophys* (1986) 24(1):127–70. doi:10.1146/annurev.aa.24.090186.001015

99. Skilling J. The axioms of maximum entropy. In: *Maximum-entropy and bayesian methods in science and engineering*. Berlin: Springer (1988). p. 173–87.

100. Burnier Y, Rothkopf A. Bayesian approach to spectral function reconstruction for euclidean quantum field theories. *Phys Rev Lett* (2013) 111:182003. doi:10.1103/PhysRevLett.111.182003

101. Harris T, Meyer HB, Robaina D. A variational method for spectral functions. *PoS LATTICE* (2016) 2016:339. doi:10.22323/1.256.0339

102. Bala D, Kaczmarek O, Larsen R, Mukherjee S, Parkar G, Petreczky P, et al. Static quark-antiquark interactions at nonzero temperature from lattice QCD. *Phys Rev D* (2022) 105(5):054513. doi:10.1103/PhysRevD.105.054513

103. Hobson M, Lasenby A. The entropic prior for distributions with positive and negative values. *Mon Not R Astron Soc* (1998) 298:905–8. doi:10.1046/j.1365-8711.1998.01707.x

104. Rothkopf A. Bayesian inference of nonpositive spectral functions in quantum field theory. *Phys Rev D* (2017) 95(5):056016. doi:10.1103/PhysRevD.95.056016

105. Haas M, Fister L, Pawlowski JM. Gluon spectral functions and transport coefficients in Yang–Mills theory. *Phys Rev D* (2014) 90:091501. doi:10.1103/PhysRevD.90.091501

106. Mishchenko A, Prokof'Ev N, Sakamoto A, Svistunov B. Diagrammatic quantum Monte Carlo study of the fröhlich polaron. *Phys Rev B* (2000) 62(10):6317–36. doi:10.1103/physrevb.62.6317

107. Ding HT, Kaczmarek O, Mukherjee S, Ohno H, Shu HT. Stochastic reconstructions of spectral functions: Application to lattice qcd. *Phys Rev D* (2018) 97(9):094503. doi:10.1103/physrevd.97.094503

108. Shao H, Sandvik AW. *Progress on stochastic analytic continuation of quantum Monte Carlo data* (2022). arXiv:2202.09870.

109. Beach K. *Identifying the maximum entropy method as a special limit of stochastic analytic continuation* (2004). arXiv preprint cond-mat/0403055.

110. Press WH, Teukolsky SA, Vetterling WT, Flannery BP. *Numerical recipes 3rd edition: The art of scientific computing*. 3rd ed. Cambridge: Cambridge University Press (2007).

111. Burnier Y, Laine M, Mether L. A Test on analytic continuation of thermal imaginary-time data. *Eur Phys J C* (2011) 71:1619. doi:10.1140/epjc/s10052-011-1619-0

112. Zhu Y, Vuorinen A. The shear channel spectral function in hot Yang-Mills theory. *J High Energ Phys* (2013) 03:002. doi:10.1007/JHEP03(2013)002

113. Burnier Y, Laine M. Massive vector current correlator in thermal QCD. *J High Energ Phys* (2012) 11:086. doi:10.1007/JHEP11(2012)086

114. Vuorinen A, Zhu Y. On the infrared behavior of the shear spectral function in hot Yang-Mills theory. *J High Energ Phys* (2015) 03:138. doi:10.1007/JHEP03(2015)138

115. Jeffreys H. An invariant form for the prior probability in estimation problems. *Proc R Soc Lond A Math Phys Sci* (1946) 186(1007):453–61. doi:10.1098/rspa.1946.0056

116. Bryan RK. Maximum entropy analysis of oversampled data problems. *Eur Biophys J* (1990) 18(3):165–74. doi:10.1007/BF02427376

117. Rothkopf A. Improved maximum entropy analysis with an extended search space. *J Comput Phys* (2013) 238:106–14. doi:10.1016/j.jcp.2012.12.023

118. Rothkopf A. Improved maximum entropy method with extended search space. *PoS LATTICE* (2012) 2012:100. doi:10.22323/1.164.0100

119. Rothkopf A. MAP Implementation of the BR method & MEM. Zenodo (2022). doi:10.5281/zenodo.7362890

120. Rothkopf A. MC Stan implementation of the BR method. Zenodo (2022). doi:10.5281/zenodo.7362907

121. Granlund T. *The GMP development team: GNU MP: The GNU multiple precision arithmetic library, 5.0.5 edn.* (2012).

122. Fousse L, Hanrot G, Lefèvre V, Pélissier P, Zimmermann P. Mpfr: A multiple-precision binary floating-point library with correct rounding. *ACM Trans Math Softw* (2007) 33(2):13. doi:10.1145/1236463.1236468

123. Ding HT, Kaczmarek O, Karsch F, Satz H, Soldner W. Charmonium correlators and spectral functions at finite temperature. *PoS LAT* (2009) 2009:169. doi:10.22323/1.091.0169

124. Malouf R. A comparison of algorithms for maximum entropy parameter estimation. In: Proceedings of the 6th Conference on Natural Language Learning - Volume 20. COLING-02. Stroudsburg, Pennsylvania, USA: Association for Computational Linguistics (2002). p. 1–7. doi:10.3115/1118853.1118871

125. Carpenter B, Gelman A, Hoffman MD, Lee D, Goodrich B, Betancourt M, et al. *Stan*: A probabilistic programming language. *J Stat Softw* (2017) 76(1). doi:10.18637/jss.v076.i01

126. Stan Development Team. *The stan core library. Version 2.18.0* (2018).

127. Burnier Y, Rothkopf A. Hard thermal loop benchmark for the extraction of the nonperturbative $Q\bar{Q}$ potential. *Phys Rev D* (2013) 87:114019. doi:10.1103/PhysRevD.87.114019

128. Boyda D, Calì S, Foreman S, Funcke L, Hackett DC, Lin Y, et al. Applications of machine learning to lattice quantum field theory. In: *2022 snowmass summer study* (2022). 2202.05838.

129. Offler S, Aarts G, Allton C, Jäger B, Kim S, Lombardo MP, et al. Reconstruction of bottomonium spectral functions in thermal QCD using Kernel Ridge Regression. *PoS LATTICE* (2022) 2021:509. doi:10.22323/1.396.0509

130. Spriggs T, Aarts G, Allton C, Burns T, Horohan D'Arcy R, Jager B, et al. A comparison of spectral reconstruction methods applied to non-zero temperature NRQCD meson correlation functions. *EPJ Web Conf* (2022) 258:05011. doi:10.1051/epjconf/202225805011

131. Fournier R, Wang L, Yazyev OV, Wu Q. Artificial neural network approach to the analytic continuation problem. *Phys Rev Lett* (2020) 124(5):056401. doi:10.1103/physrevlett.124.056401

132. Kades L, Pawlowski JM, Rothkopf A, Scherzer M, Urban JM, Wetzel SJ, et al. Spectral reconstruction with deep neural networks. *Phys Rev D* (2020) 102(9):096001. doi:10.1103/PhysRevD.102.096001

133. Chen SY, Ding HT, Liu FY, Papp G, Yang CB. *Machine learning spectral functions in lattice QCD* (2021). arXiv:2110.13521.

134. Wang L, Shi S, Zhou K. Automatic differentiation approach for reconstructing spectral functions with neural networks. In: *35th conference on neural information processing systems* (2021). 2112.06206.

135. Lechien T, Dudal D. Neural network approach to reconstructing spectral functions and complex poles of confined particles. *Scipost Phys* (2022) 13(4):097. doi:10.21468/SciPostPhys.13.4.097

136. Valentine AP, Sambridge M. Gaussian process models—I. A framework for probabilistic continuous inverse theory. *Geophys J Int* (2020) 220(3):1632–47. doi:10.1093/gji/ggz520

137. Horak J, Pawlowski JM, Rodríguez-Quintero J, Turnwald J, Urban JM, Wink N, et al. Reconstructing QCD spectral functions with Gaussian processes. *Phys Rev D* (2022) 105(3):036014. doi:10.1103/PhysRevD.105.036014

frontiers | Frontiers in Physics

TYPE Original Research
PUBLISHED 15 December 2022
DOI 10.3389/fphy.2022.1046638

OPEN ACCESS

EDITED BY
Maria Piarulli,
Washington University in St. Louis, United States

REVIEWED BY
Michele Viviani,
National Institute of Nuclear Physics of Pisa, Italy
Gregory Potel Aguilar,
Lawrence Livermore National Laboratory (DOE), United States

*CORRESPONDENCE
Nicole Vassh,
nvassh@triumf.ca

SPECIALTY SECTION
This article was submitted to Nuclear Physics, a section of the journal Frontiers in Physics

RECEIVED 16 September 2022
ACCEPTED 28 November 2022
PUBLISHED 15 December 2022

CITATION
Vassh N, McLaughlin GC, Mumpower MR and Surman R (2022), Solar data uncertainty impacts on MCMC methods for *r*-process nucleosynthesis. *Front. Phys.* 10:1046638. doi: 10.3389/fphy.2022.1046638

Solar data uncertainty impacts on MCMC methods for *r*-process nucleosynthesis

Nicole Vassh[1]*, Gail C. McLaughlin[2], Matthew R. Mumpower[3,4] and Rebecca Surman[5]

[1]TRIUMF, Vancouver, BC, Canada, [2]Department of Physics, North Carolina State University, Raleigh, NC, United States, [3]Theoretical Division, Los Alamos National Laboratory, Los Alamos, NM, United States, [4]Center for Theoretical Astrophysics, Los Alamos National Laboratory, Los Alamos, NM, United States, [5]Department of Physics, University of Notre Dame, Notre Dame, IN, United States

In recent work, we developed a Markov Chain Monte Carlo (MCMC) procedure to predict the ground state masses capable of forming the observed Solar *r*-process rare-earth abundance peak. By applying this method to nucleosynthesis calculations which make use of distinct astrophysical conditions and comparing our results to the latest precision mass measurements, we are able to shed light on the conditions/masses capable of producing a rare-earth peak which matches Solar data. Here we examine how our mass predictions change when using a few different sets of *r*-process Solar abundance residuals that have been reported in the literature. We explore how the differing error estimates of these Solar evaluations propagate through the Markov Chain Monte Carlo to our mass predictions. We find that Solar data which reports the rare-earth peak to have its highest abundance at mass number $A = 162$ can require distinctly different mass predictions from data with the peak centered at $A = 164$. Nevertheless, we find that two important general conclusions from past work, regarding the inconsistency of 'cold' astrophysical outflows with current mass measurements and the need for local stability at $N = 104$ in 'hot' scenarios, remain robust in the face of differing Solar data evaluations. Additionally, we show that the masses our procedure finds capable of producing a peak at $A < 164$ are not in line with the latest precision mass measurements.

KEYWORDS

nucleosynthesis, solar abundances, r-process, heavy elements, Markov Chain Monte Carlo (MCMC), uncertainty quantification (UQ)

The study of the origin of the heaviest elements has in recent years been buzzing with new discussions surrounding the interpretation of the multi-messenger neutron star merger event GW170817 [1–3]. This event was first detected in gravitational waves and then followed-up by the telescope community to be observed across the electromagnetic spectrum [4, 5]. The prospect of learning from real-time nucleosynthesis events such as this is indeed a direction in which the field will grow for years to come. However, if such single events are to be connected back to our own Solar System origins, the importance of messengers of heavy element synthesis

closer to home, that is Solar spectroscopic data and meteorites, must continue to be recognized. From these sources the Solar isotopic pattern, that is the relative amounts of species of a given mass number, is able to be determined [6]. This bit of observational information is unique to our Solar System with only elemental abundance patterns being available for other stars through spectroscopy [7]. The Solar isotopic pattern serves as an important benchmark for studies of the rapid neutron capture process (*r*-process), with it being common practice to compare these abundances to nucleosynthesis predictions in order to sort out the possible contributions a given astrophysical scenario or the plausibility of a given set of nuclear inputs (e.g. [8–11]). In recent work [12–17], rather than proceeding with the Solar isotopic pattern as solely a final point of comparison, we have instead made use of these abundances as the starting point for Markov Chain Monte Carlo (MCMC) methods aiming to work backwards toward deriving fundamental nuclear physics quantities. This approach is possible due to the clear impact of the properties of neutron-rich nuclei on astrophysical abundances, as evidenced by the second and third *r*-process abundance peaks seen in the Solar data at A ~130 and A ~195 from the closed neutron shells at N = 82 and N = 126 respectively [18]. Our approach therefore exploits this interplay between nuclear physics and observables by focusing on an abundance feature of uncertain origin, the *r*-process rare-earth abundance peak [19, 20], in order to probe previously unmeasured nuclear masses of rare-earth species.

Our MCMC method considers the masses needed in order to form the rare-earth abundance peak by applying the mass parameterization:

$$M(Z,N) = M_{DZ}(Z,N) + a_N e^{-(Z-C)^2/2f} \quad (1)$$

where M_{DZ} corresponds to the masses predicted by the Duflo-Zuker (DZ) mass model [21] and a_N values are the parameters being determined by the MCMC. In these calculations we set f = 10 based on fits to mass trends of the Atomic Mass Evaluation (AME) 2012 data [22] and set C = 58 or C = 60 as was determined by numerous initial runs in which this parameter was allowed to float (see [15] for a detailed discussion). Following our mass adjustments we then calculate neutron capture, β-decay, and photodissociation rates corresponding to the mass changes before performing the nucleosynthesis calculation. Additionally, as discussed in [15], we perform external checks on quantities, such as the one neutron pairing metric and the σ_{rms} deviation with respect to AME2012 mass values, in order to ensure that we do not explore unphysical solutions.

Since the astrophysical conditions present during the nucleosynthesis impact the formation of abundance features, in past work we considered our MCMC approach along with several distinct astrophysical outflows. We consider an outflow 'hot' if neutron capture and photodissociation undergo an extended equilibrium during the synthesis. If rather photodissociation falls out of equilibrium early leaving neutron capture to compete with β-decay, we consider this a 'cold' outflow. As can be seen in Figure 1, we predict distinct mass surface trends to be needed to form the rare-earth peak for each of the distinct

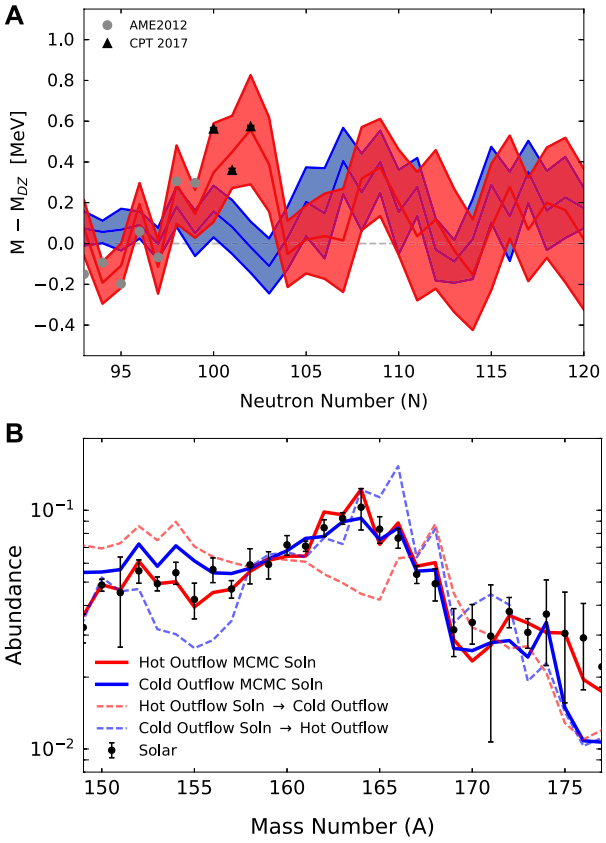

FIGURE 1
(A) The MCMC predicted masses for samarium (Z =62), relative to the DZ mass model, given two distinct moderately neutron-rich (Y_e =0.2) astrophysical outflows that could be found in accretion disk winds: a hot case which undergoes an extended (n,γ)⇄(γ,n) equilibrium (red band) and a cold case (blue band) for which photodissociation falls out of equilibrium early (adapted from Figure 20 of [15]). The AME2012 data [22] used to guide the calculation is shown along with CPT at CARIBU [14] data of which the calculation was not informed. All bands were determined from the average and standard deviation of 50 parallel, independent MCMC runs **(B)** Demonstration that the mass solutions are uniquely tied to the astrophysical conditions, with the solid red line showing the abundance results using the MCMC masses of top panel and the dotted red line showing the results when these masses are applied in a nucleosynthesis calculation with the cold trajectory. Likewise the blue solid line shows the abundances predicted by the blue band in the top panel along with the resultant abundances when this mass solution is applied to the hot trajectory (Figure 2 of [16]). Note that results in the top panel were determined from runs which applied symmetrized Solar data derived from Arnould+07 [29] (described in [15]) which is shown as black points in the bottom panel.

astrophysical outflows. Here note that since our mass predictions M are illustrated *via* the mass difference with respect to DZ ($M-M_{DZ}$) a positive value implies our MCMC requires masses less tightly bound than DZ and a negative value implies a more tightly bound system than is predicted by DZ. Since the nucleosynthesis outcome is sensitive to how the properties of a given nucleus relate to the properties of its neighbors, the most influential mass surface features will be ones that introduce strong local differences, such as the drop in the red band from positive to negative $M-M_{DZ}$ from N = 102 to N = 104 which creates a region of 'enhanced stability' at N = 104 relative to neighboring nuclei. Independent mass measurements performed by the Canadian Penning Trap (CPT) at the CAlifornium Rare Isotope Breeder Upgrade (CARIBU) of which the MCMC calculation was not informed are found to be most consistent with the masses need in hot astrophysical outflows. Therefore this method can ultimately point to the type of astrophysical conditions which dominantly produced the lanthanide elements we see in the Solar System, which can then be traced back to candidate sites such as neutron star mergers or magneto-rotationally driven supernovae through comparisons with hydrodynamics predictions (e.g. [23–28]) and multi-messenger observations.

This exciting prospect to use advancements in statistical methods in order to progress our understanding of the origins of Solar System elements however hinges on how precisely we know the *r*-process content of the Solar System. The so-called 'Solar *r*-process residuals' are derived from subtracting out the predicted contribution to the Solar System for the slow neutron capture process (*s*-process). This is accepted as the standard approach since the *s* process occurs closer to stable species and so the nuclear data of importance to this process is significantly better understood than the data of relevance to the *r* process. Such '*s*-process subtractions' have been performed over the years, taking into account new nuclear data measurements or new information on the conditions present at the astrophysical site of the *s* process, Asymptotic Giant Branch (AGB) stars. However very few of these independent Solar data evaluation sets from the literature report error estimates. The few that do report errors do so *via* propagating uncertainties from multiple sources including the observational data, neutron capture and β-decay measurement uncertainties, as well as estimates of the astrophysical variations which may be present in *s*-process sites (e.g. [30]). This procedure can thus yield different predictions for the relative abundances of neighboring nuclei as well as big differences in the reported errors depending on the error propagation treatment. Such considerations are highly relevant for our *r*-process MCMC calculations since the absolute value ($Y_\odot(A)$) and error ($\Delta Y_\odot(A)$) of the Solar *r*-process residuals at a given mass number dictates how our Markov chains evolve. This is because whether or not new masses of given step are adopted is determined by the likelihood ratio $R = \frac{\mathcal{L}_j}{\mathcal{L}_i}$ with j being the new step, i being the previous step, and the likelihood function being $\mathcal{L} \sim e^{-\chi^2/2}$ with χ^2 defined by

$$\chi^2 = \sum_{A=150}^{180} \frac{(Y_\odot(A) - Y(A))^2}{(\Delta Y_\odot(A))^2}. \quad (2)$$

Here we consider the Solar data impact on our MCMC mass predictions by applying two evaluations which report error estimates, those of Arnould+07 [29] and those of Beer+97 [31], and the data set of Sneden+08 [32] which does not report error estimates. As can be seen from Figure 2, Arnould+07 and Beer+97 not only have distinctly different trends in the shape of the relative abundances of the rare-earths, but also very different error estimates with the Beer+97 set being the case considered here with the smallest reported error. Even though the Sneden+08 dataset does not come with its own unique error estimate, this is an important set to consider given its frequent use as a comparison point for nucleosynthesis calculations in the literature. To utilize the Sneden+08 set in our MCMC approach, we must assign an abundance uncertainty in order to calculate χ^2. For our purposes, the most intriguing feature of the Sneden+08 dataset is the location of the peak of the rare-earth abundances since our calculations must find nuclear properties which can pile up nuclei at the needed mass number. Therefore for this case we take the error to be the average error of the Arnould+07 set applied equally to all points so that our MCMC analysis can investigate sensitivity to peak location rather than overall error. Thus the Beer+97 case will be most informative of the impact of error estimates and the Sneden+08 case will serve to observe how much the relative abundances and exactly placement of the highest peak point influence our MCMC.

In Table 1 we compare the χ^2 fits for each astrophysical scenario/Solar data combination reported in this work. Note that we report unnormalized χ^2 values because of the difficulty in defining the number of degrees of freedom due to the nature of how our MC parameters propagate through to the abundance values. We use 28 a_N parameters to adjust the masses of ~ 300 nuclei that are then inputs for the neutron capture rates, photodissociation rates, and β-decay rates that ultimately determine the abundances entering the χ^2 calculation for A = 150–180 (30 data points). Propagation of our 28 parameters to reaction rates introduces non-trival correlations amongst the 30 abundances being investigated, and the number of correlations introduced is a necessary ingredient to define the number of degrees of freedom (for instance standard deviations require dividing by N-1 where N is the number of points and one degree of freedom is subtracted since the average of N values enters the calculation and thus introduces one correlation). See the discussion in [15] for further details.

As can be seen in Table 1, since the errors we assume for the Sneden+08 Solar data set are based on the average of the Arnould+07 set, the χ^2 for the initial baseline nucleosynthesis abundance is similar, being between 180–286 for both the hot and cold astrophysical scenarios. The set considered here with

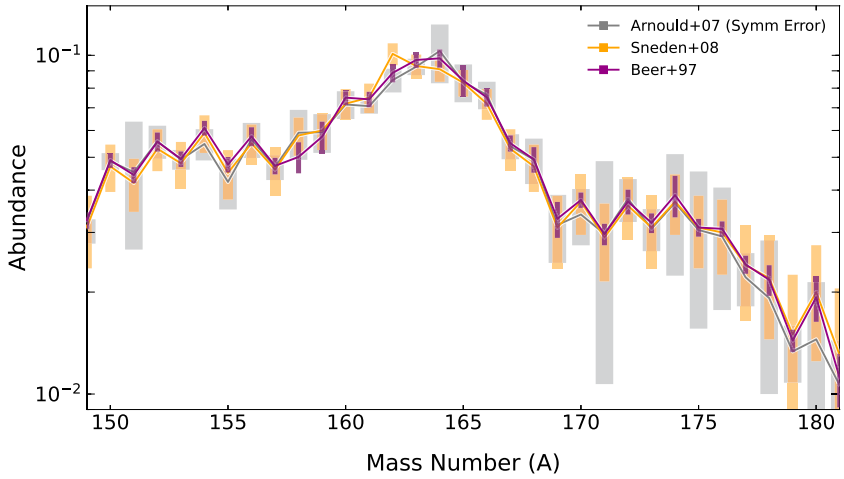

FIGURE 2
The Solar *r*-process abundance residuals for the rare-earth peak (~ A =150–180) given several evaluations and error estimates. The set applied in previous MCMC work (grey) were derived from those in Arnould+07 [29, 30] by performing a symmetrization procedure as described in [15]. Also shown is the Solar data evaluation of Beer+97 [31] (purple) which reports significantly smaller error estimates. Another set considered is the popular Sneden+08 Solar data evaluation [32] (orange) which does not report errors. For this Sneden+08 set, the average error on abundances between A =150–180 from [29, 30] was applied.

TABLE 1 Summary of the χ^2 for the DZ baseline and MCMC results for all cases presented in this work.

Description of Astro. Cond	C	Solar *r*-process evaluation	Baseline χ^2	Average χ^2	Average # of steps
Cold, low entropy, moderately neutron-rich (Y_e = 0.2)	58	Arnould+07 (Symm Error)	285.7	21.6	17,095
Cold, low entropy, moderately neutron-rich (Y_e = 0.2)	58	Sneden+08	180.4	23.9	16,020
Hot, low entropy, moderately neutron-rich (Y_e = 0.2)	60	Arnould+07 (Symm Error)	200.1	22.7	16,800
Hot, low entropy, moderately neutron-rich (Y_e = 0.2)	60	Sneden+08	184.4	18.7	17,624
Hot, low entropy, moderately neutron-rich (Y_e = 0.2)	60	Beer+97	864.9	128.9	10,714

the smallest errors, that is Beer+97, is distinct in having a much larger initial χ^2 abundance baseline of 865 for the hot astrophysical outflow. This leads to the MCMC not being able to achieve as low of χ^2 solutions as could be found in the Arnould+07 and Sneden+08 cases, despite the fact that the average number of steps taken by MCMC runs with Beer+97 was more than 10,000. Note that a few preliminary runs considered another Solar evaluation dataset in the literature of Arlandini+99 [33] which does report an error estimate for the *r*-process residuals. However in this case the error bars are especially small when compared to the sets pursued here, leading to a very large initial χ^2 of 6941.8. Such a high initial χ^2 implies that our Duflo-Zuker baseline mass model produces abundances very far off from the targeted Solar data, reported to be very precise in the Arlandini+99 case. Such a big initial discrepancy produced challenges to our current approach with all preliminary runs having a low acceptance rate. Such challenges could be overcome by, for example, exploring new baselines, but we leave such investigations to future work. Thus we concentrated our computational time on the Sneden+08 and Beer+97 cases since these already permit us to explore the influence of the unique features of each evaluation in terms of their error size and overall shape of the rare-earth peak. To provide a sense of the computational cost of a given MCMC result, we note that there are two main factors determining this: 1) the time to run the β-decay code which calculates the β-delayed neutron emission probabilities (~30 s) and 2) the time to run the nucleosynthesis network (PRISM), with both being performed for every timestep. Runtime for the network can take between 30 s and 3 min depending on whether we are considering an astrophysical scenario in which the fission products must be included in the network. Therefore a single MCMC run which takes 10,000 steps can translate into anywhere from ~2,000–10,000 core-hours depending on the speed of

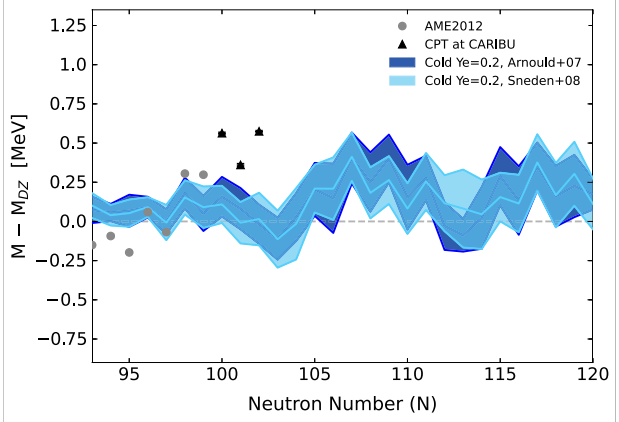

FIGURE 3
The MCMC predicted masses for samarium (Z =62) given the cold, moderately neutron-rich outflow with different sets of Solar data applied: those from Arnould+07 [29, 30] with symmeterized errors (as described in [15]) (dark blue, band derived from 50 runs) as well as the Solar residuals from Sneden+08 [32] (light blue, band derived from 25 runs) which differ in their prediction for the location of highest abundance in the rare-earths (A = 162 for [32] and A = 164 for [29, 30]).

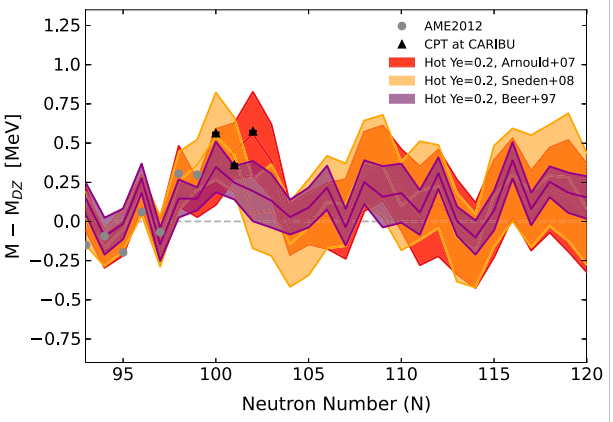

FIGURE 4
The MCMC predicted masses for samarium (Z =62) given the hot, moderately neutron-rich outflow with different sets of Solar data applied: those from Arnould+07 [29, 30] with symmeterized errors (as described in [15]) (red, band derived from 50 runs), those from Sneden+08 [32] (orange, band derived from 50 runs), and those reported in Beer+97 [31] (purple, band derived from 25 runs).

network calculation and the set-up of the computing cluster (this work made use of three distinct computing facilities). Therefore a 50 run band result ultimately requires ~100,000 to 500,000 core-hours depending on the scenario.

We now evaluate whether the Solar data applied modifies our previous conclusions regarding cold astrophysical scenarios being inconsistent with the latest mass measurements. As can be seen in Figure 3, the MCMC calculations with Arnould+07 and Sneden+08 give similar mass predictions in the cold case, with the mass surface behavior at N = 103 and N = 108 as the main features forming the peak consistently appearing in the trends of both calculations. As discussed in [15], the time evolution of peak formation in the cold case first starts with a shifted peak with highest abundance at A = 162, which is moved *via* late time neutron capture to having highest abundance at A = 164 as predicted by Arnould+07. Thus in the case of Sneden+08 data which peaks instead at A = 162, the MCMC mass solution does not have to be significantly modified as it can already accommodate an abundance pile-up at A = 162, leading to relatively minor mass differences near N = 100 where the Sneden+08 case requires some enhancement in the stability of such nuclear species in order to keep the highest abundance from shifting beyond A = 162. Most importantly, we find that the differing peak placement of these distinct r-process Solar residual evaluations does not present an avenue towards resolving the tension between the predicted masses and the latest mass measurements given this cold astrophysical outflow.

We next consider the impact of the Solar data on mass solutions in the hot astrophysical scenario. Our uncertainty bands are derived from 50 MCMC runs when applying Arnould+07 and Sneden+08 Solar data and in the case of Beer+97 data are determined from 25 runs. As can be seen in Figure 3 of [15], previous investigations demonstrated that a 20 run result can underestimate the total uncertainty band by at most 0.26 MeV or 0.05 MeV on average when considering the N = 93–110 range which influences rare-earth peak formation most strongly. For the 30 run case we find this underestimate to be only at most 0.06 MeV or 0.02 MeV on average. Therefore we estimate that our 25 run results likely underrepresent the reported total uncertainty by roughly 0.035–0.16 MeV, but still adequately capture the overall mass surface trends.

As discussed in [15], peak formation in the hot case centers around nuclei being held at neutron number N = 104 during the time evolution of the synthesis. To achieve this, in the case of Arnould+07 data, we require a strong difference in the predicted masses at N = 102 and N = 104 which can be seen as a dive in the mass surface shown in Figure 4. The latest precision measurements agree with this predicted N = 102 rise, however measurements fall just short of providing information on mass behavior at N = 104. Contrary to the result using Arnould+07 Solar data, the MCMC predictions when Sneden+08 data is applied show the drop in the mass surface is needed to instead begin at neutron number N = 100 in order for the highest abundance peak to be produced instead at A = 162. This behavior is also present in the predicted MCMC solution using the Solar data of Beer+97 since this case also requires higher abundances than Arnould+07 at A = 162, 163 and a lower abundance than Arounld+07 at A = 164. Since this drop in the predicted masses after N = 100 is inconsistent with CPT measurements, we find that Solar evaluations in which the rare-earth peak has its highest abundance at A < 164 to be in tension with

the latest mass data. Additionally, from Figure 4 we can see directly the influence of the size of the Solar data error bars. The case with Sneden+08 and Arnould+07 data show very similarly sized mass surface bands whereas significantly tighter mass surface bands are predicted in the Beer+97 case (even with accounting for the slight underestimate of the bands due to the smaller statistics of a 25 run result) which is consistent with expectations given that this set has the smallest error on average. Interestingly, we find that regardless of the differences in the Solar data values and overall errors, all MCMC solutions in hot scenarios predict a local region of enhanced stability at $N = 104$.

Here we demonstrated that studies, such as the MCMC work presented, which seek to be quantitative when using Solar abundance data are directly dependent upon a careful accounting of abundance uncertainties. The Solar *r*-process abundances are regularly used as a comparison point with theoretical nucleosynthesis calculations, however often the associated error on these abundances is not considered. Since the Solar *r*-process abundances are in actuality the 'residual' abundances remaining after subtracting the predicted *s*-process contribution from the total Solar inventory, our understanding of the Solar System *r*-process content is directly dependent on uncertainties in *s*-process nucleosynthesis predictions. More recent evaluations have demonstrated the importance of accounting for new neutron capture measurements [34] and more sophisticated treatments of the *s*-process astrophysical site [35]. Nevertheless, the *r*-process community remains in need of updated Solar *s*-process subtractions which put together all such new information while also carefully propagating the uncertainties associated with the meteoritic and spectroscopic data which are used to determine the total abundances of Solar System heavy elements.

The application of distinct Solar data evaluations reveals that the mass predictions of our MCMC are sensitive to both the location of the highest peak abundance as well as the abundance error estimates, such that both the predicted uncertainty bands and overall mass trends can be affected. Nevertheless, two important general conclusions from utilizing Arnould+07 Solar data in our previous MCMC work [15] remain robust, that is: (1) cold astrophysical outflows remain inconsistent with the latest mass measurements and (2) hot astrophysical outflows consistently point to a local enhancement in stability at $N = 104$ as the mechanism by which the rare-earth peak forms. This consistency further argues for the importance of mass measurements at this neutron number, as may be possible in the future at Argonne National Laboratory's $N = 126$ Factory, the Facility for Rare Isotopes Beams (FRIB), or the Advanced Rare Isotope Laboratory (ARIEL) at TRIUMF.

Since we have demonstrated that our MCMC method is sensitive to the overall shape and errors of the *r*-process abundances, our calculations permit us to consider what the masses of neutron-rich nuclei can teach us about Solar *r*-process evaluations. We find that in the case of Solar evaluations which predict the highest abundance of the rare-earth peak to occur before $A = 164$, our method points to the need for masses which are not consistent with the most recent measurements. Therefore, this result favors Solar *r*-process evaluations with the highest abundance of the rare-earth peak located at $A = 164$ as those which can be readily replicated given the latest nuclear data. We note that robust conclusions regarding Solar *r*-process abundances from such an MCMC approach require more exhaustively considering the uncertainties of all nuclear data inputs such as the β-decay strength function and neutron capture model. Therefore, since the interplay between β-decay, neutron capture, and photodissociation is at the heart of peak formation, future MCMC studies which consider other β-decay and neutron capture treatments when propagating mass changes to astrophysical reaction and decay rates could yield even more robust statements on whether the highest rare-earth peak abundance can occur at $A < 164$. We leave these investigations to future work, but note that such an approach could apply a more global analysis with both mass and β-decay measurements guiding the Markov chains and therefore informing uncertainty estimates. Nevertheless, the work presented here highlights how statistical methods such as our MCMC procedure can be used to explicitly link nuclear data and astrophysical observations, thereby serving to inform and drive progress in both nuclear physics and astrophysics communities.

Data availability statement

The raw data supporting the conclusions of this article will be made available by the authors, without undue reservation.

Author contributions

Development of the MCMC code was performed by MM and NV. The MCMC calculations and the analysis of results were performed by NV. NV was the primary author of the manuscript, with MM, GM, and RS participating in the writing process.

Funding

The work of NV acknowledges the support of the Natural Sciences and Engineering Research Council of Canada (NSERC). The work of NV, GM, MM, and RS was partly supported by the Fission In R-process Elements (FIRE) topical collaboration in nuclear theory, funded by the U.S. Department of Energy. RS and GM also acknowledge support by the US Department of Energy from grant LA22-ML-DE-FOA-2440. Additional support was provided by the U.S. Department of Energy through contract numbers DE-FG02-02ER41216 (GM), DE-FG02-95-ER40934 (R.S.), and DE-SC0018232 (SciDAC TEAMS collaboration, RS). RS and GM also acknowledge support by the National Science Foundation N3AS Hub Grant No.

PHY-1630782 and Physics Frontiers Center No. PHY-2020275. MM was supported by the US Department of Energy through the Los Alamos National Laboratory. Los Alamos National Laboratory is operated by Triad National Security, LLC, for the National Nuclear Security Administration of U.S. Department of Energy (Contract No. 89233218CNA000001). This work was partially enabled by the National Science Foundation under Grant No. PHY-1430152 (JINA Center for the Evolution of the Elements). This manuscript has been released via Los Alamos National Laboratory report number LA-UR-22-29364.

Acknowledgments

This work utilized the computational re- sources of the Laboratory Computing Resource Center at Argonne National Laboratory (ANL LCRC), the University of Notre Dame Center for Research Computing (ND CRC), as well as TRIUMF laboratory's Theory Group Cluster Oak (TRIUMF Oak). We specifically acknowledge the assistance of Stanislav Sergienko (ANL LCRC), Scott Hampton (ND CRC), and Kel Raywood (TRIUMF Oak).

Conflict of interest

The authors declare that the research was conducted in the absence of any commercial or financial relationships that could be construed as a potential conflict of interest.

Publisher's note

References

1. Abbott BP. Erratum: Upper limits on the stochastic gravitational-wave background from advanced LIGO's first observing run. *Phys Rev Lett* (2017) 119:029901. doi:10.1103/PhysRevLett.119.029901

2. Abbott BP, Abbott R, Abbott TD, Acernese F, Ackley K, Adams C, et al. Multi-messenger observations of a binary neutron star merger. *ApJL* (2017) 848:L12. doi:10.3847/2041-8213/aa91c9

3. Abbott BP, Abbott R, Abbott TD, et al. Erratum: Tests of general relativity with GW150914. *Phys Rev Lett* (2018) 121:129902. arXiv:1805.11581 [gr-qc]. doi:10.1103/PhysRevLett.121.129902

4. Villar VA, Guillochon J, Berger E, Metzger BD, Cowperthwaite PS, Nicholl M, et al. The combined ultraviolet, optical, and near-infrared light curves of the kilonova associated with the binary neutron star merger GW170817: Unified data set, analytic models, and physical implications. *Astrophys J* (2017) 851:L21. doi:10.3847/2041-8213/aa9c84

5. Cowperthwaite PS, Berger E, Villar VA, Metzger BD, Nicholl M, Chornock R, et al. Electromagnetic counterpart of the binary neutron star merger LIGO/Virgo GW170817. II. UV, optical, and near-infrared light curves and comparison to kilonova models. *ApJL* (2017) 848:L17. doi:10.3847/2041-8213/aa8fc7

6. Lodders K. Principles and perspectives in cosmochemistry. *Astrophysics Space Sci Proc* (2010) 16:379.

7. Frebel A. From nuclei to the cosmos: Tracing heavy-element production with the oldest stars. *Annu Rev Nucl Part Sci* (2018) 68:237–69. doi:10.1146/annurev-nucl-101917-021141

8. Mumpower MR, Surman R, Fang DL, Beard M, Möller P, Kawano T, et al. Impact of individual nuclear masses onr-process abundances. *Phys Rev C* (2015) 92:035807. doi:10.1103/physrevc.92.035807

9. Eichler M, Arcones A, Kelic A, Korobkin O, Langanke K, Marketin T, et al. The role of fission in neutron star mergers and its impact on ther-process peaks. *ApJ* (2015) 808:30. doi:10.1088/0004-637x/808/1/30

10. Goriely S. Towards more accurate and reliable predictions for nuclear applications. *Eur Phys J A* (2015) 51:172. doi:10.1140/epja/i2015-15172-2

11. Vassh N, Vogt R, Surman R, Randrup J, Sprouse TM, Mumpower MR, et al. Using excitation-energy dependent fission yields to identify key fissioning nuclei in *r*-process nucleosynthesis. *J Phys G: Nucl Part Phys* (2019) 46:065202. doi:10.1088/1361-6471/ab0bea

12. Mumpower MR, McLaughlin GC, Surman R, Steiner AW. The link between rare-earth peak formation and the astrophysical site of therprocess. *ApJ* (2016) 833:282. doi:10.3847/1538-4357/833/2/282

13. Mumpower MR, McLaughlin GC, Surman R, Steiner AW. Reverse engineering nuclear properties from rare Earth abundances in therprocess. *J Phys G: Nucl Part Phys* (2017) 44:034003. doi:10.1088/1361-6471/44/3/034003

14. Orford R, Vassh N, Clark JA, McLaughlin GC, Mumpower MR, Savard G, et al. Precision mass measurements of neutron-rich neodymium and samarium Isotopes and their role in understanding rare-earth peak formation. *Phys Rev Lett* (2018) 120:262702. doi:10.1103/physrevlett.120.262702

15. Vassh N, McLaughlin GC, Mumpower MR, Surman R. Markov chain Monte Carlo predictions of neutron-rich lanthanide properties as a probe of *r*-process dynamics. *ApJ* (2021) 90798(2021):98. doi:10.3847/1538-4357/abd035

16. Orford R, Vassh N, Clark JA, McLaughlin GC, Mumpower MR, Ray D, et al. Searching for the origin of the rare-Earth peak with precision mass measurements across Ce–Eu isotopic chains. *Phys Rev C* (2022) 105:L052802. doi:10.1103/physrevc.105.l052802

17. Vassh N, McLaughlin GC, Mumpower MR, Surman R. The need for a local nuclear physics feature in the neutron-rich rare-earths to explain Solar r-process abundances. *arXiv e-prints*, arXiv:2202.09437 (2022). doi:10.48550/arxiv.2202.09437

18. Burbidge EM, Burbidge GR, Fowler WA, Hoyle F. Synthesis of the elements in stars. *Rev Mod Phys* (1957) 29:547–650. doi:10.1103/revmodphys.29.547

19. Surman R, Engel J, Bennett JR, Meyer BS. Source of the rare-earth element peak inr-process nucleosynthesis. *Phys Rev Lett* (1997) 79:1809–12. doi:10.1103/physrevlett.79.1809

20. Mumpower MR, McLaughlin GC, Surman R. Formation of the rare-Earth peak: Gaining insight into late-timer-process dynamics. *Phys Rev C* (2012) 85:045801. doi:10.1103/physrevc.85.045801

21. Duflo J, Zuker AP. Microscopic mass formulas. *Phys Rev C* (1995) 52:R23–7. doi:10.1103/physrevc.52.r23

22. Audi G, Wang M, Wapstra AH, Kondev FG, MacCormick M, Xu X, et al. The Ame2012 atomic mass evaluation. *Chin Phys C* (2012) 36:1287–602. doi:10.1088/1674-1137/36/12/002

23. Perego A, Rosswog S, Cabezón RM, Korobkin O, Käppeli R, Arcones A, et al. Neutrino-driven winds from neutron star merger remnants. *Mon Not R Astron Soc* (2014) 443:3134–56. doi:10.1093/mnras/stu1352

24. Just O, Bauswein A, Pulpillo RA, Goriely S, Janka H-T. Comprehensive nucleosynthesis analysis for ejecta of compact binary mergers. *Mon Not R Astron Soc* (2015) 448:541–67. doi:10.1093/mnras/stv009

25. Radice D, Perego A, Hotokezaka K, Fromm SA, Bernuzzi S, Roberts LF. Binary neutron star mergers: Mass ejection, electromagnetic counterparts, and nucleosynthesis. *ApJ* (2018) 869:130. doi:10.3847/1538-4357/aaf054

26. Foucart F, Duez MD, Hebert F, Kidder LE, Pfeiffer HP, Scheel MA. Monte-carlo neutrino transport in neutron star merger simulations. *Astrophys J* (2020) 902: L27. doi:10.3847/2041-8213/abbb87

27. Reichert M, Obergaulinger M, Eichler M, Aloy MÁ, Arcones A. *Mon Not R Astron Soc* (2021) 501:5733.

28. Mösta P, Roberts LF, Halevi G, Ott CD, Lippuner J, Haas R, et al. *r*-Process nucleosynthesis from three-dimensional magnetorotational core-collapse supernovae. *ApJ* (2018) 864:171. doi:10.3847/1538-4357/aad6ec

29. Arnould M, Goriely S, Takahashi K. The r-process of stellar nucleosynthesis: Astrophysics and nuclear physics achievements and mysteries. *Phys Rep* (2007) 450: 97–213. doi:10.1016/j.physrep.2007.06.002

30. Goriely S. *Astron Astrophys* (1999) 342:881.

31. Beer H, Corvi F, Mutti P. Neutron capture of the bottleneck Isotopes^{138}Ba and ^{208}Pb, *s*-process studies, and ther-process abundance distribution. *Astrophys J* (1997) 474:843–61. doi:10.1086/303480

32. Sneden C, Cowan JJ, Gallino R. Neutron-capture elements in the early galaxy. *Annu Rev Astron Astrophys* (2008) 46:241–88. doi:10.1146/annurev.astro.46.060407.145207

33. Arlandini C, Käppeler F, Wisshak K, Gallino R, Lugaro M, Busso M, et al. Neutron capture in low-mass asymptotic giant Branch stars: Cross sections and abundance signatures. *Astrophys J* (1999) 525:886–900. arXiv:astro-ph/9906266 [astro-ph]. doi:10.1086/307938

34. Pritychenko B. Determination of solar system R-process abundances using ENDF/B-VIII.0 and TENDL-2015 libraries. *aXiv e-prints*, aXiv e-prints, arXiv: 2012.06728 [astro-ph.SR] (2020). doi:10.48550/arxiv.2012.06728

35. Prantzos N, Abia C, Cristallo S, Limongi M, Chieffi A. Chemical evolution with rotating massive star yields II. A new assessment of the solar s- and r-process components. *Mon Not R Astron Soc* (2020) 491:1832. arXiv:1911.02545 [astro-ph.GA]

frontiers | Frontiers in Physics

TYPE Review
PUBLISHED 06 January 2023
DOI 10.3389/fphy.2022.1066035

OPEN ACCESS

EDITED BY
Christian Forssén,
Chalmers University of Technology,
Sweden

REVIEWED BY
Robert B. Wiringa,
Argonne National Laboratory (DOE),
United States
Xavier Roca Maza,
University of Milan, Italy

*CORRESPONDENCE
Sonia Bacca,
s.bacca@uni-mainz.de

SPECIALTY SECTION
This article was submitted to Nuclear Physics, a section of the journal Frontiers in Physics

RECEIVED 10 October 2022
ACCEPTED 21 December 2022
PUBLISHED 06 January 2023

CITATION
Acharya B, Bacca S, Bonaiti F, Li Muli SS and Sobczyk JE (2023), Uncertainty quantification in electromagnetic observables of nuclei.
Front. Phys. 10:1066035.
doi: 10.3389/fphy.2022.1066035

Uncertainty quantification in electromagnetic observables of nuclei

Bijaya Acharya[1,2], Sonia Bacca[1,3]*, Francesca Bonaiti[1], Simone Salvatore Li Muli [1] and Joanna E. Sobczyk[1]

[1]Institut für Kernphysik and PRISMA⁺Cluster of Excellence, Johannes Gutenberg Universität, Mainz, Germany, [2]Physics Division, Oak Ridge National Laboratory, Oak Ridge, TN, United States, [3]Helmholtz-Institut Mainz, Johannes Gutenberg Universität Mainz, Mainz, Germany

We present strategies to quantify theoretical uncertainties in modern *ab initio* calculations of electromagnetic observables in light and medium-mass nuclei. We discuss how uncertainties build up from various sources, such as the approximations introduced by the few- or many-body solver and the truncation of the chiral effective field theory expansion. We review the recent progress encompassing a broad range of electromagnetic observables in stable and unstable nuclei.

KEYWORDS

uncertainty quantification, electromagnetic processes, *ab initio* theory, chiral effective field theory, few- and many-body systems

1 Introduction

Uncertainty quantification is an emerging field in nuclear theory. It is nowadays expected for any theoretical calculation of nuclear observables to have a corresponding uncertainty bar, which is vital to make progress in our understanding of strongly interacting systems through the comparison of theoretical modeling with experimental data. While this is clearly the goal, the specific approach to uncertainty quantification and its sophistication level strongly depends on the used theoretical method and on the observables under investigation. In this review, we focus on electromagnetic reactions and on how they can be calculated with corresponding uncertainty in the so-called *ab initio* methods. It is fair to say that the sub-field of quantification of theoretical uncertainties is just now developing, and while there is still much to be done there has been recent significant progress. Here, we report on such progress, discuss its philosophy and identify areas where improvements can be expected in the future.

In the *ab initio* approach to nuclear theory [1–3] the goal is to explain nuclear phenomena, including electromagnetic processes, starting from protons and neutrons as degrees of freedom and to solve the related quantum-mechanical problem in a numerical way, either exactly or within controlled approximations. To achieve this, one typically solves the Schrödinger equation for a given Hamiltonian H and then computes transition matrix elements of the electromagnetic operator J^{μ} between the eigenstates of H. Hence, before discussing the approach devised to quantify uncertainties in electromagnetic observables, we define the dynamical ingredients (Hamiltonian and currents), as well as the specific observables we want to investigate.

1.1 Hamiltonians and currents

The starting point of an *ab initio* computation of a nucleus composed of A nucleons is the nuclear Hamiltonian,

$$H = T_K + \sum_{i<j}^{A} V_{ij} + \sum_{i<j<k}^{A} W_{ijk}, \tag{1}$$

where T_K is the intrinsic kinetic energy, V_{ij} is the two-body interaction and W_{ijk} is the three-body interaction. As opposed to a phenomenological derivation of nuclear forces, effective field theories (EFT) offer a more systematic approach [4]. In this paper, we will use effective Hamiltonians which are derived in chiral effective field theory (χEFT) [5–7]. In this framework, the Hamiltonian is expanded in powers of (Q/Λ), where Q is the typical low–momentum characterizing nuclear physics and Λ is the breakdown scale of the effective field theory. The various components relevant for V_{ij} and W_{ijk} are presented in terms of Feynman diagrams in Figure 1, where ν_0 is the first power entering in the counting. The unresolved short range physics is encoded in the values of the low energy constants (LECs), which are usually calibrated by fitting to experimental data. Different optimization and fitting strategies have been used to calibrate the LECs [8–11]. Here, we will use only a selected set of different Hamiltonians obtained from χEFT. Furthermore, interactions with explicit Δ degrees of freedom are becoming available [12–17] and should be explored. In the present work we will present results with both chiral Δ-full and Δ-less interactions.

The nuclear response to external probes is described by the interaction Hamiltonian, which depends on nuclear dynamics through the nuclear current operator. The χEFT expansion exists also for the electromagnetic four-vector current $J^\mu = (\rho, \mathbf{J})$, where the time-like component is the charge operator and the space-like component is the three-vector current operator. The first diagrams entering the χEFT expansion for $(\rho, \mathbf{J})$ are shown in Figure 1, where we omit the diagrams that contribute to the elastic form factors. The reader can find more details on our implementation of the currents in Ref. [18]. While different authors adopt different power counting schemes for the currents [19–22], we follow the conventions of Ref. [22].

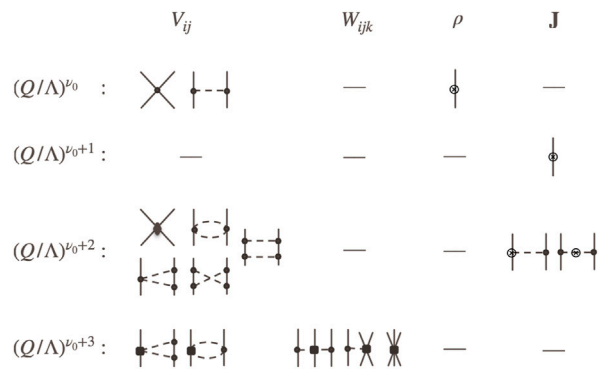

FIGURE 1
The χEFT expansion of the nuclear Hamiltonian and electromagnetic currents. The filled circles, squares and diamond denote strong-interaction vertices with chiral dimension 0,1 and 2, respectively. The $\otimes$ symbols denote the electromagnetic vertices. In the literature, ν_0 is usually taken as 0 for the potential and −3 for the currents.

1.2 Electromagnetic observables

Electromagnetic probes are key tools to study nuclear structure because measured cross sections are easily related to the few-/many-body matrix elements of electromagnetic operators *via* perturbation theory. Here, we focus on electromagnetic observables that can be explained to high precision in first order perturbation theory, i.e., processes where one single photon is exchanged between the probe and the nucleus. This is the case for the photoabsorption process and the electron scattering process, see Figure 2. The exchanged photon can in general transfer energy ω and momentum $\mathbf{q}$. In the photonuclear process, a real photon with $\omega = |\mathbf{q}| = q$ is absorbed by the nucleus, while in electron scattering a virtual photon is exchanged, where one can vary ω and q independently.

In the cases of the photoabsorption and the electron-scattering process (see also Sections 3, 5), the cross section can be written in terms of a so-called response function, which, in the inclusive unpolarized case, is defined as

$$R(\omega, q) = \sum_{\bar{0}f} \int \left| \langle \Psi_f | \Theta(q) | \Psi_0 \rangle \right|^2 \delta\left(E_f - E_0 - \omega\right). \tag{2}$$

Here, $\Theta(q)$ is the electromagnetic operator, which can be directly one of the operators $(\rho, \mathbf{J})$ or can be just a multipole of them. $|\Psi_{0/f}\rangle$ are the ground state and the excited states of the Hamiltonian H, respectively. The symbol $\sum_{\bar{0}}$ indicates an average on the initial angular momentum projection, while the symbol $\int_f$ corresponds to both a sum over discrete excited states and an integral over continuum eigenstates of the Hamiltonian. Indeed, $|\Psi_f\rangle$ may include not only bound excited states, but also states in the continuum where the nucleus is broken up into fragments.

The calculation of continuum wave functions represents a challenging task especially in an inclusive process, where one needs information on all possible fragmentation channels of the nucleus at a given energy. To avoid the issue, one can use integral transforms, such

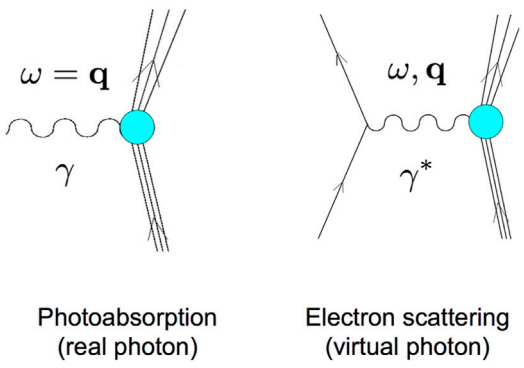

FIGURE 2
Feynman diagrams for the photoabsorption process (left), where a real photon γ is exchanged, and the electron scattering process, where a virtual photon γ^* is exchanged between the probe and the nucleus (cyan blob).

as the Lorentz integral transform (LIT) technique [23, 24]. Originally used in few-body calculations, the LIT technique is based on the calculation of the following integral of the response function $R(\omega, q)$,

$$L(\sigma, \Gamma, q) = \frac{\Gamma}{\pi}\int d\omega \ \frac{R(\omega, q)}{(\omega - \sigma)^2 + \Gamma^2}, \tag{3}$$

which can be shown to be the squared norm of the solution of a Schrödinger-like equation calculated using bound-state techniques. Once $L(\sigma, \Gamma, q)$ is calculated, a numerical inversion procedure allows one to recover $R(\omega, q)$, see Ref. [24] for details.

1.3 Numerical solvers

In order to calculate electromagnetic observables, we first need a numerical solution of the Schrödinger equation. In the applications discussed in Sections 3, 4 and 5, we will use either few-body or many-body solvers depending on the mass range A of the addressed nuclei.

We obtain the bound-state and scattering-state wave functions for the $A = 2$ problem by solving the partial-wave Lippmann-Schwinger equations for the Hamiltonian. The response functions are then calculated by directly evaluating the matrix elements of the electromagnetic operator in coordinate space.

To calculate few-body problems with $2 < A < 8$ we use hyperspherical harmonics expansions. In this framework, one expands the A-body intrinsic wave function in terms of hyperspherical harmonics $\mathcal{H}_K$ and hyperradial functions R_n as

$$\Psi = \sum_{K}^{K_{max}} \sum_{n}^{n_{max}} \alpha_{nK} R_n(\rho_r) \mathcal{H}_K(\Omega), \tag{4}$$

where α_{nK} are the coefficients of the expansion and where for the sake of simplicity we omit spin and isospin degrees of freedom. Here, ρ_r is the hyperradius while Ω is a set of hyperangles, on which the hyperspherical harmonics $\mathcal{H}_K$ with grandangular momentum K depend. The expansion is performed up to a maximal value of hyperradial functions n_{max} and a maximal value of grandangular momentum K_{max}. Reaching convergence in n_{max} is typically not difficult. The expansion in hyperspherical harmonics is instead more delicate and one needs to ensure that the dependence of the calculated observables on this truncation is under control. To accelerate convergence, an effective interaction a la Lee-Suzuki can be introduced [25], obtaining the so-called effective interaction hyperspherical harmonics (EIHH) method, which allows to eventually achieve sub-percentage accuracy in the ^{4}He calculations of binding energies and electromagentic observables [26]. Hyperspherical harmonics expansions can be conveniently used also to solve the Schrödinger-like equation obtained when applying the LIT method described above. The interested reader can consult, e.g., Refs. [2, 24–28] for more details.

For nuclei with $A \geq 8$ we use coupled-cluster theory. In this framework, for a given Hamiltonian H one starts from a Slater determinant $|\Phi_0\rangle$ of single particle states and assumes an exponential ansatz to construct the correlated many-body wave function as

$$|\Psi_0\rangle = \exp(T)|\Phi_0\rangle. \tag{5}$$

The operator T is typically expanded in n-particle-n-hole excitations (or clusters) as $T = T_1 + T_2 + \cdots + T_A$. Coupled-cluster theory is exact when the expansion of the T operator is considered up to A particle—A hole excitations (Ap–Ah) within a model space determined by the number N_{max} of oscillator shells considered [29]. Even though truncations are typically introduced, they can lead to a result very close to the exact one due to the exponential ansatz Eq. 5). Because the computational cost of this method scales polynomially with increasing mass number A, it is a very convenient solver for medium mass and even heavy nuclei [30].

For closed (sub-) shell nuclei, coupled-cluster theory truncated at the $2p$–$2h$ level, in the so called coupled-cluster singles and doubles (CCSD) scheme, captures about 90% of the full correlation energy. When including triples excitation, even at the leading order in the so-called CCSDT-1 scheme [31], one can obtain almost 97% of the correlation energy [29, 32]. It has been shown that coupled-cluster theory can be also used in conjunction with the LIT method, where one can reduce the problem to the solution of a bound-state like equation of motion [33].

2 Uncertainty quantification

In each of our computations of electromagnetic observables, the final accuracy will be controlled on the one hand by the employed χEFT (determined by Hamiltonian and currents) and on the other hand by the accuracy to which one can solve the few–body or many–body problem for a given Hamiltonian and current operator. Hence, in the following we will divide the sources of uncertainties in two broad categories:

1) χEFT uncertainties;
2) Numerical uncertainties.

Among the uncertainties in 1), there are possible dependencies on the employed interaction or current model (including cutoff dependencies), as well as uncertainties introduced by the truncation to a given order ν of the employed χEFT, and uncertainties due to extracting the LECs from experimental data or from lattice calculations. If the LECs are well constrained by experimental data, the χEFT uncertainty is typically dominated by the truncation error of the χEFT expansion. Regarding the latter, if the leading non-vanishing contribution to a calculated observable $\mathcal{O}$ enters at order ν_0 and one is able to perform calculations that include all effects up to order ν_0+k, one can naively expect to incur a relative error of $\delta_{\mathcal{O}}^{\chi\text{EFT}}/\mathcal{O} \approx (Q/\Lambda)^{k+1}$ from the neglected higher-order terms. A more rigorous estimate can be obtained by using the calculated order-by-order results $\mathcal{O}_\nu$ as "data" to inform the uncertainty analysis. For example, using the simple algorithm proposed by Ref. [34], the absolute truncation error can be estimated as

$$\delta_{\mathcal{O}}^{\chi\text{EFT}} = \max\left\{\left(\frac{Q}{\Lambda}\right)^{k+1}|\mathcal{O}_{\nu_0}|, \left(\frac{Q}{\Lambda}\right)^{k}|\mathcal{O}_{\nu_0+1} - \mathcal{O}_{\nu_0}|, \ldots, \left(\frac{Q}{\Lambda}\right)|\mathcal{O}_{\nu_0+k} - \mathcal{O}_{\nu_0+k-1}|\right\}. \tag{6}$$

More recently, Bayesian methods have been adopted for quantification of the χEFT truncation error [35–38]. These methods start from Bayesian priors that encode naturalness of the coefficients $\{c_\nu\}$ defined, using a suitable reference $\mathcal{O}_{\text{ref}}$, by

$$\mathcal{O}_{\nu_0+k} = \mathcal{O}_{\text{ref}} \sum_{\nu=0}^{k} c_\nu \left(\frac{Q}{\Lambda}\right)^{\nu}. \tag{7}$$

The priors are then updated using the calculated data to arrive at a Bayesian posterior for the truncation error $\delta_{\mathcal{O}}^{\chi\text{EFT}}$. A key advantage of this approach is that the estimates have a statistical interpretation, which allows us to validate the assumptions made and to easily combine truncation errors with other sources of uncertainties such as fitting or random sampling of parameters. This opens a possible path for a complete and consistent accounting of theory uncertainty from all dynamical ingredients in the future.

Regarding the uncertainties in 2), the protocol to evaluate them will depend on the implemented numerical solver. On the one hand, when performing a few-body calculations with hyperspherical harmonics, one needs to carefully take the convergence in K_{max} into account. When using the LIT method, one also needs to consider the uncertainty of the inversion procedure. On the other hand, when using coupled-cluster theory, one needs to account for at least two different patterns of convergence. First, there is always a truncation on the model space controlled by the maximum number of harmonic oscillator (HO) shells N_{max}, which, in a sense, is analogous to the K_{max} in hyperspherical harmonics. If convergence in N_{max} is reached, the results should in principle be independent of the underlying HO frequency $\hbar\Omega$ used for single particle states. However, in practice, one is always left with some residual $\hbar\Omega$ dependence which should be explored. Second, in coupled-cluster theory one has a cluster expansion of the operator T. Here, the most frequently adopted approximation is CCSD. When possible, one should include higher order excitations, such as leading order triples corrections with CCSDT-1. Finally, when using the LIT method, one incurs the extra numerical uncertainty coming from the inversion procedure.

In general, we expect uncertainties of 2) to be sub–percentage or at most one percent in light nuclei up to mass number 4, while for medium–mass nuclei they may increase up to a few percent, depending on the specific observable. In particular, it is to note that binding energies, because of their eigenvalue nature, can usually be obtained with higher precision, while for example quadrupole transitions are notoriously difficult in methods such as coupled-cluster theory or in-medium similarity renormalization group [39]. Beyond the lightest nuclei, whether the uncertainties of 1) dominate over those of 2) may, in principle, depend on the specific system/observable considered. Experience has shown so far that uncertainties related to the χEFT 1) are typically the largest. We will compare the specific contributions in each example below.

3 Photoabsorption cross section

Photoabsorption cross sections have been extensively studied using *ab initio* techniques, especially in the sector of light nuclei, see Ref. [2] and references therein. The photoabsorption cross section is related to the response function by

$$\sigma_\gamma(\omega) = \frac{4\pi^2}{\omega}\alpha R_T(\omega,\omega), \tag{8}$$

where $R_T(\omega,\omega)$ is the response function of Eq. 2 where the Θ operator is the transverse (with respect to photon propagation) part of the electromagnetic current operator $\mathbf{J}$ and where $\omega = q$. In the unretarded dipole approximation, the cross section can be obtained from

$$\sigma_\gamma(\omega) = 4\pi^2\alpha\omega R_D(\omega), \tag{9}$$

where $R_D(\omega)$ is the response function of the electric dipole operator D (acting only on the Z protons) in the long wavelength approximation, defined as

$$D = \sum_i^Z (z_i - Z_{cm}), \tag{10}$$

where z_i and Z_{cm} are the z-components of the ith particle and center-of-mass coordinates, respectively.

Below, we will discuss two examples. First, we will deal with the radiative capture reaction $np \to \gamma$d reaction, which is important for astrophysics and is related to the photoabsorption reaction γd $\to np$ by time-reversal. Next, we will discuss the inclusive photoabsorption of ^{4}He, for which we will present new original results obtained with chiral forces at four different orders, including an analysis of its uncertainties.

3.1 The $n\,p \leftrightarrow \gamma$d reaction

The primordial Deuterium abundance, which is very well constrained by astronomical [44] and cosmological [45] observations, can also be determined from nuclear physics by measuring or calculating the rates of the Deuterium production and burning reactions of the big-bang-nucleosynthesis network. While there is a reasonable agreement between these at the moment [46], a higher-precision comparison will search more rigorously for potential conflict which will be indicative of missing physics in one or the other and may even hint at new physics beyond the Standard Model. This elevates the importance of uncertainty quantification in the primordial Deuterium production reaction, $np \to \gamma$d.

In the relevant energy regime, $M1$ and $E1$ transitions are both important; we, therefore, evaluate the cross section using the full response function $R_T(\omega,\omega)$ with the one- and two-body current operators shown in Figure 1. The uncertainties associated with the solution of the Schrödinger equation and other numerical approximations are negligible for this system. We therefore focus on χEFT uncertainties for this reaction. Working with fixed currents, we used the semi-local momentum-space-regularized chiral interactions of Ref. [47] to study the convergence properties of the χEFT expansion of the nuclear potential in Ref. [48]. We employed the Gaussian Process (GP) error model developed in Ref. [49] to perform a Bayesian analysis of the χEFT convergence for observables that have parametric dependence on a kinematic variable, which in this case is the np relative momentum. We performed detailed diagnostic checks to quantitatively assess the adequacy of the GP model and found that it described the observed convergence very well, which allowed us to extract reliable Bayesian posteriors for $\delta_{\mathcal{O}}^{\chi\text{EFT}}$ at various orders.

In Figure 3, we show the 95% degree-of-belief bands for calculations at next-to-leading order (NLO), next-to-next-to-leading order (N2LO) and next-to-next-to-next-to-leading order (N3LO) obtained by using the leading order (LO) result as the reference $\mathcal{O}_{\text{ref}}$ (see Eq. 7). We note that the theory uncertainty from the truncation of χEFT at N2LO and N3LO are much smaller than experimental errors at the energy range of astrophysical relevance. The uncertainty from truncation of the current operator is a subject of future study.

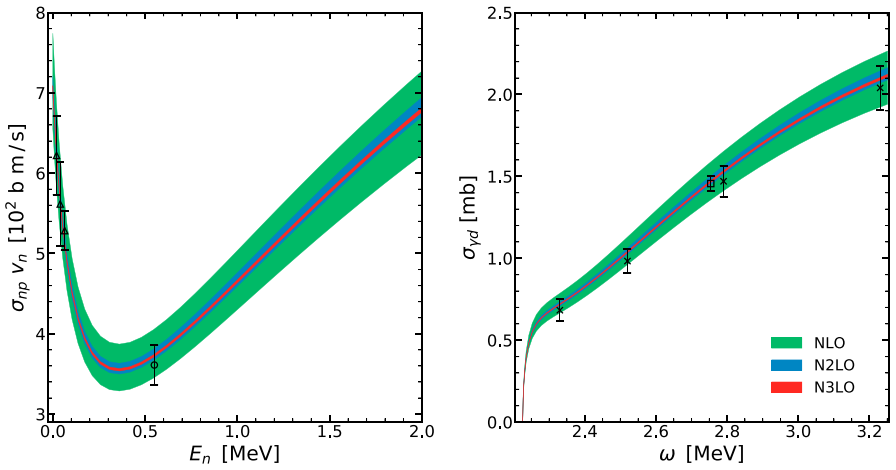

FIGURE 3
The product of p $(n, \gamma)d$ cross section σ_{np} and the neutron speed v_n *versus* the neutron energy E_n (left panel); and the deuteron photodissociation cross section $\sigma_{\gamma d}$ as a function of the photon energy ω in the rest frame of the deuteron (right panel). The bands indicate 95% Bayesian degree-of-belief intervals at the various orders. Experimental data are from Ref. [40] (triangles) [41] (circle) [42] (crosses) and [43] (square). Experimental errors in beam-energy resolution are not shown.

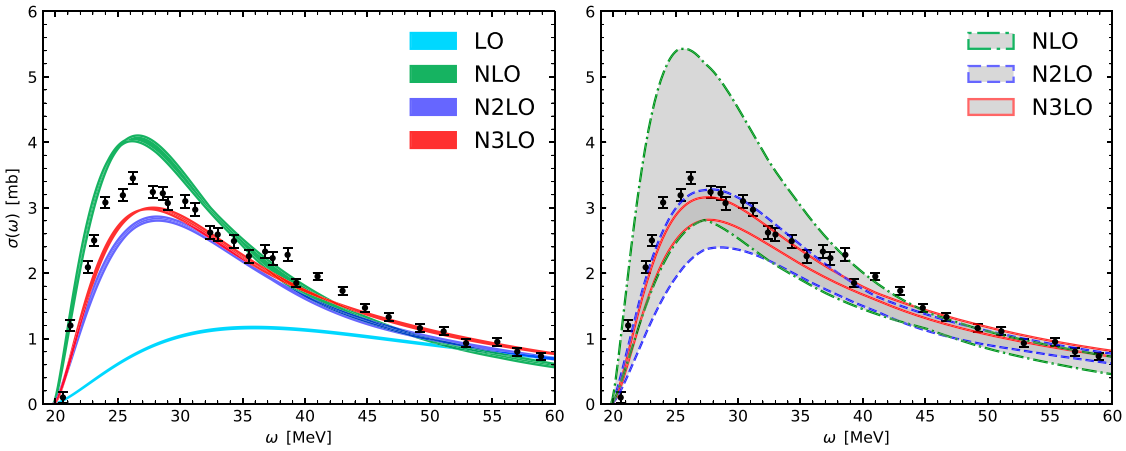

FIGURE 4
Inclusive ^{4}He photoabsorption cross section calculated at different order in the chiral interaction. Left panel: bands display the numerical uncertainty in the inversion of the LIT. Right panel: bands display the χEFT truncation uncertainty, estimated using Eq. 6. The experimental data are taken from Ref. [61].

3.2 The γ^4He $\rightarrow X$ reaction

The photodisintegration cross section of ^{4}He has been a focus of several past studies [50–55]. In this work, we provide new original results for this reaction obtained within the frameworks of χEFT using the EIHH [25, 56, 57] as a solver. We start from Eq. 9 and keep the dipole operator fixed, while changing the nuclear interaction in the Hamiltonian implementing different orders in the chiral expansion. We work up to N2LO with a maximally local version of the chiral interaction developed for the first time in Refs. [58–60], which we previously adapted to the EIHH method in Ref. [26]. In the same spirit of our work in the $n\,p \leftrightarrow \gamma$d reaction, the uncertainty coming from the numerical solution of the Schrödinger equation is neglected here, since the EIHH method has been proven to be very precise for three- and four-body systems, with uncertainties that usually are below the percent level.

To bypass the explicit calculation of the continuum wave functions, the electric dipole response $R_D(\omega)$ of Eq. 9 is obtained by first computing its LIT and then performing the inversion. This introduces a numerical uncertainty of the order of 1%–2%, which can be seen in Figure 4 (left panel), where we present the calculation of $\sigma_\gamma(\omega)$ at LO, NLO, N2LO and N3LO in different colors. The width of the band is the uncertainty introduced by the inversion.

To assess uncertainty coming from the truncation of the chiral expansion, we start from the calculations of $\sigma_\gamma(\omega)$ at the various chiral orders and implement the algorithm in Eq. 6, which requires a choice for the expansion parameter Q/Λ. A reasonable choice for Q is obtained by a smooth max-function (see Eq. 46 of Ref. [49]) of m_π

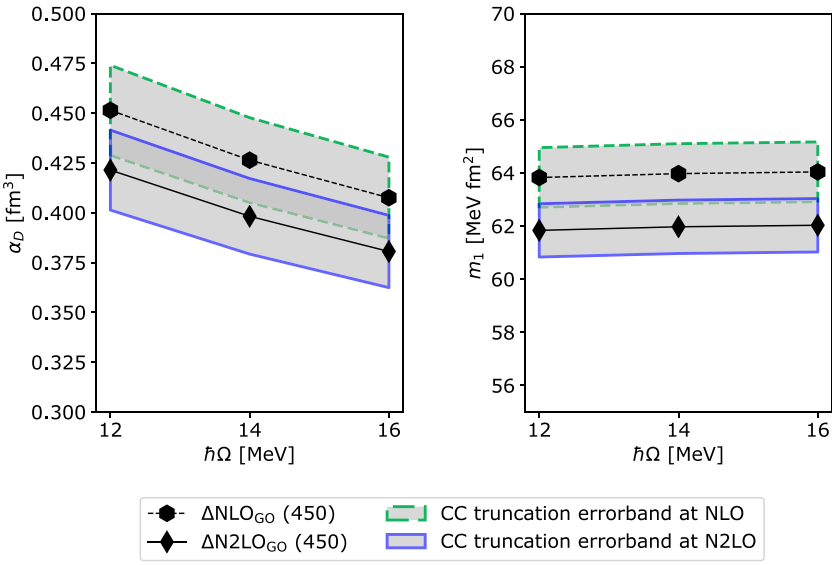

FIGURE 5
The $\hbar\Omega$-convergence pattern of α_D and m_1 for ^{8}He calculated with ΔNLO$_{GO}$ (450) and ΔN2LO$_{GO}$ (450) at fixed N_{max} =14. The green and blue bands indicate the CC truncation uncertainty. The black points are the results obtained including 3*p*-3*h* excitations in both the ground- and excited-state computations.

and $p_{rel} = \sqrt{2\mu\omega}$, where m_π is the pion-mass and μ is the reduced mass of the main photodisintegration channel, for which we take p–^{3}H. For the breakdown scale Λ we conservatively take 500 MeV, which yields an expansion parameter for the χEFT consistent with Ref. [62]. When implementing Eq. 6, we go beyond our calculations with local chiral interactions which go all the way up to N2LO, and also consider the partial N3LO calculation from Ref. [54] and use it to estimate the uncertainty also at this order.

In Figure 4 (right panel), we show the cross section with corresponding χEFT uncertainty at the NLO, N2LO and N3LO orders. For every order the threshold energies are shifted to the experimental value. Clearly, the χEFT errors account for the largest portion of the overall uncertainty budget with respect to the numerical inversion uncertainty, which are therefore not even included in the right panel of Figure 4. The χEFT truncation errors are such that the calculated photoabsorption cross section at each order is consistent with the previous order within its uncertainties, as well as with the experimental data from Ref. [61]. At NLO we get an uncertainty at the cross section maximum of roughly 30% (half width), while at N2LO it is 15% (half width). Finally, the N3LO band, which is roughly 5% (half width), is located slightly below the shown experimental data. To facilitate comparison of theory with experiment, we have chosen to show only one representative set of data [61], which covers a wide range in energy. More data exist than are shown here, see, e.g., Ref. [2] and references therein.

4 Electromagnetic sum rules

Starting from the nuclear response function, one can compute electromagnetic sum rules, i.e., the moments of the response function of Eq. 2 interpreted as a distribution function. These quantities are defined as

$$m_n(q) = \int d\omega\ \omega^n R(\omega, q), \tag{11}$$

where n is an integer. Sum rules can be calculated directly from the LIT. Since for $\Gamma \to 0$, the limit of a Lorentzian corresponds to a delta function, we get

$$L(\sigma, \Gamma \to 0, q) = \int d\omega\ R(\omega, q)\delta(\omega - \sigma) = R(q, \sigma). \tag{12}$$

This means that the moments of $R(\omega, q)$ can be obtained from the following expression

$$m_n(q) = \int d\sigma\ \sigma^n L(\sigma, \Gamma \to 0, q). \tag{13}$$

As illustrated in Ref. [63], this procedure is equivalent to the computation and subsequent integration of the response. Moreover, this strategy does not require an inversion, which represents an additional source of uncertainty.

Among the sum rules, the electric dipole polarizability α_D is an interesting one, as it is correlated to parameters in the neutron-matter equation of state [64]. The electric dipole polarizability can be obtained starting from the inverse-energy weighted sum rule

$$\alpha_D = 2\alpha \int d\omega\ \frac{R_D(\omega)}{\omega} = 2\alpha m_{-1}, \tag{14}$$

where m_{-1} is calculated using Eq. 11 and $R_D(\omega)$ is the response function of the dipole operator in the long wavelength approximation. From Eq. 14, it is clear that the polarizability is dominated by the low-energy part of the response function.

In a recent work [65], we performed coupled-cluster computations of dipole-excited state properties of the halo nucleus ^{8}He, focusing on α_D and the energy-weighted sum rule m_1 using χEFT potentials derived at N2LO. Our calculations

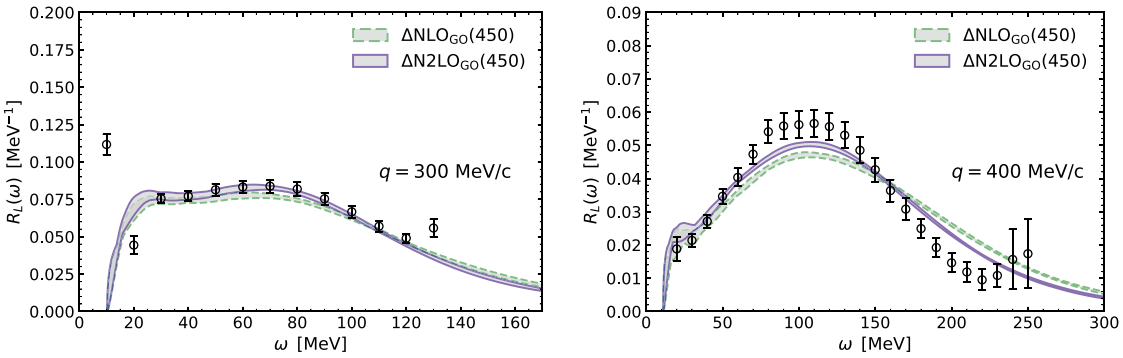

FIGURE 6
Longitudinal response functions of ^{40}Ca for the momentum transfer q =300 MeV/c (left panel) and q =400 MeV/c (right panel). Two orders of the chiral expansion of the nuclear Hamiltonian are shown. The uncertainty band originates from the inversion procedure of the LITs. The experimental data are taken from Ref. [67].

included an estimate of the theoretical uncertainty related to the model space convergence in N_{max} and to the truncation of the coupled-cluster expansion, according to the strategy illustrated in Ref. [66]. Regarding the first source of uncertainty, the maximum available model space is $N_{max} = 14$, so we consider the residual $\hbar\Omega$-dependence at this N_{max} as the uncertainty in the model space expansion. To assess the uncertainty in the coupled-cluster expansion, we take two different approximation schemes, the CCSD and the CCSDT-1, since we have no higher order coupled-cluster approximations available. The truncation uncertainty is then estimated taking half of the difference between the CCSD and CCSDT-1 results. The two contributions are then summed in quadrature.

To complement our previous analysis, we consider in this work the dependence on the order of the χEFT expansion in the case of the Δ-full interaction model, by providing a new calculation at a lower order (NLO). In Figure 5, we show the $\hbar\Omega$ convergence pattern of α_D and m_1 for the ΔNLO$_{GO}$ (450) and ΔN2LO$_{GO}$ (450) potentials [17], indicating with bands the contribution of the coupled-cluster truncation uncertainty. In the case of the dipole polarizability, the theoretical error receives substantial contributions from both the many-body method and the residual dependence on the coupled-cluster convergence parameters. The polarizability is sensitive to the outer part of the nuclear wave function, and this makes the convergence slower for a loosely-bound system like ^{8}He. ΔNLO$_{GO}$ (450) predicts a slightly larger polarizability with respect to ΔN2LO$_{GO}$ (450). Taking into account the uncertainty budget coming from the many-body solver (around 7% of the central value), the two results come out to agree within errobars.

The situation changes when turning to the energy-weighted sum rule. Here the overall uncertainty is dominated by the coupled-cluster truncation and it is estimated to be below 2%. Also in this case ΔNLO$_{GO}$ (450) leads to a larger value for m_1. However, due to the smooth convergence of this observable, the difference between the two chiral orders, amounting to 3%, can be better appreciated than in the case of the polarizability. At the moment it is possible only to compute two orders in the χEFT expansion, namely the NLO and N2LO, therefore we refrain from using the algorithm of Eq. 6 in this case. Clearly, the uncertainty analysis is then less sophisticated than for the $A = 2, 4$ nuclei, but it is reassuring to see that the NLO and N2LO error bands overlap.

5 Electron scattering cross section

Electron scattering has proven to be a powerful tool to investigate the nuclear structure and dynamics at various energy scales and for different systems. Very recently we started investigating the region of the quasielastic peak which becomes a dominating mechanism for the momentum transfer of the order of hundreds of MeV, below the pion production threshold. The inclusive electron-nucleus cross section can be expressed as

$$\frac{d^2\sigma}{d\Omega d\omega} = \sigma_{\text{Mott}}\left(\frac{\mathbf{q}^2-\omega^2}{\mathbf{q}^2}R_L(\omega,q) + \left(\frac{\mathbf{q}^2-\omega^2}{2\mathbf{q}^2} + \tan^2\frac{\theta}{2}\right)R_T(\omega,q)\right) \tag{15}$$

with the longitudinal and transverse response functions $R_{L/T}$ and the scattering angle θ. The response functions can be disentangled experimentally *via* the Rosenbluth separation technique. From the theoretical point of view, it is convenient to investigate first the longitudinal component, which is the response function of Eq. 2 where the operator $\Theta(q)$ is the charge operator

$$\rho(q) = \sum_{i=1}^{Z} e^{iq(z_i - Z_{cm})}. \tag{16}$$

Typically, then nucleon form factors are folded in (see e.g. Ref. [68]). The operator structure of ρ is simpler than that of the electromagnetic current $\mathbf{J}$ and two-body contributions appear at a high order in the chiral expansion (see Figure 1), so that it can be neglected if performing studies up to N2LO. While the *ab initio* calculations of R_L in light systems were performed in several theoretical frameworks, we recently extended these studies to the region of medium-mass nuclei [69]. We focused on ^{40}Ca, for which Rosenbluth separated response functions are available, using two different N2LO potentials [9, 17]. Here, we complement our uncertainty analysis by performing a new calculation with an NLO potential.

Similarly to the photoabsorption considered in Section 3.2, the calculation of R_L requires computing the LITs which afterwards

have to be inverted, introducing an additional source of uncertainty with respect to the sum-rule calculation. We obtain the LITs using coupled-cluster theory within the CCSD approximation. The role played by $3p$–$3h$ excitations will be a topic of the future investigation. We calculate R_L using a single model space of $N_{\max} = 14$ and harmonic oscillator frequency $\hbar\Omega = 16$ MeV. In our previous work [69] we varied the frequency of the underlying harmonic oscillator basis and its size and we found that the LITs are already well converged. In this situation, the numerical uncertainty is driven by the inversion procedure which is represented by the band shown in Figure 6.

To assess the uncertainty coming from the χEFT expansion we look at the dependence on the order of expansion of the Δ-full potential [17] at NLO and N2LO. In Figure 6 we present R_L for q = 300 MeV/c (left panel) and q = 400 MeV/c (right panel). At q = 300 MeV/c the predictions of $\Delta\text{NLO}_{\text{GO}}$ (450) and $\Delta\text{N2LO}_{\text{GO}}$ (450) agree to great extent within the uncertainty bands and with the data. In contrast, at q = 400 MeV, the uncertainty bands of $\Delta\text{NLO}_{\text{GO}}$ (450) and $\Delta\text{N2LO}_{\text{GO}}$ (450) overlap less and the agreement with data slightly deteriorates. When comparing the two interactions, we see that the $\Delta\text{N2LO}_{\text{GO}}$ (450) leads to a slightly higher and narrower quasielastic peak with respect to the $\Delta\text{NLO}_{\text{GO}}$ (450) (the difference of around 8% in the peak for q = 400 MeV/c), bringing the results closer to the data as the chiral order increases. Because a quantitative analysis would require more than two orders of the χEFT Hamiltonian, we refrain here from applying Eq. 6, which would only contain one term.

At the qualitative level, we observe that the size of the uncertainties of kind *1*) and *2*) are comparable, and those of kind *1*) seem to depend on the momentum transfer and grow at larger q value. This is, after all, not surprising, because χEFT is expected to work better at low momenta than at higher momenta.

6 Conclusion

In this paper, we review the recent progress made in uncertainty quantification for *ab initio* calculations of electromagnetic observables focusing on the one hand on our recent results and on the other hand providing also new original results to complement the uncertainty analysis. We show several examples where nuclei of different masses are scrutinized.

We first showcase the recent computations of the $n\ p \leftrightarrow \gamma$d reaction, where an uncertainty analysis of the χEFT truncation with Bayesian tools was implemented. Then, we show new results for the photoabsoprtion cross section of ^{4}He computed with χEFT potentials at LO, NLO and N2LO. The uncertainty quantification we present is based on the use of Eq. 6 and pushed to N3LO using the results from Ref. [54]. For both these examples in the sector of light nuclei, we find that numerical uncertainties are negligible and the bulk of the error stems from the truncation of the χEFT expansion. Next, we discuss sum rules in the exotic ^{8}He nucleus, where we confront the existing calculation at N2LO with a new computation at NLO in the χEFT expansion using Δ degrees of freedom. Here, we see that numerical uncertainties and χEFT truncation errors are comparable in size. Finally, we show results for the longitudinal response function of ^{40}Ca using the same interactions we used for ^{8}He. Also in this case, the uncertainty stemming from the χEFT truncation seems comparable to that coming from the numerical solver. It is important to note here that we are not yet able to fully account for the numerical uncertainties, because we have not yet included $3p$–$3h$ excitations. Furthermore, we only have two orders in the χEFT so a quantitative uncertainty cannot yet be reliably estimated. Interestingly, we qualitatively observe a momentum-transfer dependence in the difference between the calculation at NLO and N2LO, which is not unexpected given that χEFT is a low-momentum expansion. A precise quantitative description of the dependence of the χEFT expansion on the momentum transfer, which is obscured by the fact that we use phenomenological form factors to represent photon-nucleon vertices, is a subject of future study.

Clearly, the level of sophistication of our uncertainty quantification is higher for lighter nuclei and decreases as the mass grows. The most rigorous analysis was performed for A = 2, where we were able to express the truncation errors as Bayesian degree-of-belief intervals. For the range of $A \simeq 4$ one can expect that a Bayesian analysis will be implemented in the future. A quantitative analysis of nuclei with $A \geq 8$ will need more effort. We expect LO calculations to be far from experimental data for these nuclei, but if one wants to go beyond N2LO in the χEFT expansion, one would need consistent potentials that are soft enough for many-body calculations to converge. Moreover, to fully assess uncertainties in electromagnetic observables, one must also consider the χEFT expansion in the current and in the interaction simultaneously. Examples of how one can vary the χEFT expansion in the current operators can be found in the literature for example in Refs. [2, 70] and reference therein. Another consideration to take into account in a full uncertainty quantification is the variation between different χEFTs, i.e., different regularization schemes [38] or different degrees of freedom [15]. Here, we have explored only a few options and obviously more work in this direction needs to be done by the whole community. Finally, in the future statistical approaches for the variation of the LECs such as those shown in Ref. [30] should be applied broadly to the study of electroweak dynamical observables, such as response functions and cross sections.

Author contributions

All authors contributed in equal parts to this paper. BA led in the deuteron calculations, SSL the ^{4}He calculations, FB the ^{8}He calculations, and JES together with BA performed the ^{40}Ca calculations. While SB took the main responsibility for the drafting of the paper, all authors contributed to the writing of the manuscript.

Funding

This work was supported by the Deutsche Forschungsgemeinschaft (DFG) through Project-ID 279384907 - SFB 1245 and through the Cluster of Excellence "Precision Physics, Fundamental Interactions, and Structure of Matter" (PRISMA$^+$ EXC 2118/1) funded by the DFG within the German Excellence Strategy (Project ID 39083149). BA's work at ORNL is supported by the Neutrino Theory Network Fellowship Program (Grant No. DE-AC02-07CH11359). JES acknowledges the support of the

Humboldt Foundation through a Humboldt Research Fellowship for Postdoctoral Researchers and funding from the European Union's Horizon 2020 research and innovation programme under the Marie Skłodowska-Curie grant agreement No. 101026014. Computer time was provided by the Innovative and Novel Computational Impact on Theory and Experiment (INCITE) program and by the supercomputer Mogon at Johannes Gutenberg Universität Mainz. This research used resources of the Oak Ridge Leadership Computing Facility located at ORNL, which is supported by the Office of Science of the Department of Energy under Contract No. DE-AC05-00OR22725.

Acknowledgments

We would like to acknowledge Weiguang Jiang for sharing the matrix elements for the $\Delta\text{NLO}_{\text{GO}}(450)$ potential with us. We would like to thank Nir Barnea and Gaute Hagen for access to the hyperspherical harmonics and coupled-cluster codes, respectively. Finally, we would like to thank Thomas R. Richardson for a critical reading of the manuscript.

Conflict of interest

The authors declare that the research was conducted in the absence of any commercial or financial relationships that could be construed as a potential conflict of interest.

Publisher's note

References

1. Leidemann W, Orlandini G. Modern ab initio approaches and applications in few-nucleon physics with $A \geq 4$. *Prog Part Nucl Phys* (2013) 68:158–214. doi:10.1016/j.ppnp.2012.09.001

2. Bacca S, Pastore S. Electromagnetic reactions on light nuclei. *J Phys G: Nucl Part Phys* (2014) 41:123002. doi:10.1088/0954-3899/41/12/123002

3. Hebeler K, Holt JD, Menéndez J, Schwenk A. Nuclear forces and their impact on neutron-rich nuclei and neutron-rich matter. *Ann Rev Nucl Part Sci* (2015) 65:457–84. doi:10.1146/annurev-nucl-102313-025446

4. Hammer HW, Furnstahl R. Effective field theory for dilute fermi systems. *Nucl Phys A* (2000) 678:277–94. doi:10.1016/S0375-9474(00)00325-0

5. Weinberg S. Nuclear forces from chiral Lagrangians. *Phys Lett B* (1990) 251:288–92. doi:10.1016/0370-2693(90)90938-3

6. Epelbaum E, Hammer HW, Meißner UG. Modern theory of nuclear forces. *Rev Mod Phys* (2009) 81:1773–825. doi:10.1103/RevModPhys.81.1773

7. Machleidt R, Entem D. Chiral effective field theory and nuclear forces. *Phys Rep* (2011) 503:1–75. doi:10.1016/j.physrep.2011.02.001

8. Ekström A, Baardsen G, Forssén C, Hagen G, Hjorth-Jensen M, Jansen GR, et al. Optimized chiral nucleon-nucleon interaction at next-to-next-to-leading order. *Phys Rev Lett* (2013) 110:192502. doi:10.1103/PhysRevLett.110.192502

9. Ekström A, Jansen GR, Wendt KA, Hagen G, Papenbrock T, Carlsson BD, et al. Accurate nuclear radii and binding energies from a chiral interaction. *Phys Rev C* (2015) 91:051301. doi:10.1103/PhysRevC.91.051301

10. Navarro Pérez R, Amaro JE, Ruiz Arriola E. Statistical error analysis for phenomenological nucleon-nucleon potentials. *Phys Rev C* (2014) 89:064006. doi:10.1103/PhysRevC.89.064006

11. Piarulli M, Girlanda L, Schiavilla R, Pérez RN, Amaro JE, Arriola ER. Minimally nonlocal nucleon-nucleon potentials with chiral two-pion exchange including Δ resonances. *Phys Rev C* (2015) 91:024003. doi:10.1103/PhysRevC.91.024003

12. Kaiser N, Gerstendörfer S, Weise W. Peripheral nn-scattering: Role of delta-excitation, correlated two-pion and vector meson exchange. *Nucl Phys A* (1998) 637:395–420. doi:10.1016/S0375-9474(98)00234-6

13. Krebs H, Epelbaum E, Meißner UG. Nuclear forces with Δ excitations up to next-to-next-to-leading order, part i: Peripheral nucleon-nucleon waves. *Eur Phys J A* (2007) 32:127–37. doi:10.1140/epja/i2007-10372-y

14. Epelbaum E, Krebs H, Meißner UG. Δ-excitations and the three-nucleon force. *Nucl Phys A* (2008) 806:65–78. doi:10.1016/j.nuclphysa.2008.02.305

15. Piarulli M, Girlanda L, Schiavilla R, Kievsky A, Lovato A, Marcucci LE, et al. Local chiral potentials with Δ-intermediate states and the structure of light nuclei. *Phys Rev C* (2016) 94:054007. doi:10.1103/PhysRevC.94.054007

16. Ekström A, Hagen G, Morris TD, Papenbrock T, Schwartz PD. Δ isobars and nuclear saturation. *Phys Rev C* (2018) 97:024332. doi:10.1103/PhysRevC.97.024332

17. Jiang WG, Ekström A, Forssén C, Hagen G, Jansen GR, Papenbrock T. Accurate bulk properties of nuclei from $a = 2$ to ∞ from potentials with Δ isobars. *Phys Rev C* (2020) 102:054301. doi:10.1103/PhysRevC.102.054301

18. Acharya B, Bacca S. Neutrino-deuteron scattering: Uncertainty quantification and new $L_{1,\,A}$ constraints. *Phys Rev C* (2020) 101:015505. doi:10.1103/PhysRevC.101.015505

19. Pastore S, Schiavilla R, Goity JL. Electromagnetic two-body currents of one- and two-pion range. *Phys Rev* (2008) C78:064002. doi:10.1103/PhysRevC.78.064002

20. Pastore S, Girlanda L, Schiavilla R, Viviani M, Wiringa RB. Electromagnetic currents and magnetic moments in chiral effective field theory (χeft). *Phys Rev C* (2009) 80:034004. doi:10.1103/PhysRevC.80.034004

21. Kölling S, Epelbaum E, Krebs H, Meißner UG. Two-pion exchange electromagnetic current in chiral effective field theory using the method of unitary transformation. *Phys Rev C* (2009) 80:045502. doi:10.1103/PhysRevC.80.045502

22. Phillips DR. Electromagnetic structure of two- and three-nucleon systems: An effective field theory description. *Annu Rev Nucl Part Sci* (2016) 66:421–47. doi:10.1146/annurev-nucl-102014-022321

23. Efros VD, Leidemann W, Orlandini G. Response functions from integral transforms with a lorentz kernel. *Phys Lett B* (1994) 338:130–3. doi:10.1016/0370-2693(94)91355-2

24. Efros VD, Leidemann W, Orlandini G, Barnea N. The lorentz integral transform (lit) method and its applications to perturbation-induced reactions. *J Phys G: Nucl Part Phys* (2007) 34:R459–528. doi:10.1088/0954-3899/34/12/r02

25. Barnea N, Leidemann W, Orlandini G. State dependent effective interaction for the hyperspherical formalism. *Phys Rev C* (2000) 61:054001. doi:10.1103/PhysRevC.61.054001

26. Li Muli SS, Bacca S, Barnea N. Implementation of local chiral interactions in the hyperspherical harmonics formalism. *Front Phys* (2021) 9. doi:10.3389/fphy.2021.671869

27. Barnea N, Novoselsky A. Hyperspherical wave functions with orthogonal and permutational symmetry. *Phys Rev A* (1998) 57:48–58. doi:10.1103/PhysRevA.57.48

28. Ji C, Bacca S, Barnea N, Hernandez OJ, Dinur NN. *Ab initio* calculation of nuclear-structure corrections in muonic atoms. *J Phys G: Nucl Part Phys* (2018) 45:093002. doi:10.1088/1361-6471/aad3eb

29. Hagen G, Papenbrock T, Dean DJ, Hjorth-Jensen M, Asokan BV. *Ab initio* computation of neutron-rich oxygen isotopes. *Phys Rev C* (2009) 80:021306. doi:10.1103/PhysRevC.80.021306

30. Hu B, Jiang W, Miyagi T, Sun Z, Ekström A, Forssén C, et al. *Ab initio* predictions link the neutron skin of ^{208}Pb to nuclear forces *Nature Phys* (2022) 18(10):1196–1200. doi:10.1038/s41567-022-01715-8

31. Watts JD, Gauss J, Bartlett RJ. Coupled-cluster methods with noniterative triple excitations for restricted open-shell Hartree–Fock and other general single determinant reference functions. energies and analytical gradients. *J Chem Phys* (1993) 98:8718–33. doi:10.1063/1.464480

32. Bartlett RJ, Musiał M. Coupled-cluster theory in quantum chemistry. *Rev Mod Phys* (2007) 79:291–352. doi:10.1103/RevModPhys.79.291

33. Bacca S, Barnea N, Hagen G, Orlandini G, Papenbrock T. First principles description of the giant dipole resonance in ^{16}**O**. *Phys Rev Lett* (2013) 111:122502. doi:10.1103/PhysRevLett.111.122502

34. Epelbaum E, Krebs H, Meißner UG. Precision nucleon-nucleon potential at fifth order in the chiral expansion. *Phys Rev Lett* (2015) 115:122301. doi:10.1103/PhysRevLett.115.122301

35. Schindler M, Phillips D. Bayesian methods for parameter estimation in effective field theories. *Ann Phys* (2009) 324:682–708. doi:10.1016/j.aop.2008.09.003

36. Furnstahl RJ, Phillips DR, Wesolowski S. A recipe for EFT uncertainty quantification in nuclear physics. *J Phys G: Nucl Part Phys* (2015) 42:034028. doi:10.1088/0954-3899/42/3/034028

37. Ekström A. Analyzing the nuclear interaction: Challenges and new ideas. *Front Phys* (2020) 8. doi:10.3389/fphy.2020.00029

38. Epelbaum E, Krebs H, Reinert P. High-precision nuclear forces from chiral eft: State-of-the-art, challenges, and outlook. *Front Phys* (2020) 8. doi:10.3389/fphy.2020.00098

39. Stroberg SR, Henderson J, Hackman G, Ruotsalainen P, Hagen G, Holt JD. Systematics of *e*2 strength in the *sd* shell with the valence-space in-medium similarity renormalization group. *Phys Rev C* (2022) 105:034333. doi:10.1103/PhysRevC.105.034333

40. Suzuki T, Nagai Y, Shima T, Kikuchi T, Sato H, Kii T, et al. First measurement of a *p(n, γ)d* reaction cross section between 10 and 80 kev. *Astrophysical J* (1995) 439:L59. doi:10.1086/187744

41. Nagai Y, Suzuki TS, Kikuchi T, Shima T, Kii T, Sato H, et al. Measurement of ^{1}H(*n*, *γ*)^{2}H reaction cross section at a comparable *M*1/*E*1 strength. *Phys Rev C* (1997) 56:3173–9. doi:10.1103/PhysRevC.56.3173

42. Hara KY, Utsunomiya H, Goko S, Akimune H, Yamagata T, Ohta M, et al. Photodisintegration of deuterium and big bang nucleosynthesis. *Phys Rev D* (2003) 68:072001. doi:10.1103/PhysRevD.68.072001

43. Moreh R, Kennett TJ, Prestwich WV. ^{2}H(*γ*, n) absolute cross section at 2754 kev. *Phys Rev C* (1989) 39:1247–50. doi:10.1103/PhysRevC.39.1247

44. Cooke RJ, Pettini M, Steidel CC. One percent determination of the primordial deuterium abundance. *Astrophys J* (2018) 855:102. doi:10.3847/1538-4357/aaab53

45. Aghanim N, Akrami Y, Ashdown M, Aumont J, Baccigalupi C, Ballardini M, et al. Planck 2018 results. VI. Cosmological parameters. *Astron Astrophys* (2020) 641:A6. [Erratum: Astron.Astrophys. 652, C4 (2021)]. doi:10.1051/0004-6361/201833910

46. Pisanti O, Mangano G, Miele G, Mazzella P. Primordial deuterium after LUNA: Concordances and error budget. *JCAP* (2021) 04:020. doi:10.1088/1475-7516/2021/04/020

47. Reinert P, Krebs H, Epelbaum E. Semilocal momentum-space regularized chiral two-nucleon potentials up to fifth order. *Eur Phys J A* (2018) 54:86. doi:10.1140/epja/i2018-12516-4

48. Acharya B, Bacca S. Gaussian process error modeling for chiral effective-field-theory calculations of $np \leftrightarrow dy$ at low energies. *Phys Lett B* (2022) 827:137011. doi:10.1016/j.physletb.2022.137011

49. Melendez JA, Furnstahl RJ, Phillips DR, Pratola MT, Wesolowski S. Quantifying correlated truncation errors in effective field theory. *Phys Rev C* (2019) 100:044001. doi:10.1103/PhysRevC.100.044001

50. Ellerkmann G, Sandhas W, Sofianos SA, Fiedeldey H. Integral equation calculations for the photodisintegration process ^{4}He(*γ*, *n*)^{3}He. *Phys Rev C* (1996) 53:2638–44. doi:10.1103/PhysRevC.53.2638

51. Efros VD, Leidemann W, Orlandini G. Is there a pronounced giant dipole resonance in ^{4}*he*? *Phys Rev Lett* (1997) 78:4015–8. doi:10.1103/PhysRevLett.78.4015

52. Barnea N, Efros VD, Leidemann W, Orlandini G. Total ^{4}He photoabsorption cross section reexamined: Correlated versus effective interaction hyperspherical harmonics. *Phys Rev C* (2001) 63:057002. doi:10.1103/PhysRevC.63.057002

53. Quaglioni S, Leidemann W, Orlandini G, Barnea N, Efros VD. Two-body photodisintegration of ^{4}He with full final state interaction. *Phys Rev C* (2004) 69:044002. doi:10.1103/PhysRevC.69.044002

54. Quaglioni S, Navrátil P. The 4he total photo-absorption cross section with two-plus three-nucleon interactions from chiral effective field theory. *Phys Lett B* (2007) 652:370–5. doi:10.1016/j.physletb.2007.06.082

55. Gazit D, Bacca S, Barnea N, Leidemann W, Orlandini G. Photoabsorption on ^{4}He with a realistic nuclear force. *Phys Rev Lett* (2006) 96:112301. doi:10.1103/PhysRevLett.96.112301

56. Barnea N, Efros VD, Leidemann W, Orlandini G. Incorporation of three-nucleon force in the effective-interaction hyperspherical-harmonic approach. *Few-Body Syst* (2004) 35:155–67. doi:10.1007/s00601-004-0066-y

57. Barnea N, Leidemann W, Orlandini G. Improved effective interaction for the hyperspherical formalism. *Phys Rev C* (2003) 67:054003. doi:10.1103/PhysRevC.67.054003

58. Gezerlis A, Tews I, Epelbaum E, Freunek M, Gandolfi S, Hebeler K, et al. Local chiral effective field theory interactions and quantum Monte Carlo applications. *Phys Rev C* (2014) 90:054323. doi:10.1103/PhysRevC.90.054323

59. Lynn J, Tews I, Carlson J, Gandolfi S, Gezerlis A, Schmidt K, et al. Chiral three-nucleon interactions in light nuclei, neutron-α scattering and neutron matter. *Phys Rev Lett* (2016) 116:062501. doi:10.1103/PhysRevLett.116.062501

60. Lynn J, Tews I, Carlson J, Gandolfi S, Gezerlis A, Schmidt KE, et al. Quantum Monte Carlo calculations of light nuclei with local chiral two- and three-nucleon interactions. *Phys Rev C* (2017) 96:054007. doi:10.1103/PhysRevC.96.054007

61. Arkatov YM, Vatset P. I., Voloshuchuk V. I., Zolenko V. I., Prokhorets I. M., Chimil V. I. *Sov J Nucl Phys* (1974) 19:598.

62. Wesolowski S, Svensson I, Ekström A, Forssén C, Furnstahl RJ, Melendez JA, et al. Rigorous constraints on three-nucleon forces in chiral effective field theory from fast and accurate calculations of few-body observables. *Phys Rev C* (2021) 104:064001. doi:10.1103/PhysRevC.104.064001

63. Miorelli M, Bacca S, Barnea N, Hagen G, Jansen GR, Orlandini G, et al. Electric dipole polarizability from first principles calculations. *Phys Rev C* (2016) 94:034317. doi:10.1103/PhysRevC.94.034317

64. Roca-Maza X, Brenna M, Colò G, Centelles M, Viñas X, Agrawal BK, et al. Electric dipole polarizability in208Pb: Insights from the droplet model. *Phys Rev C* (2013) 88:024316. doi:10.1103/PhysRevC.88.024316

65. Bonaiti F, Bacca S, Hagen G. *Ab initio* coupled-cluster calculations of ground and dipole excited states in ^{8}He. *Phys Rev C* (2022) 105:034313. doi:10.1103/PhysRevC.105.034313

66. Simonis J, Bacca S, Hagen G. First principles electromagnetic responses in medium-mass nuclei - recent progress from coupled-cluster theory. *Eur Phys J A* (2019) 55:241. doi:10.1140/epja/i2019-12825-0

67. Williamson CF, Yates TC, Schmitt WM, Osborn M, Deady M, Zimmerman PD, et al. Quasielastic electron scattering from40Ca. *Phys Rev C* (1997) 56:3152–72. doi:10.1103/PhysRevC.56.3152

68. Bacca S, Arenhövel H, Barnea N, Leidemann W, Orlandini G. Inclusive electron scattering off ^{4}He. *Phys Rev C* (2007) 76:014003. doi:10.1103/PhysRevC.76.014003

69. Sobczyk JE, Acharya B, Bacca S, Hagen G. *Ab initio* computation of the longitudinal response function in ^{40}Ca. *Phys Rev Lett* (2021) 127:072501. doi:10.1103/PhysRevLett.127.072501

70. Krebs H. Nuclear currents in chiral effective field theory. *Eur Phys J A Eur* (2020) 56:234. doi:10.1140/epja/s10050-020-00230-9

71. Richardson TR, Schindler MR. Large-N_c analysis of magnetic and axial two-nucleon currents in pionless effective field theory. *Phys Rev C* (2020) 101:055505. doi:10.1103/PhysRevC.101.055505

frontiers | Frontiers in Physics

TYPE Original Research
PUBLISHED 06 January 2023
DOI 10.3389/fphy.2022.1054524

OPEN ACCESS

EDITED BY
Maria Piarulli,
Washington University in St. Louis, United States

REVIEWED BY
Nicolas Schunck,
Lawrence Livermore National Laboratory (DOE), United States
Ragnar Stroberg,
University of Notre Dame, United States

*CORRESPONDENCE
Pablo Giuliani,
giulia27@msu.edu
Kyle Godbey,
godbey@frib.msu.edu
Edgard Bonilla,
edgard@stanford.edu
Frederi Viens,
viens@msu.edu
Jorge Piekarewicz,
jpiekarewicz@fsu.edu

†These authors have contributed equally to this work and share first authorship

SPECIALTY SECTION
This article was submitted to Nuclear Physics, a section of the journal Frontiers in Physics

RECEIVED 26 September 2022
ACCEPTED 09 November 2022
PUBLISHED 06 January 2023

CITATION
Giuliani P, Godbey K, Bonilla E, Viens F and Piekarewicz J (2023), Bayes goes fast: Uncertainty quantification for a covariant energy density functional emulated by the reduced basis method. *Front. Phys.* 10:1054524. doi: 10.3389/fphy.2022.1054524

Bayes goes fast: Uncertainty quantification for a covariant energy density functional emulated by the reduced basis method

Pablo Giuliani[1,2*†], Kyle Godbey[1*†], Edgard Bonilla[3*], Frederi Viens[2,4*] and Jorge Piekarewicz[5*]

[1]FRIB/NSCL Laboratory, Michigan State University, East Lansing, MI, United States, [2]Department of Statistics and Probability, Michigan State University, East Lansing, MI, United States, [3]Department of Physics, Stanford University, Stanford, CA, United States, [4]Rice University, Department of Statistics, Houston, TX, United States, [5]Department of Physics, Florida State University, Tallahassee, FL, United States

A covariant energy density functional is calibrated using a principled Bayesian statistical framework informed by experimental binding energies and charge radii of several magic and semi-magic nuclei. The Bayesian sampling required for the calibration is enabled by the emulation of the high-fidelity model through the implementation of a reduced basis method (RBM)—a set of dimensionality reduction techniques that can speed up demanding calculations involving partial differential equations by several orders of magnitude. The RBM emulator we build—using only 100 evaluations of the high-fidelity model—is able to accurately reproduce the model calculations in tens of milliseconds on a personal computer, an increase in speed of nearly a factor of 3,300 when compared to the original solver. Besides the analysis of the posterior distribution of parameters, we present model calculations for masses and radii with properly estimated uncertainties. We also analyze the model correlation between the slope of the symmetry energy L and the neutron skin of ^{48}Ca and ^{208}Pb. The straightforward implementation and outstanding performance of the RBM makes it an ideal tool for assisting the nuclear theory community in providing reliable estimates with properly quantified uncertainties of physical observables. Such uncertainty quantification tools will become essential given the expected abundance of data from the recently inaugurated and future experimental and observational facilities.

KEYWORDS

bayesian, reduced basis method (RBM), relativistic mean field (RMF) theory, nuclear physics, density functional theory

1 Introduction

Nuclear science is undergoing a transformational change enabled by the commissioning of new experimental and observational facilities as well as dramatic advances in high-performance computing [1]. The newly operational Facility for Rare Isotope Beams (FRIB), together with other state-of-the-art facilities throughout the world, will produce short-lived isotopes that provide vital information on the creation of the heavy elements in the cosmos. In turn, earth and space-based telescopes operating across the entire electromagnetic spectrum will constrain the nuclear dynamics in regimes inaccessible in terrestrial laboratories. Finally, improved and future gravitational-wave detectors will provide valuable insights into the production sites of the heavy elements as well as on the properties of ultra-dense matter at both low and finite temperatures [2–9].

To fully capitalize on the upcoming discoveries, a strong synergy will need to be further developed between theory, experiment, and observation. First, theory is needed to decode the wealth of information contained in the new experimental and observational data. Second, new measurements drive new theoretical advances which, in turn, uncover new questions that motivate new experiments. From the theoretical perspective, sophisticated and highly-accurate *ab initio* methods have been developed to solve the complicated many-body problem. Besides the adoption of a many-body solver, one needs to specify a nuclear interaction that is informed by two- and three-nucleon data. A highly successful approach relies on a nuclear interaction rooted in chiral effective field theory (EFT). Chiral EFT—a theoretical framework inspired by the underlying symmetries of QCD—provides a systematic and improvable expansion in terms of a suitable small parameter, defined as the ratio of the length scale of interest to the length scale of the underlying dynamics [10–12]. During the last decade, enormous progress has been made in our understanding of the equation of state (EOS) of pure neutron matter by systematically improving the chiral expansion [13–19]. However, the chiral expansion breaks down once the relevant energy scale of the problem becomes comparable to the hard scale associated with the underlying dynamics. This fact alone precludes the use of chiral perturbation theory in the study of high density matter.

A more phenomenological approach that could be extended to higher densities is Density Functional Theory (DFT). Developed in quantum chemistry [20] but now widely used in nuclear physics, DFT is a powerful technique whose greatest virtue is shifting the focus away from the complicated many-body wave function that depends on the spatial coordinates of all particles, to an energy density functional (EDF) that depends only on the three spatial coordinates of the ground state density. Moreover, DFT guarantees that both the exact ground-state density and energy of the complicated many-body system may be obtained from minimizing a suitable functional [21, 22]. In an effort to simplify the solution of the problem, the Kohn–Sham formalism reformulates the DFT problem in favor of one-particle orbitals that may be obtained by solving self-consistently a set of equations that closely resemble the structure of the well-known Hartree equations [22]. It is important to note that the theorems behind DFT offer no guidance on how to construct the correct EDF. This fact is mitigated in nuclear physics by incorporating as many physical insights as possible into the construction of the functional, and then calibrating the parameters of the model by using the available experimental and observational data. However, unlike chiral EFT, DFT is unable to quantify systematic errors associated with missing terms in the functional that may become important at higher densities. Nevertheless, given that modern covariant EDFs are informed by the existence of two-solar mass neutron stars, the parameters of the model encode (at least partially) information on the high-density component of the EOS.

The calibrated models are not static, however, and theory must be nimble in its response to the exciting new data that will emerge from future experiments and observations. In the particular case of DFT, new data must be promptly incorporated into the refinement of the EDF to explore the full impact of the new information. This is particularly relevant given that nuclear physics has the ability to predict the structure and properties of matter in regions inaccessible to either experiment or observation. For example, one may use Bayesian inference to identify strong correlations between a desired property, which cannot be measured, and a surrogate observable that may be determined experimentally. However, Bayesian methods often require multiple evaluations of the same set of observables for many different realizations of the model parameters. If the nuclear observables informing the EDF are computationally expensive, then direct Bayesian inference is highly impractical. This computational challenge has motivated many of the recent efforts by the nuclear theory community in the development and adoption of emulators to accelerate computation speed with a minimal precision loss [23–35]. In this work we explore the application of one such class of emulators, the Reduced Basis Method (RBM) [36–38], which falls under the umbrella of the general Reduced Order Models (ROM) techniques [39, 40].

The Reduced Basis Method encapsulates a set of dimensionality reduction approaches that generally aim at speeding up computations by approximating the solution to differential equations with just a handful of active components (the reduced basis). These methods have been shown to exhibit speed increases of several orders of magnitude in various areas of science and engineering [41–44], including specific applications for uncertainty

quantification [45, 46], and have been recently demonstrated to be viable for applications in nuclear physics DFT [29]. Solving the full system of differential equations self-consistently in the framework of covariant DFT is not a particularly demanding computational task for modern computers, usually taking around a minute for a heavy nucleus such as ^{208}Pb. The computational bottleneck appears when millions of such evaluations must be carried out sequentially to perform Bayesian inference, and the problem multiplies when several nuclei are involved or if one wants to consider and compare different EDFs. A speed-up factor of three orders of magnitude or more provided by techniques such as the RBM could bridge the computational gap and enable new scientific advancements that would otherwise be impossibly or significantly more expensive. The adoption of these methods, paired together with leadership-class computing infrastructure, will enable the quick response that is needed to take full advantage of the vast wealth of experimental and observational data that will be coming in the next years.

The intent of this manuscript is to develop and showcase a pipeline for the calibration and uncertainty quantification of a nuclear model—a covariant energy density functional—enabled by the RBM emulation. To that goal, in Sec. II we provide a brief introduction to the relativistic mean field model we use, culminating with the set of differential equations that need to be solved in order to calculate nuclear observables. In Sec. III we present the reduced basis methodology, alongside an explanation on how it is used to construct an emulator that simplifies the computations of the DFT model. In Sec. IV we explain the theory and implementation of the Bayesian statistical analysis used to calibrate the model parameters, with full uncertainty quantification. In Sec. V we present and discuss the results of the calibration, displaying the Bayesian posterior distribution of the model parameters, together with the model predictions with quantified uncertainties for binding energies and charge radii, as well as the correlation between the slope of the symmetry energy L and the neutron skin thickness of both ^{208}Pb and ^{48}Ca. These two observables have been the focus of recent experimental campaigns [47–49], and its widespread implications are of great interest to the nuclear physics and astrophysics communities [50, 51]. Finally, in Sec. VI we present our conclusions and outlooks, with a perspective on the role that this class of emulators could play, in the near future, on the nuclear theory-experiment cycle enhanced by statistics and machine learning [31, 52, 53].

2 Relativistic mean field calculations

The cornerstone of covariant density functional theory is a Lagrangian density that includes nucleons and mesons as the effective degrees of freedom. Besides the photon that mediates the long-range Coulomb interaction, the model includes the isoscalar-scalar σ meson, the isoscalar-vector ω meson, and the isovector-vector ρ meson [54, 55]. The interacting Lagrangian density consists of a nucleon-nucleon interaction mediated by the various mesons alongside non-linear meson interactions [55–60]. That is,

$$\mathcal{L}_{\text{int}} = \bar{\psi}\Big[g_s\phi - \Big(g_v V_\mu + \frac{g_\rho}{2}\boldsymbol{\tau}\cdot\mathbf{b}_\mu + \frac{e}{2}(1+\tau_3)A_\mu\Big)\gamma^\mu\Big]\psi - \frac{\kappa}{3!}(g_s\phi)^3 - \frac{\lambda}{4!}(g_s\phi)^4 + \frac{\zeta}{4!}g_v^4\big(V_\mu V^\mu\big)^2 + \Lambda_v\big(g_\rho^2\,\mathbf{b}_\mu\cdot\mathbf{b}^\mu\big)\big(g_v^2 V_\nu V^\nu\big). \tag{1}$$

The first line in the above expression includes Yukawa couplings g_s, g_v, and g_ρ of the isoscalar-scalar (ϕ), isoscalar-vector (V^μ), and isovector-vector ($\mathbf{b}_\mu$) meson fields to the appropriate bilinear combination of nucleon fields. In turn, the second line includes non-linear meson interactions that serve to simulate the complicated many-body dynamics and that are required to improve the predictive power of the model [56–58]. In particular, the two isoscalar parameters κ and λ were designed to soften the equation of state of symmetric nuclear matter at saturation density. In turn, the isoscalar parameter ζ also softens the EOS of symmetric nuclear matter but at much higher densities. Finally, the mixed isoscalar-isovector parameter Λ_v was introduced to modify the density dependence of the symmetry energy, particularly it slope at saturation density. For a detailed account on the physics underlying each terms in the Lagrangian see Refs. [60, 61].

2.1 Meson field equations

In the mean-field limit, both the meson-field operators and their corresponding sources are replaced by their ground state expectation values. For spherically symmetric systems, all meson fields and the photon satisfy Klein-Gordon equations of the following form [59]:

$$\Big(\frac{d^2}{dr^2} + \frac{2}{r}\frac{d}{dr} - m_s^2\Big)\Phi_0(r) - g_s^2\Big(\frac{\kappa}{2}\Phi_0^2(r) + \frac{\lambda}{6}\Phi_0^3(r)\Big) = -g_s^2\big(\rho_{s,p}(r) + \rho_{s,n}(r)\big), \tag{2a}$$

$$\Big(\frac{d^2}{dr^2} + \frac{2}{r}\frac{d}{dr} - m_v^2\Big)W_0(r) - g_v^2\Big(\frac{\zeta}{6}W_0^3(r) + 2\Lambda_v B_0^2(r)W_0(r)\Big) = -g_v^2\big(\rho_{v,p}(r) + \rho_{v,n}(r)\big), \tag{2b}$$

$$\Big(\frac{d^2}{dr^2} + \frac{2}{r}\frac{d}{dr} - m_\rho^2\Big)B_0(r) - 2\Lambda_v g_\rho^2 W_0^2(r)B_0(r) = -\frac{g_\rho^2}{2}\big(\rho_{v,p}(r) - \rho_{v,n}(r)\big), \tag{2c}$$

$$\Big(\frac{d^2}{dr^2} + \frac{2}{r}\frac{d}{dr}\Big)A_0(r) = -e\rho_{v,p}(r), \tag{2d}$$

Where we have defined $\Phi = g_s\phi$, $W_\mu = g_v V_\mu$, and $\mathbf{B}_\mu = g_\rho \mathbf{b}_\mu$. The various meson masses, which are inversely proportional to the effective range of the corresponding meson-mediated

interaction, are given by m_s, m_v, and m_ρ. The source terms for the Klein-Gordon equations are ground-state densities with the correct Lorentz and isospin structure. Finally, the above scalar (s) and vector (v) densities are written in terms of the occupied proton and neutron Dirac orbitals:

$$\begin{pmatrix} \rho_{s,t}(r) \\ \rho_{v,t}(r) \end{pmatrix} = \sum_{n\kappa}^{occ} \left(\frac{2j_\kappa + 1}{4\pi r^2} \right) \left(g^2_{n\kappa t}(r) \mp f^2_{n\kappa t}(r) \right). \tag{3}$$

Here t identifies the nucleon species (or isospin) and n denotes the principal quantum number. We note that some of the semi-magic nuclei that will be used to calibrate the energy density functional may have open protons or neutron shells. In such case, we continue to assume spherical symmetry, but introduce a fractional occupancy for the valence shell. For example, in the particular case of ^{116}Sn, only two neutrons occupy the valence $d_{3/2}$ orbital, so the filling fraction is set to 1/2.

2.2 Dirac equations

In turn, the nucleons satisfy a Dirac equation with scalar and time-like vector potentials generated by the meson fields. The eigenstates of the Dirac equation for the spherically symmetric ground state assumed here may be classified according to a generalized angular momentum κ. The orbital angular momentum l and total angular momentum j are obtained from κ as follows:

$$j = |\kappa| - \frac{1}{2}\ ; \quad l = \begin{cases} \kappa, & \text{if } \kappa > 0; \\ -(1+\kappa), & \text{if } \kappa < 0, \end{cases} \tag{4}$$

where κ takes all integer values different from zero. For example, $\kappa = -1$ corresponds to the $s_{1/2}$ orbital. The single-particle solutions of the Dirac equation may then be written as

$$\mathcal{U}_{n\kappa mt}(\mathbf{r}) = \frac{1}{r} \begin{pmatrix} g_{n\kappa t}(r)\mathcal{Y}_{+\kappa m}(\hat{\mathbf{r}}) \\ i f_{n\kappa t}(r)\mathcal{Y}_{-\kappa m}(\hat{\mathbf{r}}) \end{pmatrix}, \tag{5}$$

where m is the magnetic quantum number and the spin-spherical harmonics $\mathcal{Y}_{\kappa m}$ are obtained by coupling the orbital angular l momentum and the intrinsic nucleon spin to a total angular momentum j. However, note that the orbital angular momentum of the upper and lower components differ by one unit, indicating that the orbital angular momentum is not a good quantum number. The functions $g_{n\kappa t}$ and $f_{n\kappa t}$ satisfy a set of first order, coupled differential equations that must be solved to obtain the single particle spectrum:

$$\left(\frac{d}{dr} + \frac{\kappa}{r} \right) g_a(r) - \left[E_a + M - \Phi_0(r) - W_0(r) \mp \frac{1}{2} B_0(r) - e \begin{Bmatrix} 1 \\ 0 \end{Bmatrix} A_0(r) \right] f_a(r) = 0, \tag{6a}$$

$$\left(\frac{d}{dr} - \frac{\kappa}{r} \right) f_a(r) + \left[E_a - M + \Phi_0(r) - W_0(r) \mp \frac{1}{2} B_0(r) - e \begin{Bmatrix} 1 \\ 0 \end{Bmatrix} A_0(r) \right] g_a(r) = 0, \tag{6b}$$

Where the upper numbers correspond to protons and the lower ones to neutrons, and we have used the shorthand notation $a = \{n\kappa t\}$ to denote the relevant quantum numbers. The mass of both nucleons is denoted by M, and it is fixed to the value 939 MeV. Finally, $g_a(r)$ and $f_a(r)$ satisfy the following normalization condition:

$$\int_0^\infty \left(g^2_a(r) + f^2_a(r) \right) dr = 1. \tag{7}$$

Looking back at Eq. 3, we observe that the proton and neutron vector densities are conserved, namely, their corresponding integrals yield the number of protons Z and the number of neutrons N, respectively. In contrast, the scalar density is not conserved.

2.3 Ground state properties

From the solution of both the Klein-Gordon equations for the mesons Eq. 2 and the Dirac equation for the nucleons Eq. 6, we can calculate all ground-state properties of a nucleus composed of Z protons and N neutrons. The proton and neutron mean square radii are determined directly in terms of their respective vector densities:

$$R^2_p \equiv \frac{4\pi}{Z} \int_0^\infty r^4 \rho_{v,p}(r) dr, \tag{8a}$$

$$R^2_n \equiv \frac{4\pi}{N} \int_0^\infty r^4 \rho_{v,n}(r) dr. \tag{8b}$$

Following [60] we approximate the charge radius of the nucleus by folding the finite size of the proton r_p as:

$$R^2_{ch} = R^2_p + r^2_p, \tag{9}$$

where we have used for the radius of a single proton r_p = 0.84 fm [62].

In turn, the total binding energy per nucleon $E/A - M$, includes contributions from both the nucleon and meson fields: $E = E_{nuc} + E_{mesons}$. The nucleon contribution is calculated directly in terms of the single particle energies obtained from the solution of the Dirac equation. That is,

$$E_{\rm nuc} = \sum_{a}^{\rm occ} (2j_a + 1)\, E_a, \tag{10}$$

where the sum is over all occupied single particle orbitals, E_a is the energy of the ath orbital, and $(2j_a + 1)$ is the maximum occupancy of such orbital. For partially filled shells, one must multiply the above expression by the corresponding filling fraction, which in the case of ^{116}Sn, is equal to one for all orbitals except for the valence $d_{3/2}$ neutron orbital where the filling fraction is 1/2.

The contribution to the energy from the meson fields and the photon may be written as

$$E_{\rm mesons} = 4\pi \int_0^\infty \Big(E_\sigma + E_\omega + E_\rho + E_\gamma + E_{\omega\rho}\Big) r^2\, dr, \tag{11}$$

where the above expression includes individual contributions from the σ, ω, and ρ mesons, the photon, and the mixed $\omega\rho$ term. In terms of the various meson fields and the ground-state nucleon densities, the above contributions are given by.

$$E_\sigma = \frac{1}{2}\Phi_0(r)\Big(\rho_{\rm s,p}(r) + \rho_{\rm s,n}(r)\Big) - \frac{\kappa}{12}\Phi_0^3(r) - \frac{\lambda}{24}\Phi_0^4(r), \tag{12a}$$

$$E_\omega = -\frac{1}{2}W_0(r)\Big(\rho_{\rm v,p}(r) + \rho_{\rm v,n}(r)\Big) + \frac{\zeta}{24}W_0^4(r), \tag{12b}$$

$$E_\rho = -\frac{1}{4}B_0(r)\Big(\rho_{\rm v,p}(r) - \rho_{\rm v,n}(r)\Big), \tag{12c}$$

$$E_\gamma = -\frac{1}{2}eA_0(r)\rho_{\rm v,p}(r), \tag{12d}$$

$$E_{\omega\rho} = \Lambda_{\rm v} W_0^2(r) B_0^2(r). \tag{12e}$$

Following [60], in this work we calibrate the relativistic mean field model by comparing the calculations of charge radii and binding energies with the experimentally measured values for the doubly magic and semi-magic nuclei: ^{16}O, ^{40}Ca, ^{48}Ca, ^{68}Ni[1], ^{90}Zr, ^{100}Sn, ^{116}Sn, ^{132}Sn, ^{144}Sm, ^{208}Pb.

2.4 Bulk properties parametrization

The Lagrangian density of Eq. 1 is defined in terms of seven coupling constants. These seven parameters plus the mass of the σ meson define the entire 8-dimensional parameter space (the masses of the two vector mesons are fixed at their respective experimental values of $m_{\rm v} = 782.5$ MeV and $m_\rho = 763$ MeV). Although historically the masses of the two vector mesons have been fixed at their experimental value to simplify the search over a complicated parameter landscape, such a requirement is no longer necessary. Bayesian inference supplemented by RBMs can easily handle two additional model parameters. Given that the aim of this contribution is to compare our results against those obtained with the traditional fitting protocol, we fix the masses of the two vector mesons to their experimental values, and defer the most ambitious calibration to a future work.

Once the theoretical model and the set of physical observables informing the calibration have been specified, one proceeds to sample the space of model parameters: $\alpha \equiv \{m_{\rm s}, g_{\rm s}, g_{\rm v}, g_\rho, \kappa, \lambda, \wedge_{\rm v}, \zeta\}$. However, given that the connection between the model parameters and our physical intuition is tenuous at best, the sampling algorithm can end up wandering aimlessly through the parameter space. The problem is further exacerbated in covariant DFT by the fact that the coupling constants are particularly large. Indeed, one of the hallmarks of the covariant framework is the presence of strong—and cancelling—scalar and vector potentials. So, if the scalar coupling $g_{\rm s}$ is modified without a compensating modification to the vector coupling $g_{\rm v}$, it is likely that no bound states will be found. To overcome this situation one should make correlated changes in the model parameters. Such correlated changes can be implemented by taking advantage of the fact that some of the model parameters can be expressed in terms of a few bulk properties of infinite nuclear matter [60, 64]. Thus, rather than sampling the model parameters α, we sample the equivalent bulk parameters $\theta = \{m_{\rm s}, \rho_0, \epsilon_0, M^\star, K, J, L, \zeta\}$. In this expression, ρ_0, ϵ_0, $M^\star$, and K are the saturation density, the binding energy, effective nucleon mass, and incompressibility coefficient of symmetric nuclear matter evaluated at saturation density. In turn, J and L are the value and slope of the symmetry energy also at saturation density. The quartic vector coupling ζ is left as a "bulk" parameter as the properties of infinite nuclear matter at saturation density are largely insensitive to the value of ζ [57]. The virtue of such a transformation is twofold: first, most of the bulk parameters given in θ are already known within a fairly narrow range, making the incorporation of Bayesian priors easier and natural, and second, a modification to the bulk parameters involves a correlated change in several of the model parameters, thereby facilitating the success of the calibration procedure.

In the context of density functional theory, Eqs 2–6 represent the effective Kohn–Sham equations for the nuclear many-body problem. Once the Lagrangian parameters α have been calculated from the chosen bulk parameters θ, these set of non-linear coupled equations must be solved self-consistently. That is, the single-particle orbitals satisfying the Dirac equation are generated from the various meson fields which, in turn, satisfy Klein-Gordon equations with the appropriate ground-state densities as the source terms. This demands an iterative procedure in which mean-field potentials of the Wood-Saxon form are initially provided to solve the Dirac equation for the occupied nucleon orbitals which are then combined to generate

1 The charge radius of ^{68}Ni was recently measured [63] and we do not include in the calibration to better compare with the previous results [60]. The charge radius of ^{100}Sn has not been measured yet. Therefore, our calibration dataset consists of 18 points, 10 binding energies and 8 charge radii.

the appropriate densities for the meson field. The Klein-Gordon equations are then solved with the resulting meson fields providing a refinement to the initial mean-field potentials. This procedure continues until self-consistency is achieved, namely, the iterative process has converged.

In the next section we show how the reduced basis method bypasses such a complex and time-consuming procedure by constructing suitable reduced bases for the solution of both the Klein-Gordon and Dirac equations.

3 The reduced basis method

A system of coupled differential equations in the one-dimensional variable r, such as Eq. 2 and Eq. 6, can be computationally solved by numerical methods such as finite element or Runge-Kutta. We shall refer to the numerical solutions obtained from those computations as high fidelity solutions for the rest of the discussion. Those approaches possess an intrinsic resolution Δr—such as the grid spacing in the case of finite element or the step size in the case of Runge-Kutta[2]. For a given interval L in which we are interested in solving the equations, each of the functions involved will have roughly $\mathcal{N} \sim \frac{L}{\Delta r}$ elements. In the case of the finite element method for example, for fixed particle densities and a given grid, the four fields involved in Eq. 2 become arrays of unknown values:

$$\begin{aligned} r &\to [r_1,\ r_2, \ldots,\ r_{\mathcal{N}}], \\ \Phi_0(r) &\to [\Phi_0(r_1),\ \Phi_0(r_2), \ldots,\ \Phi_0(r_{\mathcal{N}})], \\ W_0(r) &\to [W_0(r_1),\ W_0(r_2), \ldots,\ W_0(r_{\mathcal{N}})], \\ B_0(r) &\to [B_0(r_1),\ B_0(r_2), \ldots,\ B_0(r_{\mathcal{N}})], \\ A_0(r) &\to [A_0(r_1),\ A_0(r_2), \ldots,\ A_0(r_{\mathcal{N}})]. \end{aligned} \tag{13}$$

In turn, once the differential operators such as $\frac{d^2}{dr^2}$ are transformed into matrices of finite differences, the differential equations themselves will become matrix equations for the unknown arrays Eq. 13. The same procedure follows for the Dirac equations Eq. 6 for fixed fields, with each upper and lower components $g_{n\kappa}(r)$ and $f_{n\kappa}(r)$ for protons and neutrons becoming arrays of unknown values that must be solved for.

Both the traditional Runge-Kutta solver and the finite element solver we developed to iteratively tackle Eqs 2 and 6 have $L = 20$ fm, $\Delta r = 0.05$ fm, and therefore $\mathcal{N} = 400$. The goal of the Reduced Basis (RB) approach is to build a framework that, after a preparation period called the offline stage, can obtain approximate solutions to the differential equations with as few—or even better, none—calculations of size $\mathcal{N}$ during the evaluation period called the online stage [37]. Any observable computed from such solutions, such as binding energies and radii, should also involve as few calculations of size $\mathcal{N}$ as possible to streamline the uncertainty quantification procedure.

The RBM implementation we construct in this work consists of two principal steps: "training and projecting" [29]. In the first step we build the RB using information from high fidelity solutions, while in the second step we create the necessary equations for finding the approximate solution by projecting over a well-chosen low-dimensional subspace. The following subsections explain both steps in detail.

3.1 Training

We begin by proposing the corresponding RB expansion for each function involved in Eqs 2 and 6:

$$\Phi_0(r) \approx \hat{\Phi}_0(r) = \sum_{k=1}^{n_\Phi} a_k^\Phi\ \Phi_k(r), \tag{14a}$$

$$W_0(r) \approx \hat{W}_0(r) = \sum_{k=1}^{n_W} a_k^W\ W_k(r), \tag{14b}$$

$$B_0(r) \approx \hat{B}_0(r) = \sum_{k=1}^{n_B} a_k^B\ B_k(r), \tag{14c}$$

$$A_0(r) \approx \hat{A}_0(r) = \sum_{k=1}^{n_A} a_k^A\ A_k(r), \tag{14d}$$

$$g(r) \approx \hat{g}(r) = \sum_{k=1}^{n_g} a_k^g\ g_k(r), \tag{14e}$$

$$f(r) \approx \hat{f}(r) = \sum_{k=1}^{n_f} a_k^f\ f_k(r), \tag{14f}$$

The subscripts n and κ have been omitted from the $g_{n\kappa}$ and $f_{n\kappa}$ components for the sake of clarity, but it is important to note that the expansion will have unique coefficients a_k, and possible different number of basis n_g and n_f for each level. The functions with sub-index k, $A_k(r)$ for example, form the RB used to build their respective approximations, $\hat{A}_0(r)$ in this case. It is interesting to note that Eq.2d can be solved to explicitly obtain $A_0(r)$ as integrals of the proton density (see Eq. 7 in [59]). Nevertheless, we found that expanding $A_0(r)$ in its own RB resulted in appreciably bigger speed up gains by the RBM emulator with negligible loss in accuracy.

Once chosen, each RB is fixed and will not change when finding approximated solutions to Eqs 2 and 6 for different parameters α. The coefficients $a_k^{(\cdot)}$ do depend on the parameters α and are the ones responsible for adjusting the approximate solution as the parameter space is explored. It is important to note that, if there is a level crossing, the occupancy configuration of the nucleus will change. The RBM implementation we describe here—relying on smooth

2 Both the grid size and the step size could be adaptive instead of constant across the spatial domain. We shall assume a constant Δr for the rest of the discussion for the sake of simplicity.

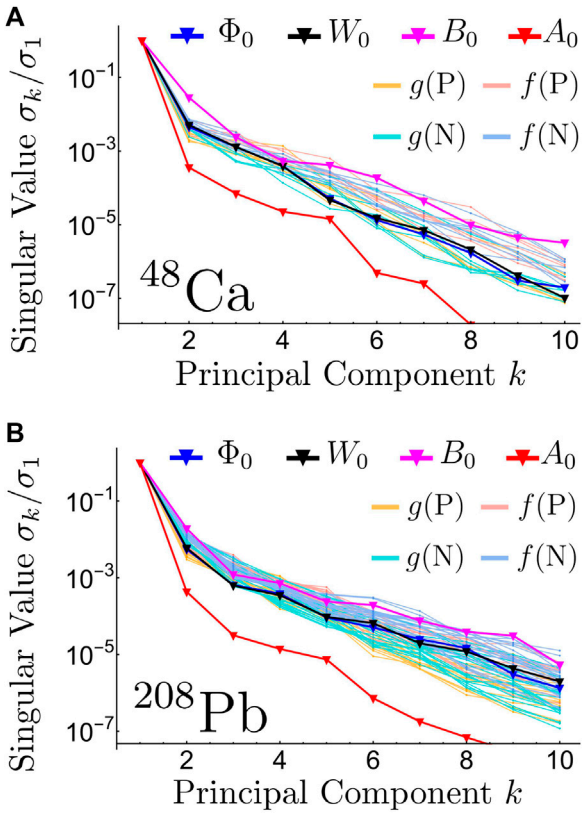

FIGURE 1
Normalized singular values σ_k/σ_1 for the fields $\Phi_0(r)$, $W_0(r)$, $B_0(r)$, and $A_0(r)$, and the single particle wave functions of the upper $g_{nk}(r)$ and lower $f_{nk}(r)$ components for ^{48}Ca **(A)** and ^{208}Pb **(B)**. The single particle proton levels are denoted as $g(P)$ and $f(P)$ for the upper and lower components, respectively, while the single particle neutron levels are denoted as g(N) and f(N) for the upper and lower components, respectively. There are six proton levels and seven neutron levels for ^{48}Ca **(A)**, while for ^{208}Pb there are sixteen proton levels and twenty-two neutron levels.

variations of the functions involved as α changes—is unable to correctly emulate the solution if suddenly an orbital looses or gains nucleons. For the parameter ranges we studied we do not expect that to happen for the closed shell magic nuclei we employed given the gap in the single particle spectrum. We did not observe level crossing either on the partially filled neutrons and protons shells of ^{116}Sn and ^{144}Sm.

For future applications going beyond the spherical approximation it will be important to modify the approach accordingly, both in expanding the number of basis states to capture the richness of the solutions and in directly including information on the occupation of the single particle orbitals. This can be done at either the Hartree-Fock-Bogoliubov or the Hartree-Fock + BCS level and will naturally address the issue of level crossings and deformation at the expense of the slower performance associated with larger bases and more coupled equations to be solved. The trade-off is tempered by the fact that, because the RBM does not depend on the original dimensionality of the problem, moving from a spherical picture to full 3D will not be as heavily penalized as the high fidelity solver.

There are several approaches for the construction of the reduced basis [36, 37], most of which involve information obtained from high fidelity solutions for a sample of the parameters α. For this work, we choose the Proper Orthogonal Decomposition (POD) approach, which consists of building the RB as the first n components (singular vectors) of a Singular Value Decomposition (SVD) [65]—see also Principal Component Analysis (PCA) [66]—performed on a set of high fidelity solutions.

For each nucleus involved we compute high fidelity evaluations for 50 parameter sets sampled from the multivariate Gaussian distributions obtained in the calibration performed in [60]. We perform the SVD on each of the four fields and each of the wave functions for the respective protons and neutron levels for all ten nuclei considered in this study. For example, for ^{48}Ca for protons and neutrons there are six and seven $f_a(r)$ and $g_a(r)$, respectively. Figure 1 shows the normalized singular values σ_k/σ_1 for the field and nucleon wave functions for ^{48}Ca and ^{208}Pb. Each singular value represents how much of the total variance in the entire sample that particular component is capable of explain [40]. A fast exponential decay of the singular values can indicate that a RB with few components should be able to approximate the full solution with good accuracy (see also the discussion on the Kolmogorov N-width in Chapter V of [36]).

Figure 2 shows the first three principal components obtained from the SVD of the 50 high fidelity evaluations for the $\Phi_0(r)$ and $A_0(r)$ fields, the upper component $g(r)$ of the first neutron level, and the lower component $f(r)$ for the last proton level for ^{48}Ca. The figure also shows the corresponding 50 high fidelity solutions, although the spread is barely noticeable for the two wave function components, and is imperceptible outside of the inset plot for the photon field $A_0(r)$. We observed a similar small spread of the fields and wave functions for all the nuclei considered for the 50 high fidelity evaluations. This is consistent with the fact that the relativistic mean field model has been calibrated to reproduce ground state experimental observables such as masses and radii within a 0.5% error[3] [60]. Appreciable variations of the solutions would deteriorate such values.

Choosing how many reduced bases to include for each field or wave function—the upper limits on the sums in Eq. 14 [n_Φ, n_W, n_B, n_A, n_g, n_f]—is a non-trivial process. In general, the more basis used the more precise the approximation will be, but that comes at the trade-off of an increased calculation time. This choice will not depend only on the relative importance of the singular values shown in Figure 1, but rather on the quantities we are

3 With an error of around 1.4%, the charge radius of ^{16}O can be treated as an outlier in which the mean field approximation might break down.

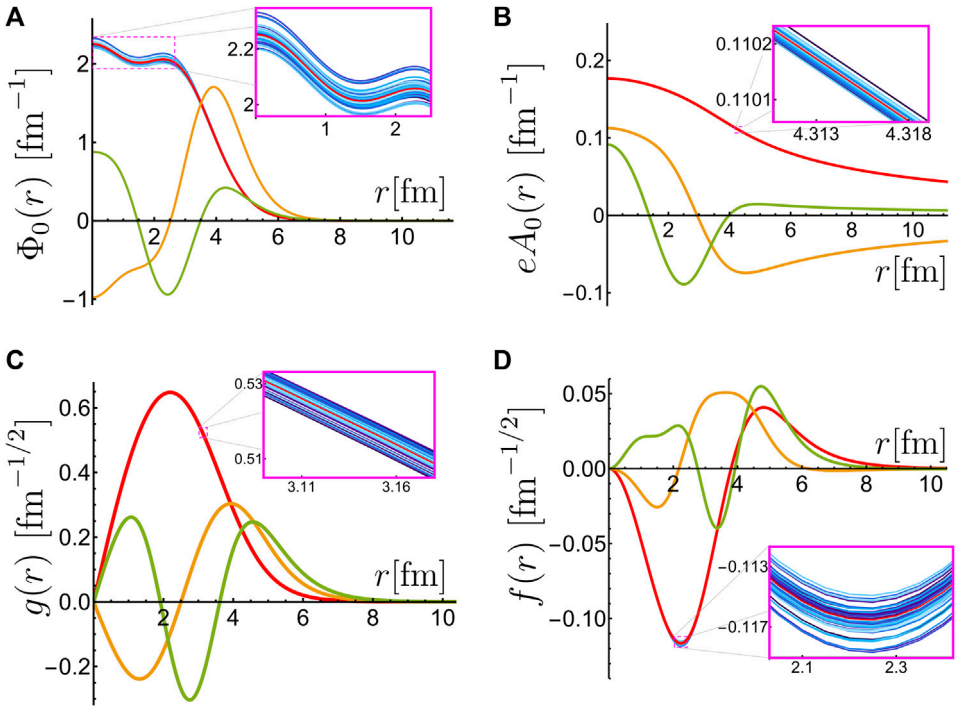

FIGURE 2
First three principal components in red, orange, and green respectively, for $\Phi_0(r)$ **(A)**, $eA_0(r)$ **(B)**, the first $g(r)$ for neutrons **(C)**, and the sixth $f(r)$ for protons **(D)** in ^{48}Ca. The second and third components (in orange and green) have been re-scaled arbitrarily for plotting convenience. The 50 solutions used in the training set are shown in different shades of blue in each figure. The spread of such solutions is barely visible for $\Phi_0(r)$ and $f(r)$, and almost undetectable for the other two cases. The spread is further enhanced in the inset plots within the magenta squares in each sub figure.

interested in calculating after solving the coupled differential equations. For example, for ^{48}Ca, the photon field $A_0(r)$ has the fastest decaying singular values shown in Figure 1, which could indicate that we need a smaller basis to reproduce it to the same level of accuracy than any of the other fields, such as $B_0(r)$. Nevertheless, if our primary objective is to obtain accurate calculations for binding energies and charge radii, for example, it might be the case that we need to reproduce $A_0(r)$ to much better precision than $B_0(r)$, requiring $n_A > n_B$. We elaborate this discussion later when we describe our method for selecting the number of basis for each function.

3.2 Projecting

For a fixed nucleus and a chosen RB configuration we have $n_\Phi + n_W + n_B + n_A$ free coefficients for the fields, $\sum_{i=1}^{l_P}(n_g^{(i,P)} + n_f^{(i,P)})$ coefficients for the single particle wave functions for protons, and $\sum_{i=1}^{l_N}(n_g^{(i,N)} + n_f^{(i,N)})$ for the single particle wave functions for neutrons. In these expressions l_P and l_N denote the total levels of protons and neutrons for the given nucleus, respectively. Additionally, since Eq. 6 are eigenvalue equations, the respective energies $E_{i,p}$ and $E_{i,N}$ for each of the protons and neutrons levels also count as unknown quantities that need to be determined. Let us denote a list of such coefficients and energies as $\boldsymbol{a} \equiv \{a_1^\Phi,\ a_2^\Phi,\ \ldots,\ a_1^W, \ldots E_{1_P},\ E_{2_P}, \ldots\}$.

For example, consider we are working with ^{48}Ca which has six proton levels and seven neutron levels. If we set three RB for every field and wave function expansion in Eq. 14, we will have 12 coefficients associated with the fields, 36 coefficients and six energies associated with the protons, and 42 coefficients and seven energies associated with the neutrons. This amounts for a total of 103 unknown quantities that must be determined from 103 equations. Each single particle level for protons and neutrons has an associated normalization condition shown in Eq. 7. These normalization equations go in par with the unknown energies. The rest of the unknown coefficients—90 in this example—are determined from the Galerkin projection equations that we now describe. The Galerkin method [67] is the traditional approach for obtaining such coefficients in the RBM [37, 39].

Let us denote the set of field functions and wave functions in the compact notation $\Xi \equiv \{\Phi_0, W_0, B_0, A_0, g, f\}$ and their respective RB approximation $\hat{\Xi} \equiv \{\hat{\Phi}_0, \hat{W}_0, \hat{B}_0, \hat{A}_0, \hat{g}, \hat{f}\}$. Let us denote the Klein-Gordon and Dirac equations as operators acting on the set Ξ, re-arrange them such that they are all equal to 0, and label them as:

$$\begin{aligned}
\text{Eq. (2a)} &\rightarrow F^{\Phi}_{\alpha}[\Xi] = 0,\\
\text{Eq. (2b)} &\rightarrow F^{W}_{\alpha}[\Xi] = 0,\\
\text{Eq. (2c)} &\rightarrow F^{B}_{\alpha}[\Xi] = 0,\\
\text{Eq. (2d)} &\rightarrow F^{A}_{\alpha}[\Xi] = 0,\\
\text{Eq. (6a)} &\rightarrow F^{g}_{\alpha}[\Xi] = 0,\\
\text{Eq. (6b)} &\rightarrow F^{f}_{\alpha}[\Xi] = 0.
\end{aligned}$$

For example, $F^{A}_{\alpha}[\Xi] = 0$ reads $(\frac{d^2}{dr^2} + \frac{2}{r}\frac{d}{dr})A_0(r) + e\rho_{\mathrm{v,p}}(r) = 0$, and it only depends explicitly on the photon field $A_0(r)$ and on the protons components $g(r)$ and $f(r)$ through the density $\rho_{\mathrm{v,p}}(r)$. There is a different associated operator for each proton and neutron level for the Dirac equations, but we omit a tracking index to keep the notation simpler.

Finding a solution Ξ for given parameters α means finding a collection of fields and wave functions such that all the operators $F^{(\cdot)}_{\alpha}[\Xi]$ acting on such list give back the function that is zero for every r. Such solution must satisfy as well the normalization condition Eq. 7. In general, these requirements cannot be satisfied by any choice of the RB coefficients under the RB approximation, i.e. $F^{(\cdot)}_{\alpha}[\hat{\Xi}] \neq 0$ simultaneously for any choice of $\boldsymbol{a}$. We can relax these conditions by projecting each operator $F_{\alpha}[\hat{\Xi}]$ over a set of "judges" $\psi^{(\cdot)}_{j}(r)$ [29] and requiring that the projections are zero:

$$\langle \psi^{\Phi}_{j} | F^{\Phi}_{\alpha}\left[\hat{\Xi}\right]\rangle = 0, \quad 1 \leq j \leq n_{\Phi}, \tag{16a}$$
$$\langle \psi^{W}_{j} | F^{W}_{\alpha}\left[\hat{\Xi}\right]\rangle = 0, \quad 1 \leq j \leq n_{W}, \tag{16b}$$
$$\langle \psi^{B}_{j} | F^{B}_{\alpha}\left[\hat{\Xi}\right]\rangle = 0, \quad 1 \leq j \leq n_{B}, \tag{16c}$$
$$\langle \psi^{A}_{j} | F^{A}_{\alpha}\left[\hat{\Xi}\right]\rangle = 0, \quad 1 \leq j \leq n_{A}, \tag{16d}$$
$$\langle \psi^{g}_{j} | F^{g}_{\alpha}\left[\hat{\Xi}\right]\rangle = 0, \quad 1 \leq j \leq n_{g}, \tag{16e}$$
$$\langle \psi^{f}_{j} | F^{f}_{\alpha}\left[\hat{\Xi}\right]\rangle = 0, \quad 1 \leq j \leq n_{f}, \tag{16f}$$

Where we have made the choice of projecting each operator $F^{(\cdot)}_{\alpha}[\Xi]$ a total of $n_{(\cdot)}$ times, where $n_{(\cdot)}$ is the number of RB expanding the associated function. Once again, there will be a different set of projection equations for every proton and neutron level for a given nucleus. The projection operation, which we write using Dirac's notation, is used here to mean the usual inner product integral over the radial variable, $r \in [0, \infty)$:

$$\langle \psi(r) | \phi(r)\rangle \equiv \int_{0}^{\infty} \psi^{\star}(r)\phi(r)dr \tag{17}$$

Following our previous approach [29], we choose the "judges" to be the same as the RB expansion, as it is common practice with the Galerkin method [68]. For example, in the case of ^{48}Ca with three basis for every field and wave function, since the photon field RB expansion $\hat{A}_0 = \sum_{k=1}^{3} a^{A}_{k} A_k$ has three unknown coefficients, there will be three "judges" projecting the operator $F^{A}_{\alpha}[\hat{\Xi}]$. These "judges" are chosen as $\psi^{A}_{j}(r) = A_j(r)$ for $1 \leq j \leq 3$. In total, for this ^{48}Ca example, we will have three projection equations for each field, three equations for each g and three for each f for each level of protons and neutrons, for a total of 90 projection equations. Such system of equations, together with the normalization conditions uniquely determines (if it has a solution) the 103 RB coefficients and energies $\boldsymbol{a}$ for each new value of the parameters α.

We also note that the dependence of Eqs 2 and 6 on the parameters α is affine, which means that every operator can be separated into a product of a function that only depends on α and a function that only depends on r. For example, the non-linear coupling between the isoscalar-vector meson ω and the isovector-vector meson ρ in Eq.2c reads: $-2(g^2_{\rho}\Lambda_{\mathrm{v}})[W_0(r)B_0(r)]$. In practice, this means that every integral in r in the projection equations Eq. 16 can be done, once the RB has been fully specified, without explicitly assigning numerical values to the parameters such as g^2_{ρ} or $\wedge_{\mathrm{v}}$. These computations are usually done once during the offline stage and then stored in memory to be used during the online stage [37]. The result of this procedure is a set of projected equations—agnostic to the r variable—that do not involve any computation in the high fidelity space of size $\mathcal{N}$. These equations will involve a small amount of linear combinations of products of the model parameters α and the unknown coefficients $\boldsymbol{a}$, usually much more computationally tractable than the original coupled equations of size $\mathcal{N}$. The two observables we study in this work, the charge radius and binding energy of each nucleus, are also affine functions of the parameters α and the solution's coefficients $\boldsymbol{a}$, see Eqs. 8 and Eqs 10–12. This means that these observables can also be pre-computed, avoiding calculations of size $\mathcal{N}$ when the emulator is used for fast evaluations[4].

For a concrete example, consider ^{48}Ca now with only two basis for all functions. Each of the two projection equations associated with the proton's g and f Eq. 16e and Eq. 16f contains a total of 22 terms. The equation for f for the first proton level—with the choice of basis we describe in the next section—with all numbers printed to two decimals precision reads:

$$\begin{aligned}
\langle g^{f}_{1}(r) | F^{f}_{\alpha}\left[\hat{\Xi}\right]\rangle = {} & 0.06a^{f}_{1} - 0.09a^{f}_{2} - E^{P}\left(0.8a^{g}_{2} + 1.66a^{g}_{1}\right)\\
& + M\left(1.66a^{g}_{1} + 0.8a^{g}_{2}\right) - 2.89a^{\Phi}_{1}a^{g}_{1} - 1.45a^{\Phi}_{2}a^{g}_{1}\\
& + 2.35a^{W}_{1}a^{g}_{1} \quad + 1.17a^{W}_{2}a^{g}_{1} - 0.03a^{B}_{1}a^{g}_{1}\\
& - 0.01a^{B}_{2}a^{g}_{1} + 0.07a^{A}_{1}a^{g}_{1} - 0.01a^{A}_{2}a^{g}_{1} - 0.8a^{\Phi}_{1}a^{g}_{2}\\
& - 2.71a^{\Phi}_{2}a^{g}_{2} + 0.64a^{W}_{1}a^{g}_{2} + 2.18a^{W}_{2}a^{g}_{2} - 0.02a^{B}_{1}a^{g}_{2}\\
& + 0.01a^{B}_{2}a^{g}_{2} + 0.03a^{A}_{1}a^{g}_{2} + 0.04a^{A}_{2}a^{g}_{2} = 0.
\end{aligned} \tag{18}$$

4 If the dependence on the parameters α of the operators involved in the system's equations, or in the observable's calculations is not affine, techniques such as the Empirical Interpolation Method [37, 69, 70] can be implemented to avoid computations of size $\mathcal{N}$ in the online stage.

3.3 Accuracy vs. speed: Basis selection

As with many other computational methods, the RBM posses a trade-off between accuracy and speed. If we use more bases for the expansions Eq. 14 we expect that our approximation will be closer to the high fidelity calculation, but that will come at the expense of more coefficients to solve for in the projection equations Eq. 16. If we use too few bases, the underlying physical model will be miss-represented when compared with experimental data, but if we use too many bases we might waste computational time to obtain an unnecessary accuracy level. To find a satisfactory balance we study the performance of the RBM, both in terms of accuracy and speed, for different basis size configurations on a validation set containing 50 new high fidelity evaluations drawn from the same distribution as the one we used for the training set [60].

As a metric of performance we define the emulator root mean squared errors as:

$$\Delta R_{ch} = \sqrt{\frac{1}{N_v}\sum_{i=1}^{N_v}\left(R_{ch\ i}^{mo} - R_{ch\ i}^{em}\right)^2} \tag{19}$$

For the charge radius, and as:

$$\Delta BE = \sqrt{\frac{1}{N_v}\sum_{i=1}^{N_v}\left(BE_i^{mo} - BE_i^{em}\right)^2}, \tag{20}$$

For the total binding energy. In both expressions N_v is the total number of samples in the validation set (50) and the superscripts "mo" and "em" stand for the high fidelity model and the RBM emulator, respectively.

A straightforward approach for exploring different basis configurations consists of setting all basis numbers $\{n_\Phi, n_W, n_B, n_A, n_g, n_f\}$ to the same value n. There are two main disadvantages of this approach. First, the basis increments can be too big, making it harder to obtain a good trade-off. For example, in the case of ^{208}Pb with $n = 2$ we have a total of 160 basis, while for $n = 3$ we jump straight to 240. Second, the accuracy in the emulation of the observables could be impacted differently by how well we reproduce each function involved in Eq. 2 and Eq. 6. Having a leverage that allows us to dedicate more resources (bases, that is) to more crucial functions could be therefore beneficial, and the simplistic approach with a common number n is unable to optimize the computational resources in that sense.

On the other hand, exploring all possible basis size configurations for a given maximum basis size is a combinatorial problem that can quickly become intractable. Therefore, we decided to follow a Greedy-type optimization procedure in which we incrementally add new basis to the current configuration, choosing the "best" local option at each step. The basis are chosen from the principal components obtained from the training set of 50 high fidelity runs. For all the nuclei the starting configuration was seven basis for each

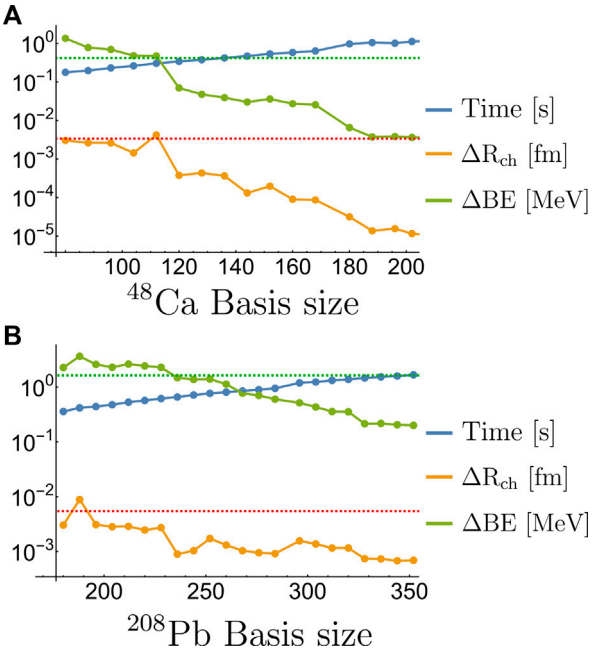

FIGURE 3
Performance of the RBM emulator for ^{48}Ca **(A)** and ^{208}Pb **(B)** as the total number of basis is increased following the Greedy algorithm described in the text. The dashed red and green lines in both plot indicate an error of 0.1% in the charge radius and total binding energy, respectively. The computation time per sample is calculated solving the RBM equations in Mathematica, which is substantially slower than the production emulator used in the calibration and detailed in Sec. IIID.

one of the fields $\{\Phi_0, W_0, B_0, A_0\}$ and two basis for each of the wave functions g and f on all the nucleus' levels. On each step, we add one more basis to both g and f to the four levels across both protons and neutrons which were reproduced most poorly in the previous iteration on the validation set. The "worst performers" are chosen alternating in terms of either the single particle energies (serving as a proxy for the total binding energy), and the L^2 norm on the wavefunctions themselves (serving as a proxy for the proton and neutron radius). The fields basis numbers are all increased by one once one of the wave functions basis number reaches their current level (7 in this case).

For example, for ^{48}Ca we start with seven basis for the four fields $\{n_\Phi, n_W, n_B, n_A\} = \{7, 7, 7, 7\}$, and $\{n_g, n_f\} = \{2, 2\}$ for every one of the six levels for protons and seven levels for neutrons. On the first step we compare the RBM calculations with the 50 high fidelity solutions from the validation set and identify the first neutron level, and the first, third, and fifth proton levels as the worse (on average) estimated single particle energies. Consequently, their respective basis are increased by their third principal components (see Figure 2): $\{n_g, n_f\} = \{3, 3\}$. On the next step, we re-calculate

TABLE 1 Results from the basis selection procedure using the 50 samples from the validation set.

Nuc	Basis Size	Time [ms]	Δ R_{ch} [10^{-3} fm]	0.1% R_{ch} [10^{-3} fm]	Δ BE [MeV]	0.1% BE [MeV]
^{16}O	68	0.7	1.8	2.7	0.1	0.1
^{40}Ca	116	2.2	1.2	3.5	0.2	0.3
^{48}Ca	120	2.4	0.4	3.5	0.1	0.4
^{68}Ni	128	3.1	1.8	3.9	0.5	0.6
^{90}Zr	168	6.6	0.9	4.3	0.2	0.8
^{100}Sn	180	8.1	1.0	4.5	0.3	0.8
^{116}Sn	176	8.0	2.4	4.6	0.8	1.0
^{132}Sn	184	9.5	1.9	4.7	0.8	1.1
^{144}Sm	216	14	1.8	4.9	0.8	1.2
^{208}Pb	236	20	0.9	5.5	1.5	1.6

The second column shows the total basis size for the selected configuration for each nucleus for the RBM emulator we use in the rest of the manuscript. Column three shows the average time to compute a single RB full solution for that nucleus using the optimized compiled emulator in Python, which we detail in the next section. Columns four and six show the root mean squared error of the emulator (see Eqs 19 and 20) when compared to the high fidelity solutions for the charge radius and the total binding energy, respectively. Columns five and seven show the target of 0.1% of the experimental value of the respective quantity used in the basis selection procedure. For the charge radius of ^{68}Ni and ^{100}Sn the central value of FSUGold2 [60] was used instead for column five.

the RBM solutions with the new updated basis and identify the fifth neutron level, and the second, third, and sixth proton levels as the worst performances in terms of the overall wave function sense (the L^2 norm). This procedure is repeated as the overall basis number increases as is illustrated in Figure 3 for ^{48}Ca and ^{208}Pb. We observed similar behaviors for the other eight nuclei involved in this study.

For the range of basis explored, the overall performance for both the charge radius and total binding energy roughly improves exponentially, although not monotonically[5], with the total basis number. The error in the radius and binding energy reduces by more than a factor of 100 for ^{48}Ca and by a factor of 10 for ^{208}Pb. The computational time also increases exponentially, expanding almost an entire order of magnitude for both nuclei.

To select an optimal configuration of bases we used as a target a 0.1% error in both observables for all nuclei involved, which is roughly three times smaller than the average deviation between the originally calibrated RMF and the available experimental values [60]. These targets are shown as the red and green dashed lines in Figure 3. Table 1 shows the basis size for the chosen basis and the results from this validation analysis. In the case where we would like to have a faster emulator at the expense of accuracy, we could choose a smaller basis size from the configurations showed in Figure 3. In the case where we need a more accurate emulator for particular calculations, configurations with more basis functions could be chosen at the expense of speed.

3.4 RBM code optimization

The offline stage consisting of the symbolic construction of the Galerkin projection equations and the expressions for the observables of interest is performed in Mathematica, resulting in polynomial equations in the parameters and RB coefficients such as Eq. 18. These equations are then parsed and converted into both Python and Fortran functions which can then be compiled into a library and evaluated in the calibration driver software. The explicit Jacobian matrix is also constructed and parsed in the same way, resulting in fewer evaluations of the polynomial equations and thus faster convergence of the root finding routine. This automated pipeline from symbolic representation in Mathematica to compiled Python library vastly simplifies the development process of the emulator and allows for various basis sizes to be included at will while ensuring an efficient implementation.

For the Python implementation Cython is used to first convert the Python code into C which is subsequently compiled into a Python compatible library. The Fortran implementation is similarly compiled using the `NumPy f2py` tool to produce a performant Fortran library with an appropriate

5 For some steps the emulator's performance -in terms of Δ R_{ch} and Δ BE-gets worse when adding the four new basis, which at first might seem counter-intuitive. It is important to note, however, that with each new basis we add we are changing the entire system of equations both by adding four new projections and by adding new elements to the previous ones. Nothing prevents the solution $\boldsymbol{a}$ to the new system to under perform in comparison to the previous one in the particular metric we are using.

Python interface. Regardless of the generating code, the resulting interface of the modules are the same and can be used interchangeably depending on the needs of the user. Each evaluation of the emulator for a given set of parameters then uses the MINPACK-derived root finding routine in `SciPy` [71] to find the optimal basis coefficients which are used as input for the observable calculations.

This procedure results in a time-to-solution on the order of hundreds of microseconds to tens of milliseconds depending on the nucleus being considered, as detailed in Table 1. The Runge-Kutta high-fidelity solver (written in Fortran) does not exhibit such a strong scaling across different nuclei, thus the relative speed-ups vary from 25,000x for ^{16}O, to 9,000x for ^{48}Ca and 1,500x for ^{208}Pb. This level of performance brings the evaluation of the surrogate model well within our time budget for the calibration procedure and also represents the simplest method in terms of developmental complexity. If the evaluation of the emulator needs to be further accelerated, a pure Fortran implementation of the root finding routine exhibits an additional decrease in time-to-solution of order 3x in comparison to the hybrid Python/compiled model detailed above at the cost of a slightly less user-friendly interface for the emulator.

Having constructed an emulator with the accuracy and calculation speed level we require, we now proceed to build the Bayesian statistical framework that will be used to perform the model calibration. In this calibration, the emulator finite accuracy will be included as part of our statistical model.

4 Framework for Bayesian uncertainty quantification

To calibrate our nuclear model properly, we need to account for the sources of error associated with each data point. We will use the well-principled Bayesian framework for this task [23, 72], which produces a full evaluation of uncertainty for every model parameter, in the form of posterior probability distributions given all the data. Its ingredients are twofold: first, a probability model, known as the likelihood model, for the statistical errors linking the physically modeled (or emulated) output to the experimental data given physical model parameters; second, another probability model for one's *a priori* assumptions about the physical model parameters. The output of the Bayesian analysis takes the form of a probability distribution for all model parameters; this is known as the parameters' posterior distribution. In this work, given the paucity of data, we choose to estimate the standard deviations of the statistical models separately, ahead of the Bayesian analysis, either using uncertainty levels reported in the literature, or using a natural frequentist statistical estimator. This minor deviation from a fully Bayesian framework is computationally very advantageous, an important consideration given this manuscript's overall objective.

The Bayesian framework can also be used as a predictive tool, by integrating the high-fidelity or emulated physical model against the posterior distribution of all model parameters, for any hypothetical experimental conditions which have not yet been the subject of an experimental campaign. Such predictions are expected also to take into account the uncertainty coming from the statistical errors in the likelihood version of the physical model. Relatively early examples of these uses of Bayesian features in nuclear physics work can be found in [73, 74].

In this section, we provide the details of our likelihood and prior models, and how they are built in a natural way, as they relate to experimental values, their associated emulated values, and all physical model parameters. We also explain in detail how the statistical model variance parameters are estimated ahead of the Bayesian analysis. All our modeling choices are justified using the physical context and the simple principle of keeping statistical models as parsimonious as possible.

4.1 Specification of the statistical errors and the likelihood model

Let us denote by y_i^{ex} the ith experimental observation—binding energies or charge radii in our case—of the 10 nuclei considered. We have a total of 10 measured binding energies and 8 charge radii (the charge radii of ^{68}Ni was not included in the calibration, while ^{100}Sn does not have a measured charge radii), therefore $1 \le i \le 18$. Let us denote by $y_i^{\mathrm{mo}}(\alpha)$ the high fidelity model calculation associated with y_i^{ex} for a given value of the model parameters α. Finally, let us denote $y_i^{\mathrm{em}}(\alpha)$ the RBM emulated calculation associated with the same observable. We identify three main sources of errors[6] in the model calibration, namely experimental, modeling, and emulation errors—the latter being the difference between $y_i^{\mathrm{mo}}(\alpha)$ and $y_i^{\mathrm{em}}(\alpha)$ — which we write into a statistical model as follows: for every i,

$$\begin{aligned} y_i^{\mathrm{ex}} &= y_i^{\mathrm{mo}}(\alpha) + \delta_i(\alpha) + \epsilon_i \\ &= y_i^{\mathrm{em}}(\alpha) + \eta_i(\alpha) + \delta_i(\alpha) + \epsilon_i. \end{aligned} \tag{21}$$

These three sources of error are represented in Figure 4 as an illustrative stylized example.

The experimental error, ϵ_i, is assumed to come from a normal distribution with mean zero and standard deviation σ_i^{ex}:

6 A fourth source of error could be, in principle, the computational error in the high fidelity solver for the physical model. We expect this error to be negligible in comparison to the other three at the level of resolution Δr our high fidelity solvers have.

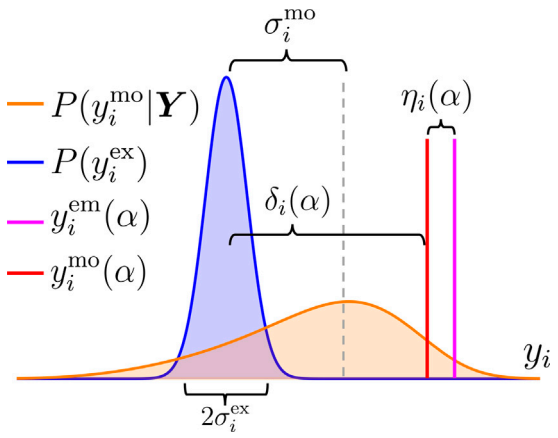

FIGURE 4
Visual representation of the statistical model with the three sources of uncertainty for an observable y_i. For a particular value of α, the model calculation, y_i^{mo} (red vertical line) deviates from the center of the experimental distribution, $P(y_i^{\mathrm{ex}})$ (blue curve) by the model error $\delta_i(\alpha)$. The size of the experimental error, characterized by σ_i^{ex}, is exaggerated in the figure to facilitate showing. The estimated value by the emulator, y_i^{em} (vertical magenta line) deviates from the model calculation, y_i^{mo}, by the emulator error, $\eta_i(\alpha)$. The model error scale, σ_i^{mo}, characterizes the expected size of $\delta_i(\alpha)$ as the parameters α are varied within their meaningful physical range. This parameter range is characterized by the Bayesian posterior distribution $P(y_i^{\mathrm{mo}}|\boldsymbol{Y})$ (orange curve), -obtained only after the analysis is done-of the observable y_i given all the calibration data $\boldsymbol{Y}$.

$\epsilon_i \sim \mathcal{N}(0,\ (\sigma_i^{\mathrm{ex}})^2)$. These errors are assumed to be uncorrelated between measurements of different nuclei and different quantities. The error scale for each measurement, σ_i^{ex}, is an estimate of the aggregate of the many uncertainty sources—both systematic and statistical—that can play a role during the experimental campaign. In principle, since each measurement comes from a different campaign i, it is important to allow σ_i^{ex} to change from i to i. Since the experiments are not conducted in consort, it is legitimate to assume these errors are uncorrelated. As shown in Figure 4, these experimental errors ϵ_i should not be interpreted as the discrepancy between the theoretical prediction and the experimental value. Rather, they represent the estimated difference between the observed experimental value during realistic conditions, compared to its (unattainable) value in ideal settings free of experimental noise. This noise is thus due for instance to the known imprecision of measurement instruments.

The modeling error, or model discrepancy term, $\delta_i(\alpha)$, represents the intrinsic failures of the physical model when reproducing reality, for a given value of α. It is an aggregate of the many simplifications made during the construction of the model, as well as any physical effects, known or unknown, which are unaccounted for by the physical model. In the limit where the experimental errors become negligible, it is the term that explains the deviation between theory and observation. Due to these model limitations, we expect that even the best regions in the parameter space—values of α that make the discrepancies as small as possible—cannot make them all vanish simultaneously ($\delta_i(\alpha) = 0$) for every observable i.

It is typically unrealistic to expect a very precise estimate of the statistical properties of the set of $\delta_i(\alpha)$ as α varies. Indeed, first, because the usual dataset in low-energy physics studies consist only of a few spherical magic or semi-magic nuclei, limiting the statistical analyses that can be made. Second, since the origin of $\delta_i(\alpha)$ has roots in phenomena not completely understood, it becomes very hard to give accurate estimates when the experimental observations are not available. This motivates us to propose a parsimonious model, in accordance with the statistical principle that parsimony promotes robustness, an idea that traces back several decades (e.g. [75]). We assume that, up to scaling at the level of observables, the modeling error variances are shared within each of the two observable categories (binding energies and charge radii), and do not depend on the parameters α within their physical meaningful range that reproduces the nuclear properties. This is represented by the scale σ_i^{mo} (to be defined precisely shortly) in Figure 4.

Finally, for a given fixed value of the parameters α, the emulator error, $\eta_i(\alpha)$, represents the difference between the model's original high fidelity calculation, and the approximate version computed by the emulator. In Figure 4 it is represented as the difference between the red and magenta vertical lines. This is the easiest error to obtain exactly, given a fixed α, since it is entirely computable, given access to the high fidelity and the emulator implementations. The challenge lies in estimating $\eta_i(\alpha)$ for new values of α *without* the use of the high fidelity solver. In the RBM literature, there exist approaches to estimate the emulator's error in terms of the properties of the underlying differential equation [37], [76] and [77], but to our knowledge they have not been yet extended to the type of coupled nonlinear equations that describe our physical model Eq. 2 and Eq. 6. Our proposal below is to model all emulator errors, including the unobserved ones, using the same statistical model, where the emulator error intensity does not depend on α, thereby circumventing the issue of developing an analytical approach to extrapolating these errors in a non-linear setting, and keeping with the principle of parsimony.

Having identified and described these three sources of errors, we proceed to propose and implement methods to estimate their combined effect in order to calibrate our physical model properly through the RBM emulator.

In the case of binding energies and charge radii, the experimental determinations are precise enough that the typical error scale σ_i^{ex} can be ignored in comparison to the typical model discrepancies[7]. Therefore, we decide to neglect the experimental errors for the rest of our analysis.

7 For example, the binding energy of ^{208}Pb is known to a precision better than 10^{-4}% [78], while its charge radius to a precision of 0.02% [79]. In contrast, the estimated model error we calculate in the following discussion for the same quantities is 0.25% and 0.26%, respectively.

We assume that the model discrepancies $\delta_i(\alpha)$ scale proportionally to the value of each individual experimental datapoint. This is because each datapoint represents a different physical reality, and while, say, two binding energies for two similar nuclei may be subject to the same intensity of modeling error, this may not be a good assumption for two nuclei which are more distant in the nuclear landscape. Specifically, we assume that each scaled model discrepancies $\tilde{\delta}_i \equiv \delta_i / y_i^{\text{ex}}$ comes from a common normal distribution with mean zero and either variance σ_{BE}^2 for a binding energy datapoint or variance σ_{R}^2 for a charge radius datapopint. Another assumption lies in our treatment of these errors being independent of each other, and thus uncorrelated. A more elaborate statistical framework could be developed to account for this correlation between errors, requiring additional information to provide structure to the correlation matrix and avoid overfitting the statistical model. In the absence of such information, our assumption of independence is consistent with an agnostic view about these errors' correlation. We estimate these errors' scales σ_{BE} and σ_{R} from the deviations between the originally calibrated RMF model FSUGold2 [60] and the experimental observations, simply by using a version of the classical unbiased variance estimator. Explicitly, for the variance of the modeling errors on the binding energy side, where the model is FSUGold2, with $N_{\text{BE}} = 10$ for the ten binding energy datapoints, we let

$$\sigma_{\text{BE}}^2 = \frac{1}{N_{\text{BE}}} \sum_{i=1}^{N_{\text{BE}}} \left(\frac{y_i^{\text{ex}} - y_i^{\text{FSUGold2}}}{y_i^{\text{ex}}} \right)^2, \tag{22}$$

And similarly for σ_{R}^2 as the variance of the modeling error for charge radii. These expressions are calculated for all the data with available experimental values in Table 2 in [60]. These formulas are the classical minimum-variance unbiased estimators (MVUE) of variances for datapoints coming from a normal distribution with known means and unknown common variance. One can view each model-calculated datapoint as the error-prone data, with the experimental value as its mean value. This results in a mathematically identical unbiased estimator as if all means were equal. In our case, since we choose to normalize the modeled data by dividing it by the experimental data, we are in fact handling a classical situation, where the data's mean value is known to equal 1. In that scenario, the classical MVUE is the one given in formula (22). Note that its leading factor is $1/N_{\text{BE}}$ rather than $1/(N_{\text{BE}} - 1)$; this is because the mean is known. In other words, the model to which this MVUE Eq. 22 responds is

$$\frac{y_i^{\text{FSUGold2}}}{y_i^{\text{ex}}} = 1 + \tilde{\delta}_i \tag{23}$$

where $\tilde{\delta}_i$ are assumed to be independent mean-zero normal errors with unknown variance σ_{BE}^2 for the binding-energy data, and similarly for σ_{R}^2. Applying the estimation to the data in [60] we obtain:

TABLE 2 Prior central values and standard deviations for the eight model parameters used in the calibration.

$\boldsymbol{\theta_j}$	$\boldsymbol{\theta_{0,j}}$	$\boldsymbol{\sigma_{\theta,j}}$
m_s [MeV]	500	50
ρ_0 [fm^{-3}]	0.15	0.04
ϵ_0 [MeV]	-16	1
$M^\star$ [MeV]	0.6	0.1
K [MeV]	230	10
ζ	0.03	0.03
J [MeV]	34	4
L [MeV]	80	40

$$\sigma_{\text{BE}} = 0.25\%, \tag{24}$$

And

$$\sigma_{\text{R}} = 0.26\%. \tag{25}$$

We express these two values as percentages since they are dimensionless. We treat the charge radius of ^{16}O as an outlier and exclude it from this estimation, assigning it its own estimated error scale of $\sigma_{\text{R},^{16}\text{O}} = 1.4\%$, so that $N_{\text{R}} = 7$. The corresponding modeling error standard deviations σ_i^{mo} for specific observables y_i are obtained by multiplying the one based on scaled data by their respective experimental values, which provides the correct standard deviations for all δ_i in accordance with how we defined $\tilde{\delta}_i$. For example, for i = BE for ^{48}Ca, $\sigma_i^{\text{mo}} = \sigma_{\text{BE}} \times (416\ \text{MeV}) = \frac{0.25}{100} \times (416\ \text{MeV}) \approx 1\ \text{MeV}$.[8]

We follow a similar parsimonious approach and model the emulator error $\eta_i(\alpha)$ as coming from a normal distribution with mean zero and scale (standard deviation) σ_i^{em} that does not depend on α. In Figure 4, σ_i^{em} would be the scale of a Gaussian distribution (not shown to keep the figure easier to read) centered at $y_i^{\text{em}}(\alpha)$. From our assumptions we would expect that such distribution will contain within one standard deviation the true model evaluation y_i^{mo} around 68% of the time both computations are made, *independent* of the exact value of α within the physically meaningful range where the emulator was trained.

We estimate the scale σ_i^{em} from the empirically observed deviations between the RBM emulator and the high fidelity solutions in the validation set used for the selection of the basis in the previous section. We select, therefore, σ_i^{em} as the values reported in the fourth column (ΔR_{ch}) and sixth column (Δ BE) in Table 1. Of potential concern is the degradation of the Reduced Basis approximation for values of α outside of the

8 The experimental values of the charge radii for ^{68}Ni was not known at the time of the calibration in [60], while the charge radii of ^{100}Sn is still not known. In these cases, we used the values reported for FSUGold2 as proxies to preserve these two nuclei in the analysis when creating predictive posterior distributions with the calibrated model.

training and validation regions. We note that such values would be outside the accepted physically meaningful range and thus are unlikely to be visited by the Monte Carlo sampling we use later for the model calibration. Additionally, as shown in similar RBM applications [24, 25, 29], the emulation error tends to change smoothly outside of the training region. This gives us confidence that even in the rare event that such parameter values are visited, they will have negligible impact on the overall calibration procedure. Finally, we assume that the emulator's errors and the model discrepancy errors are independent (and thus uncorrelated) across different quantities, and within the same observable as well.

Under the assumptions we have made about the three sources of uncertainties, including the independence of all error terms which implies that the variance of their sum is the sum of their variances, we can finally specify the likelihood function for our statistical model. To simplify the prior specification and the exploration of the parameter space, we construct our statistical modeling using the bulk matter parametrization θ, which is equivalent to the Lagrangian couplings one with α (see Secion 2). Denoting $N = N_{\mathrm{BE}} + N_{\mathrm{R}} = 18$ and denoting by $\boldsymbol{Y}$ the N-dimensional vector formed of the experimental datapoints y_i^{ex}, our likelihood model is:

$$P(\boldsymbol{Y}|\theta) \propto e^{-\chi^2/2}, \tag{26}$$

Where

$$\chi^2 = \sum_{i_1=1}^{N_{\mathrm{BE}}} \frac{\left(y_{i_1}^{\mathrm{em}}(\theta) - y_{i_1}^{\mathrm{ex}}\right)^2}{\sigma_{i_1}^{\mathrm{em}\ 2} + \sigma_{i_1}^{\mathrm{mo}\ 2}} + \sum_{i_2=1}^{N_{\mathrm{R}}} \frac{\left(y_{i_2}^{\mathrm{em}}(\theta) - y_{i_2}^{\mathrm{ex}}\right)^2}{\sigma_{i_2}^{\mathrm{em}\ 2} + \sigma_{i_2}^{\mathrm{mo}\ 2}}. \tag{27}$$

Our modeling assumptions about the error structure, plus the standardization in $\boldsymbol{Y}$, imply indeed that χ^2 is chi-squared distributed with N degrees of freedom. Note that $\sigma_{i_2}^{\mathrm{mo}}$ has the associated 0.26% value for all i_2 except for ^{16}O, for which it has the value of 1.4%.

4.2 Prior

For the prior distribution we adopt an uncorrelated multivariate normal in θ as follows:

$$P(\theta) \propto e^{-\chi_0^2/2}, \tag{28}$$

where:

$$\chi_0^2 = \sum_{j=1}^{8} \frac{\left(\theta_j - \theta_{0,j}\right)^2}{\sigma_{\theta,j}^2}. \tag{29}$$

The central values $\theta_{0,j}$ and standard deviations $\sigma_{\theta,j}$ are specified for the eight components of θ in Table 2. They were chosen to roughly cover the expected parameter region with wide ranges based on the previous calibration [60].

4.3 Posterior

With our likelihood and priors fully set up, the posterior densities $p.(\theta|\boldsymbol{Y})$ for the parameters θ are given classically by Bayes' rule [72] as being proportional to the product of the likelihood in Eq. 26 and the prior in Eq. 28, where the likelihood is evaluated at the experimentally observed datapoints labeled above as $\boldsymbol{Y}$. From here, we are interested in using the Bayesian analysis to compare the calculations of the fully calibrated model with the experimental values of the observables, to verify that our uncertainty quantification is accurate. If our uncertainty bands on these predicted values are too narrow (too optimistic), too high a proportion of our 18 observations will fall outside of the bands. If our uncertainty bands are too wide (too conservative), many or all of our 18 observations will be inside their corresponding uncertainty bands. Being slightly too conservative is easily construed as a virtue to hedge against the risk of being too optimistic. The latter should be construed as an ill-reported uncertainty quantification. The method we propose here, to gauge the accuracy our uncertainty quantification, with results described in Section 5, is a manual/visual implementation of the now classical notion of Empirical Coverage Probability (ECP, see [73] for a nuclear physics implementation), appropriate for our very small dataset with 18 points. To compute the posterior density of every predicted value corresponding to our experimental observations, we view the likelihood model as a predictive model, featuring the fact that it includes statistical noise coming from the δ's and η's (see Figure 4 and Eq. 21), not just the posterior uncertainty in the parameters, and we simply use Bayesian posterior prediction, namely

$$P\left(y_i^{\mathrm{pred}}|\boldsymbol{Y}\right) = \int P\left(y_i^{\mathrm{pred}}|\theta\right) P(\theta|\boldsymbol{Y})\, d\theta, \tag{30}$$

where $p\,(\theta|\boldsymbol{Y})$ is the posterior density of all model parameters. In this fashion, the posterior uncertainty on the parameters, and the statistical uncertainty from the likelihood model, are both taken into account in a principled way. Note that this predictive calculation can be performed for all 20 observables of interest, though ECP-type comparisons with the experimental datapoints happen only for the 18 points we have, excluding charge radii for ^{100}Sn and ^{68}Ni. The next subsection explains how all Bayesian analyses are implemented numerically.

4.4 Metropolis-Hastings and surmise

The difficulty with any Bayesian method is to know how to understand the statistical properties of the posteriors. The simplest way to answer this question is to sample repeatedly (and efficiently) from those probability distributions. To sample from the posterior densities of the model parameters θ, we use the

standard Metropolis-Hastings algorithm implemented in the `surmise` Python package [80]. For the results presented here, eight independent chains of 725,000 samples were ran using the direct Bayes calibrator within `surmise`. For the step size used, the ratio of acceptance for proposed new steps was about 30% across all chains. The first 100,000 samples of each chain were taken as a burn-in, reducing the effective sample size of the calibration to 5,000,000 evaluations. The eight chains were run in parallel and thus the 5,800,000 total evaluations took about a day on a personal computer with commodity hardware. For comparison, it would have taken nearly 6 years of continuous computation to produce the same results using the original code for the high-fidelity model.

To evaluate posterior predictive distributions to compare with the experimental data, we rely on the fact that `surmise`, like any flexible Monte-Carlo Bayesian implementation, gives us access to all Metropolis-Hastings samples. For each multivariate sample of the parameters in θ, we draw independent samples from the normal distributions in the likelihood model Eq. 21, and evaluate the corresponding value of y_i^{ex} in that model by plugging those sampled values into the right-hand side of that specification. Note that the second line in Eq. 21 must be used for this purpose, not the first line, in order to account for the uncertainty due to emulation. This procedure provides a sampling method for the distribution in Eq. 30 which has a level of accuracy consistent with the accuracy of the Metropolis-Hastings method for sampling from the parameters' posterior densities.

5 Results and discussion

Having defined the covariant density functional model in Secion 2, the reduced basis emulator in Secion 3, and the statistical framework and the computational sampling tools in Secion 4 we are in position to use the experimental data to calibrate the model under a Bayesian approach. At the time of the original calibration of the FSUGold2 functional [60], this would have represented an exceptional computational challenge, mainly because of the absence of the computational speed up of three orders of magnitude provided by the RBM. Instead, in the original calibration, one was limited to finding the minimum of the objective (or χ^2) function and the matrix of second derivatives. In this manner, it was possible to compute uncertainties and correlations between observables, but only in the Gaussian approximation. We compare and contrast our results and procedure, highlighting that with the exception of the information on the four giant monopole resonances and the maximum neutron star mass, both calibrations share the same dataset of binding energies and charge radii.

We begin by displaying in graphical form the results of our Bayesian implementation in `surmise` as a corner plot in Figure 5. The corner plot summarizes the posterior distribution of bulk parameters alongside the two-dimensional correlations. For comparison, the Gaussian distribution of parameters extracted from the original FSUGold2 calibration is displayed by the vertically scaled blue line. As expected, the width of the one-dimensional distributions has increased—in some cases significantly—relative to the Gaussian approximation that is limited to explore the parameter landscape in the vicinity of the χ^2 minimum. The inclusion of bigger estimated model errors δ_i in Eq. 21 likely also share responsibility for the increased overall uncertainty. Besides the increase in the width of the distribution, we see a relatively significant shift in the average value of the incompressibility coefficient K. We attribute this fact to the lack of information on the GMR, which is the observable that is mostly sensitive to K.

Beyond the corner plot that displays the distribution of bulk parameters and the correlations among them, we illustrate in Figure 6 and Table 3 the performance of the model as compared with the experimental data informing the calibration. Note that in Figure 6 as well as in Table 3 we have defined the binding energy as a positive quantity.

The blue histograms display the posterior predictive distributions Eq. 30 of each of the 20 observables. Included in our results is the prediction for the yet to be measured charge radius of ^{100}Sn, as well as the charge radius of ^{68}Ni not used in the calibration. The vertical red lines indicate the values of the experimental datapoints specified in [60] and [63]. These plots show excellent coverage of all datapoints within our reported uncertainty. With 19 datapoints, one would expect about one of them to fall outside of 95% credible intervals. The credible intervals are printed in Table 3, showing that none of our datapoints fall outside those intervals around the posterior means. This implies that our uncertainty quantification leans towards the conservative side, although the binding energy for ^{48}Ca and the charge radii of ^{68}Ni are very close to falling outside the 95% band. Our method has produced uncertainties which are very likely not to be overly wasteful by significantly over-reporting uncertainty, and which are very likely not to under-report uncertainty. This is exactly where a Bayesian predictive posterior coverage analysis wants to be in a study with such a small number of datapoints.

Being the lightest of all the nuclei included in the calibration, ^{16}O may be regarded as a questionable "mean-field" nucleus. As such, comparing its experimental charge radius with our posterior results is particularly interesting, since the model standard deviation we used was more than 5 times larger than for the other observables. Yet, our reported uncertainty sees the

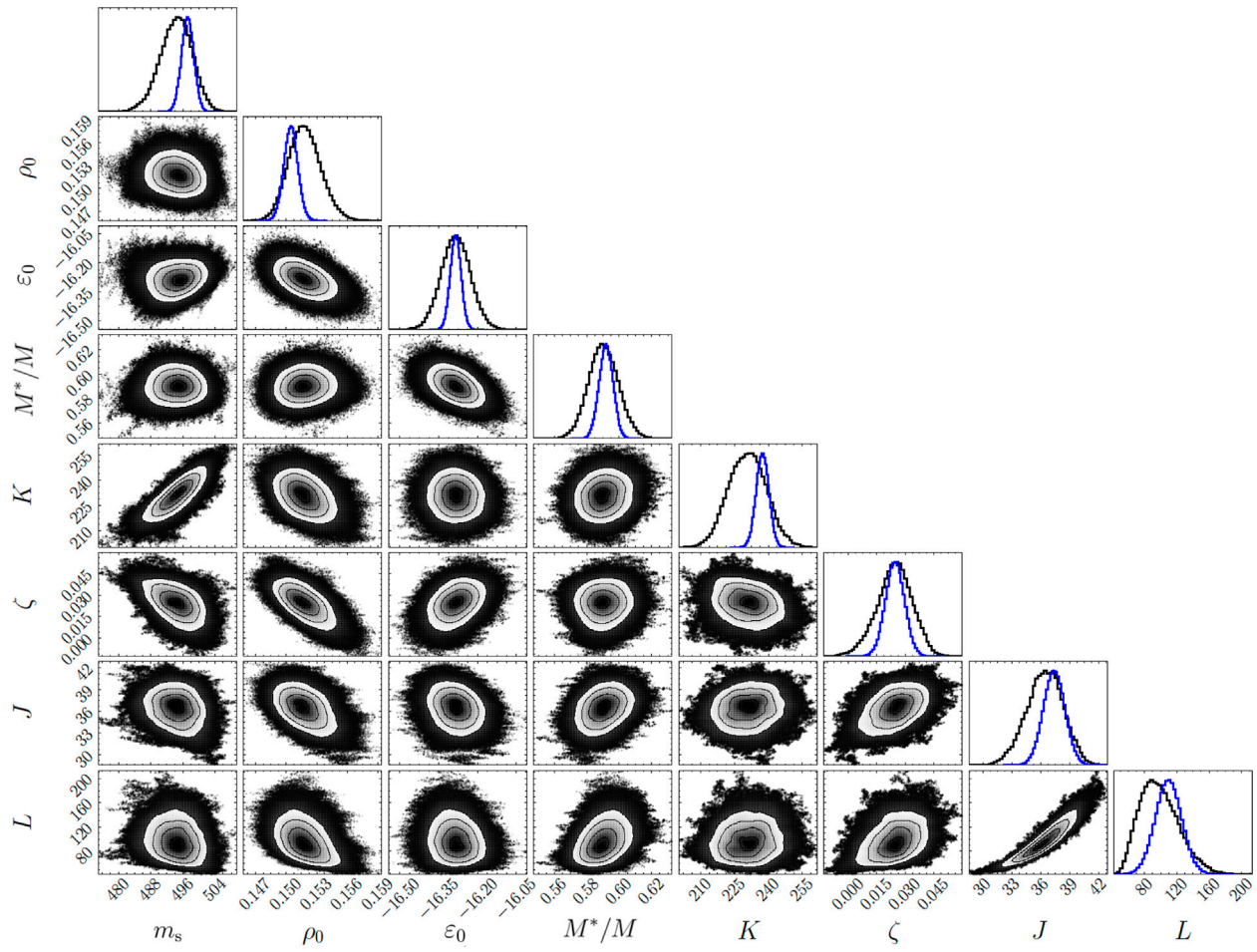

FIGURE 5
Corner plot [81] from the posterior distribution of the eight bulk matter parameters θ obtained from the Metropolis-Hasting sampling with `surmise`. A total of five million samples were used, distributed along eight independent chains. The saturation density ρ_0 is expressed in fm^{-3}, the mass of the σ meson m_s, the binding energy at saturation ε_0, the incompressibility coefficient K, the symmetry energy J and its slope L at saturation are all expressed in MeV. For comparison, the original calibration done in [60] is shown as the blue curves along the diagonal, scaled vertically to fit in the same plot as our posterior results in black.

experimental measurement fairly well reproduced. This is an indication that it was important to use the higher model variance, or our prediction could have reported too low of an uncertainty. Using a smaller variance for the model error δ_i could have also pushed the parameters too strongly towards the ^{16}O charge radius outlier, deteriorating the overall performance of the calibration on the other nuclei. The final coverage of all data points illustrates our method's ability to handle heteroskedasticity (uneven variances) well. Finally, in Figure 6, because our comparison with predictive distributions performs very well and is only mildly conservative, we can be confident that our prediction for the charge radii of ^{100}Sn is robust. How narrow these histograms are is a testament to the quality of the original modeling, its emulation, and our uncertainty quantification.

Coming back to the corner plot in Figure 5, we note that the strongest correlation between observables involves the value of the symmetry energy (J) and its slope (L) at saturation density. The symmetry energy quantifies the energy cost in transforming symmetric nuclear matter—with equal number of neutrons and protons—to pure neutron matter. In the vicinity of nuclear matter saturation density, one can expand the symmetry energy in terms of a few bulk parameters [82]:

$$\mathcal{S}(\rho) = J + Lx + \frac{1}{2}K_{\rm sym}x^2 + \cdots \tag{31}$$

where $x = (\rho - \rho_0)/3\rho_0$ is a dimensionless parameter that quantifies the deviations of the density from its value at saturation. Given that the calibration is informed by the

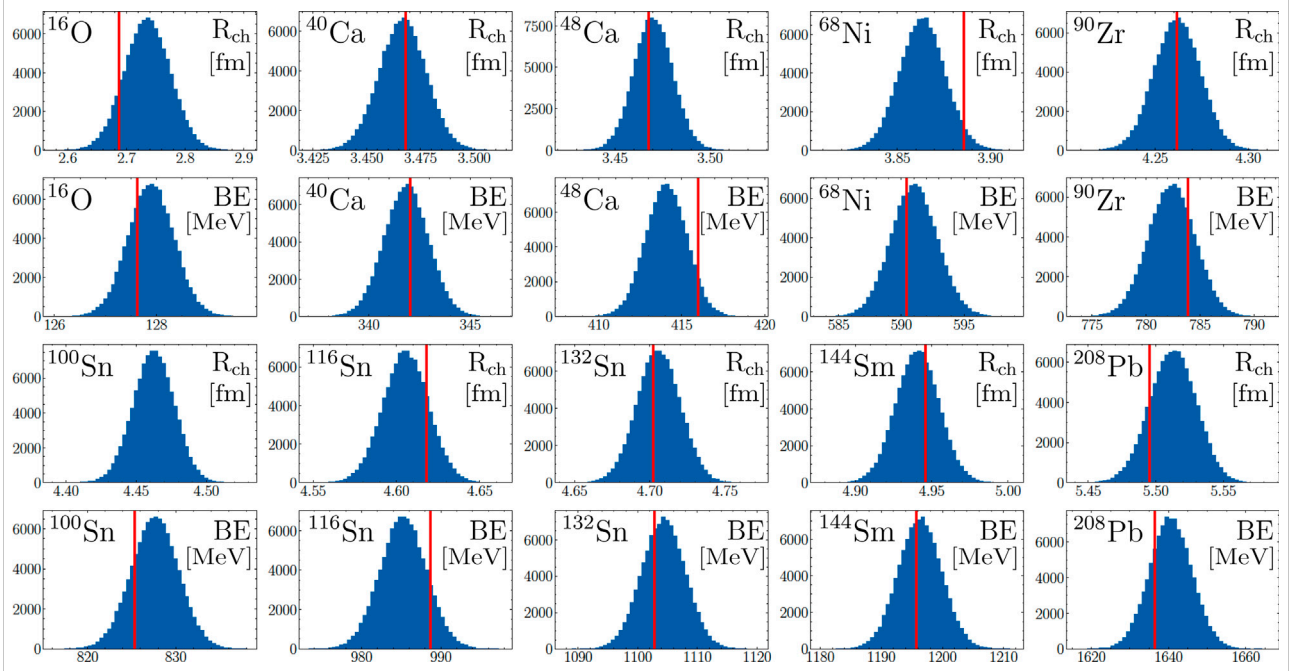

FIGURE 6
Posterior distributions for the binding energies (in MeV) and charge radii (in fm) of the ten nuclei involved in our study. A total of 100,000 samples from the 5,000,000 visited parameter values were used to make these distributions. The vertical red line in each plot represents the associated experimental values, all contained within the 95% credible interval of the model, including the charge radii of ^{68}Ni which was not included in the calibration of the model. On the other hand, ^{100}Sn does not have a measured charge radius, making its associated posterior distribution a true prediction from our calibration. The numerical values for the mean and credible intervals on all these quantities are displayed in Table 3.

TABLE 3 Mean values and 95% credible intervals of the Bayesian posteriors on charge radii (in fm) and binding energy (in MeV), showed in Figure 6. Also displayed are the 19 available experimental values [60, 63]. The credible intervals are calculated as equal-tailed intervals—such that the probabilities of falling above or below the interval are both equal to 2.5%.

Nucleus	$\langle R_{ch}^{em} \rangle$	[2.5%–97.5%]	R_{ch}^{ex}	$\langle BE^{em} \rangle$	[2.5%–97.5%]	BE^{exp}
^{16}O	2.736	[2.660–2.812]	2.690	127.90	[127.04–128.77]	127.62
^{40}Ca	3.467	[3.446–3.488]	3.471	341.83	[339.75–343.91]	342.05
^{48}Ca	3.470	[3.451–3.490]	3.470	414.05	[411.66–416.45]	416.00
^{68}Ni	3.864	[3.841–3.888]	3.887	590.99	[587.47–594.52]	590.41
^{90}Zr	4.262	[4.238–4.286]	4.264	782.34	[778.14–786.52]	783.90
^{100}Sn	4.462	[4.433–4.490]	-	827.69	[822.49–832.87]	825.30
^{116}Sn	4.606	[4.580–4.632]	4.620	985.21	[979.57–990.86]	988.68
^{132}Sn	4.705	[4.678–4.733]	4.704	1,104.3	[1,097.3–1,111.4]	1,102.84
^{144}Sm	4.941	[4.914–4.968]	4.947	1,196.3	[1,189.4–1,203.1]	1,195.73
^{208}Pb	5.512	[5.478–5.544]	5.497	1,640.7	[1,630.1–1,651.3]	1,636.43

binding energy of neutron-rich nuclei, such as ^{132}Sn and ^{208}Pb, the symmetry energy $\tilde{J} = S(\tilde{\rho}) \approx 26\,\text{MeV}$ is well constrained at an average density of about two-thirds of saturation density, or $\tilde{\rho} \approx 0.1\,\text{fm}^{-3}$ [83]. As a result, one obtains the following relation:

$$\tilde{J} = J - \frac{L}{9} + \frac{K_{\text{sym}}}{162} + \cdots \approx J - \frac{L}{9} \Rightarrow J \approx \tilde{J} + \frac{L}{9}. \tag{32}$$

Hence, accurately calibrated EDFs display a strong correlation between J and L by the mere fact that the calibration included information on the binding energy of neutron-rich nuclei. In the original calibration of FSUGold2 [60], one obtained a correlation coefficient between J and L of 0.97, while in this work we obtained a correlation coefficient of 0.92. The slight non-linearity observed in Figure 5 on the correlation between J and L is due to K_{sym}, which was neglected in the simple argument made in Eq. 32.

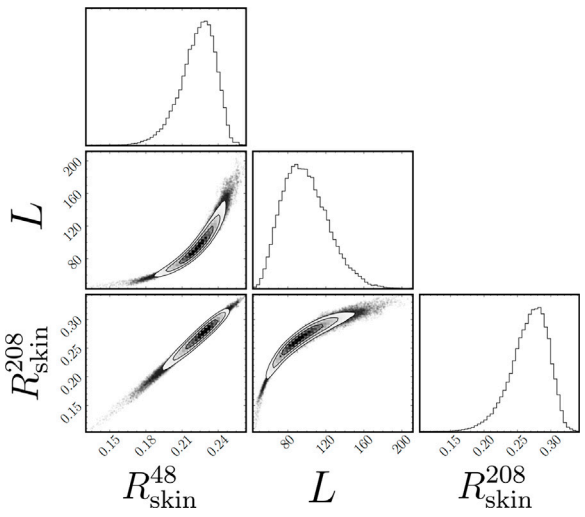

FIGURE 7
Correlation corner plot [81] between the posterior distributions for the neutron skin of ^{48}Ca and ^{208}Pb (both in fm), and the slope of the symmetry energy L (in MeV). A total of 100,000 samples from the 5,000,000 visited parameter values were used to make these distributions. Both neutron skins $R^{48}_{\rm skin}$ and $R^{208}_{\rm skin}$ are strongly correlated, each with negative skewness. The distribution for L, on the other hand, has a positive skewness and, while it is strongly correlated with both neutron skins, the correlation displays a non-linear behavior in both cases.

Although not directly an observable, L has been determined to be strongly correlated to the thickness of the neutron skin of heavy nuclei [83–85]; the neutron skin thickness is defined as the difference in the mean square radii between the neutron and proton vector densities (see Eq. 8). In Figure 7 we show the correlation plot between L and the neutron skin of ^{48}Ca and ^{208}Pb calculated directly from 100,000 random samples from our posterior distributions. It is important to note that we have not included the model error δ_i through Eq. 30 in these histograms[9], and as such we do not expect the uncertainties to be accurate, as we discuss later in Sec. VI.

The correlation between L and the thickness of the neutron skin of heavy nuclei has a strong physical underpinning. For example, in the case of ^{208}Pb, surface tension favors the formation of a spherical liquid drop containing all 208 nucleons. However, the symmetry energy increases monotonically in the density region of relevance to atomic nuclei. Hence, to minimize the symmetry energy, is energetically favorable to move some of the excess neutrons to the surface. It is then the difference in the symmetry energy at the core relative to its value at the surface that determines the thickness of the neutron skin; such a difference is encoded in the slope of the symmetry energy L. If such a difference is large enough to overcome surface tension, then some of the excess neutrons will be pushed to the surface, resulting in a thick neutron skin [86]. That the correlation between the neutron skin thickness of ^{208}Pb and L is strong has been validated using a large set of EDFs [85]. Note that L is closely related to the pressure of pure neutron matter at saturation density—a quantity that has been extensively studied using chiral effective field theory [13–19], and which is of great relevance to our understanding of the structure of neutron stars [87].

It is important to note that no information on neutron skins—or any other observable that is strongly correlated to L—was included in our calibration procedure, making it difficult to estimate the model error associated with such quantities. This also indicates that in the absence of any guidance, the class of covariant EDFs used in this work tend to produce stiff symmetry energies, in contrast to Skyrme-type EDFs and chiral effective field theories that tend to favor relatively soft symmetry energies [13–19, 88]. Particularly interesting to note is that whereas $R^{208}_{\rm skin}$ and L are strongly correlated, the correlation deviates significantly from the one obtained using a large set of both covariant and Skyrme energy density functionals [85]. It is known, however, that $R^{208}_{\rm skin}$ displays a stronger correlation with the slope of the symmetry energy at 0.1 fm^{-3} than at ρ_0; see Ref. [50] and references contained therein. However, the correlation between $R^{208}_{\rm skin}$ and $R^{48}_{\rm skin}$ we observe remains as strong as observed in Ref. [89].

Given the recently reported results from the PREX-II [48] and CREX [49] experimental campaigns, our model's average predicted neutron skin for both ^{208}Pb (0.27 fm) and ^{208}Ca (0.23 fm) might indicate that the physics encapsulated in the Lagrangian density depicted in Eq. 1 is insufficient to describe both skins simultaneously. Granted, with only two isovector parameters the model may be too rigid to break the strong observed model correlation between $R^{208}_{\rm skin}$ and $R^{48}_{\rm skin}$. However, whereas models with a more refined isovector sector may be able to reconcile both measurements at some level, a consensus is emerging that this can only be done at the expense of introducing significant tension with other calculated observables by the model.

To make a clear assessment, we will need to both include a statistical treatment of the expected model error in these quantities, as well as mitigate possible model dependencies by directly comparing with experimental observations such as the parity violating asymmetry. We are planing to do so as an immediate direction by calibrating covariant EDFs with an extended and more elaborated isovector sector that might help bridge both neutron skin results without compromising the success of the model in reproducing other nuclear observables, such as the ones displayed in Figure 6. As we discuss in the next and final section, well quantified uncertainties enabled by powerful emulators such as the RBM will be indispensable to achieve those goals and make full use of the anticipated new

9 Such procedure would require to first give an accurate estimation of the model error on *neutron* radii -a non trivial task given the lack of experimental data on neutron radii-, and second to take into account the model correlation between R_p and R_n.

laboratory experiments and astronomical observations that will be coming in the next years.

6 Conclusion and outlook

In the last few decades nuclear theory has gone through several transformational changes brought on by embracing philosophies and techniques from the fields of statistics and computational science. It is now expected that theoretical predictions should always be accompanied by uncertainties [93]. This is particularly true in theoretical nuclear physics where predictions from QCD inspired models require the calibration of several model parameters. This newly-adopted philosophy has also prompted the exploration of uncertainty quantification across the many sub-fields of nuclear theory [34, 94–97]. Furthermore, several recent advancements and discoveries have become feasible only through the successful integration of machine learning and other novel computational approaches to the large body of theoretical models developed over many decades [31, 74, 98–100]. This dedication is also exemplified by the theory community's proactive efforts to organize topical conferences, summer schools, and workshops in service of disseminating the technical know-how to every level of the community.

Aligned with these developments and efforts, our present work aimed at showcasing a pipeline for integrating a statistical framework through one such innovative computational technique. We have calibrated a covariant energy density functional within a Bayesian approach using available experimental values of binding energies and charge radii. The calibration of the model, as well as the quantification of the uncertainties of its predictions, required millions of evaluations for different values of its parameters. Such titanic computational burden was made possible—straightforward even—thanks to the emulation of the model through the reduced basis method, which decreased the necessary calculation time from months or years to a single day on a personal computer.

Our calibration's main results, which consists of posterior distributions for all the model's parameters, were presented in Figure 5. From these posteriors, and following the statistical framework we developed in Sec. IV, the model output can be estimated with well quantified uncertainties that can take into account experimental, model, and emulator errors. We showed such calculations with their respective estimated uncertainties in Figure 6 and Table 3 for the binding energies and charge radii of the 10 nuclei involved in the study. The fact that the experimental values used in the calibration, depicted as red vertical lines in Figure 6, fall within the 95% our calculated credible intervals gives us confidence that our uncertainty procedure was not biased towards being too optimistic for this dataset. This is especially true for the case of the charge radii of ^{16}O, which was treated as an outlier based on prior expert knowledge on the expectation of the limits of the mean field approach for smaller systems. Once the experimental value for the charge radii of ^{100}Sn becomes available, it will be interesting to contrast our model prediction's and gauge the success of the uncertainty level estimated.

However, the picture changes when we focus on the calculations for the neutron skin thickness of ^{48}Ca and ^{208}Pb showed in Figure 7. The recent experimental campaigns PREX [101], PREX-II [102], and CREX [49] on parity violating electron scattering have published results which suggest that the neutron skins of ^{48}Ca and ^{208}Pb stand in opposite corners. While ^{208}Pb is estimated to have a relatively thick neutron skin of around 0.28 fm [102], ^{48}Ca [49] is estimated to have a significantly smaller skin of around 0.12 fm. Albeit we have not included a model error term in the calculations shown in Figure 7, it seems that our current model is unable to satisfy both values simultaneously.

Moving forward, we envision two complementary research directions that could help mitigate the problems identified above. First, one could build a more robust statistical framework that, by including strong isovector indicators, such as information on the electric dipole response of neutron rich nuclei, will impose stringent constraints on the isovector sector. Second, and as already mentioned, we could increase the flexibility of the isovector sector by adding additional interactions that modify the density dependence of the symmetry energy. The use of dimensionality reduction techniques such as the RBM to significantly speed up the calculation time—especially if information on nuclear excitations is incorporated into the calibration of the EDF—will become a fundamental pillar of the fitting protocol.

We believe that the RBM we showcased here has the potential to further impact many of the nuclear theory areas that have already made use of similar emulators, as well as expanding the frontiers of the physical models that can be successfully emulated. Indeed, the RBM's unique combination of few high-fidelity evaluations needed to build an effective emulator, the simplicity and flexibility of the Galerkin projection, and the ability to precompute many observables and equations in the offline stage could allow the community to deploy trained emulators for use on different computer architectures and on cloud infrastructure [103]. This could effectively lower the barrier created by the need of running expensive computer models locally. This could give access of cutting edge theoretical models and simulations to an increased number of research groups, opening new opportunities to expand the network of collaborative research.

In short, the computational framework detailed in this work attempts to provide an end-to-end solution for model calibration and exploration with a focus on statistical rigor without sacrificing computational efficiency. By leveraging this efficiency to nimbly incorporate new experimental data, one can imagine the continuous calibration of models that can be updated in a matter of hours without requiring large-scale computing facilities. Finally, the heavy focus on integrating these disparate parts into a user-friendly form to generate physics-informed emulators is ultimately in service of our

wider goal to increase data availability and software accessibility, and is a necessity in the paradigmatic shift towards probability distributions—rooted in Bayesian principles—defining physical models rather than a single set of optimal parameters.

Data availability statement

The datasets presented in this study can be found in online repositories. The names of the repository/repositories and accession number(s) can be found below: https://figshare.com/projects/RBM_Calibration_Pipeline/149840.

Author contributions

PG, KG, and EB created the RBM framework. PG and KG implemented the computational pipeline. PG and FV created the Statistical Framework. KG created the computational sampling framework. JP provided the RMF physical description and insight and created the Relativistic Mean Field original code. All authors contributed to the writing and editing of the manuscript.

Funding

This work was supported by the National Science Foundation CSSI program under award number 2004601 (BAND collaboration) and the U.S. Department of Energy under Award Numbers DOE-DE-NA0004074 (NNSA, the Stewardship Science Academic Alliances program), DE-SC0013365 (Office of Science), and DE-SC0018083 (Office of Science, NUCLEI SciDAC-4 collaboration). This material is based upon work supported by the U.S. Department of Energy Office of Science, Office of Nuclear Physics under Award Number DE-FG02-92ER40750.

Acknowledgments

We are grateful to Moses Chan for guiding us on the use of the `surmise` python package, as well as for useful discussions and recommendations on good practices for the Monte Carlo sampling. We are grateful to Craig Gross for useful discussions about the reduced basis method, including the visualization of the speed up gained in terms of the high fidelity solver size $\mathcal{N}$. We thank Diogenes Figueroa for his reading of the manuscript. We thank Kei Minamisono for providing information regarding the experimentally measured charge radius of ^{68}Ni. We thank the two referees for a careful read of the manuscript and for comments and suggestions that improved it.

Conflict of interest

The authors declare that the research was conducted in the absence of any commercial or financial relationships that could be construed as a potential conflict of interest.

Publisher's note

References

1. Reaching for the Horizon: The 2015 long range plan for nuclear science," (2015).

2. Abbott BP. LIGO scientific collaboration, virgo collaboration. *Phys Rev Lett* (2017) 119:161101. doi:10.1103/physrevlett.121.129902

3. Drout MR, Piro AL, Shappee BJ, Kilpatrick CD, Simon JD, Contreras C, et al. Light curves of the neutron star merger GW170817/SSS17a: Implications for r-process nucleosynthesis. *Science* (2017) 358:1570. doi:10.1126/science.aaq0049

4. Cowperthwaite PS, Berger E, Villar VA, Metzger BD, Nicholl M, Chornock R, et al. The electromagnetic counterpart of the binary neutron star merger LIGO/virgo GW170817. II. UV, optical, and near-infrared light curves and comparison to kilonova models. *Astrophys J* (2017) 848:L17. doi:10.3847/2041-8213/aa8fc7

5. Chornock R, Berger E, Kasen D, Cowperthwaite PS, Nicholl M, Villar VA, et al. The electromagnetic counterpart of the binary neutron star merger LIGO/virgo GW170817. IV. Detection of near-infrared signatures of r-process nucleosynthesis with gemini-south. *Astrophys J* (2017) 848:L19. doi:10.3847/2041-8213/aa905c

6. Nicholl M, Berger E, Kasen D, Metzger BD, Elias J, Briceño C, et al. The electromagnetic counterpart of the binary neutron star merger LIGO/virgo GW170817. III. Optical and UV spectra of a blue kilonova from fast polar ejecta. *Astrophys J* (2017) 848:L18. doi:10.3847/2041-8213/aa9029

7. Fattoyev FJ, Piekarewicz J, Horowitz CJ. Neutron skins and neutron stars in the multimessenger era. *Phys Rev Lett* (2018) 120:172702. doi:10.1103/physrevlett.120.172702

8. Annala E, Gorda T, Kurkela A, Vuorinen A. Gravitational-wave constraints on the neutron-star-matter equation of state. *Phys Rev Lett* (2018) 120:172703. doi:10.1103/physrevlett.120.172703

9. Abbott BP. LIGO scientific collaboration, virgo collaboration). *Phys Rev Lett* (2018) 121:161101. doi:10.1103/physrevlett.121.129902

10. Weinberg S. Nuclear forces from chiral Lagrangians. *Phys Lett B* (1990) 251:288–92. doi:10.1016/0370-2693(90)90938-3

11. van Kolck U. Few-nucleon forces from chiral Lagrangians. *Phys Rev C* (1994) 49:2932–41. doi:10.1103/physrevc.49.2932

12. Ordóñez C, Ray L, van Kolck U. Two-nucleon potential from chiral Lagrangians. *Phys Rev C* (1996) 53:2086–105. doi:10.1103/physrevc.53.2086

13. Hebeler K, Schwenk A. Chiral three-nucleon forces and neutron matter. *Phys Rev C* (2010) 82:014314. doi:10.1103/physrevc.82.014314

14. Tews I, Kruger T, Hebeler K, Schwenk A. Neutron matter at next-to-next-to-next-to-leading order in chiral effective field theory. *Phys Rev Lett* (2013) 110:032504. doi:10.1103/physrevlett.110.032504

15. Kruger T, Tews I, Hebeler K, Schwenk A. Neutron matter from chiral effective field theory interactions. *Phys Rev* (2013) C88:025802. doi:10.1103/PhysRevC.88.025802

16. Lonardoni D, Tews I, Gandolfi S, Carlson J. Nuclear and neutron-star matter from local chiral interactions. *Phys Rev Res* (2020) 2:022033. doi:10.1103/physrevresearch.2.022033

17. Drischler C, Holt JW, Wellenhofer C. Chiral effective field theory and the high-density nuclear equation of state. *Annu Rev Nucl Part Sci* (2021) 71:403–32. doi:10.1146/annurev-nucl-102419-041903

18. Sammarruca F, Millerson R. Overview of symmetric nuclear matter properties from chiral interactions up to fourth order of the chiral expansion. *Phys Rev C* (2021) 104:034308. doi:10.1103/physrevc.104.064312

19. Millerson F, Millerson R. The equation of state of neutron-rich matter at fourth order of chiral effective field theory and the radius of a medium-mass neutron star. *Universe* (2022) 8:133. doi:10.3390/universe8020133

20. Kohn W. Nobel Lecture: Electronic structure of matter-wave functions and density functionals. *Rev Mod Phys* (1999) 71:1253–66. doi:10.1103/revmodphys.71.1253

21. Kohn P, Kohn W. Inhomogeneous electron gas. *Phys Rev* (1964) 136:B864–B871. doi:10.1103/physrev.136.b864

22. Sham W, Sham LJ. Self-consistent equations including exchange and correlation effects. *Phys Rev* (1965) 140:A1133–A1138. doi:10.1103/physrev.140.a1133

23. Phillips DR, Furnstahl RJ, Heinz U, Maiti T, Nazarewicz W, Nunes FM, et al. Get on the BAND wagon: A bayesian framework for quantifying model uncertainties in nuclear dynamics. *J Phys G: Nucl Part Phys* (2021) 48:072001. doi:10.1088/1361-6471/abf1df

24. Frame D, He R, Ipsen I, Lee D, Lee D, Rrapaj E. Eigenvector continuation with subspace learning. *Phys Rev Lett* (2018) 121:032501. doi:10.1103/physrevlett.121.032501

25. König S, Ekström A, Hebeler K, Lee D, Schwenk A. Eigenvector continuation as an efficient and accurate emulator for uncertainty quantification. *Phys Lett B* (2020) 810:135814. doi:10.1016/j.physletb.2020.135814

26. Furnstahl R, Garcia A, Millican P, Zhang X. Efficient emulators for scattering using eigenvector continuation. *Phys Lett B* (2020) 809:135719. doi:10.1016/j.physletb.2020.135719

27. Melendez J, Drischler C, Garcia A, Furnstahl R, Zhang X. Fast & accurate emulation of two-body scattering observables without wave functions. *Phys Lett B* (2021) 821:136608. doi:10.1016/j.physletb.2021.136608

28. Drischler C, Quinonez M, Giuliani P, Lovell A, Nunes F. Toward emulating nuclear reactions using eigenvector continuation. *Phys Lett B* (2021) 823:136777. doi:10.1016/j.physletb.2021.136777

29. Bonilla E, Giuliani P, Godbey K, Lee D, (2022), Training and projecting: A reduced basis method emulator for many-body physics. *Phys Rev C* (2022) 106:054322. doi:10.1103/PhysRevC.106.054322

30. Sarkar A, Lee D. Self-learning emulators and eigenvector continuation. *Phys Rev Res* (2022) 4:023214. doi:10.1103/physrevresearch.4.023214

31. Boehnlein A, Diefenthaler M, Sato N, Schram M, Ziegler V, Fanelli C, et al. Colloquium: Machine learning in nuclear physics. *Rev Mod Phys* (2022) 94:031003. doi:10.1103/revmodphys.94.031003

32. Tews I, Davoudi Z, Ekström A, Holt JD, Becker K, Briceño R, et al. Nuclear forces for precision nuclear physics: A collection of perspectives. *Few-body Syst* (2022) 63:1. doi:10.1007/s00601-022-01749-x

33. Higdon D, McDonnell JD, Schunck N, Sarich J, Wild SM. A Bayesian approach for parameter estimation and prediction using a computationally intensive model. *J Phys G Nucl Part Phys* (2015) 42:034009. doi:10.1088/0954-3899/42/3/034009

34. McDonnell JD, Schunck N, Higdon D, Sarich J, Wild SM, Nazarewicz W. Uncertainty quantification for nuclear density functional theory and information content of new measurements. *Phys Rev Lett* (2015) 114:122501. doi:10.1103/physrevlett.114.122501

35. Anderson AL, O'Donnell GL, Piekarewicz J. Applications of reduced-basis methods to the nuclear single-particle spectrum. *Phys Rev C* (2022) 106:L031302. doi:10.1103/physrevc.106.l031302

36. Quarteroni A, Manzoni A, Negri F. *Reduced basis methods for partial differential equations: An introduction*, 92. Springer (2015). doi:10.1007/978-3-319-15431-2

37. Hesthaven JS, Rozza G, Stamm B. *Certified reduced basis methods for parametrized partial differential equations*, 590. Springer (2016). doi:10.1007/978-3-319-22470-1

38. Melendez JA, Drischler C, Furnstahl RJ, Garcia AJ, Zhang X. Model reduction methods for nuclear emulators. *J Phys G: Nucl Part Phys* (2022) 49:102001. doi:10.1088/1361-6471/ac83dd

39. Quarteroni A, Rozza G. *Reduced order methods for modeling and computational reduction*, 9. Springer (2014). doi:10.1007/978-3-319-02090-7

40. Brunton SL, Kutz JN. *Data-driven science and engineering: Machine learning, dynamical systems, and control*. Cambridge University Press (2019). doi:10.1017/9781108380690

41. Benner P, Gugercin S, Willcox K. A survey of projection-based model reduction methods for parametric dynamical systems. *SIAM Rev* (2015) 57:483–531. doi:10.1137/130932715

42. Sartori A, Cammi A, Luzzi L, Rozza G. A reduced basis approach for modeling the movement of nuclear reactor control rods. *J Nucl Eng Radiat* (2016) 2:1062. doi:10.1115/1.4031945

43. Quarteroni A, Rozza G, Manzoni A. Certified reduced basis approximation for parametrized partial differential equations and applications. *J Math Ind* (2011) 1:1. doi:10.1186/2190-5983-1-3

44. Field SE, Galley CR, Herrmann F, Hesthaven JS, Ochsner E, Tiglio M. Reduced basis catalogs for gravitational wave templates. *Phys Rev Lett* (2011) 106:221102. doi:10.1103/physrevlett.106.221102

45. Nguyen NC, Rozza G, Huynh DBP, Patera AT. Reduced basis approximation and a posteriori error estimation for parametrized parabolic PDEs: Application to real-time bayesian parameter estimation. In: *Large-scale inverse problems and quantification of uncertainty*. John Wiley & Sons (2010). p. 151–77. Chap. 8. doi:10.1002/9780470685853.ch8

46. Jiang J, Chen Y, Narayan A. A goal-oriented reduced basis methods-accelerated generalized polynomial chaos algorithm. *Siam/asa J Uncertainty Quantification* (2016) 4:1398–420. doi:10.1137/16m1055736

47. Abrahamyan S, Ahmed Z, Albataineh H, Aniol K, Armstrong DS, Armstrong W. Measurement of the neutron radius of 208Pb through parity violation in electron scattering. *Phys Rev Lett* (2012) 108:112502. doi:10.1103/PhysRevLett.108.112502

48. Adhikari D. Accurate determination of the neutron skin Th. *Phys Rev Lett* (2021) 126:172502. doi:10.1103/PhysRevLett.126.172502

49. Adhikari D. Precision determination of the neutral weak form factor of ^{48} Ca. *Phys Rev Lett* (2022) 129:042501. doi:10.1103/PhysRevLett.129.042501

50. Reed BT, Fattoyev FJ, Horowitz CJ, Piekarewicz J. Implications of PREX-2 on the equation of state of neutron-rich matter. *Phys Rev Lett* (2021) 126:172503. doi:10.1103/physrevlett.126.172503

51. Reinhard P-G, Roca-Maza X, Nazarewicz W, Combined theoretical analysis of the parity-violating asymmetry for ^{48}Ca and ^{208}Pb. (2022), arXiv:2206.03134 [nucl-th] .

52. Ireland D, Nazarewicz W. Enhancing the interaction between nuclear experiment and theory through information and statistics. *J Phys G Nucl Part Phys* (2015) 42. doi:10.1088/0954-3899/42/3/030301

53. Bedaque P, Boehnlein A, Cromaz M, Diefenthaler M, Elouadrhiri L, Horn T, et al. *Eur Phys J A* (2021) 57:1. doi:10.1140/epja/s10050-020-00290-x

54. Walecka JD. A theory of highly condensed matter. *Ann Phys* (1974) 83:491–529. doi:10.1016/0003-4916(74)90208-5

55. Serot BD, Walecka JD. Relativistic nuclear many-body theory. *Adv Nucl Phys* (1986) 16:1. doi:10.1007/978-1-4615-3466-2_5

56. Bodmer J, Bodmer AR. Relativistic calculation of nuclear matter and the nuclear surface. *Nucl Phys A* (1977) 292:413–28. doi:10.1016/0375-9474(77)90626-1

57. Mueller H, Serot BD. Relativistic mean-field theory and the high-density nuclear equation of state. *Nucl Phys A* (1996) 606:508. doi:10.1016/0375-9474(96)00187-X

58. Piekarewicz CJ, Piekarewicz J. Neutron star structure and the neutron radius ofP208b. *Phys Rev Lett* (2001) 86:5647–50. doi:10.1103/physrevlett.86.5647

59. Todd BG, Piekarewicz J. Relativistic mean-field study of neutron-rich nuclei. *Phys Rev C* (2003) 67:044317. doi:10.1103/physrevc.67.044317

60. Chen W-C, Piekarewicz J. Building relativistic mean field models for finite nuclei and neutron stars. *Phys Rev C* (2014) 90:044305. doi:10.1103/physrevc.90.044305

61. Piekarewicz J, Piekarewicz J. Covariant density functional theory in nuclear physics and astrophysics. *Annu Rev Nucl Part Sci* (2020) 70:21–41. doi:10.1146/annurev-nucl-101918-023608

62. Tiesinga E, Mohr PJ, Newell DB, Taylor BN. CODATA recommended values of the fundamental physical constants: 2018. *J Phys Chem Reference Data* (2021) 50:033105. doi:10.1063/5.0064853

63. Kaufmann S, Simonis J, Bacca S, Billowes J, Bissell ML, Blaum K. Charge radius of the short-lived Ni 68 and correlation with the dipole plarizability. (2020). *Phys Rev Lett* (2012) 124:132502. doi:10.1103/PhysRevLett.127.182503

64. Glendenning NK. *Compact stars*. Springer-Verlag New York (2000). doi:10.1007/978-1-4684-0491-3

65. Blum A, Hopcroft J, Kannan R. *Foundations of data science*. Cambridge University Press (2020). doi:10.1017/9781108755528

66. Jolliffe IT. *Principal component analysis*. Springer (2002). doi:10.1007/b98835

67. Rawitscher G, dos Santos Filho V, Peixoto TC. Galerkin and collocation methods. In: *An introductory guide to computational methods for the solution of physics problems*. Springer (2018). p. 17–31. doi:10.1007/978-3-319-42703-4

68. Fletcher CA. *Computational Galerkin methods*. Springer (1984). doi:10.1007/978-3-642-85949-6

69. Grepl MA, Maday Y, Nguyen NC, Patera AT. Efficient reduced-basis treatment of nonaffine and nonlinear partial differential equations. *Esaim: M2an* (2007) 41:575–605. doi:10.1051/m2an:2007031

70. Barrault M, Maday Y, Nguyen NC, Patera AT. An 'empirical interpolation' method: Application to efficient reduced-basis discretization of partial differential equations. *Comptes Rendus Mathematique* (2004) 339:667–72. doi:10.1016/j.crma.2004.08.006

71. Virtanen P, Gommers R, Oliphant TE, Haberland M, Reddy T, Cournapeau D, et al. SciPy 1.0: Fundamental algorithms for scientific computing in Python. *Nat Methods* (2020) 17:261–72. doi:10.1038/s41592-019-0686-2

72. Gelman A, Carlin JB, Stern HS, Rubin DB. *Bayesian data analysis*. Chapman and Hall/CRC (1995). doi:10.1201/b16018

73. Neufcourt L, Cao Y, Nazarewicz W, Viens F. Bayesian approach to model-based extrapolation of nuclear observables. *Phys Rev C* (2018) 98:034318. doi:10.1103/physrevc.98.034318

74. Neufcourt L, Cao Y, Nazarewicz W, Olsen E, Viens F. Neutron drip line in the Ca region from bayesian model averaging. *Phys Rev Lett* (2019) 122:062502. doi:10.1103/physrevlett.122.062502

75. Ludwig D. Parsimonious asymptotics. *SIAM J Appl Math* (1983) 43:664–72. doi:10.1137/0143045

76. Veroy K, Prud'Homme C, Rovas D, Patera A. A posteriori error bounds for reduced-basis approximation of parametrized noncoercive and nonlinear elliptic partial differential equations. *Fluid Dyn Conf* (2003) 3847. 16th AIAA Comput. doi:10.2514/6.2003-3847

77. Buffa A, Maday Y, Patera AT, Prud'homme C, Turinici G. A priori convergence of the Greedy algorithm for the parametrized reduced basis method. *Esaim: M2an* (2012) 46:595–603. doi:10.1051/m2an/2011056

78. Huang W, Wang M, Kondev FG, Audi G, Naimi S. The AME 2020 atomic mass evaluation (I). Evaluation of input data, and adjustment procedures*. *Chin Phys. C* (2021) 45:030002. doi:10.1088/1674-1137/abddb0

79. Marinova I, Marinova KP. Table of experimental nuclear ground state charge radii: An update. *At Data Nucl Data Tables* (2013) 99:69–95. doi:10.1016/j.adt.2011.12.006

80. Plumlee M, Sürer Ö, Wild SM. *Tech. Rep. Version 0.1.0*. NAISE (2021). Surmise users manual. Available at: https://surmise.readthedocs.io/en/latest/introduction.html

81. Foreman-Mackey D. corner.py: Scatterplot matrices in Python. *Joss* (2016) 1:24. doi:10.21105/joss.00024

82. Piekarewicz J, Centelles M. Incompressibility of neutron-rich matter. *Phys Rev C* (2009) 79:054311. doi:10.1103/physrevc.79.054311

83. Furnstahl RJ. Neutron radii in mean-field models. *Nucl Phys A* (2002) 706:85–110. doi:10.1016/s0375-9474(02)00867-9

84. Brown BA. Neutron radii in nuclei and the neutron equation of state. *Phys Rev Lett* (2000) 85:5296–9. doi:10.1103/PhysRevLett.85.5296

85. Roca-Maza X, Centelles M, Viñas X, Warda M. Neutron skin ofPb208, nuclear symmetry energy, and the parity radius experiment. *Phys Rev Lett* (2011) 106:252501. doi:10.1103/physrevlett.106.252501

86. Horowitz CJ, Piekarewicz J. The neutron radii of Lead and neutron stars. *Phys Rev C* (2001) 64:062802. doi:10.1103/physrevc.64.062802

87. Fattoyev J, Fattoyev FJ. Neutron-rich matter in heaven and on Earth. *Phys Today* (2019) 72:30–7. doi:10.1063/pt.3.4247

88. Reinhard P-G, Roca-Maza X, Nazarewicz W. Information content of the parity-violating asymmetry in Pb208. *Phys Rev Lett* (2021) 127:232501. doi:10.1103/physrevlett.127.232501

89. Piekarewicz J. Implications of PREX-2 on the electric dipole polarizability of neutron-rich nuclei. *Phys Rev C* (2021) 104:024329. doi:10.1103/physrevc.104.024329

90. Hu B, Jiang W, Miyagi T. *Ab initio* predictions link the neutron skin of 208Pb to nuclear forces. *Nat Phys* (2022) 18:1196–200. doi:10.1038/s41567-022-01715-8

91. Zhang Z, Chen L-W, (2022), Bayesian inference of the symmetry energy and the neutron skin in 48Ca and 208Pb from CREX and PREX-2, arXiv:2207.03328 [nucl-th].

92. Mondal C, Gulminelli F, (2022), Nucleonic metamodelling in light of multimessenger, PREX-II and CREX data, arXiv:2209.05177 [nucl-th].

93. Join A. A new mass model for nuclear astrophysics: Crossing 200 keV accuracy. *Phys Rev A* (2011) 83:040001.

94. Godbey K, Umar S, Simenel C. Theoretical uncertainty quantification for heavy-ion fusion. *Phys Rev C.* (2022) 106:L0511602. doi:10.1103/PhysRevC.106.L051602

95. King G, Lovell A, Neufcourt L, Nunes F. Direct comparison between bayesian and frequentist uncertainty quantification for nuclear reactions. *Phys Rev Lett* (2019) 122:232502. doi:10.1103/physrevlett.122.232502

96. Odell D, Brune CR, Phillips DR, deBoer RJ, Paneru SN. Performing bayesian analyses with AZURE2 using BRICK: An application to the ^{7}Be system. *Front Phys* (2022) 423:888476. doi:10.3389/fphy.2022.888476

97. Drischler C, Furnstahl RJ, Melendez JA, Phillips DR. How well do we know the neutron-matter equation of state at the densities inside neutron stars? A bayesian approach with correlated uncertainties. *Phys Rev Lett* (2020) 125:202702. doi:10.1103/physrevlett.125.202702

98. Hamaker A, Leistenschneider E, Jain R, Bollen G, Giuliani S, Lund K, et al. Precision mass measurement of lightweight self-conjugate nucleus 80Zr. *Nat Phys* (2021) 17:1408–12. doi:10.1038/s41567-021-01395-w

99. Utama R, Piekarewicz J, Prosper H. Nuclear mass predictions for the crustal composition of neutron stars: A bayesian neural network approach. *Phys Rev C* (2016) 93:014311. doi:10.1103/physrevc.93.014311

100. Kuchera MP, Ramanujan R, Taylor JZ, Strauss RR, Bazin D, Bradt J, et al. Machine learning methods for track classification in the AT-TPC. *Nucl Instr Methods Phys Res Section A: Acc Spectrometers, Detectors Associated Equipment* (2019) 940:156–67. doi:10.1016/j.nima.2019.05.097

101. Abrahamyan S, Ahmed Z, Albataineh H, Aniol K, Armstrong D, Armstrong W, et al. Measurement of the neutron radius of 208Pb through parity violation in electron scattering. *Phys Rev Lett* (2012) 108:112502. doi:10.1103/PhysRevLett.108.112502

102. Adhikari D, Albataineh H, Androic D, Aniol K, Armstrong D, Averett T, et al. Accurate determination of the neutron skin thickness of Pb208 through parity-violation in electron scattering. *Phys Rev Lett* (2021) 126:172502. doi:10.1103/physrevlett.126.172502

103. Godbey K, Giuliani P, "BMEX - The Bayesian Mass Explorer", (2022). Available at: https://bmex.dev

frontiers | Frontiers in Physics

TYPE Original Research
PUBLISHED 11 January 2023
DOI 10.3389/fphy.2022.1049919

OPEN ACCESS

EDITED BY
Sonia Bacca,
Johannes Gutenberg University Mainz, Germany

REVIEWED BY
Chen Ji,
Central China Normal University, China
Bijaya Acharya,
Oak Ridge National Laboratory (DOE), United States

*CORRESPONDENCE
L. E. Marcucci,
laura.elisa.marcucci@unipi.it

SPECIALTY SECTION
This article was submitted to Nuclear Physics, a section of the journal Frontiers in Physics

RECEIVED 21 September 2022
ACCEPTED 07 November 2022
PUBLISHED 11 January 2023

CITATION
Ceccarelli L, Gnech A, Marcucci LE, Piarulli M and Viviani M (2023), Muon capture on deuteron using local chiral potentials.
Front. Phys. 10:1049919.
doi: 10.3389/fphy.2022.1049919

Muon capture on deuteron using local chiral potentials

L. Ceccarelli[1], A. Gnech[2], L. E. Marcucci[1,3]*, M. Piarulli[4,5] and M. Viviani[3]

[1]Dipartimento di Fisica "E. Fermi", Università di Pisa, Pisa, Italy, [2]Theory Center, Jefferson Lab, Newport News, Virginia, United States, [3]Istituto Nazionale di Fisica Nucleare, Pisa, Italy, [4]Physics Department, Washington University, St. Louis, MO, United States, [5]McDonnell Center for the Space Sciences at Washington University in St. Louis, St. Louis, MO, United States

The muon capture reaction $\mu^- + d \to n + n + \nu_\mu$ in the doublet hyperfine state is studied using nuclear potentials and consistent currents derived in the chiral effective field theory, which are local and expressed in coordinate space (the so-called Norfolk models). Only the largest contribution due to the $^1S_0$ *nn* scattering state is considered. Particular attention is given to the estimate of theoretical uncertainty, for which four sources have been identified: 1) the model dependence, 2) the chiral-order convergence for the weak nuclear current, 3) the uncertainty in the single-nucleon axial form factor, and 4) the numerical technique adopted to solve the bound and scattering $A = 2$ systems. This last source of uncertainty has turned out to be essentially negligible. For the $^1S_0$ doublet muon capture rate $\Gamma^D(^1S_0)$, we obtain $\Gamma^D(^1S_0) = 255.8\,(0.6)\,(4.4)\,(2.9)\ \mathrm{s}^{-1}$, where the three errors come from the first three sources of uncertainty. The value for $\Gamma^D(^1S_0)$ obtained within this local chiral framework is compared with previous calculations and found in very good agreement.

KEYWORDS

muon capture, deuteron, chiral effective field theory, *ab initio* calculation, error estimate

1 Introduction

The muon capture on a deuteron, i.e. the process

$$\mu^- + d \to n + n + \nu_\mu, \tag{1}$$

is one of the few weak nuclear reactions involving light nuclei which, on one side, are experimentally accessible, and, on the other, can be studied using *ab initio* methods. Furthermore, it is a process closely linked to the proton–proton weak capture, the so-called *pp* reaction,

$$p + p \to d + e^+ + \nu_e, \tag{2}$$

which, although being of paramount importance in astrophysics, is not experimentally accessible due to its extremely low rate and can only be calculated. Since the theoretical inputs to study reaction (2) and reaction (1) are essentially the same, the comparison between the experiment and theory for muon capture provides a strong test for the *pp* studies.

The muon capture reaction (1) can take place in two different hyperfine states, $f = 1/2$ and 3/2. Since it is well known that the doublet capture rate is about 40 times larger than the quartet one (see, for instance, Ref. [1]), we will consider the $f = 1/2$ state only, and we will focus on the doublet capture rate, Γ^D. The experimental situation for Γ^D is quite confused, with available measurements which are relatively old. These are the ones of Refs. [2–5], 365 (96) s^{-1}, 445 (60) s^{-1}, 470 (29) s^{-1}, and 409 (40) s^{-1}, respectively. All these data are consistent with each other within the experimental uncertainties, which are, however, quite large. To clarify the situation, an experiment with the aim of measuring Γ^D with 1% accuracy is currently performed at the Paul Scherrer Institute, in Switzerland, by the MuSun Collaboration [6].

Many theoretical studies are available for the muon capture rate Γ^D. A review of the available literature from up to about 10 years ago can be found in Ref. [7]. Here, we focus on the work conducted in the past 10 years. To the best of our knowledge, the capture rate Γ^D has been studied in Refs. [8–12]. The studies of Refs. [9, 11] were performed within the phenomenological approach, using phenomenological potentials and currents. In Ref. [9], the first attempt to use the chiral effective field theory (χEFT) was presented, within the so-called hybrid approach, where a phenomenological nuclear interaction is used in conjunction with χEFT weak nuclear charge and current operators. In the study we present in this contribution, though, we are interested not only in the determination of Γ^D but also an assessment of the theoretical uncertainty. This can be grasped more comfortably and robustly within a consistent χEFT approach. Therefore, we review only the theoretical works of Refs. [8, 10, 12], which were performed within a consistent χEFT. The studies of Refs. [8, 10] were essentially performed in parallel. They both employed the latest (at those times) nuclear chiral potentials and consistent weak current operators. In Ref. [8], the doublet capture rate was found to be $\Gamma^D = 388.1\ (4.3)\ s^{-1}$, when the *NN* chiral potentials of Ref. [13], obtained up to the next-to-next-to-next-to-leading order (N3LO) in the chiral expansion, were used. When only the $^1S_0$ channel of the final *nn* scattering state was retained, it was found that $\Gamma^D\,(^1S_0) = 247.7\,(2.8)\ s^{-1}$. In Ref. [10], a simultaneous study of the muon capture on a deuteron and ^{3}He was performed using the same N3LO chiral potentials, but varying the potential cutoff $\Lambda = 500, 600$ MeV [13, 14], and consequently refitting consistently for each value of Λ the low-energy constants (LECs) entering into the axial and vector current operators. For the muon capture on a deuteron, it was obtained $\Gamma^D = 399\ (3)\ s^{-1}$, the spread accounting for the cutoff sensitivity, as well as uncertainties in the LECs and electroweak radiative corrections. When only the $^1S_0$ channel is considered, $\Gamma^D\,(^1S_0) = 254.9\,(1.4)\ s^{-1}$, where, in this case, the (small) uncertainty arising from electroweak radiative corrections is not included. In the case of the muon capture on ^{3}He, an excellent agreement with the available extremely accurate experimental datum was found. Although obtained by different groups and with some differences in the axial and vector current operators adopted in the calculations, the results of Refs. [8, 10] for Γ^D and $\Gamma^D\,(^1S_0)$ should be considered in reasonable agreement. It should be mentioned that in both studies of Refs. [8, 10], a relation between the LEC entering the axial current operator (denoted by d_R) and c_D, one of the two LECs entering the three-nucleon potential (the other one being c_E) was taken from Ref. [15]. Then, the $A = 3$ binding energies and the Gamow–Teller matrix element of tritium β-decay were used to fix both c_D (and consequently d_R) and c_E for each given potential and cutoff Λ. Unfortunately, the relation between d_R and c_D of Ref. [15] is missing of a factor $-1/4$, as clearly stated in the Erratum of Ref. [10] (see also the Erratum of Ref. [15]). While the work of Ref. [8] has not yet been revisited, that of Ref. [10] has been corrected, finding very small changes in the final results, which become $\Gamma^D = 398\ (3)\ s^{-1}$ and $\Gamma^D\,(^1S_0) = 253.5\,(1.2)\ s^{-1}$.

The most recent and systematic study of reaction (1) in χEFT, even if only retaining the $^1S_0$ *nn* channel, is that of Ref. [12]. There, $\Gamma^D\,(^1S_0)$ was calculated using a pool of 42 non-local chiral potentials up to the next-to-next-to-leading order (N2LO), with a regulator cutoff Λ in the range 450–600 MeV and six different energy ranges in the *NN* scattering database [16]. The consistent axial and vector currents were constructed (with the correct relation between d_R and c_D), and a simultaneous fitting procedure for all the involved LECs was adopted. The final result was found to be $\Gamma^D\,(^1S_0) = 252.8\,(4.6)\,(3.9)\ s^{-1}$, in excellent agreement with Ref. [10]. Here, the first error is due to the truncation in the chiral expansion and the second one is due to the uncertainty in the parameterization of the single-nucleon axial form factor (see as follows). Furthermore, in Ref. [17], it has been found that a non-proper treatment of the infrared cutoff when the bound-state wave function is represented in a truncated basis (as in the case of Refs. [9, 10]) can lead to an error of the order of ~ 1% in the few-nucleon capture cross sections and astrophysical *S*-factors (as that of the *pp* reaction, the case studied in Ref. [17]). Therefore, we believe that it is also important to investigate this issue related to the present muon capture process.

The chiral nuclear potentials involved in all the aforementioned studies are highly non-local and expressed in momentum space. This is less desirable than the *r*-space in the case of the *pp* reaction, where the treatment in the momentum space of the Coulomb interaction and the higher-order electromagnetic effects is rather cumbersome. To overcome these difficulties, local chiral potentials expressed in the *r*-space would be highly desirable. These have been developed only in recent years, as discussed in the recent review of Ref. [18].

These potentials are very accurate and have proven to be extremely successful in describing the structure and dynamics of light and medium-mass nuclei. In particular, we are interested in the work of the models of Ref. [19], the so-called Norfolk potentials, for which, in these years, consistent electromagnetic and weak transition operators have been constructed [20–22]. This local chiral framework has been used to calculate energies [23] and charge radii [24] and various electromagnetic observables in light nuclei, as the charge form factors in $A = 6$, 12 [24] and the magnetic structure of few-nucleon systems [22]. It has also been used to study weak transitions in light nuclei [25, 26], the muon captures on $A = 3, 6$ nuclei [27], neutrinoless double β-decay for $A = 6$, 12 [28] and the β-decay spectra in $A = 6$ [29], and, finally, the equation of the state of pure neutron matter [30, 31]. However, the use of the Norfolk potentials to study the muon capture on a deuteron and the *pp* reaction is still lacking. One of the aims of this work is to start this path. Given the fact that $\Gamma^D(^1S_0)$ is the main contribution to Γ^D, and the $^1S_0$ channel is also the only one of interest for *pp* fusion [32, 33], we focus our attention only on $\Gamma^D(^1S_0)$. A full calculation of Γ^D, together with the rates for muon capture on $A = 3, 6$ nuclei, is currently underway. The second aim of the present study is to provide a more robust determination of the theoretical uncertainty than the work of Ref. [10], although probably not as robust as the full work presented in Ref. [12]. However, the procedure we plan to apply in the present work is much simpler and, as shown as follows, with a quite similar outcome. We will consider four sources of uncertainties: 1) the first one is due to model dependence. In this study, the use of the local Norfolk potentials will allow us to take into consideration the uncertainty arising from the cutoff variation, as well as the energy ranges in the *NN* scattering database up to which the LECs are fitted. In fact, as it will be explained in Section 2.2, we will employ four different versions of the Norfolk potentials, obtained using two different sets of short- and long-range cutoffs, and two different energy ranges, up to 125 MeV or up to 200 MeV, in the *NN* scattering database. 2) The second source of uncertainty arises from the chiral-order convergence. In principle, this should be investigated by maintaining the same order for potentials and weak nuclear currents. However, at present, the Norfolk potentials, for which weak current operators have been consistently constructed, are those obtained at N3LO. This chiral order is needed to reach good accuracy in the description of the *NN* systems and of light nuclei. Therefore, it is questionable whether a study of reaction (1) using potentials and currents at a chiral order which does not even reproduce the nuclear systems under consideration, would be of real interest. As a consequence, we will study, in the present work, only the chiral-order convergence for the weak nuclear currents, keeping fixed the chiral order of the adopted potentials. 3) The third source of uncertainty is due to the uncertainty in the parameterization of the single-nucleon axial form factor $g_A(q_\sigma^2)$ as a function of the squared four-momentum transfer q_σ^2. This aspect is discussed in detail in Section 2.2. Here, we only notice that the most recent parameterization for the single-nucleon axial form factor is given by

$$g_A(q_\sigma^2) = g_A\left(1 - \frac{1}{6}r_A^2 q_\sigma^2 + \cdots\right), \tag{3}$$

where the dots indicate higher-order terms, which are typically disregarded, and r_A is the axial charge radius, its square being given by $r_A^2 = 0.46(16)$ fm^2 [34]. The large uncertainty on r_A^2 will significantly affect the total uncertainty budget, as already found in Ref. [12]. 4) The final source of uncertainty is the one arising from the numerical technique adopted to solve the bound and scattering $A = 2$ systems. Taking into consideration the arguments of Ref. [17], we have decided to use two methods. The first one is the method already developed by Refs. [9, 10], i.e., a variational method, in which the bound and scattering wave functions are expanded on a known basis and the unknown coefficients of these expansions are obtained using variational principles. The second method is the so-called Numerov method, where the tail of the bound-state wave function is, in fact, imposed "by hand" (see Section 2.3). This last source of uncertainty will be shown to be completely negligible.

The paper is organized as follows: Section 2 presents the theoretical formalism, providing a schematic derivation for $\Gamma^D(^1S_0)$ in Section 2.1, a description of the adopted nuclear potentials and currents in Section 2.2, and a discussion of the methods used to calculate the deuteron and *nn* wave functions in Section 2.3. The results for $\Gamma^D(^1S_0)$ are presented and discussed in Section 3, and some concluding remarks and an outlook are given in Section 4.

2 Theoretical formalism

We discuss, in this section, the theoretical formalism developed to calculate the muon capture rate. In particular, Section 2.1 gives the main steps of the formalism used to derive the differential and the total muon capture rate on a deuteron in the initial doublet hyperfine state. A through discussion is given by Ref. [9]. Section 2.2 reports the main characteristics of the nuclear potentials and currents we used in the present study. Finally, Section 2.3 presents the variational and the Numerov methods used to calculate the deuteron bound and *nn* scattering wave functions.

2.1 Observables

The differential capture rate in the doublet initial hyperfine state $d\Gamma^D/dp$ can be written as [9]

$$\frac{d\Gamma^D}{dp} = E_\nu^2 \left[1 - \frac{E_\nu}{\left(m_\mu + m_d\right)}\right] \frac{p^2 d\hat{\mathbf{p}}}{8\pi^4} \overline{|T_W|^2}, \tag{4}$$

where $\mathbf{p}$ is the nn relative momentum, and

$$E_\nu = \frac{\left(m_\mu + m_d\right)^2 - 4m_n^2 - 4p^2}{2\left(m_\mu + m_d\right)}, \tag{5}$$

with m_μ, m_n, and m_d being the muon, neutron, and deuteron masses, respectively. The transition amplitude $\overline{|T_W|^2}$ reads [9]

$$\overline{|T_W|^2} = \frac{1}{2f+1} \sum_{s_1 s_2 h_\nu} \sum_{f_z} |T_W(f, f_z; s_1, s_2, h_\nu)|^2, \tag{6}$$

where f, f_z indicate the initial hyperfine state, fixed here to be $f = 1/2$, while s_1, s_2, and h_ν denote the spin z-projection for the two neutrons and the neutrino helicity state, respectively. In turn, $T_W(f, f_z; s_1, s_2, h_\nu)$ is given by

$$\begin{aligned} T_W(f, f_z; s_1, s_2, h_\nu) &\equiv \langle nn, s_1, s_2; \nu, h_\nu \mid H_W \mid (\mu, d); f, f_z \rangle \\ &\simeq \frac{G_V}{\sqrt{2}} \psi_{1s} \sum_{s_\mu s_d} \langle \tfrac{1}{2} s_\mu, 1 s_d \mid f f_z \rangle \, l_\sigma(h_\nu, s_\mu) \\ &\quad \times \langle \Psi_{p, s_1 s_2}(nn) \mid j^\sigma(\mathbf{q}) \mid \Psi_d(s_d) \rangle \,, \end{aligned} \tag{7}$$

with G_V being the vector coupling constant, chosen to be $G_V = 1.14939 \times 10^{-5}$ GeV^{-2}, consistently with what has been used in the fitting procedure of the LECs in the transition currents (see Section 2.2). With l_σ and j_σ we indicate the leptonic and hadronic current densities, respectively [9], written as

$$l_\sigma\left(h_\nu, s_\mu\right) \equiv \bar{u}(\mathbf{k}_\nu, h_\nu) \gamma_\sigma \left(1 - \gamma_5\right) u\left(\mathbf{k}_\mu, s_\mu\right), \tag{8}$$

and

$$j^\sigma(\mathbf{q}) = \int d\mathbf{x} \, e^{i\mathbf{q}\cdot\mathbf{x}} \, j^\sigma(\mathbf{x}) \equiv \left(\rho(\mathbf{q}), \mathbf{j}(\mathbf{q})\right). \tag{9}$$

Here, the leptonic momentum transfer $\mathbf{q}$ is defined as $\mathbf{q} = \mathbf{k}_\mu - \mathbf{k}_\nu \simeq -\mathbf{k}_\nu$. Furthermore, $\Psi_d(s_d)$ and $\Psi_{\mathbf{p}, s_1 s_2}(nn)$ are the initial deuteron and final nn wave functions, respectively, with s_d indicating the deuteron spin z-projection. Finally, in Eq. 7, the function ψ_{1s} represents the $1s$ solution of the Schrödinger equation for the initial muonic $\mu - d$ atom. Since the muon capture occurs in the region where the deuteron and the muon wave functions overlap, ψ_{1s} can be approximated as the average over the nuclear volume [9, 35], namely,

$$|\psi_{1s}| \simeq |\psi_{1s}^{\rm av}| \equiv |\psi_{1s}(0)| = \sqrt{\frac{\left(\alpha \mu_{\mu d}\right)^3}{\pi}}, \tag{10}$$

where $\psi_{1s}(0)$ denotes the Bohr wave function for a point charge e evaluated at the origin, $\mu_{\mu d}$ is the reduced mass of the (μ, d) system, and $\alpha = 1/137.036$ is the fine-structure constant.

The final nn wave function can be expanded in partial waves as

$$\begin{aligned} \Psi_{p, s_1 s_2}(nn) = \; & 4\pi \sum_S \langle \tfrac{1}{2} s_1, \tfrac{1}{2} s_2 \mid S S_z \rangle \\ & \times \sum_{L L_z J J_z} i^L Y^\star_{L L_z}(\hat{\mathbf{p}}) \langle S S_z, L L_z \mid J J_z \rangle \, \bar{\Psi}^{LSJJ_z}_{nn}(\mathrm{p}), \end{aligned} \tag{11}$$

where $\bar{\Psi}^{LSJJ_z}_{nn}(p)$ is the nn wave function with orbital angular momentum LL_z, total spin SS_z, and total angular momentum JJ_z. In the present work, we restrict our study to the $L = 0$ state ($^1S_0$ in spectroscopic notation).

Using standard techniques described in Refs. [9, 35], a multipole expansion of the weak charge, $\rho(\mathbf{q})$, and current, $\mathbf{j}(\mathbf{q})$, operators can be performed, resulting in

$$\begin{aligned} \langle \bar{\Psi}^{LSJJ_z}_{nn}(p) | \rho(\mathbf{q}) | \Psi_d(s_d) \rangle = \; & \sqrt{4\pi} \sum_{\Lambda \geq 0} \sqrt{2\Lambda + 1} \; i^\Lambda \\ & \times \frac{\langle 1 s_d, \Lambda 0 | J J_z \rangle}{\sqrt{2J+1}} C^{LSJ}_\Lambda(q), \end{aligned} \tag{12}$$

$$\begin{aligned} \langle \bar{\Psi}^{LSJJ_z}_{nn}(p) | j_z(\mathbf{q}) | \Psi_d(s_d) \rangle = \; & -\sqrt{4\pi} \sum_{\Lambda \geq 0} \sqrt{2\Lambda + 1} \; i^\Lambda \\ & \times \frac{\langle 1 s_d, \Lambda 0 | J J_z \rangle}{\sqrt{2J+1}} L^{LSJ}_\Lambda(q), \end{aligned} \tag{13}$$

$$\begin{aligned} \langle \bar{\Psi}^{LSJJ_z}_{nn}(p) \mid j_\lambda(\mathbf{q}) \mid \Psi_d(s_d) \rangle = \; & \sqrt{2\pi} \sum_{\Lambda \geq 1} \sqrt{2\Lambda + 1} \; i^\Lambda \\ & \times \frac{\langle 1 s_d, \Lambda - \lambda \mid J J_z \rangle}{\sqrt{2J+1}} \\ & \times \left[-\lambda M^{LSJ}_\lambda(q) + E^{LSJ}_\Lambda(q)\right], \end{aligned} \tag{14}$$

where $\lambda = \pm 1$, and $C^{LSJ}_\Lambda(q)$, $L^{LSJ}_\Lambda(q)$, $E^{LSJ}_\Lambda(q)$, and $M^{LSJ}_\Lambda(q)$ denote the reduced matrix elements (RMEs) of the Coulomb (C), longitudinal (L), transverse electric (E), and transverse magnetic (M) multipole operators, respectively, as defined in Ref. [9]. Since the weak charge and current operators have scalar/polar-vector (V) and pseudo-scalar/axial-vector (A) components, each multipole consists of the sum of the V and A terms, having opposite parity under space inversions. Given that, in this study, only the $^1S_0$ contribution is considered, the only contributing multipoles are $C_1(A)$, $L_1(A)$, $E_1(A)$, and $M_1(V)$, where the superscripts LSJ have been dropped. The integration of the matrix elements is performed using ~ 50 Gaussian points on the angles and a scaled grid on r with a maximum value $r_{\rm max} \sim 42$ fm. This permits full convergence of the integrals, and the grid of r is large enough that all the low-energy components of the current become negligible.

To calculate the differential capture rate $d\Gamma^D/dp$ in Eq. 4, we need to integrate over $\hat{\mathbf{p}}$. This is carried out numerically using the Gauss-Legendre method with a number of points of the order of 10 so that an accuracy of better than 1 part in 10^3 can be achieved. Finally, the total capture rate Γ^D is obtained as

$$\Gamma^D = \int_0^{p_{max}} \frac{d\Gamma^D}{dp} dp, \tag{15}$$

where $p_{\rm max}$ is the maximum value of the momentum p. To find the smallest needed number of grid points on p to reach convergence, we computed the capture rate by integrating over several grids starting from a minimum value of 20 points up to a maximum of 80. We verified that the results obtained by integrating over 20 or 40 points differ by about 0.1 s^{-1}, while the ones obtained with 40, 60, and 80 points differ by less than

$0.01\ s^{-1}$. Therefore, we have used 60 grid points in all the studied cases mentioned below.

2.2 Nuclear potentials and currents

In this study, we consider four different nuclear interaction models and consistent weak current operators derived in χEFT. We decided to concentrate our attention on the recent local *r*-space potentials of Ref. [19] (see also Ref. [18] for a recent review). The motivation behind this choice is that, in the future, we plan to use this same formalism to the *pp* reaction, for which the Coulomb interaction and also electromagnetic higher-order contributions play a significant role at the accuracy level reached by theory. The possibility to work in the *r*-space is clearly an advantage compared with the momentum space, which would be the unavoidable choice when using non-local potentials. However, in the momentum space, the full electromagnetic interaction between the two protons is not easy to be taken into account. The potentials of Ref. [19], which we will refer to as Norfolk potentials (denoted as NV), are chiral interactions that also include, beyond pions and nucleons, Δ-isobar degrees of freedom explicitly. The short-range (contact) part of the interaction receives contributions at the leading order (LO), next-to-leading order (NLO), and next-to-next-to-next-to-leading order (N3LO), while the long-range components arise from one- and two-pion exchanges, and are retained up to the next-to-next-to-leading order (N2LO). By truncating the expansion at N3LO, there are 26 LECs which have been fitted to the *NN* Granada database [36–38], obtaining two classes of Norfolk potentials, depending on the range of laboratory energies over which the fits have been carried out: the NVI potentials have been fitted in the range 0–125 MeV, while for the NVII potentials, the range has been extended up to 200 MeV. For each class of potential, two cutoff functions $C_{R_S}(r)$ and $C_{R_L}(r)$ have been used to regularize the short- and long-range components, respectively. These functions have been defined as

$$C_{R_S}(r) = \frac{1}{\pi^{\frac{3}{2}} R_S^3} e^{-(r/R_S)^2}, \tag{16}$$

$$C_{R_L}(r) = 1 - \frac{1}{(r/R_L)^6 e^{(r-R_L)/a_L} + 1}, \tag{17}$$

with $a_L \equiv R_L/2$. Two different sets of cutoff values have been considered, $(R_S; R_L) = (0.7; 1.0)$ and $(0.8; 1.2)$, and the resulting models have been labeled "a" and "b," respectively. All these potentials are very accurate: in fact, the χ^2/datum for the NVIa, NVIIa, NVIb, and NVIIb potentials are 1.05, 1.37, 1.07, and 1.37 [19], respectively. It should be noted that in Ref. [19], another set of NV potentials labeled NVIc and NVIIc was constructed, with $(R_S; R_L) = (0.6; 0.8)$. The reason for not considering these potential models in this work is that they have been found to lead to a poor convergence in the hyperspherical harmonics method used to calculate the ^{3}H and ^{3}He wave functions needed to predict the Gamow–Teller matrix element in tritium β-decay. This study is, in turn, necessary to fit the aforementioned d_R LEC (see as follows and Ref. [20]). Therefore, for the NVIc and NVIIc potentials, consistent currents are not available, and we have disregarded them in this work.

We now turn our attention to the weak transition operators. When only the $^1S_0$ *nn* partial wave is included, we have seen that the contributing multipoles are $C_1(A)$, $L_1(A)$, $E_1(A)$, and $M_1(V)$. Consequently, the weak vector charge operator is of no interest in the process under consideration, and we will not discuss it here. The weak vector current entering $M_1(V)$ can be obtained from the isovector electromagnetic current, performing a rotation in the isospin space, i.e., with the substitutions

$$\tau_{i,z}/2 \Rightarrow \tau_{i,\pm} = \left(\tau_{i,x} \pm i\tau_{i,y}\right)/2, \tag{18}$$

$$\left(\boldsymbol{\tau}_i \times \boldsymbol{\tau}_j\right)_z \Rightarrow \left(\boldsymbol{\tau}_i \times \boldsymbol{\tau}_j\right)_\pm = \left(\boldsymbol{\tau}_i \times \boldsymbol{\tau}_j\right)_x \pm i\left(\boldsymbol{\tau}_i \times \boldsymbol{\tau}_j\right)_y. \tag{19}$$

Therefore, we will review the various contributions to the electromagnetic current, even if we are interested only in their isovector components. The electromagnetic current operators up to one loop have been most recently reviewed in Ref. [22]. Here, we only give a synthetic summary. Following the notation of Ref. [22], we denote with Q the generic low-momentum scale. The LO contribution, at the order Q^{-2}, consists of the single-nucleon current, while at the NLO or order Q^{-1}, there is the one-pion-exchange (OPE) contribution. The relativistic correction to the LO single-nucleon current provides the first contribution of order Q^0 (N2LO). Furthermore, since the Norfolk interaction models retain explicitly Δ-isobar degrees of freedom, we take into account also the N2LO currents originating from explicit Δ intermediate states. Finally, the currents at order Q^1 (N3LO) consist of 1) terms generated by minimal substitution in the four-nucleon contact interactions involving two gradients of the nucleon fields and by non-minimal couplings to the electromagnetic field; 2) OPE terms induced by $\gamma\pi N$ interactions of sub-leading order; and 3) one-loop two-pion-exchange terms. A thorough discussion of all these contributions as well as their explicit expressions is given in Ref. [22]. Here, we only remark that 1) the various contributions are derived in momentum space and have power–law behavior at large momenta, or short range. Therefore, they need to be regularized. The procedure adopted here, as in Ref. [22], is to carry out first the Fourier transforms of the various terms. This results in *r*-space operators which are highly singular at vanishing inter-nucleon separations. Then, the singular behavior is removed by multiplying the various terms by appropriate *r*-space cutoff functions, identical to those of the Norfolk potentials of Ref. [19]. More details are given in Refs. [21, 22]. 2) There are 5 LECs in the electromagnetic currents which do not enter the nuclear potentials and need to be fitted using electromagnetic observables. These LECs enter the current operators at N3LO; in

particular, two of them are present in the currents arising from non-minimal couplings to the electromagnetic field, and three of them are present in the sub-leading isoscalar and isovector OPE contributions. In this study, these LECs are determined by a simultaneous fir to the A = 2–3 nuclei magnetic moments and the deuteron threshold electrodisintegration at backward angles over a wide range of momentum transfers [22]. In this work, we used the LECs labeled with set A in Ref. [22].

The axial current operators used in the present work are the ones of Ref. [20]. They include the LO term of order Q^{-3}, which arises from the single-nucleon axial current, and the N2LO and N3LO terms (scaling as Q^{-1} and Q^0, respectively), consisting of the relativistic corrections and Δ contributions at N2LO, and of OPE and contact terms at N3LO. It should be noted that at NLO, here of order Q^{-2}, there is no contribution in χEFT. The explicit *r*-space expression of these operators is given in Ref. [20]. Here, we only remark that all contributions have been regularized at a short and long range consistently with the regulator functions used in the Norfolk potentials. Furthermore, the N3LO contact term presents a LEC, here denoted by z_0 (but essentially equal to the d_R LEC mentioned in Section 1), defined as

$$z_0 = \frac{g_A}{2}\frac{m_\pi^2}{f_\pi^2}\frac{1}{(m_\pi R_S)^3}\left[-\frac{m_\pi}{4g_A\Lambda_\chi}c_D + \frac{m_\pi}{3}(c_3+2c_4) + \frac{m_\pi}{6m}\right]. \tag{20}$$

Here, g_A = 1.2723 (23) is the single-nucleon axial coupling constant, m = 938.9 MeV is the nucleon mass, m_π = 138.04 MeV and f_π = 97.4 MeV are the pion mass and decay constant, respectively, $\Lambda_\chi \sim 1$ GeV is the chiral-symmetry breaking scale, and $c_3 = -0.79$ and $c_4 = 1.33$ are two LECs entering the $\pi\pi N$ Lagrangian at N2LO and taken from the fit of the pion-nucleon scattering data with Δ-isobar as explicit degrees of freedom [39]. As mentioned previously, c_D is one of the two LECs which enter the three-nucleon interaction, the other being denoted by c_E. The two LECs c_D (and consequently z_0) and c_E have been fitted to simultaneously reproduce the experimental trinucleon binding energies and the central value of the Gamow–Teller matrix element in tritium β-decay. The explicit values for c_D are −0.635, −4.71, −0.61, and −5.25 for the NVIa, NVIb, NVIIa, and NVIIb potentials, respectively.

The nuclear axial charge has a much simpler structure than the axial and vector currents, and we have used the operators as derived in Ref. [40]. At LO, i.e., at the order Q^{-2}, it retains the one-body term, which gives the most important contribution. At NLO (order Q^{-1}), the OPE contribution appears, which, however, has been found to be almost negligible in this study. The N2LO contributions (order Q^0) exactly vanish, and at N3LO (order Q^1), there are two-pion-exchange terms and new contact terms where new LECs appear. N3LO has not been included in the calculation, since the new LECs have not been fixed yet. However, we have found the contribution of $C_1(A)$ to be two orders of magnitude smaller than the one from the other multipoles. Therefore, the effect of the axial current correction at N3LO can be safely disregarded.

All the axial charge and current contributions are multiplied by the single-nucleon axial coupling constant, $g_A(q_\sigma^2)$, written as a function of the squared of the four-momentum transfer q_σ^2. Contrary to the triton β-decay, in the case of the muon capture on a deuteron, the four-momentum transfer is quite large. The dependence of $g_A(q_\sigma^2)$ on q_σ^2 is, therefore, crucial and, as already mentioned in Section 1, is a source of theoretical uncertainty in this study. In the past, it has been used for $g_A(q_\sigma^2)$, a dipole form [9], but in Ref. [41], it has been argued that the dipole form introduces an uncontrolled systematic error in estimating the value of the axial form factor. Alternatively, it has been proposed to use the small-momentum expansion, which leads to the expression of Eq. 3. In our study, we decided to use the new parameterization for $g_A(q_\sigma^2)$ of Eq. 3, but with a slightly smaller uncertainty on the axial charge radius r_A compared with Ref. [41], as discussed in Ref. [34]. In this work, r_A has been chosen as the weighted average of the values obtained by two independent procedures having approximately the same accuracy, about 50%. One procedure is the one of Ref. [41] and used for the axial form factor a convergent expansion given by

$$g_A(q_\sigma^2) = \sum_{k=0}^{k_{max}} a_k z(q_\sigma^2)^k, \tag{21}$$

where the variable $z(q_\sigma^2)$ is defined as

$$z(q_\sigma^2) = \frac{\sqrt{t_{cut}-q_\sigma^2}-\sqrt{t_{cut}-t_0}}{\sqrt{t_{cut}-q_\sigma^2}+\sqrt{t_{cut}-t_0}}, \tag{22}$$

with $t_{cut} = 9\,m_\pi^2$ and $-\infty < t_0 < t_{cut}$. In Eq. 21, a_k is the expansion parameters that encode the nuclear structure information and need to be experimentally fixed. From $g_A(q_\sigma^2)$ in Eq. 21, we can obtain r_A^2 as [41]

$$\frac{1}{6}r_A^2 \equiv \frac{1}{g_A(0)}\frac{dg_A(q_\sigma^2)}{dq_\sigma^2}\bigg|_{q_\sigma^2=0}. \tag{23}$$

The value for r_A^2 is obtained by fitting experimental data of neutrino scattering on a deuterium and is found to be $r_A^2(z\ \mathrm{exp}.\nu) = 0.46(22)$ fm^2 [41].

Alternatively, it is possible to obtain r_A^2 from experiments on muonic capture on protons, as carried out by the MuCap Collaboration. To date, these experiments are characterized by an overall accuracy of 1%, but a future experiment plans to reduce this uncertainty to about 0.33% [34]. In this case, r_A^2(MuCap) = 0.46(24) fm^2 [34]. In order to take into account both $r_A^2(z\ \mathrm{exp}.\nu)$ and r_A^2(MuCap), we adopted for r_A^2 the value $r_A^2 = 0.46(16)$ fm^2, as suggested in Ref. [34]. The uncertainty on r_A^2 remains quite large, at about 35%, but it is slightly smaller than the one of Ref. [41], which has been adopted in the study of Ref. [12]. The consequences on the error budget are discussed in Section 3. We finally notice that the dipole

function for $g_A(q_\sigma^2)$, with a cutoff value of $\Lambda_A = 1$ GeV as used, for instance, in Refs. [9, 10], can be reduced to Eq. 3 by imposing $r_A^2 = 0.467$ fm^2.

2.3 Nuclear wave functions

The calculation of the nuclear wave functions of the deuteron and *nn* systems was, first of all, performed using the variational method described in Ref. [9], where all the details of the calculation can be found. Here, we summarize only the main steps.

The deuteron wave function can be written as

$$\Psi_d(\mathbf{r}, J_z) = \sum_\alpha \sum_{i=0}^{M-1} c_{\alpha,i}\, f_i(r)\, \mathcal{Y}_\alpha(\hat{\mathbf{r}}), \tag{24}$$

where the channels $\alpha \equiv (l; s; J; t)$ denote the deuteron quantum numbers, with the combination $(l = 0, 2; s = 1; J = 1; t = 0)$ corresponding to $\alpha = 1, 2$, respectively, and the functions $\mathcal{Y}_\alpha(\hat{\mathbf{r}})$ are given by

$$\mathcal{Y}_\alpha(\hat{\mathbf{r}}) \equiv \left[Y_l(\hat{\mathbf{r}}) \otimes \chi_s\right]_{JJ_z} \xi_{tt_z}. \tag{25}$$

The M radial functions $f_i(r)$, normalized to unity, with $i = 0, \ldots, M-1$, are written as

$$f_i(r) = \sqrt{\frac{i!\gamma^3}{(i+2)!}} e^{-\frac{\gamma}{2}r}\, {}^{(2)}L_i(\gamma r), \tag{26}$$

where γ is a non-variational parameter chosen to be [9] $\gamma = 0.25\,\text{fm}^{-1}$ and ${}^{(2)}L_i(\gamma r)$ are the Laguerre polynomials of the second type [42]. The unknown coefficients $c_{\alpha,i}$ are obtained using the Rayleigh–Ritz variational principle, i.e., imposing the condition

$$\frac{\partial}{\partial c_{\alpha,i}} \langle \Psi_d | H + B_d | \Psi_d \rangle = 0, \tag{27}$$

where H is the Hamiltonian and B_d is the deuteron binding energy. This reduces to an eigenvalue–eigenvector problem, which can be solved with standard numerical techniques [9].

The *nn* wave function $\bar{\Psi}_{nn}^{LSJJ_z}(p)$ in Eq. 11 is written as a sum of a core wave function $\Psi^c(p)$, and of an asymptotic wave function $\Psi^a(p)$, where we have dropped the superscript $LSJJ_z$ for ease of presentation. The core wave function $\Psi^c(p)$ describes the *nn* scattering state where the two nucleons are close to each other, and is expanded on a basis of Laguerre polynomials, similarly to what we did for the deuteron wave function. Therefore,

$$\Psi^c(p) = \sum_{i=0}^{M-1} d_i(p) f_i(r) \mathcal{Y}_\alpha(\hat{\mathbf{r}}), \tag{28}$$

where $f_i(r)$ and $\mathcal{Y}_\alpha(\hat{\mathbf{r}})$ are defined in Eqs 26, 25, respectively. It should be noted that $\alpha \equiv L = 0; S = 0, J = 0, J_z = 0$. In the unknown coefficients $d_i(p)$, we have explicitly kept the dependence on p.

The asymptotic wave function $\Psi^a(p)$ describes the *nn* scattering system in the asymptotic region, where the nuclear potential is negligible. Consequently, it can be written as a linear combination of regular (Bessel) and irregular (Neumann) spherical functions, denoted as $j_L(pr)$, $n_L(pr)$, respectively, i.e.,

$$\Psi^a(p) = \tilde{F}_L(pr)\mathcal{Y}_\alpha(\hat{\mathbf{r}}) + \sum_{L'} R_{LL'}\, \tilde{G}_{L'}(pr)\mathcal{Y}_{\alpha'}(\hat{\mathbf{r}}), \tag{29}$$

where $R_{LL'}$ is the reactance matrix, and $\tilde{F}_{L'}(pr)$ and $\tilde{G}_{L'}(pr)$ are defined as

$$\tilde{F}_{L'}(pr) \equiv \frac{j_L(pr)}{p^L}, \tag{30}$$

$$\tilde{G}_{L'}(pr) \equiv n_L(pr)(1 - e^{-\epsilon r})^{2L+1} p^{L+1}, \tag{31}$$

so that they are well defined for $p \to 0$ and $r \to 0$. The function $(1 - e^{-\epsilon r})^{2L+1}$ was found to be an appropriate regularization factor at the origin for $n_L(pr)$. We use the value $\epsilon = 0.25\,\text{fm}^{-1}$ as in Ref. [9]. It should be noted that since $L = L' = 0$ the reactance matrix is, in fact, just a number here, and $R_{00} = \tan\delta_0$, δ_0 being the phase shift.

To determine the coefficients $d_i(p)$ in Eq. 28 and the reactance matrix $R_{LL'}$ in Eq. 29, we use the Kohn variational principle [43], which states that the functional

$$[R_{LL'}(p)] = R_{LL'}(p) - \frac{m_n}{\hbar^2} \langle \bar{\Psi}_{\alpha'}(p) | H - E | \bar{\Psi}_\alpha(p) \rangle \tag{32}$$

is stationary with respect to $d_i(p)$ and $R_{LL'}$. In Eq. 32, E is the *nn* relative energy ($E = p^2/m_n$, m_n being the neutron mass) and H is the Hamiltonian operator. Performing the variation, a system of linear inhomogeneous equations for $d_i(p)$ and a set of algebraic equations for $R_{LL'}$ are derived. These equations are solved by standard techniques. The variational results presented in the following section are obtained using $M = 35$ for both the deuteron and the *nn* scattering wave functions.

To test the validity of the variational method and its numerical accuracy, in this work, we also used the Numerov method for the deuteron and the *nn* wave functions.

For the deuteron wave function, we used the so-called renormalized Numerov method, based on the work of Ref. [44]. Within this method, the Schrödinger equation is rewritten as

$$\left[I \frac{d^2}{dx^2} + Q(x)\right] \Psi(x) = 0, \tag{33}$$

where I is the identity matrix and $Q(x)$ is a matrix defined as

$$Q(x) = \left(\frac{2\mu}{\hbar^2}\right)[EI - V(x)], \tag{34}$$

and $\Psi(x)$ is also a matrix whose columns are the independent solutions of the Schrödinger equation with non-assigned boundary conditions on the derivatives. In Eq. 34, μ is the *np*

reduced mass, $E \equiv -B_d$, and $V(x)$ is the sum of the *np* nuclear potential $V^{np}(x)$ and the centrifugal barrier, i.e.,

$$V(x) = V^{np}(x) + \frac{\hbar^2 l(l+1)}{2\mu r^2}. \tag{35}$$

The Schrödinger equation is evaluated on a finite and discrete grid with a constant step h. The boundary conditions require knowing the wave function at the initial and final grid points, given by $x_0 = 0$ and $x_N = Nh$, respectively. Specifically, it is assumed that $\Psi(0) = 0$ and $\Psi(Nh) = 0$. No conditions on first derivatives are imposed.

Equation 33 can be rewritten equivalently as [44]

$$[I - T(x_{n+1})]\Psi(x_{n+1}) - [2I + 10T(x_n)]\Psi(x_n) + [I - T(x_{n-1})]\Psi(x_{n-1}) = 0, \tag{36}$$

where $x_n \in A$, $A \equiv (x_0, x_N)$, and $T(x_n)$ is a 2×2 matrix defined as [44]

$$T(x_n) = -\frac{h^2}{12}Q(x_n). \tag{37}$$

It should be noted that Eq. 36 is, in fact, the natural extension to a matrix formulation of the ordinary Numerov algorithm (see Eq. 65 as follows).

By introducing the matrix $F(x_n)$ as [44]

$$F(x_n) = [I - T(x_n)]\Psi(x_n), \tag{38}$$

Equation 36 can be rewritten as

$$F(x_{n+1}) - U(x_n)F(x_n) + F(x_{n-1}) = 0, \tag{39}$$

where the matrix $U(x_n)$ is given by

$$U(x_n) = [I - T(x_n)]^{-1}[2I + 10\,T(x_n)]. \tag{40}$$

Furthermore, we introduce the matrices $R(x_n)$ and $\hat{R}(x_n)$, defined as [44]

$$R(x_n) = F(x_{n+1})F^{-1}(x_n), \tag{41}$$

$$\hat{R}(x_n) = F(x_{n-1})F^{-1}(x_n), \tag{42}$$

and their inverse matrices as

$$R^{-1}(x_n) = F(x_n)F^{-1}(x_{n+1}), \tag{43}$$

$$\hat{R}^{-1}(x_n) = F(x_n)F^{-1}(x_{n-1}). \tag{44}$$

By using definitions (41) and (42), it is possible to derive from Eq. 39 the following recursive relations:

$$R(x_n) = U(x_n) - R^{-1}(x_{n-1}), \tag{45}$$

$$\hat{R}(x_n) = U(x_n) - \hat{R}^{-1}(x_{n+1}). \tag{46}$$

We now notice that, since $\Psi(0) = 0$, Eq. 38 implies that $F(0) = 0$ and, consequently, from Eq. 43, it follows that $R^{-1}(0) = 0$. Similarly, since $\Psi(Nh) = 0$, from Eqs 38, 44 we obtain $\hat{R}^{-1}(Nh) = 0$. Starting from the $R^{-1}(0)$ and $\hat{R}^{-1}(Nh)$ values, and iteratively using Eqs 45, 46, it is possible to calculate the $R(x_m)$ and $\hat{R}^{-1}(x_{m+1})$ values up to a matching point x_m, so that the interval A remains divided into two sub-intervals, $A_1 \equiv [x_0, x_{m+1}]$ and $A_2 \equiv [x_m, x_N]$. These values are needed to calculate the deuteron binding energy and its wave function. In fact, assuming we knew the deuteron binding energy $B_d \equiv -E$ for a given potential, then we could integrate Eq. 33 in the two sub-intervals A_1 and A_2, obtaining the outgoing (left) solution $\Psi_l(x_n)$ in A_1, and the incoming (right) solution $\Psi_r(x_n)$ in A_2. If B_d were a true eigenvalue, then the function $\Psi(x_n)$ and its derivative have to be continuous in x_m. The wave function continuity at two consecutive points, for example, x_m and x_{m+1}, implies that

$$\Psi_l(x_m) \cdot \mathbf{l} = \Psi_r(x_m) \cdot \mathbf{r} \equiv \psi(x_m), \tag{47}$$

$$\Psi_l(x_{m+1}) \cdot \mathbf{l} = \Psi_r(x_{m+1}) \cdot \mathbf{r} \equiv \psi(x_{m+1}), \tag{48}$$

where $\mathbf{l}$ and $\mathbf{r}$ are two unknown vectors. Multiplying Eq. 48 by $[I - T(x_{m+1})]$ and using Eq. 38, we obtain

$$F_l(x_{m+1}) \cdot \mathbf{l} = F_r(x_{m+1}) \cdot \mathbf{r} \equiv f(x_{m+1}). \tag{49}$$

Similarly, from Eq. 47, we can write

$$F_l(x_m) \cdot \mathbf{l} = F_r(x_m) \cdot \mathbf{r} \equiv f(x_m). \tag{50}$$

Using Eq. 41 with $x_n = x_m$ for the outgoing solution and Eq. 42 with $x_n = x_{m+1}$ for the incoming solution, we can write

$$F_l(x_{m+1}) = R(x_m)F_l(x_m), \tag{51}$$

$$F_r(x_{m+1}) = \hat{R}^{-1}(x_{m+1})F_r(x_m). \tag{52}$$

By replacing Eqs 51, 52 with Eq. 49 and using Eq. 50, we obtain that

$$R(x_m)f(x_m) = \hat{R}^{-1}(x_{m+1})f(x_m) \tag{53}$$

or equivalently that

$$\left[R(x_m) - \hat{R}^{-1}(x_{m+1})\right]f(x_m) = 0. \tag{54}$$

A non-trivial solution is only admitted if the aforementioned equation satisfies the following condition:

$$det\left[R(x_m) - \hat{R}^{-1}(x_{m+1})\right] = 0. \tag{55}$$

This determinant is a function of the energy E, i.e.,

$$det(E) = det\left[R(x_m) - \hat{R}^{-1}(x_{m+1})\right]. \tag{56}$$

Therefore, we proceed as follows: starting from an initial trial value E_1, we calculate $det(E_1)$. Fixing a tolerance factor ϵ, for example $\epsilon = 10^{-16}$, if $det(E_1) \leq \epsilon$, we assume E_1 being the eigenvalue, otherwise we compute the determinant for a second

energy value E_2. If $det\ (E_2) \leq \epsilon$, we take the deuteron binding energy as $B_d = -E_2$, otherwise it is necessary to repeat the procedure iteratively until $det\ (E_i) \leq \epsilon$. For the iterations after the second one, the energy is chosen through the relation

$$E_i = E_{i-2} - det\,(E_{i-1})\frac{E_{i-2} - E_{i-1}}{det\,(E_{i-2}) - det\,(E_{i-1})}, \tag{57}$$

which follows from a linear interpolation procedure. The procedure stops when $det\ (E_i) \leq \epsilon$, and the deuteron binding energy is taken to be $B_d = -E_i$.

To calculate the S- and D-wave components of the reduced radial wave function, denoted as $u_0\,(x_n)$ and $u_2\,(x_n)$, respectively, we notice that they are the two components of the vector $\psi(x_n)$, defined in Eq. 47 at the point x_m. The starting point is to assign an arbitrary value to one of the two components of the vector function $f\,(x_m)$ (see Eq. 50). Since $R\,(x_m)$ and $\hat{R}^{-1}\,(x_{m+1})$ are known, the value of the other component is fixed by Eq. 54. By defining the outgoing function as $f\,(x_n) = F\,(x_n)\cdot\mathbf{l}$, from Eq. 41, it follows that

$$f\,(x_n) = R^{-1}\,(x_n) f\,(x_{n+1}), \tag{58}$$

where $n = m - 1, \ldots, 0$. Similarly, we can proceed with the incoming function. By defining it as $f\,(x_n) = F\,(x_n)\cdot\mathbf{r}$, from Eq. 42 we have

$$f\,(x_n) = \hat{R}^{-1}\,(x_n) f\,(x_{n-1}), \tag{59}$$

where $n = m + 1, \ldots, N$. At this point, the vector function $f\,(x_n)$ can be calculated $\forall\ x_n \in [x_0, x_N]$, through Eqs 58, 59. The $u_0\,(x_n)$ and $u_2\,(x_n)$ functions are given from $f\,(x_n)$ by

$$\psi\,(x_n) = [I - T\,(x_n)]^{-1} f\,(x_n). \tag{60}$$

Finally, the deuteron wave function is normalized to unity.

The single-channel Numerov method, also known as a three-point algorithm, is used to calculate the nn wave function. Although the method is quite well known, to provide a comprehensive review of all the approaches to the $A = 2$ systems, we briefly summarize its main steps. Again, we start by defining a finite and discrete interval I, with constant step h, characterized by the initial and final points, $x_0 = 0$ and $x_N = Nh$, respectively. Then, the Schrödinger equation can be cast in the form

$$u''\,(x_n) \equiv \left.\frac{d^2\,u(x)}{dx^2}\right|_{x=x_n} = W\,(x_n) u\,(x_n), \tag{61}$$

where

$$W\,(x_n) = \left(\frac{2\mu}{\hbar^2}\right) V\,(x_n) - p^2, \tag{62}$$

with $V\,(x_n)$ being the nuclear potential and p the nn relative momentum. To solve Eq. 61, it is convenient to introduce the function $z\,(x_n)$, defined as

TABLE 1 Deuteron binding energies B_d, in MeV, and nn S-wave phase shift δ_0 at E =5 MeV, in deg, calculated with the Numerov (Num.) or the variational (Var.) methods using the four Norfolk chiral potentials NVIa, NVIIa, NVIb, and NVIIb. Here, we report the results up to the digit from which the two methods start to differ. The experimental value for B_d is $B_d^{exp} = 2.2245$ MeV.

Potential	B_d (Num.)	B_d (Var.)	δ_0(Num.)	δ_0(Var.)
NVIa	2.22465	2.22464	57.714	57.714
NVIIa	2.22442	2.22441	57.766	57.766
NVIb	2.22482	2.22486	57.815	57.812
NVIIb	2.22418	2.22427	57.964	57.960

$$z\,(x_n) = u\,(x_n) - \frac{h^2}{12} u''\,(x_n). \tag{63}$$

By replacing Eq. 61 with Eq. 63, $z\,(x_n)$ can be rewritten as

$$z\,(x_n) = \left(1 - \frac{h^2}{12} W\,(x_n)\right) u\,(x_n). \tag{64}$$

By expanding $z\,(x_{n-1})$ and $z\,(x_{n+1})$ in an interval around the point x_n in a Taylor series up to $O\,(h^4)$, and adding together the two expressions, we obtain

$$z\,(x_{n+1}) = 2z\,(x_n) - z\,(x_{n-1}) + h^2 u''\,(x_n) + O\left(h^6\right). \tag{65}$$

This is a three-point relation: once the $z\,(x_{n-1})$ and $z\,(x_n)$ values are known, after calculating $u''(x_n)$ using Eq. 61, we can compute $z\,(x_{n+1})$ at the order $O\,(h^6)$.

By fixing the values $u\,(0) = 0$ and $u(h) = h$, we consequently know $z\,(0)$ and $z(h)$, i.e.,

$$u\,(0) = 0 \Rightarrow z\,(0) = 0, \tag{66}$$

$$u\,(h) = h \Rightarrow z\,(h) = \left(1 - \frac{h^2}{12} W\,(h)\right) u\,(h), \tag{67}$$

and $u''(h)$ is obtained by Eq. 61. Then, $z\,(2h)$ is obtained from Eq. 65, and consequently,

$$u\,(2h) = \frac{z\,(2h)}{\left[1 - (h^2/12) W\,(2h)\right]}, \tag{68}$$

where $W\,(2h)$ is given by Eq. 62. Equation 68 can be used again to determine the $u(3h)$ value, and, proceeding iteratively, the S-wave scattering reduced radial wave function is fully determined except for an overall normalization factor. This means that for a sufficiently large value of $x_n \in A$, denoted as $x_{\bar{n}}$, we can write

$$u\,(x_{\bar{n}}) = N\left[j_0\,(k x_{\bar{n}}) + \tan\delta_0\, n_0\,(k x_{\bar{n}})\right], \tag{69}$$

where N is the sought normalization constant, and the phase shift δ_0 can be computed by taking the ratio between Eq. 69 written for $x_{\bar{n}}$ and the same equation written for x_m, m being close to $\bar{n}$ so that

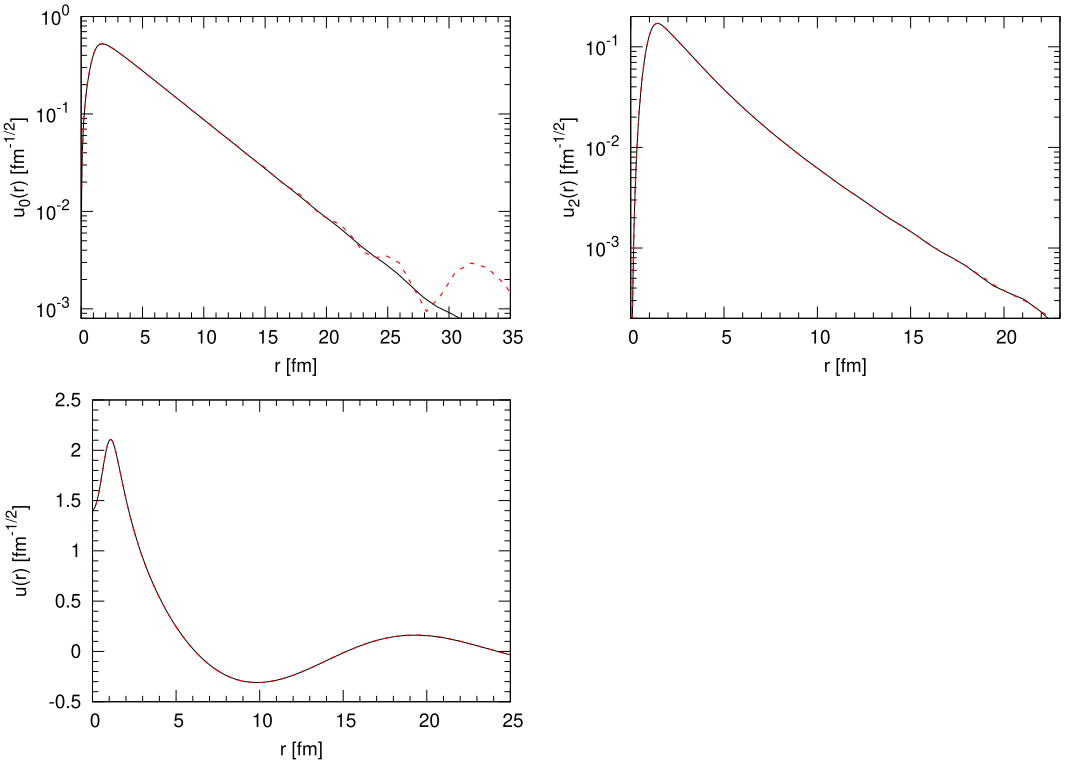

FIGURE 1
Deuteron $u_0(r)$ (left top panel) and $u_2(r)$ (right top panel) functions, and the nn $^1S_0$ function (left bottom panel) at E =5 MeV are calculated with the variational (dashed red line) and the Numerov (black solid line) methods. The NVIa potential is used. To appreciate the differences between the two methods, the function $u_0(r)$ and $u_2(r)$ are shown in a semilogarithmic scale.

$$\tan\delta_0 = \frac{u(x_m)j_0(kx_{\bar{n}}) - u(x_{\bar{n}})j_0(kx_m)}{u(x_{\bar{n}})n_0(kx_m) - u(x_m)n_0(kx_{\bar{n}})}. \tag{70}$$

Finally, using Eq. 69, the normalization constant N is given by

$$N = u(x_{\bar{n}})/\left[j_0(kx_{\bar{n}}) + \tan\delta_0 n_0(kx_{\bar{n}})\right] \tag{71}$$

so that the function $u(x_n)$ turns out to be normalized to unitary flux.

To compare the results obtained with the variational and the Numerov methods, Table 1 shows the deuteron binding energies and the nn phase shifts at the indicative relative energy E = 5 MeV for the four chiral potentials under consideration. In the table, we can see an excellent agreement between the two methods, with a difference well below 1 keV for the binding energies. The phase shifts calculated with the two methods are also in excellent numerical agreement. Furthermore, Figure 1 shows the deuteron and the nn wave functions, still at E = 5 MeV as an example, for the NVIa potential. The results obtained with the other chiral potentials present similar behavior. In the figure, we can see that the variational method fails to reproduce the $u_0(r)$ function for r > 20 fm. However, it should be noticed that in this region, the function is almost two orders of magnitude smaller than in the dominant range of $r \sim$ 0–5 fm. As we will see in the following section, we already anticipate that these discrepancies in the deuteron wave functions will have no impact on the muon capture rate.

3 Results

We present, in this section, the results for the $\Gamma^D(^1S_0)$ muon capture rate, obtained using the Norfolk potentials and consistent currents, as presented in Section 2.2. In particular, we will use the four Norfolk potentials NVIa, NVIb, NVIIa, and NVIIb, obtained varying the short- and long-range cutoffs (models a or b), and the range of laboratory energies over which the fits have been carried out (models I or II). For each model, the weak vector current and the axial current and the charge operators have been consistently constructed. In particular, we will indicate with the label LO those results obtained including only the LO contributions in the vector current and axial current and charge operators, and with NLO those obtained including, in addition, the NLO contributions to the vector current and axial charge

TABLE 2 Total doublet capture rate in the $^1S_0$ *nn* channel, $\Gamma^D(^1S_0)$ in s^{-1}, calculated using either the Numerov or the variational methods to obtain the deuteron and the *nn* scattering wave functions. Here, we report the results up to the digit for which the two methods differ. The NVIa potential and consistent currents at the various chiral order are used, and the axial charge radius is taken to be $r_A^2 = 0.46$ fm^2.

χ-order	Numerov	Variational
LO	245.43	245.42
NLO	247.59	247.58
N2LO	254.67	254.65
N3LO	255.31	255.30

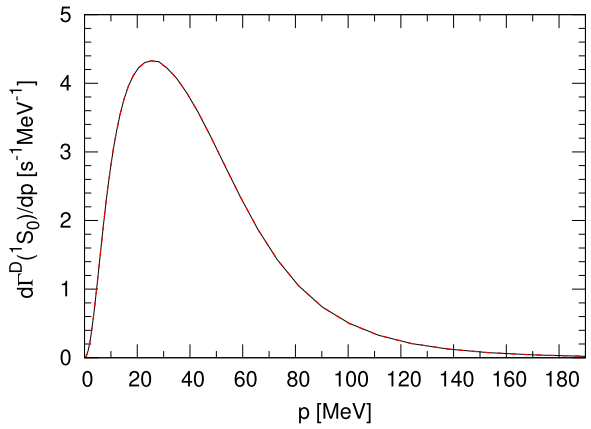

FIGURE 2
Differential doublet capture rate in the $^1S_0$ *nn* channel, $d\Gamma^D(^1S_0)/dp$ in $s^{-1}MeV^{-1}$, as a function of the *nn* relative momentum p in MeV, calculated using either the Numerov (black solid line) or the variational (red dashed line) methods in order to obtain the deuteron and the *nn* scattering wave functions. The curves are exactly on top of each other. The NVIa potential and consistent currents at N3LO are used. The axial charge radius is taken to be $r_A^2 = 0.46$ fm^2.

operators. We remind the reader that there are no NLO contributions to the axial current. With the label N2LO we will indicate those results obtained including the N2LO terms of the vector and axial currents, but not the axial charge since they vanish exactly. Finally, with N3LO we will indicate the results obtained when N3LO terms in the vector and axial currents are retained. It should be noted that this is the order in which new LECs appear. The contributions at N3LO for the axial charge are, instead, discarded for the reasons explained in Section 2.2. Finally, we will use the dependence given in Eq. 3 with $g_A = 1.2723$ and $r_A^2 = 0.46$ fm^2 for the axial single-nucleon form factor. However, to establish the uncertainty arising from the rather poor knowledge of r_A^2 (see Ref. [34] and the discussion in Section 1 and at the end of Section 2.2), we

TABLE 3 Total doublet capture rate in the $^1S_0$ *nn* channel, $\Gamma^D(^1S_0)$ in s^{-1}, calculated using the four Norfolk potentials NVIa, NVIb, NVIIa, and NVIIb, and consistent currents, at the various chiral orders. We also report the uncertainty due to the truncation of the chiral expansion in the current for each order. The axial charge radius is taken to be $r_A^2 = 0.46$ fm^2, and the variational method is applied to calculate the deuteron and the *nn* scattering wave functions.

	Potential			
χ-order	NVIa	NVIb	NVIIa	NVIIb
LO	245.4 (62.0)	245.1 (61.9)	245.7 (62.1)	246.6 (62.3)
NLO	247.6 (15.7)	247.6 (15.7)	247.9 (15.7)	249.0 (15.7)
N2LO	254.7 (4.1)	259.1 (4.4)	255.0 (4.1)	260.3 (4.4)
N3LO	255.3 (1.1)	255.6 (1.3)	255.9 (1.1)	256.4 (1.4)

will also show results obtained with $r_A^2 = 0.30, 0.46, 0.62$ fm^2, so that the 0.16 fm^2 uncertainty on r_A^2 [34] will be taken into account.

First, we begin by proving that the uncertainty arising from the numerical method adopted to study the deuteron and the *nn* scattering states is well below the 1% level. In fact, Table 2 shows the results obtained with the NVIa potential and currents with up to N3LO contributions, using either the variational or the Numerov method to solve the two-body problem (see Section 2.3). The function $d\Gamma^D(^1S_0)/dp$ (see Eq. 4) calculated with the same potential and currents is shown in Figure 2. As the figure and the table show, the agreement between the results obtained with the two methods is essentially perfect, of the order of 0.01 s^{-1} in $\Gamma^D(^1S_0)$, well below any other source of error ($\simeq 0.005\%$). Therefore, from now on, we will only present results obtained using the variational method, which is numerically less involved than the Numerov one.

Table 3 shows the results for $\Gamma^D(^1S_0)$, obtained using all four Norfolk potentials, NVIa, NVIb, NVIIa, and NVIIb, and consistent currents, from LO up to N3LO. The axial charge radius is fixed at $r_A^2 = 0.46$ fm^2. As seen in the table, we can provide our best estimate for $\Gamma^D(^1S_0)$, which we calculate simply as the average between the four values at N3LO, $\Gamma^D(^1S_0) = 255.8\ s^{-1}$. Furthermore, we would like to remark that the overall model dependence is quite small, the largest difference being of the order of 1.1 s^{-1} between the NVIa and NVIIb results, at N3LO. Going into more detail, 1) by comparing the NVIa (NVIIa) and NVIb (NVIIb) results, still at N3LO, we can get a grasp on the cutoff dependence, which turns out to be smaller than 1 s^{-1} for both models I and II. 2) By comparing the NVIa (NVIb) and NVIIa (NVIIb) results, again at N3LO, we can conclude that the dependence on the *NN* database used for the LECs' fitting procedure for the potentials is essentially of the same order. To remain conservative, we decided to define the theoretical uncertainty arising from model dependence as the half range, i.e.,

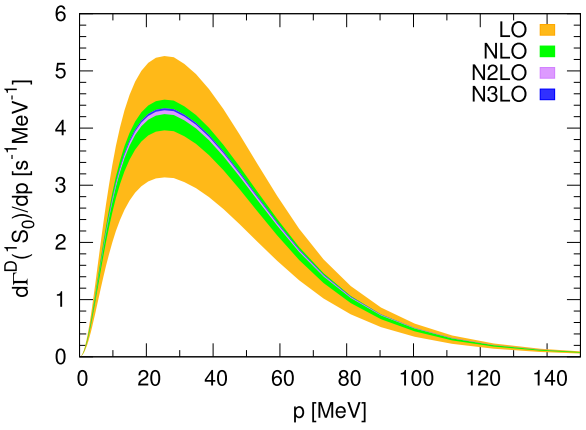

FIGURE 3
Differential doublet capture rate in the $^1S_0$ *nn* channel, $d\Gamma^D(^1S_0)/dp$ in $s^{-1}MeV^{-1}$, as a function of the *nn* relative momentum p in MeV, calculated order by order with the relative errors computed following the prescription of Ref. [45]. The axial charge radius is taken to be $r_A^2 = 0.46$ fm^2.

$$\Delta\Gamma^D(^1S_0)[\text{mod}-\text{dep}] \equiv \frac{|\Gamma^D(^1S_0)_{\text{NVIIb}} - \Gamma^D(^1S_0)_{\text{NVIa}}|}{2}. \quad (72)$$

From this, we obtain $\Delta\Gamma^D(^1S_0)[\text{mod}-\text{dep}] = 0.6\ s^{-1}$. We want to remark that this estimate of $\Delta\Gamma^D(^1S_0)[\text{mod}-\text{dep}]$ does not take into account the error on the fit of the nuclear interaction's LECs or its chiral truncation. Therefore, it should be considered just as a lower bound of the actual uncertainty.

From Table 3, we can conclude that the chiral-order convergence seems to be quite well under control for all the potential models. In fact, in going from LO to NLO, $\Gamma^D(^1S_0)$ has increased by 2.2 s^{-1} for the a models, and 2.5 s^{-1} and 2.4 s^{-1} for the models NVIb and NVIIb, respectively. This small change is because the only correction appearing at NLO comes from the vector current. Passing from NLO to N2LO, the muon capture rate increases by 7.1 s^{-1} for the interactions NVIa and NVIIa, and 11.5 s^{-1} and 11.3 s^{-1} for the models NVIb and NVIIb, respectively. This can be understood considering that the terms with the Δ-isobar contributions appear at this order for the vector and axial current. The convergence at N3LO shows instead a more involved behavior: for the models NVIa and NVIIa, an $\Gamma^D(^1S_0)$ increase of 0.6 s^{-1} and 0.9 s^{-1}, respectively, while for the models NVIb and NVIIb, the muon capture rate decreases by 3.5 s^{-1} and 3.9 s^{-1}, respectively. Even if the results are in reasonable agreement with the expected chiral convergence behavior (in particular for the models a), the chiral convergence of the current shows a significant dependence on the regularization that we tracked back to the axial current corrections and in particular to the different value of the constant c_D (see Section 2.2). We still find remarkable that the results at N3LO obtained with the various potentials, even if their chiral convergence patterns are quite different, turn out to be within 1.1 s^{-1}.

TABLE 4 Total doublet capture rate in the $^1S_0$ *nn* channel, $\Gamma^D(^1S_0)$ in s^{-1}, is calculated using all the different interactions and consistent currents up to N3LO, and three different values of r_A^2, $r_A^2 = 0.30, 0.46, 0.62$ fm^2. The variational method is applied to calculate the deuteron and the *nn* scattering wave functions.

Potential	$r_A^2 = 0.30$	$r_A^2 = 0.46$	$r_A^2 = 0.62$
NVIa	258.2	255.3	252.4
NVIb	258.5	255.6	252.8
NVIIa	258.7	255.9	253.0
NVIIb	259.3	256.4	253.6

The theoretical uncertainty arising from the chiral-order convergence of the nuclear weak transition operators can be studied using the prescription of Ref. [45]. Here, we report the formula for the error at N2LO only. At this order, for each energy, we define the error for the differential capture rate (to simplify the notation from now on we use $\Gamma^D(p) = d\Gamma^D(^1S_0)/dp$), as

$$\Delta\Gamma^D(p) \equiv \max\{Q^3|\Gamma^D_{\text{LO}}(p)|, Q^2|\Gamma^D_{\text{NLO}}(p) - \Gamma^D_{\text{LO}}(p)|, Q|\Gamma^D_{\text{N2LO}}(p) - \Gamma^D_{\text{NLO}}(p)|\}, \quad (73)$$

where we assumed

$$Q = \frac{1}{\Lambda}\frac{p^8 + m_\pi^8}{p^7 + m_\pi^7} \quad (74)$$

as in Ref. [46] for the case of the $np \leftrightarrow dy$ reaction. Here, p is the relative momentum of the *nn* system and we assume a value of $\Lambda \simeq 550$ MeV, which is of the order of the cutoff of the adopted interactions. Analogous formulas have been used to study the other orders (see Ref. [45] for details).

In Figure 3, we show the error on $d\Gamma^D(^1S_0)/dp$ order by order in the expansion of the nuclear current up to N3LO for the NVIa interaction. From the figure, the nice convergence of the chiral expansion of the currents is evident. The total error arising from the chiral truncation of the currents on $\Gamma^D(^1S_0)$ is then computed by integrating the error of the differential capture rate over p, namely,

$$\Delta\Gamma^D(^1S_0)[\text{curr}-\text{conv}] = \int_0^{p_{max}} \Delta\Gamma^D(p)dp. \quad (75)$$

Note that here we assumed the distribution of the truncation error to be uniform, this being a systematic error. Therefore, we do not square it in Eq. 75. Table 3 also shows for each order the error relative to the chiral truncation of the electroweak currents. To be the most conservative as possible, we keep as error the largest obtained with the various interaction models. In the same spirit, we consider the error computed at N2LO, since the calculation at N3LO does not contain all the contributions of the axial charge (see discussion Section

2.2). Therefore, we obtain $\Delta\Gamma^D(^1S_0)[\text{curr} - \text{conv}] = 4.4\ \text{s}^{-1}$. In comparison, the same calculation at N3LO would give as an error $\Delta\Gamma^D(^1S_0)[\text{curr} - \text{conv}]|_{\text{N3LO}} = 1.4\ \text{s}^{-1}$. We want to remark that the uncertainty computed here arises only from the chiral truncation of the currents and it represents only a lower bound of the total chiral error.

Finally, Table 4 shows the results obtained with all the interactions and consistent currents up to N3LO for the three values of the axial charge radius, $r_A^2 = 0.30, 0.46, 0.62\ \text{fm}^2$. This allows us to understand the importance of this last source of theoretical uncertainty. The three values are chosen to span the range of values proposed in Ref. [34], being the lower limit, central value, and upper limit for r_A^2. We also verified that $\Gamma^D(^1S_0)$ has a linear dependence on r_A^2. As a consequence, performing the calculation for the three mentioned values of r_A^2 is essentially equivalent to the "standard" error propagation. Again, we define the theoretical uncertainty $\Delta\Gamma^D(^1S_0)[r_A^2]$ arising from this last source as the half-range of the results, i.e.,

$$\Delta\Gamma^D(^1S_0)[r_A^2] \equiv \max_{pot}\left\{\frac{|\Gamma^D(^1S_0)_{r_A^2=0.30} - \Gamma^D(^1S_0)_{r_A^2=0.62}|}{2}\right\}, \quad (76)$$

where $\max_{pot}$ indicates that we take the maximum value among the different interactions considered. From the table, we can conclude that $\Delta\Gamma^D(^1S_0)[r_A^2] = 2.9\ \text{s}^{-1}$, which is found to be essentially model-independent.

In conclusion, our final result for $\Gamma^D(^1S_0)$ is

$$\Gamma^D(^1S_0) = 255.8(0.6)(4.4)(2.9)\ \text{s}^{-1}, \quad (77)$$

where the three uncertainties arise from model dependence, chiral convergence, and the experimental error in the axial charge radius r_A. The overall systematic uncertainty becomes $5.0\ \text{s}^{-1}$ when the various contributions are summed. The uncertainty on r_A^2 is instead statistical and, therefore, must be treated separately. This result can be compared with those of Refs. [10, 12]. In Ref. [10], we found a value of 253.5 (1.2) s^{-1}, the error taking care of the cutoff dependence and the uncertainty in the d_R LEC fitting procedure. When only the cutoff dependence is considered, it reduces to $0.2\ \text{s}^{-1}$, somewhat smaller than the present $0.6\ \text{s}^{-1}$. The central values that we obtained and the one quoted in Ref. [10], even if the chiral potentials are very different, are instead in reasonable agreement. In Ref. [12], it was found that $\Gamma^D(^1S_0) = 252.8(4.6)(3.9)\ \text{s}^{-1}$, where the first error is due to the truncation in the chiral expansion and the second is due to the uncertainty in the nucleon axial radius r_A. These two errors should be compared with our $5.0\ \text{s}^{-1}$ and $2.9\ \text{s}^{-1}$. The agreement for the first error is very nice, while the small difference in the second error is certainly due to the fact that in Ref. [12] a larger uncertainty for r_A^2 was used ($0.22\ \text{fm}^2$ vs. the present $0.16\ \text{fm}^2$). Also, in this case, the agreement between the central values is good, even if the potential models adopted are very different. This could suggest that the observable $\Gamma^D(^1S_0)$ is not sensitive to the nuclear potential model, as long as this can properly reproduce the deuteron and the *nn* scattering systems (as, in fact, any realistic modern potential usually does).

4 Conclusion and outlook

We investigated, for the first time, with local nuclear potential models derived in χEFT and consistent currents, the muon capture on deuteron, in the $^1S_0$ initial *nn* scattering state. The use of this framework allowed us to 1) provide a new estimate for the capture rate $\Gamma^D(^1S_0)$, which turned out to agree with the results already present in the literature and obtained still in χEFT, but with different (non-local) potential models [10, 12]; 2) accompany this estimate with a determination of the theoretical uncertainty, which arises from model dependence, chiral convergence, and the uncertainty in the single-nucleon axial charge radius r_A. We also verified that the uncertainty arising from the numerical technique adopted to solve the two-body bound- and scattering-state problem is completely negligible.

Our final result is $\Gamma^D(^1S_0) = 255.8(0.6)(4.4)(2.9)\ \text{s}^{-1}$, where the three errors come from the three sources of uncertainty just mentioned. To provide an indicative value for the overall uncertainty, we propose to sum the systematic uncertainties arising from sources 1) and 2), obtaining the value of $5.0\ \text{s}^{-1}$. Then, this error can be summed in quadrature with the one of source 3), $2.9\ \text{s}^{-1}$. Therefore, we obtain $\Gamma^D(^1S_0) = 255.8(5.8)\ \text{s}^{-1}$. We remark again that the value of $5.8\ \text{s}^{-1}$ for the overall uncertainty is only indicative, and the preferable procedure should be to treat the three errors, $0.6\ \text{s}^{-1}$, $4.4\ \text{s}^{-1}$, and $2.9\ \text{s}^{-1}$, separately. Moreover, it is important to remind that the errors coming from the sources 1) and 2) can be considered only as lower limits of the actual uncertainty coming from the model dependence and the chiral truncation.

Given the success of this calculation in determining $\Gamma^D(^1S_0)$ and its uncertainty, with a procedure less involved than the one of Ref. [12], which still leads to similar results, we plan to proceed with applying this framework to the calculation of Γ^D, retaining all the *nn* partial waves up to $J = 2$ and $L = 3$. These are known to provide contributions to Γ^D up to $1\ \text{s}^{-1}$ [9]. In parallel, we plan to study the muon capture processes also on ^{3}He and ^{6}Li, in the footsteps of Ref. [27]. Here, the Norfolk potentials were used in conjunction with the variational and Green's function Monte Carlo techniques to solve for the $A = 3, 6$ bound states, and the final results were found to disagree, to some level, with the experimental data. It will be interesting to verify these outcomes, using the hyperspherical harmonics method to solve for the $A = 3, 6$ nuclei [47–49]. Last but not least, we plan to apply this same

framework to weak processes of interest for solar standard models and solar neutrino fluxes, i.e., the proton weak capture on proton (reaction 2), and on ^{3}He (the so-called *hep* reaction). In this second case, it is remarkable that a consistent χEFT calculation is still missing (see Refs. [50–52]). For both reactions, we will be able to provide a value for the astrophysical *S*-factor at zero energy accompanied by an estimate of the theoretical uncertainty.

Data availability statement

The original contributions presented in the study are included in the article; further inquiries can be directed to the corresponding author.

Author contributions

LC and LM shared the idea, the formula derivation, and the computer code implementation of this work. LM was mainly responsible for the drafting of the manuscript. AG contributed to reviewing the codes and running them in order to obtain the final results presented here, while MP and MV gave valuable suggestions during the setting up of the calculation. All the authors contributed equally to reviewing and correcting the draft of the manuscript.

Funding

AG acknowledges the support provided by the U.S. Department of Energy, Office of Nuclear Science, under Contract No. DE-AC05-06OR23177, while MP acknowledges the support from the U.S. Department of Energy through the FRIB Theory Alliance Award No. DE-SC0013617.

Acknowledgments

The authors also acknowledge the Istituto Nazionale di Fisica Nucleare (INFN), Sezione di Pisa, for providing the computational resources. The final calculation was performed using resources of the National Energy Research Scientific Computing Center (NERSC), a U.S. Department of Energy Office of Science User Facility located at Lawrence Berkeley National Laboratory, operated under Contract No. DE-AC02-05CH11231.

Conflict of interest

The authors declare that the research was conducted in the absence of any commercial or financial relationships that could be construed as a potential conflict of interest.

Publisher's note

References

1. Measday DF. The nuclear physics of muon capture. *Phys Rep* (2001) 354: 243–409. doi:10.1016/s0370-1573(01)00012-6

2. Wang IT, Anderson EW, Bleser EJ, Lederman LM, Meyer SL, Rosen JL, et al. Muon capture in (p μ d)+ molecules. *Phys Rev* (1965) 139:B1528–38. doi:10.1103/physrev.139.b1528

3. Bertin A, Vitale A, Placci A, Zavattini E. Muon capture in gaseous deuterium. *Phys Rev D* (1973) 8:3774–93. doi:10.1103/physrevd.8.3774

4. Bardin G, Duclos J, Martino J, Bertin A, Capponi M, Piccinini M, et al. A measurement of the muon capture rate in liquid deuterium by the lifetime technique. *Nucl Phys A* (1986) 453:591–604. doi:10.1016/0375-9474(86)90253-8

5. Cargnelli M, et al. Workshop on fundamental μ physics, los alamos, 1986, LA 10714C. In: M Morita, H Ejiri, H Ohtsubo, T Sato, editors. *Nuclear weak process and nuclear structure, Yamada Conference XXIII*. Singapore: World Scientific (1989). p. 115.

6. Kammel P. Precision muon capture at PSI. *PoS* (2013) CD12:016.

7. Marcucci LE. Muon capture on deuteron and ^{3}He: A personal review. *Int J Mod Phys A* (2012) 27:1230006. doi:10.1142/s0217751x12300062

8. Adam J, Jr, Tater M, Truhlik E, Epelbaum E, Machleidt R, Ricci P. Calculation of doublet capture rate for muon capture in deuterium within chiral effective field theory. *Phys Lett B* (2012) 709:93–100. doi:10.1016/j.physletb.2012.01.065

9. Marcucci LE, Piarulli M, Viviani M, Girlanda L, Kievsky A, Rosati S, et al. Muon capture on deuteron and ^{3}*He. Phys Rev C* (2011) 83:014002. doi:10.1103/physrevc.83.014002

10. Marcucci LE, Kievsky A, Rosati S, Schiavilla R, Viviani M. Chiral effective field theory predictions for muon capture on deuteron and ^{3}He. *Phys Rev Lett* (2012) 108: 052502. [Erratum: Phys. Rev. Lett. 121, (2018) 049901]. doi:10.1103/physrevlett.108.052502

11. Golak J, Skibiński R, Witała H, Topolnicki K, Elmeshneb AE, Kamada H, et al. Break-up channels in muon capture on ^{3}He. *Phys Rev C* (2014) 90:024001. [Addendum: Phys.Rev.C 90, 029904 10.1103/physrevc.90.029904(2014)].

12. Acharya B, Ekström A, Platter L. Effective-field-theory predictions of the muon-deuteron capture rate. *Phys Rev C* (2018) 98:065506. doi:10.1103/physrevc.98.065506

13. Entem DR, Machleidt R. Accurate charge dependent nucleon nucleon potential at fourth order of chiral perturbation theory. *Phys Rev C* (2003) 68: 041001. doi:10.1103/physrevc.68.041001

14. Machleidt R, Entem DR. Chiral effective field theory and nuclear forces. *Phys Rep* (2011) 503:1–75. doi:10.1016/j.physrep.2011.02.001

15. Gazit D, Quaglioni S, Navrátil P. Three-nucleon low-energy constants from the consistency of interactions and currents in chiral effective field theory. *Phys Rev Lett* (2009) 103:102502. [Erratum: Phys. Rev. Lett. 122, (2019) 029901]. doi:10.1103/physrevlett.103.102502

16. Carlsson BD, Ekström A, Forssén C, Strömberg DF, Jansen GR, Lilja O, et al. Uncertainty analysis and order-by-order optimization of chiral nuclear interactions. *Phys Rev X* (2016) 6:011019. doi:10.1103/physrevx.6.011019

17. Acharya B, Ekström A, Odell D, Papenbrock T, Platter L. Corrections to nucleon capture cross sections computed in truncated Hilbert spaces. *Phys Rev C* (2017) 95:031301. doi:10.1103/physrevc.95.031301

18. Piarulli M, Tews I. Local nucleon-nucleon and three-nucleon interactions within chiral effective field theory. *Front Phys* (2020) 7:245. doi:10.3389/fphy.2019.00245

19. Piarulli M, Girlanda L, Schiavilla R, Kievsky A, Lovato A, Marcucci LE, et al. Local chiral potentials with Δ-intermediate states and the structure of light nuclei. *Phys Rev C* (2016) 94:054007. doi:10.1103/physrevc.94.054007

20. Baroni A, Schiavilla R, Marcucci LE, Girlanda L, Kievsky A, Lovato A, et al. Local chiral interactions, the tritium Gamow-Teller matrix element, and the three-nucleon contact term. *Phys Rev C* (2018) 98:044003. doi:10.1103/physrevc.98.044003

21. Schiavilla R, Baroni A, Pastore S, Piarulli M, Girlanda L, Kievsky A, et al. Local chiral interactions and magnetic structure of few-nucleon systems. *Phys Rev C* (2019) 99:034005. doi:10.1103/physrevc.99.034005

22. Gnech A, Schiavilla R. *Magnetic structure of few-nucleon systems at high momentum transfers in a χEFT approach* (2022). arXiv:2207.05528.

23. Piarulli M, Baroni A, Girlanda L, Kievsky A, Lovato A, Lusk E, et al. Light-nuclei spectra from chiral dynamics. *Phys Rev Lett* (2018) 120:052503. doi:10.1103/PhysRevLett.120.052503

24. Gandolfi S, Lonardoni D, Lovato A, Piarulli M. Atomic nuclei from quantum Monte Carlo calculations with chiral EFT interactions. *Front Phys* (2020) 8:117. doi:10.3389/fphy.2020.00117

25. King GB, Andreoli L, Pastore S, Piarulli M, Schiavilla R, Wiringa RB, et al. Chiral effective field theory calculations of weak transitions in light nuclei. *Phys Rev C* (2020) 102:025501. doi:10.1103/physrevc.102.025501

26. King GB, Andreoli L, Pastore S, Piarulli M. Weak transitions in light nuclei. *Front Phys* (2020) 8:363. doi:10.3389/fphy.2020.00363

27. King GB, Pastore S, Piarulli M, Schiavilla R. Partial muon capture rates in A=3 and A=6 nuclei with chiral effective field theory. *Phys Rev C* (2022) 105:L042501. doi:10.1103/physrevc.105.l042501

28. Cirigliano V, Dekens W, De Vries J, Graesser ML, Mereghetti E, Pastore S, et al. Renormalized approach to neutrinoless double- β decay. *Phys Rev C* (2019) 100:055504. doi:10.1103/physrevc.100.055504

29. King GB, Baroni A, Cirigliano V, Gandolfi S, Hayen L, Mereghetti E, et al. *Ab initio calculation of the* β *decay spectrum of* ^{6}*He* (2022). ArXiv:2207.11179.

30. Piarulli M, Bombaci I, Logoteta D, Lovato A, Wiringa RB. Benchmark calculations of pure neutron matter with realistic nucleon-nucleon interactions. *Phys Rev C* (2020) 101:045801. doi:10.1103/physrevc.101.045801

31. Lovato A, Bombaci I, Logoteta D, Piarulli M, Wiringa RB. Benchmark calculations of infinite neutron matter with realistic two- and three-nucleon potentials. *Phys Rev C* (2022) 105:055808. doi:10.1103/physrevc.105.055808

32. Acharya B, Platter L, Rupak G. Universal behavior of *p*-wave proton-proton fusion near threshold. *Phys Rev C* (2019) 100:021001. doi:10.1103/physrevc.100.021001

33. Marcucci LE, Schiavilla R, Viviani M. Proton-proton weak capture in chiral effective field theory. *Phys Rev Lett* (2013) 110:192503. [Erratum: Phys. Rev. Lett. 123, (2019) 019901]. doi:10.1103/physrevlett.110.192503

34. Hill RJ, Kammel P, Marciano WJ, Sirlin A. Nucleon axial radius and muonic hydrogen—A new analysis and review. *Rep Prog Phys* (2018) 81:096301. doi:10.1088/1361-6633/aac190

35. Walecka J. *Theorethical nuclear and subnuclear Physics*. London: Imperial College Press (1995).

36. Navarro Pérez R, Amaro JE, Ruiz Arriola E. Erratum: Coarse-grained potential analysis of neutron-proton and proton-proton scattering below the pion production threshold [Phys. Rev. C**88**, 064002 (2013)]. *Phys Rev C* (2013) 88:064002. [Erratum: Phys. Rev. C 91, (2015) 029901]. doi:10.1103/physrevc.91.029901

37. Navarro Pérez R, Amaro JE, Ruiz Arriola E. Coarse grained *nn* potential with chiral two-pion exchange. *Phys Rev C* (2014) 89:024004. doi:10.1103/physrevc.89.024004

38. Navarro Pérez R, Amaro JE, Ruiz Arriola E. Statistical error analysis for phenomenological nucleon-nucleon potentials. *Phys Rev C* (2014) 89:064006. doi:10.1103/physrevc.89.064006

39. Krebs H, Epelbaum E, Meissner U. Nuclear forces with Δ excitations up to next-to-next-to-leading order, part I: Peripheral nucleon-nucleon waves. *Eur Phys J A* (2007) 32:127–37. doi:10.1140/epja/i2007-10372-y

40. Baroni A, Girlanda L, Pastore S, Schiavilla R, Viviani M. Nuclear axial currents in chiral effective field theory. *Phys Rev C* (2016) 93:015501. doi:10.1103/physrevc.93.015501

41. Meyer AS, Betancourt M, Gran R, Hill RJ. Deuterium target data for precision neutrino-nucleus cross sections. *Phys Rev D* (2016) 93:113015. doi:10.1103/physrevd.93.113015

42. Abramowitz M, Stegun IA. *Handbook of mathematical functions with formulas, graphs, and mathematical tables, vol. 55*. Washington, DC, USA: US Government printing office (1964).

43. Kohn W. Variational methods in nuclear collision problems. *Phys Rev* (1948) 74:1763–72. doi:10.1103/physrev.74.1763

44. Johnson BR. The renormalized Numerov method applied to calculating bound states of the coupled-channel Schroedinger equation. *J Chem Phys* (1978) 69:4678–88. doi:10.1063/1.436421

45. Epelbaum E, Krebs H, Meißner UG. Improved chiral nucleon-nucleon potential up to next-to-next-to-next-to-leading order. *Eur Phys J A* (2015) 51:53. doi:10.1140/epja/i2015-15053-8

46. Acharya B, Bacca S. Gaussian process error modeling for chiral effective-field-theory calculations of $np \leftrightarrow dy$ at low energies. *Phys Lett B* (2022) 827:137011. doi:10.1016/j.physletb.2022.137011

47. Marcucci LE, Dohet-Eraly J, Girlanda L, Gnech A, Kievsky A, Viviani M. The hyperspherical harmonics method: A tool for testing and improving nuclear interaction models. *Front Phys* (2020) 8:69. doi:10.3389/fphy.2020.00069

48. Gnech A, Viviani M, Marcucci LE. Calculation of the ^{6}Li ground state within the hyperspherical harmonic basis. *Phys Rev C* (2020) 102:014001. doi:10.1103/physrevc.102.014001

49. Gnech A, Marcucci LE, Schiavilla R, Viviani M. Comparative study of ^{6}He β-decay based on different similarity-renormalization-group evolved chiral interactions. *Phys Rev C* (2021) 104:035501. doi:10.1103/physrevc.104.035501

50. Marcucci LE, Schiavilla R, Viviani M, Kievsky A, Rosati S, Beacom JF. Weak proton capture on ^{3}He. *Phys Rev C* (2001) 63:015801. doi:10.1103/physrevc.63.015801

51. Park TS, Marcucci LE, Schiavilla R, Viviani M, Kievsky A, Rosati S, et al. Parameter free effective field theory calculation for the solar proton fusion and hep processes. *Phys Rev C* (2003) 67:055206. doi:10.1103/physrevc.67.055206

52. Adelberger EG, Garcia A, Robertson RGH, Snover KA, Balantekin AB, Heeger K, et al. Solar fusion cross sections. II. Theppchain and CNO cycles. *Rev Mod Phys* (2011) 83:195–245. doi:10.1103/revmodphys.83.195

frontiers | Frontiers in Physics

TYPE Review
PUBLISHED 20 January 2023
DOI 10.3389/fphy.2022.1071971

OPEN ACCESS

EDITED BY
Maria Piarulli,
Washington University in St. Louis,
United States

REVIEWED BY
David Rodriguez Entem,
University of Salamanca, Spain
Carlo Barbieri,
University of Surrey, United Kingdom

*CORRESPONDENCE
Charlotte Elster,
elster@ohio.edu

SPECIALTY SECTION
This article was submitted
to Nuclear Physics,
a section of the journal
Frontiers in Physics

RECEIVED 17 October 2022
ACCEPTED 30 December 2022
PUBLISHED 20 January 2023

CITATION
Baker RB, Burrows M, Elster C, Launey KD, Maris P, Popa G and Weppner SP (2023), Chiral uncertainties in *ab initio* elastic nucleon-nucleus scattering.
Front. Phys. 10:1071971.
doi: 10.3389/fphy.2022.1071971

Chiral uncertainties in *ab initio* elastic nucleon-nucleus scattering

Robert B. Baker[1], Matthew Burrows[2], Charlotte Elster[1]*, Kristina D. Launey[2], Pieter Maris[3], Gabriela Popa[1] and Stephen P. Weppner[4]

[1]Department of Physics and Astronomy, Ohio University, Athens, OH, United States, [2]Department of Physics and Astronomy, Louisiana State University, Baton Rouge, LA, United States, [3]Department of Physics and Astronomy, Iowa State University, Ames, IA, United States, [4]Natural Sciences, Eckerd College, St. Petersburg, FL, United States

The effective interaction between a nucleon and a nucleus is one of the most important ingredients for reaction theories. Theoretical formulations were introduced early by Feshbach and Watson, and efforts of deriving and computing those 'optical potentials' in a microscopic fashion have a long tradition. However, only recently the leading order term in the Watson multiple scattering approach could be calculated fully *ab initio*, meaning that the same nucleon-nucleon (NN) interaction enters both the structure as well as the reaction pieces on equal footing. This allows the uncertainties from the underlying chiral effective NN interaction to be systematically explored in nucleon-nucleus elastic scattering observables. In this contribution the main ingredients for arriving at the *ab initio* leading order of the effective nucleon-nucleus interaction in the Watson approach will be reviewed. Concentrating on one specific chiral NN interaction from the LENPIC collaboration and light nuclei with a 0^+ ground state, the leading order nucleon-nucleus interaction is calculated using up to the third chiral order (N2LO) in the nucleon-nucleon potential, and elastic scattering observables are extracted. Then pointwise as well as correlated uncertainty quantification is used for the estimation of the chiral truncation error. Elastic scattering observables for ^{4}He, ^{12}C, and ^{16}O for between 65 and 200 MeV projectile energy will be analyzed.

KEYWORDS

elastic nucleon-nucleus scattering, multiple scattering expansion, *ab initio* optical potential, chiral nucleon-nucleon interaction, truncation uncertainty quantification

1 Introduction

Simplifying the many-body problem posed by scattering of a proton or neutron from a nucleus to a two-body problem with an effective (optical) potential was introduced already by Bethe [1] in the 1930s, and its justification summarized by Feshbach [2]. Since then differential cross sections as well as spin observables for elastic scattering played an important role in either determining the parameters in phenomenological optical models for proton or neutron scattering from nuclei or in testing validity and accuracy of microscopic models thereof. The theoretical approach to elastic scattering from a nuclear target presented in this article is based on the ansatz of a multiple scattering expansion that was pioneered by Watson [3, 4], made familiar by Kerman, McManus, and Thaler (KMT) [5]. and refined further as spectator expansion [6–8]. Specifically, elastic scattering from stable nuclei has led in the 1990s to a large body of work on microscopic optical potentials in which the nucleon-nucleon interaction and the density of the nucleus were taken as input to rigorous calculations of first-order potentials, in either a Kerman-McManus-Thaler (KMT) or a Watson expansion of the multiple scattering series (see e.g. [9–14]). Here the primary goal was a deeper understanding of the reaction

mechanism. However, a main disadvantage of that work was the lack of sophisticated nuclear structure input compared to what is available today.

Recent developments of the nucleon-nucleon (NN) and three-nucleon (3N) interactions, derived from chiral effective field theory, have yielded major progress [15–22]. These, together with the utilization of massively parallel computing resources (e.g., see [23–27]), have placed *ab initio* large-scale simulations at the frontier of nuclear structure and reaction explorations. Among other successful many-body theories, the *ab initio* no-core shell-model (NCSM) approach (see, e.g. [28–31]), has over the last decade taken center stage in the development of microscopic tools for studying the structure of atomic nuclei. The NCSM concept combined with a symmetry-adapted (SA) basis in the *ab initio* SA-NCSM [32] has further expanded the reach to the structure of intermediate-mass nuclei [33].

Following the developments in nuclear structure theory, it is very natural to again consider rigorous calculations of effective folding nucleon-nucleus (NA) potentials, since now the nuclear densities required as input for the folding with the NN scattering amplitudes can be based on the same chiral NN interaction. This development also allows to investigate effects of truncation uncertainties in the chiral expansion on NA scattering observables in a similar fashion as already successfully performed in NN scattering (see e.g. [34–36]), nucleon-deuteron scattering [37], or structure observables for light nuclei [31, 38].

The theoretical and computational developments leading to *ab initio* NA effective interactions (in leading order in the spectator expansion) are described in a serious of publications by the authors [39–43] and others (see e. g. [44–47]). Thus the aim of this review is to shed light on truncation uncertainties in the chiral expansion, and within that context give a perspective on intricacies of the spectator expansion as well as the explicit content of its leading order term, which can now be calculated *ab initio*.

Deriving *ab initio* optical potentials within a multiple scattering approach focuses on projectile energies at energies about 80 MeV or higher, since the expectation is that at those energies the leading order term may already capture the most important physics. Another recent *ab initio* approach starts from a formulation introduced by Feshbach [48] and constructs optical potentials and elastic scattering observables within a Green's function approach [49, 50]. For elastic scattering from medium-mass nuclei the coupled-cluster method [51] and the SA-NCSM [52] approach have been successfully implemented. These approaches are by design better suited for calculating scattering observables at energies below about 20–30 MeV due to restrictions on the size of the model spaces which increase with increasing projectile energy. In Ref. [53] an extensive overview of the status of the field of optical potentials and their need in the rare-isotope era is given and the current status of *ab initio* approaches is discussed. We want to encourage the reader to refer to this work, for more details.

2 Watson optical potential within the spectator expansion

The standard starting point for describing elastic scattering of a single projectile from a target of A particles within a multiple scattering approach is the separation of the Lippmann-Schwinger (LS) equation for the transition operator T,

$$T = V + VG_0(E)T \tag{1}$$

into two parts, namely an integral equation for T,

$$T = U + UG_0(E)PT, \tag{2}$$

where U is the effective potential operator defined by a second integral equation,

$$U = V + VG_0(E)QU. \tag{3}$$

Here p is a projection onto the ground state of the target, $P = \frac{|\Phi_0\rangle\langle\Phi_0|}{\langle\Phi_0|\Phi_0\rangle}$, with $P + Q = 1$ and $[G_0(E), P] = 1$. The free propagator for the projectile and target system is given by $G_0(E) = (E - h_0 - H_A + i\epsilon)^{-1}$ where h_0 is the kinetic energy of the projectile and H_A is the Hamiltonian of the target nucleus. The general solutions of the nuclear bound state problem $H_A|\Phi\rangle$ include the ground state, excited states and continuum states. For the scattering problem given by the transition amplitude T the reference energy separating bound and continuum states is chosen such that the ground state energy is set to zero. Thus energies referring to the target Hamiltonian in G_0 are excitation energies of the target. With these definitions the transition operator for elastic scattering may be redefined as $T_{\rm el} = PTP$, in which case Eq. 2 can be written as

$$T_{\rm el} = PUP + PUPG_0(E)T_{\rm el}. \tag{4}$$

2.1 Spectator expansion of the operator U

The transition operator for elastic scattering is given by a straightforward one-body integral equation, which of course requires the knowledge of PUP, which is a many-body operator. For a brief review we follow the spectator expansion of PUP as introduced in Ref. [54] in contrast to Ref. [6] where the expansion of T is considered. Following those references, we assume the presence of two-body forces only for the present discussion. The extension to many-body forces is not precluded by the formulation. With this assumption the operator U can be expanded as

$$U = \sum_{i=1}^{A} U_i, \tag{5}$$

where U_i is given by

$$U_i = v_{0i} + v_{0i}G_0(E)Q\sum_{j=1}^{A} U_j, \tag{6}$$

provided that $V = \sum_{i=1}^{A} v_{0i}$, where the two-body potential v_{0i} acts between the projectile and the ith target nucleon. Through the introduction of an operator τ_i which satisfies

$$\tau_i = v_{0i} + v_{0i}G_0(E)Q\tau_i, \tag{7}$$

Eq. 6 can be rearranged as

$$U_i = \tau_i + \tau_i G_0(E)Q\sum_{j\neq i} U_j. \tag{8}$$

This rearrangement process can be continued for all A target particles, so that the operator for the optical potential can be expanded in a series of A terms of the form

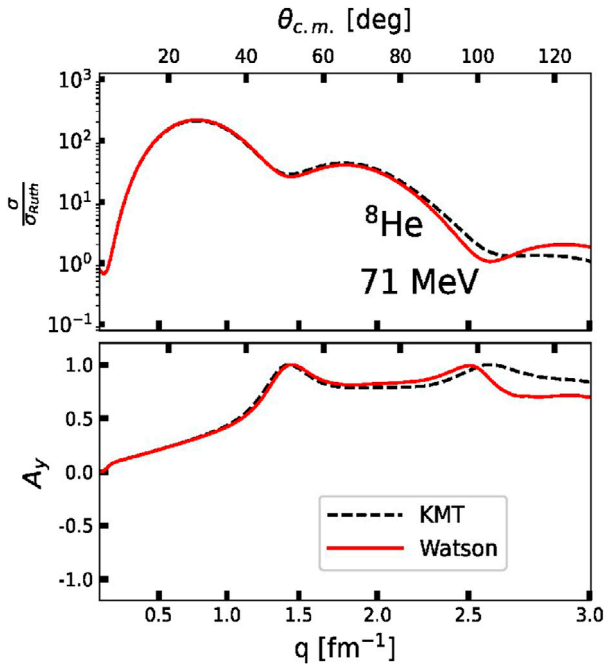

FIGURE 1
The angular distribution of the differential cross section divided by the Rutherford cross section (upper panel) and the analyzing power (A_y) for elastic proton scattering from ^{8}He at 71 MeV laboratory kinetic energy as function of the momentum transfer q and the c. m. angle calculated with the LENPIC SCS chiral interaction [19] with a cutoff R = 1 fm. The calculations are based on non-local densities using $\hbar\Omega$ = 14 MeV at N_{max} = 14. The solid (red) line stands for using the Watson optical potential while the black (dashed) line represents the KMT prescription.

$$U = \sum_{i=1}^{A} \tau_i + \sum_{i,j\neq i}^{A} \tau_{ij} + \sum_{i,j\neq i,k\neq i,j}^{A} \tau_{ijk} + \cdots . \tag{9}$$

This is the Spectator Expansion for U, where each term is treated in turn. The separation of the interactions according to the number of interacting nucleons has a certain latitude, due to the many-body nature of $G_0(E)$, which needs to be considered separately. In the following we will concentrate on the leading-order term, which is still a many-body operator due the presence of $G_0(E)$. The next-to-leading order term in this spectator expansion for U has been formally derived and connected to standard three-body equations in Ref. [54].

2.2 Propagator expansion in the leading-order term of U

When using the leading-order term of the spectator expansion as given in Eq. 7, for elastic scattering only $P\tau_i P$, or equivalently $\langle\Phi_0|\tau_i|\Phi_0\rangle$ needs be considered. With this in mind, Eq. 7 can be re-expressed as

$$\tau_i = v_{0i} + v_{0i}G_0(E)\tau_i - v_{0i}G_0(E)P\tau_i = \hat{\tau}_i - \hat{\tau}_i G_0(E)P\tau_i, \tag{10}$$

or

$$\langle\Phi_0|\tau_i|\Phi_0\rangle = \langle\Phi_0|\hat{\tau}_i|\Phi_0\rangle - \langle\Phi_0|\hat{\tau}_i|\Phi_0\rangle\frac{1}{(E-E_A)-h_0+i\varepsilon}\langle\Phi_0|\tau_i|\Phi_0\rangle, \tag{11}$$

where $\hat{\tau}_i$ is defined as the solution of

$$\hat{\tau}_i = v_{0i} + v_{0i}G_0(E)\hat{\tau}_i. \tag{12}$$

The combination of Eqs 10, 2 corresponds to the leading-order Watson optical potential [3, 4]. In *ab initio* structure calculations the one-body densities or ground state wave functions for protons and neutrons are calculated separately, so that Eq. 11 allows to combine e.g. for proton scattering of a nucleus the proton-neutron interaction ($\hat{\tau}_{i=pn}$) with the neutron one-body density and the proton-proton interaction with the proton one-body density. The sum over i then adds both to obtain the driving term $\langle\Phi_0|\hat{\tau}_i|\Phi_0\rangle$ the integral equation, Eq. 11.

If the projectile-target-nucleon interaction is assumed to be the same for all target nucleons and if iso-spin effects are neglected then the KMT approximation ($\frac{A-1}{A}\langle\Phi_0|\hat{\tau}_i|\Phi_0\rangle$) can be derived from the leading-order Watson potential [5]. When working with momentum space integral equations, the numerical implementation of Eq. 11 is straightforward [40, 41, 45, 55]. Working in coordinate space with differential equations does not allow an equally straightforward implementation, and thus the KMT prescription is the most favorable alternative. A comparison between leading-order Watson potential and the KMT prescription is shown in Figure 1 for elastic proton scattering from ^{8}He at 71 MeV laboratory kinetic energy. Despite the relatively large difference between the proton and neutron densities for this nucleus the KMT prescription agrees with the exact Watson description very well up to momentum transfers of about 2 fm^{-1}.

Since Eq. 11 is a one-body integral equation, the principal problem is to find a solution of Eq. 12, which due to many-body character of $G_0(E)$ is still a many-body integral equation, and in fact no more easily solved than the starting point of Eq. 1.

For most practical calculations the so-called closure approximation to $G_0(E)$ is implemented [56] turning Eq. 12 into a one-body integral equation. This approximation replaces H_A by a constant that is interpreted as an average excitation energy, and is justified when the projectile energy is large compared to typical excitation energies of the nucleus. The closure approximation is very successfully applied for elastic scattering around 80 MeV and higher.

Going beyond the closure approximation in the spirit of the spectator expansion we want to single out one target nucleon i and write $G_0(E)$ as

$$\begin{aligned} G_0(E) &= (E - h_0 - H_A + i\varepsilon)^{-1} \\ &= \left(E - h_0 - h_i - \sum_{j\neq i} v_{ij} - H^i + i\varepsilon\right)^{-1}, \end{aligned} \tag{13}$$

where the target Hamiltonian is expanded as $H_A = h_i + \sum_{j\neq i} v_{ij} + H^i$ with v_{ij} being the interaction between target nucleons i and j, and H^i being an (A-1)-body operator containing all higher order effects. Realizing that $\sum_{j\neq i} v_{ij} \equiv W_i$ and thus $H^i = H_A - h_i - W_i$ does not have an explicit dependence on the ith particle, then H^i may be replaced by an average energy E^i which is akin to the effective binding energy between the ith nucleon and the $A-1$ spectator. This is not an approximation since $G_0(E)$ may be regarded as

$$G_0(E) = \left[(E - E^i) - h_0 - h_i - W_i - (H^i - E^i) + i\varepsilon\right]^{-1} \tag{14}$$

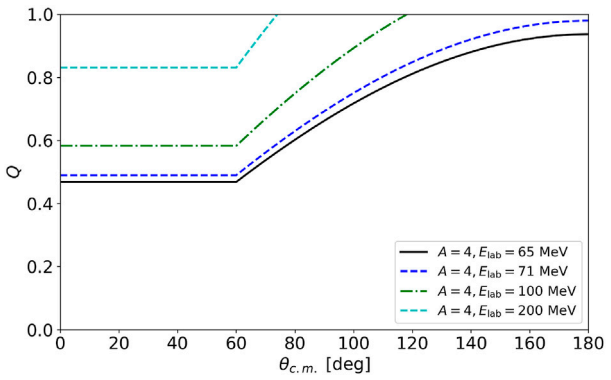

FIGURE 2
The expansion parameter Q, defined by Eq. 30 where Λ_b = x600 MeV, as a function of the center-of-mass angle $\theta_{c.m.}$ for a range of lab projectile energies E_{lab}. In this case of nucleon-nucleus (NA) elastic scattering, the transition between when the expansion parameter is dominated by the center-of-mass momentum and the momentum transfer can easily be identified.

and $(H^i–E^i)$ should be set aside to be treated in the next order of the expansion of the propagator $G_0(E)$. In this order of the expansion $G_0(E)$ becomes

$$G_i(E) = \left[\left(E - E^i\right) - h_0 - h_i - W_i + i\varepsilon\right]^{-1}, \tag{15}$$

and Eq. 12 reads

$$\hat{\tau}_i = v_{0i} + v_{0i} G_i(E) \hat{\tau}_i. \tag{16}$$

In order to connect the above expression with the free NN amplitude

$$t_{0i} = v_{0i} + v_{0i} g_i t_{0i} \tag{17}$$

with

$$g_i = \left[\left(E - E^i\right) - h_0 - h_i + i\varepsilon\right]^{-1}. \tag{18}$$

algebraic relations between the resolvents lead to

$$\hat{\tau}_i = t_{0i} + t_{0i} G_i W_i g_i(E) \hat{\tau}_i. \tag{19}$$

Defining $G_i W_i = g_i \mathcal{T}_i$ with $\mathcal{T}_i = W_i + W_i g_i \mathcal{T}_i$ leads to

$$\hat{\tau}_i = t_{0i} + t_{0i} g_i \mathcal{T}_i g_i \hat{\tau}_i. \tag{20}$$

The three-body character of the above expression becomes more evident if one defines it as a set of coupled equations as

$$\begin{aligned} \hat{\tau}_i &= t_{0i} + t_{0i} g_i X_i \\ X_i &= \mathcal{T}_i g_i \hat{\tau}_i. \end{aligned} \tag{21}$$

Though the spectator expansion of the operator U in terms of active particles is defined in Eq. 9, we see that this expansion is performed in terms of quantities which contain many-body propagators. Each of the ingredients τ_i, τ_{ij}, etc. may themselves be expanded in a spectator expansion, i.e. expanding the many-body propagator also according to the number of active participants. The corrections to the propagator in the leading-order term of U contributions that arise from the Q space, whereas the terms arising from the propagator remain in the P space at first order level. Thus their contribution may be more relevant for elastic scattering.

In an explicit treatment of $G_i(E)$ it is necessary to consider the explicit form of $\sum_{j\neq i} v_{ij} = W_i$, which is *a priori* a two-body operator. In the framework of *ab initio* nuclear structure calculations this will involve two-body densities. In earlier work [54, 57, 58] the quantity W_i was treated as one-body operator, specifically a mean-field potential. This was a physically reasonable choice, though being outside the strict demands of the spectator expansion. However, those studies revealed that the next order in the propagator expansion has little effect on elastic scattering observables at energies larger than 100 MeV, while the description of differential cross section and spin-observables for elastic scattering from ^{40}Ca at 48 MeV showed considerable improvement with respect to experiment [57]. Obviously this type of calculation will need to be explored within an *ab initio* approach. In Ref. [57] the energy E^i of Eq. 18 was set to zero.

As illustrated in this section, deriving a multiple scattering expansion for elastic NA scattering means projecting on the ground state of the target in order to obtain a Lippman-Schwinger type equation for the transition amplitude and obtaining an operator U for the effective interaction, which is defined in the space $Q = 1 - P$. In this spirit, the spectator expansion contains therefore two pieces, namely the expansion of the operator U in terms of active particles in the scattering process as well as the expansion of target Hamiltonian H_A in the propagator $G_0(E)$ in a similar fashion. Thus it is very difficult to define a single expansion parameter which governs the convergence of the expansion.

3 Leading order *ab initio* optical potential based on a chiral NN interaction

The leading order of the spectator expansion involves two active nucleons, the projectile and a target nucleon. Therefore, the leading order is driven by the NN amplitude $\bar{M}$, which in its most general form can be parameterized in terms of Wolfenstein amplitudes [59–61],

$$\begin{aligned} \bar{M}(\boldsymbol{q}, \boldsymbol{\mathcal{K}}_{NN}, \epsilon) = {} & A(\boldsymbol{q}, \boldsymbol{\mathcal{K}}_{NN}, \epsilon) \mathbf{1} \otimes \mathbf{1} \\ & + iC(\boldsymbol{q}, \boldsymbol{\mathcal{K}}_{NN}, \epsilon) \left(\boldsymbol{\sigma}^{(0)} \cdot \hat{\boldsymbol{n}}\right) \otimes \mathbf{1} \\ & + iC(\boldsymbol{q}, \boldsymbol{\mathcal{K}}_{NN}, \epsilon) \mathbf{1} \otimes \left(\boldsymbol{\sigma}^{(i)} \cdot \hat{\boldsymbol{n}}\right) \\ & + M(\boldsymbol{q}, \boldsymbol{\mathcal{K}}_{NN}, \epsilon) \left(\boldsymbol{\sigma}^{(0)} \cdot \hat{\boldsymbol{n}}\right) \otimes \left(\boldsymbol{\sigma}^{(i)} \cdot \hat{\boldsymbol{n}}\right) \\ & + \left[G(\boldsymbol{q}, \boldsymbol{\mathcal{K}}_{NN}, \epsilon) - H(\boldsymbol{q}, \boldsymbol{\mathcal{K}}_{NN}, \epsilon)\right] \\ & \quad \times \left(\boldsymbol{\sigma}^{(0)} \cdot \hat{\boldsymbol{q}}\right) \otimes \left(\boldsymbol{\sigma}^{(i)} \cdot \hat{\boldsymbol{q}}\right) \\ & + \left[G(\boldsymbol{q}, \boldsymbol{\mathcal{K}}_{NN}, \epsilon) + H(\boldsymbol{q}, \boldsymbol{\mathcal{K}}_{NN}, \epsilon)\right] \\ & \quad \times \left(\boldsymbol{\sigma}^{(0)} \cdot \hat{\boldsymbol{\mathcal{K}}}\right) \otimes \left(\boldsymbol{\sigma}^{(i)} \cdot \hat{\boldsymbol{\mathcal{K}}}\right) \\ & + D(\boldsymbol{q}, \boldsymbol{\mathcal{K}}_{NN}, \epsilon) \left[\left(\boldsymbol{\sigma}^{(0)} \cdot \hat{\boldsymbol{q}}\right) \otimes \left(\boldsymbol{\sigma}^{(i)} \cdot \hat{\boldsymbol{\mathcal{K}}}\right)\right. \\ & + \left.\left(\boldsymbol{\sigma}^{(0)} \cdot \hat{\boldsymbol{\mathcal{K}}}\right) \otimes \left(\boldsymbol{\sigma}^{(i)} \cdot \hat{\boldsymbol{q}}\right)\right], \end{aligned} \tag{22}$$

where $\boldsymbol{\sigma}^{(0)}$ describes the spin of the projectile, and $\boldsymbol{\sigma}^{(i)}$ the spin of the struck nucleon. The average momentum in the NN frame is defined as $\boldsymbol{\mathcal{K}}_{NN} = \frac{1}{2}(\boldsymbol{k}'_{NN} + \boldsymbol{k}_{NN})$. The scalar functions A, C, M, G, H, and D are referred to as Wolfenstein amplitudes and only depend on the scattering momenta and energy. Each term in Eq. 22 has two components, namely a scalar function of two vector momenta and an energy and the coupling between the operators of the projectile and the struck nucleon. The linear independent unit vectors $\hat{\boldsymbol{q}}$, $\hat{\boldsymbol{\mathcal{K}}}$, and $\hat{\boldsymbol{n}}$ are defined in terms of the momentum transfer and the average momentum as

$$\hat{\boldsymbol{q}} = \frac{\boldsymbol{q}}{|\boldsymbol{q}|} \quad , \quad \hat{\boldsymbol{\mathcal{K}}} = \frac{\boldsymbol{\mathcal{K}}}{|\boldsymbol{\mathcal{K}}|} \quad , \quad \hat{\boldsymbol{n}} = \frac{\boldsymbol{\mathcal{K}} \times \boldsymbol{q}}{|\boldsymbol{\mathcal{K}} \times \boldsymbol{q}|}, \tag{23}$$

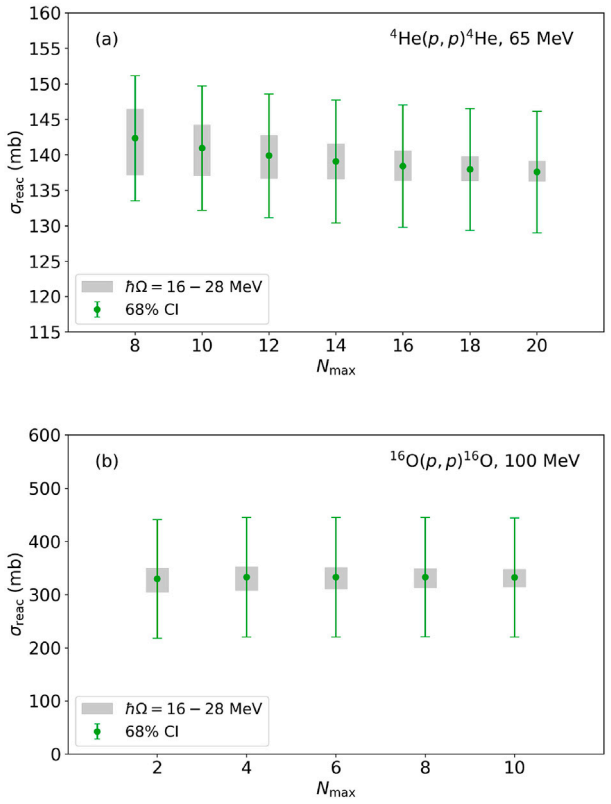

FIGURE 3
Reaction cross section for proton scattering on **(A)** ^{4}He at 65 MeV and **(B)** ^{16}O at 100 MeV, both at N2LO as a function of N_{max}. The error bars show a 68% credible interval (CI) from using a pointwise error estimation with the LO, NLO, and N2LO results. The shaded regions show variations with respect to the harmonic oscillator parameter $\hbar\Omega$. The values of the expansion parameters used were Q = .47 for ^{4}He at 65 MeV and Q = .69 for ^{16}O at 100 MeV. Note the different scales in **(A, B)**.

and span the momentum vector space. With the exception of the momentum transfer $\boldsymbol{q}$, which is invariant under frame transformation, the vectors in Eq. 23 need to be considered in their respective frame in explicit calculations [41, 62]. For the struck target nucleon the expectation values of the operator **one** and the scalar products of $\boldsymbol{\sigma}^{(i)}$ with the linear independent unit vectors of Eq. 23 need to be evaluated with the ground state wave functions of the respective nucleus when calculating the leading-order NA effective interaction. Evaluating the expectation value of the operator **one** in the ground state of the nucleus results in the scalar non-local, translationally invariant one-body density that has traditionally been used as input to microscopic or *ab initio* calculations of leading order effective interactions [11, 12, 40, 44]. The other operators from Eq. 23, namely $(\boldsymbol{\sigma}^{(i)} \cdot \hat{\boldsymbol{n}})$, $(\boldsymbol{\sigma}^{(i)} \cdot \hat{\boldsymbol{q}})$, and $(\boldsymbol{\sigma}^{(i)} \cdot \hat{\boldsymbol{\mathcal{K}}})$ need to also be evaluated for a leading-order *ab initio* NA effective interaction, in which the NN interaction is treated on equal footing in the reaction and structure calculation.

Thus, the general expression for a non-local density needs to include the spin operator $\boldsymbol{\sigma}^{(i)}$ explicitly,

$$\rho^{K_s}_{q_s}(\boldsymbol{p},\boldsymbol{p}') = \left\langle \Phi_0' \left| \sum_{i=1}^{A} \delta^3(\boldsymbol{p}_i - \boldsymbol{p}) \delta^3(\boldsymbol{p}_i' - \boldsymbol{p}') \sigma^{(i)K_s}_{q_s} \right| \Phi_0 \right\rangle, \quad (24)$$

where $\sigma^{(i)K_s}_{q_s}$ is the spherical representation of the spin operator and the wavefunction $\Phi_0\ (\boldsymbol{p}_1, \ldots, \boldsymbol{p}_A) = \langle \boldsymbol{p}_1, \ldots, \boldsymbol{p}_A | \Phi_0 \rangle$ is defined in momentum space. Evaluating this expression for K_s = 0 gives the non-local one-body scalar density and K_s = 1 becomes a non-local one-body spin density.

The Wolfenstein parameterization of Eq. 22 requires the evaluation of scalar products of the one-body spin density with unit momentum vectors. Since those only depend on the momenta $\boldsymbol{p}$ and $\boldsymbol{p}'$, those can be calculated as $\rho^{K_s}(\boldsymbol{p},\boldsymbol{p}') \cdot \hat{\boldsymbol{n}}$, $\rho^{K_s}(\boldsymbol{p},\boldsymbol{p}') \cdot \hat{\boldsymbol{q}}$, and $\rho^{K_s}(\boldsymbol{p},\boldsymbol{p}') \cdot \hat{\boldsymbol{\mathcal{K}}}$. For the explicit calculation of $\rho^{K_s}(\boldsymbol{p},\boldsymbol{p}') \cdot \hat{\boldsymbol{n}}$, we refer the reader to [41, 62]. The scalar products $(\boldsymbol{\sigma}^{(i)} \cdot \hat{\boldsymbol{q}})$ and $(\boldsymbol{\sigma}^{(i)} \cdot \hat{\boldsymbol{\mathcal{K}}})$ represent scalar products of a pseudo-vector and a vector, a construct that is not invariant under parity transformations, and thus vanish when sandwiched between ground state wave functions, which is explicitly shown in [62]. Thus the tensor contributions of the NN force only enter the leading order effective NA interaction through the Wolfenstein amplitude M as long as elastic scattering is considered. When e.g. transition amplitudes between states of different parity would be considered, the other tensor amplitudes will contribute.

Currently contributions to elastic scattering observables due to the spin-projected one-body densities have only been calculated for light nuclei with 0^+ ground states, and it was found that this contribution is very small for nuclei with equal proton and neutron numbers [41, 42]. This is likely different for nuclei with ground states of non-zero spin, which was explored for ^{10}B polarization transfer observables in Refs. [63, 64], where the authors assume a nuclear structure which consists of a core and valence nucleons. The work of Ref. [45] extends the standard leading order calculation to non-zero spin nuclei, however does not consider the inherent tensor contributions from the NN force in their formulation. This leaves the importance of a consistent treatment of the NN force on elastic scattering from non-zero spin nuclei still an open question.

The complete calculation of the leading-order effective interaction describing the scattering of a proton from a nucleus in a 0^+ ground state and which enters the integral Eq. 11 as driving term is given by

$$\begin{aligned}
\hat{U}_{\mathrm{p}}(\boldsymbol{q},\boldsymbol{\mathcal{K}}_{NA},\epsilon) = &\sum_{\alpha=\mathrm{n,p}} \int d^3\mathcal{K}\, \eta(\boldsymbol{q},\boldsymbol{\mathcal{K}},\boldsymbol{\mathcal{K}}_{NA}) A_{\mathrm{p}\alpha}\left(\boldsymbol{q}, \frac{1}{2}\left(\frac{A+1}{A}\boldsymbol{\mathcal{K}}_{NA} - \boldsymbol{\mathcal{K}}\right); \epsilon\right) \rho^{K_s=0}_{\alpha}(\boldsymbol{\mathcal{P}}', \boldsymbol{\mathcal{P}}) \\
&+ i(\boldsymbol{\sigma}^{(0)} \cdot \hat{\boldsymbol{n}}) \times \sum_{\alpha=\mathrm{n,p}} \int d^3\mathcal{K}\, \eta(\boldsymbol{q},\boldsymbol{\mathcal{K}},\boldsymbol{\mathcal{K}}_{NA}) C_{\mathrm{p}\alpha}\left(\boldsymbol{q}, \frac{1}{2}\left(\frac{A+1}{A}\boldsymbol{\mathcal{K}}_{NA} - \boldsymbol{\mathcal{K}}\right); \epsilon\right) \rho^{K_s=0}_{\alpha}(\boldsymbol{\mathcal{P}}', \boldsymbol{\mathcal{P}}) \\
&+ i \sum_{\alpha=\mathrm{n,p}} \int d^3\mathcal{K}\, \eta(\boldsymbol{q},\boldsymbol{\mathcal{K}},\boldsymbol{\mathcal{K}}_{NA}) C_{\mathrm{p}\alpha}\left(\boldsymbol{q}, \frac{1}{2}\left(\frac{A+1}{A}\boldsymbol{\mathcal{K}}_{NA} - \boldsymbol{\mathcal{K}}\right); \epsilon\right) S_{n,\alpha}(\boldsymbol{\mathcal{P}}', \boldsymbol{\mathcal{P}}) \cos\beta \\
&+ i(\boldsymbol{\sigma}^{(0)} \cdot \hat{\boldsymbol{n}}) \sum_{\alpha=\mathrm{n,p}} \int d^3\mathcal{K}\, \eta(\boldsymbol{q},\boldsymbol{\mathcal{K}},\boldsymbol{\mathcal{K}}_{NA}) \\
&\times (-i) M_{\mathrm{p}\alpha}\left(\boldsymbol{q}, \frac{1}{2}\left(\frac{A+1}{A}\boldsymbol{\mathcal{K}}_{NA} - \boldsymbol{\mathcal{K}}\right); \epsilon\right) S_{n,\alpha}(\boldsymbol{\mathcal{P}}', \boldsymbol{\mathcal{P}}) \cos\beta. \quad (25)
\end{aligned}$$

The term $\eta(\boldsymbol{q},\boldsymbol{\mathcal{K}},\boldsymbol{\mathcal{K}}_{NA})$ is the Møller factor [65] describing the transformation from the NN frame to the NA frame. The functions $A_{\mathrm{p}\alpha}$, $C_{\mathrm{p}\alpha}$, and $M_{\mathrm{p}\alpha}$ represent the NN interaction through Wolfenstein amplitudes [59]. Since the incoming proton can interact with either a proton or a neutron in the nucleus, the index α indicates the neutron (n) and proton (p) contributions, which are calculated

separately and then summed up. With respect to the nucleus, the operator $i(\boldsymbol{\sigma}^{(0)} \cdot \hat{\boldsymbol{n}})$ represents the spin-orbit operator in momentum space with respect to the projectile. As such, Eq. 25 exhibits the expected form of an interaction between a spin-$\frac{1}{2}$ projectile and a target nucleus in a $J = 0$ state [66]. The momentum variables in the problem are given as

$$\begin{aligned} \boldsymbol{q} &= \boldsymbol{p}' - \boldsymbol{p} = \boldsymbol{k}' - \boldsymbol{k}, \\ \boldsymbol{\mathcal{K}} &= \frac{1}{2}(\boldsymbol{p}' + \boldsymbol{p}), \\ \boldsymbol{\mathcal{K}}_{NA} &= \frac{A}{A+1}\left[(\boldsymbol{k}' + \boldsymbol{k}) + \frac{1}{2}(\boldsymbol{p}' + \boldsymbol{p})\right], \\ \boldsymbol{\mathcal{P}} &= \boldsymbol{\mathcal{K}} + \frac{A-1}{A}\frac{\boldsymbol{q}}{2}, \\ \boldsymbol{\mathcal{P}}' &= \boldsymbol{\mathcal{K}} - \frac{A-1}{A}\frac{\boldsymbol{q}}{2}. \end{aligned} \tag{26}$$

The two quantities representing the structure of the nucleus are the scalar one-body density $\rho_{\alpha}^{K_s=0}(\boldsymbol{\mathcal{P}}', \boldsymbol{\mathcal{P}})$ and the spin-projected momentum distribution $S_{n,\alpha}(\boldsymbol{\mathcal{P}}', \boldsymbol{\mathcal{P}}) = \rho^{K_s=1}(\boldsymbol{\mathcal{P}}', \boldsymbol{\mathcal{P}}) \cdot \hat{\boldsymbol{n}}$. Both distributions are non-local and translationally invariant. The reduced matrix elements entering the one-body densities are obtained within the NCSM (SA-NCSM) in the center-of-mass frame of the nucleus. In order to employ them in calculating the leading-order effective NA interaction, this center-of-mass variable must be removed. Within the framework of NCSM (SA-NCSM) the technique for obtaining non-local and translationally invariant one-body densities is well developed [40, 44, 67–70]. Lastly, the term $\cos\beta$ in Eq. 25 results from projecting $\hat{\boldsymbol{n}}$ from the NN frame to the NA frame. For further details, see Ref. [41].

4 Chiral truncation uncertainties in the leading order optical potential

With the emergence of nuclear forces based on chiral effective field theory (EFT), we are presented with an opportunity to study the nucleon-nucleus effective interaction as it develops order-by-order in a chiral EFT framework. Given the hierarchical nature of chiral EFT, we can combine these order-by-order results to reliably estimate truncation uncertainties associated with the higher chiral orders not included in the calculations. To this end, Refs. [35–37] first implemented uncertainty quantification for the cases of NN and Nd scattering by assuming a quantity $y(x)$ at a chiral order k can be written as

$$y_k(x) = y_{\text{ref}}(x)\sum_{n=0}^{k} c_n(x) Q^n(x) \tag{27}$$

where $y_{\text{ref}}(x)$ is a reference value that sets the scale of the problem and also includes the dimensions of the quantity $y(x)$ of interest. By construction, the coefficients $c_n(x)$ are dimensionless and are expected to be of order unity. The remaining quantity $Q(x)$ is the expansion parameter associated with the chiral EFT. The expansion parameter is usually defined as

$$Q = \frac{1}{\Lambda_b}\max(M_\pi, p) \tag{28}$$

where Λ_b is the breakdown scale of the EFT, M_π is the pion mass, and p is the relevant momentum for the problem. Various works [35–37] have identified the relevant momentum in different ways, but keeping with Ref. [43] we choose the relevant momentum as

TABLE 1 Ground state binding energies (top) and point-proton RMS radii (bottom) of ^{4}He, ^{12}C, and ^{16}O with LO, NLO, and N^{2}LO LENPIC SCS NN potentials. Both our estimated numerical uncertainties (first set of uncertainties) and chiral truncation uncertainty estimates (second set of uncertainties, not evaluated for LO) are given.

	^{4}He	^{12}C	^{16}O
	Binding energy (MeV)		
LO	45.45(.01)	137.(1.)	224.(2.)
NLO	28.53(.01)(3.5)	97.(3.)(9.)	156.(5.)(14.)
N^{2}LO	28.11(.01)(.9)	94.(4.)(3.)	149.(5.)(4.)
expt	28.30	92.16	127.62
	Point-proton radius (fm)		
LO	1.08(.02)	1.85(.17)	1.8(.2)
NLO	1.40(.02)(.08)	2.04(.16)(.09)	2.05(.16)(.10)
N^{2}LO	1.42(.02)(.02)	2.12(.15)(.03)	2.11(.15)(.03)
expt	1.46	2.32	2.58

the center-of-mass (c.m.) momentum in the nucleon-nucleus system

$$p_{NA}^2 = \frac{E_{\text{lab}} A^2 m^2 (E_{\text{lab}} + 2m)}{m^2 (A+1)^2 + 2AmE_{\text{lab}}} \tag{29}$$

where E_{lab} is the kinetic energy of the projectile in the laboratory frame, A is the target nucleus's mass number, and m is the mass of the nucleon.

Previous scattering works [36, 43] have noted that various results indicate, when identifying the relevant momentum, the momentum transfer q should also be considered. That is, the expansion parameter would be more appropriately defined as

$$Q = \frac{1}{\Lambda_b}\max(M_\pi, p_{NA}, q) \tag{30}$$

The momentum transfer in elastic scattering is defined as

$$q = 2p_{NA}\sin\left(\frac{\theta_{\text{c.m.}}}{2}\right) \tag{31}$$

where $\theta_{\text{c.m.}}$ is the scattering angle in the c. m. frame. Notably, including the momentum transfer in Eq. 30 makes the expansion parameter a function of $\theta_{\text{c.m.}}$, even though the other momentum scales in Eq. 30 are independent of the scattering angle. When considering observables such as the differential cross section or analyzing power that are functions of $\theta_{\text{c.m.}}$, this implies the expansion parameter will be larger at backward angles than at forward angles. Furthermore, since the leading order of the spectator expansion is not applicable at low energies, we only consider scattering at lab energies of 65 MeV or higher. As a result, the chiral expansion parameter becomes $Q = \max(p_{NA}, q)/\Lambda_b$. This expansion parameter is shown in Figure 2 for the case of $A = 4$ and $\Lambda_b = 600$ MeV. Because of the factorization of the c. m. momentum, there is a universal scattering angle at which the momentum transfer q begins to dominate the expansion parameter, regardless of the chosen E_{lab} or nucleus. We will exploit this behavior in later sections.

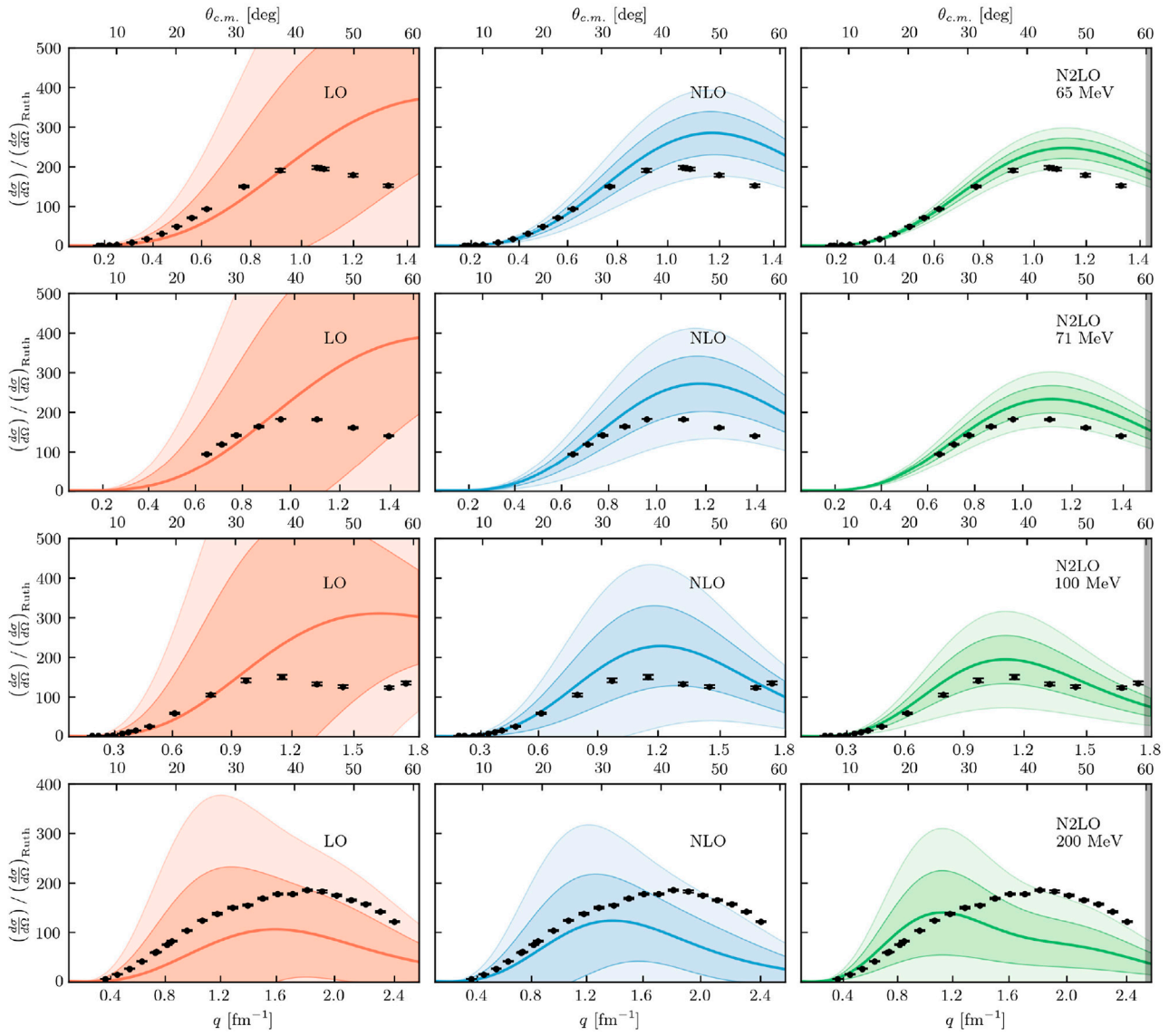

FIGURE 4
Differential cross section divided by Rutherford for proton scattering on ^{4}He at (first row) 65 MeV, (second row) 71 MeV, (third row) 100 MeV, and (fourth row) 200 MeV for LO (left column), NLO (middle column), and N2LO (right column) with corresponding 1σ (darker bands) and 2σ (lighter bands) error bands. Black dots are experimental data from Ref. [75] (65 MeV) [76], (71 MeV) [77], (100 MeV), and [78] (200 MeV).

4.1 Nuclear structure calculations

Prior to our detailed study of truncation uncertainties of a chiral NN interaction in elastic NA scattering observables we need to choose a specific chiral NN interaction. Here we want to focus on the EKM chiral NN interaction [18, 19] with a semi-local coordinate space regulator of R = 1 fm, which has a breakdown scale of $\Lambda_b = 600$ MeV. This interaction gives a slightly better description of the ground state energies in the upper p-shell than a similar, more recent interaction with a semi-local momentum space regulator. For consistency with the leading-order optical we only use the NN potentials, omitting three-nucleon forces, which appear at N2LO in the chiral expansion, both in the structure and the scattering part of the calculations. Including three-nucleon forces consistently in both, the structure and scattering calculations requires going beyond the leading-order optical potential, and is beyond the scope of this work. Though initial attempts of incorporating three-nucleon forces as an effective density-dependent NN force in the scattering part have been presented [46], they can not yet be considered as systematic consideration of three-nucleon forces in NA scattering. For similar reasons, we restrict most of our results to N2LO since three-nucleon force contributions at N3LO and N4LO are significant [71].

Next, the translationally-invariant one-body density needed for the scattering calculation can be obtained using the NCSM approach, in which the nuclear wavefunction is expanded in Slater determinants of harmonic oscillator basis functions [30]. Ideally, one uses a sufficiently large basis to ensure convergence of this expansion, but in practice observables depend on both the many-body basis truncation, $N_{\rm max}$ (defined as the total number of harmonic oscillator quanta in the many-body system above the minimal

configuration), and on the harmonic oscillator scale $\hbar\Omega$. In Table 1 we give the ground state binding energies and point-proton radii of ^{4}He, ^{12}C, and ^{16}O obtained with the EKM chiral NN potential [18, 19] with a semi-local coordinate space regulator of R = 1 fm (note that at N2LO we did not include any three-nucleon forces).

For ^{4}He we can obtain nearly converged results for both the binding energy and the proton radius, and these results agree, to within their estimated numerical uncertainties (the first set of uncertainties in Table 1), with Yakubovsky calculations using the same NN potential [71]. However, for larger nuclei such as ^{12}C and ^{16}O we are more limited in the $N_{\max}$ values that can be reached on current computational resources.[1]

4.2 Pointwise truncation uncertainties

To assess the relative size of chiral truncation uncertainties compared to other known uncertainties, e.g. the harmonic oscillator parameters $N_{\max}$ and $\hbar\Omega$, we employ a pointwise truncation procedure and study reaction observables that are not functional quantities, e.g. reaction cross sections at a specified laboratory energy. This pointwise approach was previously implemented in Refs. [36, 43] and it starts by assuming the expansion parameter Q and reference scale y_{ref} are known. From there, we can apply Eq. 27 to calculate the coefficients c_n, which are treated as independent draws from the same underlying distribution. The properties of this distribution can be learned from Bayesian techniques and the posterior distribution for the prediction can be readily calculated with its associated credible intervals. For more details, see Ref. [36].

In order to estimate the chiral truncation uncertainties of the obtained ground state binding energies and radii, we apply the pointwise approach with $Q \approx .3$ as the effective expansion parameter, following Ref. [31]. These uncertainties are listed as the second set of uncertainties in Table 1, starting from NLO. Here we see that for the energies, the chiral uncertainties are at least of the same order as the estimated numerical uncertainties; however, the uncertainties of the radii of ^{12}C and ^{16}O are clearly dominated by their systematic dependence on the basis parameter $\hbar\Omega$.

To illustrate the pointwise approach for scattering observables, Figure 3 shows the reaction cross sections for proton scattering from ^{4}He at 65 MeV and ^{16}O at 100 MeV. For each case, the result is shown as a function of $N_{\max}$, and variations with respect to $\hbar\Omega$ are indicated. While more obvious for the smaller nucleus where the NCSM can better converge, in both cases the uncertainty resulting from the chiral truncation remains larger than the uncertainty arising from the many-body method. To better illustrate this point, we present the reaction cross section for ^{4}He with a scale starting from 115 mb and with a range of only 45 mb, while using the full range of 600 mb for ^{16}O. While larger model spaces will better converge the NCSM results, smaller truncation uncertainties will only be achieved by higher chiral orders, despite the noticeable dependence of the radii on the harmonic oscillator parameter $\hbar\Omega$, in particular for the heavier nuclei, in the current calculations. Note however that even at N3LO we anticipate the chiral truncation uncertainties will be larger than the indicated variations with respect to the harmonic oscillator parameter $\hbar\Omega$ due to the rather large value of the expansion parameter Q in the scattering calculation.

4.3 Correlated truncation uncertainties

For functional quantities $y(x)$ we employ a correlated approach that includes information at nearby values of x. This approach is better for observables such as a differential cross section, which we know does not vary wildly from values at nearby angles. It also starts from Eq. 27 and treats the coefficients $c_n(x)$ as independent draws from an underlying Gaussian process. This Gaussian process encodes information about the correlation length ℓ, and the qualities of the underlying distribution can be learned from the order-by-order results. This training is followed up by testing procedures which seek to confirm the Gaussian process has been appropriately fit to the available results, and if not, to diagnose potential issues. From a well-fit Gaussian process we can then extract truncation uncertainties for the functional quantities. For more details and applications, see Refs. [36, 43].

In the following examples, we examine proton scattering for ^{4}He, ^{12}C, and ^{16}O at various projectile energies and compare to the available experimental data. In each case, we show the convergence with respect to chiral order and the resulting decrease in the size of the chiral truncation uncertainties, as well as discuss any associated physics insights. To avoid concerns about the expansion parameter increasing at larger angles, we mostly restrict our analysis to forward angles where we expect the expansion parameter to be independent of the scattering angle.

For proton scattering on ^{4}He, we see good agreement with experiment for the differential cross sections (Figure 4) at lower projectile energies. Below 100 MeV, most data points fall within the 2σ uncertainty band, and at 100 MeV a majority of the data points are within the 1σ band. At the highest energy of 200 MeV, the chosen interaction seems unable to reproduce the experimental data, though this is not uncommon for scattering from ^{4}He.

The analyzing powers for proton scattering on ^{4}He (Figure 5) is more complicated. For the lower energies of 65 and 71 MeV, the experimental data shows a near zero value, regardless of scattering angle. In the scattering of a spin-1/2 particle from a spin-0 nucleus, this indicates that there is no spin-orbit force at play. This behavior is only reproduced by the LO result, for which the chiral NN interaction only contains the one-pion exchange and contact terms, which do not produce a spin-orbit force. At NLO the two-pion exchange diagrams are responsible for reproducing the NN p-waves and thus provide a spin-orbit force that

1 One commonly applies a Similarity Renormalization Group (SRG) transformation to the NN potential in order to improve the convergence of the many-body calculation. However, this leads to induced three-nucleon forces that are non-negligible; omitting those would lead to a strong dependence on the SRG parameter. We therefore choose to not employ such a transformation here. For the binding energies we use an exponential extrapolation to the complete basis, with associated uncertainties, see Ref. [71] for details. Radii converge rather slowly in a harmonic oscillator basis, and they do not necessarily converge monotonically with increasing $N_{\max}$; furthermore, in the scattering calculations we use densities obtained at fixed values of the harmonic oscillator parameters $N_{\max}$ and $\hbar\Omega$. We therefore simply give in Table 1 our results for the point-proton radii of ^{12}C and ^{16}O at $N_{\max} = 10$, averaged over the range $16 \leq \hbar\Omega \leq 28$ MeV (the same range as is used for the scattering calculations). The numerical uncertainty estimates for the radii listed in Table 1 correspond to the spread over this $\hbar\Omega$ interval; this is a systematic uncertainty due to the Gaussian fall-off of harmonic oscillator basis functions, and is therefore strongly correlated for the different chiral orders. However, the trend of a significant increase in the radii going from LO to NLO, followed by a smaller increase going from NLO to N2LO, is robust, and correlates with the decrease in binding energies going from LO to NLO to N2LO. Note that we did not include any chiral EFT corrections to the R^2 operator; and the experimental point-proton radii are extracted from the charge radius measured in electron scattering experiments, using standard proton and neutron finite-size corrections, relativistic corrections, and meson-exchange corrections.

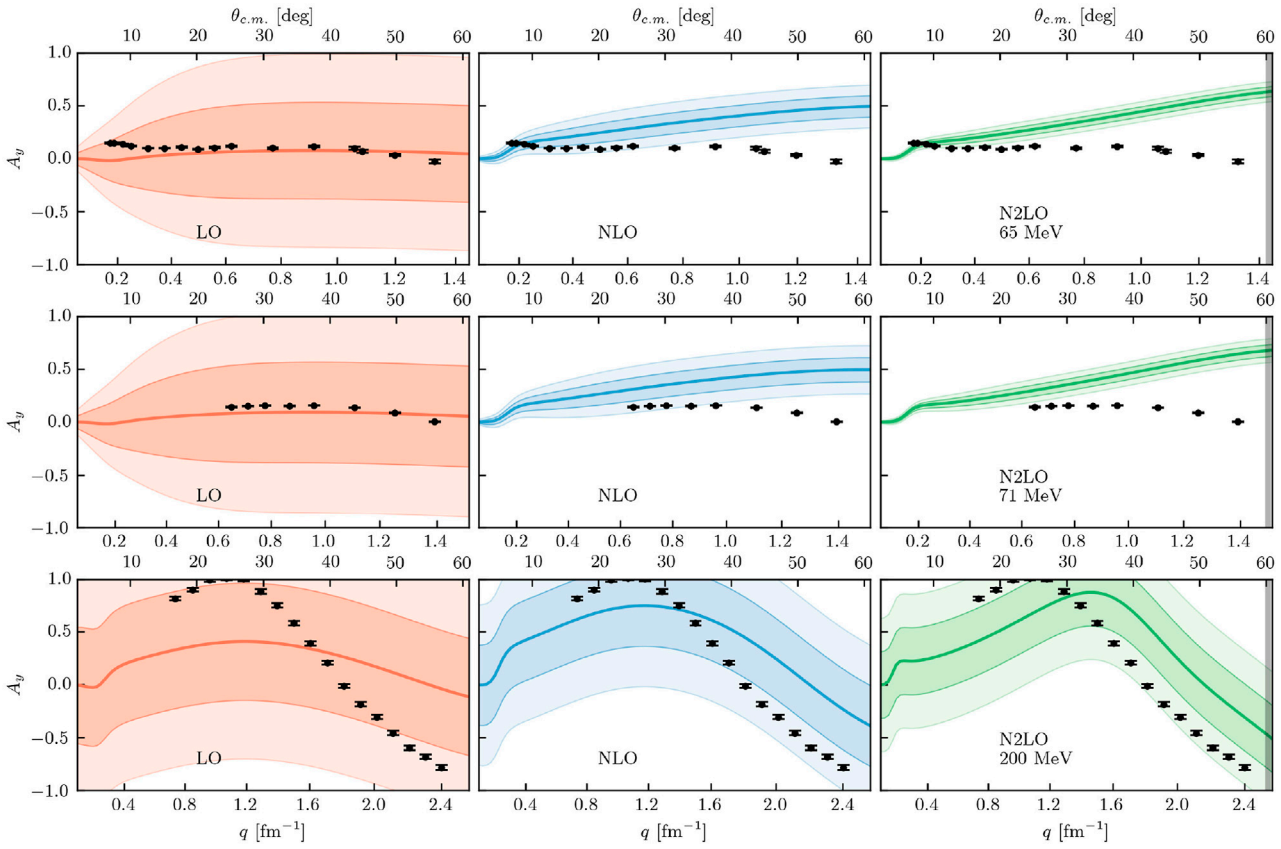

FIGURE 5
Analyzing power for proton scattering on ^{4}He at (first row) 65 MeV, (second row) 71 MeV, and (third row) 200 MeV) for LO (left column), NLO (middle column), and N2LO (right column) with corresponding 1σ (darker bands) and 2σ (lighter bands) error bands. Black dots are experimental data from Ref. [75] (65 MeV) [76], (71 MeV), and [78] (200 MeV).

leads to a non-zero value for the analyzing power in NA scattering. At N2LO there are no new terms in the two-nucleon sector, and thus A_y does not change its shape at that chiral order. Therefore, one needs to conclude that in this case other physics which goes beyond the leading order NA effective interaction may be needed to describe the analyzing power.

For the higher energy of 200 MeV, all of the experimental data points are within the 2σ uncertainty band, though there is a slight offset in the shape. In all cases, the analyzing power is more difficult to reproduce using this interaction, though other interactions have done better [39, 41].

For proton scattering from ^{12}C, the differential cross sections (Figure 6) are reliably reproduced by the central value of the N2LO calculations up to 100 MeV laboratory kinetic energy, and systematically over-predict at higher energies. As the projectile energy increases, the expansion parameter increases and as a result uncertainty bands become larger. This is most noticeable at 160 MeV: the experimental data is within the 1σ band, but the size of that band, as well as the 2σ band, are so large that they are not practically useful. The gray bars in the cross section panels for N2LO indicate the momentum transfer up to where we expect the expansion parameter to be dominated by the c. m. momentum p_{NA}. Once the momentum transfer exceeds the value given by the bar, the uncertainty is dominated by the momentum transfer q, and is thus underrepresented by the method we use. Note that the vertical bar is at the same scattering angle $\theta_{\text{c.m.}}$, but different momentum transfer q, as function of the projectile energy since p_{NA} is a function of the projectile energy as given in Eq. 29. Looking at the lower energies, the increasing agreement with experiment in the first peak and minimum as higher orders in the chiral NN interaction are included gives the correct trend. Minima in the differential cross section correlate with the size of the target nucleus. It is well well known [31], and also evident from Table 1, that the nuclear binding energy calculated with the LO of the chiral NN interaction is way too large and correspondingly the radius much too small. Only when going to NLO and N2LO the binding energy as well as the radius move into the vicinity of their experimental values. This finding from structure calculations is corroborated by the calculations in Figure 6, where with increasing chiral order the calculated first diffraction minimum moves towards smaller momentum transfers indicating a larger nuclear size.

The analyzing powers for proton scattering on ^{12}C are at 65 MeV also almost zero for small momentum transfers and rise at $q = 1.2$ fm^{-1} to its maximum value of +1. This is captured by the NLO calculation where spin-contributions occur in the NN interaction (Figure 7). For 65 MeV, the experimental data is mostly within the 2σ band until approximately $\theta_{\text{c.m.}} = 60^{\circ}$, where we expect the expansion parameter to being increasing and the uncertainty bands to thus be underestimates. For 122 MeV, the very forward direction is inside the 1σ band, but the overall shape of the experimental data is not well captured by this interaction.

For proton scattering from ^{16}O, the differential cross sections (Figure 8) are similar to the ^{12}C case. Namely, the lower energies do reasonably well at describing the data within the 2σ bands, but as the projectile energy increases the uncertainty bands increase to unhelpful

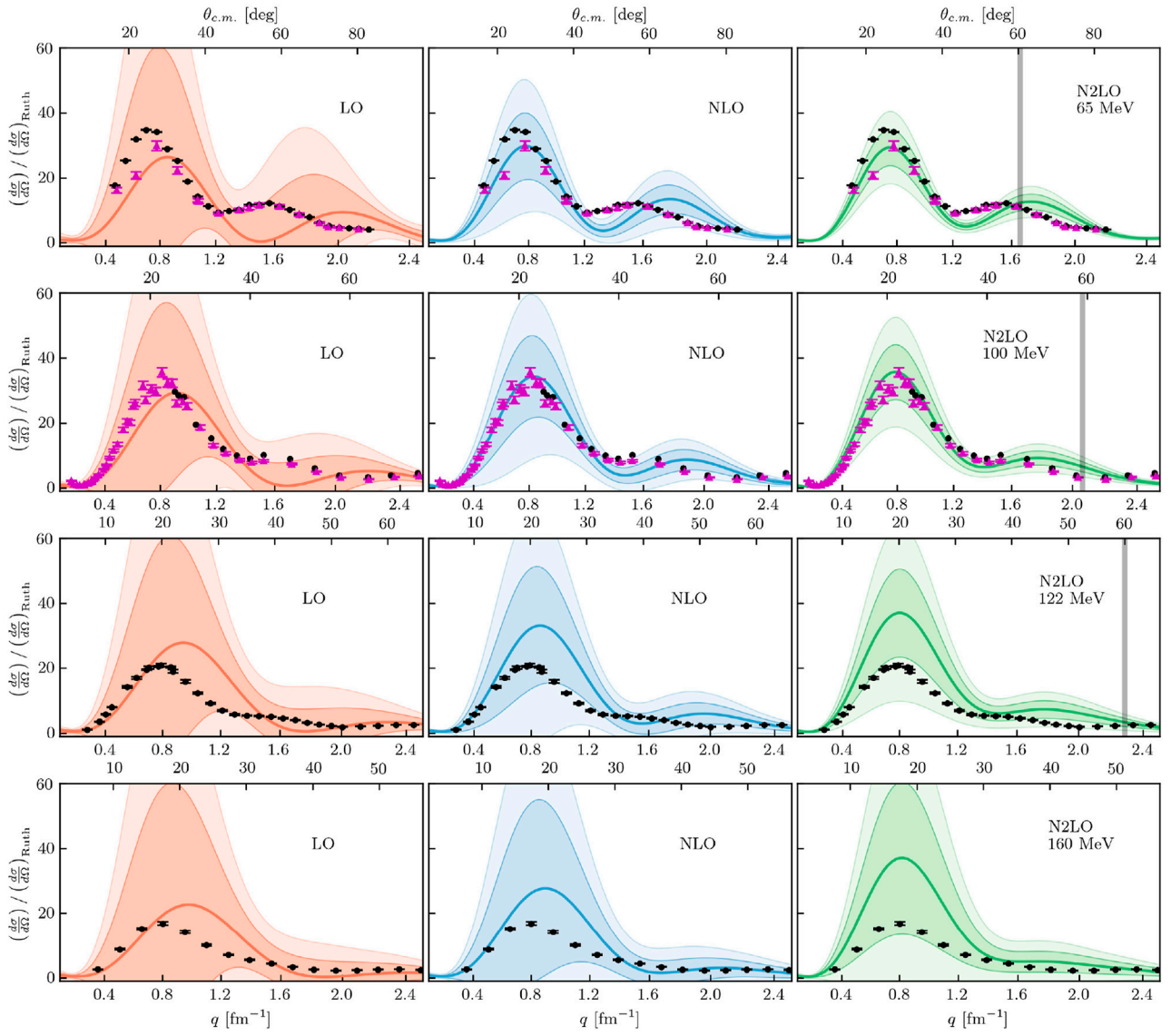

FIGURE 6
Differential cross section divided by Rutherford for proton scattering on ^{12}C at (first row) 65 MeV, (second row) 100 MeV, (third row) 122 MeV, and (fourth row) 160 MeV for LO (left column), NLO (middle column), and N2LO (right column) with corresponding 1σ (darker bands) and 2σ (lighter bands) error bands. Black dots/purple triangles are experimental data from Ref. [79] (65 MeV, black dots) [80], (65 MeV, purple triangles) [81], (96 MeV, purple triangles) [82], (99 MeV, black dots), and [83] (122 MeV and 160 MeV). Figure from Ref. [43].

sizes. At the lowest energy of 65 MeV, we see a better and better reproduction of the first minimum in the differential cross section as the chiral order increases. Again, this first minimum is known to be related to the size of the nucleus, so this is an important feature to reproduce from both a structure, see Table 1, and reaction perspective.

The analyzing powers for proton scattering on ^{16}O (Figure 9) are again similar to the ^{12}C case. At lower energies (65 and 100 MeV), we again see a good reproduction to within 1σ or 2σ of the forward direction data, but beyond $\theta_{\text{c.m.}} = 60^{\circ}$, the experimental data is outside the uncertainty bands. At the higher energy of 135 MeV, many of the experimental data are within the uncertainty bands but for a nucleus of this size, the expansion parameter has already increased such that the resulting uncertainty bands are unhelpfully large.

As stated toward the beginning of the section we omit three-nucleon forces for consistency with the leading-order optical potential which only treats two active nucleons. Those three-nucleon forces already appear at N2LO in the chiral expansion, however, including them consistently in the structure as well as reaction calculation requires going beyond the leading-order optical potential and is beyond the scope of this work. For the sake of investigating truncation errors in the chiral NN force, one may carry out inconsistent calculation in the sense that the structure part of the calculation is kept fixed at N2LO, and in the reaction part higher orders in the NN force are used. Proceeding in this fashion is sensible, since the scattering calculation is more sensitive to the NN force compared to the structure calculation, provided this structure calculation gives a reasonable description of the ground state one-body density. To show how the chiral truncation error develops when higher chiral orders in the NN interaction are introduced, we show in Figure 10 proton scattering from ^{16}O at 100 MeV projectile energy, where the higher chiral orders are only employed in the scattering part through the corresponding Wolfenstein

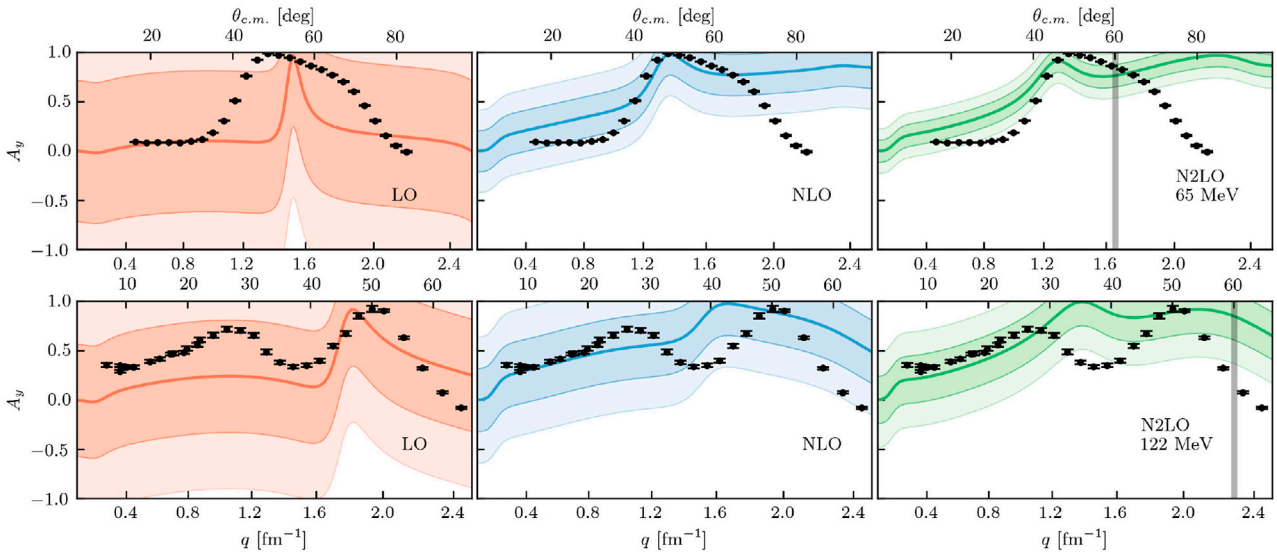

FIGURE 7
Analyzing power for proton scattering on ^{12}C at (first row) 65 MeV and (second row) 122 MeV for LO (left column), NLO (middle column), and N2LO (right column) with corresponding 1σ (darker bands) and 2σ (lighter bands) error bands. Black dots are experimental data from Ref. [84] (65 MeV) and [83] (122 MeV). Figure taken from Ref. [43].

amplitudes. In both, the differential cross section as well as the analyzing power the two most right panels depicting the inconsistent calculation show that the uncertainty bands become smaller when higher chiral orders in the NN interaction are included. However, these uncertainty bands are not necessarily realistic due to missing higher-body effects, which include higher orders in the chiral force as well as higher orders in the multiple scattering expansion. Therefore, we can not draw firm conclusions from the fact that data are outside the uncertainty estimates. Nevertheless, it is obvious that the decrease in the uncertainties in the chiral truncation is rather slow due to the large expansion parameter. Furthermore, the medians of the calculations shown in Figures 8, 9 do not change when higher chiral orders are considered in Figure 10, which further indicates that the smaller error bands of the higher order chiral truncations may be artificial.

4.4 Analysis of posteriors

Even while restricting our analysis to a region where we expect the expansion parameter to be constant, we can still observe effects on the uncertainty bands if the expansion parameter is large, as noted in many of the results at larger projectile energies. In fact, this behavior will place limits on the size of nucleus that can be considered with this approach, since p_{NA} as defined by Eq. 29 will continue to increase as A increases, yielding $Q > 1$ eventually. While this situation is not ideal, we non-etheless find support for it in our analysis after examining the posteriors for Q, in accordance with Refs. [36, 43].

In Figure 11, we calculated posteriors for the differential cross sections in proton scattering from ^{4}He, ^{12}C, and ^{16}O at the energies previously discussed. From these, we can extract a single best guess for the value of Q based on the order-by-order calculations and compare that to the expectation for Q based on Eq. 30. For ^{16}O, the largest nucleus considered, we see generally good agreement between the expected value of Q and the best guess value from the posteriors (Figure 11C). However, as the nucleus decreases in size and as the laboratory energy decreases, some differences begin to emerge between the two values. In Figure 11B for ^{12}C, the comparisons are roughly similar to the ^{16}O case, but for the ^{4}He analysis (Figure 11A), the differences are more pronounced, especially for the lower laboratory energies. A similar analysis of neutron scattering on ^{12}C did not show any significant differences between the two values [43], which implies ^{4}He may be the outlier in this approach. This analysis may imply scattering from ^{4}He with projectiles at lower energies could be analyzed with a smaller expansion parameter Q, though the higher energy results still favor the larger expansion parameter. As the smallest nucleus considered here, it may also point to the few-body character of ^{4}He, which has not historically been well captured in an optical potential approach.

5 Outlook

Procedures that quantify the theoretical uncertainties associated with the underlying chiral EFT NN interaction are by now well established for the NN and nucleon-deuteron systems as well as nuclear structure calculations, while the systematic study of chiral truncation uncertainty is not as widely used in *ab initio* effective interaction employed to describe the scattering of protons or neutrons from nuclei. Contributing factors for this relatively slow development include that when considering a multiple scattering approach to deriving this effective NA interaction in an *ab initio* fashion only recent progress in calculating the leading-order term in the multiple scattering approach has allowed to treat the NN interaction on the same footing in the structure and reaction part [41] by considering the spin of the struck target nucleon. Though calculations showed that the latter does not contribute significantly to observables when considering scattering from nuclei with a 0^+ ground state, one nevertheless needs a consistent *ab initio* implementation of the leading-order term of the effective NA interaction in order to study the

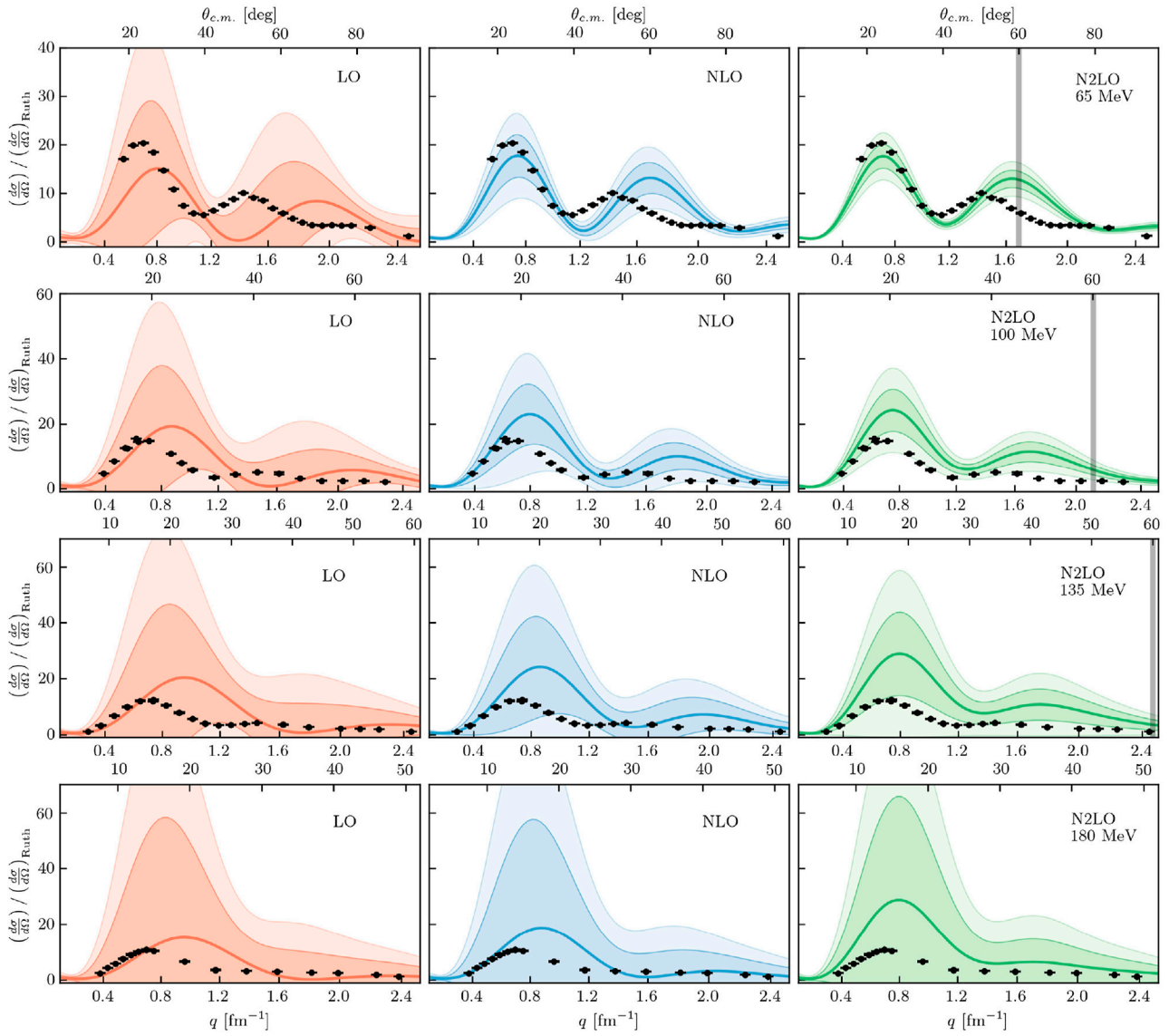

FIGURE 8
Differential cross section divided by Rutherford for proton scattering on ^{16}O at (first row) 65 MeV, (second row) 100 MeV, (third row) 135 MeV, and (fourth row) 180 MeV for LO (left column), NLO (middle column), and N2LO (right column) with corresponding 1σ (darker bands) and 2σ (lighter bands) error bands. Black dots are experimental data from Ref. [85] (65 MeV) [86], (100 MeV) [87], (135 MeV), and [88] (180 MeV). Figure taken from Ref. [43].

theoretical uncertainties imprinted on NA observables by the chiral EFT NN interaction.

In this work we carry out a systematic study of chiral truncation uncertainties of the EKM chiral interaction on the *ab initio* effective NA interaction calculated in leading order of the spectator expansion for ^{4}He, ^{12}C, and ^{16}O. We find that this interaction allows for a good description of experiment at energies around 100 MeV projectile kinetic energy and slightly lower, provided we focus on regions of momentum transfer where the analysis of the EFT truncation uncertainty is valid. When considering the lower energy of 65 MeV, the agreement with data starts to deteriorate. This is an indication that errors other than the truncation error in the chiral interaction should come into play, specifically errors that result from the spectator expansion itself. Theoretical consideration of the next-to-leading-order term in the spectator expansion are described in some detail in this work in order to lay out necessary theoretical and computational developments for this non-trivial endeavor. At at the next-to-leading order three-nucleon forces will naturally enter the effective interaction. At present this step has only been attempted in approximative fashions, namely by approximating the next-to-leading order in the propagator expansion *via* a nuclear mean field force [54] or by introducing an effective, density dependent NN potential in the scattering part of the calculation [46]. Since we are not considering next-to-leading order terms in the spectator expansion, we restrict our analysis to N2LO in the chiral interaction and only consider two-nucleon forces. In this case the choice of the EKM interaction with a semi-local coordinate space regulator of 1.0 fm is advantageous [38], since this specific interaction gives a slightly better description of the ground state energies in the upper *p*-shell compared to other more recent chiral EFT interactions when using two-nucleon interactions only.

In our study the chiral truncation errors at energies larger than 100 MeV increase considerably and the agreement with experiment

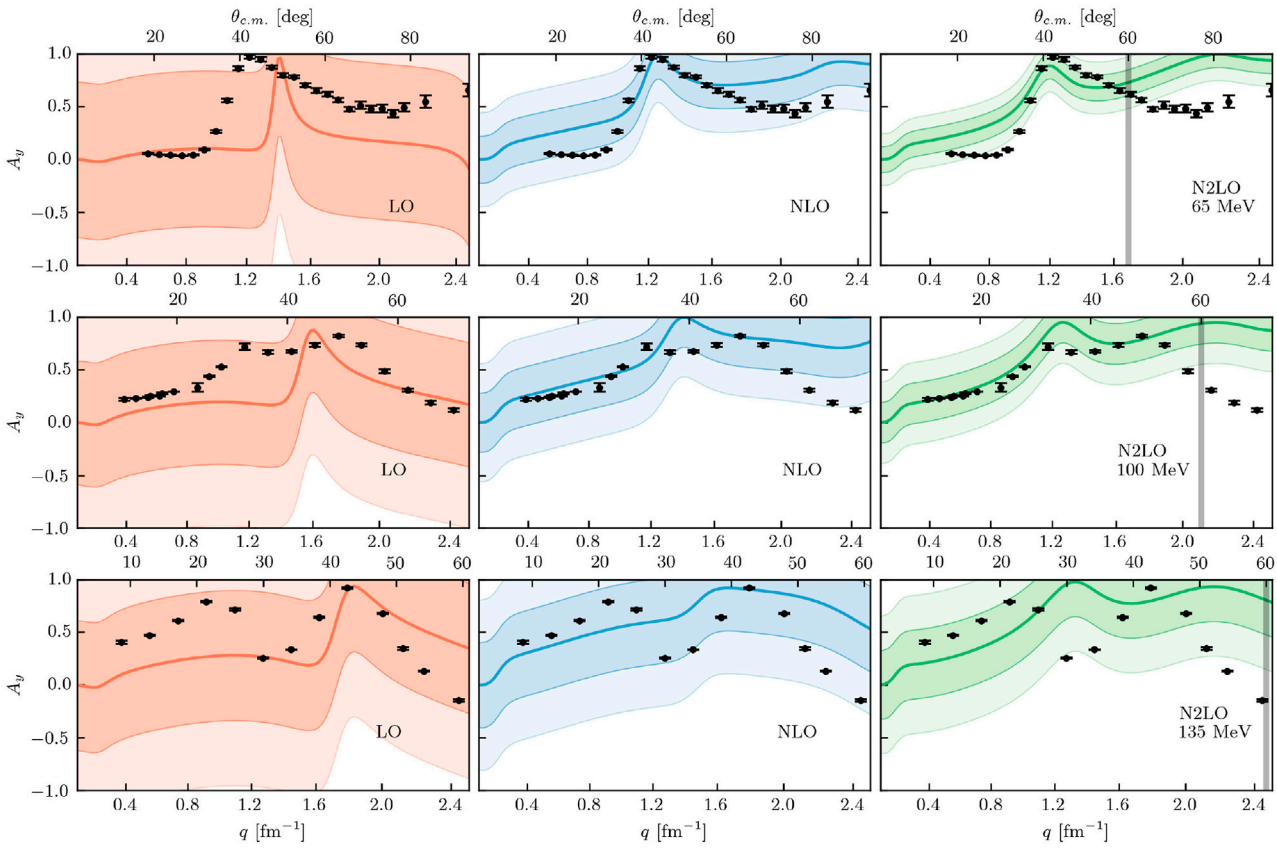

FIGURE 9
Analyzing power for proton scattering on ^{16}O at (first row) 65 MeV, (second row) 100 MeV, and (third row) 135 MeV for LO (left column), NLO (middle column), and N2LO (right column) with corresponding 1σ (darker bands) and 2σ (lighter bands) error bands. Black dots are experimental data from Ref. [85] (65 MeV) [86], (100 MeV), and [87] (135 MeV). Figure taken from Ref. [43].

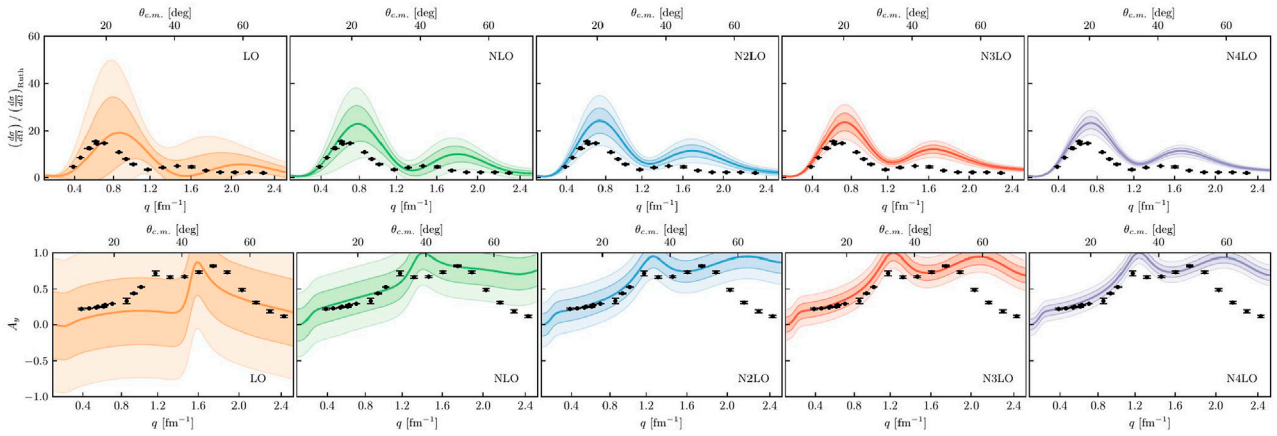

FIGURE 10
Differential cross section divided by the Rutherford cross section (top) and analyzing power (bottom) for proton scattering from ^{16}O at 100 MeV. The first three columns are the same as the second rows of Figures 8, 9. The additional two rightmost panels are inconsistent calculations with use up to N2LO in the structure calculations and up to N3LO (fourth column) or N4LO (fifth column) in the reaction calculation. Due to the inconsistency of the calculation the uncertainty bands are not fully realistic. The data are the same as cited in Figures 8, 9.

deteriorates. The increase in the chiral truncation error can simply be traced back to the expansion parameter in our approach is getting too large. The deterioration of the agreement with experiment when going to higher energies is more difficult to answer. One conclusion may be that the specific EKM chiral interaction employed here in using the leading-order in the spectator expansion is not well suited to describe

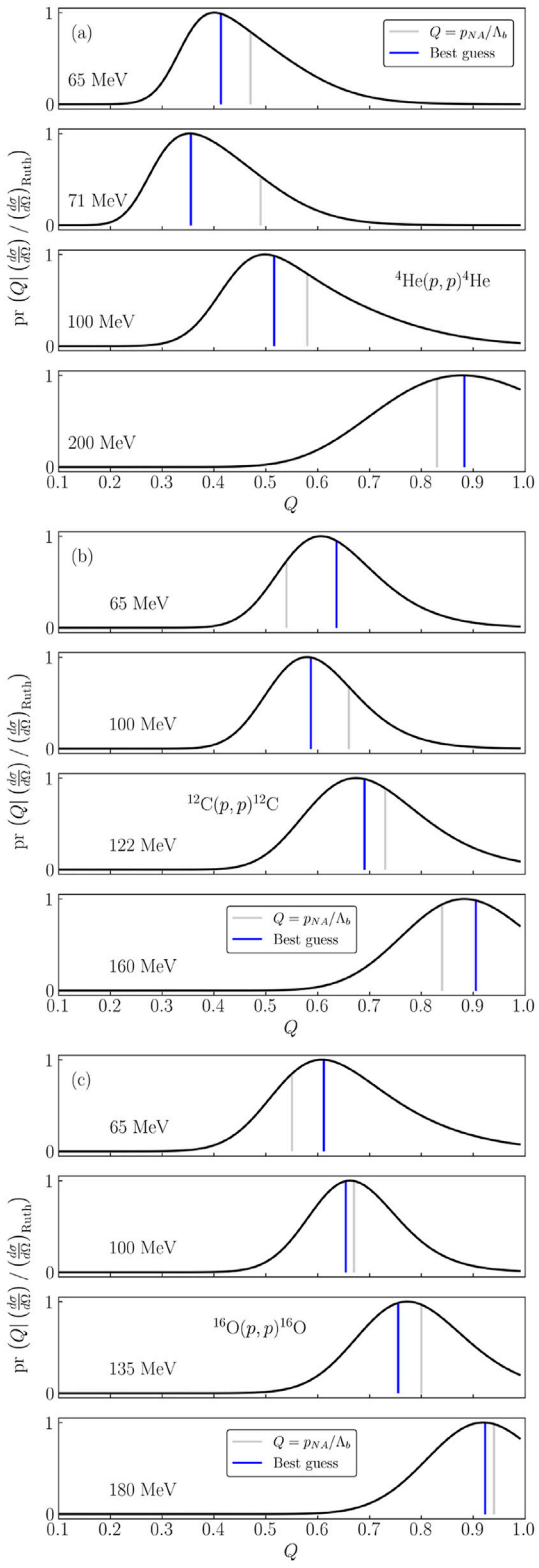

FIGURE 11
Posterior plots for the expansion parameter Q given the differential cross sections for proton scattering on **(A)** ^{4}He, **(B)** ^{12}C, and **(C)** ^{16}O.

proton-nucleus scattering observables for ^{4}He, ^{12}C, and ^{16}O at higher energies. For the chiral NN interaction from Ref. [72] this is not the case as shown in Refs. [40, 41]. Therefore one will have to investigate what features of a chiral NN interaction are most relevant for a description of NA scattering observables for light nuclei.

To put this in perspective, let us reconsider the basic ideas of the spectator expansion. By design, the leading-order term should be dominant at energies 150 MeV projectile kinetic energy and higher, since the reaction time of the projectile with nucleons inside the nucleus is short, and thus an 'impulse approximation' is in general very good. However, we do not want to consider here projectile energies larger than 400 MeV, where a relativistic treatment e.g. *via* the Dirac equation may be preferred [73, 74]. Thus at energies around 200 MeV the leading order term by design should give a reasonably good description of NA scattering data. This has been the case in the microscopic calculations of the 1990s (see e.g. [9–14]) and a set of recent calculations with specific chiral NN interactions [40, 41, 46]. Attempts to go beyond the leading order by incorporating 3NFs in a density dependent fashion into the many-body propagator [46] indicate that effects at 200 MeV are only visible at higher momentum transfer. In a similar fashion, investigations going beyond the leading order term in Ref. [54] indicate that those effects become important at around 100 MeV and at higher momentum transfers. Thus, if the 3NFs inherent in the chiral expansion are needed to influence calculations with chiral NN forces in the leading order of the spectator expansion at higher energies, then a new look at the interplay between NN and 3NFs in the leading-order spectator expansion must be developed.

Author contributions

All authors listed have made a substantial, direct, and intellectual contribution to the work and approved it for publication.

Funding

This work was performed in part under the auspices of the U. S. Department of Energy under contract Nos. DE-FG02-93ER40756, DE-SC0018223, and DE-SC0023495, and by the U. S. NSF (PHY-1913728). The numerical computations benefited from computing resources provided by the Louisiana Optical Network Initiative and HPC resources provided by LSU, together with resources of the National Energy Research Scientific Computing Center, a U. S. DOE Office of Science User Facility located at Lawrence Berkeley National Laboratory, operated under contract No. DE-AC02-05CH11231.

Acknowledgments

RB and CE gratefully acknowledge fruitful discussions with R.J. Furnstahl and D.R. Phillips about quantifying truncation errors in EFTs. CE acknowledges useful discussions with A. Nogga about the LENPIC chiral NN interactions.

Conflict of interest

The authors declare that the research was conducted in the absence of any commercial or financial relationships that could be construed as a potential conflict of interest.

Publisher's note

References

1. Bethe HA. Theory of disintegration of nuclei by neutrons. *Phys Rev* (1935) 47:747–59. doi:10.1103/PhysRev.47.747

2. Feshbach H. The optical model and its justification. *Annu Rev Nucl Sci* (1958) 8: 49–104. doi:10.1146/annurev.ns.08.120158.000405

3. Watson KM. Multiple scattering and the many-body problem-applications to photomeson production in complex nuclei. *Phys Rev* (1953) 89:575–87. doi:10.1103/physrev.89.575

4. Francis NC, Watson KM. The elastic scattering of particles by atomic nuclei. *Phys Rev* (1953) 92:291–303. doi:10.1103/physrev.92.291

5. Kerman AK, McManus H, Thaler RM. The scattering of fast nucleons from nuclei. *Ann Phys* (1959) 8:551–635. doi:10.1016/0003-4916(59)90076-4

6. Siciliano ER, Thaler RM. Spectator expansion in multiple scattering theory. *Phys Rev C* (1977) 16:1322–32. doi:10.1103/PhysRevC.16.1322

7. Ernst DJ, Londergan JT, Miller GA, Thaler RM. Correlation expansion of the optical potential. *Phys Rev C* (1977) 16:537–55. doi:10.1103/PhysRevC.16.537

8. Tandy PC, Thaler RM. Multiple scattering expansion with distortion. *Phys Rev C* (1980) 22:2321–9. doi:10.1103/PhysRevC.22.2321

9. Crespo R, Johnson RC, Tostevin JA. Multiple scattering theory of proton elastic scattering at intermediate energies. *Phys Rev C* (1992) 46:279–97. doi:10.1103/PhysRevC.46.279

10. Crespo R, Johnson RC, Tostevin JA. Full folding calculations for proton-nucleus elastic scattering at intermediate energies. *Phys Rev C* (1990) 41:2257–62. doi:10.1103/PhysRevC.41.2257

11. Elster C, Weppner SP, Chinn CR. Full-folding optical potentials for elastic nucleon-nucleus scattering based on realistic densities. *Phys Rev C* (1997) 56:2080–92. doi:10.1103/PhysRevC.56.2080

12. Elster C, Cheon T, Redish EF, Tandy PC. Full-folding optical potentials in elastic proton-nucleus scattering. *Phys Rev C* (1990) 41:814–27. doi:10.1103/PhysRevC.41.814

13. Arellano HF, Brieva FA, Love WG. Nonrelativistic full-folding model of nucleon elastic scattering at intermediate energies. *Phys Rev C* (1990) 41:2188–201. 10.1103/PhysRevC.42.1782. [Erratum: Phys. Rev.C 42, 1782 (1990)]. doi:10.1103/PhysRevC.41.2188

14. Arellano HF, Brieva FA, Love WG. Role of nuclear densities in nucleon elastic scattering. *Phys Rev C* (1990) 42:652–8. doi:10.1103/PhysRevC.42.652

15. Entem DR, Machleidt R. *Phys Rev C* (2003) 68:041001. doi:10.1103/physrevc.68.041001

16. Epelbaum E. Few-nucleon forces and systems in chiral effective field theory. *Prog Part Nucl Phys* (2006) 57:654–741. doi:10.1016/j.ppnp.2005.09.002

17. Epelbaum E, Hammer HW, Meißner UG. Modern theory of nuclear forces. *Rev Mod Phys* (2009) 81:1773–825. doi:10.1103/RevModPhys.81.1773

18. Epelbaum E, Krebs H, Meißner UG. Precision nucleon-nucleon potential at fifth order in the chiral expansion. *Phys Rev Lett* (2015) 115:122301. doi:10.1103/PhysRevLett.115.122301

19. Epelbaum E, Krebs H, Meißner UG. Improved chiral nucleon-nucleon potential up to next-to-next-to-next-to-leading order. *Eur Phys J A* (2015) 51:53. doi:10.1140/epja/i2015-15053-8

20. Reinert P, Krebs H, Epelbaum E. Semilocal momentum-space regularized chiral two-nucleon potentials up to fifth order. *Eur Phys J A* (2018) 54:86. doi:10.1140/epja/i2018-12516-4

21. Machleidt R, Entem DR. Chiral effective field theory and nuclear forces. *Phys Rep* (2011) 503:1–75. doi:10.1016/j.physrep.2011.02.001

22. Entem DR, Machleidt R, Nosyk Y. High-quality two-nucleon potentials up to fifth order of the chiral expansion. *Phys Rev C* (2017) 96:024004. doi:10.1103/PhysRevC.96.024004

23. Langr D, Dytrych T, Draayer JP, Launey KD, Tvrdík P. Efficient algorithm for representations of U(3) in U(N). *Comput Phys Commun* (2019) 244:442–7. doi:10.1016/j.cpc.2019.05.018

24. Langr D, Dytrych T, Launey KD, Draayer JP. Accelerating many-nucleon basis generation for high performance computing enabled *ab initio* nuclear structure studies. *Int J High Perform Comput Appl* (2019) 33:522–33. doi:10.1177/1094342019838314

25. Shao M, Aktulga HM, Yang C, Ng EG, Maris P, Vary JP. Accelerating nuclear configuration interaction calculations through a preconditioned block iterative eigensolver. *Comput Phys Commun* (2018) 222:1–13. doi:10.1016/j.cpc.2017.09.004

26. Aktulga HM, Yang C, Ng EG, Maris P, Vary JP. Improving the scalability of a symmetric iterative eigensolver for multi-core platforms. *Concurrency Computat.: Pract Exper* (2014) 26:2631–51. doi:10.1002/cpe.3129

27. Jung M, Wilson EH, III, Choi W, Shalf J, Aktulga HM, Yang C, et al. Exploring the future of out-of-core computing with compute-local non-volatile memory. In: SC '13: Proceedings of the International Conference on High Performance Computing, Networking, Storage and Analysis. New York, NY, USA: ACM (2013). p. 75:1–75:11. doi:10.1145/2503210.2503261

28. Navrátil P, Vary JP, Barrett BR. Properties of12Cin theAb InitioNuclear shell model. *Phys Rev Lett* (2000) 84:5728–31. doi:10.1103/PhysRevLett.84.5728

29. Roth R, Navrátil P. Ab InitioStudy ofCa40with an importance-truncated No-core shell model. *Phys Rev Lett* (2007) 99:092501. doi:10.1103/PhysRevLett.99.092501

30. Barrett B, Navrátil P, Vary J. *Ab initio* no core shell model. *Prog Part Nucl Phys* (2013) 69:131–81. doi:10.1016/j.ppnp.2012.10.003

31. Binder S, Calci A, Epelbaum E, Furnstahl RJ, Golak J, Hebeler K, et al. Few-nucleon and many-nucleon systems with semilocal coordinate-space regularized chiral nucleon-nucleon forces. *Phys Rev C* (2018) 98:014002. doi:10.1103/PhysRevC.98.014002

32. Launey KD, Dytrych T, Draayer JP. Symmetry-guided large-scale shell-model theory. *Prog Part Nucl Phys* (2016) 89:101–36. doi:10.1016/j.ppnp.2016.02.001

33. Dytrych T, Launey KD, Draayer JP, Rowe DJ, Wood JL, Rosensteel G, et al. Physics of nuclei: Key role of an emergent symmetry. *Phys Rev Lett* (2020) 124:042501. doi:10.1103/PhysRevLett.124.042501

34. Furnstahl RJ, Klco N, Phillips DR, Wesolowski S. Quantifying truncation errors in effective field theory. *Phys Rev C* (2015) 92:024005. doi:10.1103/PhysRevC.92.024005

35. Melendez JA, Wesolowski S, Furnstahl RJ. Bayesian truncation errors in chiral effective field theory: Nucleon-nucleon observables. *Phys Rev C* (2017) 96:024003. doi:10.1103/PhysRevC.96.024003

36. Melendez JA, Furnstahl RJ, Phillips DR, Pratola MT, Wesolowski S. Quantifying correlated truncation errors in effective field theory. *Phys Rev C* (2019) 100:044001. doi:10.1103/PhysRevC.100.044001

37. Epelbaum E, Golak J, Hebeler K, Kamada H, Krebs H, Meißner G, et al. Towards high-order calculations of three-nucleon scattering in chiral effective field theory. *Eur Phys J A* (2020) 56:92. doi:10.1140/epja/s10050-020-00102-2

38. Maris P, Epelbaum E, Furnstahl RJ, Golak J, Hebeler K, Hüther T, et al. Light nuclei with semilocal momentum-space regularized chiral interactions up to third order. *Phys Rev C* (2021) 103:054001. doi:10.1103/PhysRevC.103.054001

39. Burrows M, Elster C, Popa G, Launey KD, Nogga A, Maris P. *Ab initio* translationally invariant nonlocal one-body densities from No-core shell-model theory. *Phys Rev C* (2018) 97:024325. doi:10.1103/PhysRevC.97.024325

40. Burrows M, Elster C, Weppner SP, Launey KD, Maris P, Nogga A, et al. *Ab initio* folding potentials for nucleon-nucleus scattering based on NCSM one-body densities. *Phys Rev C* (2019) 99:044603. doi:10.1103/physrevc.99.044603

41. Burrows M, Baker RB, Elster C, Weppner SP, Launey KD, Maris P, et al. *Ab initio* leading order effective potentials for elastic nucleon-nucleus scattering. *Phys Rev C* (2020) 102:034606. doi:10.1103/PhysRevC.102.034606

42. Baker RB, Burrows M, Elster C, Launey KD, Maris P, Popa G, et al. Nuclear spin features relevant to *ab initio* nucleon-nucleus elastic scattering. *Phys Rev C* (2021) 103:054314. doi:10.1103/PhysRevC.103.054314

43. Baker RB, McClung B, Elster C, Maris P, Weppner SP, Burrows M, et al. *Ab initio* nucleon-nucleus elastic scattering with chiral effective field theory uncertainties. *Phys Rev C* (2022) 106:064605. doi:10.1103/PhysRevC.106.064605

44. Gennari M, Vorabbi M, Calci A, Navrátil P. Microscopic optical potentials derived from *ab initio* translationally invariant nonlocal one-body densities. *Phys Rev C* (2018) 97:034619. doi:10.1103/PhysRevC.97.034619

45. Vorabbi M, Gennari M, Finelli P, Giusti C, Navrátil P, Machleidt R. Elastic proton scattering off nonzero spin nuclei. *Phys Rev C* (2022) 105:014621. doi:10.1103/PhysRevC.105.014621

46. Vorabbi M, Gennari M, Finelli P, Giusti C, Navrátil P, Machleidt R. Impact of three-body forces on elastic nucleon-nucleus scattering observables. *Phys Rev C* (2021) 103:024604. doi:10.1103/PhysRevC.103.024604

47. Arellano HF, Blanchon G. On the separability of microscopic optical model potentials and emerging bell-shape Perey-Buck nonlocality. *Eur Phys J A* (2022) 58:119. doi:10.1140/epja/s10050-022-00777-9

48. Feshbach H. Unified theory of nuclear reactions. *Ann Phys* (1958) 5:357–90. doi:10.1016/0003-4916(58)90007-1

49. Dickhoff WH, Barbieri C. Self-consistent Green's function method for nuclei and nuclear matter. *Prog Part Nucl Phys* (2004) 52:377–496. doi:10.1016/j.ppnp.2004.02.038

50. Idini A, Barbieri C, Navrátil P. *Ab initio* optical potentials and nucleon scattering on medium mass nuclei. *Phys Rev Lett* (2019) 123:092501. doi:10.1103/PhysRevLett.123.092501

51. Rotureau J, Danielewicz P, Hagen G, Nunes FM, Papenbrock T. Optical potential from first principles. *Phys Rev C* (2017) 95:024315. doi:10.1103/PhysRevC.95.024315

52. Launey KD, Mercenne A, Dytrych T. Nuclear dynamics and reactions in the ab initio symmetry-adapted framework. *Annu Rev Nucl Part Sci* (2021) 71:253–77. doi:10.1146/annurev-nucl-102419-033316

53. Hebborn C, Nunes FM, Potel G, Dickhoff WH, Holt JW, Atkinson MC, et al. *Optical potentials for the rare-isotope beam era* (2022). arXiv:2210.07293.

54. Chinn CR, Elster C, Thaler RM, Weppner SP. Propagator modifications in elastic nucleon-nucleus scattering within the spectator expansion. *Phys Rev C* (1995) 52:1992–2003. doi:10.1103/PhysRevC.52.1992

55. Chinn CR, Elster C, Thaler RM. Isospin effects in elastic proton-nucleus scattering. *Phys Rev C* (1993) 47:2242–9. doi:10.1103/PhysRevC.47.2242

56. Miller GA, Austern N, Silver M. Vanishing closure correction in the second-order optical potential. *Phys Rev C* (1978) 17:835–6. doi:10.1103/PhysRevC.17.835

57. Chinn CR, Elster C, Thaler RM. Microscopic formulation of medium contributions to the first-order optical potential. *Phys Rev C* (1993) 48:2956–66. doi:10.1103/PhysRevC.48.2956

58. Chinn CR, Elster C, Thaler RM, Weppner SP. Application of multiple scattering theory to lower-energy elastic nucleon-nucleus scattering. *Phys Rev C* (1995) 51:1418–24. doi:10.1103/PhysRevC.51.1418

59. Wolfenstein L, Ashkin J. Invariance conditions on the scattering amplitudes for spin ½ particles. *Phys Rev* (1952) 85:947–9. doi:10.1103/physrev.85.947

60. Fachruddin I, Elster C, Glöckle W. Nucleon-nucleon scattering in a three dimensional approach. *Phys Rev C* (2000) 62:044002. doi:10.1103/PhysRevC.62.044002

61. Golak J, Glöckle W, Skibiński R, Witała H, Rozpędzik D, Topolnicki K, et al. Two-nucleon systems in three dimensions. *Phys Rev C* (2010) 81:034006. doi:10.1103/PhysRevC.81.034006

62. Burrows M. *Ab initio leading order effective interactions for scattering of nucleons from light nuclei*. Ph.D. thesis. Athens, Ohio: Ohio University (2020).

63. Cunningham ES, Al-Khalili JS, Johnson RC. Role of the tensor exchange potential in nucleon-nucleus scattering. *Phys Rev C* (2011) 84:041601. doi:10.1103/PhysRevC.84.041601

64. Cunningham ES, Al-Khalili JS, Johnson RC. Effect of spin-spin interactions on nucleon-nucleus scattering. *Phys Rev C* (2013) 87:054601. doi:10.1103/PhysRevC.87.054601

65. Møller C. *K Dan Vidensk Sels Mat Fys Medd* (1945) 23:1.

66. Rodberg L, Thaler R. Introduction of the quantum theory of scattering. In: *Pure and applied physics*, Vol. 26. Cambridge, MA, USA: Academic Press (1967).

67. Navrátil P. Translationally invariant density. *Phys Rev C* (2004) 70:014317. doi:10.1103/PhysRevC.70.014317

68. Cockrell C, Vary JP, Maris P. Lithium isotopes within theab initiono-core full configuration approach. *Phys Rev C* (2012) 86:034325. doi:10.1103/PhysRevC.86.034325

69. Mihaila B, Heisenberg JH. Center-of-mass corrections reexamined: A many-body expansion approach. *Phys Rev C* (1999) 60:054303. doi:10.1103/PhysRevC.60.054303

70. Navrátil P. Translationally invariant matrix elements of general one-body operators. *Phys Rev C* (2021) 104:064322. doi:10.1103/PhysRevC.104.064322

71. Binder S, Calci A, Epelbaum E, Furnstahl RJ, Golak J, Hebeler K, et al. Few-nucleon systems with state-of-the-art chiral nucleon-nucleon forces. *Phys Rev C* (2016) 93:044002. doi:10.1103/PhysRevC.93.044002

72. Ekström A, Baardsen G, Forssén C, Hagen G, Hjorth-Jensen M, Jansen GR, et al. Optimized chiral nucleon-nucleon interaction at next-to-next-to-leading order. *Phys Rev Lett* (2013) 110:192502. doi:10.1103/physrevlett.110.192502

73. Cooper ED, Hama S, Clark BC, Mercer RL. Global Dirac phenomenology for proton-nucleus elastic scattering. *Phys Rev C* (1993) 47:297–311. doi:10.1103/PhysRevC.47.297

74. Hynes MV, Picklesimer A, Tandy PC, Thaler RM. Relativistic (Dirac equation) effects in microscopic elastic scattering calculations. *Phys Rev C* (1985) 31:1438–63. doi:10.1103/PhysRevC.31.1438

75. Imai K, Hatanaka K, Shimizu H, Tamura N, Egawa K, Nisimura K, et al. Polarization and cross section measurements for p-4he elastic scattering at 45, 52, 60 and 65 mev. *Nucl Phys A* (1979) 325:397–407. doi:10.1016/0375-9474(79)90023-X

76. Burzynski S, Campbell J, Hammans M, Henneck R, Lorenzon WB, Pickar MA, et al. p–4He scattering: New data and a phase-shift analysis between 30 and 72 MeV. *Phys Rev C* (1989) 39:56–64. doi:10.1103/PhysRevC.39.56

77. Goldstein NP, Held A, Stairs DG. Elastic scattering of 100 mev protons from 3he and 4he. *Can J Phys* (1970) 48:2629–39. doi:10.1139/p70-326

78. Moss GA, Greeniaus LG, Cameron JM, Hutcheon DA, Liljestrand RL, Miller CA, et al. Proton-He4elastic scattering at intermediate energies. *Phys Rev C* (1980) 21:1932–43. doi:10.1103/PhysRevC.21.1932

79. Ieiri M, Sakaguchi H, Nakamura M, Sakamoto H, Ogawa H, Yosol M, et al. A multifoil carbon polarimeter for protons between 20 and 84 mev. *Nucl Instr Methods Phys Res Section A: Acc Spectrometers, Detectors Associated Equipment* (1987) 257:253–78. doi:10.1016/0168-9002(87)90744-3

80. Kato S, Okada K, Kondo M, Hosono K, Saito T, Matsuoka N, et al. Inelastic scattering of 65 mev protons from ^{12}C, ^{24}Mg, ^{28}Si, and ^{32}S. *Phys Rev C* (1985) 31:1616–32. doi:10.1103/PhysRevC.31.1616

81. Strauch K, Titus F. Direct excitation of nuclear energy states in carbon by 96-mev protons. *Phys Rev* (1956) 103:200–8. doi:10.1103/PhysRev.103.200

82. Gerstein G, Niederer J, Strauch K. Elastic scattering of 96-mev protons. *Phys Rev* (1957) 108:427–32. doi:10.1103/PhysRev.108.427

83. Meyer HO, Schwandt P, Jacobs WW, Hall JR. Proton scattering fromC12between 120 and 200 MeV and the optical potential. *Phys Rev C* (1983) 27:459–69. doi:10.1103/PhysRevC.27.459

84. Ieiri M, Sakaguchi H, Nakamura M, Sakamoto H, Ogawa H, Yosol M, et al. A multifoil carbon polarimeter for protons between 20 and 84 mev. *Nucl Instr Methods Phys Res Section A: Acc Spectrometers, Detectors Associated Equipment* (1987) 257:253–78. doi:10.1016/0168-9002(87)90744-3

85. Sakaguchi H, Nakamura M, Hatanaka K, Goto A, Noro T, Ohtani F, et al. 65 MeV polarized proton elastic scattering and the effective two-body interaction range. *Phys Lett B* (1979) 89:40–3. doi:10.1016/0370-2693(79)90071-6

86. Seifert H. *Energy dependence of the effective interaction for nucleon-nucleus scattering*. Ph.D. thesis. College Park, Maryland: University of Maryland (1990).

87. Kelly JJ, Bertozzi W, Buti TN, Finn JM, Hersman FW, Hyde-Wright C, et al. Density dependence in the two-nucleon effective interaction at 135 MeV. *Phys Rev C* (1989) 39:1222–41. doi:10.1103/PhysRevC.39.1222

88. Kelly JJ, Finn JM, Bertozzi W, Buti TN, Hersman FW, Hyde-Wright C, et al. Effective interactions and nuclear structure using 180 MeV protons. I.O16(p,p'). *Phys Rev C* (1990) 41:2504–13. doi:10.1103/PhysRevC.41.2504

frontiers | Frontiers in Physics

TYPE Review
PUBLISHED 17 February 2023
DOI 10.3389/fphy.2022.1092931

OPEN ACCESS

EDITED BY
Maria Piarulli,
Washington University in St. Louis,
United States

REVIEWED BY
Alexander Rothkopf,
University of Stavanger, Norway
Bingyu Ni,
Hunan University, China

*CORRESPONDENCE
C. Drischler,
drischler@ohio.edu

SPECIALTY SECTION
This article was submitted to Nuclear Physics, a section of the journal Frontiers in Physics

RECEIVED 08 November 2022
ACCEPTED 15 December 2022
PUBLISHED 17 February 2023

CITATION
Drischler C, Melendez JA, Furnstahl RJ, Garcia AJ and Zhang X (2023), BUQEYE guide to projection-based emulators in nuclear physics.
Front. Phys. 10:1092931.
doi: 10.3389/fphy.2022.1092931

BUQEYE guide to projection-based emulators in nuclear physics

C. Drischler[1,2]*, J. A. Melendez[3], R. J. Furnstahl[3], A. J. Garcia[3] and Xilin Zhang[2]

[1]Department of Physics and Astronomy & Institute of Nuclear and Particle Physics, Ohio University, Athens, OH, United States, [2]Facility for Rare Isotope Beams, Michigan State University, East Lansing, MI, United States, [3]Department of Physics, The Ohio State University, Columbus, OH, United States

The BUQEYE collaboration (Bayesian Uncertainty Quantification: Errors in Your effective field theory) presents a pedagogical introduction to projection-based, reduced-order emulators for applications in low-energy nuclear physics. The term *emulator* refers here to a fast surrogate model capable of reliably approximating high-fidelity models. As the general tools employed by these emulators are not yet well-known in the nuclear physics community, we discuss variational and Galerkin projection methods, emphasize the benefits of offline-online decompositions, and explore how these concepts lead to emulators for bound and scattering systems that enable fast and accurate calculations using many different model parameter sets. We also point to future extensions and applications of these emulators for nuclear physics, guided by the mature field of model (order) reduction. All examples discussed here and more are available as interactive, open-source Python code so that practitioners can readily adapt projection-based emulators for their own work.

KEYWORDS

emulators, reduced-order models, model order reduction, nuclear scattering, uncertainty quantification, effective field theory, variational principles, Galerkin projection

1 Introduction

Nuclear systems are notoriously complex. But typically, our theoretical modeling of nuclear phenomena contains superfluous information for quantities of interest. Model order reduction (MOR) refers to powerful techniques that enable us to reduce a system's complexity systematically (*e.g.*, see Refs. [1–3] for comprehensive introductions). These techniques enable emulators, which are low-dimensional surrogate models capable of rapidly and reliably approximating high-fidelity models, making practical otherwise impractical calculations. But the nuclear physics community has barely scratched the surface of the types of emulators that could be crafted or explored their full range of applications.

A fertile area for new emulators is uncertainty quantification (UQ) [4–13] in nuclear physics, which is the general theme of this Frontiers Research Topic [14]. Quantifying theoretical uncertainties rigorously is crucial for comparing theory predictions with experimental and/or observational constraints and performing model comparison and/or mixing [15]. However, UQ has only recently drawn much attention as nuclear theory has entered the precision era. Bayesian parameter estimation for nuclear effective field theory (EFT) and optical models, UQ for nuclear structure pushing toward larger masses and for reactions across the chart of nuclides, experimental design [15–17] for the next-generation of precision experiments probing the nuclear dripline, and many other applications will all benefit from emulators. This Research Topic [14] already contains several new applications of emulators for nuclear physics. Key to the wider adoption of these tools is the evangelization of their potential

and the creation of pedagogical guides for those first starting in this field [18]. This article is aimed at both goals.

To do so, the BUQEYE collaboration (Bayesian Uncertainty Quantification: Errors in Your EFT) [19] has created a rather unconventional document comprised of the article you are reading now along with a companion website [20] containing interactive supplemental material and source code that generates all the results shown, and much more. Interested individuals can dynamically generate different versions of this document based on tunable parameters. We hope that this format encourages readers to experiment and build upon the examples presented here, thereby facilitating new applications.

Various types of emulators have already been applied with success within nuclear physics. A non-exhaustive list of applications includes Refs. [7, 9, 21–42]. But as emphasized in Refs. [18, 43], there is a broad and relatively mature MOR literature outside of nuclear physics waiting to be exploited (*e.g.*, see Ref. [44] for an overview of the Universe of MOR approaches). Our goal in this guide will be to facilitate this exploitation through a selective treatment of physics-informed, projection-based emulators relevant to a wide range of nuclear physics problems.

To this end, we organize this guide as follows. Section 2 focuses on emulators for bound-state calculations using subspace-projection methods. We then provide a more general introduction to MOR for solving differential equations in Section 3, which leads to our discussion of scattering emulators in Section 4. Section 5 concludes with a summary and outlook. Throughout, we draw connections between variational and Galerkin projection methods and illustrate these concepts with pedagogical examples, supplemented by source code on the companion website [20].

2 Eigen-emulators

In this section, we discuss the construction of fast and accurate emulators for bound-state calculations. Given a (Hermitian) Hamiltonian $H(\boldsymbol{\theta})$ parameterized by $\boldsymbol{\theta}$, we aim to find the solutions $\{E(\boldsymbol{\theta}), |\psi(\boldsymbol{\theta})\rangle\}$ of the Schrödinger Equation

$$H(\boldsymbol{\theta})|\psi(\boldsymbol{\theta})\rangle = E(\boldsymbol{\theta})|\psi(\boldsymbol{\theta})\rangle, \tag{1}$$

subject to the normalization $\langle\psi(\boldsymbol{\theta})|\psi(\boldsymbol{\theta})\rangle = 1$. The components of the vector $\boldsymbol{\theta}$ may be model parameters, such as the low-energy couplings of a nuclear EFT, or other parameters describing the system of interest [33, 40]. We consider here cases in which Eq. 1 can be solved with high fidelity, but doing so requires a significant amount of compute time. This compute time is compounded when repeated solutions are required throughout the parameter space, *e.g.*, during optimization routines or Monte Carlo sampling. In the following, we will discuss how the Ritz variational principle and the Galerkin method can be used to construct rapid and reliable[1] emulators that facilitate these calculations.

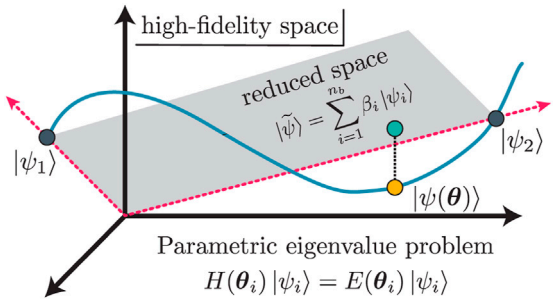

FIGURE 1
Illustration of a projection-based emulator using only two snapshots $|\psi_i\rangle \equiv |\psi(\boldsymbol{\theta}_i)\rangle$ (dark gray points). These snapshots are high-fidelity solutions of the Schrödinger Eq. 1, which span the subspace of the reduced-order model, as indicated by the red arrows and the gray plane. The trajectory of a high-fidelity eigenvector is denoted by the blue curve. The orange dot depicts an eigenvector $|\psi(\boldsymbol{\theta})\rangle$ along the trajectory that, when projected onto the reduced space, corresponds to the turquoise point; hence, the difference between the orange and turquoise points represents the error due to the emulator's subspace projection (*i.e.*, the dotted line). Inspired by Figure 2.1 in Ref. [2].

2.1 Variational approach

To construct an emulator for bound state calculations, we use here the Rayleigh–Ritz method[2] and thus consider the energy functional

$$\mathcal{E}[\tilde{\psi}] = \langle\tilde{\psi}|H(\boldsymbol{\theta})|\tilde{\psi}\rangle - \tilde{E}(\boldsymbol{\theta})\big(\langle\tilde{\psi}|\tilde{\psi}\rangle - 1\big), \tag{2}$$

where the Lagrange multiplier $\tilde{E}(\boldsymbol{\theta})$ (also known as Ritz value) imposes the normalization condition $\langle\tilde{\psi}|\tilde{\psi}\rangle = 1$ for bound states. The Generalized Ritz Theorem [47][3] states that the functional (Eq. 2) is stationary about all (discrete) solutions of the Eq. 1, not just the ground state solution, which can be seen by imposing the stationary condition

$$\delta\mathcal{E}[\tilde{\psi}] \equiv 0 = 2\langle\delta\tilde{\psi}|\big[H(\boldsymbol{\theta}) - \tilde{E}(\boldsymbol{\theta})\big]|\tilde{\psi}\rangle - \delta\tilde{E}(\boldsymbol{\theta})\big[\langle\tilde{\psi}|\tilde{\psi}\rangle - 1\big], \tag{3}$$

and noting that Eq. 3 is only fulfilled for arbitrary variations $\langle\delta\tilde{\psi}|$ if $|\tilde{\psi}\rangle$ is a solution of the Schrödinger Eq. 1 with $\tilde{E}(\boldsymbol{\theta}) = E(\boldsymbol{\theta})$.

Let us now define the trial wave function we use in conjunction with the functional (2):

$$|\tilde{\psi}\rangle = \sum_{i=1}^{n_b} \beta_i |\psi_i\rangle \equiv X\vec{\beta}, \tag{4a}$$

$$X = \big[\,|\psi_1\rangle \;\; |\psi_2\rangle \;\; \cdots \;\; |\psi_{n_b}\rangle\,\big], \tag{4b}$$

where the column-vector $\vec{\beta}$ contains the to-be-determined coefficients and the row-vector[4] X the (in principle) arbitrary basis states. Here, we use *snapshots* of high-fidelity solutions of the Eq. 1 at a set of given parameter values; *i.e.*, $\{|\psi_i\rangle \equiv |\psi(\boldsymbol{\theta}_i)\rangle\}_{i=1}^{n_b}$ [2, 48–50]. No assumption has been made as to how to obtain the high-fidelity solutions.

1 A *reliable* emulator may not necessarily be required to be highly accurate, *e.g.*, if the other uncertainties of the theoretical calculation dominate the overall uncertainty budget

2 For a critical commentary on the history of the method's name, see, *e.g.*, Refs. [45, 46].

3 Many helpful theorems relevant to the Rayleigh–Ritz method can be found in Section 3 in Ref. [47].

4 In a representation of H, the ψ_i corresponding to $|\psi_i\rangle$ are the n_b columns of the matrix X in that representation

Figure 1 motivates the efficacy of snapshot-based trial functions. Although a given eigenvector $|\psi(\boldsymbol{\theta})\rangle$ obtained from a high-fidelity solver resides in a high-dimensional (or even infinite-dimensional) space, the trajectory traced out by continuous variations in $\boldsymbol{\theta}$ remains in a relatively low-dimensional subspace (as illustrated by the gray plane). Hence, linear combinations of high-fidelity eigenvectors spanning this subspace (*i.e.*, the snapshots) make extremely effective trial wave functions for variational calculations. In nuclear physics, snapshot-based emulators already have accurately approximated ground-state properties, such as binding energies, charge radii [7, 9, 25], and transition matrix elements [9, 29], and have been explored for applications to excited states [51].

Given the trial wave function (4), we determine the coefficients $\vec{\beta}_\star$ that render $\mathcal{E}[\tilde{\psi} = X\vec{\beta}]$ stationary under variations $|\delta\tilde{\psi}\rangle = X|\delta\vec{\beta}\rangle$ of the trial wave function, as opposed to arbitrary variations. Solving for the optimal $\vec{\beta}_\star$ occurs then in the low-dimensional space spanned by the basis elements in X (*i.e.*, the red arrows in Figure 1) rather than in the high-dimensional space in which $|\psi\rangle$ resides. From the stationarity condition Eq. 3, we obtain the reduced-order model [52],

$$\tilde{H}(\boldsymbol{\theta})\vec{\beta}_\star(\boldsymbol{\theta}) = \tilde{E}(\boldsymbol{\theta})\tilde{N}\vec{\beta}_\star(\boldsymbol{\theta}), \tag{5a}$$

$$\vec{\beta}_\star^\dagger(\boldsymbol{\theta})\tilde{N}\vec{\beta}_\star(\boldsymbol{\theta}) = 1, \tag{5b}$$

where $\tilde{H}(\boldsymbol{\theta}) \equiv X^\dagger H(\boldsymbol{\theta})X$ is the subspace-projected Hamiltonian and $\tilde{N} \equiv X^\dagger X$ the norm matrix in the snapshot basis. As opposed to $H(\boldsymbol{\theta})$ in Eq. 1, $\tilde{H}(\boldsymbol{\theta})$ (and likewise $\tilde{N}$) is a $n_b \times n_b$ Hermitian matrix,

$$\tilde{H}(\boldsymbol{\theta}) = \begin{bmatrix} \langle\psi_1|H(\boldsymbol{\theta})|\psi_1\rangle & \cdots & \langle\psi_1|H(\boldsymbol{\theta})|\psi_{n_b}\rangle \\ \vdots & \ddots & \vdots \\ \langle\psi_{n_b}|H(\boldsymbol{\theta})|\psi_1\rangle & \cdots & \langle\psi_{n_b}|H(\boldsymbol{\theta})|\psi_{n_b}\rangle \end{bmatrix}. \tag{6}$$

In practice, the generalized eigenvalue problem Eq. 5 may experience numerical instabilities due to small singular values in $\tilde{N}$. (The instabilities also appear in reduced-order modeling of differential equations, see Section 3). One way to ameliorate these instabilities is to orthonormalize the snapshots in X, hence yielding $\tilde{N} = 1$. This approach could also permit some efficiency gains, by excluding the least important vectors as measured by their singular values. Alternatively, Ref. [53] recently introduced a trimmed sampling algorithm that can substantially reduce the effects of noise in solving generalized eigenvalue problems. Finally, a well-known approach to regularize both generalized eigenvalue problems and matrix inversion is through the use of a nugget [54, 55]. Here, a regularization parameter $\nu \ll 1$ (called a nugget) is added to the diagonal of the ill-conditioned matrix one wishes to invert (here, $\tilde{N}$), thus shifting its singular values.

By solving the generalized eigenvalue problem Eq. 5, one obtains n_b pairs $\{\tilde{E}(\boldsymbol{\theta}), \vec{\beta}_\star(\boldsymbol{\theta})\}$ consisting of a Lagrange multiplier (*i.e.*, an eigenvalue) and its corresponding coefficient vector. Let us index the eigenvalues of the Eq. 5 and Eq. 1 in ascending order; that is, $\tilde{E}_n \leqslant \tilde{E}_{n+1}$ and $E_n \leqslant E_{n+1}$, respectively, with $n = 1$ indicating the lowest eigenvalue. If the snapshot basis X in the trial wave function (Eq. 4) contains n_b linearly independent states, then the Min–Max Theorem [47] asserts that each Lagrange multiplier,

$$\tilde{E}_n(\boldsymbol{\theta}) \geqslant E_n(\boldsymbol{\theta}) \quad \text{for } 1 \leqslant n \leqslant n_b, \tag{7}$$

provides an upper bound on its corresponding eigenvalue of the Schrödinger Eq. 1.[5] Furthermore, the Generalized Ritz Theorem implies that the $\tilde{E}_n(\boldsymbol{\theta})$ provide not only the variational bounds (Eq. 7) but also stationary approximations for these high-fidelity eigenvalues. Adding another basis state to X can only improve these approximations, which converge to the high-fidelity eigenvalues as the projected subspace approaches the high-fidelity space [47].

Although excited states can also be emulated, especially when adding excited-state snapshots to the trial wave function to improve the emulator's accuracy (see also Ref. [51]), we focus on ground-state properties and thus use only ground-state snapshots in the trial wave function. For brevity, we will omit the subscripts henceforth. To obtain the approximate ground-state wave function associated with $\tilde{E}(\boldsymbol{\theta})$, one evaluates the Ritz vector $|\psi(\boldsymbol{\theta})\rangle \approx X\vec{\beta}_\star(\boldsymbol{\theta})$. Expectations values of operators O can then be straightforwardly computed using

$$\langle\psi(\boldsymbol{\theta})|O(\boldsymbol{\theta})|\psi(\boldsymbol{\theta})\rangle \approx \vec{\beta}_\star^\dagger(\boldsymbol{\theta})\tilde{O}\vec{\beta}_\star(\boldsymbol{\theta}), \tag{8}$$

with the subspace-projected $\tilde{O}(\boldsymbol{\theta}) = X^\dagger O(\boldsymbol{\theta})X$. However, these expectation values generally do not provide variational bounds unless $O = H$ is the Hamiltonian, as discussed (see, *e.g.*, Figure 5 in Ref. [25] for emulated ^{4}He ground-state radii).

2.2 Galerkin approach

The reduced-order model (5) can be alternatively derived *via* a Galerkin projection, as we will also see with the variational emulators for scattering in Section 4. To this end, we construct the *weak form* of the Eq. 1 by left-multiplying it by an arbitrary test function $\langle\zeta|$ and asserting that

$$\langle\zeta|H(\boldsymbol{\theta}) - E(\boldsymbol{\theta})|\psi\rangle = 0, \quad \forall\langle\zeta|. \tag{9}$$

If the weak form (9) is satisfied for all $\langle\zeta|$ for a given set $\{E, |\psi\rangle\}$, then the set must also satisfy the Eq. 1. The proof of this statement can be obtained *via* a contrapositive: if Eq. 1 were not satisfied, then one could find a $\langle\zeta|$ such that Eq. 9 is nonzero.

The weak form of the high-fidelity system is the starting point for deriving a reduced-order model. Although Eq. 9 still operates in the large space in which $|\psi\rangle$ resides (cf. Figure 1), we can reduce its dimension by replacing $|\psi\rangle \to |\tilde{\psi}\rangle$, where $|\tilde{\psi}\rangle$ is defined in Eq. 4. With the degrees of freedom for $|\psi\rangle$ reduced, we enforce a less strict orthogonality condition: we select n_b test functions ζ_i and assert that the residual due to the trial wave function (cf. Figure 1) should be orthogonal to the subspace $\mathcal{Z}$ spanned by these test functions $Z = [|\zeta_1\rangle, \ldots, |\zeta_{n_b}\rangle]$:

$$\left(H(\boldsymbol{\theta}) - \tilde{E}(\boldsymbol{\theta})\right)|\tilde{\psi}\rangle \perp \mathcal{Z}, \tag{10}$$

or likewise

5 For non-Hermitian Hamiltonians, one generally does not obtain the variational bounds (Eq. 7) as can be observed in, *e.g.*, the subspace-projected coupled-cluster method developed in Ref. [7].

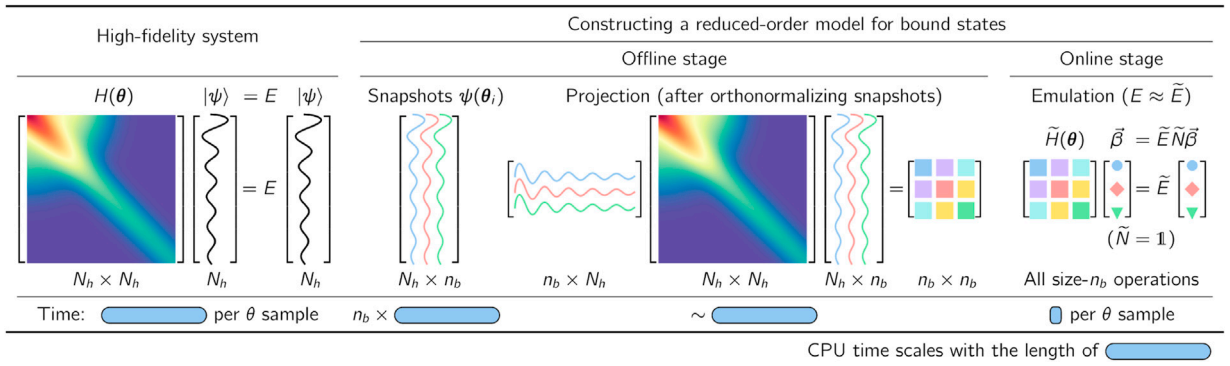

FIGURE 2
Illustration of the workflow for implementing fast and accurate emulators, including a high-fidelity solver (left) and an intrusive, projection-based emulator with efficient offline-online decomposition (right), for sampling the (approximate) solutions of the Schrödinger Eq. 1 in the parameter space $\boldsymbol{\theta}$. For brevity, the figure assumes that the snapshots are orthonormalized during the offline stage such that $\tilde{N} = \mathbb{1}$ in the emulator Eq. 5. See the main text for details.

$$\langle\zeta|H(\boldsymbol{\theta}) - \tilde{E}(\boldsymbol{\theta})|\tilde{\psi}\rangle = 0, \quad \forall|\zeta\rangle \in \mathcal{Z}. \tag{11}$$

But replacing $|\psi\rangle \to |\tilde{\psi}\rangle$ also implies that the true eigenvalue E is in general not exactly reproduced unless $\mathcal{X}$ contains $|\psi(\boldsymbol{\theta})\rangle$. Hence, we also had to apply the approximation $\tilde{E} \approx E$ in Eqs. 10 and 11.

In the Galerkin method, which is also known as the "method of weighted residuals," the test and trial function bases are chosen to be equivalent; *i.e.*, $\mathcal{Z} = \mathcal{X}$. The so-called Galerkin condition Eq. 11 is then equivalent to imposing that $\langle\psi_i|H - \tilde{E}|\tilde{\psi}\rangle = 0$ holds for $i \in [1, n_b]$. This yields a system of n_b equations with n_b unknowns $\vec{\beta}$ and, together with the normalization condition, reduces to Eq. 5 obtained from the variational principle in Section 2.1. However, we stress that the test and trial function bases can be chosen differently (*i.e.*, $|\zeta_i\rangle \neq |\psi_i\rangle$), which makes the Galerkin method more general than the variational approach. Note that the normalization condition does not affect the Galerkin condition Eq. 11 and can be implemented by normalizing the trial function.

2.3 Emulator workflow and offline-online decomposition

Figure 2 illustrates the workflow for implementing fast and accurate emulators as described in Section 2.1. The workflow involves

1. a computational framework capable of reliably solving the high-fidelity system Eq. 1,
2. the snapshot-based trial wave function Eq. 4 with the optimal coefficients (*i.e.*, the weights) determined by the Eq. 5, and
3. an efficient offline-online decomposition in which the computational heavy lifting is performed once *before* the emulator is invoked.

Several computational frameworks exist in nuclear physics (and quantum chemistry) for solving the few- and many-body Schrödinger Eq. 1 [56]. For illustration, Figure 2 assumes that the high-fidelity solver performs a direct diagonalization of the $N_h \times N_h$ Hamiltonian in a chosen (truncated) model basis of length N_h. The corresponding runtime t_s per sampling point $\boldsymbol{\theta}_i$ is indicated by the width of the blue bar in Figure 2. In nuclear physics, such approaches are referred to as Configuration Interaction (CI). However, the following discussion will be independent of how the high-fidelity solutions of the Eq. 1 are obtained in practice.

Using the high-fidelity solver, one constructs a set of snapshots $\{|\psi(\boldsymbol{\theta}_i)\rangle\}_{i=1}^{n_b}$ in the truncated model basis to build the columns of the $N_h \times n_b$ matrix X. The runtime for this task is $n_b \times t_s$. For simplicity, Figure 2 assumes $n_b = 3$ and depicts the basis functions schematically in different colors. This phase of the emulator needs to be completed only once before the emulator is invoked and is thus called the *offline stage* as opposed to the *online stage* of the emulator. The predictions are made quickly and with little memory footprint in the online stage.

The appearance of the full-order Hamiltonian during the offline stage, where the projected Hamiltonian $\tilde{H}(\boldsymbol{\theta}) \equiv X^\dagger H(\boldsymbol{\theta}) X$ is computed (see Figure 2), implies that this class of projection-based emulators is *intrusive* in nature. In general, intrusive emulators apply the basis expansions and projections to the operators implemented in the high-fidelity model [57]. On the other hand, *non-intrusive* emulators use only outputs of the full-order solver without access to the full-order operators such as the Hamiltonian. Non-intrusive emulators include Gaussian processes [58], Dynamic Mode Decompositions [59, 60], and other machine learning methods [61–63]. More details on this classification scheme can be found in Section 8 in Ghattas and Willcox [57].

The emulator's efficiency greatly benefits from moving all size-N_h operations into the offline stage, which can easily be achieved for Hamiltonians $H(\boldsymbol{\theta})$ with an affine parameter dependence. These affine operators can be written as a sum of products of parameter-dependent functions $h_n(\boldsymbol{\theta})$ and parameter-independent operators H_n,

$$H(\boldsymbol{\theta}) = \sum_n h_n(\boldsymbol{\theta}) H_n. \tag{12}$$

Note that the functions $h_n(\boldsymbol{\theta})$ are only required to be smooth but not necessarily linear in $\boldsymbol{\theta}$. The affine parameter dependence in Eq. 12 then allows one to store the subspace-projected operators $\tilde{H}_n = X^\dagger H_n X$ separately up front in the offline phase, from which

$$\tilde{H}(\boldsymbol{\theta}) = \sum_n h_n(\boldsymbol{\theta}) \tilde{H}_n, \tag{13}$$

can be efficiently constructed for each $\boldsymbol{\theta}_i$ during the *online* stage to solve the emulator equation 5. For instance, Hamiltonians derived from chiral EFT can be cast into the form (12) due to their affine dependence on the low-energy couplings. The runtime per sample $\boldsymbol{\theta}_i$ in the online phase is therefore typically just a small fraction of that of the high-fidelity solver, as depicted by the small blue box in Figure 2. Likewise, emulating expectation values of other operators with an affine parameter dependence *via* Eq. 8 also benefits from this offline-online decomposition. For non-affine operators, various hyperreduction methods have been developed to construct approximate affine representations [50, 64], including the empirical interpolation (EIM) [65–68] and gappy proper orthogonal decomposition [69, 70]. See also Refs [48, 71–73] for hyperreduction methods that interpolate X or $\tilde{H}(\boldsymbol{\theta})$ directly, and Refs [33, 74] for recent applications of machine learning tools for hyperreduction.

How should one choose the snapshots in the trial wave function Eq. 4 effectively? For relatively small parameter spaces, one can use Latin hypercube sampling to obtain space-filling snapshots or choose the snapshots in the proximity of the to-be-emulated parameter ranges, keeping $n_b \ll N_h$ in practice. A chosen set of snapshots expressed in the (truncated) model basis can be optimized by applying a singular value decomposition (SVD) or the closely related proper orthogonal decomposition (POD) [75] to the $N_h \times n_b$ matrix X. One then creates a new set of snapshots from the (orthonormal) left-singular vectors associated with the singular values greater than a chosen threshold [64]. This (optional) preprocessing step can be performed during the offline stage, as illustrated in Figure 2, thereby rendering the Eq. 5 an eigenvalue problem (*i.e.*, $\tilde{N} = 1$) and less sensitive to numerical noise.

The basis states of the trial wave function can also be obtained iteratively, using a greedy algorithm [64, 76, 77]. These algorithms estimate and then minimize the emulator's overall error by adding basis states (obtained from a high-fidelity solver) in the parameter space where the error is expected to be the largest. Greedy algorithms require fast approximations of the emulator's error and terminate when either a requested error tolerance or a maximum number of iterations has been achieved. Uncertainty quantification for reduced-order models has been studied in various contexts, including differential equations [64, 77, 78] and nuclear physics problems [24, 43].

2.4 Illustrative example

The formal results so far in this Section can be illuminated by a simple example, which allows us to compare results from a snapshot-based emulator to more conventional approaches, such as direct diagonalization in a harmonic oscillator basis and Gaussian process emulation. Let us define the system we would like to solve as a single particle with zero angular momentum in three dimensions and trapped in an anharmonic oscillator potential. This example can be directly generalized to few- and many-body systems. The potential operator is the sum of a conventional harmonic oscillator (HO) potential and a finite-range piece:

$$V(r;\boldsymbol{\theta}) = V_{\mathrm{HO}}(r) + \sum_{n=1}^{3} \theta_n \exp\left(-r^2/\sigma_n^2\right), \tag{14}$$

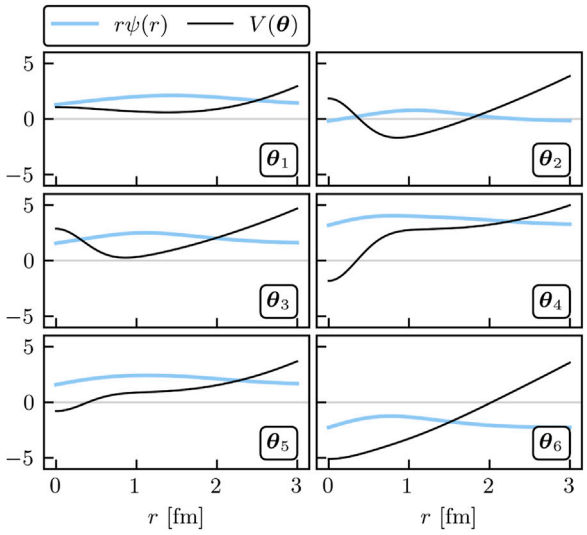

FIGURE 3
Basis functions for training the snapshot-based eigen-emulator. The black curves show the potential, and the blue curves show the wave functions as functions of the radial coordinate r. The wave functions are offset vertically by their corresponding energies for clarity. See the main text for details.

with $\sigma_n = [0.5, 2, 4]$ fm. The potential Eq. 14 has the affine structure defined in Eq. 12 for $\boldsymbol{\theta}$ and hence can be emulated rapidly after projecting into the snapshot basis during the offline stage. Even the high-fidelity system considered here is still small enough to be solved quickly and accurately using a fine radial mesh on a standard laptop. However, this provides an illuminating setting within which we can observe many qualities seen in more complicated scenarios.

Following the MOR paradigm, we take snapshots of the high-fidelity wave function at various training parameters $\{\boldsymbol{\theta}_i\}$ and collect them into our basis X. Here, we choose $n_b = 6$ training points randomly and uniformly distributed in the range $[-5, 5]$ MeV for all θ_n; 50 validation parameter sets are chosen within the same range. The snapshots and the corresponding potentials are shown in Figure 3. These snapshots are then used to construct the reduced-order system as in Eq. 5. All of this, and more, is made simple by the `EigenEmulator` Python class provided in the supplemental material [20].

Once the reduced system has been constructed and the affine structure of the Hamiltonian exploited to store the projected matrices during the offline stage, we can begin rapid emulation during the online stage. To help provide a baseline to a common approach in nuclear physics, we provide an emulator constructed with the first $n_b = 6$ HO wave functions as the trial basis X in Eq. 5. We label this approach the HO emulator and the snapshot-based approach the reduced-basis method (RBM) emulator. See Ref. [18] for a guide to the extensive literature on RBMs. One can emulate quantities with this HO approach *via* our `OscillatorEmulator` class [20].

For example, we take three of the validation parameter sets we sampled and compare the exact and emulated wave functions for both emulators. Figure 4 shows the results. The gray lines depict the n_b wave functions used to create the reduced-order models, and the colored lines show the emulated results on top of the high-fidelity solutions (black lines). Although both the reduced basis and HO basis are rich

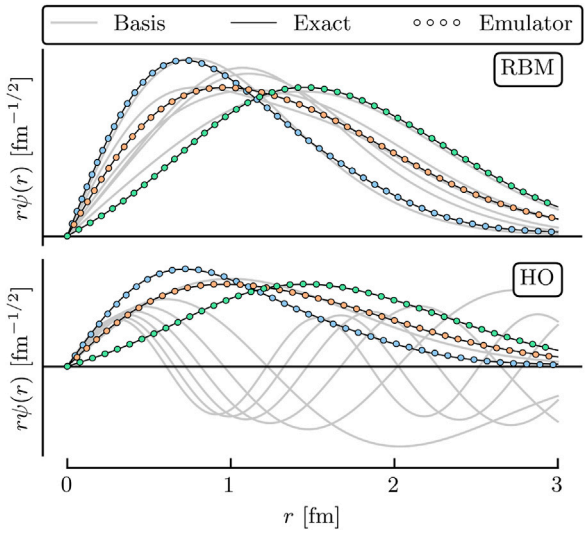

FIGURE 4
Emulated wave functions for the RBM emulator (top panel) and HO emulator (bottom panel) as a function of the radius. The solid black lines represent the exact solution, and the dots represent the emulator result. The gray lines give the wave functions used to train the emulator. See the main text for details.

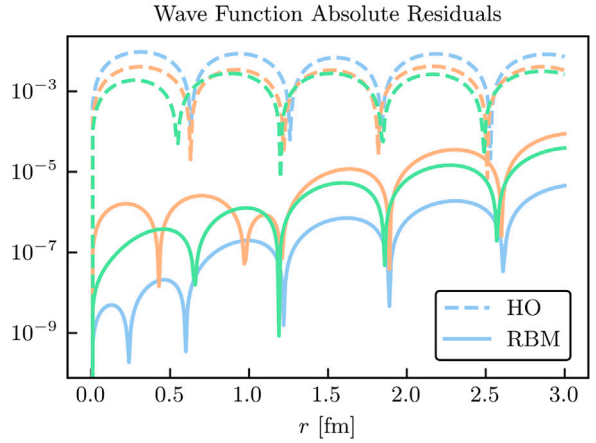

FIGURE 5
Absolute residuals of the emulated wave functions (in fm$^{-1/2}$) based on the RBM and HO emulator as a function of r, with colors corresponding to those in Figure 4. The emulator results are compared to the exact solutions. See the main text for details.

enough to capture the main effects of varying $\boldsymbol{\theta}$, the RBM emulator is much more effective at capturing the fine details of the wave function. This can be seen in more detail in Figure 5, where the absolute residuals of the RBM emulator are orders of magnitude smaller than those of the HO emulator. The sensitivity of the emulator accuracy as n_b is varied can be readily studied using the Python code provided on the companion website [20].

The quality of the emulators can be understood by noting in Figure 4 that the basis functions of the RBM emulator match much more closely with the emulated wave functions than the HO emulator, whose wave functions have nodes not seen in the ground state (see the gray lines). Thus, although the HO basis functions may be better at spanning the space of all possible wave functions, they are, in fact, a poor basis for spanning the set of all possible ground states as $\boldsymbol{\theta}$ are varied. The RBM emulator constructs an extremely effective basis almost automatically, with minimal input required by the modeler. This can prove particularly effective for cases where the system's complexity limits the quality of the basis that can be constructed from intuition or expertise alone.

Next, we discuss the emulation of bound-state observables. Straightforward to emulate are the eigen-energies $E(\boldsymbol{\theta})$, whose emulated values $\tilde{E}(\boldsymbol{\theta})$ are the result of solving the Eq. 5. But as discussed in Section 2.1, other observables associated with the operator O can be emulated *via* $\langle\psi(\boldsymbol{\theta})|O|\psi(\boldsymbol{\theta})\rangle \approx \langle\tilde{\psi}(\boldsymbol{\theta})|O|\tilde{\psi}(\boldsymbol{\theta})\rangle$ using the $\tilde{\psi}(\boldsymbol{\theta})$ found from Eq. 5. We choose to show the results of emulating the radius-squared operator R^2, defined here to be

$$\langle\psi|R^2|\psi\rangle = \frac{1}{\mathcal{N}}\int_0^\infty r^2\,\mathrm{d}r\,r^2\psi^2(r), \tag{15}$$

with the normalization $\mathcal{N} = \int_0^\infty r^2\,\mathrm{d}r\,\psi^2(r)$. As stated previously, the bulk of the numerical effort in the evaluation of this matrix element is handled during the offline stage, where the integration is performed once,

$$\tilde{R}^2_{ij} \equiv \langle\psi_i|R^2|\psi_j\rangle = \frac{1}{\mathcal{N}}\int_0^\infty r^2\,\mathrm{d}r\,r^2\psi_i(r)\psi_j(r), \tag{16}$$

and then the online stage emulation can occur quickly *via* Eq. 8; *i.e.*, $\langle\psi(\boldsymbol{\theta})|R^2|\psi(\boldsymbol{\theta})\rangle \approx \sum_{ij}\vec{\beta}^{(i)}_\star(\boldsymbol{\theta})\tilde{R}^2_{ij}\vec{\beta}^{(j)}_\star(\boldsymbol{\theta})$.

For illustrative purposes, we continue our example using the trained RBM and HO emulators, but add a popular emulation tool to the discussion: Gaussian processes (GPs). GPs are non-parametric, non-intrusive machine learning models for both regression and classification tasks [58, 79, 80]. Their popularity stems partly from their convenient analytical form and flexibility in effectively modeling various types of functions. GPs benefit from treating the underlying set of codes as a black box [57]; as we will soon see, this is a double-edged sword. We employ two independent GPs to emulate the ground-state energy and the corresponding radius expectation value. Each GP uses a Gaussian covariance kernel and is fit to the observable values at the same values of $\boldsymbol{\theta}_i$ used to train the RBM emulator. We use the maximum likelihood values for the hyperparameters.

The absolute residuals at the validation points for each of the RBM, HO, and GP emulators are shown in Figures 6 and 7 for the energy and radius, respectively. Among these emulators, the GP emulators perform the worst, despite being trained on the values of the energies and radii themselves to perform this very emulation task. Furthermore, its ability to extrapolate beyond the support of its training data is often poor unless great care is taken in the design of its kernel and mean function (see Figures 1 and 2 in Ref. [25]). The GP suffers from what, in other contexts, could be considered its strength: because it treats the high-fidelity system as a black box, it cannot use the structure of the high-fidelity system to its advantage (although some information can be conveyed *via* physics-informed priors for the hyperparameters). Note that the point here is not that it is impossible to find some GP that can be competitive with other RBM emulators after using expert judgment and careful (*i.e.*, physics-informed) hyperparameter tuning. Rather, we emphasize that with the reduced-order models, remarkably high accuracy is achieved *without* the need for such expertise.

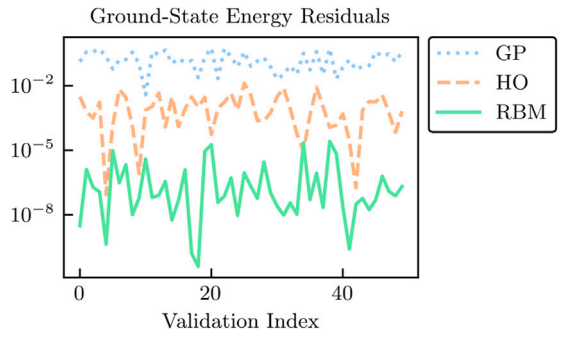

FIGURE 6
Absolute residuals in the energy (in MeV) at the 50 validation points for the RBM, HO, and GP emulators. The validation points are chosen randomly from a uniform distribution within the same range as the training points. See the main text for details.

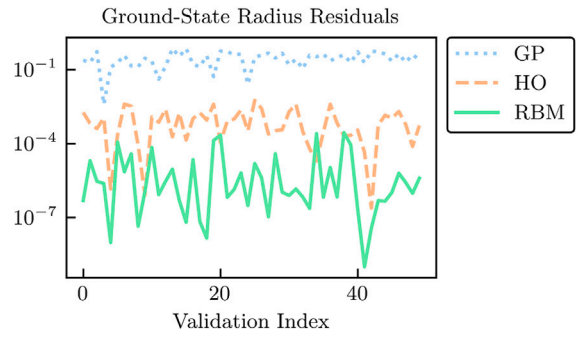

FIGURE 7
Similar to Figure 6 but for the root-mean-squared radius $\sqrt{\langle R^2 \rangle}$ and in units of fm.

The HO emulator performs better than the GP emulator, but it was not "trained" *per se*, it was merely given a basis of the lowest six HO wave functions as a trial basis, from which a reduced-order model was derived. However, the HO emulator can still outperform the GP emulator because it takes advantage of the *structure* of the high-fidelity system: it is aware that the problem to be solved is an eigenvalue problem, for this is built into the emulator itself. This feature permits a single HO emulator to emulate the wave function, energy, and radius simultaneously.

Coming in first in the comparison of the emulators' performances is the RBM emulator, which typically results in higher accuracies than the HO and GP emulators by multiple orders of magnitude. The RBM emulator combines the best ideas from the other emulators. Like the GP, the RBM emulator uses evaluations of the eigenvalue problem as training data. However, its "training data" are *curves* (*i.e.*, the wave functions) rather than scalars (*e.g.*, eigen-energies), like the GP is trained upon. Like the HO emulator, the RBM emulator takes advantage of the structure of the system when projecting the high-fidelity system to create the reduced-order model. With these strengths, the RBM emulator is highly effective in emulating bound-state systems, even with only a few snapshots and far from the support of the snapshots (see Figures 1 and 2 in Ref. [25]). As we will see in Section 4, many of these strengths carry over to systems of differential equations.

3 Model reduction

In this Section, we provide a more general discussion of variational principles and the Galerkin method as the foundations for constructing highly efficient emulators for nuclear physics (see also Ref. [18]). The general methods discussed here will be used as a springboard to develop emulators for the specific case of scattering systems in Section 4.

We consider (time-independent) differential equations that depend on the parameter vector $\boldsymbol{\theta}$ and aim to find the solution ξ of

$$D(\xi;\boldsymbol{\theta}) = 0 \quad \text{in } \Omega, \tag{17a}$$
$$B(\xi;\boldsymbol{\theta}) = 0 \quad \text{on } \Gamma, \tag{17b}$$

where $\{D, B\}$ are differential operators and Ω is the domain with boundary Γ. See Ref. [18] for illustrative examples. Here, we use the generic function ξ because different choices of ξ will be made in Section 4. In what follows, we will discuss two related methods for constructing emulators from Eq. 17, which states the physics problem in a *strong form* (*i.e.*, Eq. 17 holds for each point in the domain and on the boundary). The first begins by finding a variational principle whose stationary solution implies Eq. 17. The second instead constructs the corresponding *weak form* of Eq. 17.

3.1 Variational principles

Variational principles (VPs) have a long history in physics and play a central role in a wide range of applications; *e.g.*, for deriving equations of motion using stationary-action principles and Euler–Lagrange equations in classical mechanics (see, *e.g.*, Ref. [81] for a historical overview). Here, we use VPs as an alternate way of solving the differential Eq. 17.

Variational principles are based on scalar functionals of the form

$$\mathcal{S}[\xi] = \int_\Omega \mathrm{d}\Omega\, F[\xi] + \int_\Gamma \mathrm{d}\Gamma\, G[\xi], \tag{18}$$

where F and G are differential operators. Many differential Eq. 17 can be solved by finding stationary solutions of a corresponding functional Eq. 18; *i.e.*, the solution $\xi_\star$ that leads to $\delta\mathcal{S}[\xi_\star] = 0$.

However, VPs can also lead straightforwardly to a reduced-order model. This follows from the following trial ansatz

$$|\tilde{\xi}\rangle \equiv \sum_{i=1}^{n_b} \beta_i |\xi_i\rangle = X\vec{\beta}, \tag{19a}$$
$$X \equiv \left[\, |\xi_1\rangle \;\; |\xi_2\rangle \;\; \cdots \;\; |\xi_{n_b}\rangle \,\right], \tag{19b}$$

with the to-be-determined coefficients vector $\vec{\beta}$. Rather than stipulate that $\delta\mathcal{S} = 0$ for any arbitrary variation $\delta\xi$, we instead extract the optimal coefficients, $\vec{\beta}_\star$, as those for which $\mathcal{S}$ is stationary under variations in $\vec{\beta}$:[6]

$$\delta\mathcal{S} = \sum_{i=1}^{n_b} \frac{\partial\mathcal{S}}{\partial\beta_i}\delta\beta_i = 0. \tag{20}$$

6 For simplicity we consider ξ to be a real variable; for complex variables, independent variations $\delta\vec{\beta}^*$ should be included in the discussion

The general case would involve a numerical search for the solution to Eq. 20 but if $\mathcal{S}$ is quadratic in ξ, as are all the examples considered here, then the solution can be determined exactly. In this case, $\mathcal{S}$ can be written as

$$\mathcal{S}[\vec{\beta}] = \frac{1}{2}\vec{\beta}^{\top} A\vec{\beta} + \vec{b}\cdot\vec{\beta} + c \tag{21}$$

for some matrix A, vector $\vec{b}$, and scalar c. Symmetrizing the quadratic portion—if it is not already symmetric—by rewriting $A \leftarrow (A + A^{\top})/2$ can be desirable for numerical purposes. It then follows that the optimal coefficients, $\vec{\beta}_\star$ are those for which

$$\delta\mathcal{S} = A\vec{\beta}_\star + \vec{b} = 0, \tag{22}$$

which can be solved for $\vec{\beta}_\star$ using standard linear algebra methods. Solving for $\vec{\beta}_\star$ occurs only in a space of size n_b, the number of basis elements $\{\xi_i\}_{i=1}^{n_b}$, rather than in the much larger space of ξ itself. Therefore, as long as $\{\xi_i\}_{i=1}^{n_b}$ approximately spans the space in which ξ lives, the trial function constructed by Eqs. 19a and 22 will be both a fast and accurate emulator of ξ.

Similar to the discussion in Section 2.1, the matrix A in Eq. 22 may be ill-conditioned and require regularization. A nugget $\nu \ll 1$ can be added to the diagonal elements of A to help stabilize the solution for $\vec{\beta}_\star$ [54, 55].

3.2 Galerkin emulators

The Galerkin approach, also more broadly called the "method of weighted residuals," relies on the *weak* formulation of the differential Eq. 17. To obtain the weak form, the differential equation and boundary condition (in Eq. 17) are left-multiplied by arbitrary test functions ζ and $\bar{\zeta}$ and integrated over the domain and boundary, respectively, and then their sum is set to zero:

$$\int_\Omega \mathrm{d}\Omega\, \zeta D(\xi) + \int_\Gamma \mathrm{d}\Gamma\, \bar{\zeta} B(\xi) = 0. \tag{23}$$

If Eq. 23 holds for all ζ and $\bar{\zeta}$, then Eq. 17) must be satisfied as well. The form of Eq. 23 is often rewritten using integration by parts to reduce the order of derivatives and simplify the solution. Importantly, the weak form has the integral form needed for our emulator application. The weak form and its Galerkin projection are used extensively, *e.g.*, in the finite element method; see Refs. [82–84] for an in-depth study and examples. For a discussion of the convergence properties of the Galerkin method, its relation to abstract variational problems, and other salient mathematical details, see Refs. [64, 85–87]. Here, we follow the introduction of Galerkin methods as provided in Ref. [82].

Starting with the weak form, we can construct an emulator that avoids the need for an explicit variational principle. It begins by first noting that substituting our trial function Eq. 4 into $D(\xi)$ and $B(\xi)$ will not, in general, satisfy Eq. 17 regardless of the choice of $\vec{\beta}$. Therefore, there will be some *residual*, and the goal is to find the $\vec{\beta}_\star$ which minimizes that residual across a range of test functions ζ and $\bar{\zeta}$. This system would be over-determined in the case of truly arbitrary test functions, so instead, we propose the test bases

$$|\zeta\rangle = \sum_{i=1}^{n_b} \delta\beta_i |\zeta_i\rangle, \qquad |\bar{\zeta}\rangle = \sum_{i=1}^{n_b} \delta\beta_i |\bar{\zeta}_i\rangle, \tag{24}$$

where $\delta\beta_i$ are arbitrary parameters, not related to the β_i in Eq. 19a. The $\delta\beta_i$ will play the same role as those in Eq. 20, namely as a bookkeeping method for determining the set of equations that are equivalently zero. By enforcing that the residuals against these test functions vanish for arbitrary $\delta\beta_i$, the bracketed expression in

$$\delta\beta_i \left[\int_\Omega \mathrm{d}\Omega\, \zeta_i D\big(X\vec{\beta}_\star\big) + \int_\Gamma \mathrm{d}\Gamma\, \bar{\zeta}_i B\big(X\vec{\beta}_\star\big) \right] = 0, \tag{25}$$

is zero for all $i \in [1, n_b]$, from which the optimal $\vec{\beta}_\star$ are extracted. Because this approximately satisfies the weak formulation, we have found an approximate solution to Equation (17).

In a variety of cases [82], the subspace $\mathcal{Z}$ spanned by the test function basis is chosen to coincide with the subspace $\mathcal{X}$ spanned by the trial function basis X; *i.e.*, $\mathcal{Z} = \mathcal{X}$. This particular choice is known as *the* Galerkin method, but it is sometimes further specified as the Ritz–Galerkin or Bubnov–Galerkin methods. The Galerkin method is more general than the variational methods described in Section 3.1 because the test space need not be equivalent to the trial space (*i.e.*, $\mathcal{Z} \neq \mathcal{X}$). In these cases, the approach is described as the Petrov–Galerkin method [82]; this can result in more efficient emulators for some differential equations (84).

4 Scattering emulators

In this Section, we describe various reduced-basis emulators one could construct for quantum scattering systems. Throughout, we note how the variational principles used to construct emulators in recent works are related [30–33, 88]. We also describe how each of the results from VPs could instead be derived from Galerkin projections.

For scattering problems, the Equation 1 is no longer an eigenvalue problem. The task is to solve the differential equation for the wave function at a given energy E rather than searching for discrete energies with normalizable wave functions. Differential equations are well studied in the field of MOR, where parametric reduced-order models have been constructed with great success across a multitude of fields [44, 89]. This is a relatively mature field whose formal results are quite extensive. For example, UQ for the RBM has been well studied, along with the development of effective algorithms for choosing the best training points [64, 76, 77, 90].

One can formulate the Schrödinger equation in multiple ways, including any flavor of Lippmann-Schwinger (LS) integral equation (which builds in boundary conditions) or as a differential equation in either homogeneous or inhomogeneous form. This freedom, along with the freedom of trial and test bases for the Galerkin projection, leads to multiple alternative emulators that one could construct for quantum scattering systems. For simplicity, we restrict our discussion to two-body scattering for Hermitian Hamiltonians. (See, however, Section 4.6.2 for an extension to higher-body systems.) As a concise reference, we provide Table 1 to show the connections between the fundamental differential or integral equations, variational principles, and Galerkin projections. This section thus provides multiple distinct examples of using Galerkin projections to create emulators, which may prove useful to newcomers wishing to apply model reduction to their own systems, and ends with an example for an emulator applied to a separable potential.

TABLE 1 Description of common variational principles (VPs) in quantum scattering, and how to relate them to a Galerkin projection. The quantities are defined as the free wave function $|\phi\rangle$, the full wave function $|\psi\rangle$, the scattered wave function $|\chi\rangle$, and the reactance matrix K along with its on-shell form K_E. Tildes denote trial quantities. The expressions for the Newton VP are written in operator rather than scalar form; any matrix element can be made individually stationary (see Section 4.4 for details). To compute the weak form of the Schwinger and Newton VPs, one must first left multiply by $V(\boldsymbol{\theta})$ and G_0, respectively, before orthogonalizing against the test basis. The rightmost column specifies whether a constraint for the trial wave function has to be imposed (*e.g.*, using a Lagrange multiplier λ).

Variational principle		Galerkin projection information			
Name	Functional for K	Strong form	Trial basis	Test basis	Constrained?
Kohn (λ)	$\tilde{K}_E + \langle\tilde{\psi}\|H - E\|\tilde{\psi}\rangle$	$H\|\psi\rangle = E\|\psi\rangle$	$\|\psi_i\rangle$	$\langle\psi_i\|$	Yes
Kohn (No λ)	$\langle\tilde{\chi}\|H - E\|\tilde{\chi}\rangle + \langle\phi\|V\|\tilde{\chi}\rangle$ $+\langle\phi\|H - E\|\phi\rangle + \langle\tilde{\chi}\|V\|\phi\rangle$	$[E-H]\|\chi\rangle = V\|\phi\rangle$	$\|\chi_i\rangle$	$\langle\chi_i\|$	No
Schwinger	$\langle\tilde{\psi}\|V\|\phi\rangle + \langle\phi\|V\|\tilde{\psi}\rangle$ $-\langle\tilde{\psi}\|V - VG_0V\|\tilde{\psi}\rangle$	$\|\psi\rangle = \|\phi\rangle + G_0V\|\psi\rangle$	$\|\psi_i\rangle$	$\langle\psi_i\|$	No
Newton	$V + VG_0\tilde{K} + \tilde{K}G_0V$ $-\tilde{K}G_0\tilde{K} + \tilde{K}G_0VG_0\tilde{K}$	$K = V + VG_0K$	K_i	K_i	No

4.1 Constrained Kohn emulators

The Kohn variational principle (KVP) [91, 92] is one of the most well-known VPs for quantum scattering systems. Here we focus on the KVP flavor that relates a trial wave function to the reactance matrix K. However, alternative flavors exist for other matrices such at $T^{\pm}$ and S (see Section 4.6). Analogously to the Ritz VP for bound states, the KVP then allows us to guess effective wave functions by finding those that make the KVP stationary. This Section will discuss a style of KVP emulator that relies on the homogeneous Schrödinger equation, which requires a normalization constraint during emulation; an alternative style without such a constraint will be discussed in Section 4.2.

We start with a rescaled version of the KVP discussed in Ref. [30]:

$$\mathcal{K}[\tilde{\psi}] = \tilde{K}_E + \langle\tilde{\psi}|H - E|\tilde{\psi}\rangle, \tag{26}$$

where $|\tilde{\psi}\rangle$ is the trial wave function (denoted by $|\tilde{\xi}\rangle$ in Section 3) and $\tilde{K}_E \equiv \sum_i \beta_i K_{E,i}$ the associated on-shell trial K matrix with on-shell energy $E = q^2/2\mu$. This flavor of KVP applies when ψ satisfies the asymptotic normalization condition in position space

$$\psi_\ell(r) \xrightarrow[r\longrightarrow\infty]{} j_\ell(qr) + n_\ell(qr)\tan\delta_\ell, \tag{27}$$

where $\phi(r) = j_\ell(qr)$ is the (regular) free-space wave function, and $j_\ell(qr)$ and $n_\ell(qr)$ are spherical Bessel and Neumann functions, respectively. [7] Note that we define the on-shell K_E matrix as

$$K_E = -\frac{\tan\delta_\ell}{2\mu q}, \tag{28}$$

which differs from the convention in Ref. [30]. The KVP is stationary about exact solutions ψ, such that $\mathcal{K}[\psi + \delta\psi] = K_E + \mathcal{O}(\delta K)^2$.

Eq. 26 can be cast into the form of the generic functional (Eq. 18) by noting that, in position space,

$$\begin{aligned}\int_\Gamma \mathrm{d}\Gamma\, G[\tilde{\psi}] \to G[\tilde{\psi}]\big|_{r=0}^{\infty} &\equiv \frac{W(r\phi, r\tilde{\psi}; r)}{2\mu}\bigg|_{r=0}^{\infty} \\ &= \tilde{K}_E,\end{aligned} \tag{29}$$

which has defined the surface functional G in Eq. 18 and where we have used the Wronskian

$$W(\phi, \psi; r) \equiv \phi(r)\psi'(r) - \phi'(r)\psi(r). \tag{30}$$

Both $r\phi(r)$ and $r\tilde{\psi}(r)$ vanish at $r = 0$ so only the limit of $r \to \infty$ contributes, from which we can use Eq. 27 when evaluating Eq. 29.

Because the Schrödinger equation is a linear, homogeneous differential equation, the normalization of $r\psi(r)$ is proportional to its derivative at, say, $r = 0$. Therefore, a constraint on the normalization of ψ is equivalent to a boundary condition on ψ'. However, to satisfy this boundary condition we must include a constraint on Eq. 26 if we are to ensure that the trial function $\tilde{\psi}$ continues to satisfy the normalization condition of Eq. 27. If we assume that each snapshot ψ_i satisfies Eq. 27, then

$$\tilde{\psi}_\ell(r) = \left[\sum_i \beta_i\right] j_\ell(qr) + n_\ell(qr) \sum_i \beta_i \tan\delta_{\ell,i}, \tag{31}$$

whose first term implies that we must impose the constraint $\sum_i \beta_i = 1$.

We are now in a position to find the $\vec{\beta}$ that make Eq. 26 stationary. If we insert the definition of $\tilde{\psi}$ and $\tilde{K}$ into Eq. 26, along with the Lagrange multiplier, we have (with repeated indices indicating summations)

$$\mathcal{K}[\vec{\beta}] = \beta_i K_{E,i} + \frac{1}{2}\beta_i \Delta\tilde{U}_{ij}\beta_j + \lambda\left[\sum_i \beta_i - 1\right], \tag{32}$$

where we define $V_i = V(\boldsymbol{\theta}_i)$ and

$$\begin{aligned}\Delta\tilde{U}_{ij} &\equiv \langle\psi_i|H - E|\psi_j\rangle + (i \leftrightarrow j) \\ &= \langle\psi_i|V(\boldsymbol{\theta}) - V_j|\psi_j\rangle + (i \leftrightarrow j).\end{aligned} \tag{33}$$

In the second line we have used that the $|\psi_j\rangle$ are eigenstates with the corresponding V_j. If $V(\boldsymbol{\theta})$ is affine in $\boldsymbol{\theta}$, then $\Delta\tilde{U}$ can be projected once in the emulator's offline stage, and reconstructed quickly during the online stage.

7 We focus here on examples with real-valued potentials and without long-range Coulomb interactions. Cases with complex-valued potentials and/or the Coulomb interaction may be analyzed in similar ways; relevant discussions specific to Kohn emulators can be found in Refs. [30, 32].

Now we can follow the steps outlined in Section 3.1 to determine $\vec{\beta}_\star$. Taking the gradient of Eq. 32 with respect to $\vec{\beta}$ and setting it equal to 0 yields

$$\vec{K}_E + \Delta\tilde{U}\vec{\beta}_\star + \lambda_\star = 0, \tag{34}$$

where $\vec{K}_E$ are the n_b on-shell K-matrices used to train the emulator, and $\vec{\beta}_\star$ are the optimal coefficients of the trial wave function. The gradient with respect to λ simply returns the constraint. This system can be solved *via* the system of equations

$$\begin{bmatrix} \Delta\tilde{U} & \vec{1} \\ \vec{1}^{\,\top} & 0 \end{bmatrix} \begin{bmatrix} \vec{\beta}_\star \\ \lambda_\star \end{bmatrix} = \begin{bmatrix} -\vec{K}_E \\ 1 \end{bmatrix}, \tag{35}$$

where $\vec{1}$ is an $n_b \times 1$ vector of ones. If the n_b number of basis functions is much smaller than the size of ψ, then Eq. 35 can be a highly computationally efficient emulator for scattering systems and requires little computer memory to store. The on-shell K matrix can then be emulated *via*

$$K_E \approx \mathcal{K}\left[\vec{\beta}_\star\right] = \vec{\beta}_\star \cdot \vec{K}_E + \frac{1}{2}\vec{\beta}_\star^{\,\top}\Delta\tilde{U}\vec{\beta}_\star, \tag{36}$$

whose operations all occur quickly in the size-n_b space during the online stage.

The derivation above followed closely that of Refs [30, 93], but one could instead arrive at exactly Eq. 35 from a Galerkin projection [43]. Rather than begin with the VP, we start here with (the *strong form* of) the homogeneous Schrödinger equation, *i.e.*, $H(\boldsymbol{\theta})|\psi\rangle = E|\psi\rangle$. To construct the weak form, we multiply with a test function $|\zeta\rangle$ and assert that the residual vanishes:

$$\langle\zeta|H - E|\psi\rangle = 0, \qquad \forall|\zeta\rangle. \tag{37}$$

To make explicit the boundary conditions, we make use of the relation

$$\begin{aligned} 0 &= \langle\zeta|H - E|\psi\rangle \\ &= \langle\zeta|\overleftarrow{H} - E|\psi\rangle - \frac{W(r\zeta, r\psi; r)}{2\mu}\bigg|_{r=0}^{\infty}, \end{aligned} \tag{38}$$

where we have again used the Wronskian from Eq. 30, and assigned $\overleftarrow{H}$ as the operator acting, after integration by parts, on $\langle\zeta|$ instead of $|\psi\rangle$. By adding Eqs. 38 and 37, we have

$$\langle\zeta|H - E|\psi\rangle + \langle\zeta|\overleftarrow{H} - E|\psi\rangle = \frac{W(r\zeta, r\psi; r)}{2\mu}\bigg|_{r=0}^{\infty}. \tag{39}$$

This is the weak form of the homogeneous Schrödinger equation that we will use to construct the emulator, although the asymptotic normalization condition Eq. 27 still needs to be enforced. This will be imposed *via* a Lagrange multiplier after inserting our trial basis.

Now that we have a weak form, the next step to construct the reduced-order model equations is to define our trial and test bases to project the weak form into the finite space of these bases. To align with the Kohn emulator from the variational argument above, we choose the trial and test basis to be identical as snapshots ψ_i. Then we can evaluate

$$\frac{W(r\psi_i, r\psi_j; r)}{2\mu}\bigg|_{r=0}^{\infty} = K_j - K_i \tag{40}$$

and thus, it follows after including the Lagrange multiplier that

$$\lambda + \left[\langle\psi_i|H - E|\psi_j\rangle + \langle\psi_i|\overleftarrow{H} - E|\psi_j\rangle\right]\beta_j = \sum_j \beta_j K_j - K_i \sum_j \beta_j. \tag{41}$$

The sum in the rightmost term can be evaluated using the constraint $\sum_j \beta_j = 1$, and we can make the redefinition $\lambda' \equiv \lambda - \sum_j \beta_j K_j$ without impacting the solution because this term does not depend on i. Thus, we have

$$\lambda' + \vec{K}_E + \Delta\tilde{U}\vec{\beta}_\star = 0, \tag{42}$$

which is exactly Eq. 34 found by making the KVP stationary. This simplification can be understood by noting that if $\{\vec{\beta}_\star, \lambda_\star\}$ satisfy Eq. 41, then we know that $\{\vec{\beta}_\star, \lambda'_\star\}$ is the unique solution to Eq. 42. Therefore, we can solve Eq. 42 to obtain $\vec{\beta}_\star$ rather than Eq. 41. In conclusion, using the Galerkin projection of the homogeneous Schrödinger equation with trial and test bases of ψ_i, we were able to obtain the same coefficients as the KVP in Eq. 35, which yield the same on-shell K matrix when used in Eq. 36.

4.2 Unconstrained Kohn emulators

The Kohn emulators from Section 4.1 start with the homogeneous Schrödinger equation, which does not enforce any specific normalization of the wave function; hence this requirement needs to be enforced at the time of emulation. This effectively takes the n_b degrees of freedom $\{\psi_i\}$—which were potentially costly to obtain—and reduces the degrees of freedom to n_b–1. However, one can instead build in the normalization from the very start, thus removing the need to constrain our basis *via* $\sum_{j=1}^{n_b}\beta_j = 1$ during emulation. The unconstrained emulator is fundamentally different from any approach that constrains the coefficients (*e.g.*, explicit substitution of $\beta_1 = 1 - \sum_{j=2}^{n_b}\beta_j$), regardless of if a Lagrange multiplier is explicitly used as in Section 4.1. This is the topic of the current section.

The full wave function $|\psi\rangle$ can be written as the sum of the free wave function $|\phi\rangle$ and the scattered wave $|\chi\rangle$, that is, $|\psi\rangle = |\phi\rangle + |\chi\rangle$. Thus, we can rewrite the KVP as

$$\begin{aligned} \mathcal{K} &= K + \langle\psi|[H - E]|\psi\rangle \\ &= K + \langle\chi|[H - E]|\chi\rangle + \langle\phi|[H - E]|\chi\rangle \\ &\quad + \langle\phi|[H - E]|\phi\rangle + \langle\chi|[H - E]|\phi\rangle \\ &= \langle\chi|[H - E]|\chi\rangle + \langle\phi|V|\chi\rangle + \langle\phi|[H - E]|\phi\rangle + \langle\chi|V|\phi\rangle, \end{aligned} \tag{43}$$

where we used (*via* integration by parts)

$$\langle\phi|[H - E]|\chi\rangle - \langle\phi|\left[\overleftarrow{H} - E\right]|\chi\rangle = -K. \tag{44}$$

We choose our trial function as $|\tilde{\chi}\rangle$, which always enforces the normalization condition $|\tilde{\psi}\rangle = |\phi\rangle + |\tilde{\chi}\rangle$, and so no additional constraint needs to be included in the variational principle.

Now we can construct the set of linear equations that makes Eq. 43 stationary in $|\tilde{\chi}\rangle = \sum_i \beta_i|\chi_i\rangle$. By taking the gradient with respect to β_i, we find

$$\Omega\vec{\beta}_\star = \vec{\omega}, \tag{45}$$

where

$$\Omega_{ij} = \langle\chi_i|[E-H]|\chi_j\rangle, \tag{46a}$$
$$\omega_i = \langle\chi_i|V|\phi\rangle, \tag{46b}$$

which is the set of equations used to obtain $\vec{\beta}_\star$. The matrix elements Ω_{ij} can be evaluated with the help of

$$\begin{aligned}[E-H]|\chi_j\rangle &= \big[E-H_j\big]|\chi_j\rangle + \big[V_j - V\big]|\chi_j\rangle \\ &= V_j|\phi\rangle + \big[V_j - V\big]|\chi_j\rangle,\end{aligned} \tag{47}$$

with $H_j = H(\boldsymbol{\theta}_j)$ and $V_j = V(\boldsymbol{\theta}_j)$.

An equivalent approach follows from a Galerkin orthogonalization procedure. We begin by writing the homogeneous Schrödinger equation in inhomogeneous form using $|\psi\rangle = |\phi\rangle + |\chi\rangle$:

$$[E-H]|\chi\rangle = V|\phi\rangle. \tag{48}$$

We can construct the weak form by multiplying by a generic test function $|\zeta\rangle$, which yields

$$\langle\zeta|E-H|\chi\rangle = \langle\zeta|V|\phi\rangle. \tag{49}$$

Next, we insert the trial function $|\tilde{\chi}\rangle$ and choose the test basis of $\{|\chi_i\rangle\}_i$, which is the same as the trial basis. This yields a reduced weak form that is identical to Eq. 45.

We have shown that the coefficients $\vec{\beta}_\star$ found *via* the appropriate Galerkin procedure aligns exactly with the KVP. However, we can go one step further and in fact derive an estimate for the K matrix that is equivalent to $\mathcal{K}[\vec{\beta}_\star]$. By inserting the optimal coefficients into $K|\phi\rangle = V|\psi\rangle$,

$$\begin{aligned}\langle\phi'|K|\phi\rangle &\approx \langle\phi'|V|\phi\rangle + \langle\phi'|V|\tilde{\chi}\rangle \\ &= \langle\phi'|V|\phi\rangle + \sum_{ij}\langle\phi'|V|\chi_i\rangle\Big[\left(\Omega^{-1}\right)_{ij}\langle\chi_j|V|\phi\rangle\Big],\end{aligned} \tag{50}$$

with the factors in brackets equating to β_i using Eq. 45. The equivalence to the KVP is demonstrated in Refs. [94, 95].

4.3 Schwinger emulators

The Schwinger variational principle (SVP) is given by [94].

$$\mathcal{K}[\tilde{\psi}] = \langle\tilde{\psi}|V|\phi\rangle + \langle\phi|V|\tilde{\psi}\rangle - \langle\tilde{\psi}|V - VG_0V|\tilde{\psi}\rangle, \tag{51}$$

where G_0 is the Green's operator. This too has the stationary property $\mathcal{K}[\psi+\delta\psi] = K + \mathcal{O}(\delta K)^2$ when ψ is a wave function satisfying the LS equation. Following the MOR philosophy and inserting a trial function $\tilde{\psi}$, the stationary condition becomes

$$W\vec{\beta}_\star = \vec{w}, \tag{52}$$

where

$$W_{ij} = \langle\psi_i|V - VG_0V|\psi_j\rangle \tag{53a}$$
$$w_i = \langle\psi_i|V|\phi\rangle, \tag{53b}$$

for all $i \in [1, \ldots, n_b]$.

The system of Eq. 52 can also be determined by a Galerkin projection procedure. In this case, we start with the LS equation for wave functions,

$$|\psi\rangle = |\phi\rangle + G_0V|\psi\rangle, \tag{54}$$

and create a weak form by left-multiplying by $V(\boldsymbol{\theta})$ along with the test function $|\zeta\rangle$:

$$\langle\zeta|V|\psi\rangle = \langle\zeta|V|\phi\rangle + \langle\zeta|VG_0V|\psi\rangle. \tag{55}$$

The weak form can then be converted to its discrete form by setting $\psi \to \tilde{\psi}$ and enforcing orthogonality against $|\zeta_i\rangle = |\psi_i\rangle$ for $i \in [1, \ldots, n_b]$. [8] This yields then Eq. 52, and so the coefficients found by making Eq. 51 stationary are indeed identical to those found *via* the Galerkin procedure for Eq. 54.

Using the emulation of ψ, which is calculated by inserting the optimal coefficients obtained from Eq. 52 into the definition of $\tilde{\psi}$, we can get the associated K through

$$\begin{aligned}\langle\phi'|K|\phi\rangle &= \langle\phi'|V|\psi\rangle \\ &\approx \langle\phi'|V|\tilde{\psi}\rangle \\ &= \sum_{ij}\langle\phi'|V|\psi_i\rangle\left(W^{-1}\right)_{ij}\langle\psi_j|V|\phi\rangle.\end{aligned} \tag{56}$$

This Equation is exactly the solution for K found *via* the LS equation while assuming a finite-rank approximation for V:

$$V^f = \sum_{ij} V|\psi_i\rangle\Lambda_{ij}\langle\psi_j|V, \tag{57}$$

where

$$\left(\Lambda^{-1}\right)_{ij} = \langle\psi_i|V|\psi_j\rangle. \tag{58}$$

It is known that the SVP yields a K matrix that is equivalent to that found *via* a finite-rank approximation to V [94, 95], which shows that the Galerkin projection described in this Section is identical to the SVP.

4.4 Newton emulators

The Newton variational principle (NVP) for the K matrix is given by [31, 96].

$$\mathcal{K}\big[\tilde{K}\big] = V + VG_0\tilde{K} + \tilde{K}G_0V - \tilde{K}G_0\tilde{K} + \tilde{K}G_0VG_0\tilde{K}, \tag{59}$$

where $\tilde{K}$ is a trial matrix. If desired, one could instead emulate $T^{(\pm)}$ by imposing the associated boundary conditions on G_0. Here it is assumed that we have chosen an on-shell energy E, which will remain implicit throughout. A separate emulator can be constructed for each choice of E. The functional Eq. 59 is stationary about exact solutions of the LS equation, *i.e.*, $\mathcal{K}[K+\delta K] = K + (\delta K)^2$. If we write the trial matrix as a linear combination of exact snapshots

$$\tilde{K} = \sum_{i=1}^{n_b}\beta_iK_i, \tag{60}$$

then we can construct an emulator of the K matrix in the spirit of the RBM.

Unlike some of the VPs discussed so far, the NVP is written here in operator form, without yet projecting it into a basis. This gives us

8 Note that left-multiplying by $V(\boldsymbol{\theta})$ and enforcing orthogonality against $|\zeta_i\rangle = |\psi_i\rangle$ is different than simply defining $|\zeta\rangle = V|\psi\rangle$ and enforcing orthogonality against $|\zeta_i\rangle = V_i|\psi_i\rangle$ because $V(\boldsymbol{\theta})$ depends on $\boldsymbol{\theta}$. Thus, this is indeed a purely Galerkin approach, rather than a Petrov-Galerkin approach

the freedom to assert that any component $\langle\phi'|\mathcal{K}|\phi\rangle$ constructed from Eq. 59 is stationary, which yields an emulator for $\langle\phi'|K|\phi\rangle$. For example, one could choose $|\phi\rangle$ to be a plane-wave partial-wave basis $|k\ell m\rangle$ with momentum k and angular momentum quanta (l, m), or one could keep the angular dependence explicit *via* $|\phi\rangle = |\mathbf{k}\rangle$ in a single-particle basis. Coupled channels could be emulated by choosing the angular momentum quanta differently between $|\phi'\rangle$ and $|\phi\rangle$. In fact, the NVP does not even require $|\phi\rangle$ and $|\phi'\rangle$ to be free-space states; one can impose stationarity of Eq. 59 between any two states due to its operator form. Note that the *independent* coefficients $\vec{\beta}$ are found for each choice of $|\phi'\rangle$ and $|\phi\rangle$. Thus, in the case of coupled partial waves, for example, each channel is emulated independently. To compute phase shifts, we must emulate K at the on-shell energy $E = q^2/2\mu$ and thus, $k = k' = q$ for $|\phi\rangle = |k\ell m\rangle$ and $\langle\phi'| = \langle k'\ell' m'|$.

Expressed in the chosen basis, simplifying the functional Eq. 59 after inserting Eq. 60 yields [31]

$$\langle\phi'|\mathcal{K}\big(\boldsymbol{\theta},\vec{\beta}\big)|\phi\rangle = \langle\phi'|V(\boldsymbol{\theta})|\phi\rangle + \vec{\beta}^{\top}\vec{m}(\boldsymbol{\theta}) - \frac{1}{2}\vec{\beta}^{\top}M(\boldsymbol{\theta})\vec{\beta}, \tag{61}$$

with

$$m_i(\boldsymbol{\theta}) = \langle\phi'|[K_i G_0 V(\boldsymbol{\theta}) + V(\boldsymbol{\theta}) G_0 K_i]|\phi\rangle, \tag{62a}$$

$$M_{ij}(\boldsymbol{\theta}) = \langle\phi'|\big[K_i G_0 K_j - K_i G_0 V(\boldsymbol{\theta}) G_0 K_j\big]|\phi\rangle + (i \leftrightarrow j). \tag{62b}$$

If the potential $V(\boldsymbol{\theta})$ has an affine parameter dependence, $\vec{m}$ and M can be efficiently constructed by linear combinations of matrices pre-computed during the emulator's offline stage, resulting in substantial improvements in CPU time, *e.g.*, for chiral interactions.

By imposing the stationary condition $\partial\mathcal{K}/\partial\vec{\beta} = 0$, one then finds $\vec{\beta}_\star(\boldsymbol{\theta})$ such that $M\vec{\beta}_\star = \vec{m}$. Given that the optimal $\vec{\beta}_\star(\boldsymbol{\theta})$ yields a trial matrix Eq. 60 with an error δK, one can insert $\vec{\beta}_\star$ in Eq. 61 to obtain an error $(\delta K)^2$. The resulting emulator $\mathcal{K}_\star(\boldsymbol{\theta}) \equiv \mathcal{K}(\boldsymbol{\theta},\vec{\beta}_\star)$ is then [31]

$$\langle\phi'|K|\phi\rangle \approx \langle\phi'|\mathcal{K}|\phi\rangle = \langle\phi'|V|\phi\rangle + \frac{1}{2}\vec{m}^{\top}M^{-1}\vec{m}. \tag{63}$$

Reference [31] studied several applications of the emulator Eq. 63 to short-range potentials with and without the Coulomb interaction and partial-wave coupling. They demonstrated that the NVP emulator has remarkable extrapolation capabilities (see Figure 2 in Ref. [31]) and can quickly reproduce high-fidelity calculations of neutron-proton cross sections based on modern chiral interactions with negligible error.

We now repeat the derivation for the NVP emulator, but instead from the perspective of a Galerkin projection. Here, we will focus on the case where $\langle\phi'| = \langle\phi|$. We start with the LS equation

$$K = V + VG_0K, \tag{64}$$

which, in this context, constitutes the strong form of the integral equation. Although Eq. 64 is written in terms of abstract operators, it can be turned into a vector equation in a specific representation after right-multiplying by $|\phi\rangle$. To derive the weak form we left-multiply by G_0 and a test function $\langle\zeta|$:

$$\langle\zeta|G_0K - G_0VG_0K|\phi\rangle = \langle\zeta|G_0V|\phi\rangle. \tag{65}$$

The trial function in this case is $K|\phi\rangle$, which can be expanded in a discrete (snapshot) basis using Eq. 60. We further employ the Galerkin prescription, where the test basis is equivalent to the trial basis, making $\langle\zeta_i| = \langle\phi|K_i$. With these assumptions, the reduced weak form becomes

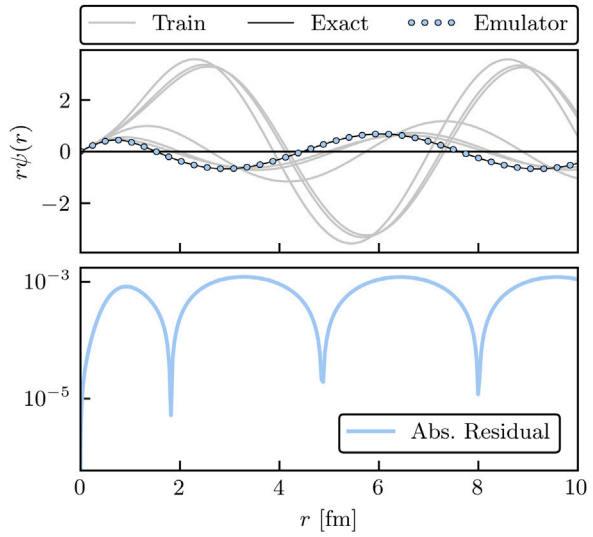

FIGURE 8
Results for the scattering emulator with origin boundary conditions in arbitrary units. Six basis functions are shown as gray lines, and the exact wave function as a black line. Each of the basis functions and the emulated wave function satisfy the constraints at the origin.

$$M\vec{\beta}_\star = \vec{m}, \tag{66}$$

with M and $\vec{m}$ defined in Equation (62), again with $\langle\phi'| = \langle\phi|$. Thus, we find the same $\vec{\beta}_\star$ using either the NVP or the Galerkin projection.

Given the optimal coefficients $\vec{\beta}_\star$, the emulator can be derived by substituting $\tilde{K}$ into the right-hand side of Eq. 64:

$$\begin{aligned}\langle\phi|K|\phi\rangle &\approx \langle\phi|V|\phi\rangle + \langle\phi|VG_0\tilde{K}|\phi\rangle \\ &= \langle\phi|V|\phi\rangle + \frac{1}{2}\vec{m}^{\top}M^{-1}\vec{m},\end{aligned} \tag{67}$$

which is equivalent to Eq. 63 under the assumption that $\langle\phi'| = \langle\phi|$. Therefore, both the NVP and Galerkin projection lead to identical emulators for the K matrix.

4.5 Origin emulators

The scattering emulators discussed so far are best known as VPs but are equivalent to various types of Galerkin projections of the Schrödinger or LS equation (see Table 1). However, other types of emulators can be constructed *via* Galerkin projections, even if they do not necessarily correspond to any well-known VP.

Starting from the Schrödinger equation—a second-order differential equation—we must impose two boundary conditions. The first is that $r\psi(r)$ vanishes at $r = 0$; this constraint has been automatically satisfied by our choice of trial bases in all VPs considered above. But the second constraint is yet to be chosen. In the KVP, for example, the second constraint was obtained *via* the normalization of $r\psi(r)$ as $r \to \infty$, which, in the constrained KVP, led to a normalization constraint for the coefficients β_i. Because the Schrödinger equation is linear and homogeneous, this normalization condition is equivalent to

imposing a constraint on the derivative of $r\psi(r)$, *e.g.*, evaluated at the origin.

Thus, an alternative weak form for the Schrödinger equation could be constructed using only constraints at the origin. Let us construct a coordinate-space emulator with $(r\psi)'(0) = 1$. Starting from the generic weak form (23), we obtain

$$\langle\zeta|H - E|\psi\rangle + \bar{\zeta}\left[(r\psi)' - 1\right]\big|_{r=0} = 0, \tag{68}$$

where ζ and $\bar{\zeta}$ are the (independent) test functions in the domain and on the boundary, respectively, and the boundary condition is only evaluated at the origin. Here, we can make the Galerkin choice of (domain) test functions, where $\langle\zeta| = \langle\psi|$, but make a Petrov-Galerkin choice for the boundary, with $\bar{\zeta}(0) = 1$.

Thus, the discretized weak form, from which our emulator equations follow, is given by

$$\langle\psi_i|H - E|\psi_j\rangle\beta_j + \sum_j \beta_j - 1 = 0, \tag{69}$$

where we have assumed that the trial basis is constructed such that each snapshot satisfies $(r\psi_j)'(0) = 1$.

As an example, we show the output of such an s-wave ($\ell = 0$) emulator in Figure 8. Here, the potential is given by a sum of two Gaussians,

$$V(r, \boldsymbol{\theta}) = \theta_1 \exp\left(-\kappa_1 r^2\right) + \theta_2 \exp\left(-\kappa_2 r^2\right), \tag{70}$$

with $\kappa_1 = 0.5$ and $\kappa_2 = 1$. The parameters to be varied are $\boldsymbol{\theta} = \{\theta_1, \theta_2\}$. The six training and one validation parameters are selected randomly from a uniform distribution in the range of $[-5, 5]$. To obtain the snapshots, the partial-wave decomposed radial Schrödinger equation for $\ell = 0$ can be expressed as the system of coupled first-order differential equations,

$$\begin{pmatrix} y'_0(r) \\ y'_1(r) \end{pmatrix} = \begin{pmatrix} (r\psi)'(r) \\ 2\mu\left[V(r;\boldsymbol{\theta}_i) - E\right](r\psi)(r) \end{pmatrix}, \tag{71}$$

and numerically solved with Runge-Kutta methods. For more details on solving the radial Schrödinger equation and matching the solutions to the asymptotic boundary condition (27), see, *e.g.*, Ref. [97]. As we can see from Figure 8, each training and emulated wave function has matching boundary conditions at the origin, and the discrepancy from the true wave function is less than 10^{-3}.

4.6 General Kohn variational principle

The KVP functional given in Eq. 26 can be extended to include arbitrary boundary conditions [32, 98]. For simplicity, let us consider short-range potentials $V(\boldsymbol{\theta})$ that have been partial-wave decomposed into an uncoupled channel with angular momentum ℓ. The general asymptotic form of the (coordinate-space) radial wave functions will be linear combinations of free-space solutions[9]

$$\psi_{\ell,E}(r) \xrightarrow[r\longrightarrow\infty]{} \bar{\phi}^{(0)}_{\ell,E}(r) + L_{\ell,E}\,\bar{\phi}^{(1)}_{\ell,E}(r), \tag{72}$$

where

$$\begin{pmatrix} \bar{\phi}^{(0)}_{\ell,E}(r) \\ \bar{\phi}^{(1)}_{\ell,E}(r) \end{pmatrix} = \mathcal{N}^{-1}\begin{pmatrix} u_{00} & u_{01} \\ u_{10} & u_{11} \end{pmatrix}\begin{pmatrix} j_\ell(qr) \\ \eta_\ell(qr) \end{pmatrix}, \tag{73}$$

with $q = \sqrt{2\mu E}$ and an arbitrary normalization constant $\mathcal{N} \neq 0$. Here, $L_{\ell,E}$ is a generic scattering matrix that is determined by the boundary condition, as parametrized by the non-singular matrix $\boldsymbol{u}$.

We now define $\mathcal{L}$ as a general functional for the generic L-matrix in Eq. 72 [32, 88, 98],

$$\mathcal{L}[\tilde{\psi}] = L_{\ell,E} + \frac{2\mu\mathcal{N}^2}{q\det\boldsymbol{u}}\langle\tilde{\psi}_{\boldsymbol{u}}|H - E|\tilde{\psi}_{\boldsymbol{u}}\rangle. \tag{74}$$

Note that Eq. 74 is not restricted to coordinate space, e.g., it also holds for scattering in momentum space (see Ref. [88]). With Eq. 26, one can follow the process described in Section 4.1 to emulate any asympototic boundary condition. Obtaining an emulator prediction for different boundary conditions does not mean that Eq. 74 has to be solve multiple times. In fact, it only needs to be solved once and each term in the functional *rescaled* using the relations derived in Ref. [32]:

$$\Delta\tilde{U}^{(\boldsymbol{u}')} = C'^{-1}(L_i)\,C'^{-1}\big(L_j\big)\frac{\det\boldsymbol{u}}{\det\boldsymbol{u}'}\Delta\tilde{U}^{(\boldsymbol{u})}, \tag{75}$$

$$C'(L) = \frac{\det\boldsymbol{u}}{\det\boldsymbol{u}'}\frac{u'_{11} - u'_{10}K(L)}{u_{11} - u_{10}K(L)}. \tag{76}$$

The non-primed terms refer to the initial state and primed terms refer to the final state (explained below). The snapshots used to train the emulator in the offline stage are transformed using the Möbius (or linear fractional) transform

$$L'(L) = \frac{-u'_{01} + u'_{00}K(L)}{u'_{11} - u'_{10}K(L)}. \tag{77}$$

Let us consider solving Eq. 74 using the K-matrix boundary condition, but then wanting a prediction for the T-matrix. We would first rescale $\Delta\tilde{U}$ using Eq. 75. Here, $\boldsymbol{u}$ and $\boldsymbol{u}'$ would correspond to $\boldsymbol{u}_K$ and $\boldsymbol{u}_T$, respectively, given by

$$\boldsymbol{u}_K = \begin{bmatrix} 1 & 0 \\ 0 & 1 \end{bmatrix}, \quad \boldsymbol{u}_T = \begin{bmatrix} 1 & 0 \\ i & 1 \end{bmatrix}. \tag{78}$$

Once $\Delta\tilde{U}^{(\boldsymbol{u}')}$ is calculated and the snapshots transformed from the K- to the T-matrix according to Eq. 77, we apply Eq. 35 to obtain the emulator prediction for the T-matrix. One can also inverse transform the new emulated solution back to its K-matrix equivalent by using

$$K(L) = \frac{u_{01} + u_{11}L}{u_{00} + u_{10}L}. \tag{79}$$

Variational principles may not always provide a (unique) stationary approximation, causing the appearance of spurious singularities known as Kohn (or Schwartz) anomalies [32, 98, 101], which can render applications of VPs ineffective; especially for sampling of a model's parameter space.[10] The appearance of these anomalies depends on the parameters $\boldsymbol{\theta}$ used to train the emulator in the offline stage, the scattering energy, and the evaluation set used in the online stage. However, Ref. [32]

9 We follow the conventions for scattering matrices in Refs. [99, 100]. Thus, the K matrix in this section is dimensionless and defined without the negative sign in Eq. 28.

10 These anomalies are not restricted to the KVP but also appear in other VPs such as the NVP and SVP [102].

demonstrated that a KVP-based emulator that simultaneously emulates an array of KVPs with different boundary conditions can be used to systematically detect and remove these anomalies. The anomalies can be detected by assessing the (relative) consistency of the different emulated results for, *e.g.*, the scattering S-matrix. The results that do not pass the consistency check are discarded and the remaining ones averaged to obtain an anomaly-free estimate of the S matrix (or any other matrix). If all possible consistency checks fail, one can change the basis size of the trial wave function iteratively, which typically shifts the locations of the Kohn anomalies in the parameter space in each iteration. The basic idea for removing Kohn anomalies is general and can be applied to other emulators, including the NVP-based emulator discussed in Section 4.4, as long as multiple scattering boundary conditions can be emulated independently and efficiently. Alternatively, one might also consider comparing the consistency of emulated results obtained from different VPs such as the ones summarized in Table 1.

4.6.1 Generalization to coupled systems

Following Ref. [88], let us now extend the generalized KVP in Section 4.6 to coupled systems, which could be coupled partial-wave or reaction channels. The stationary approximation to the high-fidelity L-matrix then reads

$$\mathcal{L}^{ss'} = \beta_i L_i^{ss'} + \frac{1}{2}\beta_i \Delta\tilde{U}_{ij}^{ss'}\beta_j, \tag{80}$$

where

$$\begin{aligned}\Delta\tilde{U}_{ij}^{ss'} &\equiv \frac{2\mu\mathcal{N}^2}{q\det \boldsymbol{u}}\left[\langle\psi_i^s|H(\boldsymbol{\theta})-E|\psi_j^{s'}\rangle + (i\leftrightarrow j)\right] \\ &= \frac{2\mu\mathcal{N}^2}{q\det \boldsymbol{u}}\left[\langle\psi_i^s|V(\boldsymbol{\theta})-V_j|\psi_j^{s'}\rangle + (i\leftrightarrow j)\right],\end{aligned} \tag{81}$$

with s and s' corresponding to the entrance and exit channels. The uncoupled case is retrieved by replacing $ss' \to \ell$. Solving for $\vec{\beta}$ now proceeds as in Eq. 35 but for a specific choice of ss' channels. Note that the coefficients $\vec{\beta}$ are to be determined *independently* for each ss' pair.

The coefficients are independent because $\mathcal{L}^{ss'}$ is independently stationary for each ss' pair. This becomes apparent when considering how one would solve for the coefficients in the case where there are two uncoupled channels, where $ss' \to \ell$ in Eqs. 80 and 81. Here, each partial wave is completely independent of one another, and thus each VP and their corresponding coefficients $\vec{\beta}$ are independent of one another across values of ℓ. Without loss of generality, let the two channels be labeled as $\ell = 0$ and $\ell = 1$, and let $\vec{\beta}^{(0)}$ and $\vec{\beta}^{(1)}$ denote the independent sets of coefficients found by making each channel's KVP stationary. Now consider adiabatically turning on a coupling between two partial waves: the coefficients $\vec{\beta}^{(0)}$ and $\vec{\beta}^{(1)}$ should remain nearly fixed to their previously uncoupled values, but now there is a new set of coefficients to determine, which one could label as $\vec{\beta}^{(01)}$. Thus, even in the coupled case, there are multiple independent sets of coefficients to determine: one for each pair of incoming and outgoing channels.

An alternative way to understand how the $\vec{\beta}$ enter in the coupled case is to instead start with the Schrödinger equation and enforce (Petrov-)Galerkin orthogonalization as in Section 4.1. For the diagonal channels, the test functions are chosen to have the same outgoing channel as the trial functions, making the procedure of standard Galerkin form. But for the off-diagonal channels, the test functions have a different outgoing channel (s) than the trial functions (s'). Because the basis of test functions differs from the basis of the trial function, this is instead a Petrov–Galerkin approach. The linear equations to be solved are exactly what one would obtain from enforcing stationarity in Eq. 80 for each ss' independently. See Ref. [88] for more information on coupled channel emulation.

4.6.2 Generalizations to higher-body systems

The variational emulators for two-body scattering described so far can be generalized to higher-body scattering. In fact, the KVP, as a powerful method for solving scattering problems, has been applied in developing high-fidelity solvers (as opposed to a KVP-based emulator) for studying three- and four-nucleon systems (*e.g.*, nucleon-deuteron elastic scattering below and above the deuteron break-up threshold) [103, 104].[11] It is then natural to combine the KVP with the variational emulation strategy to develop fast and accurate emulators beyond just two-body scattering.

Here, we follow Ref. [33], which developed KVP-based emulators for three-body systems. We focus on systems of three identical spinless bosons, particularly the elastic scattering between boson and two-boson bound state in the channel without any relative angular momenta and below the bound state's break-up threshold. The corresponding scattering S-matrix can be estimated *via* a variational functional that resembles Eq. 74 in the two-body case:

$$\mathcal{S}[\tilde{\psi}] = S - \frac{i}{3\mathcal{N}^2}\langle\tilde{\psi}|[H-E]|\tilde{\psi}\rangle. \tag{82}$$

Here, S is the S-matrix associated with the trial three-body wave function $|\tilde{\psi}\rangle$, H and E the full Hamiltonian and energy, respectively. The trial wave function has the following asymptotic behavior [33]:

$$\langle R_1, r_1|\tilde{\psi}\rangle \overset{R_1\to\infty}{\to} \frac{\mathcal{N}}{\sqrt{v}}\frac{u_B(r_1)}{r_1 R_1}\left(-e^{-iPR_1} + S\,e^{iPR_1}\right), \tag{83}$$

with R_1, r_1 as one of three different Jacobi coordinate sets; v and P as the relative velocity and momentum between the scattering particles, $\mathcal{N}$ the normalization constant that also appeared in Eq. 82, and $u_B(r_1)$ the radial wave function of the two-body bound state.

The emulation procedure is generally similar to those for two-body emulations. We first collect high-fidelity calculations of $|\tilde{\psi}_i\rangle$ at various points in the Hamiltonian's parameter space during the offline (*i.e.*, training) stage and then use these snapshots as the basis to construct the trial solution (see Eq. 19b) to be used in the variational functional during the online emulation stage. A similar set of the low-dimensional linear equations as in Eq. 35 can be derived to fix the weights β_i. The variational functional with these inputs produce accurate results for the S-matrix at the emulation points [33]. This is all straightforward if we vary only the three-body interactions in $H(\boldsymbol{\theta})$ when exploring its parameter space. If the two-body interactions are also changed, the two-body bound states of those snapshots are different among themselves and therefore the trial wave functions based on Eq. 19b

11 The other high-fidelity solvers in this context solve problems in momentum or coordinate space based on the Faddeev formalism [105–107].

fails to satisfy the asymptotic behavior described in Eq. 83. In Ref. [33], proper modifications were applied to the constructions of the trial wave functions to satisfy the asymptotic condition. The resulting emulator is again a low-dimensional equation system, but the projected $\tilde{H}(\boldsymbol{\theta})$ matrices and the $\Delta\tilde{U}$ matrices lose the affine structure as needed for fast emulation (see Eq. 13). To mitigate this issue, the GP emulation method was employed to interpolate and extrapolate the $\Delta\tilde{U}$'s matrix elements in the parameter space (note that this dependence is much smoother than the parameter dependence of the observables). Other hyperreduction approaches [48] could also be explored in this context.

The results in Ref. [33] are encouraging: the time cost for emulating three-boson scattering is on the order of milliseconds (on a laptop), while the emulation's relative errors vary from 10^{-13} to 10^{-4} depending on the case. It is straightforward to generalize it to elastic scattering above the break-up threshold, but more studies need to be done for emulating the break-up processes and even higher-body systems. Of course, the Fermi statistics, spin and isospin degrees of freedom, and partial waves beyond the s-wave need to be included to realize emulation for realistic three and higher-body scatterings (*e.g.* for three-nucleon systems).

4.7 A scattering example

We have covered the reduced-order models that can be constructed from the Kohn, Schwinger, and Newton VPs, and now we put them into action. This example is given in the context of a rank-n separable potential where simple analytic forms are available for the snapshots. This provides a sandbox to explore many aspects of the RBM for quantum scattering without the complicating details of more realistic systems. All of the source code that generates the results shown here is available to explore on the companion website [20].

Separable potentials lead to simple formulas for the K matrix and the scattering wave function [108]. A rank-n separable potential in momentum space is given by

$$V_\ell = \sum_{ij}^{n} |v_i^\ell\rangle \Lambda_{ij} \langle v_j^\ell|, \tag{84}$$

where $\Lambda_{ij} = \Lambda_{ji}$ are the coefficients of the potential that will be varied during emulation. For simplicity, we consider here only s-wave scattering (*i.e.*, $\ell = 0$). The potential (Eq. 84) leads to an affine structure that lends itself to the offline-online decomposition discussed in Section 3. From the potential (Eq. 84), simple expressions for K and ψ can be derived [109]. For instance, the K matrix is given in operator form by

$$K = \sum_{ijk}^{n} |v_i\rangle \Lambda_{ij} [\mathbb{1} - J\Lambda]^{-1}_{jk} \langle v_k|, \tag{85}$$

with the identity matrix $\mathbb{1}$ and the matrix

$$J_{ij} \equiv \langle v_i | G_0 | v_j \rangle, \tag{86}$$

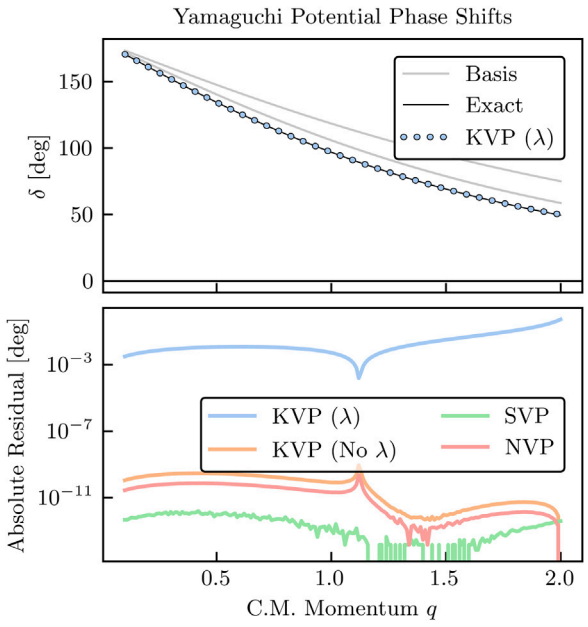

FIGURE 9
Phase shifts (top panel) and absolute residuals (bottom panel) in arbitrary units for the Yamaguchi potential Eq. 87 for each scattering emulator discussed above. The solid black lines represent the high-fidelity solution and the dots represent the emulator results. The emulators are so accurate that they are indistinguishable unless looking at residuals. The training set is given by the two gray lines.

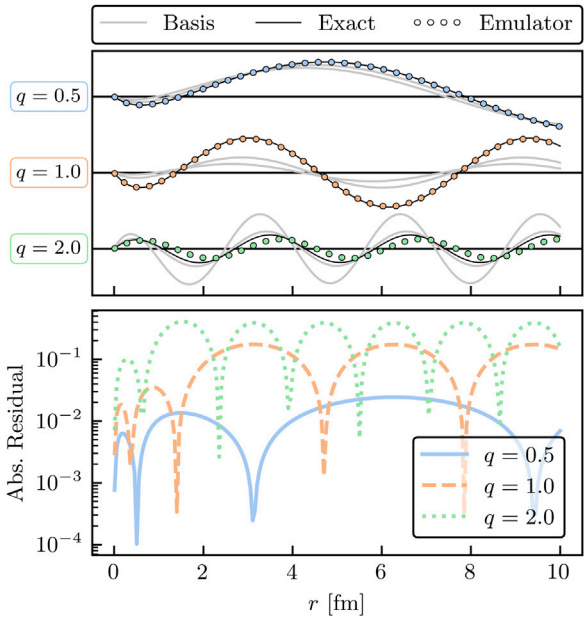

FIGURE 10
Wave functions (top panel) and absolute residuals (bottom panel) for the Yamaguchi potential Eq. 87 in arbitrary units using the constrained KVP. The top panel legend description is similar to Figure 9, but for three different values of q. The bottom panel shows the relative residuals of the three values previously mentioned.

where the Green's function G_0 implicitly depends on the on-shell energy E. Thus, it follows that K is separable if V is separable.

We choose to study the Yamaguchi potential [110].

$$\langle p|v_i^\ell\rangle \equiv v_i^\ell(p) = \frac{p^\ell}{\left(p^2+b_i^2\right)^{\ell+1}} \tag{87}$$

with $\ell = 0$ and assume a rank-2 potential with $b_i = [2, 4]$ and $2\mu = 1$. In this case,

$$J_{ij} = \frac{\pi}{2}\frac{\left(q^2 - b_i b_j\right)}{\left(b_i+b_j\right)\left(q^2+b_i^2\right)\left(q^2+b_j^2\right)}, \tag{88}$$

which permits all phase shifts, wave functions, and reduced-order matrices (*e.g.*, $\Delta\tilde{U}$) to be evaluated analytically. The training parameters $\{\Lambda_{00}, \Lambda_{01}, \Lambda_{11}\}$ are sampled randomly from a uniform distribution in $[-50, 50]$. The companion website [20] provides the following Python classes that implement the scattering emulators: {`Newton`, `Schwinger`, `Kohn`, `UnconstrainedKohn`}`Emulator`.

Figure 9 shows the phase shifts and the absolute residuals for the Yamaguchi potential Eq. 87 for emulators constructed with $n_b = 2$ training points. The top panel depicts the high-fidelity solution (solid black curve) and the emulator results (dots). Here, only the constrained KVP is shown because the others would be indistinguishable. In gray we show the basis states used to train the emulator in the offline stage. The bottom panel shows the absolute residuals for each of the emulators. We can see that all but the constrained KVP are extremely accurate, with the residuals mostly governed by the choice of nugget used to regularize the matrix inversion (see also Section 2.1). For the constrained KVP, we see that the loss of a degree of freedom to implement the constraint significantly impacts its predictive power given that we only have two basis states, although it is still quite accurate in this case. Increasing the basis to $n_b = 5$ yields predictions that are accurate to 10^{-13} degrees, or better, for all emulators.

Figure 10 shows the high-fidelity (solid black line), emulated (dots), and basis (solid gray line) wave functions for three values of q with their absolute residuals using the constrained KVP constructed with $n_b = 5$ training points. The emulator reproduces the high-fidelity solution at all three values of q, with $q = 2.0$ having the smallest residual. The sensitivity of the emulator accuracy as n_b is varied can be readily studied using the Python code provided on the companion website [20]. An example of how the accuracy is affected when varying n_b is also given in Ref. [88].

While all emulators described in this Section are applicable to scattering problems in general, their efficacy will depend in practice on various factors, such as their computational complexity and the potential to be emulated. The constrained KVP has the advantage that terms constant in $\boldsymbol{\theta}$, such as the (long-range) Coulomb potential, cancel in the computation of Eq. 33 but it loses one degree of freedom due to the normalization constraint of the coefficients. On the other hand, both the NVP and SVP involve the computation of Green's functions, which makes them computationally more complex than the KVP—especially the SVP since it also depends quadratically on the potential.

5 Summary and outlook

We have presented a pedagogical introduction to projection-based, reduced-order emulators and general MOR concepts suitable for a wide range of applications in low-energy nuclear physics. Emulators are fast surrogate models capable of reliably approximating high-fidelity models due to their reduced content of superfluous information. By making practical otherwise impractical calculations, they can open the door to the various techniques and applications central to the overall theme of this Frontiers Research Topic [14], such as Bayesian parameter estimation for UQ, experimental design, and many more.

In particular, we have discussed variational and Galerkin methods combined with snapshot-based trial (or test) functions as the foundation for constructing fast and accurate emulators. These emulators enable repeated bound state and scattering calculations, *e.g.*, for sampling a model's parameter space when high-fidelity calculations are computationally expensive or prohibitively slow. A crucial element in this emulator workflow, as summarized in Figure 2, is an efficient offline-online decomposition in which the heavy computational lifting is performed only once before the emulator is invoked. Chiral Hamiltonians allow for such efficient decompositions due to their affine parameter dependence on the low-energy couplings. Furthermore, we discussed the high efficacy of projection-based emulators in extrapolating results far from the support of the snapshot data, as opposed to the GPs.

While MOR has already reached maturity in other fields, it is still in its infancy in nuclear physics—although rapidly growing—and there remains much to explore and exploit [18, 35, 36, 43]. In the following, we highlight some of the many interesting research avenues for emulator applications in nuclear physics. All of these avenues can benefit from the rich MOR literature and software tools available (*e.g.*, see Refs. [1–3]):

- Emulator uncertainties need to be robustly quantified and treated on equal footing with other uncertainties in nuclear physics calculations, such as EFT truncation errors. This will be facilitated by the extensive literature on the uncertainties in the RBM [76, 77, 90, 111].
- The performance of competing emulators (*e.g.*, the Newton vs. Kohn variational principle) is typically highly implementation dependent. Best practices for efficient implementation of nuclear physics emulators should be developed. This may include exploiting MOR software libraries from other fields, such as `pyMOR` [112], when possible.
- Galerkin emulators are equivalent to variational emulators for bound-state and scattering calculations if the test and trial basis are properly chosen. But Galerkin (and especially Petrov-Galerkin) emulators are more general and exploring their applications in non-linear problems may be fruitful in nuclear physics. Emulator applied to non-linear problems will have challenges in terms of both speed and accuracy: 1) the basis size will, in general, need to be large(r) resulting in lower speed-up factors and longer offline stages; 2) using hyperreduction methods will lead to additional approximations that worsen the accuracy of the emulator and whose uncertainties need to be quantified.
- Many technical aspects should be further explored, such as greedy (or active-learning) [24] and SVD-based algorithms for choosing the training points more effectively, hyperreduction methods for non-affine problems, and improved convergence analyses.
- Scattering emulators could play pivotal roles in connecting reaction models and experiments at new-generation rare-

isotope facilities (*e.g.*, the Facility for Rare Isotope Beams). In this regard, further studies on incorporating long-range Coulomb interactions and optical potentials beyond two-body systems will be valuable. Furthermore, emulators for time-dependent density functional theories could see extensive applications in interpreting fission measurements. At facilities such as Jefferson Lab and the future Electron-Ion Collider, explorations of nuclear dynamics at much higher energy scales should also benefit from emulators.

- The emulator framework can be used to extrapolate observables far away from the support of the training data, such as the discrete energy levels of a many-body system calculated in one phase to those of another, as demonstrated in Ref. [22]. Using emulators as a resummation tool to increase the convergence radius of series expansions [26] falls into this category as well, and so does using them to extrapolate finite-box simulations of quantum systems across wide ranges of box sizes [40]. Moreover, for general quantum continuum states, emulation in the complex energy plane can enable computing scattering observables with bound-state methods [113]. Extrapolation capabilities of emulators should be investigated further.
- While projection-based emulators have had successes (*e.g.*, see Refs. [7, 9, 25]), it is also important to understand their limitations and investigate potential improvements. The synergy between projection-based and machine learning methods [114] is a new direction being undertaken in the field of MOR for this purpose (*e.g.*, see Ref. [63]). Nuclear physics problems, with and without time dependence, will provide ample opportunities for such explorations.
- Emulators run fast, often with a small memory footprint, and can be easily shared. These properties make emulators effective interfaces for large expensive calculations, through which users can access sophisticated physical models at a minimum cost of computational resources and without specialized expertise, creating a more efficient workflow for nuclear science. As such, emulators can become a collaboration tool [33, 34] that can catalyze new direct and indirect connections between different research areas and enable novel studies.

To help foster the exploration of these (and other) research directions in nuclear physics, we have created a companion website [20] containing interactive supplemental material and source code so that the interested reader can experiment with and extend the examples discussed here.

We look forward to seeing more of the MOR methodology implemented as these research directions are being pursued. But especially we look forward to the exciting applications of emulators in nuclear physics that are currently beyond our grasp.

Author contributions

All authors listed have made a substantial, direct, and intellectual contribution to the work and approved it for publication.

Funding

This material is based upon work supported by the U.S. Department of Energy, Office of Science, Office of Nuclear Physics, under the FRIB Theory Alliance award DE-SC0013617. This work was supported in part by the National Science Foundation under award numbers PHY-1913069 and PHY-2209442 and the NSF CSSI program under award number OAC-2004601 (BAND Collaboration [115]), and the NUCLEI SciDAC Collaboration under U.S. Department of Energy MSU subcontract RC107839-OSU.

Acknowledgments

We thank the Editors Maria Piarulli, Evgeny Epelbaum, and Christian Forssén for the kind invitation to contribute to this Frontiers Research Topic [14]. We are also grateful to our BUQEYE [19] and BAND [115] collaboration colleagues for sharing their invaluable insights with us, and especially to Pablo Giuliani and Daniel Phillips for fruitful discussions. C.D. thanks Petar Mlinarić for sharing his deep insights into the software library pyMOR [112] for building MOR applications with the Python.

Conflict of interest

The authors declare that the research was conducted in the absence of any commercial or financial relationships that could be construed as a potential conflict of interest.

Publisher's note

References

1. Benner P, Ohlberger M, Patera A, Rozza G, Urban K. *Reduction of parametrized systems*. Berlin, Germany: Springer (2017).

2. Benner P, Cohen A, Ohlberger M, Willcox K. *Reduction and approximation*. Philadelphia, PA: Society for Industrial and Applied Mathematics: Computational Science & Engineering (2017).

3. Benner P, Gugercin S, Willcox K. A survey of projection-based model reduction methods for parametric dynamical systems. *SIAM Rev* (2015) 57:483–531. doi:10.1137/130932715

4. Zhang X, Nollett KM, Phillips DR. Halo effective field theory constrains the solar ^{7}Be + p → ^{8}B + γ rate. *Phys Lett B* (2015) 751:535–40. arXiv:1507.07239. doi:10.1016/j.physletb.2015.11.005

5. Neufcourt L, Cao Y, Nazarewicz W, Olsen E, Viens F. Neutron drip line in the Ca region from bayesian model averaging. *Phys Rev Lett* (2019) 122:062502. arXiv:1901.07632 [nucl-th]. doi:10.1103/physrevlett.122.062502

6. King GB, Lovell AE, Neufcourt L, Nunes FM. Direct comparison between bayesian and frequentist uncertainty quantification for nuclear reactions. *Phys Rev Lett* (2019) 122:232502. arXiv:1905.05072 [nucl-th]. doi:10.1103/physrevlett.122.232502

7. Ekström A, Hagen G. Global sensitivity analysis of bulk properties of an atomic nucleus. *Phys Rev Lett* (2019) 123:252501. arXiv:1910.02922 [nucl-th]. doi:10.1103/physrevlett.123.252501

8. Catacora-Rios M, King GB, Lovell AE, Nunes FM. Statistical tools for a better optical model. *Phys Rev C* (2021) 104:064611. arXiv:2012.06653 [nucl-th]. doi:10.1103/physrevc.104.064611

9. Wesolowski S, Svensson I, Ekström A, Forssén C, Furnstahl RJ, Melendez JA, et al. Rigorous constraints on three-nucleon forces in chiral effective field theory from fast and accurate calculations of few-body observables. *Phys Rev C* (2021) 104:064001. arXiv:2104.04441 [nucl-th]. doi:10.1103/physrevc.104.064001

10. Svensson I, Ekström A, Forssén C. Bayesian parameter estimation in chiral effective field theory using the Hamiltonian Monte Carlo method. *Phys Rev C* (2022) 105:014004. arXiv:2110.04011 [nucl-th]. doi:10.1103/physrevc.105.014004

11. Odell D, Brune CR, Phillips DR, deBoer RJ, Paneru SN. Performing bayesian analyses with AZURE2 using BRICK: An application to the 7Be system. *Phys Rev C* (2022) 105:014625. arXiv:2105.06541 [nucl-th]. doi:10.3389/fphy.2022.888476

12. Djärv T, Ekström A, Forssén C, Johansson HT. Candidate entanglement invariants for two Dirac spinors. *Phys Rev C* (2022) 105:032402. arXiv:2108.13313 [nucl-th]. doi:10.1103/physreva.105.032402

13. Alnamlah IK, Pérez EAC, Phillips DR. Analyzing rotational bands in odd-mass nuclei using effective field theory and Bayesian methods. *Front Phys* (2022) 10:901954. arXiv:2203.01972 [nucl-th]. doi:10.3389/fphy.2022.901954

14. Frontiers in Physics. Research topic: Uncertainty quantification in nuclear physics (2022) (Online; accessed November 2, 2022)

15. Phillips DR, Furnstahl RJ, Heinz U, Maiti T, Nazarewicz W, Nunes FM, et al. Get on the BAND wagon: A bayesian framework for quantifying model uncertainties in nuclear dynamics. *J Phys G* (2021) 48:072001. arXiv:2012.07704 [nucl-th]. doi:10.1088/1361-6471/abf1df

16. Melendez JA, Furnstahl RJ, Grießhammer HW, McGovern JA, Phillips DR, Pratola MT. Designing optimal experiments: An application to proton compton scattering. *Eur Phys J A* (2021) 57:81. arXiv:2004.11307 [nucl-th]. doi:10.1140/epja/s10050-021-00382-2

17. Farr JN, Meisel Z, Steiner AW. Decision theory for the mass measurements at the facility for rare isotope beams. arXiv:2111.11536 [nucl-th]. doi:10.48550/arXiv.2111.11536

18. Melendez JA, Drischler C, Furnstahl RJ, Garcia AJ, Zhang X. Model reduction methods for nuclear emulators. *J Phys G* (2022) 49:102001. arXiv:2203.05528 [nucl-th]. doi:10.1088/1361-6471/ac83dd

19. BUQEYE collaboration. Buqeye (2021). Available at: https://buqeye.github.io/ (Accessed December 15, 2022).

20. BUQEYE collaboration. Frontiers emulator review (2022). Available at: https://github.com/buqeye/frontiers-emulator-review (Accessed December 15, 2022).

21. Higdon D, McDonnell JD, Schunck N, Sarich J, Wild SM. A Bayesian approach for parameter estimation and prediction using a computationally intensive model. *J Phys G* (2015) 42:034009. arXiv:1407.3017. doi:10.1088/0954-3899/42/3/034009

22. Frame D, He R, Ipsen I, Lee D, Lee D, Rrapaj E. Eigenvector continuation with subspace learning. *Phys Rev Lett* (2018) 121:032501. arXiv:1711.07090. doi:10.1103/physrevlett.121.032501

23. Sarkar A, Lee D. Convergence of eigenvector continuation. *Phys Rev Lett* (2021) 126:032501. arXiv:2004.07651 [nucl-th]. doi:10.1103/physrevlett.126.032501

24. Sarkar A, Lee D. Self-learning emulators and eigenvector continuation. *Phys Rev Res* (2022) 4:023214. arXiv:2107.13449 [nucl-th]. doi:10.1103/physrevresearch.4.023214

25. König S, Ekström A, Hebeler K, Lee D, Schwenk A. Eigenvector continuation as an efficient and accurate emulator for uncertainty quantification. *Phys Lett B* (2020) 810:135814. arXiv:1909.08446 [nucl-th]. doi:10.1016/j.physletb.2020.135814

26. Demol P, Duguet T, Ekström A, Frosini M, Hebeler K, König S, et al. Improved many-body expansions from eigenvector continuation. *Phys Rev C* (2020) 101:041302. arXiv:1911.12578. doi:10.1103/physrevc.101.041302

27. Bai D, Ren Z. Generalizing the calculable R-matrix theory and eigenvector continuation to the incoming-wave boundary condition. *Phys Rev C* (2021) 103:014612. arXiv:2101.06336 [nucl-th]. doi:10.1103/physrevc.103.014612

28. Demol P, Frosini M, Tichai A, Somà V, Duguet T. Bogoliubov many-body perturbation theory under constraint. *Ann Phys* (2021) 424:168358. arXiv:2002.02724 [nucl-th]. doi:10.1016/j.aop.2020.168358

29. Yoshida S, Shimizu N. Constructing approximate shell-model wavefunctions by eigenvector continuation. arXiv:2105.08256 [nucl-th]. doi:10.48550/arXiv.2105.08256

30. Furnstahl RJ, Garcia AJ, Millican PJ, Zhang X. Efficient emulators for scattering using eigenvector continuation. *Phys Lett B* (2020) 809:135719. arXiv:2007.03635 [nucl-th]. doi:10.1016/j.physletb.2020.135719

31. Melendez J, Drischler C, Garcia A, Furnstahl R, Zhang X. Fast and accurate emulation of two-body scattering observables without wave functions. *Phys Lett B* (2021) 821:136608. doi:10.1016/j.physletb.2021.136608

32. Drischler C, Quinonez M, Giuliani PG, Lovell AE, Nunes FM. Toward emulating nuclear reactions using eigenvector continuation. *Phys Lett B* (2021) 823:136777. arXiv:2108.08269 [nucl-th]. doi:10.1016/j.physletb.2021.136777

33. Zhang X, Furnstahl RJ. Fast emulation of quantum three-body scattering. *Phys Rev C* (2021) 105:064004. arXiv:2110.04269 [nucl-th]. doi:10.1103/physrevc.105.064004

34. Tews I, Davoudi Z, Ekström A, Holt JD, Becker K, Briceño R, et al. Nuclear forces for precision nuclear physics – A collection of perspectives. *Few-Body Syst* (2022) 63:67. arXiv:2202.01105. doi:10.1007/s00601-022-01749-x

35. Anderson AL, O'Donnell GL, Piekarewicz J. Applications of reduced-basis methods to the nuclear single-particle spectrum. *Phys Rev C* (2022) 106:L031302. arXiv:2206.14889 [nucl-th]. doi:10.1103/physrevc.106.l031302

36. Giuliani P, Godbey K, Bonilla E, Viens F, Piekarewicz J. Bayes goes fast: Uncertainty quantification for a covariant energy density functional emulated by the reduced basis method. *Front. Phys.* (2022) 13039. arXiv:2209[nucl-th]. doi:10.48550/arXiv.2209.13039

37. Sürer O, Nunes FM, Plumlee M, Wild SM. Uncertainty quantification in breakup reactions. *Phys Rev C* (2022) 106:024607. arXiv:2205.07119 [nucl-th]. doi:10.1103/physrevc.106.024607

38. Bai D, Ren Z. Entanglement generation in few-nucleon scattering. *Phys Rev C* (2022) 106:064005. doi:10.1103/physrevc.106.064005

39. Kravvaris K, Quinlan KR, Quaglioni S, Wendt KA, Navratil P. Quantifying uncertainties in neutron-α scattering with chiral nucleon-nucleon and three-nucleon forces. *Phys Rev C* (2020) 102:024616. arXiv:2004.08474 [nucl-th]. doi:10.1103/physrevc.102.024616

40. Yapa N, König S. Volume extrapolation via eigenvector continuation. *Phys Rev C* (2022) 106:014309. arXiv:2201.08313 [nucl-th]. doi:10.1103/physrevc.106.014309

41. Francis A, Agrawal AA, Howard JH, Kökcü E, Kemper AF. Subspace diagonalization on quantum computers using eigenvector continuation. 10571. arXiv:2209[quant-ph]. doi:10.48550/arXiv.2209.10571

42. Zare A, Wirth R, Haselby CA, Hergert H, Iwen M. Modewise johnson-lindenstrauss embeddings for nuclear many-body theory. 01305. arXiv:2211. doi:10.48550/arXiv.2211.01305

43. Bonilla E, Giuliani P, Godbey K, Lee D. Training and projecting: A reduced basis method emulator for many-body physics. *Phys Rev C* (2022) 106:054322. arXiv:2203.05284 [nucl-th]. doi:10.1103/physrevc.106.054322

44. Benner P, Schilders W, Grivet-Talocia S, Quarteroni A, Rozza G, Miguel Silveira L. *System- and data-driven methods and algorithms*. Berlin, Germany: De Gruyter (2021).

45. Leissa A. The historical bases of the Rayleigh and Ritz methods. *J Sound Vibration* (2005) 287:961–78. doi:10.1016/j.jsv.2004.12.021

46. Ilanko S. Comments on the historical bases of the Rayleigh and Ritz methods. *J Sound Vibration* (2009) 319:731–3. doi:10.1016/j.jsv.2008.06.001

47. Suzuki Y, Varga K. *Stochastic variational approach to quantum-mechanical few-body problems*. Berlin, Germany: Springer Berlin Heidelberg (1998).

48. Benner P, Schilders W, Grivet-Talocia S, Quarteroni A, Rozza G, Miguel Silveira L. *Order reduction: Volume 2: Snapshot-based methods and algorithms*. Berlin, Germany: De Gruyter (2020). p. 1–348.

49. Buchan AG, Pain CC, Fang F, Navon IM. A POD reduced-order model for eigenvalue problems with application to reactor physics. *Int J Numer Methods Eng* (2013) 95:1011–32. doi:10.1002/nme.4533

50. Quarteroni A, Manzoni A, Negri F. Reduced basis methods for partial differential equations. In: *An Introduction, La Matematica per il 3+2*. Berlin, Germany: Springer International Publishing (2016). p. 92.

51. Franzke MC, Tichai A, Hebeler K, Schwenk A. Excited states from eigenvector continuation: The anharmonic oscillator. *Phys Lett B* (2022) 830:137101. arXiv:2108.02824. doi:10.1016/j.physletb.2022.137101

52. Melendez J. *Effective field theory truncation errors and why they matter*. Ph.D. thesis. Columbus, Ohio: Ohio State U. (2020).

53. Hicks C, Lee D. Trimmed sampling algorithm for the noisy generalized eigenvalue problem. 02083. arXiv:2209. doi:10.48550/arXiv.2209.02083

54. Neumaier A. Solving ill-conditioned and singular linear systems: A tutorial on regularization. *SIAM Rev* (1998) 40:636–66. doi:10.1137/s0036144597321909

55. Engl H, Hanke M, Neubauer A. Regularization of inverse problems. In: *Mathematics and its applications*. Netherlands: Springer (1996).

56. Hergert H. A guided tour of *ab initio* nuclear many-body theory. *Front Phys* (2020) 8:37905061. arXiv:2008. doi:10.3389/fphy.2020.00379

57. Ghattas O, Willcox K. Learning physics-based models from data: Perspectives from inverse problems and model reduction. *Acta Numerica* (2021) 30:445–554. doi:10.1017/s0962492921000064

58. Rasmussen CE, Williams CKI. *Gaussian processes for machine learning, adaptive computation and machine learning series*. Cambridge, MA: University Press Group Limited (2006).

59. Mezić I. Analysis of fluid flows via spectral properties of the koopman operator. *Annu Rev Fluid Mech* (2013) 45:357–78. doi:10.1146/annurev-fluid-011212-140652

60. Kutz JN, Brunton SL, Brunton BW, Proctor JL. Dynamic mode decomposition. In: *Other titles in applied mathematics*. Pennsylvania, United States: SIAM-Society for Industrial and Applied Mathematics (2016).

61. Raissi M, Perdikaris P, Karniadakis GE. Physics-informed neural networks: A deep learning framework for solving forward and inverse problems involving nonlinear partial differential equations. *J Comput Phys* (2019) 378:686–707. doi:10.1016/j.jcp.2018.10.045

62. Chen W, Wang Q, Hesthaven JS, Zhang C. Physics-informed machine learning for reduced-order modeling of nonlinear problems. *J Comput Phys* (2021) 446:110666. doi:10.1016/j.jcp.2021.110666

63. Fresca S, Manzoni A. POD-DL-ROM: Enhancing deep learning-based reduced order models for nonlinear parametrized PDEs by proper orthogonal decomposition. *Comp Methods Appl Mech Eng* (2022) 388:114181. doi:10.1016/j.cma.2021.114181

64. Hesthaven J, Rozza G, Stamm B. Certified reduced basis methods for parametrized partial differential equations. In: *SpringerBriefs in mathematics*. Berlin, Germany: Springer International Publishing (2015).

65. Barrault M, Maday Y, Nguyen NC, Patera AT. An 'empirical interpolation' method: Application to efficient reduced-basis discretization of partial differential equations. *Comptes Rendus Mathematique* (2004) 339:667–72. doi:10.1016/j.crma.2004.08.006

66. Grepl MA, Maday Y, Nguyen NC, Patera AT. Efficient reduced-basis treatment of nonaffine and nonlinear partial differential equations. *ESAIM: M2AN* (2007) 41:575–605. doi:10.1051/m2an:2007031

67. Horacio LC, Solis-Daun J. Synthesis of positive controls for the global CLF stabilization of systems. In: Proceedings of the 48h IEEE Conference on Decision and Control (CDC) held jointly with 2009 28th Chinese Control Conference; 15-18 December 2009; Shanghai, China (2009). p. 4316–21.

68. Chaturantabut S, Sorensen DC. Nonlinear model reduction via discrete empirical interpolation. *SIAM J Scientific Comput* (2010) 32:2737–64. doi:10.1137/090766498

69. Bui-Thanh T, Damodaran M, Willcox K. Proper orthogonal decomposition extensions for parametric applications in compressible aerodynamics. In: 21st AIAA Applied Aerodynamics Conference; 23 June 2003 - 26 June 2003; Orlando, Florida (2003).

70. Carlberg K, Bou-Mosleh C, Farhat C. Efficient non-linear model reduction via a least-squares Petrov-Galerkin projection and compressive tensor approximations. *Int J Numer Methods Eng* (2011) 86:155–81. doi:10.1002/nme.3050

71. Amsallem D, Cortial J, Farhat C. Towards real-time computational-fluid-dynamics-based aeroelastic computations using a database of reduced-order information. *AIAA J* (2010) 48:2029–37. doi:10.2514/1.j050233

72. An SS, Kim T, James DL. Session details: Character animation II. *ACM Trans Graph* (2008) 27:3262975. doi:10.1145/3262975

73. Farhat C, Avery P, Chapman T, Cortial J. Dimensional reduction of nonlinear finite element dynamic models with finite rotations and energy-based mesh sampling and weighting for computational efficiency. *Int J Numer Methods Eng* (2014) 98:625–62. doi:10.1002/nme.4668

74. Guo M, Hesthaven JS. Reduced order modeling for nonlinear structural analysis using Gaussian process regression. *Comp Methods Appl Mech Eng* (2018) 341:807–26. doi:10.1016/j.cma.2018.07.017

75. Gubisch M, Volkwein S. Chapter 1: Proper orthogonal decomposition for linear-quadratic optimal control. In: *Reduction and approximation* (2017). p. 3–63.

76. Rozza G, Huynh DBP, Patera AT. Reduced basis approximation and a posteriori error estimation for affinely parametrized elliptic coercive partial differential equations. *Arch Comput Methods Eng* (2008) 15:229–75. doi:10.1007/s11831-008-9019-9

77. Chen P, Quarteroni A, Rozza G. Reduced basis methods for uncertainty quantification. *SIAM/ASA J Uncertainty Quantification* (2017) 5:813–69. doi:10.1137/151004550

78. Horger T, Wohlmuth B, Thomas D. Simultaneous reduced basis approximation of parameterized elliptic eigenvalue problems. *ESAIM: M2AN* (2017) 51:443–65. doi:10.1051/m2an/2016025

79. MacKay DJC. Neural networks and machine learning. In: CM Bishop, editor. *NATO ASI series*. Berlin: Springer (1998). p. 133–66.

80. MacKay DJC. *Information theory, inference, and learning algorithms*. Cambridge, UK: Cambridge University Press (2003).

81. Gander MJ, Wanner G. From euler, Ritz, and Galerkin to modern computing. *SIAM Rev* (2012) 54:627–66. doi:10.1137/100804036

82. Zienkiewicz O, Taylor R, Zhu J. *The finite element method: Its basis and fundamentals*. 7th ed. Oxford: Butterworth-Heinemann (Butterworth-Heinemann (2013).

83. Zienkiewicz O, Taylor R, Fox D. *The finite element method for solid and structural mechanics*. 7th ed. Oxford: Butterworth-Heinemann (2014).

84. Zienkiewicz O, Taylor R, Nithiarasu P. *The finite element method for fluid dynamics*. 7th ed. Oxford: Butterworth-Heinemann (2014).

85. Mikhlin SG. *Variational methods in mathematical physics*. Oxford: Cambridge University Press (1967). [Translated by T. Boddington for Pergamon Press, Oxford, 1964].

86. Evans JD. *Straightforward statistics for the behavioral sciences*. Pacific Grove, CA: Brooks/Cole Publishing (1996).

87. Brenner SC, Scott LR. The mathematical theory of finite element methods. In: *Texts in applied mathematics*. Berlin, Germany: Springer (2008).

88. Garcia AJ, Drischler C, Furnstahl RJ, Melendez JA, Zhang X. Wave function-based emulation for nucleon-nucleon scattering in momentum space. arXiv:2301.05093.

89. Benner P, Schilders W, Grivet-Talocia S, Quarteroni A, Rozza G, Miguel Silveira L. *Order reduction: Volume 3: Applications*. Berlin, Germany: De Gruyter (2020).

90. Huynh D, Rozza G, Sen S, Patera A. A successive constraint linear optimization method for lower bounds of parametric coercivity and inf–sup stability constants. *Comptes Rendus Mathematique* (2007) 345:473–8. doi:10.1016/j.crma.2007.09.019

91. Kohn W. Variational methods in nuclear collision problems. *Phys Rev* (1948) 74:1763–72. doi:10.1103/physrev.74.1763

92. Kohn W. Variational scattering theory in momentum space I. Central field problems. *Phys Rev* (1951) 84:495–501. doi:10.1103/physrev.84.495

93. Drischler C, Holt JW, Wellenhofer C. Chiral effective field theory and the high-density nuclear equation of state. *Annu Rev Nucl Part Sci* (2021) 71:403–32. arXiv:2101.01709. doi:10.1146/annurev-nucl-102419-041903

94. Takatsuka K, Lucchese RR, McKoy V. Relationship between the schwinger and kohn-type variational principles in scattering theory. *Phys Rev A* (1981) 24:1812–6. doi:10.1103/physreva.24.1812

95. Takatsuka K, McKoy V. Variational scattering theory using a functional of fractional form. I. General theory. *Phys Rev A* (1981) 23:2352–8. doi:10.1103/physreva.23.2352

96. Newton RG. *Scattering theory of waves and particles*. Illinois, United States: Dover (2002).

97. Thompson IJ, Nunes FM. *Nuclear reactions for astrophysics: Principles, calculation and applications of low-energy reactions*. Cambridge, United Kingdom: Cambridge University Press (2009).

98. Lucchese RR. Anomalous singularities in the complex kohn variational principle of quantum scattering theory. *Phys Rev A* (1989) 40:6879–85. doi:10.1103/physreva.40.6879

99. Taylor JR. *Scattering theory: The quantum theory of nonrelativistic collisions*. Illinois, United States: Dover (2006).

100. Morrison MA, Feldt AN. Through scattering theory with gun and camera: Coping with conventions in collision theory. *Am J Phys* (2007) 75:67–80. doi:10.1119/1.2358156

101. Nesbet R. *Variational methods in electron-atom scattering theory, Physics of atoms and molecules*. Plenum Press (1980).

102. Adhikari SK. Anomalies of variational phase shifts. *Chem Phys Lett* (1991) 181:435–40. doi:10.1016/0009-2614(91)90376-k

103. Marcucci LE, Dohet-Eraly J, Girlanda L, Gnech A, Kievsky A, Viviani M. The hyperspherical harmonics method: A tool for testing and improving nuclear interaction models. *Front Phys* (2020) 8:69. arXiv:1912.09751 [nucl-th]. doi:10.3389/fphy.2020.00069

104. Kievsky A, Rosati S, Viviani M, Marcucci LE, Girlanda L. A high-precision variational approach to three- and four-nucleon bound and zero-energy scattering states. *J Phys G* (2008) 35:063101. arXiv:0805.4688. doi:10.1088/0954-3899/35/6/063101

105. Gloeckle W, Witala H, Huber D, Kamada H, Golak J. A New look into the partial wave decomposition of three nucleon forces. *Phys Rept* (1996) 274:107. doi:10.1007/s006010050057

106. Deltuva A, Fonseca AC, Lazauskas R. Faddeev equation approach for three-cluster nuclear reactions. In: *Lecture notes in physics*. Berlin, Germany: Springer (2014). p. 1. arXiv:1201.4979 [nucl-th].

107. Lazauskas R, Carbonell J. The faddeev–yakubovsky symphony. *Few Body Syst* (2019) 60:62. arXiv:1908.04861 [quant-ph]. doi:10.1007/s00601-019-1529-5

108. Tabakin F. Inverse scattering problem for separable potentials. *Phys Rev* (1969) 177:1443–51. doi:10.1103/physrev.177.1443

109. Kwong NH, Köhler HS. SeparableNNpotentials from inverse scattering for nuclear matter studies. *Phys Rev C* (1997) 55:1650–64. doi:10.1103/physrevc.55.1650

110. Göbel M, Hammer HW, Ji C, Phillips DR. Momentum-space probability density of {}6He in halo effective field theory. *Few Body Syst* (2019) 60:61. arXiv:1904.07182 [nucl-th]. doi:10.1007/s00601-019-1528-6

111. Haasdonk B. Chapter 2: Reduced basis methods for parametrized pdes—A tutorial introduction for stationary and instationary problems. In: *Reduction and approximation*. Philadelphia, PA: Computational Science & Engineering (2017). p. 65–136.

112. Milk R, Rave S, Schindler F. pyMOR -- generic algorithms and interfaces for model order reduction. *SIAM J Scientific Comput* (2016) 38:S194–216. doi:10.1137/15m1026614

113. Zhang X, Low Energy Community Meeting. *Recent developments in the emulations of quantum continuum states*. USA: Argonne National Laboratory (2022).

114. Boehnlein A, Diefenthaler M, Sato N, Schram M, Ziegler V, Fanelli C, et al. *Colloquium*: Machine learning in nuclear physics. *Rev Mod Phys* (2022) 94:031003. arXiv:2112.02309 [nucl-th]. doi:10.1103/revmodphys.94.031003

115. BAND. Bayesian analysis of nuclear dynamics (BAND) framework project (2020). Available at: https://bandframework.github.io/ (Accessed December 15, 2022).

frontiers | Frontiers in Physics

TYPE Review
PUBLISHED 20 February 2023
DOI 10.3389/fphy.2023.1129094

OPEN ACCESS

EDITED BY
Paul Stevenson,
University of Surrey, United Kingdom

REVIEWED BY
Andreas Nogga,
Helmholtz Association of German Research Centres (HZ), Germany
Tobias Frederico,
Instituto de Tecnologia da Aeronáutica (ITA), Brazil
Richard Furnstahl,
The Ohio State University, United States

*CORRESPONDENCE
A. Ekström,
andreas.ekstrom@chalmers.se

SPECIALTY SECTION
This article was submitted to Nuclear Physics, a section of the journal Frontiers in Physics

RECEIVED 21 December 2022
ACCEPTED 07 February 2023
PUBLISHED 20 February 2023

CITATION
Ekström A, Forssén C, Hagen G, Jansen GR, Jiang W and Papenbrock T (2023), What is *ab initio* in nuclear theory? *Front. Phys.* 11:1129094.
doi: 10.3389/fphy.2023.1129094

What is *ab initio* in nuclear theory?

A. Ekström[1]*, C. Forssén[1], G. Hagen[2,3], G. R. Jansen[2,4], W. Jiang[1] and T. Papenbrock[2,3]

[1]Department of Physics, Chalmers University of Technology, Göteborg, Sweden, [2]Physics Division, Oak Ridge National Laboratory, Oak Ridge, TN, United States, [3]Department of Physics and Astronomy, University of Tennessee, Knoxville, TN, United States, [4]National Center for Computational Sciences, Oak Ridge National Laboratory, Oak Ridge, TN, United States

Ab initio has been used as a label in nuclear theory for over two decades. Its meaning has evolved and broadened over the years. We present our interpretation, briefly review its historical use, and discuss its present-day relation to theoretical uncertainty quantification.

KEYWORDS

***ab initio* nuclear theory, effective field theory, Bayesian inference, many-body methods, uncertainty quantication**

1 Introduction

The literal meaning of the latin term *ab initio* implies that one starts from the beginning. In computations of atomic nuclei, this means that the relevant degrees of freedom should be quarks and gluons. However, the history of physics tells us that we do not need to know everything to describe something and that we have some freedom in choosing the starting point. As such, we do not necessarily have to employ Standard Model degrees of freedom. In fact, many nuclear properties were successfully analyzed in terms of hadronic degrees of freedom before we even knew about the existence of quarks [1–3]. Today, we know how to explain this using renormalization group (RG) ideas [4, 5]. One may wonder about the exact meaning of the *ab initio* method and what should constitute the beginning. However, it is safe to say that a hallmark of this approach is its promise of precise and accurate predictions, with quantified uncertainties, across the multiple energy scales relevant to nuclei. Examples range from low-energy collective phenomena such as deformation and rotation [6–10], to loosely bound and unbound nuclei [11–16], and to lepton nucleus scattering in the quasi-elastic energy regime [17–19]. We expect the *ab initio* method to reliably extrapolate, in a controlled and systematic way, to regions outside the ones used for inferring the model parameters. Following the ideas from effective field theory (EFT) [20], *we interpret the ab initio method to be a systematically improvable approach for quantitatively describing nuclei using the finest resolution scale possible while maximizing its predictive capabilities.* A key part of this interpretation is the possible tension between the two latter aspects. In a nuclear physics context, we therefore let nucleons, and possibly other relevant hadronic degrees of freedom, define the beginning. Lattice quantum chromodynamics (QCD) might one day be the optimal starting point for predicting nuclear phenomena. Presently, Lattice QCD continues to provide useful input for EFTs based on hadronic degrees of freedom. However, it currently lacks predictive power for describing atomic nuclei [21–25].

We acknowledge that the *ab initio* method is interpreted differently by different people; see, e.g., Refs. [26–33]. In nuclear physics, the evolution of *ab initio* and its wide application

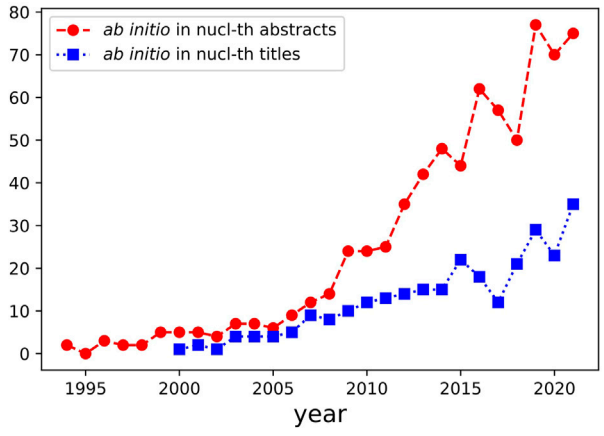

FIGURE 1
Number of times the term *ab initio* appears in the abstract (red circles) and titles (blue squares) of papers on arXiv:nucl-th in a given year.

reflect the creativity and innovation of the scientists who perform *ab initio* computations. In this sense, *ab initio* is unlike Tennessee Whiskey or French Champagne, which are internationally protected labels, but rather like Gruyère cheese, i.e., a generic expression that benefits a "vibrant, competitive marketplace"[1]. In this review we provide a brief history of *ab initio* nuclear physics (Section 2), clarify our interpretation of this label (Section 3), explain how this approach creates an inferential advantage (Section 4), and provide examples in connection with some remaining challenges (Section 5).

2 A brief history of *ab initio* nuclear physics

A search of the term *ab initio* in the title on arXiv:nucl-th returns about 300 papers, with the earliest one by Navrátil, Vary, and Barrett (Ref. [34]) dating back to the year 2000. When the search includes abstracts, the count increases to more than 700, and papers by Leinweber (Ref. [35]) and Friar (Ref. [36]) are the earliest published in the mid-1990s. Since then, an ever-increasing number of authors have used the term *ab initio* to characterize their work. In Figure 1, we show a plot of the data for the yearly use of this term in titles and abstracts.

The authors of Ref. [34] did not explain what distinguished their *ab initio* no-core shell model computations from quite similar earlier approaches [37, 38] (see also Ref. [39]). Whatever the reason, the term *ab initio* stuck and has been popular ever since. Colloquially, we often use *ab initio* to label theoretical analyses of nuclei based on "realistic" nucleon-nucleon, and three-nucleon potentials, with solutions to the nuclear many-body problem obtained either "virtually" exactly or with controlled approximations. Over the years, however, the small number of available "realistic" or "high-precision" nucleon-nucleon potentials [40, 41] have been replaced by nucleon-nucleon potentials *plus* three-nucleon potentials from chiral effective field theories (χEFTs) of QCD [42–44].

Because of the power counting in χEFT the potentials are recognized as approximate with a fidelity that presumably increases with increasing chiral order. This presented an opportunity for systematically improvable many-body methods that scale polynomially with increasing mass number [26, 30, 45–52]. Why solve an approximate potential virtually exactly? This class of gently-scaling methods has now extended the reach of many-body calculations to medium-mass and heavy-mass nuclei [13, 53–58]. The computational cost of these calculations is kept manageable by also approximating three-nucleon potentials as normal-ordered, i.e., "density-dependent," two-body potentials [53, 57, 59, 60], and using the intrinsic kinetic energy alleviated problems with the center of mass in the laboratory system [61–63]. These efforts also revealed the need for nuclear potentials that accurately reproduce bulk observables beyond the lightest-mass nuclei [64, 65]. This spurred the development of many new potentials differing by the degrees of freedom they used, how the numerical values of the low-energy constants (LECs) were determined, the choice of regulator function, power counting, and degree of locality [64–79].

Since the mid-to-late 1990s, this two-decades-long struggle to describe nuclei has brought nuclear structure and reactions closer together [11, 12, 80, 81]. Ideas from EFT [82] and RG [83, 84] have changed our views on what is observable [85], the importance of understanding the intrinsic resolution-scale and scheme dependencies [86, 87], how we can systematically account for finite-size corrections [88, 89], and estimate the effects of truncating the EFT expansion [69, 72, 90, 91]. These ideas have also led to the advent of the in-medium similarity renormalization group [49, 51, 52] and nuclear lattice EFT [92, 93] as the latest many-body methods. What we nowadays refer to as *ab initio* computations of nuclei [16, 56, 58, 94] is intimately linked to the ideas of EFT and uncertainty quantification. Clearly, what we considered *ab initio* two decades ago does not necessarily pass as *ab initio* today, and *vice versa*.

3 Our interpretation of the *ab initio* method

The methods of EFT [82] and RG [83, 84] provide a valuable foundation for the idea that the physics at a given energy scale does not explicitly depend on the details at much higher energies. The beginning can therefore be marked by identifying a scale separation, specifying the relevant degrees of freedom and symmetries, and allowing interactions accordingly. A power counting facilitates meaningful truncations.

We interpret the *ab initio* method as employing Lagrangians, Hamiltonians, or energy density functionals based on EFT principles and with degrees of freedom chosen such that it maximizes our predictive capabilities. *Ab initio* descriptions of atomic nuclei concern the physics of multi-hadron systems in an energy range from keV to a few hundreds of MeV. As such, it is reasonable to start from hadronic degrees of freedom with interactions derived from

1 https://www.nytimes.com/2022/01/12/business/gruyere-cheese-us-court-ruling.html

the Standard Model using the principles of EFT. While hadrons are composite systems, and QCD is the underlying theory of the strong nuclear force, Lattice QCD calculations of two-hadron systems are not yet under control [21, 22]. This might change, and one could imagine computing nuclei *ab initio* from QCD. Moving *the beginning* from hadronic degrees of freedom to quarks and gluons would extend the upper limit of the applicable energy scale by several orders of magnitude and thus increase predictive capabilities significantly. It is, however, an open question whether this ansatz will capture emergent phenomena like the saturation of nuclear forces [95]. Even if this were possible, it is another question how much understanding would be gained about emergent phenomena that involve novel (low-resolution) degrees of freedom from such a high-resolution perspective. The usefulness of the tower of EFTs will most likely remain [96].

Assuming that *ab initio* descriptions of nuclei inherit the physics of the Standard Model *via* EFT methods, we expect to obtain more reliable predictions compared to complementary and phenomenological approaches. Also, building on an EFT, the *ab initio* method should be systematically improvable, organizing the relevant physics according to importance following the principles of power counting. To use this advantage, we must obtain observables using numerically exact methods or, if necessary, using controlled approximations that allow for a systematic analysis. By controlled approximations, we mean ignoring, in a graded way, what we believe to be less essential physics. Doing so, we obtain a handle on what we discard and a more meaningful estimate of our prediction uncertainty. We would like to emphasize the distinction between ignored physics and unresolved physics. An example of the latter is short-range physics that, although unresolved, is accounted for in the Hamiltonian *via* contact interactions [97].

It is pivotal to incorporate and declare our knowledge base and assumptions in analyzing uncertainties. The *ab initio* method does not emerge from a vacuum. That would be an *ex nihilo* method, of which we cannot find any example in science. Quantifying theoretical uncertainties grounded in systematicity should create an advantage when assessing discrepancies between theory and experiment. Note that according to our interpretation, the *ab initio* method does not guarantee that we can find absolute bounds on the theoretical uncertainties nor that we approach the true data-generating mechanism by gradually reducing all truncations. Indeed, should tensions between experiment and theory remain despite our best efforts to quantify uncertainties and keep the truncations at a minimum, we obtain quantitative evidence that we should contest at least one of our assumptions.

4 How the *ab initio* method creates an inferential advantage

The use of probability theory to quantify uncertainty plays a central role in the scientific endeavor of inferring new knowledge about the Universe. In this context, the *ab initio* method has evolved significantly over the last few years and now offers a distinct advantage. However, before we can elaborate on the topic of inductive inference and its relation to the *ab initio* method, we must briefly discuss the nature of science in terms of data, theories, and models. This topic is expanded upon in the context of EFTs much more thoroughly in, e.g., Refs. [98, 99].

Let us start with the data $\mathcal{D}$ obtained through a measurement process. All data are equipped with uncertainties of various origins; let us denote this $\delta\mathcal{D}$. Given some data $\mathcal{D}$, one could ask what this data can tell us about future data $\mathcal{F}$. At present, the future data is uncertain and must therefore be described with a conditional probability $p(\mathcal{F}|\mathcal{D}, I)$ [100]. Here I denotes all available background information. The obvious question is: How does one go from this abstract probability to something that can be evaluated quantitatively? The answer is to develop a theory within which we can formulate a model that allows for numerical evaluation.

In physics, a theory is very often some framework that postulates or deduces from some foundational principles the spacetime dependence of a system of interacting bodies, e.g., Einstein's field equations in the general theory of relativity or Heisenberg's equations of motion in quantum mechanics. A physical theory always comes with some prior probability of being wrong and this probability should never be exactly zero or one. Otherwise no new evidence/data will ever influence the validity of the theory. In this sense, all theories are wrong, i.e., never correct with absolute certainty. This provocative statement is designed to draw attention to the fact that all theories can be improved or replaced as we progress and gather more data.

A physical model M allows quantitative evaluation of the system under study. Any model we employ will always depend on model parameters $\boldsymbol{\theta}$ with uncertain numerical values. Moreover, like theories: "all models are wrong" [101]. Indeed, there will always be some physics that we still need to include or are unaware of today. If we denote the mismatch between model predictions and data as δM, we can write

$$\mathcal{D} = M(\boldsymbol{\theta}) + \delta\mathcal{D} + \delta M. \tag{1}$$

We often refer to the mismatch term δM as the model discrepancy [102]. Naturally, we are uncertain about this term, so we represent it by a probability distribution following our beliefs about the limitations of M. It is no trivial task to incorporate model discrepancies in the analysis of scientific models and data. Nevertheless, it is crucial to avoid overfitting the model parameters $\boldsymbol{\theta}$ and making overly confident model predictions [103]. It is in this context that the *ab initio* method creates an inferential advantage. The promise of systematicity grounded in EFT, and the controlled approximations underlying the computation of nuclear observables, allows us to be quantitative about the distribution that governs δM as we increase the fidelity of M. For simplicity we sometimes refer to EFTs as models. However, an EFT is more than a physical model in the traditional sense. Indeed, within its domain of applicability an EFT prediction reflects the underlying theory up to a truncation error. In this sense, the EFT is complete, which is a distinct advantage compared to traditional models. This is sometimes referred to as model-independence. Of course, the underlying theory might be wrong, and such model discrepancies cannot be remedied at the level of the EFT.

For example, assume that we operate with an EFT of QCD to derive the potential for the nuclear interaction up to some order in the relevant power counting. In addition, suppose that we use a systematically improvable many-body method at some well-defined truncation level to solve the many-body Schrödinger equation for

the ground-state energy in our favorite nucleus. Then we can say more about δM than if we use a shell model description grounded in phenomenologically defined interaction matrix elements tailored to a specific model space. We are not saying that the latter calculation cannot provide valuable guidance or insight. However, we are saying that it is possible to systematically test the underlying assumptions within the *ab initio* method. Having quantified δM also tells us the significance of a possible discrepancy or tension between experiment and theory.

The distribution of future data conditioned on past data and background information I, i.e., $p(\mathcal{F}|\mathcal{D}, I)$, is referred to as a posterior predictive distribution (PPD). Assuming that we have a model M ($\boldsymbol{\theta}$) for the data-generating mechanism, then we can express the PPD by marginalizing over the uncertain model parameters $\boldsymbol{\theta}$ belonging to some parameter space Ω

$$p(\mathcal{F}|\mathcal{D}, I) = \int_{\Omega} p(\mathcal{F}|\boldsymbol{\theta}, I)\, p(\boldsymbol{\theta}|\mathcal{D}, I)\, \mathrm{d}\boldsymbol{\theta}. \tag{2}$$

By performing this integral, we average all predictions with respect to our uncertainty of the model parameters $\boldsymbol{\theta}$. To evaluate the posterior probability density function (PDF) $p(\boldsymbol{\theta}|\mathcal{D}, I)$ for the model parameters, we can employ Bayes' theorem, i.e.,

$$p(\boldsymbol{\theta}|\mathcal{D}, I) = \frac{p(\mathcal{D}|\boldsymbol{\theta}, I)\, p(\boldsymbol{\theta}|I)}{p(\mathcal{D}|I)}. \tag{3}$$

This requires a likelihood function $p(\mathcal{D}|\boldsymbol{\theta}, I)$ and a prior distribution of the model parameters $p(\boldsymbol{\theta}|I)$. The denominator, $p(\mathcal{D}|I)$, does not explicitly depend on $\boldsymbol{\theta}$ and is only needed for proper normalization. Quantifying the posterior is called Bayesian parameter estimation and is a staple of Bayesian inference. It is a probabilistic generalization of parameter optimization and maximum likelihood estimation.

In the historical developments of "high-precision" nucleon-nucleon potentials, one often employed a χ^2-measure to quantify the goodness of fit to nucleon-nucleon scattering data [40, 41]. Although such an approach has several drawbacks, most notably its limited use in uncertainty quantification and non-trivial incorporation of prior knowledge and model discrepancy, it is undoubtedly less demanding computationally than quantifying a multi-dimensional posterior PDF. Evaluating the posterior requires numerical methods like Markov Chain Monte Carlo [104, 105], which is no silver bullet and by no means guaranteed to succeed. To compute the denominator in Eq. (3), i.e., the marginal likelihood, is even more difficult. There is significant progress in linking *ab initio* methods to the Bayesian inferential approach in the nucleon-nucleon and few-nucleon sectors [106]. The development of efficient and accurate emulators [107–110] should provide us with sufficient leverage to continue applying Bayesian methods for analyzing and quantifying uncertainties for non-trivial nuclear structure observables and reaction cross sections. Access to emulators also opens the door to detailed experimental design studies [111–116].

5 A few examples

We will briefly discuss a few examples and highlight some remaining challenges to clarify our interpretation of the *ab initio* method to analyze nuclei.

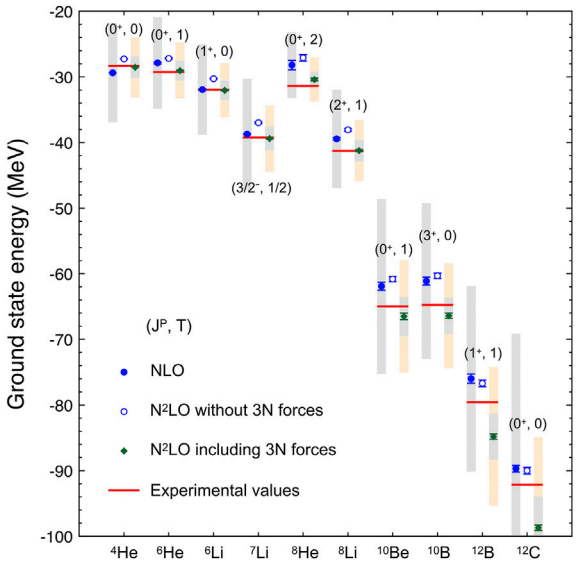

FIGURE 2
Predictions for ground-state energies of selected light nuclei using interactions up to next-to-next-to-leading order in χEFT. The grey (coral) bands indicate 68% (95%) credible intervals for the theoretical uncertainty stemming from truncating the χEFT expansion. Figure from Ref. [121], where additional details can be found.

For light-mass nuclei, methods like the Faddeev-Yakubovsky equations [117], hyperspherical harmonics expansion [27], no-core shell model [39], and quantum Monte Carlo [118] yield virtually exact solutions to the many-body Schrödinger equation [119], barring systematic truncations of the single-particle basis and the Hilbert space of many-body wave functions, or limited sampling statistics. As such, the fidelity of the prediction is mainly limited by the available computational resources [120]. When we employ these methods with interactions that can be systematically improved, we obtain the prototypical *ab initio* calculation of a nucleus. As an example, in Figure 2, we show the predictions for ground-state energies in selected nuclei with mass numbers $A = 4$–12 as obtained in a systematic study [77] of light nuclei using two-plus three-nucleon interactions up to next-to-next-to-leading order in χEFT. The parameters of the employed interactions, i.e., the LECs, were calibrated to reproduce selected two- and three-nucleon data. The authors of that study recognized the well-known trend [54] of over-binding starting at $A \approx 10$ and increasing with A. Whether going to higher orders in χEFT ameliorates this issue remains to be understood. A recent paper [122] shows that ground-state energies are better reproduced when going to the next order, but nuclear radii remain challenging to describe.

In contrast to increasing the chiral order of the nuclear potential, which also introduces additional LECs to be inferred, it was demonstrated in Ref. [64] that one could obtain accurate predictions for binding energies and nuclear radii in medium-mass nuclei using a chiral interaction at next-to-next-to-leading order ($\mathrm{NNLO_{sat}}$), which is calibrated

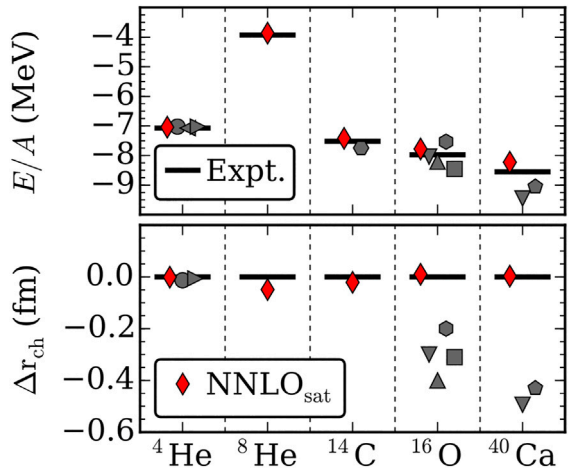

FIGURE 3
Ground-state energy (negative of binding energy) per nucleon (top), and residuals (differences between computed and experimental values) of charge radii (bottom) for selected nuclei computed with chiral interactions. In most cases, theory predicts too-small radii and too-large binding energies. Figure from Ref. [123], where additional details can be found.

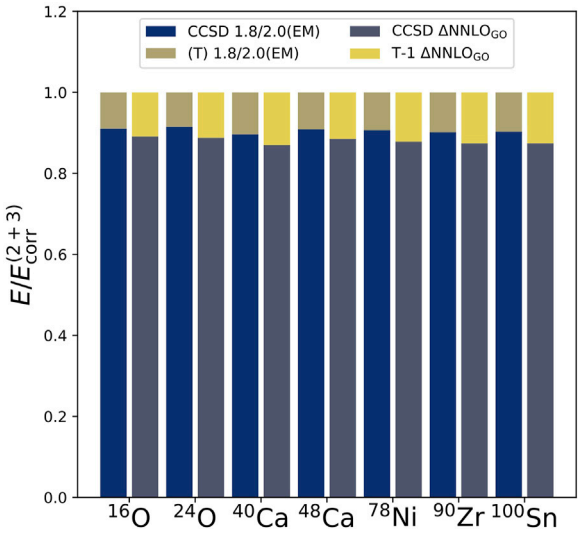

FIGURE 4
Relative contributions to the correlation energy $E_{\text{corr}}^{(2+3)}$ of several closed-shell nuclei from coupled cluster with singles and doubles (CCSD) and triples using the CCSD(T) approximation for the 1.8/2.0 (EM) interaction of Ref. [67] (left bars) and CCSDT-1 for the $\Delta\text{NNLO}_{\text{GO}}$ (394) interaction of Ref. [65] (right bars). The CCSD result accounts for about 90% of the correlation energy for different nuclei and interactions, and this visualizes the systematic improvements of the coupled-cluster expansion. The data is taken from Ref. [132].

to reproduce data for bulk observables in nuclei with A = 2–16, see Figure 3, in addition to nucleon-nucleon scattering cross sections. Calibrating the LECs to reproduce this wider class of nuclear data residing in the domain of applicability of χEFT, has been very fruitful and informative. This approach was expanded upon in Ref. [65] by exploiting empirical information from nuclear matter at saturation densities and including the $\Delta(1232)$-isobar in the chiral expansion of the nuclear interaction. The strategy of inferring LECs to also reproduce bulk properties of medium-mass nuclei runs the risk of overfitting but there are Bayesian methods to mitigate this, as discussed in the next paragraph. The interactions in Refs. [64, 65] account for rudimentary theory and method errors and can be systematically improved. Therefore we characterize them, and ensuing predictions utilizing controlled approximations, as *ab initio*. On the contrary, nuclear interactions designed to maximize the data likelihood of nucleon-nucleon scattering cross sections at any cost, invoking, e.g., unphysical parameters of the regulator for fitting purposes [78], cannot be considered as an *ab initio* approach despite being based on EFT Lagrangians. A smaller χ^2-value does not imply greater *ab initio* content.

Utilizing Bayesian inference methods, one can express the PDF for the LECs conditioned on low-energy data while accounting for the truncation errors of χEFT and our knowledge about the accuracy of the employed many-body methods. The challenge, however, is to quantify these uncertainties. There are methods based on, e.g., Gaussian processes to account for correlated EFT truncation errors in nucleon-nucleon scattering [124] and nuclear matter predictions [125]. However, studies of the χEFT truncation error for finite nuclei deserve more attention [126]. Hu et al. [58] took the first step in this direction to analyze heavy-mass nuclei, where they quantified an *ab initio* PPD for the neutron-skin thickness in ^{208}Pb. This distribution is conditioned on low-energy data from light- and medium-mass nuclei together with assigned uncertainties of the employed nuclear interactions and the many-body methods.

To enable predictions for nuclei with $A \gtrsim 10$, one must use methods whose computational complexity scales gently with A and the size of the single-particle basis. Still, these methods must retain essential many-body physics to describe the observable of interest. Three-nucleon interactions can be challenging to handle computationally [127]. Operating with truncated model spaces and normal-order-approximated interactions goes well with the ideas of the *ab initio* method. Here, we exemplify our discussion using the coupled cluster method [30] with polynomial scaling in A, but we note that several methods [128, 129] of this kind exist. The coupled cluster method exploits an exponentiated cluster operator $\hat{T}$ expanded on particle-hole excitations of some many-body reference state. Truncating the expansion of $\hat{T}$ at some level of n-particle n-hole excitations, and solving for the remaining excitation amplitudes, constitutes a systematically improvable description of the many-body wave function. Although a formal bound on the effect of higher-order particle-hole excitations is lacking, it is clear how to improve. This recipe for improvement is what we seek in an *ab initio* method. Unfortunately, the convergence pattern might be irregular and vary significantly depending on the observable considered. For example, a rapid convergence for the ground- and first excited-state energies does not imply that their respective wave functions yield a converged description of non-stationary observables [130]. Convergence must be inspected empirically by either gradually increasing the

number of particle-hole excitations, or defining a more appropriate starting point (reference state) for the expansion, see, e.g., Ref. [131]. Understanding this kind of convergence pattern is important for proper uncertainty quantification and remains an open question that requires significant domain knowledge.

In Figure 4, we show how the 2p-2h and 3p-3h excitations of the coupled-cluster method contribute to the correlation energy of various closed-shell nuclei. The correlation energy is defined as the difference between the predicted binding energies and the Hartree-Fock energy. Here, the correlation energy $E_{\mathrm{corr}}^{(2+3)}$ is the sum of the 2p-2h correlation energy from CCSD and the 3p-3h correlation energy from the triples, namely the Λ-CCSD(T) approximation [133] (for the 1.8/2.0 (EM) interaction of Ref. [67]) and the CCSDT-1 approximation [134] (for the interaction of Ref. [65]). We see that CCSD accounts for about 90% of the correlation energy for different nuclei and interactions. Various quantum chemistry applications [135] have obtained similar results. This strongly suggests that coupled-cluster theory provides us with a systematic approximation when truncated at the doubles, triples, etc levels. While we do not (yet), have an understanding of the hierarchy (i.e. triples yield much smaller energy contributions than doubles) shown in Figure 4, Sun et al. [132] proposed RG arguments as a possible explanation: Lowering the resolution scale in the three-body subsystems of a many-body system corresponds to removing (short-ranged) triples excitations. Extending the arguments by Lepage [5] and Bogner and Roscher [136] from two to three-body systems then suggests that removal of short-ranged triples excitation can be compensated by a renormalization of the three-body contact.

As discussed, the *ab initio* method aims at maximizing its predictive power over multiple energy scales relevant to nuclei. If we increase the resolution scale to resolve quarks and gluons, we can use Lattice QCD to study nuclear interactions [137, 138] and currents [139, 140]. However, the method is not yet operational for accurate predictions of atomic nuclei [21-25] at physical quark masses. Nevertheless, short of practical and computational challenges, some of the pion-nucleon couplings of χEFT have been computed on the lattice [141]. Although still operating at unphysical pion masses, lattice results can be extrapolated in the infrared using EFT methods [142]. This extrapolative approach has turned out to be particularly valuable in the data-scarce hyperon sector [143] to, e.g., elucidate the role of strangeness in dense nuclear matter [144]. If we instead decrease the resolution scale, likely at the cost of predictive power, we can integrate out the pion to obtain a systematically improvable pionless EFT [145, 146] for which we can solve the Schrödinger equation and perform *ab initio* computations of processes at very low external momenta. Continuing in this direction, one can devise halo EFT [147, 148], and EFTs for collective phenomena [149–153]. Although these latter two methods are systematically improvable, i.e., they are equipped with a power-counting scheme, they have even less predictive power because they exhibit a relatively small breakdown scale and are tailored to analyze a particular class of low-energy phenomena.

The traditional shell model can be formulated as an *ab initio* approach if one derives the valence-space interaction from a few-nucleon Hamiltonian, based on χEFT, using a systematically improvable prescription [52, 154–156]. Likewise, coarse-grained representations of nuclear phenomena, like those provided by density functional theory, might be cast as an *ab initio* method one day if we can link them to low-energy interactions derived from χEFT [157, 158]. However, this has not yet come to fruition [159, 160].

Finally, it is essential to point out that different and sometimes conflicting assumptions regarding the power counting scheme and its meaning are in use. Besides the foundations, which are covered at length in, e.g., Refs. [79, 161–165], all power counting schemes strive to furnish an EFT description of the nuclear interaction that become increasingly refined at higher orders of the expansion. To test this, we must perform calculations to predict nuclear observables. This is an important example of how the nuclear *ab initio* method and nuclear EFTs are intimately connected and how they can benefit from each other.

6 Summary

The *ab initio* method should not be confused with nuclear EFT. The *ab initio* method includes the ideas of EFT in the sense that it is systematically improvable, and one starts from degrees of freedom determined by the relevant scale separation and resolution. However, the *ab initio* method is also something more. What this "more" is, has not been specified or discussed much in our community. Naturally, misunderstandings and controversies often arise, and one may meet questions like: "Is this really *ab initio*?" With this paper we hope to bring some clarity to that question.

In our view, the *ab initio* method should set *the beginning* at a resolution scale that maximizes the method's predictive power and enables reliable predictions for phenomena at multiple energy scales ranging from a few tens of keV's to hundreds of MeV's. This implies that nucleons are currently the appropriate degrees of freedom for the *ab initio* method. However, it is an open question whether the beginning can be shifted to an even finer resolution scale, e.g., quarks and gluons while increasing the predictive power across energy scales significantly. We interpret the *ab initio* method as a systematically improvable approach employing Lagrangians, Hamiltonians, or energy density functionals derived from the Standard Model according to the principles of EFT. Subsequently solving for observables using numerically exact methods or, if necessary, controlled approximations that allow for systematic predictions with quantified uncertainties.

Despite our best efforts, tensions between theoretical predictions and experimental results remain. It is however clear that the *ab initio* method offers a unique advantage for estimating the uncertainties necessary for assessing the significance of discrepancies between theory and experiment.

Author contributions

All authors listed have made a substantial, direct, and intellectual contribution to the work and approved it for publication.

Funding

This work was supported by the European Research Council (ERC) under the European Unions Horizon 2020 research and innovation program (Grant agreement No. 758027), the Swedish Research Council (Grants Nos. 2017-04234, 2020-05127, and 2021-04507), the U.S. Department of Energy, Office of Science, Office of Nuclear Physics, under Award Nos. DE-FG02-96ER40963 and DE-SC0018223. This research used resources of the Oak Ridge Leadership Computing Facility at the Oak Ridge National Laboratory, which is supported by the Office of Science of the U.S. Department of Energy under Contract No. DE-AC05-00OR22725.

Conflict of interest

The authors declare that the research was conducted in the absence of any commercial or financial relationships that could be construed as a potential conflict of interest.

Publisher's note

References

1. Bethe HA, Bacher RF. Nuclear physics a. stationary states of nuclei. *Rev Mod Phys* (1936) 8:82–229. doi:10.1103/RevModPhys.8.82

2. Bethe HA. Nuclear physics b. nuclear dynamics, theoretical. *Rev Mod Phys* (1937) 9:69–244. doi:10.1103/RevModPhys.9.69

3. Livingston MS, Bethe HA. Nuclear physics c. nuclear dynamics, experimental. *Rev Mod Phys* (1937) 9:245–390. doi:10.1103/RevModPhys.9.245

4. Wilson KG. The renormalization group: Critical phenomena and the kondo problem. *Rev Mod Phys* (1975) 47:773–840. doi:10.1103/RevModPhys.47.773

5. Lepage GP. How to renormalize the schrodinger equation. 8th jorge andre swieca summer school on nuclear physics (1997), 135–180. doi:10.48550/arXiv.nucl-th/9706029

6. Caprio MA, Maris P, Vary JP. Emergence of rotational bands in *ab initio* no-core configuration interaction calculations of light nuclei. *Phys Lett B* (2013) 719:179–84. doi:10.1016/j.physletb.2012.12.064

7. Dytrych T, Launey KD, Draayer JP, Maris P, Vary JP, Saule E, et al. Collective modes in light nuclei from first principles. *Phys Rev Lett* (2013) 111:252501. doi:10.1103/PhysRevLett.111.252501

8. Hagen G, Novario SJ, Sun ZH, Papenbrock T, Jansen GR, Lietz JG, et al. Angular-momentum projection in coupled-cluster theory: Structure of ^{34}Mg. *Phys Rev C* (2022) 105:064311. doi:10.1103/PhysRevC.105.064311

9. Yuan Q, Fan SQ, Hu BS, Li JG, Zhang S, Wang SM, et al. Deformed in-medium similarity renormalization group. *Phys Rev C* (2022) 105:L061303. doi:10.1103/PhysRevC.105.L061303

10. Frosini M, Duguet T, Ebran JP, Bally B, Mongelli T, Rodríguez TR, et al. Multi-reference many-body perturbation theory for nuclei. *The Eur Phys J A* (2022) 58:63. doi:10.1140/epja/s10050-022-00693-y

11. Nollett KM, Pieper SC, Wiringa RB, Carlson J, Hale GM. Quantum Monte Carlo calculations of neutron-α scattering. *Phys Rev Lett* (2007) 99:022502. doi:10.1103/PhysRevLett.99.022502

12. Quaglioni S, Navrátil P. *Ab initio* many-body calculations of n –^{3}H, n –^{4}He, p –^{3,4}He, and n –^{10}Be scattering. *Phys Rev Lett* (2008) 101:092501. doi:10.1103/PhysRevLett.101.092501

13. Hagen G, Jansen GR, Papenbrock T. Structure of ^{78}Ni from first-principles computations. *Phys Rev Lett* (2016) 117:172501. doi:10.1103/PhysRevLett.117.172501

14. Li JG, Michel N, Hu BS, Zuo W, Xu FR. *Ab initio* no-core gamow shell-model calculations of multineutron systems. *Phys Rev C* (2019) 100:054313. doi:10.1103/PhysRevC.100.054313

15. Li JG, Michel N, Zuo W, Xu FR. Resonances of $a = 4t = 1$ isospin triplet states within the *ab initio* no-core gamow shell model. *Phys Rev C* (2021) 104:024319. doi:10.1103/PhysRevC.104.024319

16. Stroberg SR, Holt JD, Schwenk A, Simonis J. *Ab initio* limits of atomic nuclei. *Phys Rev Lett* (2021) 126:022501. doi:10.1103/PhysRevLett.126.022501

17. Lovato A, Gandolfi S, Carlson J, Pieper SC, Schiavilla R. Neutral weak current two-body contributions in inclusive scattering from ^{12}C. *Phys Rev Lett* (2014) 112:182502. doi:10.1103/PhysRevLett.112.182502

18. Lovato A, Carlson J, Gandolfi S, Rocco N, Schiavilla R. *Ab initio* study of (ν_ℓ, ℓ^-) and ($\bar{\nu}\ell$,ℓ^+) inclusive scattering in ^{12}C: Confronting the miniboone and t2k ccqe data. *Phys Rev X* (2020) 10:031068. doi:10.1103/PhysRevX.10.031068

19. Sobczyk JE, Acharya B, Bacca S, Hagen G. *Ab initio* computation of the longitudinal response function in ^{40}Ca. *Phys Rev Lett* (2021) 127:072501. doi:10.1103/PhysRevLett.127.072501

20. Weinberg S. Phenomenological Lagrangians. *Physica A* (1979) 96:327–40. doi:10.1016/0378-4371(79)90223-1

21. Drischler C, Haxton W, McElvain K, Mereghetti E, Nicholson A, Vranas P, et al. Towards grounding nuclear physics in qcd. *Prog Part Nucl Phys* (2021) 121:103888. doi:10.1016/j.ppnp.2021.103888

22. Nicholson A, Berkowitz E, Bulava J, Cheng Chang C, Clark K, Hanlon A, et al. Toward a resolution of the NN controversy. In: PoS LATTICE 2021 (2022). p. 098. doi:10.22323/1.396.0098

23. Barnea N, Contessi L, Gazit D, Pederiva F, van Kolck U. Effective field theory for lattice nuclei. *Phys Rev Lett* (2015) 114:052501. doi:10.1103/PhysRevLett.114.052501

24. McIlroy C, Barbieri C, Inoue T, Doi T, Hatsuda T. Doubly magic nuclei from Lattice QCD forces at M_{PS} =469 MeV/c^2. *Phys Rev C* (2018) 97:021303. doi:10.1103/PhysRevC.97.021303

25. Bansal A, Binder S, Ekström A, Hagen G, Jansen GR, Papenbrock T. Pion-less effective field theory for atomic nuclei and lattice nuclei. *Phys Rev C* (2018) 98:054301. doi:10.1103/PhysRevC.98.054301

26. Hagen G, Papenbrock T, Dean DJ, Hjorth-Jensen M. *Ab initio* coupled-cluster approach to nuclear structure with modern nucleon-nucleon interactions. *Phys Rev C* (2010) 82:034330. doi:10.1103/PhysRevC.82.034330

27. Leidemann W, Orlandini G. Modern *ab initio* approaches and applications in few-nucleon physics with $A \geq 4$. *Prog Part Nucl Phys* (2013) 68:158–214. doi:10.1016/j.ppnp.2012.09.001

28. Roth R, Calci A, Langhammer J, Binder S. *Ab initio* nuclear structure theory: From few to many. *Few Body Syst* (2014) 55:659–65. doi:10.1007/s00601-014-0860-0

29. Roth R. *Ab initio* approaches to nuclear structure. *Lect Notes Phys* (2022) 1005:87–139. doi:10.1007/978-3-031-10751-1_3

30. Hagen G, Papenbrock T, Hjorth-Jensen M, Dean DJ. Coupled-cluster computations of atomic nuclei. *Rep Prog Phys* (2014) 77:096302. doi:10.1088/0034-4885/77/9/096302

31. Launey KD, Dytrych T, Draayer JP. Symmetry-guided large-scale shell-model theory. *Prog Part Nucl Phys* (2016) 89:101–36. doi:10.1016/j.ppnp.2016.02.001

32. Somà V. Self-consistent green's function theory for atomic nuclei. *Front Phys* (2020) 8:340. doi:10.3389/fphy.2020.00340

33. Coraggio L, Itaco N. Perturbative approach to effective shell-model Hamiltonians and operators. *Front Phys* (2020) 8:345. doi:10.3389/fphy.2020.00345

34. Navrátil P, Vary JP, Barrett BR. Properties of ^{12}c in the *ab initio* nuclear shell model. *Phys Rev Lett* (2000) 84:5728–31. doi:10.1103/PhysRevLett.84.5728

35. Leinweber DB. Essential strangeness in nucleon magnetic moments. *Nucl Phys A* (1995) 585:341C–2. doi:10.1016/0375-9474(94)00597-G

36. Friar JL. Nuclear forces and chiral theories. *Few Body Syst Suppl* (1995) 8:471–482. doi:10.48550/arXiv.nucl-th/9601012

37. Zheng DC, Barrett BR, Vary JP, Haxton WC, Song CL. Large-basis shell model studies of light nuclei with a multivalued g-matrix effective interaction. *Phys Rev C* (1995) 52:2488–98. doi:10.1103/PhysRevC.52.2488

38. Navrátil P, Barrett BR. Large-basis shell-model calculations for *p*-shell nuclei. *Phys Rev C* (1998) 57:3119–28. doi:10.1103/PhysRevC.57.3119

39. Barrett BR, Navrátil P, Vary JP. *Ab initio* no core shell model. *Prog Part Nucl Phys* (2013) 69:131–81. doi:10.1016/j.ppnp.2012.10.003

40. Wiringa RB, Stoks VGJ, Schiavilla R. Accurate nucleon-nucleon potential with charge-independence breaking. *Phys Rev C* (1995) 51:38–51. doi:10.1103/PhysRevC.51.38

41. Machleidt R. High-precision, charge-dependent Bonn nucleon-nucleon potential. *Phys Rev C* (2001) 63:024001. doi:10.1103/PhysRevC.63.024001

42. Epelbaum E, Hammer HW, Meißner UG. Modern theory of nuclear forces. *Rev Mod Phys* (2009) 81:1773–825. doi:10.1103/RevModPhys.81.1773

43. Machleidt R, Entem D. Chiral effective field theory and nuclear forces. *Phys Rep* (2011) 503:1–75. doi:10.1016/j.physrep.2011.02.001

44. Hammer HW, König S, van Kolck U. Nuclear effective field theory: Status and perspectives. *Rev Mod Phys* (2020) 92:025004. doi:10.1103/RevModPhys.92.025004

45. Mihaila B, Heisenberg JH. Microscopic calculation of the inclusive electron scattering structure function in ^{16}O. *Phys Rev Lett* (2000) 84:1403–6. doi:10.1103/PhysRevLett.84.1403

46. Dickhoff W, Barbieri C. Self-consistent green's function method for nuclei and nuclear matter. *Prog Part Nucl Phys* (2004) 52:377–496. doi:10.1016/j.ppnp.2004.02.038

47. Dean DJ, Hjorth-Jensen M. Coupled-cluster approach to nuclear physics. *Phys Rev C* (2004) 69:054320. doi:10.1103/PhysRevC.69.054320

48. Epelbaum E, Krebs H, Lee D, Meißner UG. Lattice calculations for a = 3, 4, 6, 12 nuclei using chiral effective field theory. *Eur Phys J A* (2010) 45:335–52. doi:10.1140/epja/i2010-11009-x

49. Tsukiyama K, Bogner SK, Schwenk A. In-medium similarity renormalization group for nuclei. *Phys Rev Lett* (2011) 106:222502. doi:10.1103/PhysRevLett.106.222502

50. Somà V, Barbieri C, Duguet T. *Ab initio* gorkov-green's function calculations of open-shell nuclei. *Phys Rev C* (2013) 87:011303. doi:10.1103/PhysRevC.87.011303

51. Hergert H, Bogner SK, Morris TD, Schwenk A, Tsukiyama K. The in-medium similarity renormalization group: A novel *ab initio* method for nuclei. *Phys Rep* (2016) 621:165–222. doi:10.1016/j.physrep.2015.12.007

52. Stroberg SR, Calci A, Hergert H, Holt JD, Bogner SK, Roth R, et al. Nucleus-dependent valence-space approach to nuclear structure. *Phys Rev Lett* (2017) 118:032502. doi:10.1103/PhysRevLett.118.032502

53. Roth R, Binder S, Vobig K, Calci A, Langhammer J, Navrátil P. Medium-mass nuclei with normal-ordered chiral *NN*+3*N* interactions. *Phys Rev Lett* (2012) 109:052501. doi:10.1103/PhysRevLett.109.052501

54. Binder S, Langhammer J, Calci A, Roth R. *Ab initio* path to heavy nuclei. *Phys Lett B* (2014) 736:119–23. doi:10.1016/j.physletb.2014.07.010

55. Lähde TA, Epelbaum E, Krebs H, Lee D, Meißner UG, Rupak G. Lattice effective field theory for medium-mass nuclei. *Phys Lett B* (2014) 732:110–5. doi:10.1016/j.physletb.2014.03.023

56. Morris TD, Simonis J, Stroberg SR, Stumpf C, Hagen G, Holt JD, et al. Structure of the lightest tin isotopes. *Phys Rev Lett* (2018) 120:152503. doi:10.1103/PhysRevLett.120.152503

57. Miyagi T, Stroberg SR, Holt JD, Shimizu N. *Ab initio* multishell valence-space Hamiltonians and the island of inversion. *Phys Rev C* (2020) 102:034320. doi:10.1103/PhysRevC.102.034320

58. Hu B, Jiang W, Miyagi T, Sun Z, Ekström A, Forssén C, et al. *Ab initio* predictions link the neutron skin of 208pb to nuclear forces. *Nat Phys* (2022) 18:1196–200. doi:10.1038/s41567-022-01715-8

59. Hagen G, Papenbrock T, Dean DJ, Schwenk A, Nogga A, Włoch M, et al. Coupled-cluster theory for three-body Hamiltonians. *Phys Rev C* (2007) 76:034302. doi:10.1103/PhysRevC.76.034302

60. Ripoche J, Tichai A, Duguet T. Normal-ordered *k*-body approximation in particle-number-breaking theories. *Eur Phys J A* (2020) 56:40. doi:10.1140/epja/s10050-020-00045-8

61. Hagen G, Papenbrock T, Dean DJ. Solution of the center-of-mass problem in nuclear structure calculations. *Phys Rev Lett* (2009) 103:062503. doi:10.1103/PhysRevLett.103.062503

62. Parzuchowski NM, Stroberg SR, Navrátil P, Hergert H, Bogner SK. *Ab initio* electromagnetic observables with the in-medium similarity renormalization group. *Phys Rev C* (2017) 96:034324. doi:10.1103/PhysRevC.96.034324

63. Djärv T, Ekström A, Forssén C, Jansen GR. Normal-ordering approximations and translational (non)invariance. *Phys Rev C* (2021) 104:024324. doi:10.1103/PhysRevC.104.024324

64. Ekström A, Jansen GR, Wendt KA, Hagen G, Papenbrock T, Carlsson BD, et al. Accurate nuclear radii and binding energies from a chiral interaction. *Phys Rev C* (2015) 91:051301. doi:10.1103/PhysRevC.91.051301

65. Jiang WG, Ekström A, Forssén C, Hagen G, Jansen GR, Papenbrock T. Accurate bulk properties of nuclei from $a = 2$ to ∞ from potentials with Δ isobars. *Phys Rev C* (2020) 102:054301. doi:10.1103/PhysRevC.102.054301

66. Roth R, Langhammer J, Calci A, Binder S, Navrátil P. Similarity-transformed chiral *NN* + 3*N* interactions for the *ab initio* description of ^{12}**C** and ^{16}**O**. *Phys Rev Lett* (2011) 107:072501. doi:10.1103/PhysRevLett.107.072501

67. Hebeler K, Bogner SK, Furnstahl RJ, Nogga A, Schwenk A. Improved nuclear matter calculations from chiral low-momentum interactions. *Phys Rev C* (2011) 83:031301. doi:10.1103/PhysRevC.83.031301

68. Ekström A, Baardsen G, Forssén C, Hagen G, Hjorth-Jensen M, Jansen GR, et al. Optimized chiral nucleon-nucleon interaction at next-to-next-to-leading order. *Phys Rev Lett* (2013) 110:192502. doi:10.1103/PhysRevLett.110.192502

69. Epelbaum E, Krebs H, Meißner UG. Precision nucleon-nucleon potential at fifth order in the chiral expansion. *Phys Rev Lett* (2015) 115:122301. doi:10.1103/PhysRevLett.115.122301

70. Piarulli M, Girlanda L, Schiavilla R, Pérez RN, Amaro JE, Arriola ER. Minimally nonlocal nucleon-nucleon potentials with chiral two-pion exchange includingΔresonances. *Phys Rev C* (2015) 91:024003. doi:10.1103/PhysRevC.91.024003

71. Piarulli M, Girlanda L, Schiavilla R, Kievsky A, Lovato A, Marcucci LE, et al. Local chiral potentials with Δ-intermediate states and the structure of light nuclei. *Phys Rev C* (2016) 94:054007. doi:10.1103/PhysRevC.94.054007

72. Carlsson BD, Ekström A, Forssén C, Strömberg DF, Jansen GR, Lilja O, et al. Uncertainty analysis and order-by-order optimization of chiral nuclear interactions. *Phys Rev X* (2016) 6:011019. doi:10.1103/PhysRevX.6.011019

73. Ekström A, Hagen G, Morris TD, Papenbrock T, Schwartz PD. Δ isobars and nuclear saturation. *Phys Rev C* (2018) 97:024332. doi:10.1103/PhysRevC.97.024332

74. Reinert P, Krebs H, Epelbaum E. Semilocal momentum-space regularized chiral two-nucleon potentials up to fifth order. *Eur Phys J A* (2018) 54:86. doi:10.1140/epja/i2018-12516-4

75. Lu BN, Li N, Elhatisari S, Lee D, Epelbaum E, Meißner UG. Essential elements for nuclear binding. *Phys Lett B* (2019) 797:134863. doi:10.1016/j.physletb.2019.134863

76. Somà V, Navrátil P, Raimondi F, Barbieri C, Duguet T. Novel chiral Hamiltonian and observables in light and medium-mass nuclei. *Phys Rev C* (2020) 101:014318. doi:10.1103/PhysRevC.101.014318

77. Maris P, Epelbaum E, Furnstahl RJ, Golak J, Hebeler K, Huther T, et al. Light nuclei with semilocal momentum-space regularized chiral interactions up to third order. *Phys Rev C* (2021) 103:054001. doi:10.1103/PhysRevC.103.054001

78. Nosyk Y, Entem DR, Machleidt R. Nucleon-nucleon potentials from Δ-full chiral effective-field-theory and implications. *Phys Rev C* (2021) 104:054001. doi:10.1103/PhysRevC.104.054001

79. Yang CJ, Ekström A, Forssén C, Hagen G. Power counting in chiral effective field theory and nuclear binding. *Phys Rev C* (2021) 103:054304. doi:10.1103/PhysRevC.103.054304

80. Elhatisari S, Lee D, Rupak G, Epelbaum E, Krebs H, Lähde TA, et al. *Ab initio* alpha–alpha scattering. *Nature* (2015) 528:111–4. doi:10.1038/nature16067

81. Navrátil P, Quaglioni S, Hupin G, Romero-Redondo C, Calci A. Unified *ab initio* approaches to nuclear structure and reactions. *Physica Scripta* (2016) 91:053002. doi:10.1088/0031-8949/91/5/053002

82. Bedaque PF, van Kolck U. Effective field theory for few-nucleon systems. *Annu Rev Nucl Part Sci* (2002) 52:339–96. doi:10.1146/annurev.nucl.52.050102.090637

83. Bogner SK, Kuo TTS, Schwenk A. Model-independent low momentum nucleon interaction from phase shift equivalence. *Phys Rep* (2003) 386:1–27. doi:10.1016/j.physrep.2003.07.001

84. Bogner SK, Furnstahl RJ, Perry RJ. Similarity renormalization group for nucleon-nucleon interactions. *Phys Rev C* (2007) 75:061001. doi:10.1103/PhysRevC.75.061001

85. Furnstahl R, Hammer HW. Are occupation numbers observable? *Phys Lett B* (2002) 531:203–8. doi:10.1016/S0370-2693(01)01504-0

86. Jurgenson ED, Navrátil P, Furnstahl RJ. Evolution of nuclear many-body forces with the similarity renormalization group. *Phys Rev Lett* (2009) 103:082501. doi:10.1103/PhysRevLett.103.082501

87. More SN, Bogner SK, Furnstahl RJ. Scale dependence of deuteron electrodisintegration. *Phys Rev C* (2017) 96:054004. doi:10.1103/PhysRevC.96.054004

88. Furnstahl RJ, Hagen G, Papenbrock T. Corrections to nuclear energies and radii in finite oscillator spaces. *Phys Rev C* (2012) 86:031301. doi:10.1103/PhysRevC.86.031301

89. König S, Lee D. Volume dependence of n-body bound states. *Phys Lett B* (2018) 779:9–15. doi:10.1016/j.physletb.2018.01.060

90. Schindler MR, Phillips DR. Bayesian methods for parameter estimation in effective field theories. *Ann Phys* (2009) 324:682–708. doi:10.1016/j.aop.2008.09.003

91. Furnstahl RJ, Klco N, Phillips DR, Wesolowski S. Quantifying truncation errors in effective field theory. *Phys Rev C* (2015) 92:024005. doi:10.1103/PhysRevC.92.024005

92. Lee D. Lattice simulations for few- and many-body systems. *Prog Part Nucl Phys* (2009) 63:117–54. doi:10.1016/j.ppnp.2008.12.001

93. Lähde TA, Meißner UG. *Nuclear lattice effective field theory: An introduction*. Berlin: Springer (2019). doi:10.1007/978-3-030-14189-9

94. Hagen G, Ekström A, Forssén C, Jansen GR, Nazarewicz W, Papenbrock T, et al. Neutron and weak-charge distributions of the ^{48}Ca nucleus. *Nat Phys* (2016) 12:186–90. doi:10.1038/nphys3529

95. Hagen G, Hjorth-Jensen M, Jansen GR, Papenbrock T. Emergent properties of nuclei from *ab initio* coupled-cluster calculations. *Phys Scr* (2016) 91:063006. doi:10.1088/0031-8949/91/6/063006

96. Bontems V, Duguet T, Hagen G, Somà V. Topical issue on the tower of effective (field) theories and the emergence of nuclear phenomena. *Eur Phys J A* (2021) 57:42. doi:10.1140/epja/s10050-021-00356-4

97. Tropiano AJ, Bogner SK, Furnstahl RJ. Short-range correlation physics at low renormalization group resolution. *Phys Rev C* (2021) 104:034311. doi:10.1103/PhysRevC.104.034311

98. Hartmann S. Effective field theories, reductionism and scientific explanation. *Stud Hist Philos Sci B: Stud Hist Philos Mod Phys* (2001) 32:267–304. doi:10.1016/s1355-2198(01)00005-3

99. Rivat S, Grinbaum A. Philosophical foundations of effective field theories. *Eur Phys J A* (2020) 56:90. doi:10.1140/epja/s10050-020-00089-w

100. Lindley D. The philosophy of statistics. *J R Stat Soc Ser D (The Statistician)* (2000) 49:293–337. doi:10.1111/1467-9884.00238

101. Box GEP. Science and statistics. *J Am Stat Assoc* (1976) 71:791–9. doi:10.1080/01621459.1976.10480949

102. Kennedy MC, O'Hagan A. Bayesian calibration of computer models. *J R Stat Soc Ser B (Statistical Methodology)* (2001) 63:425–64. doi:10.1111/1467-9868.00294

103. Brynjarsdóttir J, O'Hagan A. Learning about physical parameters: The importance of model discrepancy. *Inverse Probl* (2014) 30:114007. doi:10.1088/0266-5611/30/11/114007

104. Brooks S, Gelman A, Jones G, Meng XL. *Handbook of Markov chain Monte Carlo*. Florida: CRC Press (2011).

105. Svensson I, Ekström A, Forssén C. Bayesian parameter estimation in chiral effective field theory using the Hamiltonian Monte Carlo method. *Phys Rev C* (2022) 105:014004. doi:10.1103/PhysRevC.105.014004

106. Wesolowski S, Svensson I, Ekström A, Forssén C, Furnstahl RJ, Melendez JA, et al. Rigorous constraints on three-nucleon forces in chiral effective field theory from fast and accurate calculations of few-body observables. *Phys Rev C* (2021) 104:064001. doi:10.1103/PhysRevC.104.064001

107. König S, Ekström A, Hebeler K, Lee D, Schwenk A. Eigenvector continuation as an efficient and accurate emulator for uncertainty quantification. *Phys Lett B* (2020) 810:135814. doi:10.1016/j.physletb.2020.135814

108. Ekström A, Hagen G. Global sensitivity analysis of bulk properties of an atomic nucleus. *Phys Rev Lett* (2019) 123:252501. doi:10.1103/PhysRevLett.123.252501

109. Witała H, Golak J, Skibiński R. Efficient emulator for solving three-nucleon continuum Faddeev equations with chiral three-nucleon force comprising any number of contact terms. *Eur Phys J A* (2021) 57:241. doi:10.1140/epja/s10050-021-00555-z

110. Furnstahl R, Garcia A, Millican P, Zhang X. Efficient emulators for scattering using eigenvector continuation. *Phys Lett B* (2020) 809:135719. doi:10.1016/j.physletb.2020.135719

111. Chaloner K, Verdinelli I. Bayesian experimental design: A review. *Statist Sci* (1995) 10:273–304. doi:10.1214/ss/1177009939

112. Santner TJ, Williams BJ, Notz WI. *The design and analysis of computer experiments*. Berlin: Springer (2003). doi:10.1007/978-1-4757-3799-8

113. Farrow M, Goldstein M. Trade-off sensitive experimental design: A multicriterion, decision theoretic, bayes linear approach. *J Stat Plan Inference* (2006) 136:498–526. doi:10.1016/j.jspi.2004.07.008

114. Vernon I, Liu J, Goldstein M, Rowe J, Topping J, Lindsey K. Bayesian uncertainty analysis for complex systems biology models: Emulation, global parameter searches and evaluation of gene functions. *BMC Syst Biol* (2018) 12:1. doi:10.1186/s12918-017-0484-3

115. Melendez JA, Furnstahl RJ, Griesshammer HW, McGovern JA, Phillips DR, Pratola MT. Designing optimal experiments: An application to proton compton scattering. *Eur Phys J A* (2021) 57:81. doi:10.1140/epja/s10050-021-00382-2

116. Pablo G, Jorge P. From noise to information: The transfer function formalism for uncertainty quantification in reconstructing the nuclear density. *Phys Rev C* (2021) 104:024301. doi:10.1103/PhysRevC.104.024301

117. Glöckle W. *The quantum mechanical few-body problem*. Berlin: Springer-Verlag (1983).

118. Carlson J, Gandolfi S, Pederiva F, Pieper SC, Schiavilla R, Schmidt KE, et al. Quantum Monte Carlo methods for nuclear physics. *Rev Mod Phys* (2015) 87:1067–118. doi:10.1103/RevModPhys.87.1067

119. Kamada H, Nogga A, Glöckle W, Hiyama E, Kamimura M, Varga K, et al. Benchmark test calculation of a four-nucleon bound state. *Phys Rev C* (2001) 64:044001. doi:10.1103/PhysRevC.64.044001

120. Forssén C, Carlsson BD, Johansson HT, Sääf D, Bansal A, Hagen G, et al. Large-scale exact diagonalizations reveal low-momentum scales of nuclei. *Phys Rev C* (2018) 97:034328. doi:10.1103/PhysRevC.97.034328

121. Maris P, Epelbaum E, Furnstahl RJ, Golak J, Hebeler K, Hüther T, et al. Light nuclei with semilocal momentum-space regularized chiral interactions up to third order. *arXiv:nucl-th* 2012.12396 (2020). doi:10.48550/arXiv.2012.12396

122. Maris P, Roth R, Epelbaum E, Furnstahl RJ, Golak J, Hebeler K, et al. Nuclear properties with semilocal momentum-space regularized chiral interactions beyond N2LO. *Phys Rev C* (2022) 106:064002. doi:10.1103/PhysRevC.106.064002

123. Ekström A, Jansen GR, Wendt KA, Hagen G, Papenbrock T, Carlsson BD, et al. Accurate nuclear radii and binding energies from a chiral interaction. *arXiv:nucl-th* 1502.04682 (2015). doi:10.48550/arXiv.1502.04682

124. Melendez JA, Furnstahl RJ, Phillips DR, Pratola MT, Wesolowski S. Quantifying correlated truncation errors in effective field theory. *Phys Rev C* (2019) 100:044001. doi:10.1103/PhysRevC.100.044001

125. Drischler C, Furnstahl RJ, Melendez JA, Phillips DR. How well do we know the neutron-matter equation of state at the densities inside neutron stars? A bayesian approach with correlated uncertainties. *Phys Rev Lett* (2020) 125:202702. doi:10.1103/PhysRevLett.125.202702

126. Tews I, Davoudi Z, Ekström A, Holt JD, Lynn JE. New ideas in constraining nuclear forces. *J Phys G* (2020) 47:103001. doi:10.1088/1361-6471/ab9079

127. Miyagi T, Stroberg SR, Navrátil P, Hebeler K, Holt JD. Converged *ab initio* calculations of heavy nuclei. *Phys Rev C* (2022) 105:014302. doi:10.1103/PhysRevC.105.014302

128. Hergert H. A guided tour of *ab initio* nuclear many-body theory. *Front Phys* (2020) 8:379. doi:10.3389/fphy.2020.00379

129. Tichai A, Roth R, Duguet T. Many-body perturbation theories for finite nuclei. *Front Phys* (2020) 8:164. doi:10.3389/fphy.2020.00164

130. Stroberg SR, Henderson J, Hackman G, Ruotsalainen P, Hagen G, Holt JD. Systematics of *e*2 strength in the *sd* shell with the valence-space in-medium similarity renormalization group. *Phys Rev C* (2022) 105:034333. doi:10.1103/PhysRevC.105.034333

131. Novario SJ, Hagen G, Jansen GR, Papenbrock T. Charge radii of exotic neon and magnesium isotopes. *Phys Rev C* (2020) 102:051303. doi:10.1103/PhysRevC.102.051303

132. Sun ZH, Bell CA, Hagen G, Papenbrock T. How to renormalize coupled cluster theory. *Phys Rev C* (2022) 106:L061302. doi:10.1103/PhysRevC.106.L061302

133. Taube AG, Bartlett RJ. Improving upon ccsd(t): Lambda ccsd(t). i. potential energy surfaces. *J Chem Phys* (2008) 128:044110. doi:10.1063/1.2830236

134. Lee YS, Kucharski SA, Bartlett RJ. A coupled cluster approach with triple excitations. *J Chem Phys* (1984) 81:5906–12. doi:10.1063/1.447591

135. Bartlett RJ, Musiał M. Coupled-cluster theory in quantum chemistry. *Rev Mod Phys* (2007) 79:291–352. doi:10.1103/RevModPhys.79.291

136. Bogner SK, Roscher D. High-momentum tails from low-momentum effective theories. *Phys Rev C* (2012) 86:064304. doi:10.1103/PhysRevC.86.064304

137. Illa M, Beane SR, Chang E, Davoudi Z, Detmold W, Murphy DJ, et al. Low-energy scattering and effective interactions of two baryons at $m_\pi \sim 450$ MeV from lattice quantum chromodynamics. *Phys Rev D* (2021) 103:054508. doi:10.1103/PhysRevD.103.054508

138. Aoki S, Doi T. Lattice qcd and baryon-baryon interactions: Hal qcd method. *Front Phys* (2020) 8:307. doi:10.3389/fphy.2020.00307

139. Davoudi Z, Detmold W, Shanahan P, Orginos K, Parreño A, Savage MJ, et al. Nuclear matrix elements from lattice qcd for electroweak and beyond-standard-model processes. *Phys ReportsNuclear matrix Elem lattice QCD electroweak beyond–Standard-Model Process* (2021) 900:1–74. doi:10.1016/j.physrep.2020.10.004

140. Parreño A, Shanahan PE, Wagman ML, Winter F, Chang E, Detmold W, et al. Axial charge of the triton from lattice qcd. *Phys Rev D* (2021) 103:074511. doi:10.1103/PhysRevD.103.074511

141. Chang CC, Nicholson AN, Rinaldi E, Berkowitz E, Garron N, Brantley DA, et al. A per-cent-level determination of the nucleon axial coupling from quantum chromodynamics. *Nature* (2018) 558:91–4. doi:10.1038/s41586-018-0161-8

142. Eliyahu M, Bazak B, Barnea N. Extrapolating lattice qcd results using effective field theory. *Phys Rev C* (2020) 102:044003. doi:10.1103/PhysRevC.102.044003

143. Beane SR, Chang E, Cohen SD, Detmold W, Lin HW, Luu TC, et al. Light nuclei and hypernuclei from quantum chromodynamics in the limit of SU(3) flavor symmetry. *Phys Rev D* (2013) 87:034506. doi:10.1103/PhysRevD.87.034506

144. Beane SR, Chang E, Cohen SD, Detmold W, Lin HW, Luu TC, et al. Hyperon-nucleon interactions from quantum chromodynamics and the composition of dense nuclear matter. *Phys Rev Lett* (2012) 109:172001. doi:10.1103/PhysRevLett.109.172001

145. Kaplan DB, Savage MJ, Wise MB. Two-nucleon systems from effective field theory. *Nucl Phys B* (1998) 534:329–55. doi:10.1016/S0550-3213(98)00440-4

146. van Kolck U. Effective field theory of short-range forces. *Nucl Phys A* (1999) 645: 273–302. doi:10.1016/S0375-9474(98)00612-5

147. Bertulani CA, Hammer HW, van Kolck U. Effective field theory for halo nuclei: Shallow -wave states. *Nucl Phys A* (2002) 712:37–58. doi:10.1016/S0375-9474(02)01270-8

148. Hammer HW, Ji C, Phillips DR. Effective field theory description of halo nuclei. *J Phys G: Nucl Part Phys* (2017) 44:103002. doi:10.1088/1361-6471/aa83db

149. Coello Pérez EA, Papenbrock T. Effective field theory for nuclear vibrations with quantified uncertainties. *Phys Rev C* (2015) 92:064309. doi:10.1103/PhysRevC.92.064309

150. Papenbrock T. Effective theory for deformed nuclei. *Nucl Phys A* (2011) 852: 36–60. doi:10.1016/j.nuclphysa.2010.12.013

151. Chen QB, Kaiser N, Meißner UG, Meng J. Effective field theory for triaxially deformed nuclei. *Eur Phys J A* (2017) 53:204. doi:10.1140/epja/i2017-12404-5

152. Alnamlah IK, Coello Pérez EA, Phillips DR. Effective field theory approach to rotational bands in odd-mass nuclei. *Phys Rev C* (2021) 104:064311. doi:10.1103/PhysRevC.104.064311

153. Papenbrock T. Effective field theory of pairing rotations. *Phys Rev C* (2022) 105: 044322. doi:10.1103/PhysRevC.105.044322

154. Jansen GR, Engel J, Hagen G, Navratil P, Signoracci A. *Ab initio* coupled-cluster effective interactions for the shell model: Application to neutron-rich oxygen and carbon isotopes. *Phys Rev Lett* (2014) 113:142502. doi:10.1103/PhysRevLett.113.142502

155. Sun ZH, Morris TD, Hagen G, Jansen GR, Papenbrock T. Shell-model coupled-cluster method for open-shell nuclei. *Phys Rev C* (2018) 98:054320. doi:10.1103/PhysRevC.98.054320

156. Sun ZH, Hagen G, Jansen GR, Papenbrock T. Effective shell-model interaction for nuclei "southeast" of ^{100}Sn. *Phys Rev C* (2021) 104:064310. doi:10.1103/PhysRevC.104.064310

157. Bogner SK, Furnstahl RJ, Platter L. Density matrix expansion for low-momentum interactions. *Eur Phys J A* (2009) 39:219–41. doi:10.1140/epja/i2008-10695-1

158. Dobaczewski J. *Ab initio* derivation of model energy density functionals. *J Phys G: Nucl Part Phys* (2016) 43:04LT01. doi:10.1088/0954-3899/43/4/04lt01

159. Furnstahl RJ. Turning the nuclear energy density functional method into a proper effective field theory: Reflections. *Eur Phys J A* (2020) 56:85. doi:10.1140/epja/s10050-020-00095-y

160. Salvioni G, Dobaczewski J, Barbieri C, Carlsson G, Idini A, Pastore A. Model nuclear energy density functionals derived from *ab initio* calculations. *J Phys G: Nucl Part Phys* (2020) 47:085107. doi:10.1088/1361-6471/ab8d8e

161. Nogga A, Timmermans RGE, van Kolck U. Renormalization of one-pion exchange and power counting. *Phys Rev C* (2005) 72:054006. doi:10.1103/PhysRevC.72.054006

162. Epelbaum E, Meißner UG. On the renormalization of the one–pion exchange potential and the consistency of weinberg's power counting. *Few-Body Syst* (2013) 54: 2175–90. doi:10.1007/s00601-012-0492-1

163. Epelbaum E, Gasparyan AM, Gegelia J, Meißner UG. How (not) to renormalize integral equations with singular potentials in effective field theory. *Eur Phys J A* (2018) 54:186. doi:10.1140/epja/i2018-12632-1

164. Yang CJ. Do we know how to count powers in pionless and pionful effective field theory? *Eur Phys J A* (2020) 56:96. doi:10.1140/epja/s10050-020-00104-0

165. van Kolck U. The problem of renormalization of chiral nuclear forces. *Front Phys* (2020) 8:79. doi:10.3389/fphy.2020.00079

frontiers | Frontiers in Physics

TYPE Original Research
PUBLISHED 01 March 2023
DOI 10.3389/fphy.2023.1064601

OPEN ACCESS

EDITED BY
Maria Piarulli,
Washington University in St. Louis,
United States

REVIEWED BY
Heiko Hergert,
Michigan State University, United States
Praveen C Srivastava,
Indian Institute of Technology Roorkee,
India

*CORRESPONDENCE
K. S. Becker,
kbeck13@lsu.edu

SPECIALTY SECTION
This article was submitted
to Nuclear Physics,
a section of the journal
Frontiers in Physics

RECEIVED 08 October 2022
ACCEPTED 13 January 2023
PUBLISHED 01 March 2023

CITATION
Becker KS, Launey KD, Ekström A and
Dytrych T (2023), *Ab initio* symmetry-
adapted emulator for studying emergent
collectivity and clustering in nuclei.
Front. Phys. 11:1064601.
doi: 10.3389/fphy.2023.1064601

Ab initio symmetry-adapted emulator for studying emergent collectivity and clustering in nuclei

K. S. Becker[1]*, K. D. Launey[1], A. Ekström[2] and T. Dytrych[1,3]

[1]Department of Physics and Astronomy, Louisiana State University, Baton Rouge, LA, United States, [2]Department of Physics, Chalmers University of Technology, Gothenburg, Sweden, [3]Nuclear Physics Institute, Academy of Sciences of the Czech Republic, Řež, Czech Republic

We discuss emulators from the *ab initio* symmetry-adapted no-core shell-model framework for studying the formation of alpha clustering and collective properties without effective charges. We present a new type of an emulator, one that utilizes the eigenvector continuation technique but is based on the use of symplectic symmetry considerations. This is achieved by using physically relevant degrees of freedom, namely, the symmetry-adapted basis, which exploits the almost perfect symplectic symmetry in nuclei. Specifically, we study excitation energies, point-proton root-mean-square radii, along with electric quadrupole moments and transitions for ^{6}Li and ^{12}C. We show that the set of parameterizations of the chiral potential used to train the emulators has no significant effect on predictions of dominant nuclear features, such as shape and the associated symplectic symmetry, along with cluster formation, but slightly varies details that affect collective quadrupole moments, asymptotic normalization coefficients, and alpha partial widths up to a factor of two. This makes these types of emulators important for further constraining the nuclear force for high-precision nuclear structure and reaction observables.

KEYWORDS

***ab initio* symmetry-adapted no-core shell model, nuclear collectivity, nuclear clustering, eigenvector continuation, emulators, 6Li, 12C**

Introduction

Ab initio approaches to nuclear structure and reactions (for an overview, see Ref. [1]) aim to provide accurate predictions based on few-nucleon forces, such as the ones derived from chiral effective field theory (EFT) [for a review, see e.g. Ref. [2] and references therein]. To achieve this, it is imperative to utilize high-precision nuclear forces that accurately describe nuclear correlations, from short- to long-range correlations, as well as to quantify uncertainties that arise from the nuclear force and the controlled approximations in solving the many-body Schrödinger equation [3]. Such developments use statistical tools, including, for example, Bayesian analysis [4], global sensitivity methods [5], and uncertainty estimates based on regression [6, 7], that sometimes require a large number of computationally intensive calculations which often poses a challenge.

In this paper, we seek to overcome some of these difficulties by combining the symmetry-adapted no-core shell model (SA-NCSM) framework [8–10] with the methodology of eigenvector continuation (EVC) [5, 11, 12]. The SA-NCSM uses a physically relevant basis that, in manageable model spaces, achieves descriptions of light to medium-mass nuclei, including challenging nuclear features, such as collectivity, clustering, and related continuum effects. Similarly, EVC further reduces the sizes of Hamiltonian matrices by mapping them onto much smaller matrices referred to as emulators, low-dimensional manifolds built upon a set of characteristic solutions to the many-body Schrödinger equation. The proposed

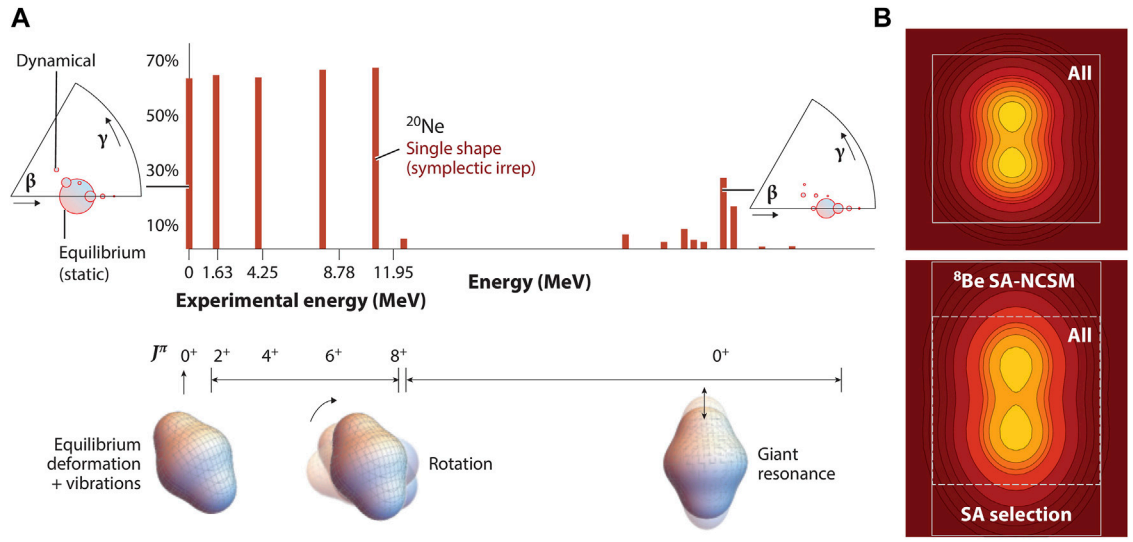

FIGURE 1
(A) Emergent symplectic symmetry in nuclei: Contribution of the most dominant shape to the 0^+ ground state of ^{20}Ne and its rotational band (2^+, 4^+, 6^+, and 8^+), as well as to excited 0^+ states, pointing to a fragmented giant monopole resonance [8]; for selected states, the deformation distribution within a shape is shown in terms of the shape parameters, the average deformation β and triaxiality angle γ (based on *ab initio* SA-NCSM calculations with NNLO$_{\text{opt}}$ in a model space of 11 HO shells with $\hbar\Omega$ = 15 MeV inter-shell distance). **(B)** Schematic illustration of the SA concept shown for ^{8}Be: a smaller model space (square) includes all possible shapes (labeled as "All") and yields spatially compressed wave functions (top); a larger model space (rectangle in lower panel) accommodates, in a well prescribed way, spatially extended modes ("SA selection") that are neglected in smaller model spaces. Figure from Ref. [9] under the terms of its CC BY license.

symmetry-adapted eigenvector continuation (SA-EVC) method opens the door to calculations up through the medium-mass region and studies of collective and clustering nuclear features that otherwise might be computationally infeasible.

With a view toward inferring new knowledge of the nuclear forces relevant to structure and reaction observables, we construct novel SA-EVC emulators to study collective and clustering nuclear properties in ^{6}Li and ^{12}C (an emulator for the ^{6}Li binding energy is validated in Ref. [13]). Because this study focuses on the method validity, we utilize SA-NCSM calculations for a single harmonic oscillator (HO) strength $\hbar\Omega$, for which and for a specific parameterization of the chiral potential we show that the observables under consideration converge with the number of HO excitations, including point-proton root-mean-square (rms) radii and $E2$ transitions. The SA-NCSM utilizes a symplectic Sp(3,$\mathbb{R}$)-adapted basis and selected model spaces[1] that are significantly reduced in size due to symmetry considerations without sacrificing the physics of interest. Moreover, we show that the set of chiral potential parameterizations used to train the emulators has no significant effect on dominant nuclear features such as the nuclear shape (and associated symplectic symmetry) and cluster formation, making the SA model spaces highly suitable for this study. However, from one parameterization to another we find that probability amplitudes of wave functions and cluster peak distance vary slightly, affecting by a factor of two or less collective quadrupole moments, asymptotic normalization coefficients (ANCs), and alpha partial widths (which provide the probability for the alpha decay among all possible decays of a state). This suggests that these types of observables, and associated emulators, are important to inform and construct the nuclear forces for high-precision nuclear calculations.

Theoretical methods

Ab initio symmetry-adapted no-core shell model

Ab initio large-scale calculations [8, 9] have recently revealed a remarkably ubiquitous and almost perfect symmetry, the Sp(3,$\mathbb{R}$) symplectic symmetry, in nuclei that naturally emerges from first principles up through the calcium region (anticipated to hold even stronger in heavy nuclei [14]). Since this symmetry does not mix nuclear shapes, this novel nuclear feature provides important insight from first principles into the physics of nuclei and their low-lying excitations as dominated by only one or two collective shapes—equilibrium shapes with their vibrations—that rotate (Figure 1A).

The SA-NCSM theory [8, 10, 15] capitalizes on these findings and exploits the idea that the infinite Hilbert space can be equivalently spanned by "microscopic" nuclear shapes and their rotations [or symplectic irreducible representations (irreps), subspaces that preserve the symmetry], where "microscopic" refers to the fact that these configurations track with the position and momentum coordinates of each particle. A collective nuclear shape can be viewed as an equilibrium ("static") deformation and its vibrations ("dynamical" deformations) of the giant-resonance type, as illustrated in the β-γ plots of Figure 1A [8, 16]. A key ingredient of the SA concept is illustrated in Figure 1B, namely, while many shapes relevant to low-lying states are included in typical shell-model spaces (Figure 1B, top),

1 Throughout the paper, we will refer to the selected SA-NCSM model spaces as SA model spaces.

the vibrations of largely deformed equilibrium shapes and spatially extended modes like clustering often lie outside such spaces. The selected model space in the SA-NCSM remedies this, and includes, in a well prescribed way, those configurations. Note that this is critical for enhanced deformation, since spherical and less deformed shapes, including relevant single-particle effects, easily develop in comparatively small model-space sizes.

In this study, we utilize the *ab initio* SA-NCSM theory [8–10] that is based on the NCSM concept [17, 18] with nuclear interactions typically derived from the chiral EFT (e.g. [2, 19–23]). We use SA-NCSM model spaces, which are reorganized to a correlated basis that respects the shape-preserving Sp (3,$\mathbb{R}$) symmetry and its embedded symmetry, the deformation-related SU(3) [8–10]. We note that while the model utilizes symmetry groups to construct the basis and calculate matrix elements, descriptions are not limited *a priori* to any symmetry and can account for significant symmetry breaking.

The SA-NCSM is reviewed in Refs. [9, 10] and has been applied to light and medium-mass nuclei using SU(3)- and Sp(3,$\mathbb{R}$)-adapted bases. The many-nucleon basis states of the SA-NCSM are constructed using efficient group-theoretical algorithms and are labeled according to SU(3) × SU(2) by the proton, neutron and total intrinsic spins, S_p, S_n, and S, respectively, and $(\lambda_\omega\ \mu_\omega)$ quantum numbers with $\lambda_\omega = N_z - N_x$ and $\mu_\omega = N_x - N_y$, where $N_x + N_y + N_z = N_0 + N$, for a total of $N_0 + N$ HO quanta distributed in the x, y, and z directions[2]. Here, $N_0\hbar\Omega$ is the lowest total HO energy for all particles ("valence-shell configuration") and $N\hbar\Omega$ ($N \leq N_{\max}$) is the additional energy of all particle-hole excitations. Thus, for example, $(\lambda_\omega\ \mu_\omega) = (0\ 0)$, for which $N_x = N_y = N_z$, describes a spherical configuration, while N_z larger than $N_x = N_y$ ($\mu_\omega = 0$) indicates prolate deformation. In addition, a closed-shell configuration has (0 0). Indeed, spherical shapes, or no deformation, are a part of the SA basis. However, most nuclei—from light to heavy—are deformed in the *body-fixed* frame, which for 0^+ states appear spherical in the *laboratory* frame.

Furthermore, considering the embedding symmetry Sp(3,$\mathbb{R}$) ⊃SU(3), one can further organize SU(3) deformed configurations into subspaces that preserve Sp(3,$\mathbb{R}$) symmetry. Each of these subspaces (symplectic irrep, labeled by σ) is characterized by a given equilibrium shape, labeled by a single deformation $N_\sigma(\lambda_\sigma\ \mu_\sigma)$. For example, the symplectic irrep $N_\sigma(\lambda_\sigma\ \mu_\sigma) = 0(8\ 0)$ in ^{20}Ne consists of a prolate 0(8 0) equilibrium shape (static deformation) with $\lambda_\omega = 8$ and $\mu_\omega = 0$ in the valence-shell 0p-0h (0-particle-0-hole) subspace, along with many other SU(3) deformed configurations or dynamical deformation (vibrations), such as $N_\omega(\lambda_\omega\ \mu_\omega) = 2(10\ 0)$, 2(6 2), and 8 (16 0), which include particle-hole excitations of the equilibrium shape to higher shells [8, 14, 16]. These vibrations are multiples of $2\hbar\Omega$ 1p-1h excitations of the giant-resonance monopole and quadrupole types, that is, induced by the monopole $r^2 = \sum_{i=1}^{A} \vec{r}_i \cdot \vec{r}_i$ and quadrupole $Q_2 = \sqrt{16\pi/5}\sum_{i=1}^{A} r_i^2 Y_2(\hat{r}_i)$ operators, respectively (for further details, see Refs. [10, 24]).

An advantage of the SA-NCSM is that the SA model space can be down-selected from the corresponding ultra-large $N_{\max}$ complete model space to a subset of SA basis states that describe static and dynamical deformation, and within this SA model space the spurious center-of-mass motion can be factored out exactly [25, 26]. Another benefit is the use of group theory for constructing the basis and calculating matrix elements, including the Wigner-Eckart theorem, which allows for calculations with SU(3) reduced matrix elements that depend only on $(\lambda\ \mu)$, along with computationally efficacious group-theoretical algorithms and data structures, as detailed in Refs. [27–31]. A third advantage is that deformation and collectivity are examined and treated in the approach *without* the need for breaking and restoring rotational symmetry. The reason is that basis states utilize the $SU(3)_{(\lambda\ \mu)} \supset SO(3)_L$ reduction chain that has a good orbital angular momentum L, whereas all SU(3) reduced matrix elements can be calculated in the simpler canonical $SU(3)_{(\lambda\ \mu)} \supset SU(2)_I$ reduction chain (for details, see Refs. [32, 33]). The canonical reduction chain provides a natural reduction to the x and y degrees of freedom, it is simple to work with, and most importantly, provides a complete labeling of a basis state that includes the single-shell quadrupole moment eigenvalue that measures the deformation along the body-fixed symmetry z-axis [34]. SU(3) reduced matrix elements calculated within this scheme yield, in turn, matrix elements for the SA-NCSM basis by invoking the Wigner-Eckart theorem with the appropriate $SU(3)_{(\lambda\ \mu)} \supset SO(3)_L$ Clebsch-Gordan coefficients that are readily available [32].

We emphasize that all basis states are kept up to some $N_{\max}^{C}$, yielding results equivalent to the corresponding $N_{\max}^{C}$ NCSM calculations. Building upon this complete $N_{\max}^{C}$ model space, we expand the model space to $N_{\max}$ by adding selected basis states to include only the necessary vibrations of largely deformed equilibrium shapes that lie outside this $N_{\max}^{C}$ (such SA-NCSM model spaces are denoted as $\langle N_{\max}^{C} \rangle N_{\max}$).

Eigenvector continuation method in the symmetry-adapted framework

As introduced in Ref. [11], the EVC method utilizes the fact that if a Hamiltonian is a smooth function of some real-valued parameters, its eigenvectors will also be well-behaved functions of those parameters. In practice, this means that one can use a relatively small number of known wave functions to construct an accurate emulator well-approximated by a low-dimensional manifold, and with it accurately predict observables for an arbitrary chiral potential parameterization [12]. To compute these initial wave functions from first principles, it is advantageous to use SA model spaces that can accommodate deformation, including spatially expanded modes, as well as medium-mass regions.

An advantage of the EVC method is that solutions are achieved by diagonalizing matrices with sizes that are many orders of magnitude smaller than those used in exact calculations. This results in a drastically reduced computational time with practically no discrepancies from the exact results. EVC thus provides a means of generating large samples of nuclear observables from variations in the Hamiltonian parameters. This, in turn, makes computationally intensive statistical analyses, such as sensitivity studies [5, 12], possible. It also allows for a reduced computational load for quantifying uncertainties of *ab initio* predictions.

In this study, we construct emulators capable of probing collective and clustering features by employing the EVC method with SA model spaces. As illustrated in Table 1, the SA-NCSM reduces the sizes of Hamiltonian matrices by up to four orders of magnitude, or equivalently by more than 97%. The application of EVC to these SA spaces results in an additional reduction of up to 3 more orders of

2 We follow the notations of Ref. [15].

TABLE 1 Model space dimensions (labeled as "Dim"), excitation energy E_X, point-proton rms radius r_{rms}, electric quadrupole moment Q, and B ($E2\uparrow$) transition strengths from the ground state (g.s.) to the first excited state of ^{6}Li and ^{12}C, calculated with NNLO$_{opt}$ and $\hbar\Omega$ = 15 MeV in SA and complete model spaces. $\langle 2_{All}\rangle 8_{13}$ denotes an N_{max} = 2 model space with all symplectic irreps (complete), 13 Sp (3,$\mathbb{R}$) irreps of which extend to N_{max} = 8; 6_3 denotes 3 Sp (3,$\mathbb{R}$) irreps up to N_{max} = 6.

Nucleus	J^π	SA						Complete					
		N_{max}	Dim	E_X [MeV]	r_{rms} [fm]	Q [e fm^2]	B ($E2\uparrow$) [e^2 fm^4]	N_{max}	Dim	E_X [MeV]	r_{rms} [fm]	Q [e fm^2]	B ($E2\uparrow$) [e^2 fm^4]
^{6}Li	$1^+_{g.s.}$	$\langle 2_{All}\rangle 8_{13}$	4,898	–	2.20	−0.25	9.75	8	2×10^5	–	2.22	−0.028	10.04
^{6}Li	3^+_1	$\langle 2_{All}\rangle 8_{13}$	9,108	2.20	2.20	−4.12	–	8	3×10^5	2.65	2.22	−4.21	–
^{12}C	$0^+_{g.s.}$	6_3	552	–	2.41	0	35.31	6	1×10^6	–	2.43	0	35.22
^{12}C	2^+_1	6_3	238	5.73	2.41	+5.67	–	6	5×10^6	3.38	2.43	+5.56	–

magnitude, or as much as 99%. In this combined framework, the final size of the resulting matrices are as much as 10^{-5} times smaller than they would be in the corresponding N_{max} complete spaces. As the first step, we consider a chiral EFT nucleon-nucleon (NN) interaction truncated at next-to-next-to-leading order (NNLO), which depends on 14 low-energy constants (LECs). It turns out that we can write the chiral Hamiltonian as $H(\vec{c}) = \sum_{i=0}^{14} c_i h_i$, where $\vec{c}$ is a vector representing a unique combination of the LECs, h_i are the constituent chiral potentials, h_0 is the LEC-independent part of the chiral potential plus relative kinetic energy and the Coulomb interaction, and $c_0 = 1$.

A state $|\psi(\vec{c})\rangle$ can be well-approximated as a linear combination of known "training" wave functions $\sum_j^{N_T} \alpha_j(\vec{c})|\psi(\vec{c_T}_j)\rangle$, where each $|\psi(\vec{c_T}_j)\rangle$ in this study is the lowest-energy eigenvector of $H(\vec{c_T}_j)$ for a given J^π, $\vec{c_T}$ corresponds to a training point in the LEC parameter space, and N_T is the number of training points. The chiral Hamiltonian matrices h_i are constructed in the representation of the training wave functions. These $N_T \times N_T$ matrices are used to emulate the wave function for any set of LECs $\vec{c}$ by solving the Schrödinger equation for the unknown $\alpha_j(\vec{c})$ as a generalized eigenvalue problem that uses the norm matrix for the training wave functions, $M_{ij} = \langle\psi(\vec{c_T}_i)|\psi(\vec{c_T}_j)\rangle$.

The new features here are that we generate the emulator for the electric quadrupole moment Q by constructing the Q matrix in the representation of the training eigenvectors (as done for rms radii in Ref. [5]), and that these are calculated using SA model spaces. The quadrupole moment is then approximated by computing $\langle\psi(\vec{c})|Q|\psi(\vec{c})\rangle = \sum_{ij}\alpha_i(\vec{c})\alpha_j(\vec{c})\langle\psi(\vec{c_T}_i)|Q|\psi(\vec{c_T}_j)\rangle$.

Results and discussions

The results presented in this paper use the SA-NCSM in an Sp(3,$\mathbb{R}$) basis with an NN chiral potential up to NNLO as used in [21]. The consistent treatment of NN and three-nucleon (3N) forces at this order is feasible but outside the scope of the present study, which aims to show the validity of the SA-EVC method. We also include the outcomes for a specific NN parameterization, NNLO$_{opt}$ [21], for which the 3N forces have been shown to contribute minimally to the 3- and 4-nucleon binding energy [21]. Furthermore, the NNLO$_{opt}$ NN potential has been found to reproduce various observables, including the ^{4}He electric dipole polarizability [35]; the challenging analyzing power for elastic proton scattering on ^{4}He, ^{12}C, and ^{16}O [36]; neutron-deuteron scattering cross-sections [37]; along with B (E2) transition strengths for ^{21}Mg and ^{21}F [38] in the SA-NCSM without effective charges.

For the EVC calculations, we use N_T = 32 training points within the 14-dimensional parameter space for NNLO. We restrict the ranges of the LECs to lie within ±10% of their values for NNLO$_{opt}$ [21] and adopt the regularization for NNLO$_{opt}$. We sample training points using a randomly seeded latin hypercube design, and validate the emulators for 256 points that are different from the training points but within the same range of the LECs.

The SA-EVC results start with SA model spaces that are reduced by three to four orders of magnitude compared to the corresponding N_{max} complete model space (or, equivalently, NCSM calculations), as outlined in Table 1. Moreover, the associated observables are in good agreement for SA and complete model spaces, with differences that are typically comparable to differences resulting from varying $\hbar\Omega$ (see Ref. [8], supplemental material). Specifically, for the example of NNLO$_{opt}$, we report in Table 1 excitation energies, point-proton rms radii, electric quadrupole moments, and B ($E2\uparrow$) transition strengths between the two lowest energy states of ^{6}Li and ^{12}C. We also show that for the SA spaces used to train the emulators all of the above observables are converged with N_{max} (Figure 2).

Thus, for example, as shown in Table 1, collectivity-driven observables agree within 0.3%–2.9%, and radii agree at the sub-percent level. The largest deviation is observed for the ^{6}Li 1^+ quadrupole moment, however, it is important that its sign and very small magnitude are reproduced in both calculations. Furthermore, such differences are expected to decrease in richer model spaces; indeed, in a series of benchmark studies for light nuclei such as ^{4}He, ^{6}Li, ^{12}C, and ^{16}O (reviewed in Ref. [9]), we have shown that the SA-NCSM uses significantly smaller model spaces in comparison to the corresponding large complete N_{max} model spaces without compromising the accuracy for various observables (including electron scattering form factors [39] and sum rules [35]), as well as for effective inter-cluster potentials [31]. Reference [9] has also shown that for light nuclei, the SA-NCSM is in reasonable agreement with other *ab initio* approaches, such as hyperspherical harmonics [40, 41], the NCSM [17, 18], and quantum Monte Carlo [42].

Collectivity and clustering of training wave functions

An important feature of the training wave functions is that the dominant deformed configurations, or the SU(3) content of the states

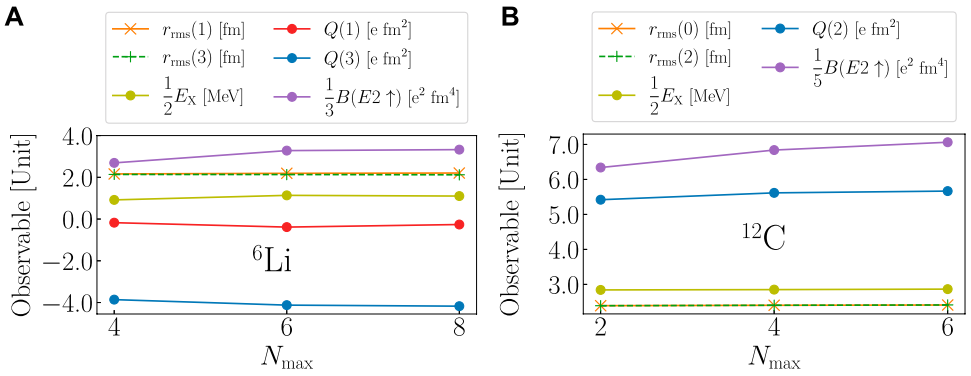

FIGURE 2
Convergence with $N_{\rm max}$ of the quadrupole moments $Q(J)$, point-proton rms radii $r_{rms}(J)$, excitation energies E_X, and B ($E2\uparrow$) transition strengths for the two lowest-lying states in **(A)** ^{6}Li and **(B)** ^{12}C. Observables are computed with the NNLO$_{\rm opt}$ parameterization for $\hbar\Omega$ = 15 MeV in SA model spaces reported in Table 1.

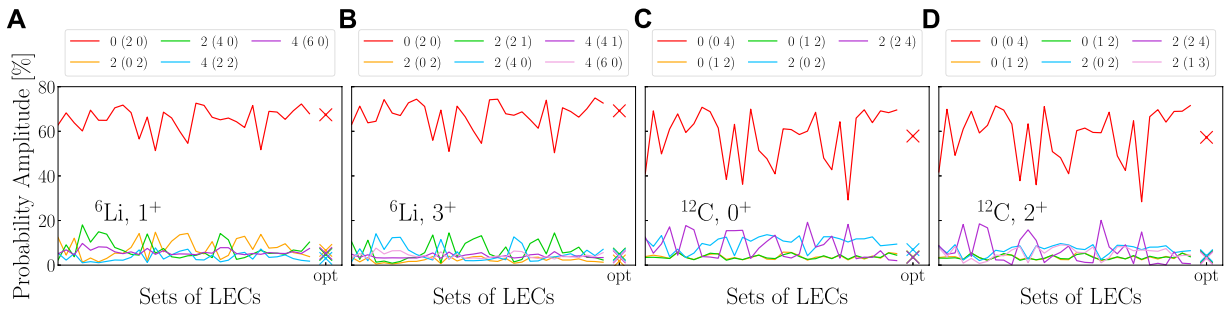

FIGURE 3
The largest SU (3) probability amplitudes (solid lines) as a function of emulator training LECs sets for **(A)** ^{6}Li 1$^+$ ground state and **(B)** ^{6}Li 3^+_1 state in $N_{\rm max}$ = $\langle 2_{\rm All}\rangle 8_{13}$ model space [all SU(3) states have $\{S_p, S_n, S\} = \{\frac{1}{2}, \frac{1}{2}, 1\}$], as well as for **(C)** ^{12}C 0$^+$ ground state and **(D)** ^{12}C 2^+_1 state in $N_{\rm max} = 6_3$ [all SU(3) states have $\{S_p, S_n, S\}$ = {0, 0, 0} except for 0 (1 2) with $\{S_p, S_n, S\}$ = {0, 1, 1} (orange) and {1, 0, 1} (green)]. Results are also shown for the NNLO$_{\rm opt}$ parameterization in the corresponding $N_{\rm max}$ complete model space (labeled as "opt").

under consideration, remain practically the same for all of the training wave functions (Figure 3). In addition, the SU(3) content agrees with the probabilities obtained with NNLO$_{\rm opt}$ in the corresponding $N_{\rm max}$ complete model space, also shown in Figure 3. This ensures that the same static and dynamical deformed modes govern the physics for all LECs sets under considerations, thereby justifying the use of the same SA selection for all the training wave functions.

Specifically, we find that one SU(3) irrep dominates the dynamics of each state at the 50%–60% level, with several additional configurations each contributing from 1% to 20% depending on the LECs set. Moreover, when the basis states are further organized into Sp(3,$\mathbb{R}$) irreps, we find that a single symplectic irrep—which contains the dominant SU(3) configurations—contributes at practically the same level from one training wave function to another. For example, the (2 0) symplectic irrep in ^{6}Li accounts for 83%–88% of each 1$^+$ training wave function, whereas the (2 0) contributes at the 85%–88% level in the case of the 3$^+$, out of thirteen available different irreps. Similarly, the probability of the (0 4) irrep in each of the ^{12}C training ground states is between 80%–88%, and between 82%–94% for the first 2$^+$ states. This is a strong indicator that the emulators are trained on wave functions that retain the symmetry-preserving and symmetry-breaking patterns that are observed in nuclei [8] and that the SA model spaces used in this study are sufficient to capture nuclear collectivity. Indeed, the fact that the Sp(3,$\mathbb{R}$) symmetry remains a near perfect symmetry for each of the training wave functions, retaining the same shape from one wave function to another, further supports the use of SA selections in the EVC method, or otherwise, the SA model spaces would need to be re-examined.

Another important feature of the training wave functions is that cluster formation is largely unaffected by the choice of interaction parameters. To study this, we project the ^{6}Li states onto the $\alpha + d$ system, following Ref. [43]: we use a ground state for each cluster that is renormalized to the most dominant SU(3) configuration, and we adopt R-matrix theory to match the amplitude of the cluster wave function and its derivative to those of the exact Coulomb eigenfunctions at large distances. We note that we are primarily interested in the effect of the LECs on the correlations in the training wave functions; hence, we fix the threshold energy to the experimental one. For the $^3S_1$ partial wave, we observe about 20%

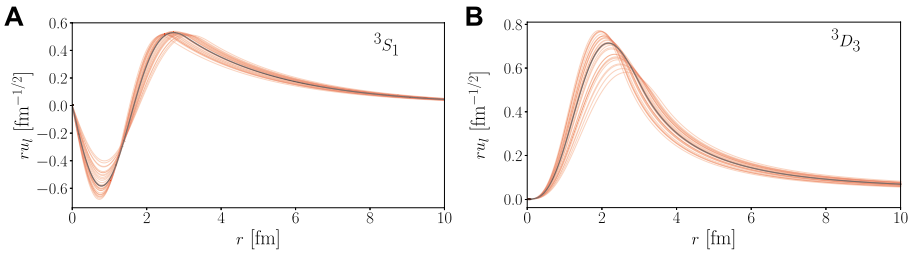

FIGURE 4
$\alpha + d$ **(A)** $^3S_1$-wave and **(B)** $^3D_3$-wave as functions of the relative distance r, computed from the ^{6}Li training wave functions for SA model spaces reported in Table 1. The spread of the curves is given by the $\pm$ 10% variation in the LECs. The case for NNLO$_{\text{opt}}$ is shown in black.

variations in the calculated asymptotic normalization coefficients (C_0 = 1.45–2.07 fm$^{-1/2}$) around their average value and 10% variations in the spectroscopic factor, namely, SF = 0.75–0.90 (Figure 4A). This tracks with the ±10% variation in the LECs. For comparison, the NNLO$_{\text{opt}}$ ANC for this particular channel is C_0 = 1.77 fm$^{-1/2}$ with SF = 0.87. Interestingly, the height of the second peak, which is located near the nuclear surface and informs the probability of cluster formation, remains fixed for all the parameterizations and coincides with the one for the NNLO$_{\text{opt}}$ case, only its position slightly varies with the LECs.

While the $^3D_3$ spectroscopic factors (SF = 0.73–0.92, with 0.90 for NNLO$_{\text{opt}}$) vary approximately at the 15% level (Figure 4B), which is practically the same as for the $^3S_1$ partial wave, α widths of the 3^+ state range from Γ_α = 6.34 keV–14.05 keV, which is about ±40% from Γ_α = 9.81 keV calculated for this particular channel with NNLO$_{\text{opt}}$ (similarly to the ANCs, we use the experimental threshold energy). We note that the NNLO$_{\text{opt}}$ values for C_0 and Γ_α are reported for a single channel without taking excitations of the clusters into account (e.g., see Ref. [44]) and should not be compared directly to experiment. Of particular interest for this study is that the LECs sets induce a change in both the location and magnitude of the peak, to which the probability for alpha decay is typically sensitive to.

To summarize, the behavior of the surface peaks in both channels and the nuclear shapes of the 1^+ and 3^+ states in ^{6}Li (as well as the shapes of the 0^+ and 2^+ states in ^{12}C) are relatively consistent. This suggests that the terms of the nuclear potential that are independent of the LECs, including parts of the long-range interaction, are largely responsible for cluster formation, along with the development of the nuclear shape [equivalently, almost perfect Sp(3,$\mathbb{R}$) symmetry]. In contrast, the LECs, which capture the unresolved short-ranged interactions between nucleons, fine-tune collective and clustering features, and affect the associated observables by only a factor, namely, 1.4 for the $1^+_{\text{g.s.}}$ ANCs, 2.2 for the 3^+_1 alpha width, and 1.4 for the 3^+_1 quadrupole moment in ^{6}Li. Similarly, the quadrupole moment for the 2^+_1 in ^{12}C is affected by a factor of 2.1. While the clustering features are explored in this study for the training points only, the SA-EVC approach—the validation of which is discussed next—enables uncertainty quantification of such collective and reaction observables if the probability distributions for the LECs are available.

Validation of the symmetry-adapted eigenvector continuation

To validate the SA-EVC approach, we show that for the quadrupole moments of the ^{6}Li 1^+ ground state and first excited 3^+ state, as well as for the 3^+ excitation energy, the emulators provide very accurate results compared to the exact outcomes (Figure 5). The average relative errors over all 256 validation LECs sets are respectively 6.91 × 10^{-2}, 7.70 × 10^{-4}, and 1.20 × 10^{-4}. It is clear that any deviations of the emulators from the expected values are negligible, especially considering that, as mentioned above, the SA selection reduces the Hamiltonian dimension by more than 97%, and the EVC projection by an additional 99% or more.

It is worth noting that the average error for the ground state quadrupole moment is two orders of magnitude larger than that of the 3^+ state. We note that $Q(1^+)$ of ^{6}Li is very similar in nature to the deuteron quadrupole moment. The extremely small value in both nuclei results from a small mixing of an L = 2 component into the ground state of ^{6}Li (and of the deuteron), which is not collective in essence like, e.g., the quadrupole moments of the 3^+ state in ^{6}Li or the 2^+ state in ^{12}C (discussed below). Indeed, the results of Figure 5A reflect the high sensitivity of the underlying NN interaction (and likely 3N forces [46]) to the L = 2 mixing in the ground state wave function.

Similar to ^{6}Li, the SA-EVC emulated 2^+_1 quadrupole moment and excitation energy for ^{12}C are in very close agreement to the exact results (Figure 6). Namely, the average relative errors are given by 1.02 × 10^{-4} and 6.72 × 10^{-5}, respectively. Compared to the average errors reported above for the 3^+_1 quadrupole moment and excitation energy for ^{6}Li, we find eight and two times improvement in the emulator's predictions for ^{12}C, respectively. The reason is likely related to the much smaller SA selection in ^{12}C and the stronger collective nature observed in the low-lying states of ^{12}C. Specifically, in ^{6}Li the SA-EVC uses thousands of basis states, whereas in ^{12}C only hundreds of basis states (see Table 1). We therefore expect the mixing of configurations to exert a more noticeable effect on ^{6}Li than on ^{12}C. The result is that the eigenvectors of ^{12}C vary in fewer directions than those of ^{6}Li, suggesting that more training points for ^{6}Li may be beneficial to improve errors. While this warrants further study, this speaks to an advantage of merging the SA and EVC frameworks.

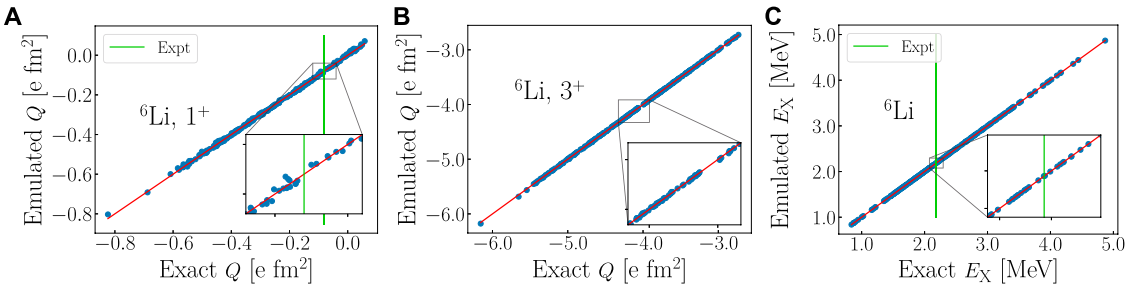

FIGURE 5
Exact vs. SA-EVC observables in ^{6}Li (blue circles) for the quadrupole moment Q of **(A)** the 1^+ ground state and **(B)** the first excited 3^+ state, as well as **(C)** for the excitation energy E_X of the 3^+ state, in $\langle 2_{All}\rangle 8_{13}$ SA model spaces and for $\hbar\Omega$ = 15 MeV. Also shown is the agreement between the exact and emulated values to guide the eye (red line), and experimental results (vertical green line) where available. Insets show 5%-regions surrounding reported experimental data [45] or the NNLO$_{opt}$ result where data is not available [a 50%-region is used for the very small Q in **(A)**].

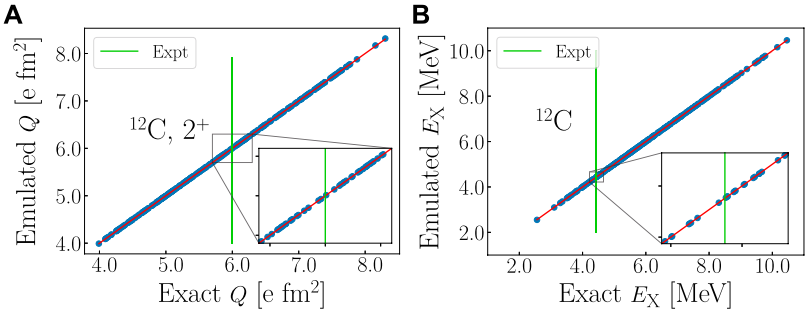

FIGURE 6
The same as in Figure 5 but for **(A)** the quadrupole moment Q and **(B)** the excitation energy of the first 2^+ state in ^{12}C, calculated in 6_3 SA model spaces and for $\hbar\Omega$ = 15 MeV. Insets show 5%-regions surrounding reported experimental data [47].

Conclusion

We have for the first time combined the framework of the SA-NCSM with the EVC procedure into the SA-EVC method for studies of collective and clustering observables. This builds upon earlier SA-NCSM explorations that have shown that an Sp(3,$\mathbb{R}$)-adapted model space selection can successfully capture nuclear collectivity while significantly reducing the sizes of Hamiltonian matrices [8]. Here, we show that excitation energies, point-proton rms radii, electric quadrupole moments and $E2$ transitions in the two lowest-lying states of ^{6}Li and ^{12}C calculated with the specific parameterization NNLO$_{opt}$ for $\hbar\Omega$ = 15 MeV in SA model spaces are in reasonable agreement with those calculated in the corresponding N_{max} complete model space (or equally, to NCSM outcomes). We also show that these observables are converged with N_{max} for the SA selections under consideration.

Further, we demonstrate that SA-EVC emulators trained on SA model spaces are capable of accurately predicting such observables as the LECs are varied, while further reducing the dimensions of operator matrices by an additional 2-3 orders of magnitude. Combined with the initial reduction provided by the SA-NCSM, the emulator matrices have a dimension as much as 10^{-5} times smaller than the corresponding N_{max} complete model spaces. They are small enough to perform linear algebra operations using a single CPU thread on a standard laptop without difficulty. Moreover, the SA-EVC approach will be critical for nuclei beyond the lightest systems; thus, e.g. in ^{20}Ne, the complete N_{max} = 8 model space has dimension of 1.52 × 10^{11}, while the *ab initio* SA-NCSM solutions are achieved when using 112 million basis states for $J^\pi = 0^+, 2^+, 4^+$. This can be further reduced to emulators of dimension 10^2 especially given the predominance of a single symplectic irrep in the ground-state rotational band of this nucleus. Comparing the emulator results to exact calculations performed in the same SA spaces, we find that the average relative errors are typically 10^{-4}. A larger error ($\sim 10^{-2}$) is found for the quadrupole moment of the ^{6}Li ground state, which is highly sensitive to the L = 2 admixture and hence to the underlying nuclear force, as discussed in the text. A future study that utilizes larger training sets may provide further insight.

In addition to validating the SA-EVC procedure, we show that the symmetry patterns and clustering features in the emulator training wave functions do not respond strongly to variations in the LECs. Across all of the training wave functions, there is a single nuclear shape (approximate symplectic symmetry) that accounts for 81%–94% of the total probability. Furthermore, the dominance of important SU(3) configurations is preserved from one training wave function to

another. Projecting the training wave functions for ^{6}Li onto the $\alpha + d$ system, we find that the likelihood of cluster formation in both the $^3S_1$- and $^3D_3$-wave channels is largely unaffected by the choice of LECs. Spectroscopic factors, ANCs and α-widths extracted from the cluster wave functions all vary within relatively narrow ranges around their average values, ranges that track reasonably well with the 10% variation of the LECs. This suggests that the part of the nuclear potential that is independent of the LECs and is practically the same for all chiral potentials (up to the regularization and related cutoffs employed) provides the dominant features of the wave function, such as Sp(3,$\mathbb{R}$) symmetry patterns and clustering formation, while varying the LECs and associated unresolved short-range interactions has an effect on, e.g., collective quadrupole moments, asymptotic normalization coefficients (ANCs), and alpha partial widths up to a factor of two.

In order to better understand the relationships between collectivity and clustering explored in this study, and how both relate to the underlying nuclear forces, sensitivity analyses are required. As we enter the era of high-precision nuclear physics, this is also an important step towards constructing accurate interactions, with quantified uncertainties. We note that properly accounting for clustering features is important for the *ab initio* modeling of nuclear reactions, and related processes from fusion to fission. The SA-EVC method provides a clear and now verified framework for generating the huge number of chiral parameterizations required for such analyses. Hence, the door is now open to perform *ab initio* calculations with quantified uncertainties that emerge from the interaction and the controlled many-body approximations, from exotic light nuclei up to medium-mass isotopes, as well from spherical to highly enhanced collective and clustering modes.

Data availability statement

The raw data supporting the conclusion of this article will be made available by the authors, without undue reservation.

Author contributions

All authors listed have made a substantial, direct, and intellectual contribution to the work and approved it for publication.

Acknowledgments

We acknowledge invaluable discussions with Jerry P. Draayer, George Rosensteel, David Rowe, and Daniel Langr. This work was supported in part by the U.S. National Science Foundation (PHY-1913728, PHY-2209060), the European Research Council (ERC) under the European Unions Horizon 2020 research and innovation program (Grant agreement No. 758027), the Czech Science Foundation (22-14497S). KSB greatly appreciates the financial support of a research fellowship from the Louisiana Board of Regents. This work benefited from high performance computational resources provided by LSU (www.hpc.lsu.edu), the National Energy Research Scientific Computing Center (NERSC), a U.S. Department of Energy Office of Science User Facility operated under Contract Nos. DE-AC02-05CH11231, as well as the Frontera computing project at the Texas Advanced Computing Center, made possible by National Science Foundation award OAC-1818253.

Conflict of interest

The authors declare that the research was conducted in the absence of any commercial or financial relationships that could be construed as a potential conflict of interest.

Publisher's note

References

1. Johnson CW, Launey KD, Auerbach N, Bacca S, Barrett BR, Brune C, et al. From bound states to the continuum. *J Phys G* (2020) 47:23001. arXiv:1912.00451.

2. van Kolck PF, van Kolck U. Effective field theory for few-nucleon systems. *Annu Rev Nucl Part Sci* (2002) 52:339–96. arXiv:nucl-th/0203055. doi:10.1146/annurev.nucl.52.050102.090637

3. Tews I, Davoudi Z, Ekström A, Holt JD, Becker K, Briceño R, et al. Nuclear forces for precision nuclear physics: A collection of perspectives. *Few-Body Syst* (2022) 63:67. arXiv:2202.01105. doi:10.1007/s00601-022-01749-x

4. Furnstahl RJ, Klco N, Phillips DR, Wesolowski S. Quantifying truncation errors in effective field theory. *Phys Rev C* (2015) 92. doi:10.1103/physrevc.92.024005

5. Hagen A, Hagen G. Global sensitivity analysis of bulk properties of an atomic nucleus. *Phys Rev Lett* (2019) 123:252501. arXiv:1910.02922. doi:10.1103/physrevlett.123.252501

6. Sargsyan GH, Launey KD, Burkey MT, Gallant AT, Scielzo ND, Savard G, et al. Impact of clustering on the Li8 β decay and recoil form factors. *Phys Rev Lett* (2022) 128:202503. arXiv:2107.10389. doi:10.1103/physrevlett.128.202503

7. Stroberg SR, Holt JD, Schwenk A, Simonis J. *Ab initio* limits of atomic nuclei. *Phys Rev Lett* (2021) 126:022501. doi:10.1103/physrevlett.126.022501

8. Dytrych T, Launey KD, Draayer JP, Rowe DJ, Wood JL, Rosensteel G, et al. Physics of nuclei: Key role of an emergent symmetry. *Phys Rev Lett* (2020) 124:042501. arXiv:1810.05757. doi:10.1103/physrevlett.124.042501

9. Launey KD, Mercenne A, Dytrych T. Nuclear dynamics and reactions in the ab initio symmetry-adapted framework. *Annu Rev Nucl Part Sci* (2021) 71:253–77. doi:10.1146/annurev-nucl-102419-033316

10. Launey KD, Dytrych T, Draayer JP. Symmetry-guided large-scale shell-model theory. *Prog Part Nucl Phys* (2016) 89:101–36. arXiv:1612.04298. doi:10.1016/j.ppnp.2016.02.001

11. Frame D, He R, Ipsen I, Lee D, Lee D, Rrapaj E. Eigenvector continuation with subspace learning. *Phys Rev Lett* (2018) 121:032501. arXiv:1711.07090. doi:10.1103/physrevlett.121.032501

12. König S, Ekström A, Hebeler K, Lee D, Schwenk A. Eigenvector continuation as an efficient and accurate emulator for uncertainty quantification. *Phys Lett B* (2020) 810:135814. arXiv:1909.08446. doi:10.1016/j.physletb.2020.135814

13. Djärv T, Ekström A, Forssén C, Johansson HT. Bayesian predictions for $A = 6$ nuclei using eigenvector continuation emulators. *Phys Rev C* (2022) 105. arXiv:2108.13313. doi:10.1103/physrevc.105.014005

14. Rowe DJ. Microscopic theory of the nuclear collective model. *Rep Prog Phys* (1985) 48:1419–80. doi:10.1088/0034-4885/48/10/003

15. Dytrych T, Sviratcheva KD, Bahri C, Draayer JP, Vary JP. Evidence for symplectic symmetry inAb InitioNo-core shell model results for light nuclei. *Phys Rev Lett* (2007) 98:162503. arXiv:0704.1108. doi:10.1103/physrevlett.98.162503

16. Rowe D. The fundamental role of symmetry in nuclear models. *AIP Conf Proc* (2013) 1541:104. arXiv:1304.6115.

17. Navrátil P, Vary JP, Barrett BR. Properties of12Cin theAb InitioNuclear shell model. *Phys Rev Lett* (2000) 84:5728–31. arXiv:nucl-th/0004058. doi:10.1103/physrevlett.84.5728

18. Barrett B, Navrátil P, Vary J. *Ab initio* no core shell model. *Prog Part Nucl Phys* (2013) 69:131–81. doi:10.1016/j.ppnp.2012.10.003

19. Epelbaum E, Nogga A, Glöckle W, Kamada H, Meißner U-G, Witala H. Three-nucleon forces from chiral effective field theory. *Phys Rev C* (2002) 66:064001. arXiv:nucl-th/0208023. doi:10.1103/physrevc.66.064001

20. Entem DR, Machleidt R. Accurate charge-dependent nucleon-nucleon potential at fourth order of chiral perturbation theory. *Phys Rev C* (2003) 68:041001. arXiv:nucl-th/0304018. doi:10.1103/physrevc.68.041001

21. Ekström A, Baardsen G, Forssén C, Hagen G, Hjorth-Jensen M, Jansen GR, et al. Optimized chiral nucleon-nucleon interaction at next-to-next-to-leading order. *Phys Rev Lett* (2013) 110:192502. arXiv:1303.4674. doi:10.1103/physrevlett.110.192502

22. Epelbaum E, Krebs H, Meißner UG. Precision nucleon-nucleon potential at fifth order in the chiral expansion. *Phys Rev Lett* (2015) 115:122301. doi:10.1103/physrevlett.115.122301

23. Schiavilla R, Girlanda L, Gnech A, Kievsky A, Lovato A, Marcucci LE, et al. Two- and three-nucleon contact interactions and groundstate energies of light- and medium-mass nuclei. *Phys Rev C* (2021) 103:054003. arXiv:2102.02327. doi:10.1103/physrevc.103.054003

24. Launey KD, Dytrych T, Sargsyan GH, Baker RB, Draayer JP. Emergent symplectic symmetry in atomic nuclei. *Eur Phys J Spec Top* (2020) 229:2429–41. arXiv:2108.04900. doi:10.1140/epjst/e2020-000178-3

25. Verhaar BJ. A method for the elimination of spurious states in the nuclear harmonic oscillator shell model. *Nucl Phys* (1960) 21:508–25. doi:10.1016/0029-5582(60)90073-0

26. Hecht KT. The use of SU(3) in the elimination of spurious center of mass states. *Nucl Phys A* (1971) 170:34–54. doi:10.1016/0375-9474(71)90681-6

27. Draayer JP, Leschber Y, Park SC, Lopez R. Representations of U(3) in U(N). *Comput Phys Commun* (1989) 56:279–90. doi:10.1016/0010-4655(89)90024-6

28. Langr D, Dytrych T, Launey KD, Draayer JP. Accelerating many-nucleon basis generation for high performance computing enabled *ab initio* nuclear structure studies. *Int J High Perform Comput Appl* (2019) 33:522–33. doi:10.1177/1094342019838314

29. Oberhuber T, Dytrych T, Launey KD, Langr D, Draayer JP. *Discrete and Continuous Dynamical Systems-S* (2021) 14:1111.

30. Dytrych T, Langr D, Draayer JP, Launey KD, Gazda D. SU3lib: A C++ library for accurate computation of wigner and racah coefficients of SU(3). *Comput Phys Commun* (2021) 269:108137. doi:10.1016/j.cpc.2021.108137

31. Mercenne A, Launey K, Dytrych T, Escher J, Quaglioni S, Sargsyan G, et al. Efficacy of the symmetry-adapted basis for *ab initio* nucleon-nucleus interactions for light- and intermediate-mass nuclei. *Comput Phys Commun* (2022) 280:108476. doi:10.1016/j.cpc.2022.108476

32. Akiyama JP, Akiyama Y. Wigner and racah coefficients for SU3. *J Math Phys* (1973) 14:1904–12. doi:10.1063/1.1666267

33. Draayer C, Draayer JP. SU(3) reduced matrix element package. *Comput Phys Commun* (1994) 83:59–94. doi:10.1016/0010-4655(94)90035-3

34. Carvalho J, Le Blanc R, Vassanji M, Rowe D, McGrory J. The symplectic shell-model theory of collective states. *Nucl Phys A* (1986) 452:240–62. doi:10.1016/0375-9474(86)90308-8

35. Baker RB, Launey KD, Bacca S, Dinur NN, Dytrych T. Benchmark calculations of electromagnetic sum rules with a symmetry-adapted basis and hyperspherical harmonics. *Phys Rev C* (2020) 102:014320. arXiv:2003.05865. doi:10.1103/physrevc.102.014320

36. Burrows M, Elster C, Weppner SP, Launey KD, Maris P, Nogga A, et al. *Ab initio* folding potentials for nucleon-nucleus scattering based on no-core shell-model one-body densities. *Phys Rev C* (2019) 99:044603. arXiv:1810.06442. doi:10.1103/physrevc.99.044603

37. Miller S, Ekström A, Hebeler K. Neutron-deuteron scattering cross-sections with chiral *NN* interactions using wave-packet continuum discretization. *Phys Rev C* (2022) 106:024001. arXiv:2201.09600. doi:10.1103/PhysRevC.106.024001

38. Ruotsalainen P, Henderson J, Hackman G, Sargsyan GH, Launey KD, Saxena A, et al. Isospin symmetry in $B(E2)$ values: Coulomb excitation study of ^{21}Mg. *Phys Rev C* (2019) 99:051301. arXiv:1811.00774. doi:10.1103/physrevc.99.051301

39. Dytrych T, Hayes AC, Launey KD, Draayer JP, Maris P, Vary JP, et al. Electron-scattering form factors for ^{6}Li in the *ab initio* symmetry-guided framework. *Phys Rev C* (2015) 91:024326. arXiv:1502.03066. doi:10.1103/physrevc.91.024326

40. Kievsky A, Rosati S, Viviani M, Marcucci LE, Girlanda L. A high-precision variational approach to three- and four-nucleon bound and zero-energy scattering states. *J Phys G: Nucl Part Phys* (2008) 35:063101. arXiv:0805.4688. doi:10.1088/0954-3899/35/6/063101

41. Bacca S, Marchisio MA, Barnea N, Leidemann W, Orlandini G. Crystalline order on a sphere and the generalized thomson problem. *Phys Rev Lett* (2002) 89:052502. doi:10.1103/PhysRevLett.89.185502

42. Carlson J, Gandolfi S, Pederiva F, Pieper SC, Schiavilla R, Schmidt KE, et al. Quantum Monte Carlo methods for nuclear physics. *Rev Mod Phys* (2015) 87:1067–118. arXiv:1412.3081. doi:10.1103/revmodphys.87.1067

43. Dreyfuss AC, Launey KD, Escher JE, Sargsyan GH, Baker RB, Dytrych T, et al. Clustering and α-capture reaction rate from *ab initio* symmetry-adapted descriptions of ^{20}Ne. *Phys Rev C* (2020) 102:044608. arXiv:2006.11208. doi:10.1103/physrevc.102.044608

44. Hupin G, Quaglioni S, Navrátil P. Unified description of ^{6}Li Structure and deuterium-^{4}He Dynamics with chiral two- and three-nucleon forces. *Phys Rev Lett* (2015) 114:212502. doi:10.1103/physrevlett.114.212502

45. Tilley D, Cheves C, Godwin J, Hale G, Hofmann H, Kelley J, et al. Energy levels of light nuclei A=5, 6, 7. *Nucl Phys A* (2002) 708:3–163. doi:10.1016/s0375-9474(02)00597-3

46. Filin AA, Möller D, Baru V, Epelbaum E, Krebs H, Reinert P. High-accuracy calculation of the deuteron charge and quadrupole form factors in chiral effective field theory. *Phys Rev C* (2021) 103:024313. arXiv:2009.08911. doi:10.1103/physrevc.103.024313

47. Kelley J, Purcell J, Sheu C. Energy levels of light nuclei A= 12. *Nucl Phys A* (2017) 968:71–253. doi:10.1016/j.nuclphysa.2017.07.015

frontiers | Frontiers in Physics

TYPE Original Research
PUBLISHED 16 March 2023
DOI 10.3389/fphy.2023.1098262

OPEN ACCESS

EDITED BY
Maria Piarulli,
Washington University in St. Louis,
United States

REVIEWED BY
Daniel Phillips,
Ohio University, United States
Andreas Ekström,
Chalmers University of Technology,
Sweden

*CORRESPONDENCE
P. Maris,
pmaris@iastate.edu

SPECIALTY SECTION
This article was submitted to Nuclear Physics, a section of the journal Frontiers in Physics

RECEIVED 14 November 2022
ACCEPTED 20 February 2023
PUBLISHED 16 March 2023

CITATION
Maris P, Le H, Nogga A, Roth R and Vary JP (2023), Uncertainties in *ab initio* nuclear structure calculations with chiral interactions.
Front. Phys. 11:1098262.
doi: 10.3389/fphy.2023.1098262

Uncertainties in *ab initio* nuclear structure calculations with chiral interactions

P. Maris[1]*, H. Le[2], A. Nogga[2,3], R. Roth[4] and J. P. Vary[1]

[1]Department of Physics and Astronomy, Iowa State University, Ames, IA, United States, [2]Institut für Kernphysik, Institute for Advanced Simulation and Jülich Center for Hadron Physics, Jülich, Germany, [3]Centre for Advanced Simulation and Analytics (CASA), Jülich, Germany, [4]Institut für Kernphysik, Technische Universität Darmstadt, Darmstadt, Germany

We present theoretical ground state energies and their uncertainties for *p*-shell nuclei obtained from chiral effective field theory internucleon interactions as a function of chiral order, fitted to two- and three-body data only. We apply a Similary Renormalization Group transformation to improve the numerical convergence of the many-body calculations, and discuss both the numerical uncertainties arising from basis truncations and those from omitted induced many-body forces, as well as chiral truncation uncertainties. With complete Next-to-Next-to-Leading (N^2LO) order two- and three-body interactions, we find significant overbinding for the ground states in the upper *p*-shell, but using higher-order two-body potentials, in combination with N^2LO three-body forces, our predictions agree with experiment throughout the *p*-shell to within our combined estimated uncertainties. The uncertainties due to chiral order truncation are noticeably larger than the numerical uncertainties, but they are expected to become comparable to the numerical uncertainties at complete N^3LO.

KEYWORDS

chiral effective field theory, nucleon-nucleon interactions, three-nucleon interactions, yakubovsky, no-core shell model, uncertainty quantification

1 Introduction

An atomic nucleus, consisting of Z protons and N neutrons, is a self-bound quantum many-body system with $A = N + Z$ strongly interacting nucleons. The interactions between these nucleons are in principle governed by QCD–but it is impractical to describe nuclei in terms of quarks and gluons, except for the very lightest systems. Even a microscopic description of nuclei using realistic two-body (NN), three-body (3N) and possibly higher *n*-body interactions between point-like nucleons remains a formidable task, both in terms of high-performance computing, and in terms of determining realistic nuclear interactions in tractable terms. In order to confront such a description with experimental data, one needs honest assessments of all uncertainties, both those arising from the numerical solution of a many-body problem, and those arising from a necessarily approximate theory of the effective interactions between nucleons.

Any *ab initio* theory of nuclei in terms of interacting nucleons requires a high-quality NN potential providing an accurate description of NN scattering data. Highly accurate NN potentials have been in existence for several decades now, all incorporating one-pion exchange, and often inspired by one-boson-exchange (OBE) models, adjusted and augmented by phenomenological terms as necessary to fit the available NN data, such as

the Argonne [1], (CD)-Bonn [2, 3], and Nijmegen [4] potentials. Although there exist highly accurate NN potentials in terms of describing the NN phase-shift data, that at the same time accurately describe the spectra of light nuclei [5], most realistic NN potentials require more or less phenomenological 3N forces (3NFs) [6–8] for a good description of nuclei in the *p*-shell and beyond. However, in order to quantify any uncertainties associated with the choice of the NN potential (and 3NFs), we need a more systematic method of arriving at the potential.

Chiral Effective Field Theory (χEFT) allows us to derive nuclear interactions in a systematic way, in terms of an expansion in the pion mass (or the relevant nucleon momentum) over the hadronic or breakdown scale [9–12]; and in principle, it also allows for a quantification of the uncertainties arising from truncating this expansion. However, this chiral expansion is by no means unique, and different choices for e.g., the degrees of freedom to include in the χEFT can lead to very different χEFT interactions, with a different ordering of various types of diagrams, and indeed different orders at which higher *n*-body forces have to be included. Furthermore, different choices on e.g., how to regulate the various expressions for loop integrals lead to different versions of the NN potentials (and 3NFs) at any given order, even if the ordering of the various diagrams is the same. Each of these different versions of χEFT comes with its own parameters (Low-Energy Constants or LECs) that need to be fitted to data (or, eventually, calculated from e.g., lattice QCD), and with its own uncertainty quantification.

Just like there are different ways to obtain (effective) nuclear interactions, there are different quantum many-body methods being used for *ab initio* nuclear structure calculations. For up to four nucleons, one can use the Faddeev–Yakubovsky method (the 3- and 4-body reformulation of the Schrödinger equation that permits the incorporation of the appropriate boundary condition for 3- and 4-body systems that are asymptotically clustered), but this has not been extended to $A = 6$ or beyond. Broadly speaking, the computational methods applicable to nuclei beyond ^{4}He, fall into one of three categories: Quantum Monte Carlo simulations (both variational, VMC [13], and Green's function, GFMC [13]), non-relativistic lattice simulations with nucleons (Nuclear Lattice Effective Field Theory, NLEFT [14, 15]), and Configuration Interaction (CI) methods (No-Core Shell Model (NCSM) [16], Coupled-Cluster (CC) [17], In-Medium Similarity Renormalization Group (IM-SRG) [18]), which are based on an expansion of the many-body wave-functions in terms of basis functions (configurations). Each of these methods has their own uncertainties: Monte Carlo simulations are typically dominated by statistical uncertainties, though there is also a dependence on the variational wave function; lattice simulations have both statistical and systematic (lattice size and lattice spacing) uncertainties; and CI methods are generally dominated by systematic uncertainties due to the truncation of the many-body basis, though one can make use of statistical sampling of the many-body basis [19]. Because each of these methods have different sources of uncertainties, and they are not always easy to identify and quantify, it is very valuable to use two or more of these many-body methods for the same nucleus, using the same interactions.

In this paper we use the NCSM to perform *ab initio* nuclear structure calculations for the ground state energies of nearly all stable *p*-shell nuclei (excluding mirror nuclei) from $A = 4$ to $A = 16$ using the χEFT interactions from Ref. [20]. We perform a systematic set of order-by-order calculations in the chiral expansion to determine the uncertainties associated with the truncation of the chiral expansion; more details about the χEFT and how we estimate the truncation uncertainty can be found in Section 2. In order to assess the numerical uncertainties in our NCSM calculations, we make a detailed comparison with Faddeev–Yakubovsky calculations for ^{3}H and ^{4}He using the same interactions; this is described in Section 3, together with details about the NCSM. Our results for the binding energies of *p*-shell nuclei are presented in Section 4. Finally, we give some concluding remarks in Section 5.

2 Nuclear interactions from chiral effective field theory

In recent years two different formulations of χEFT have emerged that are being used in *ab initio* nuclear structure calculations. The most commonly used χEFT is based on only pions and nucleon degrees of freedom [10, 11], for which the Leading Order (LO) and Next-to-Leading Order (NLO) terms consists of just two-body interactions; three-body interactions first appear at Next-to-Next-to-Leading order (N^{2}LO). Alternatively, one can include Δ degrees of freedom into the EFT, in which case three-body interactions appear already at NLO [21, 22]; see Refs. [23, 24] for nuclear structure calculations with these NN plus 3N interactions. The reordering of contributions possibly speeds up the convergence of the chiral expansion.

Here we use the formulation of χEFT based on only pion and nucleon degrees of freedom since high order potentials have already been developed for this approach. This implies that we work with the conventional power-counting scheme, and with only NN potentials at LO and NLO, while 3N interactions arise at N^{2}LO. Specifically, within the Low-Energy Nuclear Physics International Collaboration (LENPIC) we use the semilocal momentum-space (SMS) regulated NN potentials from Ref. [20], which have been developed completely up through N^{4}LO; and the most accurate LENPIC-SMS NN potential, referred to as N^{4}LO$^+$, including some contributions from the 6th order in the chiral expansion. The N^{4}LO$^+$ potential gives a near-perfect description of the mutually compatible neutron-proton and proton-proton scattering data below $E_{\rm lab} = 300$ MeV with a $\chi^2_{\rm datum} = 1.01$. At the moment, the accompanying higher *n*-body forces have not yet been developed to the same chiral order.

Right now, consistent N^{2}LO 3NFs exist, implying that the regularization of the 3N interactions is consistent with that of the NN potential, all relevant symmetries are respected, and the same LEC values are used in the NN and 3N interactions. The strength of the 2π exchange in the N^{2}LO 3NFs (c_1, c_3, and c_4) has been determined from πN scattering, see Table 1 of Ref. [20]. (Note that, for the 3NF, these values need to be shifted as given in Eq. (2.8) of Ref. [25]). We have not taken uncertainties of these c_i's into account; this should be part of the N^{3}LO uncertainty estimate given below. These 3NFs have already been used for nucleon-deuteron scattering [26], as well as select light nuclei [27, 28]. Consistent N^{3}LO 3NFs are being developed and tested, and are expected to be available for use in many-body calculations soon; similarly, consistent electroweak operators are also under development.

The 3NFs at N^{2}LO depend on two LECs, generally referred to as c_D and c_E; these two LECs have been determined in Ref. [28] by fitting the ^{3}H binding energy (using the Faddeev approach), as well as the experimental proton-deuteron scattering data [29] for the differential cross-section minimum at the proton beam energy of E = 70 MeV. Note that for the determination of c_D and c_E it is important to identify observables that a) provide sufficiently independent constraints, i.e., are sensitive to the 3NFs and are sufficiently uncorrelated; b) can be predicted accurately at N^{2}LO; and c) are measured experimentally with sufficiently high accuracy. This can be achieved by e.g., incorporating properties of ^{4}He (and other nuclei), in addition to A = 3 observables, in the fitting of c_D and c_E [30]. However, here we prefer to only use A = 3 data for the determination of c_D and c_E in order to obtain parameter-free predictions for A > 3, and to avoid interference of 4N (and higher-body) interactions at N^{3}LO and higher. In Ref. [31], it has been observed that the triton binding energy and the proton-deuteron scattering cross section minimum at 70 MeV are fulfilling these requirements.

Note that we keep all LECs in the NN potentials fixed at their values determined from NN scattering; and we do not propagate any uncertainties in these LECs through the many-body calculations. Similarly, we have not explicitly propagated uncertainties in the LECs c_D and c_E for the 3NFs through the many-body calculations. In Ref. [31] we did vary c_D and c_E while keeping the ^{3}H binding energy fixed with the LENPIC Semilocal Coordinate Space interaction at N^{2}LO, and the resulting variation in the ^{4}He and ^{12}C binding energies, while not negligible and in opposite directions, stayed within the chiral truncation uncertainty estimate for a variation of c_D between 6 and 8, the preferred range based on Nd scattering data for that interaction. Furthermore, in Ref. [32] it was shown that the uncertainties in many-body observables of ^{4}He and ^{16}O due to propagation of the uncertainties in determining the LECs at N^{2}LO are much smaller than the chiral truncation errors in those many-body observables at N^{2}LO. We therefore assume here that any variation of the LECs of the NN and 3N interaction is an effect that is of higher order than N^{2}LO and thus those uncertainties are included in the uncertainty due to missing higher chiral orders.

2.1 Chiral truncation uncertainty estimates

Assuming that the chiral expansion of the nuclear interactions translates into a similar expansion for the physical observables, one expects that an observable X follows a similar expansion pattern. Consider therefore an observable X, and write it as

$$X = X^{(0)} + \Delta X^{(2)} + \Delta X^{(3)} + \cdots, \tag{1}$$

where $X^{(0)}$ is the LO term, $\Delta X^{(2)} = X^{(2)} - X^{(0)}$ and $\Delta X^{(3)} = X^{(3)} - X^{(2)}$ are the NLO and N^{2}LO correction terms, respectively, and the dots represent higher-order corrections. If this observable indeed follows the same expansion pattern as the nuclear interaction itself, then the correction terms $\Delta X^{(i)}$ behave like Q^i for increasing i, where $Q = \max(p, M_\pi)/\Lambda_B$ is the chiral expansion parameter (typically the maximum of the relevant momentum p and the pion mass M_π over the breakdown scale Λ_B). Note that there is no term linear in Q in this expansion: the first correction, at NLO, is quadratic in the expansion parameter Q, at least for observables governed solely by the strong interaction. For electroweak observables, the power-counting is different.

For the purpose of a Bayesian analysis, it is more convenient to rewrite this in terms of dimensionless expansion coefficient c_i, with the scale set by an overall reference value $X_{\rm ref}$. Thus we can rewrite the expansion for X as

$$X = X_{\rm ref}\left(c_0 + c_2 Q^2 + c_3 Q^3 + \cdots\right). \tag{2}$$

Now we can use Bayesian analysis on the coefficients c_i to estimate the chiral truncation uncertainties. Here we follow the Bayesian model of Ref. [33] for pointwise truncation errors with hyperparameters ν_0 = 1.5 and τ_0 = 1.5 [28]. We apply this to the ground state energy of the p-shell nuclei, with the experimental value as our reference value $X_{\rm ref}$. Furthermore, we use an effective pion mass of $M_\pi^{\rm eff} \approx 200$ MeV and a breakdown scale of $\Lambda_B \approx 650$ MeV [27, 28], and therefore a dimensionless expansion parameter $Q \approx 0.31$. Note that in Ref. [34] it was observed that the average momentum of the nucleons inside a nucleus increases with A, and one might therefore have to increase Q with A as well; but up to ^{16}O this average momentum remains below 200 MeV so we use the same value for Q throughout the p-shell. Nevertheless, a Bayesian analysis of correlated uncertainties for ground states and excited states of a subset of p-shell nuclei does suggest a slightly larger value of Q for the upper p-shell [25].

Finally, although we use the LENPIC-SMS NN potentials from LO up to N^{4}LO$^+$, we only have the corresponding 3NFs at N^{2}LO. We therefore perform our chiral truncation uncertainty analysis for the N^{2}LO through N^{4}LO$^+$ NN potentials, all in combination with the N^{2}LO 3NFs, as if they were all N^{2}LO interactions; that is, we include only the coefficients c_0, c_2, and c_3 in Eq. 2 (and again, there is no term linear in Q).

3 No-core shell model

3.1 Numerical method

In the No-Core Shell Model (NCSM) [16], the wavefunction Ψ of a nucleus consisting of Z protons and N neutrons is expanded in a finite $A = Z + N$-body basis of Slater determinants Φ_k of single-particle wavefunctions $\phi_{nljm}(\vec{r})$

$$\Psi\left(\vec{r}_1, \ldots, \vec{r}_A\right) = \sum a_k \Phi_k\left(\vec{r}_1, \ldots, \vec{r}_A\right). \tag{3}$$

With such an expansion, the many-body Schrödinger equation

$$\hat{\mathbf{H}}\,\Psi\left(\vec{r}_1, \ldots, \vec{r}_A\right) = E\,\Psi\left(\vec{r}_1, \ldots, \vec{r}_A\right) \tag{4}$$

becomes an eigenvalue problem

$$H_{ik}\,a_k = E\,a_i, \tag{5}$$

for the coefficients a_k of the expansion in Eq. 3. The matrix H_{ik} consists of matrix elements $\Phi_i \hat{\mathbf{H}} \Phi_k$ (where integration over all spatial degrees of freedom is understood) of the many-body hamiltonian

$$\hat{\mathbf{H}} = \hat{\mathbf{T}}_{\rm rel} + \hat{\mathbf{V}}_{NN} + \hat{\mathbf{V}}_{3N} + \cdots \tag{6}$$

consisting of the relative kinetic-energy operator, a two-body potential, and, in general three-body and higher n-body interaction terms. If the interaction is limited to n-body terms, the matrix H_{ik} for a nucleus with $A > n$ becomes a sparse matrix; in practice, the NCSM is generally applied with up to three-body interactions, and the corresponding Hamiltonian matrices are extremely sparse for $A \geq 6$. For any finite basis expansion, the obtained eigenvalue E gives a strict upper bound for the energy in the complete (though infinitely large) basis, at least for the lowest states of a given Z, N, and spin-parity quantum numbers J^P; and the corresponding eigenvector $\vec{a}$ gives an approximation to the A-body wavefunction $\Psi(\vec{r}_1, \ldots, \vec{r}_A)$. As one increases the basis size, the obtained eigenvalues E of the matrix H_{ik} approach the exact eigenvalues for a given Hamiltonian $\hat{\mathbf{H}}$.

In the conventional NCSM one uses a harmonic oscillator (HO) basis for the single-particle wavefunctions $\phi_{nljm}(\vec{r})$, characterised by its scale parameter $\hbar\omega$. One particular advantage of a HO basis is that one can treat the center-of-mass motion exactly: the Talmi–Moshinksy brackets [35, 36] can be used to convert between HO matrix elements in single-particle coordinates and relative plus center-of-mass coordinates; furthermore, with a many-body truncation on the total number of oscillator quanta in the many-body basis, the obtained wavefunctions factorize exactly into a center-of-mass wavefunction and a relative wavefunction [37, 38]. The single-particle wavefunctions $\phi_{nljm}(\vec{r})$ are labelled by their radial quantum number n, orbital motion quantum number l, total single-particle spin $j = l \pm \frac{1}{2}$, and magnetic projection m which satisfies $-j \leq m \leq j$. In a HO basis, the combination $(2n + l)$ gives the number of HO quanta for each state; thus, in a HO basis with a truncation on $\sum_i(2n_i + l_i)$ over all A nucleons, the factorization of the center-of-mass wavefunction is guaranteed. We add a Lagrange multiplier acting on the center-of-mass coordinates of the many-body system to the Hamiltonian $\hat{\mathbf{H}}$ to remove center-of-mass excited states from the low-lying spectrum [37, 38]; thus all low-lying states will have a 0s HO center-of-mass wavefunction. Note that this does not alter the eigenvalues nor the eigenvectors for these states, it merely separates the center-of-mass excited states from the states with the lowest center-of-mass motion.

All NCSM calculations presented here were performed using the code Many-Fermion Dynamics–nuclear physics [39–41]. It solves the eigenvalue problem Eq. (5) for the lowest eigenvalues, starting from two- and three-body matrix elements in a HO basis. MFDn is a platform-independent Fortran 90 code using a hybrid MPI+OpenMP programming model. The actual calculations have been performed on Theta at the Argonne Leadership Computing Facility (ALCF) and Cori at the National Energy Research Scientific Computing center (NERSC). For each nucleus and interaction, we performed a series of calculations, using a range of different values of $\hbar\omega$ and the truncation parameter $N_{\max}$, which is defined as the number of HO quanta above the minimal number of HO quanta in the many-body basis for that nucleus. That is, an $N_{\max} = 0$ calculation corresponds to a calculation in the lowest oscillator configuration. Here we are only interested in the normal or natural parity states (the parity of the $N_{\max} = 0$ space), and we increase $N_{\max}$ in steps of 2 starting from $N_{\max} = 0$ up to at least $N_{\max} = 8$. Some of the largest calculations for this study were for ^{14}N and ^{15}N at $N_{\max} = 8$, both with dimensions of over one billion, and about 76×10^{12} nonzero matrix elements, i.e., less than 1 in 10,000 matrix elements is nonzero with three-body interactions for these largest computations.

Of course, for two- and three-body systems it is more efficient and straightforward to work with wavefunctions in relative coordinates, rather than in single-particle wavefunctions. However, beyond four nucleons, the necessary anti-symmetrization becomes increasingly cumbersome in relative coordinates, whereas the NCSM in single-particle coordinates is straightforward to implement for an arbitrarily large number of nucleons; however, the size of the matrix does grow dramatically with the number of nucleons. Nevertheless, in recent years the NCSM has been implemented in Jacobi coordinates (J-NCSM) [42] and applied to (hyper)nuclei with up to eight (hyper)nucleons [43]. The codes MFDn and J-NCSM have been benchmarked against each other, and generally agree to within 10–20 keV for $A = 3$ and 4, and to within about 30 keV for $A = 6$, i.e., to within 0.1% of the obtained eigenvalues. The differences of up to about 0.1% have been attributed to differences in the implementations of transforming the three-body forces from their momentum-space expressions to HO matrix elements, including differences in the implementations of the Similarity Renormalization Group (SRG) transformations discussed next.

3.2 Convergence and similarity renormalization group evolution

In the left panel of Figure 1 we show the obtained ground state energy of ^{4}He at NLO and N^{2}LO for two different values of the regulator Λ as a function of $N_{\max}$ at $\hbar\omega = 24$ MeV; as illustration of the effect of the 3NFs, we also include results using only the NN potential at N^{2}LO, without the 3NFs (while at NLO, there are no 3NFs, so there is only the NN potential). Even at $N_{\max} = 16$, the NCSM results are still several MeV above the corresponding Yakubovsky results, and far from being converged with $N_{\max}$; and for the upper half of the p-shell nuclei, for $A \geq 10$ we are restricted to $N_{\max} = 8$ in the presence of 3NFs due to computational limitations. Clearly, we have to improve the numerical convergence while keeping the computational needs under control in order to obtain meaningful results for the ground state energies and other observables. There are several methods to do so, which generally fall into four categories (and of course one can also use a combination of these techniques!)

- modify the underlying single-particle wavefunctions to improve the numerical convergence, e.g., start with a Hartree–Fock basis, and/or use natural orbitals [44–46];
- modify the truncation scheme, e.g., select only the most important basis states at each step in $N_{\max}$ (importance-truncated NCSM) [47], or use symmetries to reduce the number of basis states as $N_{\max}$ increases (symmetry-adapted NCSM) [48–50];
- reduce the 3N interaction to an effective NN interaction by normal-ordering the 3N interaction, which typically gains one step in $N_{\max}$ in terms of computational needs [51, 52];
- apply a unitary transformation on the Hamiltonian to improve the convergence at (relatively) small values of $N_{\max}$ [53, 54].

Each of these methods has its advantages and drawbacks; and each of them is likely to obfuscate any uncertainty quantification of the numerical results; furthermore, with the first two methods listed above one might lose the exact factorization of the center-of-mass motion. Here we choose to improve the numerical convergence in finite bases by applying a suitable SRG transformation on the Hamiltonian.

The SRG approach [54–57] provides a robust framework for consistently evolving (softening) the Hamiltonian, including three-body terms [58–61], as well as operators for other observables, by applying a unitary transformation on the operator(s) of interest. This unitary transformation is formulated in terms of a flow equation

$$\frac{d}{d\alpha}\hat{\mathbf{H}}_\alpha = \left[\eta_\alpha, \hat{\mathbf{H}}_\alpha\right], \tag{7}$$

with a continuous flow parameter α. The physics of the SRG evolution is governed by the anti-hermitian generator η_α. A specific form widely used in nuclear physics [54] is given by

$$\eta_\alpha = m_N^2\left[\hat{\mathbf{T}}_{\rm rel}, \hat{\mathbf{H}}_\alpha\right], \tag{8}$$

where m_N is the (average) nucleon mass and $\hat{\mathbf{T}}_{\rm rel}$ is the relative kinetic-energy operator. This generator drives the Hamiltonian towards a diagonal form in a basis of eigenstates of the intrinsic kinetic energy, i.e., towards a diagonal in momentum space. The initial (or 'bare') Hamiltonian provides the initial condition at $\alpha = 0$ for this flow equation; at NLO, this is just an NN-potential, but at N^{2}LO (and higher orders) it also includes the explicit 3NFs. The width of the diagonal of the potential matrix elements in momentum space is proportional to $\lambda_{\rm SRG} = 1/\alpha^4$ [62]. For a typical value of $\alpha = 0.04$ fm^4, $\lambda_{\rm SRG} \approx 2.24$ fm^{-1}, which can be considered as an effective cutoff in momentum space; lowering this cutoff improves the convergence of NCSM calculations.

Along with a decoupling of low-momentum and high-momentum components, this SRG induces many-body operators beyond the rank of the initial Hamiltonian. In principle, all induced terms up to the A-body level should be retained to ensure that the transformation is a unitary transformation, such that the spectrum of the Hamiltonian is independent of the flow parameter α. In practice however, one has to truncate these many-body forces induced by the SRG evolution; here we follow the common practice of truncating the SRG evolution at the 3N level, omitting induced four-nucleon (and higher) induced interactions. Of course, this violates unitarity, and therefore introduces a fictitious dependence on the SRG parameter α for $A \geq 4$ which we have to monitor, and include in our uncertainty budget. Unfortunately, it is as of yet unclear how to identify an expansion parameter that allows for an estimate of uncertainties due to missing higher-body induced interactions in $A \geq 4$ nuclei.

The flow equation for the three-nucleon system is solved numerically using a HO basis in Jacobi-coordinates [60] at a fixed HO basis parameter of $\hbar\omega = 36$ MeV. The intermediate sums in this three-body Jacobi basis are truncated at $N_{\rm max} = 40$ for channels with $J < 9/2$, $N_{\rm max} = 38$ for $J = 9/2$, and $N_{\rm max} = 36$ for all $J > 9/2$. (Note that the flow equation at the two-nucleon level is solved numerically to a much higher numerical accuracy.) The SRG evolution and transformations first from $\hbar\omega = 36$ MeV to the desired $\hbar\omega$ value in the range from 14 to 32 MeV, and subsequently from Jacobi coordinates to single-particle coordinates, were all performed on a single multicore CPU node using an efficient OpenMP parallelized code.

In the right panel of Figure 1 we show the ground state energy of ^{4}He for the same initial interactions, and the same $\hbar\omega = 24$ MeV, as in the left panel, but after first performing an SRG evolution of the Hamiltonian to $\alpha = 0.04$ fm^4, and including induced 3N interactions, but omitting any induced 4N interactions. Comparing these two panels it is immediately evident that the SRG evolution has indeed dramatically improved the convergence: after the SRG evolution to $\alpha = 0.04$ fm^4, the obtained ground state energies at $N_{\rm max} = 4$ are already closer to the Yakubovsky results than the ground states energies at $N_{\rm max} = 16$ without any SRG evolution, and at $N_{\rm max} = 14$ they appear to be almost converged and in agreement with the Yakubovsky results to within a fraction of an MeV. Empirically, α in the range of $0.04 \leq \alpha \leq 0.08$ fm^4 appears to be a good compromise between the convergence of the NCSM calculations and minimizing the contributions of the SRG-induced four- and higher-body forces.

3.3 Extrapolating to the complete basis

Although the right-hand panel of Figure 1 looks converged to well within 100 keV, it is not completely converged; furthermore, in the upper half of the p-shell we are limited to at most $N_{\rm max} = 8$, at which point the results are clearly not yet converged. However, the approach to convergence appears to be smooth, and if we plot the difference between our results at successive $N_{\rm max}$ values, at fixed $\hbar\omega$ values near the variational minimum in the largest basis, see Figure 2, it is evident that these differences decrease almost exponentially with increasing $N_{\rm max}$. Inspired by this behavior, we therefore use exponential extrapolation in $N_{\rm max}$ at fixed $\hbar\omega$,

$$E^{\hbar\omega}(N_{\rm max}) \approx E_\infty^{\hbar\omega} + a\, e^{(-bN_{\rm max})} \tag{9}$$

based on three consecutive values of $N_{\rm max}$ at or slightly above the variational minimum in $\hbar\omega$ to extract binding energies in the complete (but infinitely large) basis. Indeed, such an empirical exponential has been widely used for a range of different interactions [63–65], and appears to be reasonably reliable and accurate, at least for true bound states. Furthermore, an exponential approach to convergence for the binding energy is also suggested by various analytic investigations into the asymptotic behavior [66–69]. Insights into the approach to convergence allows one to improve the extrapolation [70], but these analytic expressions generally depend on the underlying structure of the state. Here, we restrict ourselves to the simple ansatz Eq. (9) since it works well for all ground state energies considered, without the need to adapt the extrapolation to the specific structure of each nucleus.

Following Refs. [25, 28, 34], we take as our best estimate for E_∞ in the complete basis the value of $E_\infty^{\hbar\omega}$ near the variational minimum in $\hbar\omega$ for which $|E_\infty^{\hbar\omega} - E^{\hbar\omega}(N_{\rm max})|$ is minimal. Of course, this extrapolation is not exact, and will depend (slightly) on the $\hbar\omega$ value; furthermore, we have to include an extrapolation uncertainty in our uncertainty budget. Again, we resort to an empirical estimate

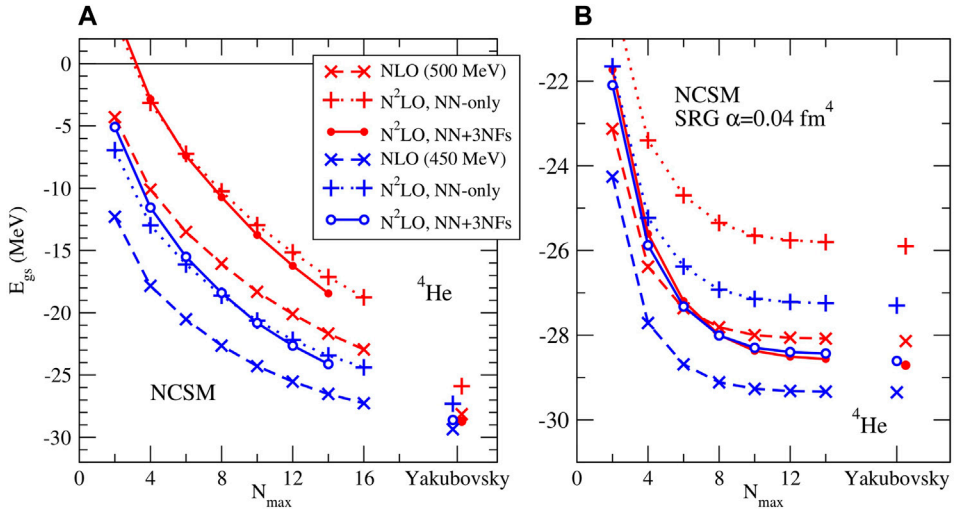

FIGURE 1
Convergence of NCSM calculations for ^{4}He without **(A)** and with **(B)** SRG evolution of the interactions. Induced 3NFs are included in the calculations in the right-hand panel; for comparison results obtained with Yakubovsky calculations in momentum space are shown for the same interactions as well.

TABLE 1 SRG dependence of ground state energies in MeV for $A = 3$ and 4, compared to Faddeev–Yakubovsky calculations [25]. Explicit N^{2}LO 3NFs are included in the N^{2}LO through N^{4}LO$^+$ calculations. Quoted uncertainties are the estimated NCSM extrapolation uncertainties only.

	NLO	N^{2}LO	N^{3}LO	N^{4}LO	N^{4}LO$^+$
^{3}H			Λ = 450 MeV		
Faddeev	−8.515(.001)	−8.483(.001)	−8.483(.001)	−8.483(.001)	−8.483(.001)
α = 0.04 fm^4	−8.54(.04)	−8.51(.06)	−8.50(.05)	−8.51(.06)	−8.50(.05)
α = 0.08 fm^4	−8.517(.008)	−8.489(.017)	−8.483(.010)	−8.484(.010)	−8.488(.016)
^{3}H			Λ = 500 MeV		
Faddeev	−8.325(.001)	−8.482(.001)	−8.483(.001)	−8.483(.001)	−8.484(.001)
α = 0.04 fm^4	−8.39(.10)	−8.52(.08)	−8.51(.06)	−8.51(.06)	−8.51(.06)
α = 0.08 fm^4	−8.327(.012)	−8.489(.019)	−8.485(.013)	−8.485(.011)	−8.491(.020)
^{4}He			Λ = 450 MeV		
Yakubovsky	−29.36(.01)	−28.61(.01)	−28.35(.01)	−28.29(.01)	−28.31(.01)
α = 0.04 fm^4	−29.339(.003)	−28.447(.004)	−28.284(.006)	−28.190(.004)	−28.195(.004)
α = 0.08 fm^4	−29.365(.001)	−28.527(.001)	−28.376(.002)	−28.285(.002)	−28.289(.002)
$\lvert E(\alpha = 0.04) - E(0)\rvert$	0.02	0.16	0.07	0.10	0.12
$\lvert E(\alpha = 0.08) - E(0)\rvert$	0.01	0.08	0.03	0.01	0.02
$\lvert E(0.04) - E(0.08)\rvert$	0.01	0.08	0.04	0.09	0.10
^{4}He			Λ = 500 MeV		
Yakubovsky	−28.15(.01)	−28.71(.01)	−28.56(.01)	−28.48(.01)	−28.52(.01)
α = 0.04 fm^4	−28.087(.003)	−28.585(.005)	−28.365(.003)	−28.236(.003)	−28.227(.003)
α = 0.08 fm^4	−28.122(.001)	−28.631(.003)	−28.447(.002)	−28.312(.002)	−28.301(.002)
$\lvert E(\alpha = 0.04) - E(0)\rvert$	0.06	0.13	0.20	0.24	0.29
$\lvert E(\alpha = 0.08) - E(0)\rvert$	0.03	0.08	0.11	0.17	0.22
$\lvert E(0.04) - E(0.08)\rvert$	0.03	0.05	0.08	0.07	0.07

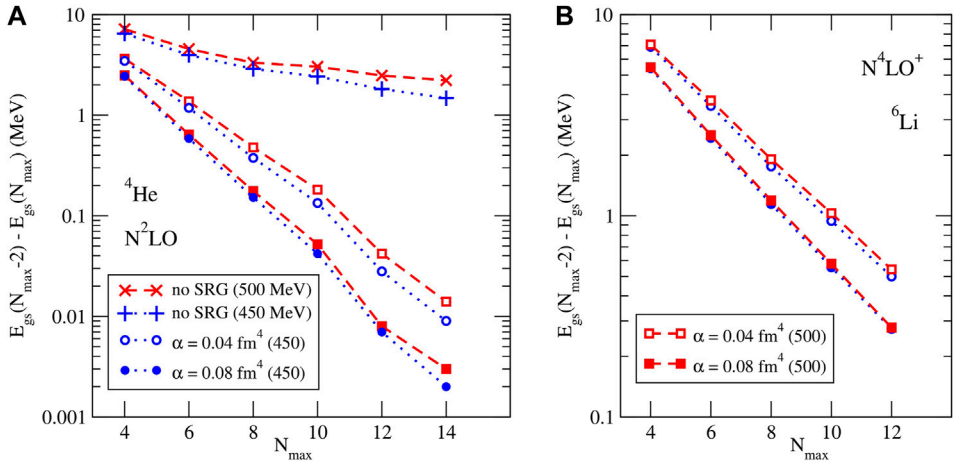

FIGURE 2
Convergence of NCSM calculations for ^{4}He **(A)** and ^{6}Li **(B)**: Difference in obtained ground energies for successive N_{max} values for different SRG evolution parameters α.

of this uncertainty based on the variation with $\hbar\omega$ and N_{max}, and our estimate of the corresponding extrapolation uncertainty is the maximum of

- the difference in $E_\infty^{\hbar\omega}$ for two successive extrapolations using data for ($N_{max} - 6$, $N_{max} - 4$, $N_{max} - 2$) and ($N_{max} - 4$, $N_{max} - 2$, N_{max}) respectively;
- half the variation in $E_\infty^{\hbar\omega}$ over a 8 MeV interval in $\hbar\omega$ around the variational minimum;
- 20% of $|E_\infty^{\hbar\omega} - E^{\hbar\omega}(N_{max})|$.

Note that this empirical uncertainty estimate is a conservative estimate, based on calculations with several different interactions [65, 71], and has been shown to give decreasing uncertainties with increasing N_{max}, with the higher-N_{max} results generally within the uncertainty estimates of the lower-N_{max} results. However, these uncertainty estimates cannot be interpreted statistically; for that one should use e.g., the Bayesian analysis of [72].

3.4 Combined numerical uncertainties

In Table 1 we give our extrapolated NCSM ground state energies for ^{3}H and ^{4}He, with our extrapolation uncertainty estimates, together with results obtained in momentum space with the Faddeev–Yakubovsky equations [25]. For ^{3}H the NCSM and Faddeev results agree very well, comfortably within the estimated extrapolation uncertainties of the NCSM calculations; and the results obtained with SRG $\alpha = 0.08\,\text{fm}^4$ are more precise than those obtained with $\alpha = 0.04\,\text{fm}^4$, judging by their smaller uncertainties. For the ground state energy of ^{4}He we do see differences between the NCSM results and the Yakubovsky calculations, beyond the 10 keV uncertainty in the Yakubovsky calculations and the estimated NCSM uncertainties. These differences can be attributed to the omitted induced 4NFs. They are generally larger with the $\Lambda = 500$ MeV regulator than with the $\Lambda = 450$ MeV regulator, as one might expect, given that the $\Lambda = 500$ MeV interactions are converging slower than the $\Lambda = 450$ MeV interactions (see Figure 1); and it may be counter-intuitive that the effects of omitted 4NFs are larger for $\alpha = 0.04\,\text{fm}^4$ than for $\alpha = 0.08\,\text{fm}^4$, but this accidental, as can be seen from Figure 3. This figure also shows good agreement between the Yakubovsky and NCSM calculations.

For $A \geq 6$ we do not have any calculations without SRG evolution for comparisons–or rather, NCSM calculations for these interactions without SRG evolution are so far from convergence for $A \geq 6$ that they are not very useful for comparison. However, we can gain insight in effects of omitted induced many-body forces by comparing results obtained with different values for the SRG parameter α, see Tables 2, 3. Table 2 shows a differences of about 0.2 MeV in the binding energies due to the two different SRG parameters α, both for ^{6}He and ^{6}Li, and almost independent of the chiral order of the NN potential; though at NLO the difference is somewhat smaller, probably due to the lack of an explicit 3N interaction at NLO. However, this difference of about 0.2 MeV is the same order of magnitude as our estimated extrapolation uncertainties at $\alpha = 0.04\,\text{fm}^4$, which prevents one from making firm conclusions.

Note that the extrapolation uncertainties for ^{6}He and ^{6}Li at $\alpha = 0.08\,\text{fm}^4$ are a factor of two to three smaller than those obtained with $\alpha = 0.04\,\text{fm}^4$, clearly indicating the improved convergence as the interaction is further evolved with SRG. The exception are the results for $A = 6$ at NLO; this is most likely caused by the fact that the obtained binding energies at NLO are actually above threshold for ^{6}He, and right around threshold for ^{6}Li, as was already observed in Ref. [28]. Indeed, for states above threshold, the simple exponential extrapolation may not be very reliable since neglected continuum effects could be significant.

In Table 3 we show the ground state energies for selected stable nuclei with $6 < A < 16$ using the N^{2}LO interaction (including 3NFs), SRG evolved to $\alpha = 0.04\,\text{fm}^4$ and $\alpha = 0.08\,\text{fm}^4$. As is the case for $A = 6$, the convergence improves with the SRG evolution:

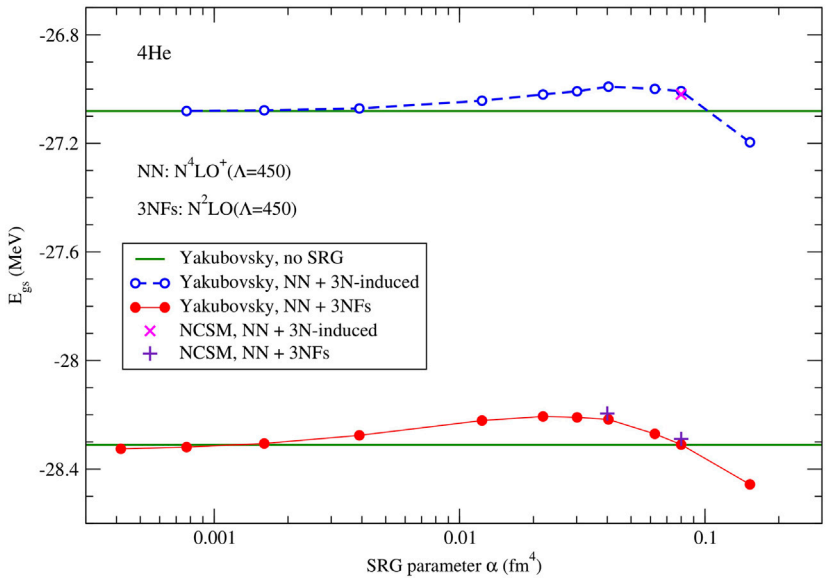

FIGURE 3
SRG depenence of the ground state energy of ^{4}He, with the N^{4}LO$^+$ NN potentials plus the N^{2}LO 3NFs and Λ = 450 MeV.

TABLE 2 SRG dependence for A = 6 ground state energies in MeV for SRG parameter α = 0.04 fm^4 and α = 0.08 fm^4, together with their difference. Quoted uncertainties are the estimated NCSM extrapolation uncertainties only.

	NLO	N^{2}LO	N^{3}LO	N^{4}LO	N^{4}LO$^+$
^{6}He			Λ = 450 MeV		
α = 0.04 fm^4	−28.73(.16)	−28.84(.17)	−28.16(.16)	−28.06(.16)	−28.11(.16)
α = 0.08 fm^4	−28.86(.14)	−29.05(.06)	−28.39(.07)	−28.28(.07)	−28.33(.07)
Δ	0.13	0.21	0.23	0.22	0.22
^{6}He			Λ = 500 MeV		
α = 0.04 fm^4	−27.27(.15)	−29.08(.17)	−28.35(.17)	−28.19(.17)	−28.23(.16)
α = 0.08 fm^4	−27.39(.10)	−29.21(.06)	−28.54(.06)	−28.37(.06)	−28.41(.07)
Δ	0.12	0.13	0.23	0.22	0.22
^{6}Li			Λ = 450 MeV		
α = 0.04 fm^4	−31.79(.11)	−31.85(.15)	−31.18(.14)	−31.07(.14)	−31.10(.14)
α = 0.08 fm^4	−31.93(.09)	−32.04(.05)	−31.41(.06)	−31.28(.06)	−31.32(.06)
Δ	0.14	0.19	0.23	0.21	0.22
^{6}Li			Λ = 500 MeV		
α = 0.04 fm^4	−30.33(.12)	−32.17(.16)	−31.42(.15)	−31.24(.15)	−31.26(.15)
α = 0.08 fm^4	−30.45(.06)	−32.29(.05)	−31.60(.06)	−31.41(.05)	−31.43(.05)
Δ	0.12	0.12	0.18	0.17	0.17

the extrapolation uncertainty estimates are a factor of 3–8 smaller at α = 0.08 fm^4 than at α = 0.04 fm^4. This effect of improved convergence becomes more pronounced as A increases, and is consistent with what we saw for A = 6 in Table 2. Furthermore, at α = 0.04 fm^4, starting from A = 10, the Λ = 450 MeV interaction converges noticeably better than the Λ = 500 MeV interaction; in qualitative agreement with the picture for ^{4}He (see Figure 2); however, at α = 0.08 fm^4 this difference has washed away, and

TABLE 3 SRG dependence for select $6 < A < 16$ ground state energies in MeV at N^{2}LO for SRG parameter $\alpha = 0.04$ fm^4 and $\alpha = 0.08$ fm^4, together with their difference. Quoted uncertainties are the estimated NCSM extrapolation uncertainties only.

	8Li	10Be	11B	12C	14C	15N
α	Λ = 450 MeV					
0.04	−40.9(0.4)	−66.1(1.2)	−79.3(1.1)	−98.3(1.8)	−119.9(1.9)	−134.4(2.4)
0.08	−41.23(0.16)	−66.5(0.5)	−79.8(0.4)	−98.7(0.4)	−120.1(0.4)	−135.1(0.5)
Δ	0.3	0.4	0.5	0.4	0.2	0.7
α	Λ = 500 MeV					
0.04	−41.6(0.4)	−67.0(1.5)	−82.1(2.0)	−101.8(2.8)	−123.3(2.5)	−138.3(4.2)
0.08	−41.85(0.15)	−67.5(0.4)	−82.3(0.4)	−101.9(0.4)	−123.9(0.4)	−138.9(0.5)
Δ	0.3	0.5	0.2	0.1	0.6	0.6

both regulators give a similar level of convergence for the ground state energies.

Somewhat surprisingly, the difference in ground state energies between the two SRG values, $\alpha = 0.04$ fm^4 and $\alpha = 0.08$ fm^4, remains almost constant, at around 0.5 MeV, from $A = 10$ to $A = 15$, at least for the nuclei considered in Table 3, with only a slight tendency to increase with A, and with similar tendencies for both regulator values. Furthermore, this difference is similar to the estimated NCSM uncertainty at $\alpha = 0.08$ fm^4 (which also increases slowly with A), but a factor of 3–8 smaller than the NCSM uncertainty at $\alpha = 0.04$ fm^4, which makes it hard to draw a firm conclusion. Nevertheless, based on these observations, we conclude that, for the calculations described here, it is realistic to include an SRG uncertainty that is equal to the NCSM extrapolation uncertainty estimate for stable $A = 10$ to $A = 16$ p-shell nuclei.

On the other hand, for $A = 6$ and ^{8}Li the difference in ground state energies between the two SRG values is noticeably larger than the NCSM extrapolation uncertainty for $\alpha = 0.08$ fm^4: for ^{8}Li it is a factor of two larger; and for $A = 6$ it is approximately a factor of three larger. Note that this coincides with a larger $N_{\max}$ value used for the lower half of the p-shell: for $A = 6$ and 7 we can perform our calculations up to $N_{\max} = 12$ (and are in fact limited by the size of the input files with three-body HO matrix elements) and the calculations for $A = 8$ and 9 extend up to $N_{\max} = 10$, whereas for $A \geq 10$ we are limited to $N_{\max} = 8$. Of course this upper limit in $N_{\max}$ also determines the level of numerical convergence that can be achieved, and hence the order of magnitude of the NCSM extrapolation uncertainty. Again, based on these observations we estimate the SRG uncertainty in the binding energy to be about 0.2 MeV for $A = 6$ and 7, and about 0.3 MeV for $A = 8$ and 9.

4 Ground state energies of p-shell nuclei

In Tables 4–8 we present our results for the ground state energies of most stable p-shell nuclei, excluding mirror nuclei. We also include ^{8}Be, despite it being above the 2α threshold. All calculations were done in the NCSM approach, extrapolated to the (infinitely-large) complete basis, using NN (and 3N) potentials, SRG evolved to $\alpha = 0.08$ fm^4, including induced 3N interactions, but omitting higher-body induced interactions. The first set of uncertainties in these tables is our estimate of the combined numerical uncertainties; the second is our estimate of the chiral truncation uncertainty; both as described in the previous section. The numerical uncertainty is estimated strictly based on the numerical convergence pattern and the SRG dependence, and cannot be interpreted statistically. The chiral truncation uncertainty is based on a Bayesian model. We give here the 68% degree of belief (DoB) values.

The NCSM calculations for the nuclei presented in Table 4 were performed up to $N_{\max} = 14$ for ^{4}He, and up to $N_{\max} = 12$ for $A = 6$ and 7, which is generally sufficient to reach convergence for the ground state energies to within 0.1% (or even better) for a given set of input HO two- and three-body matrix elements, thanks to the interaction being SRG evolved to $\alpha = 0.08$ fm^4. Therefore, the numerical uncertainties (the first set of quoted uncertainties in Table 4) are dominated by the uncertainties in the SRG evolution, which is mostly coming from the omission of induced 4-body forces (as well as higher-body forces for $A > 4$), as well as from the numerical implementation of the SRG evolution and transformations from momentum space expressions to HO matrix elements.

The exceptions are the $A = 6$ and 7 ground state energies at LO, because it turns out that at LO, these states are not bound, as indicated by the * in the tables: they are all above threshold for decays into α plus two neutrons, or plus a deuteron or a triton, respectively. Hence the numerical convergence of the NCSM calculations is poor (at best it would converge to a quasi-bound state), and neither the extrapolation to the complete basis (nor its uncertainty estimate) is likely to be accurate, which is why the extrapolation uncertainties at LO are noticeably higher than at higher chiral orders. Since we only include the LO results to improve our estimate of the chiral truncation uncertainties, an approximate bound state, or rather, resonance energy is sufficient for our purpose. Similarly, ^{6}He appears to be unbound at NLO; but again, for estimating the chiral uncertainty at N^{2}LO that is not a real problem.

The estimated chiral truncation uncertainties are significantly larger than any of the numerical uncertainty estimates. At NLO, these uncertainties are too large to draw any meaningful conclusions, but at N^{2}LO they are, as expected, more than a

TABLE 4 Ground state energies in MeV of ^{4}He, ^{6}He, ^{6}Li, and ^{7}Li, for LO through N^{4}LO$^+$ NN potentials, with 3NFs at N^{2}LO, for N^{2}LO through N^{4}LO$^+$, for $\Lambda = 450$ MeV (top) and $\Lambda = 500$ MeV (bottom). Both our estimated numerical uncertainties (first set of uncertainties) and chiral truncation uncertainty estimates (second set of uncertainties, not available for LO) are given. Entries with an * indicate energies above threshold, indicating a resonance, rather than a bound state.

V_{NN}	^{4}He(0^+)	^{6}He(0^+)	^{6}Li(1^+)	^{7}Li($\frac{1}{2}^-$)
	$\Lambda = 450$ MeV			
LO	−49.73(0.20)(−)	−46.7*(0.4)(−)	−50.4*(0.4)(−)	−61.35*(0.25)(−)
NLO	−29.37(0.20)(4.3)	−28.86*(0.24)(3.9)	−31.93(0.22)(4.0)	−38.72(0.22)(4.9)
N^{2}LO	−28.53(0.20)(1.2)	−29.04(0.21)(1.0)	−32.04(0.21)(1.1)	−39.39(0.21)(1.3)
N^{3}LO	−28.38(0.20)(1.2)	−28.39(0.21)(1.0)	−31.41(0.21)(1.1)	−38.43(0.21)(1.3)
N^{4}LO	−28.29(0.20)(1.2)	−28.28*(0.21)(1.0)	−31.28(0.21)(1.1)	−38.25(0.21)(1.3)
N^{4}LO$^+$	−28.29(0.20)(1.2)	−28.33(0.21)(1.0)	−31.32(0.21)(1.1)	−38.28(0.21)(1.3)
	$\Lambda = 500$ MeV			
LO	−51.17(0.20)(−)	−47.6*(0.5)(−)	−51.1*(0.4)(−)	−62.1*(0.3)(−)
NLO	−28.12(0.20)(4.9)	−27.39*(0.21)(4.3)	−31.45(0.21)(4.2)	−36.82(0.23)(5.4)
N^{2}LO	−28.63(0.20)(1.3)	−29.21(0.21)(1.2)	−32.29(0.20)(1.1)	−39.73(0.21)(1.5)
N^{3}LO	−28.45(0.20)(1.3)	−28.54(0.21)(1.2)	−31.61(0.21)(1.1)	−38.72(0.21)(1.5)
N^{4}LO	−28.31(0.20)(1.3)	−28.37(0.21)(1.2)	−31.41(0.21)(1.1)	−38.42(0.21)(1.5)
N^{4}LO$^+$	−28.30(0.20)(1.3)	−28.41(0.21)(1.2)	−31.43(0.21)(1.1)	−38.43(0.21)(1.5)
Expt.	−28.30	−29.27	−31.99	−39.24

TABLE 5 Ground state energies in MeV of $A = 8$ and ^{9}Li, for LO through N^{4}LO$^+$ NN potentials, with 3NFs at N^{2}LO, for N^{2}LO through N^{4}LO$^+$, for $\Lambda = 450$ MeV (top) and $\Lambda = 500$ MeV (bottom). Both our estimated numerical (first) and chiral truncation (second) uncertainties are given; and an * indicates ground states with energies above threshold.

V_{NN}	^{8}He(0^+)	^{8}Li(2^+)	^{8}Be(0^+)	^{9}Li($\frac{3}{2}^-$)
	$\Lambda = 450$ MeV			
LO	−41.6*(0.9)(−)	−59.5*(0.4)(−)	−95.7*(0.7)(−)	−60.0*(0.4)(−)
NLO	−28.2*(0.7)(3.0)	−39.44(0.36)(4.5)	−56.70*(0.36)(8.3)	−41.55(0.45)(4.2)
N^{2}LO	−30.42(0.36)(0.9)	−41.23(0.34)(1.2)	−56.48*(0.38)(2.2)	−45.14(0.34)(1.3)
N^{3}LO	−28.69(0.38)(0.8)	−39.62(0.34)(1.2)	−55.31*(0.42)(2.2)	−42.27(0.37)(1.1)
N^{4}LO	−28.62(0.38)(0.8)	−39.45(0.34)(1.2)	−54.95*(0.42)(2.2)	−42.11(0.36)(1.1)
N^{4}LO$^+$	−28.75(0.38)(0.8)	−39.53(0.34)(1.2)	−54.98*(0.42)(2.2)	−42.24(0.37)(1.1)
	$\Lambda = 500$ MeV			
LO	−41.6*(1.0)(−)	−59.6*(0.4)(−)	−97.7*(0.7)(−)	−59.8*(0.5)(−)
NLO	−26.3*(0.6)(3.4)	−37.24(0.34)(4.9)	−53.77*(0.36)(9.4)	−38.94(0.38)(4.7)
N^{2}LO	−30.92(0.34)(1.2)	−41.85(0.34)(1.5)	−56.96*(0.37)(2.5)	−46.18(0.33)(1.8)
N^{3}LO	−29.06(0.36)(1.0)	−39.94(0.36)(1.4)	−55.70*(0.38)(2.5)	−43.06(0.36)(1.4)
N^{4}LO	−28.91(0.35)(1.0)	−39.65(0.36)(1.4)	−55.10*(0.38)(2.5)	−42.80(0.36)(1.4)
N^{4}LO$^+$	−29.04(0.34)(1.0)	−39.72(0.36)(1.4)	−55.09*(0.42)(2.5)	−42.91(0.36)(1.4)
Expt.	−31.41	−41.28	−56.50	−45.32

factor of three smaller. Remember that we use N^{2}LO 3NFs in combination with the higher-order NN potentials, and we therefore apply the N^{2}LO power-counting rules for estimating the chiral uncertainties for these higher-order NN potentials. It should therefore not be surprising that the obtained chiral uncertainty estimates are the same at these higher order as those

TABLE 6 Ground state energies in MeV of ^{9}Be, ^{10}Be, ^{10}B, and ^{11}B, for LO through N^{4}LO$^+$ NN potentials, with 3NFs at N^{2}LO, for N^{2}LO through N^{4}LO$^+$, for Λ = 450 MeV (top) and Λ = 500 MeV (bottom). Both our estimated numerical (first) and chiral truncation (second) uncertainties are given; and an * indicates ground states with energies above threshold.

V_{NN}	^{9}Be ($\frac{3}{2}^-$)	^{10}Be(0^+)	^{10}B(3^+)	^{11}B ($\frac{3}{2}^-$)
	Λ = 450 MeV			
LO	−91.83*(0.8)(−)	−97.7*(2.1)(−)	−92.8*(2.3)(−)	−112.6(1.7)(−)
NLO	−56.97*(0.36)(7.5)	−61.9(0.8)(7.8)	−61.1(0.8)(7.0)	−72.2(0.8)(8.9)
N^{2}LO	−58.82(0.37)(2.0)	−66.5(0.7)(2.2)	−66.4(0.6)(2.1)	−79.8(0.6)(2.7)
N^{3}LO	−56.50*(0.40)(2.0)	−62.4(0.8)(2.1)	−62.5(0.7)(1.9)	−73.8(0.8)(2.4)
N^{4}LO	−56.12*(0.41)(2.0)	−62.0(0.8)(2.1)	−62.1(0.7)(1.9)	−73.4(0.8)(2.3)
N^{4}LO$^+$	−56.18*(0.41)(2.0)	−62.1(0.8)(2.1)	−62.2(0.8)(1.9)	−73.4(0.8)(2.3)
	Λ = 500 MeV			
LO	−93.00*(0.7)(−)	−98.1*(2.4)(−)	−92.5*(2.8)(−)	−112.0*(2.1)(−)
NLO	−53.68*(0.37)(8.4)	−57.9(0.8)(8.6)	−57.0*(0.7)(7.7)	−67.2(0.8)(9.7)
N^{2}LO	−59.73(0.36)(2.4)	−67.5(0.6)(2.8)	−68.4(0.6)(2.8)	−82.3(0.6)(3.6)
N^{3}LO	−57.20(0.40)(2.3)	−63.6(0.8)(2.5)	−64.1(0.7)(2.4)	−75.8(0.8)(3.0)
N^{4}LO	−56.59*(0.40)(2.3)	−62.9(0.8)(2.4)	−63.4(0.8)(2.3)	−74.7(0.7)(2.9)
N^{4}LO$^+$	−56.61(0.40)(2.3)	−63.0(0.8)(2.4)	−63.4(0.8)(2.3)	−74.6(0.8)(2.9)
Expt.	−58.16	−64.98	−64.75	−76.21

with the N^{2}LO NN potential. The central values however do change: all of the A = 4, 6, and 7 nuclei become less bound when using NN potentials beyond N^{2}LO in combination with the N^{2}LO 3NFs. This brings the ground state energy of ^{4}He in closer agreement with experiment, whereas the ground state energies of ^{6}He, ^{6}Li, and ^{7}Li are reasonably close to experiment with the N^{2}LO NN potential, and move away from their experimental values when including higher-order for the NN potential, to the point that ^{6}He appears to be barely bound, or maybe even slightly unbound, with these higher-order NN potentials. However, they all still agree with their corresponding experimental values, to within our combined numerical and chiral uncertainty estimates, and it is therefore too early to draw firm conclusions.

Finally, it is interesting to note that the estimated chiral truncation uncertainties are very similar for each of the four nuclei in Table 4. This can be easily understood in terms of their structure: ^{6}He, ^{6}Li, and ^{7}Li can be described as bound states of an α plus two neutrons, an α plus a deuteron, and an α plus a triton, respectively. It is therefore not surprising that the chiral uncertainties of these states follow that of the ^{4}He ground state energy (remember, the deuteron binding energy is fitted exactly, and the triton binding energies is fitted at N^{2}LO and up). However, there are subtle but important details that can make a difference: whereas the ground state energy of ^{4}He changes only by about 150–200 keV going from the N^{2}LO to the N^{3}LO NN potential, the difference between these two potentials for the A = 6 ground state energies is about 600–700 keV, and that for the ^{7}Li ground state is about 1 MeV, for both regulators.

In Table 5 we give our results the ground state energies of ^{8}He, ^{8}Li, ^{8}Be, and ^{9}Li. The NCSM calculations for these nuclei were performed up to N_{max} = 10, making the extrapolation uncertainties for these nuclei somewhat larger than those in Table 4, and they become of the same order as the estimated numerical uncertainties coming from the SRG evolution. This increased numerical uncertainty is reflected in the first set of error estimates in Table 5. And just as for the A = 6 and 7 nuclei, at LO none of these nuclei are actually bound–leading to larger extrapolation uncertainties. Again, the main purpose for the LO calculations is to set the scale for the estimate of the chiral truncation uncertainties; and for that purpose, an approximate ground state energy is sufficient. Furthermore, ^{8}Be is unbound at all chiral orders considered here, in agreement with experiment.

As for the A = 4, 6, and 7 nuclei, the estimated chiral truncation uncertainties for these A = 8 and 9 nuclei is significantly larger than the estimated numerical uncertainties. Again, at NLO, these uncertainties are too large to draw any meaningful conclusions, but at N^{2}LO they are about a factor of three smaller. The agreement with experiment is best with the N^{2}LO NN plus 3N interaction; moving to higher orders for the NN potential while retaining the N^{2}LO 3NFs leads to significant underbinding for ^{8}He, ^{8}Li, and ^{9}Li, with the experimental values outside combined numerical and chiral uncertainty estimates for the N^{3}LO and higher NN potentials. It will be very interesting to see whether or not consistent 3NFs at N^{3}LO can restore or improve on the level of agreement for these ground state energies obtained with N^{2}LO NN plus 3N interactions.

Beryllium-8 remains unbound according to our calculations, for all of these interactions, in qualitative agreement with experiment; and the extracted ground state energies may therefore be not as precise as for the other three nuclei in Table 5. Still, given the combined numerical and chiral uncertainty estimates, our results for the ^{8}Be ground state

TABLE 7 Ground state energies in MeV of $A = 12$ and $A = 13$ nuclei, for LO through N^{4}LO$^+$ NN potentials, with 3NFs at N^{2}LO, for N^{2}LO through N^{4}LO$^+$, for $\Lambda = 450$ MeV (top) and $\Lambda = 500$ MeV (bottom). Both our estimated numerical (first) and chiral truncation (second) uncertainties are given; and an * indicates ground states with energies above threshold.

V_{NN}	$^{12}B(1^+)$	$^{12}C(0^+)$	$^{13}B(\frac{3}{2}^-)$	$^{13}C(\frac{1}{2}^-)$
	$\Lambda = 450$ MeV			
LO	−113.7(1.8)(−)	−145.0*(1.3)(−)	−120.8*(1.7)(−)	−146.4*(1.1)(−)
NLO	−76.0(1.0)(8.4)	−89.7(0.7)(12.0)	−82.5(1.3)(8.6)	−94.3(0.7)(11.4)
N^{2}LO	−84.8(0.6)(2.7)	−98.7(0.6)(3.5)	−93.2(0.8)(2.9)	−108.3(0.6)(3.9)
N^{3}LO	−77.3(0.8)(2.2)	−90.6(0.8)(3.2)	−83.2(1.0)(2.3)	−96.7(0.8)(3.0)
N^{4}LO	−76.8(0.8)(2.2)	−89.9(0.8)(3.2)	−82.6(1.0)(2.3)	−96.2(0.8)(3.0)
N^{4}LO$^+$	−77.0(1.0)(2.2)	−90.0(1.0)(3.2)	−82.7(1.0)(2.3)	−96.3(0.8)(3.0)
	$\Lambda = 500$ MeV			
LO	−111.7*(2.3)(−)	−144.6*(1.8)(−)	−117.4*(2.1)(−)	−143.8*(1.6)(−)
NLO	−70.4(0.8)(9.1)	−83.3*(0.7)(13.1)	−76.1(1.1)(9.1)	−87.0(0.7)(12.3)
N^{2}LO	−87.5(0.6)(3.8)	−101.8(0.6)(4.7)	−95.8(1.0)(4.2)	−112.2(0.6)(5.4)
N^{3}LO	−79.5(0.8)(2.9)	−92.7(0.8)(3.8)	−85.5(1.0)(2.9)	−99.8(0.7)(3.9)
N^{4}LO	−78.8(0.8)(2.8)	−91.6(0.8)(3.7)	−84.6(1.0)(2.8)	−98.8(0.7)(3.8)
N^{4}LO$^+$	−78.8(1.0)(2.9)	−91.5(0.8)(3.7)	−84.6(1.0)(2.8)	−98.7(0.7)(3.8)
Expt.	−79.58	−92.16	−84.45	−97.11

TABLE 8 Ground state energies in MeV of ^{14}C, ^{14}N, ^{15}N, and ^{16}O, for LO through N^{4}LO$^+$ NN potentials, with 3NFs at N^{2}LO, for N^{2}LO through N^{4}LO$^+$, for $\Lambda = 450$ MeV (top) and $\Lambda = 500$ MeV (bottom). Both our estimated numerical (first) and chiral truncation (second) uncertainties are given.

V_{NN}	$^{14}C(0^+)$	$^{14}N(1^+)$	$^{15}N(\frac{1}{2}^-)$	$^{16}O(0^+)$
	$\Lambda = 450$ MeV			
LO	−160.2(0.7)(−)	−160.1(0.8)(−)	−182.1(0.6)(−)	−218.3(0.3)(−)
NLO	−104.9(0.8)(12.2)	−104.2(0.6)(12.3)	−119.4(0.8)(13.8)	−135.1(0.8)(17.9)
N^{2}LO	−120.1(0.6)(4.1)	−121.4(0.6)(4.4)	−135.1(0.5)(4.5)	−149.1(1.0)(5.3)
N^{3}LO	−106.3(0.8)(3.2)	−106.9(0.7)(3.3)	−118.8(0.8)(3.6)	−131.7(1.3)(4.8)
N^{4}LO	−105.5(0.8)(3.2)	−106.2(0.8)(3.3)	−117.8(0.8)(3.6)	−130.2(1.3)(4.8)
N^{4}LO$^+$	−105.7(0.8)(3.2)	−106.4(0.8)(3.3)	−118.0(0.8)(3.6)	−130.4(1.3)(4.8)
	$\Lambda = 500$ MeV			
LO	−156.1(1.1)(−)	−155.4(1.3)(−)	−175.5(0.8)(−)	−209.2(0.6)(−)
NLO	−96.2(0.7)(13.0)	−95.5(0.6)(13.0)	−109.3(1.0)(14.4)	−123.5(1.0)(18.3)
N^{2}LO	−123.9(0.6)(5.9)	−125.6(0.6)(6.2)	−138.9(0.7)(6.3)	−153.2(1.4)(7.0)
N^{3}LO	−109.8(0.8)(4.1)	−110.8(0.8)(4.3)	−122.5(1.0)(4.4)	−135.4(1.4)(5.2)
N^{4}LO	−108.5(0.8)(4.0)	−109.5(0.8)(4.2)	−120.8(1.0)(4.3)	−133.0(1.7)(5.1)
N^{4}LO$^+$	−108.5(0.8)(4.0)	−109.4(0.8)(4.2)	−120.7(1.0)(4.3)	−132.8(1.8)(5.1)
Expt.	−105.28	−104.66	−115.49	−127.62

energy are in good agreement with experiment. Furthermore it is interesting to note that the chiral uncertainty estimates for ^{8}Be are approximately twice that of ^{4}He, whereas the other three nuclei have chiral uncertainty estimates that are quite similar to those in Table 4. This can be easily understood by realizing that ^{8}Be is a loosely bound state, or rather, slightly unbound state, of two α particles, so the uncertainty is simply twice that of one α particle. It may be more surprising that the chiral uncertainties of ^{8}Li and ^{9}Li, neither of which are α-cluster states, are qualitatively similar to that of the $A = 4$, 6, and 7; and it is also surprising that

the estimated chiral uncertainties of ^{8}He is smaller than that of any of the other p-shell nuclei.

Moving to the middle of the p-shell, in Table 6 we have our results for the ground state energies of ^{9}He, ^{10}Be, ^{10}B, and ^{11}B. Starting from A = 10, the NCSM calculations are limited to N_{max} = 8, and therefore the extrapolation uncertainties become a significant factor in the uncertainty budget. Nevertheless, qualitatively, the overall picture remains the same: at LO all nuclei are unbound, but at NLO and beyond, they are generally bound, with the exception of ^{9}Be. Also, the estimated chiral truncation uncertainties for these nuclei remains significantly larger than the estimated numerical uncertainties; at NLO, these uncertainties are too large to draw any meaningful conclusions, but at N^{2}LO and beyond they are about a factor of three smaller. Here, we also start to see significant differences between the chiral uncertainties with the N^{2}LO NN plus 3N interaction, vs. using an NN potential at N^{3}LO or higher in combination with the N^{2}LO 3NFs (and remember, we are using the N^{2}LO counting rules for all these calculations with higher-order NN potential)—the effect of the higher-order NN potentials is becoming more pronounced with increasing A, and more so with Λ = 500 MeV than with Λ = 450 MeV. (This trend is already noticeable for e.g., ^{9}Li, see Table 5.).

Around A = 10, the agreement with experiment is no longer uniformly better with the N^{2}LO NN plus 3N interaction than with the higher-order NN potentials. The N^{2}LO NN plus 3N interaction is the only combination for which ^{9}Be is truly bound with respect to two α particles plus a neutron, for both regulator values, whereas with the higher-order NN potentials ^{9}Be becomes unbound or right at threshold in contrast with experiment where it is bound by about 1.6 MeV. Within the combined uncertainty estimates however, it is still in agreement with experiment for all of these interactions. For the A = 10 ground state energies the situation is different: at Λ = 450 MeV, the N^{2}LO NN plus 3N interaction gives slightly better agreement with experiment than the higher-order NN potentials, but at Λ = 500 MeV, it is the N^{3}LO NN plus N^{2}LO 3N interaction that gives the best agreement with experiment. In fact, the ^{10}B ground state energy with the N^{2}LO NN plus 3N potential is just outside the combined uncertainty estimates. Furthermore, the N^{2}LO NN potential plus 3NFs give a ground state energy for ^{11}B that is just outside the combined uncertainty estimates with both the Λ = 450 MeV and Λ = 500 MeV regulators.

This trend becomes more pronounced for $A \geq 12$, see Tables 7, 8. At LO, the ground states are still unbound, except for ^{12}B at Λ = 450 MeV; at NLO they are bound and in agreement with experiment, given the (granted, rather large) uncertainty estimates; and at N^{2}LO they are all significantly overbound, with the experimental values outside the combined numerical and chiral uncertainty estimates. Increasing the chiral order of the NN potential improves the agreement with experiment again: for A = 12 and 13 our results with the N^{3}LO and higher NN potentials, in combination with the N^{2}LO 3NFs, agree with experiment, well within our uncertainty estimates, with both the Λ = 450 MeV and Λ = 500 MeV regulators. For A = 14 this is also the case with Λ = 450 MeV, but Λ = 500 MeV leads to modest overbinding, though still within our uncertainty estimates. Also for ^{15}N and ^{16}O the ground state energies agree with experiment with Λ = 450 MeV, but with Λ = 500 MeV there is significant overbinding, with the experimental values just at the edge of our uncertainty intervals.

We have visually summarized our findings in Figure 4, which clearly shows that with the N^{2}LO NN plus 3N interaction one finds good agreement with experiment for the ground state energies of nuclei up to about A = 9, but significant overbinding starting from about A = 11, more than the estimated uncertainties for A = 13 and beyond. On the other hand, using higher-order NN potentials, in combination with N^{2}LO 3NFs, reduces this overbinding in the upper half of the p-shell, while maintaining reasonable agreement, taking into account both numerical and chiral truncation uncertainties, in the lower half of the p-shell, with only a few exceptions, out of the 20 nuclei considered here.

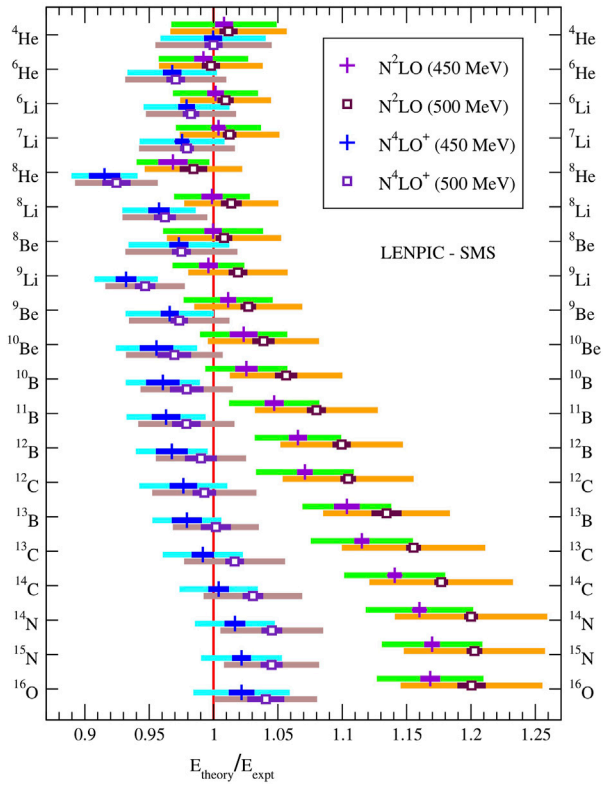

FIGURE 4
Comparison of ground state energies of p-shell nuclei between chiral EFT calculations at N^{2}LO and N^{4}LO$^+$, each for two values of the regulator Λ, and experiment. Both numerical uncertainty estimates (dark colored) and chiral truncation uncertainties (light colored, corresponding to 68% DoB) are shown.

Clearly, for A > 12 our uncertainty estimates for the N^{2}LO NN plus 3N interaction are noticeably smaller than the deviation from both the experimental data and from the calculations with higher-order NN potentials. We speculate that this may be caused by the N^{2}LO fit to the NN scattering data not being sufficiently accurate, and that discrepancies between the N^{2}LO fit and NN data should be taken into account as uncertainties in the LECs, whereas at higher orders in the NN potential, the NN scattering data are described much more accurately, and this is therefore not necessary. (Note that the N^{2}LO NN potential was fitted only up to E_{lab} = 125 MeV, whereas the N^{4}LO$^+$ potential was fitted to 260 MeV in Ref. [20].) Of course, one should then also incorporate the uncertainties in the 3NFs, c_D and c_E [30], and propagate all these uncertainties through the many-body bound state calculations [32, 72].

Another possible explanation could be that NN (and 3N) systems cannot sufficiently constrain the LECs–in which case one necessarily has to include properties of $A \geq 4$ nuclei for fitting some (or even all) of

the LECs. Indeed, impressive progress has been made in recent years along this way, extending *ab initio* calculations all the way to ^{208}Pb [73], but one loses some of the predictive power of χEFT by incorporating select many-body observables in the fitting procedures, and the results will depend on exactly which observables are included in the fitting. Yet another cause could be that the actual expansion parameter increases with A, as suggested in Ref. [34]. Calculations with consistent 3NFs at N^{3}LO, propagation of the uncertainties in the LECs through the many-body calculations, and Bayesian inference for both the chiral truncation uncertainties and the numerical uncertainties should help to resolve this issue.

Besides this general trend of increasing deviations with increasing A at N^{2}LO, ^{8}He and ^{9}Li clearly stand out among the N^{4}LO$^+$ results in Figure 4; and also our predictions for ^{8}Li do not agree, to within their estimated uncertainties, with experiment. Interestingly, ^{8}He and ^{9}Li are two of the most neutron-rich nuclei, out of the 20 nuclei shown in Figure 4, with $N - Z = 4$ and 3, respectively; and also ^{8}Li is a neutron-rich nucleus. This could be an indication of some deficiencies in the neutron-neutron (or three-neutron) part of the interactions. Unfortunately, there are no accurate neutron-neutron data, let alone three-neutron data, to constrain the LECs; the LECs of the interactions were all fitted to 2- and 3-body data involving at least one proton.

5 Concluding remarks and outlook

We have performed systematic calculations for the binding energies of p-shell nuclei using LENPIC-SMS χEFT NN and 3N interactions complete up through N^{2}LO, and with NN potentials up to N^{4}LO$^+$ in combination with N^{2}LO 3NFs. We have made a careful analysis of all sources of uncertainties, and incorporated our best estimates of these uncertainties in our comprehensive tables with order-by-order results and in Figure 4. Note that all LECs in the χEFT had been fitted to $A = 2$ and $A = 3$ data prior to these many-body calculations, and the obtained binding energies are therefore parameter-free predictions. Although our results with the N^{2}LO NN plus 3N interaction do not agree with the experimental binding energies for the upper p-shell, our results with the N^{4}LO$^+$ NN potential plus N^{2}LO 3NFs do agree with experiment throughout the p-shell within the combined numerical uncertainty estimates and the chiral truncation uncertainty estimates at the 68% DoB.

In future work we plan to extend these calculations to include consistent N^{3}LO 3NFs, which should bring the chiral truncation uncertainties down, and they may become comparable to the estimated numerical uncertainties. We therefore also intend to further reduce our numerical uncertainties; promising new developments include, among others, the use of Artificial Neural Networks [74–76] and Bayesian inference [72] for extrapolating NCSM binding energies to the complete basis. The latter is particularly interesting, since with Bayesian methods for both the numerical and the chiral truncation uncertainties one can consider correlated uncertainties of different states. This naturally leads to reduced uncertainties for excitation energies (compared to the uncertainties on the binding energies themselves), as well as e.g., neutron separation energies and various cluster thresholds.

Last but not least, we plan to use the obtained wavefunctions, in combination with consistent χEFT operators, to evaluate other observables, in particular radii, charge densities, magnetic and quadrupole moments, and electroweak transitions.

Data availability statement

The original contributions presented in the study are included in the article, further inquiries can be directed to the corresponding author.

Author contributions

All authors contributed to the calculations presented in this article, utilizing several different codes, developed at Iowa State University, the Forschungszentrum Jülich, and the Technische Universität Darmstadt. The initial draft for this article was written by PM, and all authors contributed to the subsequent discussions and final version of this article.

Funding

This work was supported by the US Department of Energy under Grants DE-FG02-87ER40371, DE-SC0018223 and DE-SC0023495, by the Deutsche Forschungsgemeinschaft (DFG, German Research Foundation) Project-ID 279384907, SFB 1245, by DFG and NSFC through funds provided to the Sino-German CRC 110 "Symmetries and 329 the Emergence of Structure in QCD" (NSFC Grant No. 12070131001, Project-ID 196253076–TRR 110), by the BMBF through Verbundprojekt 05P2021 (ErUM-FSP T07, Contract No. 05P21RDFNB), and by the MKW NRW under the funding code NW21-024-A. This research used resources of the National Energy Research Scientific Computing Center (NERSC) and the Argonne Leadership Computing Facility (ALCF), which are US Department of Energy Office of Science user facilities, supported under Contracts No. DE-AC02-05CH11231 and No. DE-AC02-06CH11357, and computing resources provided under the INCITE award 'Nuclear Structure and Nuclear Reactions' from the US Department of Energy, Office of Advanced Scientific Computing Research. Further computing resources were provided on LICHTENBERG II at the TU Darmstadt and on JURECA and the JURECA Booster of the Jülich Supercomputing Center, Jülich, Germany.

Acknowledgments

We thank all members of the LENPIC collaboration for useful and inspiring discussions. In particular, we would like to thank Evgeny Epelbaum, Dick Furnstahl, Kai Hebeler, Hermann Krebs and Jordan Melendez.

Conflict of interest

The authors declare that the research was conducted in the absence of any commercial or financial relationships that could be construed as a potential conflict of interest.

Publisher's note

References

1. Wiringa RB, Stoks VGJ, Schiavilla R. Accurate nucleon-nucleon potential with charge-independence breaking. *Phys Rev C* (1995) 51:38–51. doi:10.1103/PhysRevC.51.38

2. Machleidt R, Holinde K, Elster C. The Bonn meson exchange model for the nucleon nucleon interaction. *Phys Rept* (1987) 149:1–89. doi:10.1016/S0370-1573(87)80002-9

3. Machleidt R. High-precision, charge-dependent Bonn nucleon-nucleon potential. *Phys Rev C* (2001) 63:024001. doi:10.1103/PhysRevC.63.024001

4. Stoks VGJ, Klomp RAM, Terheggen CPF, de Swart JJ. Construction of high quality NN potential models. *Phys Rev C* (1994) 49:2950–62. doi:10.1103/PhysRevC.49.2950

5. Shirokov AM, Shin IJ, Kim Y, Sosonkina M, Maris P, Vary JP. N3LO NN interaction adjusted to light nuclei in ab exitu approach. *Phys Lett B* (2016) 761:87–91. doi:10.1016/j.physletb.2016.08.006

6. Coon SA, Scadron MD, McNamee PC, Barrett BR, Blatt DWE, McKellar BHJ. The two pion exchange, three nucleon potential and nuclear matter. *Nucl Phys A* (1979) 317:242–78. doi:10.1016/0375-9474(79)90462-7

7. Pudliner BS, Pandharipande VR, Carlson J, Pieper SC, Wiringa RB. Quantum Monte Carlo calculations of nuclei with A<~7. *Phys Rev C* (1997) 56:1720–50. doi:10.1103/PhysRevC.56.1720

8. Pieper SC, Pandharipande VR, Wiringa RB, Carlson J. Realistic models of pion exchange three nucleon interactions. *Phys Rev C* (2001) 64:014001. doi:10.1103/PhysRevC.64.014001

9. Weinberg S. Nuclear forces from chiral Lagrangians. *Phys Lett B* (1990) 251:288–92. doi:10.1016/0370-2693(90)90938-3

10. Epelbaum E, Hammer HW, Meißner UG. Modern theory of nuclear forces. *Rev Mod Phys* (2009) 81:1773–825. doi:10.1103/RevModPhys.81.1773

11. Machleidt R, Entem DR. Chiral effective field theory and nuclear forces. *Phys Rept* (2011) 503:1–75. doi:10.1016/j.physrep.2011.02.001

12. Hammer HW, König S, van Kolck U. Nuclear effective field theory: Status and perspectives. *Rev Mod Phys* (2020) 92:025004. doi:10.1103/RevModPhys.92.025004

13. Carlson J, Gandolfi S, Pederiva F, Pieper SC, Schiavilla R, Schmidt KE, et al. Quantum Monte Carlo methods for nuclear physics. *Rev Mod Phys* (2015) 87:1067–118. doi:10.1103/RevModPhys.87.1067

14. Lähde TA, Meißner UG. *Nuclear lattice effective field theory: An introduction*. Cham: Springer (2019). doi:10.1007/978-3-030-14189-9

15. Lee D. Recent progress in nuclear lattice simulations. *Front Phys* (2020) 8:174. doi:10.3389/fphy.2020.00174

16. Barrett BR, Navratil P, Vary JP. *Ab initio* no core shell model. *Prog Part Nucl Phys* (2013) 69:131–81. doi:10.1016/j.ppnp.2012.10.003

17. Hagen G, Papenbrock T, Hjorth-Jensen M, Dean DJ. Coupled-cluster computations of atomic nuclei. *Rept Prog Phys* (2014) 77:096302. doi:10.1088/0034-4885/77/9/096302

18. Hergert H, Bogner SK, Morris TD, Schwenk A, Tsukiyama K. The in-medium similarity renormalization group: A novel ab initio method for nuclei. *Phys Rept* (2016) 621:165–222. doi:10.1016/j.physrep.2015.12.007

19. Otsuka T, Honma M, Mizusaki T, Shimizu N, Utsuno Y. Monte Carlo shell model for atomic nuclei. *Prog Part Nucl Phys* (2001) 47:319–400. doi:10.1016/S0146-6410(01)00157-0

20. Reinert P, Krebs H, Epelbaum E. Semilocal momentum-space regularized chiral two-nucleon potentials up to fifth order. *Eur Phys J A* (2018) 54:86. doi:10.1140/epja/i2018-12516-4

21. van Kolck U. Few nucleon forces from chiral Lagrangians. *Phys Rev C* (1994) 49:2932–41. doi:10.1103/PhysRevC.49.2932

22. Piarulli M, Girlanda L, Schiavilla R, Navarro Pérez R, Amaro JE, Ruiz Arriola E. Minimally nonlocal nucleon-nucleon potentials with chiral two-pion exchange including Δ resonances. *Phys Rev C* (2015) 91:024003. doi:10.1103/PhysRevC.91.024003

23. Piarulli M, Girlanda L, Schiavilla R, Kievsky A, Lovato A, Marcucci LE, et al. Local chiral potentials with Δ-intermediate states and the structure of light nuclei. *Phys Rev C* (2016) 94:054007. doi:10.1103/PhysRevC.94.054007

24. Piarulli M, Baroni A, Girlanda L, Kievsky A, Lovato A, Lusk E, et al. Light-nuclei spectra from chiral dynamics. *Phys Rev Lett* (2018) 120:052503. doi:10.1103/PhysRevLett.120.052503

25. Bernard V, Epelbaum E, Krebs H, Meißner UG. Subleading contributions to the chiral three-nucleon force: Long-range terms. *Phys Rev C* (2008) 77:064004. doi:10.1103/PhysRevC.77.064004

26. Epelbaum E, Golak J, Hebeler K, Kamada H, Krebs H, Meißner UG, et al. Towards high-order calculations of three-nucleon scattering in chiral effective field theory. *Eur Phys J A* (2020) 56:92. doi:10.1140/epja/s10050-020-00102-2

27. Maris P, Roth R, Epelbaum E, Furnstahl RJ, Golak J, Hebeler K, et al. Nuclear properties with semilocal momentum-space regularized chiral interactions beyond N2LO. *Phys Rev C* (2022) 106:064002. doi:10.1103/PhysRevC.106.064002

28. Maris P, Epelbaum E, Furnstahl RJ, Golak J, Hebeler K, Hüther T, et al. Light nuclei with semilocal momentum-space regularized chiral interactions up to third order. *Phys Rev C* (2021) 103:054001. doi:10.1103/PhysRevC.103.054001

29. Sekiguchi K, Sakai H, Witala H, Glöckle W, Golak J, Hatano M, et al. Complete set of precise deuteron analyzing powers at intermediate energies: Comparison with modern nuclear force predictions. *Phys Rev C* (2002) 65:034003. doi:10.1103/PhysRevC.65.034003

30. Wesolowski S, Svensson I, Ekström A, Forssén C, Furnstahl RJ, Melendez JA, et al. Rigorous constraints on three-nucleon forces in chiral effective field theory from fast and accurate calculations of few-body observables. *Phys Rev C* (2021) 104:064001. doi:10.1103/PhysRevC.104.064001

31. Epelbaum E, Golak J, Hebeler K, Hüther T, Kamada H, Krebs H, et al. Few- and many-nucleon systems with semilocal coordinate-space regularized chiral two- and three-body forces. *Phys Rev C* (2019) 99:024313. doi:10.1103/PhysRevC.99.024313

32. Carlsson BD, Ekström A, Forssén C, Strömberg DF, Jansen GR, Lilja O, et al. Uncertainty analysis and order-by-order optimization of chiral nuclear interactions. *Phys Rev X* (2016) 6:011019. doi:10.1103/PhysRevX.6.011019

33. Melendez JA, Furnstahl RJ, Phillips DR, Pratola MT, Wesolowski S. Quantifying correlated truncation errors in effective field theory. *Phys Rev C* (2019) 100:044001. doi:10.1103/PhysRevC.100.044001

34. Binder S, Calci A, Epelbaum E, Furnstahl RJ, Golak J, Hebeler K, et al. Few-nucleon and many-nucleon systems with semilocal coordinate-space regularized chiral nucleon-nucleon forces. *Phys Rev C* (2018) 98:014002. doi:10.1103/PhysRevC.98.014002

35. Talmi I. Nuclear spectroscopy with harmonic oscillator wave-functions. *Helv Phys Acta* (1952) 25:185–234. doi:10.3929/ethz-a-000089257

36. Moshinsky M. Transformation brackets for harmonic oscillator functions. *Nucl Phys* (1959) 13:104–16. doi:10.1016/0029-5582(59)90143-9

37. Lipkin HJ. Center-of-Mass motion in the nuclear shell model. *Phys Rev* (1958) 110:1395–7. doi:10.1103/PhysRev.110.1395

38. Gloeckner DH, Lawson RD. Spurious center-of-mass motion. *Phys Lett B* (1974) 53:313–8. doi:10.1016/0370-2693(74)90390-6

39. Aktulga HM, Yang C, Ng EG, Maris P, Vary JP. Improving the scalability of a symmetric iterative eigensolver for multi-core platforms. *Concurrency Comput Pract Experience* (2014) 26:2631–51. doi:10.1002/cpe.3129

40. Shao M, Aktulga HM, Yang C, Ng EG, Maris P, Vary JP. Accelerating nuclear configuration interaction calculations through a preconditioned block iterative eigensolver. *Comput Phys Commun* (2017) 222:1–13. doi:10.1016/j.cpc.2017.09.004

41. Cook B, Maris P, Shao M, Wichmann N, Wagner M, O'Neill J, et al. High performance optimizations for nuclear physics MFDn on KNL. In: M Taufer, B Mohr, JM Kunkel, editors. *High performance computing*. Cham: Springer International Publishing (2016). p. 366–77.

42. Liebig S, Meißner UG, Nogga A. Jacobi no-core shell model for p-shell nuclei. *Eur Phys J A* (2016) 52:103. doi:10.1140/epja/i2016-16103-5

43. Le H, Haidenbauer J, Meißner UG, Nogga A. Jacobi no-core shell model for *p*-shell hypernuclei. *Eur Phys J A* (2020) 56:301. doi:10.1140/epja/s10050-020-00314-6

44. Constantinou C, Caprio MA, Vary JP, Maris P. Natural orbital description of the halo nucleus ^{6}He. *Nucl Sci Tech* (2017) 28:179. doi:10.1007/s41365-017-0332-6

45. Tichai A, Müller J, Vobig K, Roth R. Natural orbitals for *ab initio* no-core shell model calculations. *Phys Rev C* (2019) 99:034321. doi:10.1103/PhysRevC.99.034321

46. Fasano PJ, Constantinou C, Caprio MA, Maris P, Vary JP. Natural orbitals for the *ab initio* no-core configuration interaction approach. *Phys Rev C* (2022) 105:054301. doi:10.1103/PhysRevC.105.054301

47. Roth R. Importance truncation for large-scale configuration interaction approaches. *Phys Rev C* (2009) 79:064324. doi:10.1103/PhysRevC.79.064324

48. Dytrych T, Sviratcheva KD, Bahri C, Draayer JP, Vary JP. Evidence for symplectic symmetry in *ab initio* no-core shell model results for light nuclei. *Phys Rev Lett* (2007) 98:162503. doi:10.1103/PhysRevLett.98.162503

49. McCoy AE, Caprio MA, Dytrych T. Symplectic no-core configuration interaction framework for *ab initio* nuclear structure. *Ann Acad Rom Sci Ser Phys Chem Sci* (2018) 3:17. arXiv.1802.01771

50. Launey KD, Mercenne A, Dytrych T. Nuclear dynamics and Reactions in the ab initio symmetry-adapted framework. *Ann Rev Nucl Part Sci* (2021) 71:253–77. doi:10.1146/annurev-nucl-102419-033316

51. Hagen G, Papenbrock T, Dean DJ, Schwenk A, Nogga A, Wloch M, et al. Coupled-cluster theory for three-body Hamiltonians. *Phys Rev C* (2007) 76:034302. doi:10.1103/PhysRevC.76.034302

52. Roth R, Binder S, Vobig K, Calci A, Langhammer J, Navratil P. Medium-mass nuclei with normal-ordered Chiral NN+3N Interactions. *Phys Rev Lett* (2012) 109:052501. doi:10.1103/PhysRevLett.109.052501

53. Roth R, Reinhardt S, Hergert H. Unitary correlation operator method and similarity renormalization group: Connections and differences. *Phys Rev C* (2008) 77:064003. doi:10.1103/PhysRevC.77.064003

54. Bogner SK, Furnstahl RJ, Schwenk A. From low-momentum interactions to nuclear structure. *Prog Part Nucl Phys* (2010) 65:94–147. doi:10.1016/j.ppnp.2010.03.001

55. Glazek SD, Wilson KG. Renormalization of Hamiltonians. *Phys Rev D* (1993) 48:5863–72. doi:10.1103/PhysRevD.48.5863

56. Wegner F. Flow-equations for Hamiltonians. *Annalen der Physik* (1994) 506:77–91. doi:10.1002/andp.19945060203

57. Bogner SK, Furnstahl RJ, Maris P, Perry RJ, Schwenk A, Vary JP. Convergence in the no-core shell model with low-momentum two-nucleon interactions. *Nucl Phys A* (2008) 801:21–42. doi:10.1016/j.nuclphysa.2007.12.008

58. Jurgenson ED, Navratil P, Furnstahl RJ. Evolution of nuclear many-body forces with the similarity renormalization group. *Phys Rev Lett* (2009) 103:082501. doi:10.1103/PhysRevLett.103.082501

59. Roth R, Langhammer J, Calci A, Binder S, Navratil P. Similarity-transformed chiral NN+3N interactions for the ab initio description of 12-C and 16-O. *Phys Rev Lett* (2011) 107:072501. doi:10.1103/PhysRevLett.107.072501

60. Roth R, Calci A, Langhammer J, Binder S. Evolved chiral NN+3N Hamiltonians for ab initio nuclear structure calculations. *Phys Rev C* (2014) 90:024325. doi:10.1103/PhysRevC.90.024325

61. Binder S, Langhammer J, Calci A, Roth R. *Ab initio* path to heavy nuclei. *Phys Lett B* (2014) 736:119–23. doi:10.1016/j.physletb.2014.07.010

62. Bogner SK, Furnstahl RJ, Perry RJ, Schwenk A. Are low-energy nuclear observables sensitive to high-energy phase shifts? *Phys Lett B* (2007) 649:488–93. doi:10.1016/j.physletb.2007.04.048

63. Maris P, Vary JP, Shirokov AM. *Ab initio* no-core full configuration calculations of light nuclei. *Phys Rev C* (2009) 79:014308. doi:10.1103/PhysRevC.79.014308

64. Jurgenson ED, Maris P, Furnstahl RJ, Navratil P, Ormand WE, Vary JP. Structure of *p*-shell nuclei using three-nucleon interactions evolved with the similarity renormalization group. *Phys Rev C* (2013) 87:054312. doi:10.1103/PhysRevC.87.054312

65. Maris P, Shin IJ, Vary JP. *Ab initio* structure of p-shell nuclei with chiral effective field theory and Daejeon16 interactions. In: 6th International Conference Nuclear Theory in the Supercomputing Era (2019). arXiv.1908.00155

66. Coon SA, Avetian MI, Kruse MKG, van Kolck U, Maris P, Vary JP. Convergence properties of *ab initio* calculations of light nuclei in a harmonic oscillator basis. *Phys Rev C* (2012) 86:054002. doi:10.1103/PhysRevC.86.054002

67. Furnstahl RJ, Hagen G, Papenbrock T. Corrections to nuclear energies and radii in finite oscillator spaces. *Phys Rev C* (2012) 86:031301. doi:10.1103/PhysRevC.86.031301

68. More SN, Ekström A, Furnstahl RJ, Hagen G, Papenbrock T. Universal properties of infrared oscillator basis extrapolations. *Phys Rev C* (2013) 87:044326. doi:10.1103/PhysRevC.87.044326

69. Wendt KA, Forssén C, Papenbrock T, Sääf D. Infrared length scale and extrapolations for the no-core shell model. *Phys Rev C* (2015) 91:061301. doi:10.1103/PhysRevC.91.061301

70. Forssén C, Carlsson BD, Johansson HT, Sääf D, Bansal A, Hagen G, et al. Large-scale exact diagonalizations reveal low-momentum scales of nuclei. *Phys Rev C* (2018) 97:034328. doi:10.1103/PhysRevC.97.034328

71. Maris P, Vary JP. Ab initio nuclear structure calculations of p-shell nuclei with JISP16. *Int J Mod Phys E* (2013) 22:1330016. doi:10.1142/S0218301313300166

72. Gazda D, Htun TY, Forssén C. Nuclear physics uncertainties in light hypernuclei. *Phys Rev C* (2022) 106:054001. doi:10.1103/PhysRevC.106.054001

73. Hu B, Jiang W, Miyagi T, Sun Z, Ekstrom A, Forssen C, et al. *Ab initio* predictions link the neutron skin of ^{208}Pb to nuclear forces. *Nat Phys* (2022) 18:1196–200. doi:10.1038/s41567-022-01715-8

74. Negoita GA, Vary JP, Luecke GR, Maris P, Shirokov AM, Shin IJ, et al. Deep learning: Extrapolation tool for *ab initio* nuclear theory. *Phys Rev C* (2019) 99:054308. doi:10.1103/PhysRevC.99.054308

75. Jiang WG, Hagen G, Papenbrock T. Extrapolation of nuclear structure observables with artificial neural networks. *Phys Rev C* (2019) 100:054326. doi:10.1103/PhysRevC.100.054326

76. Knöll M, Wolfgruber T, Agel ML, Wenz C, Roth R. Machine learning for the prediction of converged energies from ab initio nuclear structure calculations. *Phys Lett B* (2023) 839:137781. doi:10.1016/j.physletb.2023.137781

frontiers | Frontiers in Physics

TYPE Original Research
PUBLISHED 04 May 2023
DOI 10.3389/fphy.2023.1084040

OPEN ACCESS

EDITED BY
Giuseppe Verde,
Universities and Research, Italy

REVIEWED BY
Alejandro Kievsky,
National Institute of Nuclear Physics, Pisa, Italy
Daniel Phillips,
Ohio University, United States

*CORRESPONDENCE
Evgeny Epelbaum,
evgeny.epelbaum@rub.de

RECEIVED 29 October 2022
ACCEPTED 06 April 2023
PUBLISHED 04 May 2023

CITATION
Skibiński R, Golak J, Witała H, Chahar V, Epelbaum E, Nogga A and Soloviov V (2023), The nucleon-induced deuteron breakup process as a laboratory for chiral dynamics.
Front. Phys. 11:1084040.
doi: 10.3389/fphy.2023.1084040

The nucleon-induced deuteron breakup process as a laboratory for chiral dynamics

Roman Skibiński[1], Jacek Golak[1], Henryk Witała[1], Vaibhav Chahar[1,2], Evgeny Epelbaum[3]*, Andreas Nogga[4,5] and Volodymyr Soloviov[1]

[1]M. Smoluchowski Institute of Physics, Jagiellonian University, Kraków, Poland, [2]Doctoral School of Exact and Natural Sciences, Jagiellonian University, Kraków, Poland, [3]Ruhr-Universität Bochum, Fakultät für Physik und Astronomie, Institut für Theoretische Physik II, Bochum, Germany, [4]Institut für Kernphysik, Institute for Advanced Simulation and Jülich Center for Hadron Physics, Forschungszentrum Jülich, Jülich, Germany, [5]CASA, Forschungszentrum Jülich, Jülich, Germany

The nucleon-induced deuteron breakup reaction is studied within the Faddeev approach at incoming nucleon laboratory energies of 135 and 200 MeV. The chiral semilocal momentum-space (SMS) potential developed up to N^{4}LO$^+$, supplemented by the N^{2}LO three-nucleon interaction, is used. Our investigation is focused on the determination of theoretical uncertainties in a predicted cross section related to its dependence on the value of the cutoff parameter of the regulator. We also compare predictions based on the complete N^{2}LO potential with those based on the two-nucleon force upgraded to the N^{4}LO$^+$ order and augmented with the N^{2}LO three-nucleon force. In addition, we study the three-nucleon force effects predicted by this model of interaction. Our systematic study covers the entire kinematically allowed phase space; however, our main results are obtained when additional restrictions on energies and cross section values are imposed. In such a case, we observe that the dependence of the differential cross sections on the regulator cutoff is moderate at 135 MeV and much stronger at 200 MeV. For the latter energy, it can amount to up to 45% in specific kinematic configurations. Taking into account terms beyond, N^{2}LO in a two-body interaction changes the cross section up to 20% (27%) at E = 135(200) MeV. The inclusion of the three-nucleon force leads to effects of approximately 27% at both energies. We illustrate these dependencies with a few examples of the exclusive cross section as a function of the arc length of the S-curve.

KEYWORDS

deuteron breakup, nuclear forces, three-nucleon interaction, theoretical uncertainty, Faddeev approach

1 Introduction

The precise determination of the nature of interactions between nucleons is a long-standing problem of nuclear physics. H. Yukawa's meson exchange theory in 1935 was the catalyst for the first attempts to solve this problem [1]. Over time, it was understood that nuclear forces are residual interactions stemming from those between quarks and gluons, and therefore, the theory of nuclear forces, dealing with nucleons and mesons, should have an effective character. This idea was further developed by S. Weinberg, who in seminal papers [2, 3] showed how to derive nuclear interactions from the effective chiral Lagrangian. This gave a new impetus to the development of the modern theory of nuclear forces and current operators. Soon after the pioneering work by S. Weinberg, C. Ordóñez,

et al. presented the first applications of the proposed formalism to nucleon–nucleon scattering using time-ordered perturbation theory [4]. These important steps laid the foundations on which D. R. Entem and R. Machleidt [5], and later E. Epelbaum, W. Glöckle, and Ulf-G. Meißner [6–8] built the chiral effective field theory (EFT) of nuclear forces, developing the first generation of the chiral two-nucleon (NN) interactions up to N^{3}LO. The N^{3}LO NN potential of [8] provided a good description of the NN data, but it was clear that to obtain results of quality that surpass the predictions of non-chiral phenomenological models, such as the AV18 [9] or CD-Bonn [10] potentials, it was necessary to take into account contributions from higher orders in the chiral expansion.

A number of attempts have been made to improve various aspects of these chiral interactions, resulting in the development of new potentials by several groups, for example, [11–14]. These interactions differ from the first generation of chiral NN potentials and each other in many ways, including but not limited to different regularization approaches, fitting strategies, values of the pion-nucleon low-energy constants (LECs), and treatment of the $\Delta(1232)$ degrees of freedom. In [12, 14, 15], the chiral EFT expansion for NN potentials was pushed to the fifth order of the chiral expansion (N^{4}LO). The N^{4}LO potentials of [12, 14] benefit from using the most reliable determination of the pion-nucleon LECs by matching the chiral perturbation theory to the solution of the Roy–Steiner equation at the subthreshold kinematic point [16]. The latest version of the potentials developed by the Bochum group [12] employs semi-local momentum-space (SMS) regularization, which reduces the amount of cutoff artifacts. At the highest order considered, N^{4}LO$^+$, the four N^{5}LO contact interactions in F-waves are taken into account. These additional contact terms are needed from a partial wave analysis point of view to describe certain very precise proton–proton scattering data at intermediate and higher energies. The same N^{5}LO contact interactions are also included in the N^{4}LO version of the non-locally regularized potentials in [14]. Finally, the SMS potentials of [12] have been updated in [17] to take into account isospin-breaking interactions up to N^{4}LO.

The leading contributions of the three-nucleon force (3NF) at N^{2}LO were derived using the chiral EFT [18, 19]. In [20–22], the sub-leading 3NF contributions were worked out using dimensional regularization in the calculation of loop integrals. The first application of the leading chiral 3NF to Nd scattering is shown in [19], while the first results for the triton using the non-locally regularized N^{3}LO 3NF are presented in [23], based on the previous generation of NN chiral potentials [8]. An efficient algorithm for performing partial wave decomposition of the 3NF was developed in [24]. Notably, while the expressions for the 3NF are available for N^{4}LO [20, 21, 25–28] (except for one topology), their application to few- and many-nucleon systems requires additional effort. Specifically, it was shown that the use of dimensional regularization in the derivation of the 3NF in combination with cutoff regulators in the Schrödinger equation leads to inconsistent results that violate chiral symmetry [29, 30]. Consequently, the 3NF and current operators beyond N^{2}LO need to be rederived using a symmetry-preserving cutoff regularization consistent with the SMS NN potentials of [12, 17].

In the meantime, exploratory studies on the role of higher-order short-range 3NF terms in the 3N continuum have been carried out [31–33], showing very promising results. These terms were, in particular, found to be important for solving the nucleon-analyzing power puzzle at low energies [31, 33]. However, complete calculations beyond the NN system are currently only available at N^{2}LO. In particular, the application of the SMS NN force along with the N^{2}LO 3NF regularized in the same way to 3N scattering observables and high- and medium-mass nuclei has been carried out [34]. For more details on the aforementioned applications and related topics, see the review articles [29, 30, 35, 36] and the references therein. In [37], the discussion of a simultaneous determination of the free parameters entering the NN and 3N forces can be found.

The functional form of the regulator and the choice of the cutoff values have attracted considerable attention in the community, both in connection with conceptual issues related to a proper renormalization of the Schrödinger equation in chiral EFT and in the context of an efficient treatment of the nuclear many-body problem. For a collection of different views on these and related topics, see [38] and the references therein. The most recent SMS potentials developed by the Bochum group in [12, 17] are available for the cutoff values in the range of $\Lambda = 400 - 550$ MeV, with $\Lambda = 450$ MeV giving the best description of the NN data. Smaller cutoff values were shown in [12] to introduce significant cutoff artifacts and degrade the description of NN scattering data. On the other hand, cutoff values larger than $\Lambda = 550$ MeV were found to lead to spurious deeply bound states, resulting in strongly non-perturbative interactions that are difficult to apply beyond the NN system. Clearly, the calculated observables show some residual dependence on the regulator value, which can be used to perform *a posteriori* consistency checks by confronting it with the estimated truncation uncertainty [39–41] (see [32, 34, 42] for some examples).

While in [43] we showed examples of our predictions for differential cross sections, for the nucleon analyzing power $A_Y(N)$, and for the deuteron analyzing power A_{XX} at a few chosen kinematic configurations, in this work we present more systematic studies. Therefore, we performed a search over the whole kinematically available phase space at two reaction energies: $E = 135$ MeV and $E = 200$ MeV. This phase space is spanned by five independent kinematic variables, which can be chosen as four angles defining the directions of the momenta of two outgoing nucleons and the energy of one of the nucleons. Our study allows us to identify regions where predictions based on different cutoff values differ substantially.

This approach can also be applied to other features of the potential. In the following, in addition to the cutoff dependence, we also examine how the predictions change with the chiral order and discuss the role played by the three-nucleon force. Performing calculations at two energies (135 and 200 MeV) gives additional information on how the quality of predictions based on the chiral SMS potential depends on the reaction energy. This, in turn, allows us to specify the applicability range of the chiral expansion.

Of particular interest is the possible existence of kinematic configurations for which the observables show an enhanced dependence on the chiral order or the sensitivity to the value of

the regulator. Such configurations provide an opportunity to test the theory by comparing theoretical predictions with experimental data and validating the estimated truncation uncertainties. Thus, in this work, we not only show the uncertainties associated with the cutoff values and the chiral order but also give details of the most interesting configurations. This establishes a guide for experimental groups interested in the nucleon-induced deuteron breakup process.

Our article is organized as follows. In the next section, we discuss the formalism used to obtain the breakup observables. Section 3 covers the results for the differential cross section, first for E = 200 MeV and then for E = 135 MeV. We summarize the aforementioned results in Section 4.

2 Formalism

The framework of the Faddeev equation has proven to be a precise method for solving the 3N problem with all realistic interactions, including the chiral ones. Since we are working in momentum space, the SMS interaction can be immediately incorporated into our codes. In the following, we provide the most fundamental steps of our approach (for details, see, e.g., [44–46]).

In this approach, the Faddeev equation for an auxiliary state, $T|\psi\rangle$, plays a key role. It reads

$$\begin{aligned} T|\psi\rangle &= tP|\psi\rangle + tPG_0T|\psi\rangle + (1+tG_0)V_4^{(1)}(1+P)|\psi\rangle \\ &\quad + (1+tG_0)V_4^{(1)}(1+P)T|\psi\rangle, \end{aligned} \tag{1}$$

where the initial state $|\psi\rangle$consists of a deuteron and the relative momentum eigenstate of the projectile neutron, $V_4^{(1)}$ is part of a 3N force that is symmetric under an exchange of particles 2 and 3, P is a permutation operator that takes into account the identity of the nucleons, and G_0 is the free 3N propagator. The 2N t-matrix is, for a given 2N interaction V, a solution of the Lippmann–Schwinger equation,

$$t = V + V\tilde{G}_0 t, \tag{2}$$

where $\tilde{G}_0$ is the 2N free propagator. Once Eq. 1 is solved, the transition amplitude U_0 to the final three-body scattering state $|\psi'\rangle$ is calculated as

$$\langle\psi'|U_0|\psi\rangle = \langle\psi'|(1+P)T|\psi\rangle \tag{3}$$

and used to find observables [45].

We solve Eq. 1 in the momentum space partial wave scheme. We work with the $|p, q, \alpha\rangle$ states, with $p = |\vec{p}|$ and $q = |\vec{q}|$ being the magnitudes of the relative Jacobi momenta $\vec{p}$ and $\vec{q}$. Furthermore, α represents a set of discrete quantum numbers for the 3N system in the jI-coupling

$$\alpha = \left((l,s)j;\left(\lambda,\frac{1}{2}\right)I;(j,I)JM_J;\left(t\frac{1}{2}\right)TM_T\right). \tag{4}$$

Here, l, s, j, and t denote the orbital angular momentum, total spin, total angular momentum, and total isospin of the 2–3 subsystem, respectively. Furthermore, λ and I are the orbital and total angular momenta of spectator nucleon 1, with respect to the center of mass of the 2–3 subsystem. Finally, J, M_J, T, and M_T are the total angular momentum of the 3N system, its projection on the quantization axis, the total 3N isospin, and its projection, respectively.

We solve Eq. 1 by generating its Neumann series and summing it up by using the Pade method [45]. For the results presented here, we use all partial waves with $j \le 5$ and $J \le \frac{25}{2}$, including the three-nucleon interaction up to $J = \frac{7}{2}$. More details about our numerical performance are shown in [45].

The unambiguous definition of the kinematic configuration of three free nucleons requires *a priori* knowledge of nine kinematic variables, which can be reduced to five using the conservation laws. We follow a common choice and use four angular variables: θ_1, ϕ_1, θ_2, and ϕ_2 to define the directions of the momenta of nucleons 1 and 2. As the fifth variable, we chose the position on the S-curve, that is, curves located in the E_1–E_2 plane and defined by kinematically allowed (E_1 and E_2) pairs. The possible positions of the S-curve in the E_1–E_2 plane and a convention for the location of its starting point (S = 0) are discussed, e.g., in [45]. Some points on the curve correspond to particularly interesting kinematic configurations. The final-state interaction (FSI) configuration is the one in which the momenta of two nucleons are equal, leading to vanishing relative energy. This makes the cross section for this configuration sensitive to the $^1S_0$ interaction, which results in an enhancement of the cross section referred to as the FSI peaks. The QFS configuration, in which one of the nucleons serves as a spectator particle, is also noteworthy. The quasi-free scattering mechanism also increases the cross section; however, here different partial waves contribute.

In the following section, we show the results of our search over the entire kinematically available phase space for the nucleon-deuteron breakup process. We use the same grid for θ_1, θ_2, and ϕ_2 values taken in the range [2.5°, 177.5°] and with a step of 5°, assuming that $\phi_1 = 0$ since the unpolarized observables only depend on $\phi_{12} = \phi_1 - \phi_2$. For the energies studied here, the S-curve length is typically in the range of 50–200 MeV. We have checked that the observables are accurately described when we use a step of 0.5 MeV along each S-curve.

3 Results for the differential cross section

3.1 E = 200 MeV: Cutoff dependence

To study the dependence of our predictions on the regulator value Λ, we choose the five-fold differential cross sections $\left(\frac{d^5\sigma}{d\Omega_1 d\Omega_2 dS}\right)^{400}$ and $\left(\frac{d^5\sigma}{d\Omega_1 d\Omega_2 dS}\right)^{550}$ obtained with Λ = 400 MeV and Λ = 550 MeV, respectively. Having them at our disposal, we construct ($\phi_1 = 0°$)

$$\delta^{400-550}(\theta_1,\theta_2,\phi_2,S) \equiv \frac{\left(\frac{d^5\sigma}{d\Omega_1 d\Omega_2 dS}\right)^{400} - \left(\frac{d^5\sigma}{d\Omega_1 d\Omega_2 dS}\right)^{550}}{\frac{1}{2}\left(\left(\frac{d^5\sigma}{d\Omega_1 d\Omega_2 dS}\right)^{400} + \left(\frac{d^5\sigma}{d\Omega_1 d\Omega_2 dS}\right)^{550}\right)} \tag{5}$$

and then, for given θ_1 and θ_2, we find its maximum over the remaining variables

$$\Delta^{400-550} \equiv \Delta^{400-550}(\theta_1,\theta_2) \equiv \max_{\{\phi_2,S\}} \delta^{400-550}(\theta_1,\theta_2,\phi_2,S). \tag{6}$$

Here and in the following, the calculations are performed with the NN interaction at the highest available order, that is, at N^{4}LO$^+$, supplemented by the 3NF at N^{2}LO.

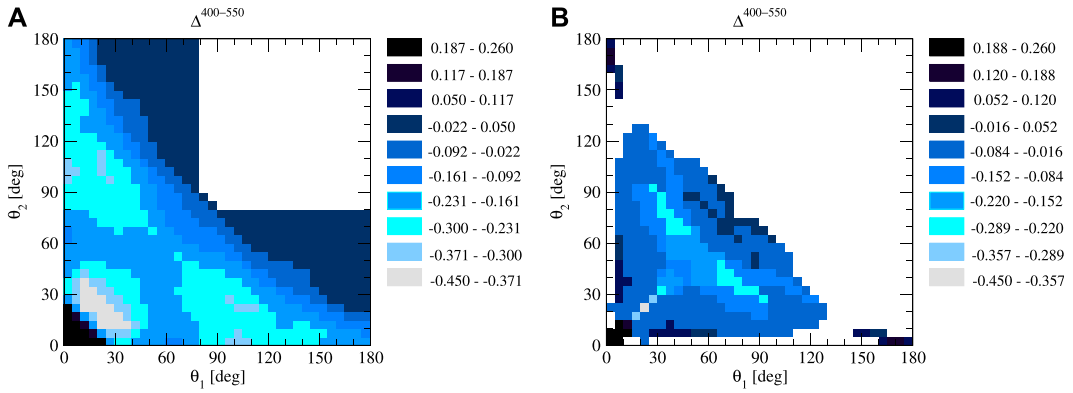

FIGURE 1
$\Delta^{400-550}$ in the incoming nucleon lab. Kinetic energy E_{lab} = 200 MeV. **(A)** shows predictions based on all the configurations studied, while for **(B)**, additional thresholds for the energies of the detected neutrons and the magnitude of the cross sections have been imposed: $E_1 > 10$ MeV and $E_2 > 10$ MeV, $(\frac{d^5\sigma}{d\Omega_1 d\Omega_2 dS})^{400} > 0.01$ [mb sr^{-2} MeV^{-1}], and $(\frac{d^5\sigma}{d\Omega_1 d\Omega_2 dS})^{550} > 0.01$ [mb sr^{-2} MeV^{-1}].

The resulting $\Delta^{400-550}$ at $E = 200$ MeV is shown in Figure 1A. The white area shows the kinematically forbidden region. The symmetry with respect to the diagonal, as shown in Figure 1, reflects the fact that two nucleons (1 and 2) are indistinguishable. Some small deviations from symmetry seen in the figure are due to the finite grid of points on the S-curves used in the calculations. When interpreting the results obtained for $\Delta^{400-550}$, it is important to keep in mind that the differences have already been maximized with respect to the not explicitly shown kinematic variables ϕ_2 and S. This implies that the actual residual cutoff dependence of the calculated cross sections, encoded in the quantity $\delta^{400-550}$, is on average much smaller than the deviations shown in Figure 1 for $\Delta^{400-550}$. The same comment applies to the results shown for the dependence on the chiral order and the effects of the 3NF.

We observe that $\Delta^{400-550}$ is spread over the range (−0.440, 0.260), so the two regulator values can yield predictions that diverge by more than 30%. In the majority of the available area in the (θ_1 and θ_2) subspace $\Delta^{400-550} \in (-30\% - 5\%)$, the maximal $\Delta^{400-550}$ values are concentrated at small θ_1 and θ_2 angles. It is interesting to note that the lowest $\Delta^{400-550}$ values also occur at relatively small polar angles. The particular configurations with extreme $\Delta^{400-550}$ in these regions are related to the FSI.

Among the configurations leading to $\Delta^{400-550}$ shown in Figure 1A, there are very likely some with very small cross sections, which can result in large $\Delta^{400-550}$. Such configurations are not of interest when planning feasible measurements. Thus, in Figure 1B, we show the same $\Delta^{400-550}$ but after imposing additional conditions on the cross sections: $(\frac{d^5\sigma}{d\Omega_1 d\Omega_2 dS})^{400} > 0.01$ [mb sr^{-2} MeV^{-1}] and $(\frac{d^5\sigma}{d\Omega_1 d\Omega_2 dS})^{550} > 0.01$ [mb sr^{-2} MeV^{-1}] and on the energies: $E_1 > 10$ MeV and $E_2 > 10$ MeV. Notably, these conditions remove many configurations, producing more white space in the graph, and $\Delta^{400-550}$ decreases on average. While the spread of the $\Delta^{400-550}$ variation remains nearly unchanged, the distribution of the $\Delta^{400-550}$ values changes, resulting in, on average, smaller in magnitude values of $\Delta^{400-550}$. In particular, the configurations with $|\Delta^{400-550}| \geq 0.289$ occupy less than 1% of the θ_1–θ_2 phase space shown.

To display the full information on the specific configurations leading to the $\Delta^{400-550}$ values shown in Figure 1B, Figure 2 shows the corresponding energy E_1 and the relative azimuthal angle ϕ_{12}, which by our choice of $\phi_1 = 0^\circ$ is equivalent to ϕ_2, as functions of the polar angles θ_1 and θ_2. The analogous figure not shown for E_2 is a mirror image of that for E_1 with respect to the diagonal $\theta_1 = \theta_2$. In most cases, E_1 takes on small (below approximately 30 MeV) or large (above approximately 160 MeV) values, and only in about a quarter of configurations, do the largest $\Delta^{400-550}$ occur at intermediate E_1 energies. The ϕ_{12} angles corresponding to the most pronounced $\Delta^{400-550}$ are usually above approximately 130°; however, for some combinations (θ_1 and θ_2), the smallest ϕ_{12} is preferred.

Figure 3 shows the differential cross section $\frac{d^5\sigma}{d\Omega_1 d\Omega_2 dS}$ as a function of the arc-length S for three configurations that maximize $\Delta^{400-550}$ at one S point. The left panel shows a configuration where both θ_i are small ($\theta_1 = 12.5^\circ$ and $\theta_2 = 7.5^\circ$), while the central panel shows the case where $\theta_1 = \theta_2 = 27.5^\circ$. For the first configuration, the maximal $\delta^{400-550}(\theta_1, \theta_2, \phi_2, S)$ occurs in the maximum of the FSI peak at S ≈ 134 MeV. In this case, the softer interaction yields a larger cross section. On the contrary, in the case of the configuration shown in Figure 3B, predictions based on the SMS potential with Λ = 400 MeV are smaller around S = 111 MeV than those with the cutoff Λ = 550 MeV. Finally, in Figure 3C, we give an example of the configuration from a different position in the $\theta_1 - \theta_2$ plane, namely, for large θ_1 and small θ_2. Here, again, the cross section resulting from the interaction at Λ = 400 MeV exceeds the one obtained at Λ = 550 MeV, leading to $\delta^{400-550}(172.5^\circ, 2.5^\circ, 177.5^\circ, 92\text{ MeV}) = 0.128$.

3.2 E = 200 MeV: Changes with the chiral order

Similar to the previously defined $\Delta^{400-550}$, we also studied

$$\Delta^{N2LO-N4LO+} \equiv \Delta^{N2LO-N4LO+}(\theta_1, \theta_2) \equiv \max_{\{\phi_2, S\}} \delta^{N2LO-N4LO+}(\theta_1, \theta_2, \phi_2, S) \tag{7}$$

with

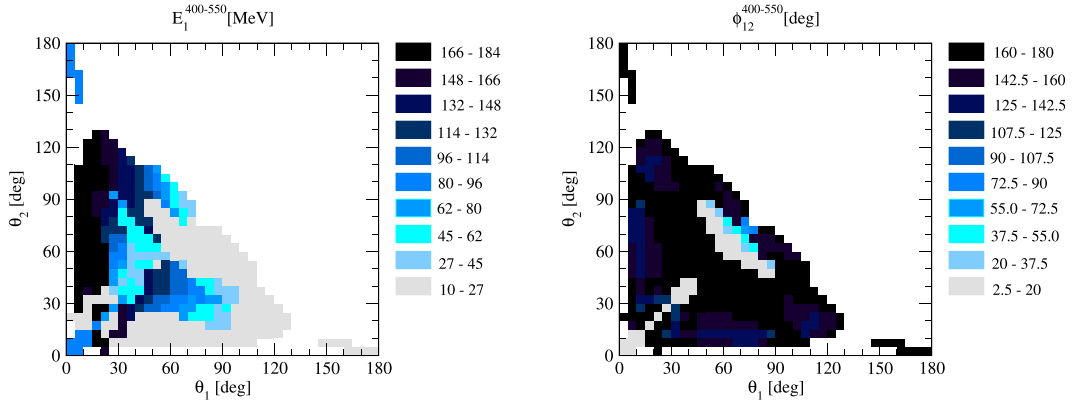

FIGURE 2
Values of nucleon 1 energy E_1 (left) and the azimuthal angle ϕ_2 (right) in the θ_1–θ_2 plane corresponding to the kinematic configurations from the right panel of Figure 1.

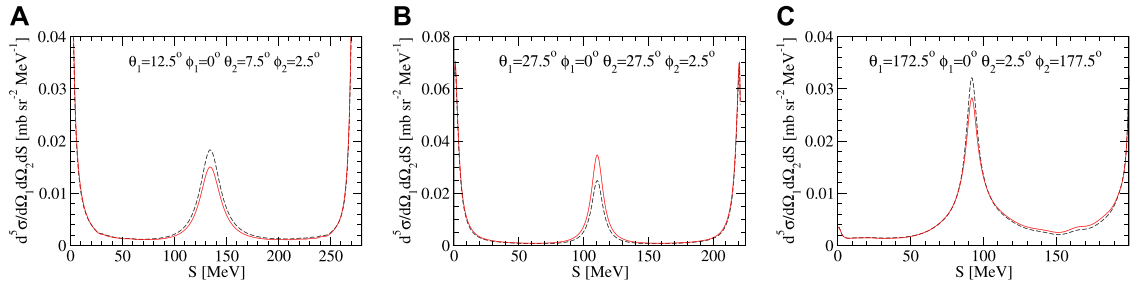

FIGURE 3
Differential cross sections maximizing $\Delta^{400-550}$ at three selected kinematic configurations defined by **(A)** $\theta_1 = 12.5^\circ$, $\theta_2 = 7.5^\circ$, $\phi_{12} = 2.5^\circ$, **(B)** $\theta_1 = 27.5^\circ$, $\theta_2 = 27.5^\circ$, $\phi_{12} = 2.5^\circ$, and **(C)** $\theta_1 = 172.5^\circ$, $\theta_2 = 2.5^\circ$, $\phi_{12} = 177.5^\circ$. The dashed black (solid red) curve represents the N^{4}LO$^+$ results at $\Lambda = 400(550)$ MeV.

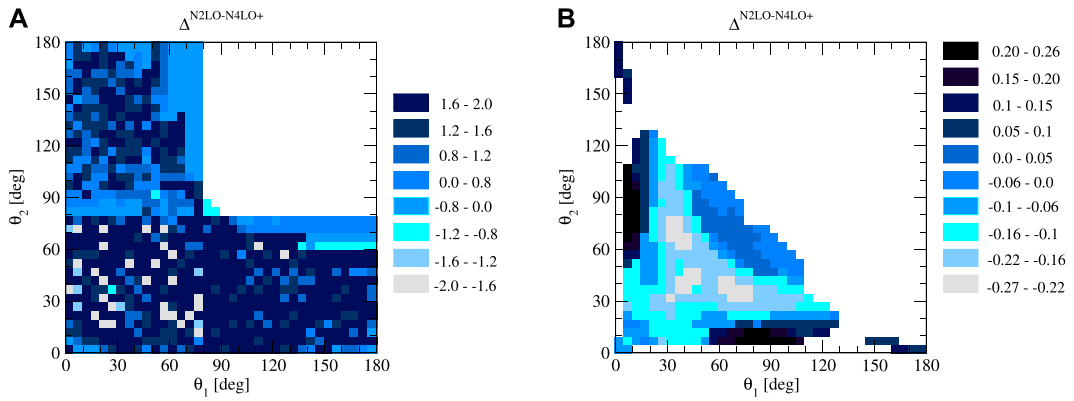

FIGURE 4
$\Delta^{N2LO-N4LO+}$ in the incoming nucleon lab. Kinetic energy E_{lab} = 200 MeV. **(A)** shows predictions based on all the configurations studied, while for **(B)**, additional thresholds for the energies of the detected neutrons and the magnitude of the cross sections have been imposed: $E_1 > 10$ MeV, $E_2 > 10$ MeV, $(\frac{d^5\sigma}{d\Omega_1 d\Omega_2 dS})^{N2LO} > 0.01$ [mb sr^{-2} MeV^{-1}], and $(\frac{d^5\sigma}{d\Omega_1 d\Omega_2 dS})^{N4LO+} > 0.01$ [mb sr^{-2} MeV^{-1}].

$$\delta^{N2LO-N4LO+}(\theta_1,\theta_2,\phi_2,S) \equiv \frac{\left(\frac{d^5\sigma}{d\Omega_1 d\Omega_2 dS}\right)^{N2LO} - \left(\frac{d^5\sigma}{d\Omega_1 d\Omega_2 dS}\right)^{N4LO+}}{\frac{1}{2}\left(\left(\frac{d^5\sigma}{d\Omega_1 d\Omega_2 dS}\right)^{N2LO} + \left(\frac{d^5\sigma}{d\Omega_1 d\Omega_2 dS}\right)^{N4LO+}\right)} \quad (8)$$

and where $(\frac{d^5\sigma}{d\Omega_1 d\Omega_2 dS})^{N2LO}$ ($(\frac{d^5\sigma}{d\Omega_1 d\Omega_2 dS})^{N4LO+}$) are the differential cross sections obtained with the NN force at N^{2}LO (N^{4}LO$^+$) supplemented in both cases by the 3NF at N^{2}LO. The regulator value $\Lambda = 450$ MeV is used. The free parameters of the 3NF, c_D and

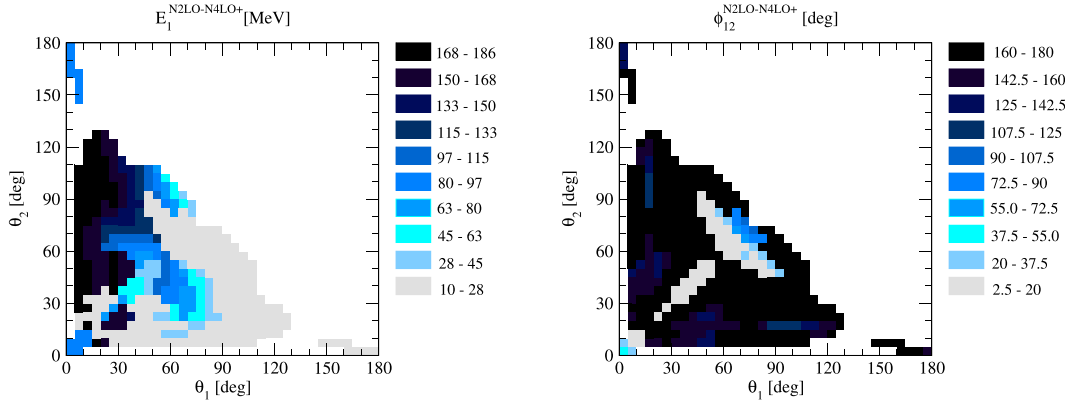

FIGURE 5
Values of nucleon 1 energy E_1 (left) and the azimuthal angle ϕ_2 (right) in the θ_1–θ_2 plane corresponding to the kinematic configurations from the right panel of Figure 4.

c_E, were determined separately when the 3NF was combined with the N^{2}LO or N^{4}LO$^+$ NN force, in such a way that the ^{3}H binding energy [47] and the differential cross section for the neutron-deuteron elastic scattering data [48] are properly described. The definition (8) shows that both $\delta^{N2LO-N4LO+}(\theta_1, \theta_2, \phi_2, E_1)$ and subsequently $\Delta^{N2LO-N4LO+}$ carry partial information about the convergence of the results to the chiral order.

Figure 4A shows that there are big differences between the predictions based on both combinations of two- and three-nucleon forces in the whole available kinematic area when no additional constraints are imposed on the cross sections and nucleon energies. $\Delta^{N2LO-N4LO+}$ varies in the range (−200%, 200%). The picture is not as symmetric as in Figure 1A. This shows that in many cases, the magnitude of $\Delta^{N2LO-N4LO+}$ depends on a very precise position on the S-curve, which is understandable when we deal with small values of the cross sections. In fact, once the additional conditions on the cross sections and energies are applied, the symmetry is restored, as shown in Figure 4B. The values of $\Delta^{N2LO-N4LO+}$ are now substantially smaller and range approximately from −30%, 30%. The inclusion of the higher chiral order contributions in the NN interaction decreases the breakup cross section, which leads to positive $\Delta^{N2LO-N4LO+}$, in configurations where one of the θ_i is small (below 20°) and the second θ_j takes intermediate values in the range $\theta_i \in (60°, 120°)$. In the other parts of the allowed θ_1 and θ_2 space, the negative $\Delta^{N2LO-N4LO+}$ values prevail. Specifically, for one of the θ_i in the range (30°, 60°) and another one in the range (30°, 90°), $\Delta^{N2LO-N4LO+}$ takes the smallest values corresponding to $(\frac{d^5\sigma}{d\Omega_1 d\Omega_2 dS})^{N4LO+} > (\frac{d^5\sigma}{d\Omega_1 d\Omega_2 dS})^{N2LO}$.

Figure 5 shows E_1 and ϕ_{12} for configurations maximizing $\Delta^{N2LO-N4LO+}$ for given θ_1 and θ_2. The picture is similar to that of Figure 2—again, the energy of the first nucleon takes the largest possible values, while the energy of the second nucleon remains small. ϕ_{12} is above 150° for most of the configurations; however, there are also configurations, clustered around the diagonal or around a straight line intersecting the diagonal at $\theta_1 = \theta_2 = 60°$ with ϕ_{12} below 20°.

A few examples of $\frac{d^5\sigma}{d\Omega_1 d\Omega_2 dS}$ with large $|\Delta^{N2LO-N4LO+}|$ are shown in Figure 6. In all the cases, a clear difference between N^{2}LO + N^{2}LO and N^{4}LO$^+$+N^{2}LO predictions is observed in one of the maxima of the cross section; however, for the configuration shown in the central panel, the largest (negative) $\delta^{N2LO-N4LO+}(\theta_1, \theta_2, \phi_2, S)$ occurs at the slope of the cross section around S = 160 MeV. A relatively large spread of cross sections and the angles defining this configuration make it, in our opinion, an encouraging case for experimental efforts. In the future, it would be interesting to investigate the origin of the enhanced sensitivity of these configurations to the details of the nuclear Hamiltonian and to study the effects of the isospin-breaking corrections to the NN force considered in ref. [17].

3.3 E = 200 MeV: 3NF effects

Finally, for the predictions at Λ = 450 MeV, we define accordingly

$$\delta^{3NF}(\theta_1, \theta_2, \phi_2, S) \equiv \frac{\left(\frac{d^5\sigma}{d\Omega_1 d\Omega_2 dS}\right)^{NN} - \left(\frac{d^5\sigma}{d\Omega_1 d\Omega_2 dS}\right)^{NN+3NF}}{\frac{1}{2}\left(\left(\frac{d^5\sigma}{d\Omega_1 d\Omega_2 dS}\right)^{NN} + \left(\frac{d^5\sigma}{d\Omega_1 d\Omega_2 dS}\right)^{NN+3NF}\right)} \quad (9)$$

and

$$\Delta^{3NF} \equiv \Delta^{3NF}(\theta_1, \theta_2) \equiv \max_{\{\phi_2, S\}} \delta^{3NF}(\theta_1, \theta_2, \phi_2, S). \quad (10)$$

In Eq. 9, the two cross sections are obtained at Λ = 450 MeV, with the N^{4}LO$^+$ NN force alone or combined with the N^{2}LO 3NF.

Our results for Δ^{3NF} are shown in Figures 7, 8. The Δ^{3NF} values are in the range (−0.378, 0.386) without constraints on the cross sections and energies and in the range (−0.270, 0.386) when these restrictions are taken into account. Initially, in most of the $\theta_1 - \theta_2$ regions, Δ^{3NF} is negative or close to zero. For almost half of the $\theta_1 - \theta_2$ combinations, we observe the importance of the 3NF as Δ^{3NF} is in the range (−0.378, − 0.150). Only for both polar angles below ≈ 25° Δ^{3NF} becomes positive. If configurations with small cross sections and energies are neglected, we find in the most typical case $-0.14 < \Delta^{3NF} < -0.07$. The largest positive Δ^{3NF} value occurs either when both polar angles are small or when one of them is small and the other one is very large. The distribution of nucleon energies in

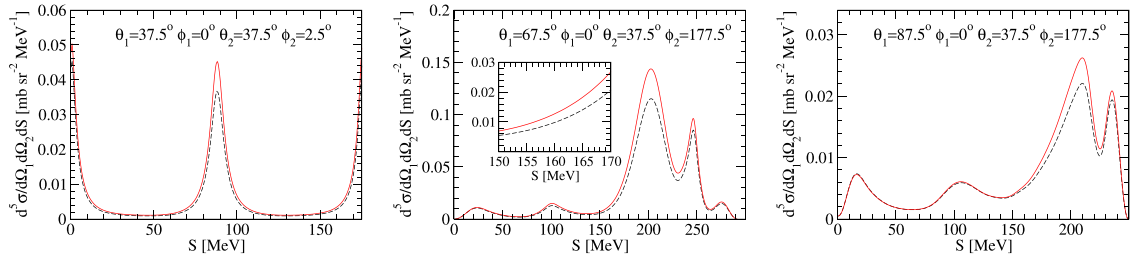

FIGURE 6
Differential cross sections at three selected kinematic configurations with maximal $\Delta^{N2LO-N4LO+}$ values. The dashed black (solid red) curve represents predictions based on the N^{2}LO (N^{4}LO$^+$) NN force supplemented in both cases by the N^{2}LO 3NF. Λ = 450 MeV was used.

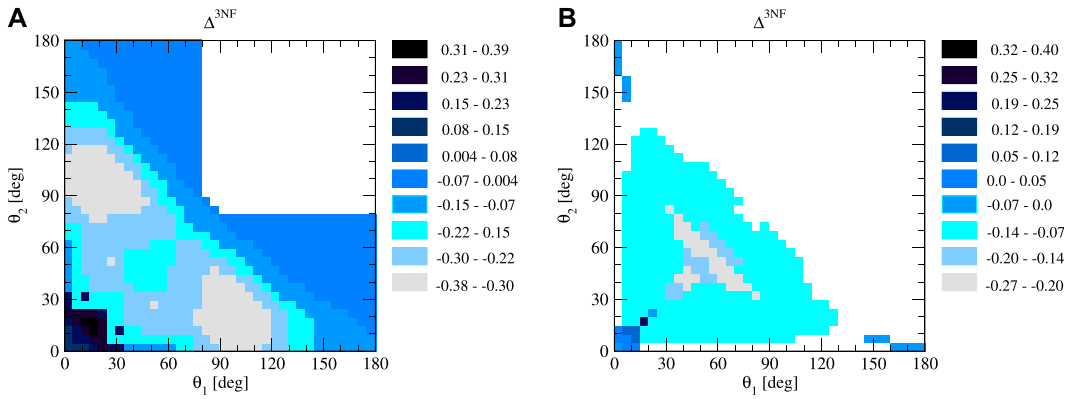

FIGURE 7
Δ^{3NF} in the incoming nucleon lab. Kinetic energy E_{lab} = 200 MeV. **(A)** shows predictions based on all the configurations studied, while for **(B)**, additional thresholds for the energies of the detected neutrons and the magnitude of the cross sections have been imposed: $E_1 > 10$ MeV, $E_2 > 10$ MeV, $(\frac{d^5\sigma}{d\Omega_1 d\Omega_2 dS})^{400} > 0.01$ [mb sr^{-2} MeV^{-1}], and $(\frac{d^5\sigma}{d\Omega_1 d\Omega_2 dS})^{550} > 0.01$ [mb sr^{-2} MeV^{-1}].

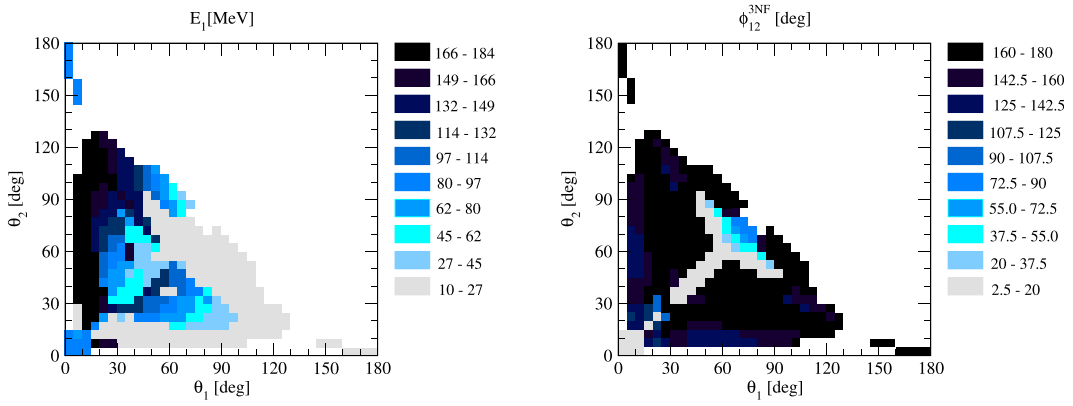

FIGURE 8
Values of nucleon 1 energy E_1 (left) and the azimuthal angle ϕ_2 (right) in the θ_1–θ_2 plane corresponding to the kinematic configurations from the right panel of Figure 7.

the configurations contributing to Figure 7B reveals that the largest $|\Delta^{3NF}|$ is observed when one of the observed nucleons absorbs nearly all of the kinetic energy, while the energy of the remaining observed nucleon becomes close to the imposed threshold of 10 MeV. For most of the configurations, ϕ_{12} is large, and only for configurations close to this diagonal $\theta_1 = \theta_2$ or close to the line

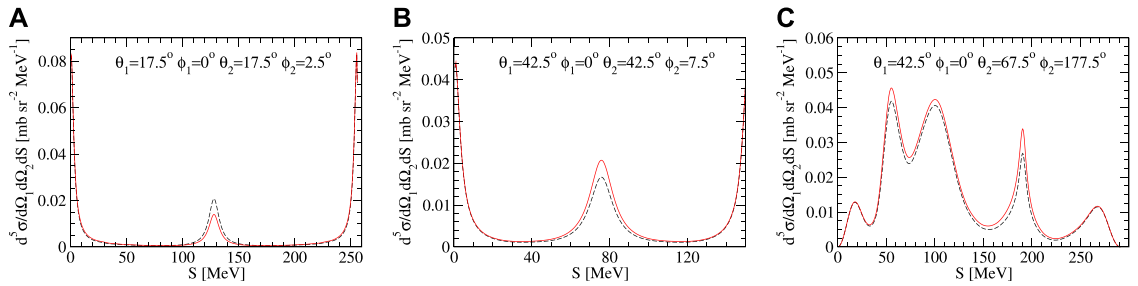

FIGURE 9
Differential cross sections maximizing Δ^{3NF} at three selected kinematic configurations defined by **(A)** $\theta_1 = 17.5^\circ$, $\theta_2 = 17.5^\circ$, $\phi_{12} = 2.5^\circ$, **(B)** $\theta_1 = 42.5^\circ$, $\theta_2 = 42.5^\circ$, $\phi_{12} = 7.5^\circ$, and **(C)** $\theta_1 = 42.5^\circ$, $\theta_2 = 67.5^\circ$, $\phi_{12} = 177.5^\circ$. The dashed black curve represents predictions based on the N^{4}LO$^+$ NN force only. The red solid curve stands for predictions based on the N^{4}LO$^+$ NN force supplemented by the N^{2}LO 3NF. Λ = 450 MeV was used.

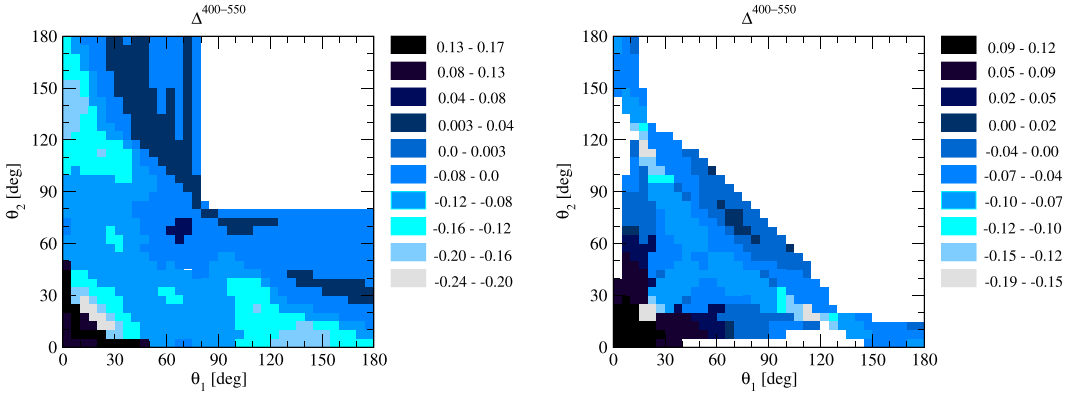

FIGURE 10
$\Delta^{400-550}$ in the incoming nucleon lab. Kinetic energy E_{lab} = 135 MeV. The left panel shows predictions based on all the configurations studied, while for the right panel, additional thresholds for the energies of the detected neutrons and the magnitude of the cross sections have been imposed: $E_1 >$ 10 MeV, $E_2 >$ 10 MeV, $(\frac{d^5\sigma}{d\Omega_1 d\Omega_2 dS})^{400} > 0.01$ [mb sr^{-2} MeV^{-1}], and $(\frac{d^5\sigma}{d\Omega_1 d\Omega_2 dS})^{550} > 0.01$ [mb sr^{-2} MeV^{-1}].

perpendicular to that diagonal at $\theta_1 = 60^\circ$small relative azimuthal angles are preferred.

Figure 9 shows the differential cross section at three configurations selected from those that maximize Δ^{3NF}. Figure 9A shows a case where 3NF lowers the cross section by about 39% at S = 128 MeV. In the two remaining configurations, 3NF increases the cross section by 22% at S = 71 MeV (Figure 9B) and by 23% at S = 187.5 MeV (Figure 9C).

This concludes our discussion of the cross section at E = 200 MeV, and in the remaining part of Section 3, we present similar maps as above, but for the deuteron breakup reaction induced by nucleons with a lower kinetic energy of E = 135 MeV.

3.4 E = 135 MeV: Cutoff dependence

Figure 10 shows $\Delta^{400-550}$, both before and after implementing the cutoff conditions on the energies E_1 and E_2 and the exclusive cross sections, obtained with Λ = 400 MeV or Λ = 550 MeV. As in the case of E = 200 MeV, the N^{4}LO$^+$ NN interaction is used, complemented by the N^{2}LO 3NF. We also maintain the same thresholds for energies and the same cross sections as were used at E = 200 MeV.

Initially, $\Delta^{400-550}$ varies between −24%, 17% but most often remains in the (−12%, 4%) intervals. The interesting configurations with $\Delta^{400-550} < -20\%$ are typically those with one of the θ_i below at approximately 30° and another θ_i in the (45°, 100°) range. The maximal positive $\Delta^{400-550}$ occurs only in the part of the $\theta_1 - \theta_2$ plane where both θ_i are small. After reducing the number of allowed configurations by applying the threshold conditions, $\Delta^{400-550}$ is found in the (−19%, 12%) range. Maximal values, around $\Delta^{400-550}$ = 10%, survive at both θ_i small. On the contrary, regions with large negative $\Delta^{400-550}$ are significantly shrunk. In most of the phase space, $\Delta^{400-550}$ belongs to (−10%, 0%). Comparing the resulting picture and numbers with those at E = 200 MeV, there is a significant increase in the magnitude of $\Delta^{400-550}$ when moving to higher energies, on average by a factor of two. This is, of course, perfectly in line with the expectations based on the fact that the truncation uncertainty of the chiral EFT grows with energy.

The pattern of E_1 for configurations leading to maximal $\Delta^{400-550}$ at E = 135 MeV is similar to that at E = 200 MeV, as shown in Figure 11. Of course, the lower reaction energy results in

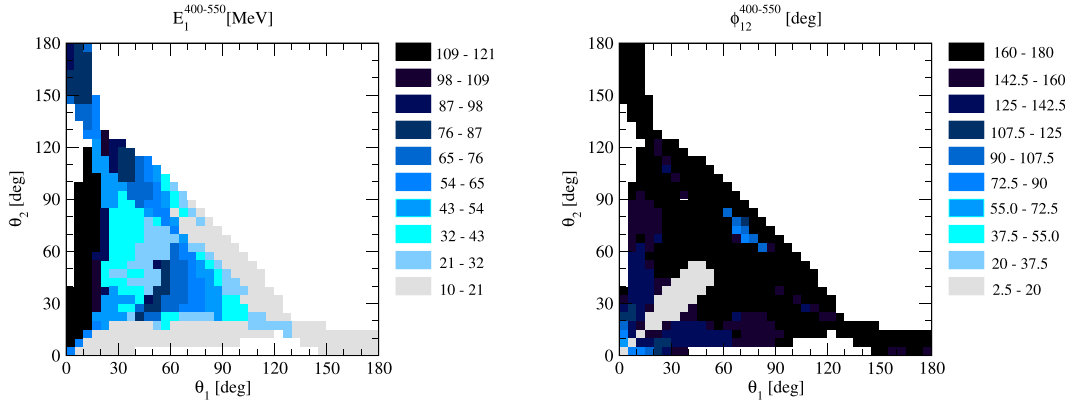

FIGURE 11
Values of the nucleon 1 energy E_1 (left) and the azimuthal angle ϕ_2 (right) in the θ_1–θ_2 plane corresponding to the kinematic configurations from the right panel of Figure 10.

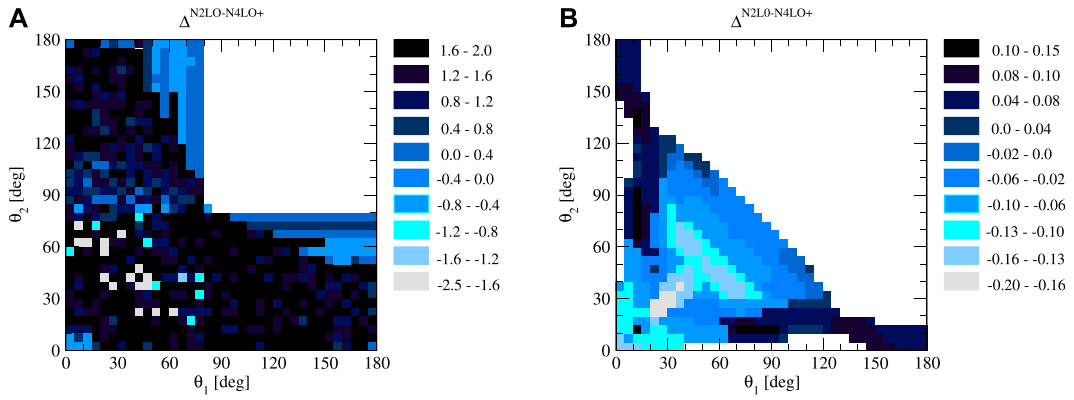

FIGURE 12
$\Delta^{N2LO-N4LO+}$ in the incoming nucleon lab. Kinetic energy E_{lab} = 135 MeV. **(A)** shows predictions based on all studied configurations, while for **(B)**, additional thresholds for the energies of the detected neutrons and the magnitude of the cross sections have been imposed: $E_1 > 10$ MeV, $E_2 > 10$ MeV, $(\frac{d^5\sigma}{d\Omega_1 d\Omega_2 dS})^{400} > 0.01$ [mb sr^{-2} MeV^{-1}], and $(\frac{d^5\sigma}{d\Omega_1 d\Omega_2 dS})^{550} > 0.01$ [mb sr^{-2} MeV^{-1}].

lower final state nucleon energies, but again, in some $\theta_1 - \theta_2$ regions, we obtain combinations of small E_1 and medium or large E_2 values, or *vice versa*, or both energies are about half of the maximal available energy. The pattern for ϕ_{12} is even more similar to that for E = 200 MeV—large relative angles dominate the picture, and only for $\theta_1 \approx \theta_2 \lessapprox 60^\circ$ ϕ_{12} is small. These similarities and the similar patterns shown in Figures 4B, 12B suggest that the considered observables at these two energies may exhibit sizeable correlations.

3.5 E = 135 MeV: Changes with the chiral order

Next, Figures 12, 13 show the analysis of $\Delta^{N2LO-N4LO+}$ and the corresponding kinematic configurations maximizing it. Similar to the case of E = 200 MeV, $\Delta^{N2LO-N4LO+}$ is huge: $\Delta^{N2LO-N4LO+} \in (-2.5, 2)$ for E = 135 MeV if no additional conditions are imposed on the energies and the cross sections. For most of $\theta_1 - \theta_2$ pairs, we find configurations where $\Delta^{N2LO-N4LO+}$ takes values above 80%. Imposing the threshold conditions used here, which limits the possible number of configurations, leads to a much smaller $\Delta^{N2LO-N4LO+}$ between −20% and +15%. For a significant part of the phase space, the N^{4}LO$^+$ NN force increases the cross sections, which results in negative $\Delta^{N2LO-N4LO+}$. Similar to the results at E = 200 MeV, the highest values of $\Delta^{N2LO-N4LO+}$ appear at one of the small azimuthal angles, below approximately 20°, and another one in the range of (70°, 180°). Configurations with the largest negative $\Delta^{N2LO-N4LO+}$ have at E = 135 MeV a slightly different distribution than observed in Figure 4B—in addition to the previously observed patterns, now also configurations with $\theta_1 = \theta_2 \in (20^\circ, 30^\circ)$ contribute. The full range for $\Delta^{N2LO-N4LO+}$ at E = 135 MeV is slightly narrower than that at E = 200 MeV.

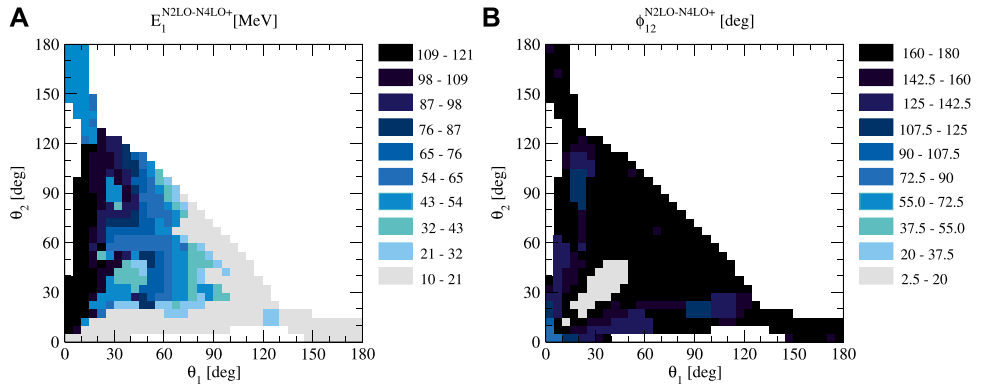

FIGURE 13
Values of nucleon 1 energy E_1 **(A)** and the azimuthal angle ϕ_2 **(B)** in the θ_1–θ_2 plane corresponding to the kinematic configurations from the right panel of Figure 12.

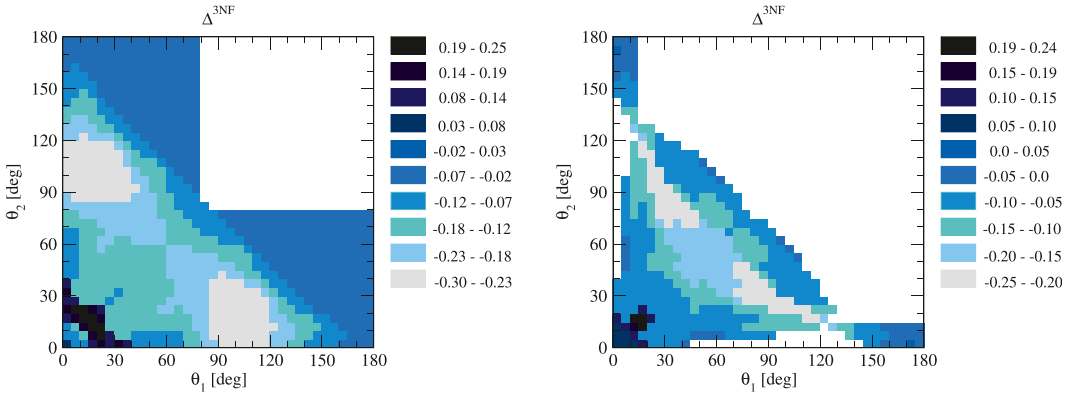

FIGURE 14
Δ^{3NF} at the incoming nucleon lab. Kinetic energy E_{lab} = 135 MeV. The left panel shows predictions based on all the configurations studied, while for the right panel, additional thresholds for the energies of the detected neutrons and the magnitude of the cross sections have been imposed: $E_1 > 10$ MeV, $E_2 > 10$ MeV, $(\frac{d^5\sigma}{d\Omega_1 d\Omega_2 dS})^{400} > 0.01$ [mb sr^{-2} MeV^{-1}], and $(\frac{d^5\sigma}{d\Omega_1 d\Omega_2 dS})^{550} > 0.01$ [mb sr^{-2} MeV^{-1}].

The distribution of nucleon energies at E = 135 MeV is again reminiscent of that observed at E = 200 MeV, taking into account a different absolute energy scale. More deviations are observed for ϕ_{12}, as shown in Figure 13B. At E = 135 MeV, the smallest ϕ_{12} survives only in one of the two large regions observed for higher energies in Figure 5. Also, for the smallest θ_1 and θ_2 medium values of ϕ_{12} are now preferred instead of small ϕ_{12}.

3.6 E = 135 MeV: 3NF effects

The effects of the 3N interaction at E = 135 MeV are shown in Figure 14. With no additional constraints on energies and cross sections, we find $|\Delta^{3NF}|$ up to 30%. Actions of the 3NF are possible in both directions —there are configurations where the three-body potential decreases the cross section (positive Δ^{3NF}) or where the cross section is increased (negative Δ^{3NF}). The first configurations are those with θ_1 and θ_2 below ≈ 30° but above 5°. In the other dominant part of the $\theta_1 - \theta_2$ plane, Δ^{3NF} is negative and in many cases remains below −10%. This does not change much when only cross sections above 0.01 [mb sr^{-2} MeV^{-1}] and energies above 10 MeV are considered. Nearly, for all the allowed configurations contributing to Figure 14 $\Delta^{3NF} < -5\%$. The largest 3NF effects are clustered around the line parallel to the diagonal in $\theta_1 = \theta_2 \approx 60°$. Δ^{3NF} above +10% requires both θ_i small. Comparing the results in Figure 14 with those in Figure 7, we observe that the maximal 3NF effects change slightly between E = 135 MeV and E = 200 MeV but are on average larger at higher energies.

The pattern of nucleon energies at which Δ^{3NF} is minimized shows that two detected nucleons have intermediate energies in the approximate range of 30 – 70 MeV, as shown in Figure 15. The large ϕ_{12} dominates almost all the configurations examined. The only exceptions are some of the configurations on the diagonal $\theta_1 = \theta_2$ including those yielding the largest positive Δ^{3NF}. The medium nucleon's energies and large relative azimuthal angles again provide good opportunities for measurements.

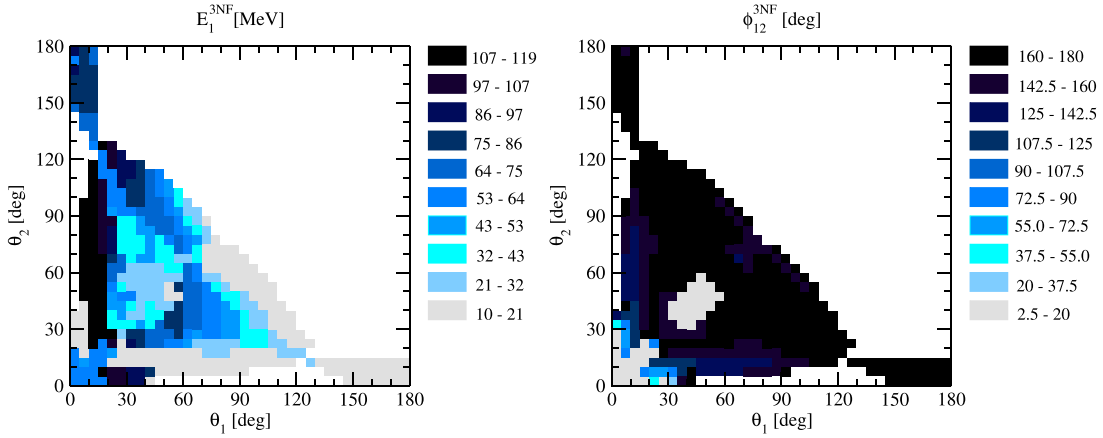

FIGURE 15
Values of nucleon 1 energy E_1 (left) and the azimuthal angle ϕ_2 (right) in the θ_1–θ_2 plane corresponding to the kinematic configurations from the right panel of Figure 14.

4 Conclusions

Recent progress in the derivation of nuclear forces from the chiral effective field theory has reduced substantially uncertainties in model predictions. The inclusion of higher-order terms of the chiral expansion in the NN interaction significantly improves the description of the NN data and extends the energy range in which chiral forces can be reliably applied. However, some questions remain. In this article, we address the problem of the regulator's dependence on nucleon-deuteron predictions. More precisely, we use the SMS interaction [12] up to N^{4}LO$^+$ and supplement it with the N^{2}LO three-nucleon interaction [34], which is fully consistent with the SMS NN force up to this order. Within this interaction model, we study the exclusive cross section for the nucleon-deuteron breakup process at two energies of the incoming nucleon: E = 135 MeV and E = 200 MeV. We do not restrict ourselves to selected final kinematic configurations, but perform a systematic search over the whole kinematically allowed phase space, defining dense grids of momenta directions and energies of two outgoing nucleons. This yields a total of 36^3 = 46656 combinations of (θ_1, θ_2, and ϕ_{12}), and for each of them, we have on average approximately 100 grid points on the S-curve; thus, the total number of studied configurations amounts to five million. Having such a rich set of predictions, we present them in the form of maps in $\theta_1 - \theta_2$ planes, identifying the configurations for which there are the largest differences between cross sections based on different cutoff values. Keeping in mind that such maps can serve as a guide for experimental studies, we impose additional conditions on the magnitudes of the cross sections and energies of the detected nucleons. We find that at E = 200(135) MeV, the cutoff dependence can spread the resulting predictions significantly. The most significant effects appear for configurations that appear to be relatively easily accessible experimentally. The maps included in the article allow one to unambiguously read out all the details of such configurations. The observed cutoff variations should be tamed by adding 3NFs of order N^{4}LO. It is well known that additional 3N contact interactions appear in this order [25, 26]. The configurations with the largest cutoff dependence will be good candidates to determine the corresponding low energy constants.

A similar approach allowed us to investigate the sensitivity of the cross sections to upgrading the two-body interaction from N^{2}LO to N^{4}LO$^+$. We observed that the inclusion of higher-order terms in the NN interaction is necessary at the relatively high energies studied here, as it changes the cross section by up to approximately 20% (27%) at E = 135(200) MeV. Finally, we observed that the inclusion of the three-nucleon interaction leads to effects of up to 27% at both energies studied.

The present work focuses on the configurations that show the highest sensitivity to different features of the nuclear Hamiltonian. The differences between the predictions we have found exceed typical experimental uncertainties achievable today. Thus, measurements of the cross section in the configurations discussed here may help to further constrain the chiral nuclear forces. It would also be interesting to confront the observed residual dependence of the breakup observables on the cutoff values and the EFT expansion order with the estimated truncation errors.

Data availability statement

The raw data supporting the conclusion of this article will be made available by the authors, without undue reservation.

Author contributions

RS—conceptualization of the work, coding, performing computations, analyzing results, preparing figures, and writing the manuscript; JG—writing code, analyzing results, and writing the manuscript; HW—writing code, analyzing results, and writing the manuscript; VC—writing code, performing computations, analyzing results, and preparing figures; EE—writing code, analyzing results, and writing the manuscript; AN—writing code, computing 3NF matrix elements, analyzing results, and writing the manuscript; VS—writing code, performing computations, and preparing figures.

Funding

This work was supported in part by the BMBF (grant no. 05P21PCFP4), by the DFG, and the NSFC through funds provided to the Sino-German CRC 110 "Symmetries and the Emergence of Structure in QCD" (NSFC grant no. 12070131001, project-ID 196253076—TRR 110), and by the ERC Nuclear Theory (grant no. 885150), by the MKW NRW under funding code NW21-024-A, and by the EU Horizon 2020 research and innovation program (STRONG-2020, GA 824093).

Acknowledgments

The numerical calculations were performed on the JURECA and the JURECA Booster at the Jülich Supercomputing Center in Jülich, Germany. We are grateful to the members of the LENPIC collaboration for sharing their insights into the considered topics.

Conflict of interest

The authors declare that the research was conducted in the absence of any commercial or financial relationships that could be construed as a potential conflict of interest.

Publisher's note

All claims expressed in this article are solely those of the authors and do not necessarily represent those of their affiliated organizations, or those of the publisher, the editors, and the reviewers. Any product that may be evaluated in this article, or claim that may be made by its manufacturer, is not guaranteed or endorsed by the publisher.

References

1. Yukawa H. On the interaction of elementary particles. i. *Proc Physico-Mathematical Soc Jpn* (1935) 17:48. 3rd Series. doi:10.11429/ppmsj1919.17.0_48

2. Weinberg S. Nuclear forces from chiral Lagrangians. *Phys Lett B* (1990) 251:288–92. doi:10.1016/0370-2693(90)90938-3

3. Weinberg S. Effective chiral Lagrangians for nucleon-pion interactions and nuclear forces. *Nucl Phys B* (1991) 363:3–18. doi:10.1016/0550-3213(91)90231-L

4. Ordóñez C, Ray L, van Kolck U. Two-nucleon potential from chiral Lagrangians. *Phys Rev C* (1996) 53:2086–105. doi:10.1103/PhysRevC.53.2086

5. Entem DR, Machleidt R. Accurate charge dependent nucleon potential at fourth order of chiral perturbation theory. *Phys Rev C* (2003) 68:041001. doi:10.1103/PhysRevC.68.041001

6. Epelbaoum E, Glöckle W, Meißner U-G. Nuclear forces from chiral Lagrangians using the method of unitary transformation (i): Formalism. *Nucl Phys A* (1998) 637:107–34. doi:10.1016/S0375-9474(98)00220-6

7. Epelbaum E, Glöckle W, Meißner U-G. Nuclear forces from chiral Lagrangians using the method of unitary transformation ii: The two-nucleon system. *Nucl Phys A* (2000) 671:295–331. doi:10.1016/S0375-9474(99)00821-0

8. Epelbaum E, Glöckle W, Meißner U-G. The two-nucleon system at next-to-next-to-next-to-leading order. *Nucl Phys A* (2005) 747:362–424. doi:10.1016/j.nuclphysa.2004.09.107

9. Wiringa RB, Stoks VGJ, Schiavilla R. Accurate nucleon-nucleon potential with charge-independence breaking. *Phys Rev C* (1995) 51:38–51. doi:10.1103/PhysRevC.51.38

10. Machleidt R. High-precision, charge-dependent bonn nucleon-nucleon potential. *Phys Rev C* (2001) 63:024001. doi:10.1103/PhysRevC.63.024001

11. Ekström A, Baardsen G, Forssén C, Hagen G, Hjorth-Jensen M, Jansen GR, et al. Optimized chiral nucleon-nucleon interaction at next-to-next-to-leading order. *Phys Rev Lett* (2013) 110:192502. doi:10.1103/PhysRevLett.110.192502

12. Reinert P, Krebs H, Epelbaum E, Krebs H. Semilocal momentum-space regularized chiral two-nucleon potentials up to fifth order. *Eur Phys J A* (2018) 54:86. doi:10.1140/epja/i2018-12516-4

13. Piarulli M, Girlanda L, Schiavilla R, Kievsky A, Lovato A, Marcucci LE, et al. Local chiral potentials with Δ-intermediate states and the structure of light nuclei. *Phys Rev C* (2016) 94:054007. doi:10.1103/PhysRevC.94.054007

14. Entem DR, Machleidt R, Nosyk Y. High-quality two-nucleon potentials up to fifth order of the chiral expansion. *Phys Rev C* (2017) 96:024004. doi:10.1103/PhysRevC.96.024004

15. Epelbaum E, Krebs H, Meißner U-G. Precision nucleon-nucleon potential at fifth order in the chiral expansion. *Phys Rev Lett* (2015) 115:122301. doi:10.1103/PhysRevLett.115.122301

16. Hoferichter M, Ruiz de Elvira J, Kubis B, Meißner U-G. Matching pion-nucleon roy-steiner equations to chiral perturbation theory. *Phys Rev Lett* (2015) 115:192301. doi:10.1103/PhysRevLett.115.192301

17. Reinert P, Krebs H, Epelbaum E. Precision determination of pion-nucleon coupling constants using effective field theory. *Phys Rev Lett* (2021) 126:092501. doi:10.1103/PhysRevLett.126.092501

18. van Kolck U. Few-nucleon forces from chiral Lagrangians. *Phys Rev C* (1994) 49:2932–41. doi:10.1103/PhysRevC.49.2932

19. Epelbaum E, Nogga A, Glöckle W, Kamada H, Meißner U-G, Witała H. Three-nucleon forces from chiral effective field theory. *Phys Rev C* (2002) 66:064001. doi:10.1103/PhysRevC.66.064001

20. Bernard V, Epelbaum E, Krebs H, Meißner U-G. Subleading contributions to the chiral three-nucleon force: Long-range terms. *Phys Rev C* (2008) 77:064004. doi:10.1103/PhysRevC.77.064004

21. Bernard V, Epelbaum E, Krebs H, Meißner U-G. Subleading contributions to the chiral three-nucleon force. ii. short-range terms and relativistic corrections. *Phys Rev C* (2011) 84:054001. doi:10.1103/PhysRevC.84.054001

22. Ishikawa S, Robilotta MR. Two-pion exchange three-nucleon potential: O(q**4) chiral expansion. *Phys Rev C* (2007) 76:014006. doi:10.1103/PhysRevC.76.014006

23. Skibiński R, Golak J, Topolnicki K, Witała H, Epelbaum E, Glöckle W, et al. Triton with long-range chiral n^3lo three-nucleon forces. *Phys Rev C* (2011) 84:054005. doi:10.1103/PhysRevC.84.054005

24. Hebeler K, Krebs H, Epelbaum E, Golak J, Skibiński R. Efficient calculation of chiral three-nucleon forces up to n^3LO for *ab initio* studies. *Phys Rev C* (2015) 91:044001. doi:10.1103/PhysRevC.91.044001

25. Girlanda L, Kievsky A, Viviani M. Subleading contributions to the three-nucleon contact interaction. *Phys Rev C* (2011) 84:014001. doi:10.1103/PhysRevC.84.014001

26. Girlanda L, Kievsky A, Viviani M. Erratum: Subleading contributions to the three-nucleon contact interaction. *Phys Rev C* (2020) 102:019903. doi:10.1103/PhysRevC.102.019903

27. Krebs H, Gasparyan A, Epelbaum E. Chiral three-nucleon force at n^4lo: Longest-range contributions. *Phys Rev C* (2012) 85:054006. doi:10.1103/PhysRevC.85.054006

28. Krebs H, Gasparyan A, Epelbaum E. Chiral three-nucleon force at n^4lo. ii. intermediate-range contributions. *Phys Rev C* (2013) 87:054007. doi:10.1103/PhysRevC.87.054007

29. Epelbaum E, Krebs H, Reinert P. High-precision nuclear forces from chiral EFT: State-of-the-art, challenges and outlook. *Front Phys* (2020) 8:98. doi:10.3389/fphy.2020.00098

30. Epelbaum E, Krebs H, Reinert P. Semi-local nuclear forces from chiral eft: State-of-the-art & challenges. In: Tanihata I, Toki H, Kajino T, editors. *Handbook of nuclear Physics*. Singapore: Springer (2022). p. 0000.

31. Girlanda L, Kievsky A, Viviani M, Marcucci LE. Short-range three-nucleon interaction from $a = 3$ data and its hierarchical structure. *Phys Rev C* (2019) 99:054003. doi:10.1103/PhysRevC.99.054003

32. Epelbaum E, Golak J, Hebeler K, Kamada H, Krebs H, Meißner U-G, et al. Towards high-order calculations of three-nucleon scattering in chiral effective field theory. *Eur Phys J A* (2020) 56:92. doi:10.1140/epja/s10050-020-00102-2

33. Witała H, Golak J, Skibiński R. Significance of chiral three-nucleon force contact terms for understanding of elastic nucleon-deuteron scattering. *Phys Rev C* (2022) 105:054004. doi:10.1103/PhysRevC.105.054004

34. Maris P, Epelbaum E, Furnstahl RJ, Golak J, Hebeler K, Hüther T, et al. Light nuclei with semilocal momentum-space regularized chiral interactions up to third order. *Phys Rev C* (2021) 103:054001. doi:10.1103/PhysRevC.103.054001

35. Epelbaum E, Hammer H-W, Meissner U-G. Modern theory of nuclear forces. *Rev Mod Phys* (2009) 81:1773–825. doi:10.1103/RevModPhys.81.1773

36. Machleidt R, Entem DR. Chiral effective field theory and nuclear forces. *Phys Rept* (2011) 503:1–75. doi:10.1016/j.physrep.2011.02.001

37. Ekström A, Jansen GR, Wendt KA, Hagen G, Papenbrock T, Carlsson BD, et al. Accurate nuclear radii and binding energies from a chiral interaction. *Phys Rev C* (2015) 91:051301. doi:10.1103/PhysRevC.91.051301

38. Tews I, Davoudi Z, Ekström A, Holt JD, Becker K, Briceño R, et al. Nuclear forces for precision nuclear Physics: A collection of perspectives. *Few Body Syst* (2022) 63:67. doi:10.1007/s00601-022-01749-x

39. Epelbaum E, Krebs H, Meißner U-G. Improved chiral nucleon-nucleon potential up to next-to-next-to-next-to-leading order. *Eur Phys J A* (2015) 51:53. doi:10.1140/epja/i2015-15053-8

40. Furnstahl RJ, Klco N, Phillips DR, Wesolowski S. Quantifying truncation errors in effective field theory. *Phys Rev C* (2015) 92:024005. doi:10.1103/PhysRevC.92.024005

41. Melendez JA, Furnstahl RJ, Phillips DR, Pratola MT, Wesolowski S. Quantifying correlated truncation errors in effective field theory. *Phys Rev C* (2019) 100:044001. doi:10.1103/PhysRevC.100.044001

42. Filin AA, Baru V, Epelbaum E, Krebs H, Möller D, Reinert P. Extraction of the neutron charge radius from a precision calculation of the deuteron structure radius. *Phys Rev Lett* (2020) 124:082501. doi:10.1103/PhysRevLett.124.082501

43. Maris P, Roth R, Epelbaum E, Furnstahl RJ, Golak J, Hebeler K, et al. Nuclear properties with semilocal momentum-space regularized chiral interactions beyond N^2LO. *Phys Rev C* (2022) 106:064002. doi:10.48550/ARXIV.2206.13303

44. Glöckle W. *The quantum mechanical few-body problem*. Berlin Heidelberg New York Tokyo: Springer-Verlag (1983).

45. Glöckle W, Witała H, Hüber D, Kamada H, Golak J. The three-nucleon continuum: Achievements, challenges and applications. *Phys Rep* (1996) 274:107–285. doi:10.1016/0370-1573(95)00085-2

46. Witała H, Glöckle W, Golak J, Nogga A, Kamada H, Skibiński R, et al. Nd elastic scattering as a tool to probe properties of 3*n* forces. *Phys Rev C* (2001) 63:024007. doi:10.1103/PhysRevC.63.024007

47. Wang M, Audi G, Kondev FG, Huang W, Naimi S, Xu X. The AME2016 atomic mass evaluation (II). tables, graphs and references. *Chin Phys C* (2017) 41:030003. doi:10.1088/1674-1137/41/3/030003

48. Sekiguchi K, Sakai H, Witała H, Glöckle W, Golak J, Hatano M, et al. Complete set of precise deuteron analyzing powers at intermediate energies: Comparison with modern nuclear force predictions. *Phys Rev C* (2002) 65:034003. doi:10.1103/PhysRevC.65.034003

Frontiers in Physics

Investigates complex questions in physics to understand the nature of the physical world

Addresses the biggest questions in physics, from macro to micro, and from theoretical to experimental and applied physics.

Discover the latest Research Topics

See more →

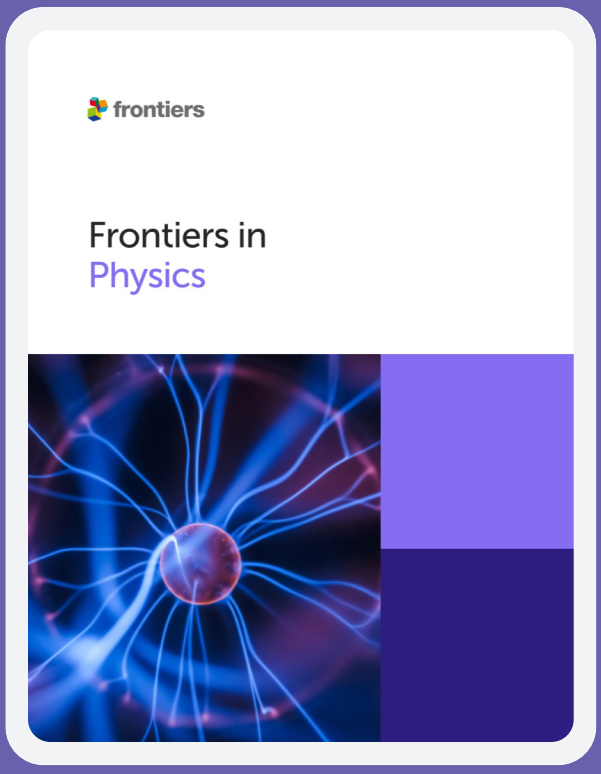

Frontiers

Avenue du Tribunal-Fédéral 34
1005 Lausanne, Switzerland
frontiersin.org

Contact us

+41 (0)21 510 17 00
frontiersin.org/about/contact